

Lecture Notes in Civil Engineering

Nikolai Vatin *Editor*

Proceedings of STCCE 2022

Selected Papers

 Springer

Lecture Notes in Civil Engineering

Volume 291

Series Editors

Marco di Prisco, Politecnico di Milano, Milano, Italy

Sheng-Hong Chen, School of Water Resources and Hydropower Engineering,
Wuhan University, Wuhan, China

Ioannis Vayas, Institute of Steel Structures, National Technical University of
Athens, Athens, Greece

Sanjay Kumar Shukla, School of Engineering, Edith Cowan University, Joondalup,
WA, Australia

Anuj Sharma, Iowa State University, Ames, IA, USA

Nagesh Kumar, Department of Civil Engineering, Indian Institute of Science
Bangalore, Bengaluru, Karnataka, India

Chien Ming Wang, School of Civil Engineering, The University of Queensland,
Brisbane, QLD, Australia

Lecture Notes in Civil Engineering (LNCE) publishes the latest developments in Civil Engineering—quickly, informally and in top quality. Though original research reported in proceedings and post-proceedings represents the core of LNCE, edited volumes of exceptionally high quality and interest may also be considered for publication. Volumes published in LNCE embrace all aspects and subfields of, as well as new challenges in, Civil Engineering. Topics in the series include:

- Construction and Structural Mechanics
- Building Materials
- Concrete, Steel and Timber Structures
- Geotechnical Engineering
- Earthquake Engineering
- Coastal Engineering
- Ocean and Offshore Engineering; Ships and Floating Structures
- Hydraulics, Hydrology and Water Resources Engineering
- Environmental Engineering and Sustainability
- Structural Health and Monitoring
- Surveying and Geographical Information Systems
- Indoor Environments
- Transportation and Traffic
- Risk Analysis
- Safety and Security

To submit a proposal or request further information, please contact the appropriate Springer Editor:

- Pierpaolo Riva at pierpaolo.riva@springer.com (Europe and Americas);
- Swati Meherishi at swati.meherishi@springer.com (Asia - except China, and Australia, New Zealand);
- Wayne Hu at wayne.hu@springer.com (China).

All books in the series now indexed by Scopus and EI Compendex database!

Nikolai Vatin
Editor

Proceedings of STCCE 2022

Selected Papers

 Springer

Editor

Nikolai Vatin
Peter the Great St. Petersburg
Polytechnic University
Saint-Petersburg, Russia

ISSN 2366-2557

ISSN 2366-2565 (electronic)

Lecture Notes in Civil Engineering

ISBN 978-3-031-14622-0

ISBN 978-3-031-14623-7 (eBook)

<https://doi.org/10.1007/978-3-031-14623-7>

© The Editor(s) (if applicable) and The Author(s), under exclusive license
to Springer Nature Switzerland AG 2023

This work is subject to copyright. All rights are solely and exclusively licensed by the Publisher, whether the whole or part of the material is concerned, specifically the rights of translation, reprinting, reuse of illustrations, recitation, broadcasting, reproduction on microfilms or in any other physical way, and transmission or information storage and retrieval, electronic adaptation, computer software, or by similar or dissimilar methodology now known or hereafter developed.

The use of general descriptive names, registered names, trademarks, service marks, etc. in this publication does not imply, even in the absence of a specific statement, that such names are exempt from the relevant protective laws and regulations and therefore free for general use.

The publisher, the authors, and the editors are safe to assume that the advice and information in this book are believed to be true and accurate at the date of publication. Neither the publisher nor the authors or the editors give a warranty, expressed or implied, with respect to the material contained herein or for any errors or omissions that may have been made. The publisher remains neutral with regard to jurisdictional claims in published maps and institutional affiliations.

This Springer imprint is published by the registered company Springer Nature Switzerland AG
The registered company address is: Gewerbestrasse 11, 6330 Cham, Switzerland

Preface

Proceedings contains reports of the Third International Scientific Conference on Socio-Technical Construction and Civil Engineering, STCCE-2022” (April 21–29, 2022, Kazan State University of Architecture and Engineering, Kazan, Russia).

Proceedings includes reports of scientists, representatives of the construction industry and postgraduate students from different technical universities not only from the Russian Federation. The conference aroused great interest among scientists, postgraduate students and specialists from various fields of science.

Representatives from more than 20 countries of the world attended the conference (Australia, Armenia, the Great Britain, Vietnam, Germany, Greece, Egypt, Israel, India, Iraq, Italy, Kazakhstan, Kirgizia, the USA, Taiwan, Uzbekistan, Check Republic, Sweden, South Korea, Japan, etc.).

Such a wide geography of the conference participants is valuable for the exchange of experience and knowledge on the issues of construction, building materials, as well as their application in various fields of construction industry and confirms the relevance of topics of the conference.

Within the framework of the conference, the following main branches were discussed:

- building constructions, buildings and structures
- bridges, roads and tunnels
- building materials and products
- construction technology and organization
- energy efficiency and thermal protection of buildings
- heat supply, ventilation, air conditioning, gas supply and lighting.

The reports of the conference touched upon the issues of research in the field of 3D concrete printing; calculating the roof trusses nodes, made of both from steel and from composite materials; experimental studies in the field of the stress state of a multilayer massif under slab foundations and field tests of pile foundations for cyclic loading; developments in the field of the stress state of hinged thin-walled structures; research in the field of the geometric modeling of coil heat exchanger based on spring-twisted channel; development of effective materials for the construction of structural

elements of the coatings of bridge structures, asphaltene, as the main element of oil dispersion systems, influence on the structure formation of asphaltenes, etc. Thus, the choice of the declared directions of the conference is quite logical and justified, since the topics discussed touch upon the main problems in the construction industry.

All articles included in the collection have been reviewed by highly qualified scientists in the relevant scientific fields. The forty best scientific manuscripts corresponding to the profile of the conference and reflecting the results of theoretical and experimental studies of the authors are recommended for publication.

Annual conference is to be organized on the main topics of the construction industry.

Saint-Petersburg, Russia

Nikolai Vatin

Contents

Assessment of the Endurance of the Normal Sections of Reinforced Concrete Bending Elements by the Method of Maximum Stresses	1
Ilizar Mirsayapov	
Study of Physical and Mechanical Properties of Asphalt Concrete with the Addition of Artificial Asphaltite	15
Anatoly Novik, Aleksei Ismailov, and Igor Sentsov	
Experimental Studies of the Endurance of Reinforced Concrete Beams	31
Ilizar Mirsayapov	
Bearing Capacity of a Glass Facade Systems, Including Stiffness of Nodes and Work of Filling	43
Alexander Galyamichev	
Regularities for Resistance of Supply and Exhaust Ventilation Cross Junctions	65
Arslan Ziganshin, Timur Karimullin, Emil Yagfarov, and Konstantin Logachev	
Load-Bearing Capacity of Raft-Pile Foundations, Taking into Account the Redistribution of Forces Between Piles During Cyclic Loading	73
Ilizar Mirsayapov	
Improvement of Technology and Quality Control of 3DCP	83
Rustem Mukhametrakhimov and Liliya Ziganshina	
Clay Soil Deformations Under Regime Long-Term Triaxial Compression Taking into Account Initial Defects	99
Ilizar Mirsayapov and Niyaz Aysin	

Special Aspects of Stress–Strain Analysis of Combined Piled-Raft Foundation Under Performance Static and Cyclic Loading	109
Mirsayapov Ilizar Talgatovich and Garaev Almaz Ilgamovich	
Physical and Mechanical Characteristics of Modified Soil Cement with Polycarboxylate Superplasticizers	125
Evgenii Vdovin, Pavel Bulanov, Victor Stroganov, and Lenar Mavliev	
Theoretical Foundations of Fatigue Destruction of Steel Reinforcement of Reinforced Concrete Structures	135
Ilizar Mirsayapov	
Unmanned Aerial Vehicle – An Element of Technology for Obtaining Spatial Data	149
Vladimir Bezmenov, Kamil Safin, and Sergey Stepanov	
Performance Characteristics of Styrene-Acrylic Polymer Compositions and Coatings Filled with Dispersive Components	155
Victor Stroganov, Evgenii Vdovin, Maxim Amel’chenko, and Radmilla Tabaeva	
Activation of Fillers for Cement-Mineral Systems	169
Evgenii Vdovin, Victor Stroganov, and Nikita Konovalov	
Adiabatic Efficiency of Monoblock Air Supply Unit with Humidification Module Based on Porous Rotating Atomizers	181
Nazir Sibgatullin and Rinat Safiullin	
Polyvinyl Chloride Compounds for Construction Industry	191
Karina Khuziakhmetova, Lyaylya Abdrakhmanova, Rashit Nizamov, and Anvar Islamov	
Modification of Wood-Polymer Composites with Silica Sols of Different Nature	201
Ayaz Khantimirov, Lyaylya Abdrakhmanova, Vadim Khozin, and Rashit Nizamov	
Solution of the Problem of Modeling Acid Hydraulic Fracturing with a Planned Technological Stop During the Pumping Process Using Standard Software	209
Irik Fattakhov, Alexander Kochetkov, and Julia Kareeva	
Optimization of Technological Solutions for Underground Space Construction of Existing Buildings	219
Leysan Zigangirova, Ilyas Galiev, and Ruslan Ibragimov	
Thermophysical Properties of Aerated Concrete Enclosing Structures	227
Olga Barysheva and Alina Barysheva	

Investigation of Polymer Composite Cage for Reinforcement of Concrete Columns	245
Dmitriy Erohin, Tagir Zinnurov, and Iliya Grishin	
Processing of Thermal Power Waste into Composite Materials Using Coke Waste	255
Galina Medvedeva, Alsu Yusupova, Kamilya Giniyatova, and Kamilla Minikaeva	
Economic Efficiency Substantiation of the Use of a Sectional Coil Exchanger in an Individual Heating Point System	263
Elvira Shagiakhmetova, Anna Romanova, Yakov Zolotonosov, Pavel Martynov, and Ella Biktemirova	
A Study of the Structure and Properties of a Fine Bitumen Emulsion via an Anionactive Emulsifier	273
Aidar Garipov, Dmitry Makarov, Vadim Khozin, and Sergey Stepanov	
The Use of Surface Laser Scanning as a Standard Operating Procedure for Assessing the Quality of Construction and Installation Work	285
Andrey Bogdanov and Sergey Stepanov	
Increasing the Energy Efficiency of Ventilated Facades Using Different Insulators	299
Dmitriy Kraynov, Galina Medvedeva, Renat Sadykov, and Aigul Ibragimova	
Planning Field Development Using Optimization Algorithms	311
Alexander Semanov, Aigul Semanova, Irik Fattakhov, Farit Iangirov, and Juliya Kareeva	
Method of Assessing the Pressure Generated by the Water Packer Saturated Packer	321
Alfred Suleymanov, Rashit Kayumov, Denis Smirnov, Ilya Grishin, and Kamilya Belayeva	
Dry Plaster Mixes Using Local Mineral Components	333
Marat Khaliullin and Alsu Gilmanshina	
Verification and Validation of Numerical Model of Flow in Supply Opening with Elbow Unit	343
Juliya Kareeva, Arslan Ziganshin, and Kseniya Narsova	
Concrete Beams with External Reinforcement of Composite Materials	353
Gleb Ogurtsov, Gleb Averchenko, Sergey Alekseev, Aleksei Ismailov, Anna Zanina, and Irshat Mukharyamov	

Full-Scale Tests of the Bearing Capacity of a Composite I-Beam with a Solid Web of Pultruded Fiberglass Profiles (PFP)	363
Marat Salakhutdinov, Daler Aripov, and Arslan Khanekov	
The Possibility of Vibrodynamic Data from Phone Accelerometers for the Rapid Assessment of the Technical Condition of Buildings and Structures Use	371
Andrey Savinov, Gennadiy Nigmatov, Temir Nigmatov, and Rinat Galliulun	
Experimental and Theoretical Analysis of Crack Resistance and Deformability of Concrete Beams Reinforced with Fiber-Reinforced Polymer Bars	381
Ilshat Mirsayapov, Igor Antakov, and Alexey Antakov	
Complex Modification of Bituminous Binders by Linear Styrene-Butadiene-Styrene Copolymer and Sulfur	405
Pavel Bulanov, Evgenii Vdovin, Victor Stroganov, Lenar Mavliev, and Igor Juravlev	
Fiber-Reinforced Building Composites Based on Mineral Binders	415
Albert Galautdinov and Rustem Mukhametrakhimov	
Structure of 3D-Printed Concrete by X-ray Computed Tomography	425
Rustem Mukhametrakhimov, Liliya Ziganshina, Rail Kadyrov, and Evgeny Statsenko	
Economic Feasibility of Manufacturing of Multi-hollow Floor Slabs from High-Strength Sand Concrete	437
Nikolai Palagin and Marat Akhmetov	
Perspectives of Interactions CAD and GIS Systems	449
Liliia Talipova, Egor Grebenyuk, Gleb Ogurtsov, Aleksei Ismailov, and Yuriy Lazarev	
Corrosion Processes in Building Materials, Products and Structures ...	465
Vladimir Berdnikov, Victor Stroganov, Evgenii Vdovin, Ilya Stroganov, and Viktor Gasilov	
Author Index	483

Assessment of the Endurance of the Normal Sections of Reinforced Concrete Bending Elements by the Method of Maximum Stresses



Ilizar Mirsayapov 

Abstract The aim of the work is theoretical study of the fatigue strength of the normal sections of the reinforced concrete bending elements in stationary and non-stationary modes of cyclic loading, taking into account the continuous change in the state and limits of the endurance of materials. It is currently not enough to develop methods for calculating research results in such formulation.

Theoretical studies of changes in the stress–strain state of normal sections of reinforced concrete bending elements under stationary and non-stationary modes of repetitive cyclic loading have been carried out. It has been established that, regardless of the loading mode, there is a change in stresses and asymmetry coefficients of the stress cycle in concrete of the compressed zone and longitudinal tensile reinforcement. Based on the results of the studies performed, a methodology for evaluating the endurance of the normal sections of reinforced concrete bending elements was developed, as well as analytical equations for describing the change in stresses and asymmetry of the stress cycle in concrete of the compressed zone and in stretched reinforcement.

The significance of the results for the construction industry lies in the fact that the developed technique makes it possible to adequately and accurately evaluate the stress-deformed state and endurance of normal sections, which is a significant contribution to the theory of design of structures under the action of cyclic loads and ensures up to 15% saving of concrete and reinforcement compared existing calculation methods.

Keywords Reinforced concrete bending element · Normal section · Concrete of compressed zone · Maximum stress · Cyclic loading · Asymmetry of the stress cycle · Non-stationary and stationary loading

I. Mirsayapov (✉)

Kazan State University of Architecture and Engineering, Zelenaya Street 1, 420043 Kazan, Russia
e-mail: mirsayapov1@mail.ru

1 Introduction

When designing buildings and structures made of reinforced concrete, during the operation of which cyclic loads occur, the endurance calculation is necessary. However, currently there is no generally accepted methodology for calculating the endurance of reinforced concrete structures taking into account the features of structural behavior under such loads [1–5]. In this regard, numerous experimental studies have been completed. On their basis, various calculation methods are proposed, which differ in the types of diagrams and limit values of stresses in concrete and reinforcement according to endurance requirements. Therefore, on the basis of previously performed studies, firstly it is necessary to establish the provisions of fatigue phenomena in reinforced concrete structures and develop more modern calculation methods taking into account these results [6–10]. Repeated cyclic loading is accompanied by the redistribution of the efforts between concrete of the compressed zone and the longitudinal stretched reinforcement [11], which leads to an increase in the stresses and coefficients of the asymmetry of the stress cycle in the reinforcement and a decrease in stress and coefficients of the asymmetry of the stress cycle in concrete. Therefore, both the stress and asymmetry coefficients of the stress cycle do not coincide with the initial values accepted in the design standards for calculation [12–16]. The design concepts are reduced to the stress value that correspond to the achievement of the limit state as a whole and determining the diagram along which the stresses will be distributed in the compressed zone [17–20]. However, the overall safety factor remains unknown. In connection with the above, the development of a new methodology for calculating the endurance of the normal sections of reinforced concrete bending elements is an urgent and timely task.

The purpose of the study is to develop a methodology for calculating the endurance of the normal sections of reinforced concrete bending elements in stationary and non-stationary cyclic loads. To do this, it is necessary to establish the basic patterns of changes in the efforts in the concrete of the compressed zone and stretched reinforcement in stationary and non-stationary modes of cyclic loading; develop analytical equations of changes in stresses in concrete of compressed zone and longitudinal stretched reinforcement in normal section in stationary and non-stationary modes of cyclic loading; develop analytical equations of changes in the asymmetry of the stress cycle in concrete of the compressed zone and in longitudinal stretched reinforcement in stationary and non-stationary modes of cyclic loading.

2 Materials and Methods

To solve these tasks, theoretical methods of limit equilibrium of reinforced concrete structures were used as well as methods of theory of fatigue strength of concrete, reinforcement and reinforced concrete and methods of the theory of creep and vibrational creep of concrete and reinforced concrete.

3 Results

Stresses and coefficients of the stress cycle in concrete of the compressed zone and stretched reinforcement, taking into account their changes in the process of cyclic loading, can be represented in the following form:

$$\sigma_b^{max}(t, t_0) = \sigma_b^{max}(t_0) \cdot (1 - H_{\sigma_b}), \quad (1)$$

$$\sigma_s^{max}(t, t_0) = \sigma_s^{max}(t_0) \cdot (1 + H_{\sigma_s}), \quad (2)$$

$$\mathcal{P}_{bt} = \frac{\frac{M_{min}}{M_{max}} - H_{\sigma_b}}{1 - H_{\sigma_b}}, \quad (3)$$

$$\mathcal{P}_{st} = \frac{\frac{M_{min}}{M_{max}} + H_{\sigma_s}}{1 + H_{\sigma_s}}, \quad (4)$$

where $\sigma_b^{max}(t_0)$, $\sigma_s^{max}(t_0)$ —The initial stress values in the concrete of the compressed zone and stretched reinforcement, respectively;

M_{min} —The bending moment with a minimum cycle load;

M_{max} —The bending moment at the maximum load of the cycle;

H_{σ_b} and H_{σ_s} —the functions of accumulation of stresses during cyclic loading in concrete of the compressed zone and stretched reinforcement.

Based on the equilibrium conditions, the system of equations for calculating stresses has the form:

$$0,5(1 + \lambda) \cdot \sigma_b^{max}(t) \cdot b \cdot x - \sigma_s^{max}(t) \cdot A_s = 0, \quad (5)$$

$$0,5\sigma_b^{max}(t) \cdot b \cdot x \cdot [(1 + \lambda) \cdot h_0 - 0,33 \cdot x \cdot (1 + \lambda + \lambda^2)] - M_{max} = 0, \quad (6)$$

$$\sigma_s^{max}(t) = \frac{\alpha \cdot \sigma_b^{max}(t)(h_0 - x)}{(1 - \lambda) \cdot x}, \quad (7)$$

$$\lambda = 1 - \frac{\sigma_b(t)}{E_b \cdot \varepsilon_b}. \quad (8)$$

Due to the manifestation of vibrational creep deformations, in coherent conditions, additional stresses occur in concrete of the compressed zone and stretched longitudinal reinforcement (Fig. 1), formulas (9) and (10). In this case, the deformations are calculated by a simplified way.

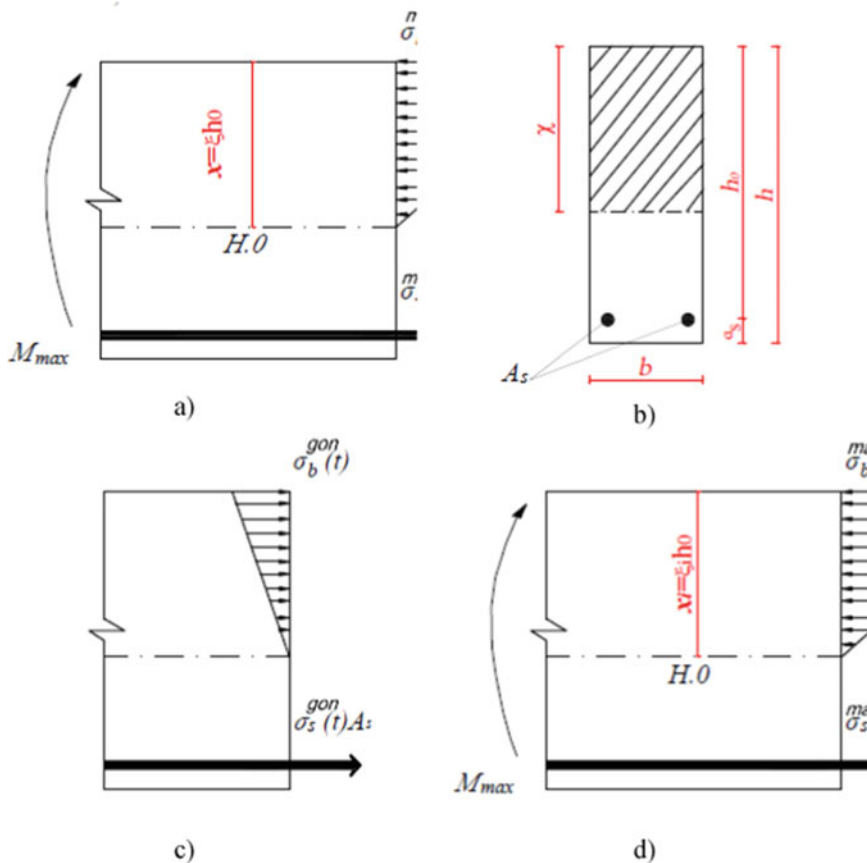


Fig. 1 Diagrams of stresses in the cross section of the reinforced concrete beam when calculating endurance in stationary mode (illustrations of the authors): **a** diagram of the initial stresses; **b** cross section; **c** diagram of additional stresses; **d** current stress diagrams

Then the expressions for calculating additional stresses in the concrete of the compressed zone take the form:

$$\sigma_b^{gon}(t) = \sigma_b^{max}(t, t_0) \left\{ \begin{array}{l} C_\infty(t, \tau) \mathcal{P}_b [1 - e^{-\gamma(t, t_0)}] + \\ + C_\infty(t, \tau) [1 - (1 - a)^N] (1 - \mathcal{P}_b) \\ + 0,566 \frac{l^2(t, t_0)}{E_b} \cdot 10^{-3} \end{array} \right\} \quad (9)$$

$$\cdot \frac{h_0 - x}{x} E_s A_s \left[\frac{1}{A_{red}} - \frac{(k_{red} - a_s)(h - k_{red})}{\mathcal{J}_{red}} \right],$$

where $k_{red} = S_{red} / A_{red}$.

Expressions for calculating additional stresses in the longitudinal stretched reinforcement take the form:

$$\sigma_s^{gon}(t) = \sigma_b^{max}(t, t_0) \left\{ \begin{array}{l} C_\infty(t, \tau) \mathcal{P}_b [1 - e^{-\gamma(t, t_0)}] \\ + C_\infty(t, \tau) [1 - (1 - a)^N] (1 - \mathcal{P}_b) \\ + 0,566 \frac{l^2(t, t_0)}{E_b} \cdot 10^{-3} \end{array} \right\} \cdot \frac{h_0 - x}{x} E_s A_s. \quad (10)$$

Substituting in Eqs. (1) and (2) expressions for $\sigma_b^{gon}(t)$, and $\sigma_s^{gon}(t)$, calculated by formulas (9) and (10), after some transformations we get:

$$\sigma_b^{max}(t, t_0) = \sigma_b^{max}(t_0) \cdot H_{6b} \quad (11)$$

$$\sigma_s^{max}(t, t_0) = \sigma_s^{max}(t_0) \cdot H_{6s} \quad (12)$$

$$\mathcal{P}_{bt} = \frac{\left\{ \mathcal{P}_M + A_s \frac{1-\xi}{\xi} H_\varepsilon \left[\frac{1}{A_{red}} - \frac{(k_{red}-a_s)(h-k_{red})}{\mathcal{J}_{red}} \right] \right\} \sigma_b^{max}(t_0)}{\left\{ 1 + A_s \frac{1-\xi}{\xi} H_\varepsilon \left[\frac{1}{A_{red}} - \frac{(k_{red}-a_s)(h-k_{red})}{\mathcal{J}_{red}} \right] \right\} \sigma_b^{max}(t_0)}, \quad (13)$$

where $\alpha = \frac{E_s}{E_b}$; E_b , E_s —The elasticity modules of concrete and reinforcement, respectively.

After a series of transformations from Eqs. (10) and (13), we determine the initial stresses in compressed fibers of the section:

$$\sigma_b^{max}(t_0) = \frac{2M_{max}}{x[(1 + \lambda) - 0.33\xi(1 + \lambda + \lambda^2)]b \cdot h_0}. \quad (14)$$

In the working reinforcement of the stretched area:

$$\sigma_s^{max}(t_0) = \frac{E_s}{E_b} \sigma_b^{max}(t_0) \cdot \frac{h_0 - x}{V \cdot x}, \quad (15)$$

Where

λ —concrete plasticity, taking into account the increase in the area of the compressed concrete zone;

ξ —relative height of the compressed zone;

x —The height of the compressed zone of normal section;

V —The coefficient of elasticity.

The function of accumulation of deformations in concrete and reinforcement is determined by the formula:

$$H_{\varepsilon s} = 1 + \frac{2(1 - \xi)}{\xi^2} \cdot \frac{\mu}{(1 + \lambda)} \cdot H_{\varepsilon}, \quad (16)$$

In the formula (16) H_{ε} is determined as follows:

$$H_{\varepsilon} = C_{\infty}(t, \tau) \cdot \mathcal{P}_b [1 - e^{-\gamma(t, t_0)}] + C_{\infty}(t, \tau) [1 - (1 - a)^N] (1 - \mathcal{P}_b) + 0,566 \frac{l^2(t, t_0)}{E_b} \cdot 10^{-3}.$$

After a series of transformations of expression (13) and (18), we lead to a form convenient for practical calculations:

$$H_{\varepsilon b} = 1 + \mu \Delta b \cdot b \cdot h \cdot H_{\varepsilon}; \quad (17)$$

$$H_{\varepsilon s} = 1 + \mu \Delta S \cdot H_{\varepsilon}; \quad (18)$$

$$\mathcal{P}_{bt} = \frac{\frac{M_{min}}{M_{max}} + A_s \Delta b \cdot H_{\varepsilon}}{1 + A_s \cdot \Delta b \cdot H_{\varepsilon}}; \quad (19)$$

$$\mathcal{P}_{St} = \frac{\frac{M_{min}}{M_{max}} + \frac{A_s}{bh_0} \Delta S \cdot H_{\varepsilon s}}{1 + \frac{A_s}{bh_0} \cdot \Delta S \cdot H_{\varepsilon s}}; \quad (20)$$

where $\Delta b = \frac{1-\xi}{\xi} \left[\frac{1}{A_{red}} - \frac{(k_{red}-\alpha_s)(h-k_{red})}{\frac{bh_0^3}{12} + \frac{E_s}{E_b} \cdot A_s} \right]$; $\Delta S = \frac{2(h_0-x)h_0}{x^2(1+\lambda)}$; A_s —The cross-sectional area of the longitudinal stretched reinforcement.

The endurance of reinforced concrete structures is evaluated based on the conditions:

$$\sigma_b^{max}(t_0) \leq \frac{1}{k_{\omega} H_{\delta b}} \cdot R_{b,rep} \quad (21)$$

$$\sigma_s^{max}(t_0) \leq \frac{1}{k_{\omega} H_{\delta s}} \cdot R_{s,rep} \quad (22)$$

where $R_{b,rep}$, $R_{s,rep}$ —the endurance limits of concrete and reinforcement are calculated accordingly, depending on the physical values \mathcal{P}_{bt} and \mathcal{P}_{St} ;

at $\mu \leq 0,035$ $k_{\omega} = 1$;

at $\mu \geq 0,035$ $k_{\omega} = 1,4 - 1,5$.

With sequentially increasing and sequentially decreasing modes of block non-stationary loading of the stress in concrete and reinforcement, it is possible to represent in the form:

$$\sigma_b^{max}(t, t_0) = \sigma_b^{max}(t_0) \cdot (1 - H_{\sigma_b}) \pm \Delta\sigma_{bi}(t, \tau), \quad (23)$$

$$\sigma_s^{max}(t, t_0) = \sigma_s^{max}(t_0) \cdot (1 + H_{\sigma_s}) \pm \Delta\sigma_{si}(t, \tau), \quad (24)$$

Where

$\sigma_b^{max}(t, t_0)$ —The initial stress in the concrete of the compressed zone at the maximum load of the cycle at the first block of non-stationary loading;

$\sigma_s^{max}(t, t_0)$ —The initial stress in the stretched reinforcement at the maximum load of the cycle at the first block of non-stationary loading;

$\Delta\sigma_{bi}(t, \tau)$ —increasing initial stresses in concrete when the loading mode changes;

$\Delta\sigma_{si}(t, \tau)$ —increment of initial stresses in reinforcement when changing the loading mode;

H_{σ_b} —The function of accumulation of stresses in the concrete of the compressed zone during cyclic loading within the first (initial) loading unit;

H_{σ_s} —The function of accumulation of stresses in stretched reinforcement during cyclic loading within the first (initial) loading unit.

In Eqs. (23) and (24), the “+” sign is accepted with a sequentially increasing mode of non-stationary loading, “−” with a sequential decreasing regime. The calculation process is conditionally divided into two stages. In the first stage, the initial stresses are determined, and at the second stage additional and current stresses are determined (Fig. 2).

4 Discussion

Let the bending moment act in the section of the bending element, the value of which is equal to the maximum value of the cyclically applied moment on the first loading block with the characteristics $M_{I_{max}}$, \mathcal{P}_{M1} , in accordance with the calculated scheme of the presented normal section (Fig. 3). Stresses in the concrete of compressed zone and working reinforcement of the stretched zone within the first block of non-stationary loading are determined for stationary cyclic loading according to formulas (14) and (15).

Changing stresses in concrete of compressed zone when changing the non-stationary cyclic loading mode:

$$\Delta\sigma_{bi}(t, \tau) = \sigma_{bi}^{max}(t_0) \cdot H_{\sigma_{bi}} - \sigma_{bi-1}^{max}(t, t_0), \quad (25)$$

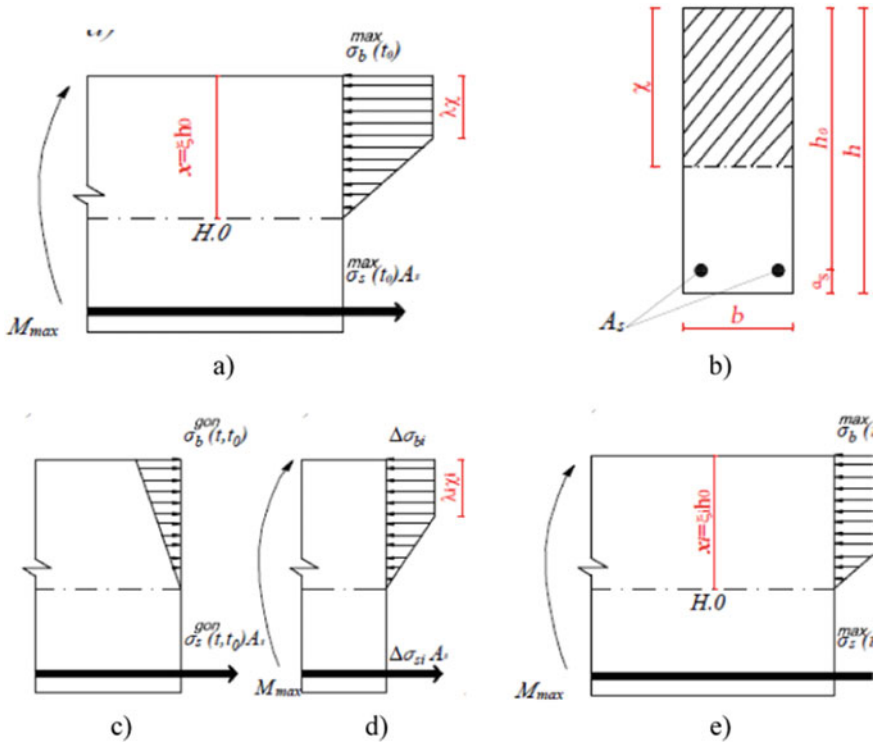


Fig. 2 Diagrams of stress in the cross section of the reinforced concrete beam, when calculating endurance with non-stationary modes of block cyclic loading **a** diagram of the initial stresses; **b** cross section; **c** diagram of additional stresses due to the manifestation of vibrational creep; **d** diagram of additional stresses when changing the regime; **e** current stress diagrams

where $\sigma_{bi}^{max}(t, t_0)$, $\sigma_{bi-1}^{max}(t, t_0)$ —The maximum stresses of the cycle in the considered and previous loading blocks.

Changing stresses in longitudinal stretched reinforcement when changing the non-stationary cyclic loading mode:

$$\Delta\sigma_{si}(t, \tau) = \sigma_{si}^{max}(t, t_0) \cdot H_{\sigma_{si}} - \sigma_{si-1}^{max}(t, t_0), \quad (26)$$

where $\sigma_{si}^{max}(t, t_0)$, $\sigma_{si-1}^{max}(t, t_0)$ —The maximum cycle stress in the considered and previous loading blocks.

In the second stage, additional stresses are determined on the basis of the same prerequisites as under the action of stationary cyclic loads. Within each load block, they can be represented by:

in longitudinal stretched reinforcement:

$$\sigma_{si}^{gon}(t, t_0) = \varepsilon_{pl}(N) \frac{1 - \xi}{\xi} E_s A_s; \quad (27)$$

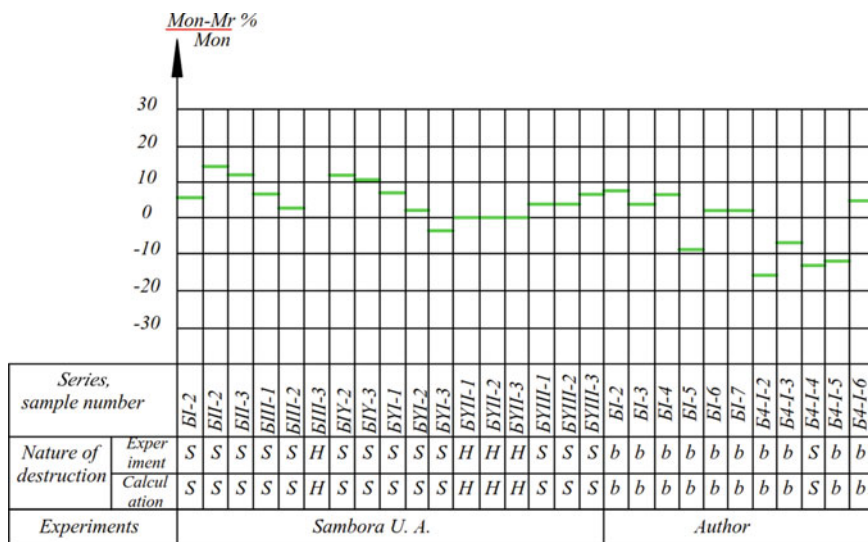


Fig. 3 Comparison of the experimental and calculated values of the endurance of reinforced concrete beams when calculating by the method of maximum stresses

in concrete of compressed zone:

$$\sigma_{bi}^{gon}(t, t_0) = \sigma_{si}^{gon}(t, t_0) \left[\frac{1}{A_{red}} - \frac{(k_{red} - a_s)(h - k_{red})}{\mathcal{J}_{red}} \right] \tag{28}$$

$$= \varepsilon_{pl}(N) \frac{1 - \xi}{\xi} E_s A_s \left[\frac{1}{A_{red}} - \frac{(k_{red} - a_s)(h - k_{red})}{\mathcal{J}_{red}} \right],$$

where $\varepsilon_{pl}(N)$ —vibrational creep deformation with regime cyclic loading.

Equations for additional stresses in concrete of compressed zone and longitudinal stretched reinforcement can be written in the following form:

a) in concrete of a compressed zone with a sequentially increasing regime:

$$\sigma_{bi}^{gon}(t, t_0) = \left\{ \begin{aligned} & C_{\infty}(t, \tau) \sigma_b^{min}(t, t_0) [1 - e^{-\gamma(t, t_0)}] + C_{\infty}(t, \tau) \sigma_b^{max}(t, t_0) (1 - \mathcal{P}_{bi}) \\ & \cdot [1 - (1 - a)^N] + \sum_2^i C_{\infty}(t, \tau) \Delta \sigma_{bi} (1 - \mathcal{P}_{bi}) [1 - (1 - a)^{N_i}] \\ & + \frac{\sigma_b^{max}(t, t_0)}{E_b} \cdot [0,566 \cdot l^2(t, t_0) \cdot 10^{-3}] \end{aligned} \right\}$$

$$\frac{1 - \xi}{\xi} E_s A_s \left[\frac{1}{A_{red}} - \frac{(k_{red} - a_s)(h - k_{red})}{\mathcal{J}_{red}} \right]; \tag{29}$$

b) in the longitudinal stretched reinforcement in a sequentially increasing mode:

$$\sigma_s^{gon}(t, t_0) = \left[\begin{aligned} & C_\infty(t, \tau) \sigma_b^{min}(t, t_0) [1 - e^{-\gamma(t, t_0)}] + C_\infty(t, \tau) \sigma_b^{max}(t, t_0) (1 - \mathcal{P}_{bi}) \\ & \cdot [1 - (1 - a)^N] + \sum_2^i C_\infty(t, \tau) \Delta \sigma_{bi} (1 - \mathcal{P}_{bi}) [1 - (1 - a)^{Ni}] \\ & + \frac{\sigma_{bi}^{max}(t, t_0)}{E_b} \cdot [0, 566 \cdot l^2(t, t_0) \cdot 10^{-3}] + \end{aligned} \right] \cdot \frac{1 - \xi}{\xi} E_s A_s; \quad (30)$$

c) in concrete of a compressed zone with a sequential mode:

$$\begin{aligned} \sigma_{bi}^{gon}(t, t_0) = & C_\infty(t, \tau) \sigma_b^{min}(t, t_0) [1 - e^{-\gamma(t, t_0)}] \\ & + C_\infty(t, \tau) \sigma_{b1}^{max}(t, t_0) (1 - \mathcal{P}_{bi}) \cdot [1 - (1 - a)^N] \\ & + \sum_2^i C_\infty(t, \tau) \Delta \sigma_{bi} (1 - \mathcal{P}_{bi}) [1 - (1 - a)^{Ni}] \\ & + \frac{\sigma_{bi}^{max}(t, t_0)}{E_b} \cdot [0, 566 \cdot l^2(t, t_0) \cdot 10^{-3}] \\ & - \sum_2^i \Delta \sigma_{bi} \left\{ \begin{aligned} & b_1 [1 - e^{-\beta_1(t, t_0)}] \\ & + b_2 [1 - e^{-\beta_1(t, t_0)}] \end{aligned} \right\} \\ & \cdot \frac{1 - \xi}{\xi} E_s A_s \left[\frac{1}{A_{red}} - \frac{(k_{red} - a_s)(h - k_{red})}{\mathcal{J}_{red}} \right]; \end{aligned} \quad (31)$$

d) in the longitudinal stretched reinforcement in a sequential mode:

$$\begin{aligned} \sigma_s^{gon}(t, t_0) = & C_\infty(t, \tau) \sigma_b^{min}(t, t_0) [1 - e^{-\gamma(t - t_0)}] \\ & + C_\infty(t, \tau) \sigma_{b1}^{max}(t, t_0) (1 - \mathcal{P}_{b1}) \cdot [1 - (1 - a)^N] \\ & + \frac{\sigma_{bi}^{max}(t, t_0)}{E_b} \cdot [0, 566 \cdot l^2(t, t_0) \cdot 10^{-3}] \\ & - \sum_2^i \Delta \sigma_{bi} \left\{ \begin{aligned} & b_1 [1 - e^{-\beta_1(t, t_0)}] \\ & + b_2 [1 - e^{-\beta_1(t, t_0)}] \end{aligned} \right\} \cdot \frac{1 - \xi}{\xi} E_s A_s. \end{aligned} \quad (32)$$

The redistribution of the efforts between concrete of the compressed zone and the stretched working reinforcement leads to a change in the coefficients of the asymmetry of the stress cycle in the concrete of the compressed zone and the working longitudinal reinforcement, which does not correspond to the coefficient of asymmetry of the load cycle $\mathcal{P}_M = M_{min} / M_{max}$.

The asymmetry coefficients of the stress cycle with non-stationary loading modes are determined by the formulas:

$$\mathcal{P}_{bi}(t) = \frac{\sigma_{b1}^{max}(t_0)\mathcal{P}_{M1} \pm \sum_{i=2}^k \Delta\sigma_{bi}(t, t_0)\mathcal{P}_{Mi} + \sum_{i=1}^k \sigma_{bi}^{gon}(t, t_0)}{\sigma_{b1}^{max}(t_0) \pm \sum_{i=2}^k \Delta\sigma_{bi}(t, t_0)\mathcal{P}_{Mi} + \sum_{i=1}^k \sigma_{bi}^{gon}(t, t_0)}, \quad (33)$$

$$\mathcal{P}_{si}(t) = \frac{\sigma_{s1}^{max}(t_0)\mathcal{P}_{M1} \pm \sum_{i=2}^k \Delta\sigma_{si}(t, t_0)\mathcal{P}_{Mi} + \sum_{i=1}^k \sigma_{si}^{gon}(t, t_0)}{\sigma_{s1}^{max}(t_0) \pm \sum_{i=2}^k \Delta\sigma_{si}(t, t_0)\mathcal{P}_{Mi} + \sum_{i=1}^k \sigma_{si}^{gon}(t, t_0)}, \quad (34)$$

where \mathcal{P}_{M1} \mathcal{P}_{Mi} —The asymmetry coefficient of the external load cycle.

Substituting in (33) and (34) numerical values $\sigma_{bi}^{gon}(t, t_0)$ and $\sigma_{si}^{gon}(t, t_0)$, we determine the coefficients of asymmetry of the stress cycle in concrete of the compressed zone and longitudinal stretched reinforcement. Then, taking into account (29)–(32), the current (total) stresses in the concrete of the compressed zone and the stretched reinforcement are calculated with the sequentially increasing and consistent decreasing modes of block non-stationary loading (Fig. 3).

The endurance of reinforced concrete structures is evaluated based on the conditions:

$$\sigma_b^{max}(t, t_0) \leq R_{bi,rep} \frac{1}{k_\omega}; \quad (35)$$

$$\sigma_s^{max}(t, t_0) \leq R_{si,rep}, \quad (36)$$

where $R_{bi,rep}$ and $R_{si,rep}$ —transformed limits of the endurance of concrete and reinforcement, respectively, depending on the loading regime and actual values \mathcal{P}_{bt} \mathcal{P}_{st} .

5 Conclusion

1. Theoretical studies of the fatigue strength of the normal sections of reinforced concrete structures in stationary and non-stationary modes of cyclic loading were carried out using maximum balance methods, the theory of fatigue strength, the theory of creep and vibrational creep of concrete and reinforced concrete, taking into account the redistribution of the efforts between concrete of the compressed zone and the longitudinal reinforcement. The stresses and coefficients of the asymmetry of the stress cycle in the concrete of the compressed zone and stretched reinforcement are determined taking into account their changes in the process of cyclic loading. The functions of changes in stresses and coefficients of asymmetry of the stress cycle were obtained, which allowed developing a new method for calculating the endurance of normal sections.
2. The proposed method makes it possible to evaluate endurance quite accurately (the deviation between theoretical and experimental data does not exceed 15%)

in simplified production, and thereby reduce the time and complexity of design of structures subject to cyclic effects.

References

1. Atutis, E., Valivonis, J., Atutis, M.: Deflection determination method for BFRP prestressed concrete beams under fatigue loading **226** (2019)
2. Kim, G., Loreto, G., Kim, J.Y., Kurtis, K.E., Wall, J.J., Jacobs, L.J.: In situ nonlinear ultrasonic technique for monitoring microcracking in concrete subjected to creep and cyclic loading. *Ultrasonics* **88** (2018)
3. Li, Q., Liu, M., Lu, Z., Deng, X.: Creep model of high-strength high-performance concrete under cyclic loading. *J. Wuhan Univ. Technol. Sci. Ed.* **34** (2019)
4. Chen, P., Zhou, X., Zheng, W., Wang, Y., Bao, B.: Influence of high sustained loads and longitudinal reinforcement on long-term deformation of reinforced concrete beams. *J. Build. Eng.* **30** (2020)
5. Bouziadi, F., Boulekbache, B., Haddi, A., Hamrat, M., Djelal, C.: Finite element modeling of creep behavior of FRP-externally strengthened reinforced concrete beams. *Eng. Struct.* **204** (2020)
6. Mirsayapov, I.T.: Detection of stress concentration regions in cyclic loading by the heat monitoring method. *Mech. Solids.* **45** (2010)
7. Song, L., Fan, Z., Hou, J.: Experimental and analytical investigation of the fatigue flexural behavior of corroded reinforced concrete beams. *Int. J. Concr. Struct. Mater.* **13** (2019)
8. Zamaliev, F.S., Zakirov, M.A.: Stress-strain state of a steel-reinforced concrete slab under long-term. *Mag. Civil Eng.* (2018)
9. Tang, H., Chen, Z., Avinesh, O., Guo, H., Meng, Z., Engler-Pinto, C., Kang, H.: Notch insensitivity in fatigue failure of chopped carbon fiber chip-reinforced composites using experimental and computational analysis. *Compos. Struct.* **10** (2020)
10. Mirsayapov Ilizar, T., Garifullin, D.R.: Engineering methods for calculating elastic modulus deformations and limits of concrete endurance under cyclic loading. *News KSUAE* (53), 15–26 (2020)
11. Mirsayapov Ilizar, T., Garifullin, D.R.: Stress-strain state of normal sections of reinforced concrete elements under cyclic inelastic deformation of reinforcement. *News KSUAE* (54), 44–53 (2020)
12. Augeard, E., Ferrier, E., Michel, L.: Mechanical behavior of timber-concrete composite members under cyclic loading and creep. *Eng. Struct.* **210** (2020)
13. Trekin, N.N., Kodysh, E.N., Mamin, A.N., Trekin, D.N., Onana, J.: Improving methods of evaluating the crack resistance of concrete structures. *ACI Spec. Publ.* **326** (2018)
14. Liang, J., Nie, X., Masud, M., Li, J., Mo, Y.L.: A study on the simulation method for fatigue damage behavior of reinforced concrete structures. *Eng. Struct.* **150** (2017)
15. Zhang, G., Zhang, Y., Zhou, Y.: Fatigue tests of concrete slabs reinforced with stainless steel bars. *Adv. Mater. Sci. Eng.* (2018)
16. Zhang, G., Zhang, Y., Zhou, Y.: Fatigue tests of concrete slabs reinforced with stainless steel bars. *Adv. Mater. Sci. Eng.* **1** (2018)
17. Barclely, L., Kowalsky, M.: Critical bending strain of reinforcing steel and the buckled bar tension test. *ACI Mater. J.* **113** (2019)
18. Luo, X., Tan, Z., Chen, Y.F., Wang, Y.: Comparative study on fatigue behavior between unbonded prestressed and ordinary reinforced reactive powder concrete beams. *Mater. Test.* **61** (2019)
19. Tang, S.W., Yao, Y., Andrade, C., Li, Z.: Recent durability studies on concrete structure. *CCR* **78** (2015)

20. Berrocal, C.G., Fernandez, I., Lundgren, K., Lofgren, I.: Corrosion-induced cracking and bond behavior of corroded reinforcement bars in SFRC. *Compos. B Eng.* **113** (2017)
21. Chen, E., Berrocal, C.G., Löfgren, I., Lundgren, K.: Correlation between concrete cracks and corrosion characteristics of steel reinforcement in pre-cracked plain and fibre-reinforced concrete beams. *Mater. Struct. Constr.* **53** (2020)

Study of Physical and Mechanical Properties of Asphalt Concrete with the Addition of Artificial Asphaltite



Anatoly Novik , Aleksei Ismailov , and Igor Sentsov 

Abstract The article is devoted to the study of the physical and mechanical properties of asphalt concrete mixtures with the addition of asphaltite into the binder and into the asphalt mixing plant. The process of preparing materials for research has been described, the selection and design of the composition of the asphalt concrete mixture has been made. A step-by-step technology for the production of an asphalt concrete mixture with artificial asphaltite has been presented. Results of the experiment have shown a significant increase in the physical, mechanical and operational properties of asphalt concrete pavements modified with artificial asphaltite of the asphalt concrete mixture. It leads to the increase in the service life of roads. On the basis of the experiment and analysis the optimal formulation of the asphalt concrete mixture using artificial asphaltite has been proposed and the optimal method of introducing the additive at the asphalt concrete plant has been determined.

Keywords Road pavement · Artificial asphaltite · Asphalt concrete · Oil bitumen · Modification · Bituminous astringent

1 Introduction

Currently, there is a difficult situation with the construction, operation and maintenance of roads with asphalt concrete pavement in a safe condition. Due to the increase in the number of vehicles, the load on the road has increased. The quality and durability of the pavement depends on natural and climatic factors [1–3], the quality of the materials used [4–6], correct and reliable calculation, and the technology used. Therefore, to improve these parameters, it is necessary to expand the

A. Novik · A. Ismailov (✉)
Peter the Great St. Petersburg Polytechnic University,
Polytechnicheskaya Street, 29, St. Petersburg 195251, Russian Federation
e-mail: ismailov-aleksei@mail.ru

I. Sentsov
FAU “Russian Road Research Institute”, Street Smolnaya, 2, Moscow 125493, Russian Federation

range of applications of various additives, use new materials, and update existing regulations and standards.

When building a road surface, it is important to achieve and expand the range of performance characteristics of asphalt by increasing its stability without compromising other properties. To address the issue of quality and durability of road pavement in the Russian Federation, various additives have been used for the preparation of asphalt concrete mix. Additives are divided according to the method of their introduction: introduced into bitumen and introduced into the asphalt mixture. The most expensive component of asphalt concrete is bitumen, so it is more popular to use additives that improve the physical and mechanical properties of bitumen.

The use of asphaltite as a part of hot asphalt mixes is widespread all over the world. Asphaltite is successfully used in the construction of coatings in difficult areas that combine heavy loads and traffic with frequent stops. Indicators of water fastness and prolonged water fastness with the introduction of asphaltite increase [18], when it is introduced into bitumen, the properties of adhesion and cohesion increase. The speed of track formation is reduced by half, and also increases the shear stability of the clutch when shifting by 25%. The introduction of this additive does not worsen the low temperature properties according to State Standard 9128–2013.

Research shows that the introduction of an asphaltite additive can have a significant impact not only on the properties of asphalt concrete, but also directly on bitumen, increasing its viscosity [7, 8]. It is necessary to study the complex effect of asphaltite on asphalt concrete in order to understand how the physical and mechanical characteristics of the finished product change. Despite the fact that artificial asphalt is more expensive than natural, it is necessary to use it. The characteristics of natural asphaltite change from batch to batch and it is impossible to guarantee physical and mechanical properties in the future. Artificial asphaltite has a lower risk of getting a low-quality product, since it is a product, not a raw material.

2 Materials and Methods

2.1 Experiment Program

The test program includes:

Experiment Planning. The design of the experiment is based on the hypothesis that it is possible to introduce artificial asphaltite addition directly into the asphalt mixing plant and into the bitumen. The artificial asphaltite additive is introduced into the asphalt mixing plant using the screw method or in hot melt bags. The asphaltite is added to bitumen directly at the refinery.

Before carrying out a full-scale experiment, mathematical modeling was performed and a matrix was compiled taking into account the interaction of factors.

Selected optimization parameters:

y_1 —shear stability, shear adhesion index, MPa. y_2 —rut depth after 20,000 wheel passes, mm.

Variation factors:

x_1 —adding artificial asphaltite to an asphalt mixing plant. x_2 —adding artificial asphaltite into bituminous binder.

The equation that links the factors:

$$y = f(x_1, x_2) \tag{1}$$

Optimization parameters refer to the physical and mechanical characteristics of the product. The boundaries of the area for determining the factors x_1, x_2 , in this experiment, are considered from 2 to 10% of the mass of bitumen. The coding is presented in Table 1. The information on the range of variation was taken from the study of the effect of the addition of artificial asphaltite on the bituminous binder [9–11], since in the previous study, when artificial asphaltite was added to the bitumen binder, the Fraas brittle temperature increased, °C and went beyond the limits specified in State Standard 33143-2014 [12–14]. The choice of the main level of 6% is based on the subregion in which the physical and mechanical characteristics of bitumen with the addition of artificial asphalt meet State Standard 33143-2014 [15, 16].

In accordance with the theory of experiment planning, all possible non-repeating combinations of the levels of independent factors, which are presented in Table 2, were implemented, as a result, a response function was obtained.

Table 1 Coding of factors x_1 and x_2

Factors	x_1 (%)	X_1	x_2 (%)	X_2
Variation interval	4	1	4	1
Top level	10	+1	10	+1
Lower level	2	-1	2	-1
Main level	6	0	6	0

Table 2 Matrix for planning a multifactorial experiment 22 taking into account the interaction of factors

Experiment number	X_1	X_2	X_1X_2	Y_1	Y_2
1	-	-	+	y_1	y_1
2	+	-	-	y_2	y_2
3	-	+	-	y_3	y_3
4	+	+	+	y_4	y_4

2.2 Selection of the Composition of the Asphalt Concrete Mixture

For a comparative analysis of the effect of asphaltite in the composition of asphalt concrete within the framework of this study, type A asphalt concrete grade I was selected. This asphalt concrete was selected on the basis of previously conducted tests at the ABZ-1 plant, Pushkin, st. Gusarskaya, 30. It is necessary to determine the convergence of test results. State Standard 12801-98 “Materials based on organic binders for road and airfield construction. Test methods.” [17] was adopted as the normative base for making samples in laboratory conditions. The composition of the asphalt concrete mixture is presented in Table 3.

Mineral powder meets the requirements of State Standard 16557-78 “Mineral powder for asphalt concrete mixtures”. Crushed stone and gravel correspond to State Standard 8267-93 “Crushed stone and gravel from dense rocks for construction work”. The sand meets the requirements of State Standard 8736-93 “Sand for construction work”. Oil road bitumen complies with State Standard 11955-82 “Oil road liquid bitumen”. Bitumen for the experiment was taken from the company “Kinef”. Crushed stone and sand were taken from the company “CAREER-SCHELEIKI”.

The selection of the composition of the asphalt concrete mixture was carried out after washing, drying in a drying chamber at a temperature of 110 °C, sifting and weighing the raw materials on sieves. After sifting, the design and selection of the composition of mineral materials for the production of samples and subsequent testing was carried out.

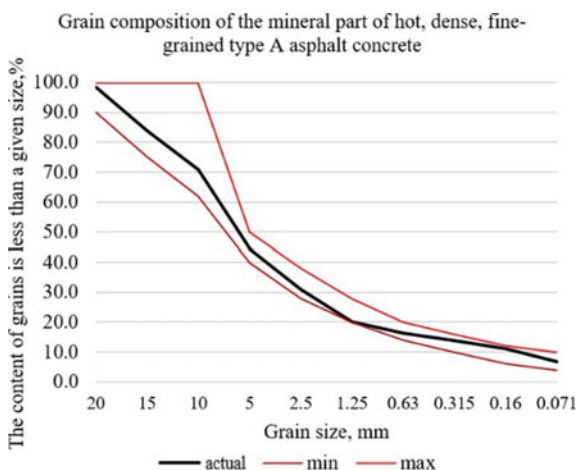
Tables 3 and 4 were compiled for the selection of grain size composition. The resulting granulometric curve is shown in Fig. 1. This curve corresponds the requirements of State Standard 9128-2013 for the selection of uninterrupted mineral composition. After analyzing Fig. 1, we can conclude that the resulting curve after design corresponds the limiting values of State Standard 9128-2013. Since the granulometric curve does not go beyond the limiting values, it can be assumed that the selection and design of the composition of the mineral part of the asphalt concrete mixture was made correctly [18, 19].

Table 3 Composition of asphalt concrete mixture type A grade I

Name	Percentage (%)
Crushed stone gabbro-diabase	55.7
Sand and screenings of gabbro-diabase	37.4
Bitumen BND 70/100 + 0.3% “AMDOR-10”	5
Smaller than 0.071 mm, % by weight	6.9
incl. Mineral powder	4.9

Table 4 Grain composition of the mineral part of the asphalt concrete mixture

Grain composition		Content of grains finer than a given size, (mm), in% by weight									
		20	15	10	5	2.5	1.25	0.63	0.315	0.16	0.071
Actual		98.3	83.9	70.9	44.3	30.9	20.0	16.3	13.8	11.1	6.9
State Standard 9128-2013	Min	90	75	62	40	28	20	14	10	6	4
	Max	100	100	100	50	38	28	20	16	12	10

**Fig. 1** Granulometric curve of the selected grain composition

2.3 Preparation of Laboratory Modified Sample

Artificial Asphaltite Preparation. Asphaltite from production comes in the form of an amorphous body. Before use, this body must be cleaned of dust and dirt (Fig. 2). After thorough cleaning, artificial asphaltite is crushed to the state of a fine powder for the best dissolution in a bitumen binder (Fig. 3). This powder sinters during long-term storage, therefore, after grinding, it must be immediately used for the preparation of an asphalt concrete mixture.

Technology of Production of Asphalt Concrete Mixture with Asphaltite Modifier

The asphaltite is introduced into the asphalt mixer by an auger loader.

1. Procurement of materials (crushed stone, sand, mineral powder, bitumen) of the required quality and their proper storage;
2. Preparation (heating) of bitumen up to 160 °C;
3. Preliminary dosing of sand of crushing screenings and crushed stone in the feed unit;



Fig. 2 Artificial asphaltite from production

4. Drying and heating of sand from crushing screenings and crushed stone to a given temperature;
5. Screening of hot sand from crushing screenings and crushed stone of gabbro-diabase into fractions of 0–2, 2–5, 5–10, 10–15, 15–20 mm and sorting them into sections of the hot bunker;
6. Weight dosing of each fraction of mineral materials and mineral powder in a given proportion into an asphalt mixer (8 s), dry mixing of components (3 s);
7. Dosing of asphaltite into an asphalt mixer;
8. Dosing and injection of prepared bitumen, (3 s);
9. Stirring a mixture of mineral materials with bitumen (24 s); The total mixing time is 38 s.
10. Unloading of ready-made asphalt concrete mixture into a storage hopper or vehicle.



Fig. 3 Artificial asphaltite after grinding

3 Results

This table shows the average values of the data from three samples obtained as a result of the experiment described above (Table 5).

For this study, bitumen BND 70/100 was used, with an adhesive additive “Amdor—10” in an amount of 0.3 of the mass of bitumen.

Adding 10% artificial asphaltite to bituminous binder on Figs. 4, 5, 6, 7, 8, 9, 10, 11, 12 and 13:

1. Reduces the average rut depth by 76% from 10 to 2.4 mm.
2. Doesn't significantly affect water saturation, and it is in the range from 2.0 to 2.5.
3. Ultimate compression resistance at a temperature of 0 °C increases by 16% from 8.01 to 9.51 MPa, not more than 11 MPa.
4. Ultimate compression resistance at a temperature of 20 °C increases by 28% from 3.54 to 4.55 MPa, at a temperature of 50 °C increases by 46% from 1.01 to 1.48 MPa.
5. Water fastness increases from 0.9 to 0.99 units with the required 0.9 units.
6. Water fastness with prolonged water saturation increases from 0.84 to 0.87, units at the required 0.85.

Table 5 Test results

Amount of added asphaltite/PMB-60	0%	2%	4%	6%	8%	10%	6%*	PMB-60	
Average density of asphalt concrete, g/cm ³	2.645	2.656	2.662	2.653	2.653	2.635	2.647	2.676	
Water saturation in% by volume	2.72	2.12	1.90	2.35	2.19	2.68	2.34	2.5	
Compressive strength, MPa	R0	8.01	7.60	6.93	8.19	9.37	9.51	8.95	11.0
	R20	3.54	3.86	3.26	3.68	3.99	4.55	3.66	5.1
	R50	1.01	1.07	1.11	1.17	1.47	1.48	1.07	1.5
	R, water saturation	3.14	3.40	3.30	3.61	4.54	4.52	4.01	4.69
	R, long-term water saturation	2.99	3.33	2.91	3.03	4.18	3.97	3.43	4.59
Water resistance	0.89	0.88	1.01	0.98	1.14	0.99	1.10	0.92	
Water resistance with long-term water saturation	0.84	0.86	0.89	0.82	1.05	0.87	0.94	0.90	
Shear resistance by coefficient internal friction	0.92	0.89	0.88	0.88	0.82	0.90	0.91	0.956	
Shear resistance of adhesion at shear at a temperature of 50 °C, MPa	0.30	0.37	0.31	0.33	0.44	0.45	0.31	0.46	
Average rut depth after 20000 wheel passes, mm according to preliminary national standard 181-2016	10.00	7.3	6.0	4.2	2.7	2.4	4.3	2.5	
Tensile split at 0 °C, MPa	3.48	4.56	4.69	3.88	4.71	4.96	4.23	4.75	

* asphaltite added to an asphalt mixing plant in b

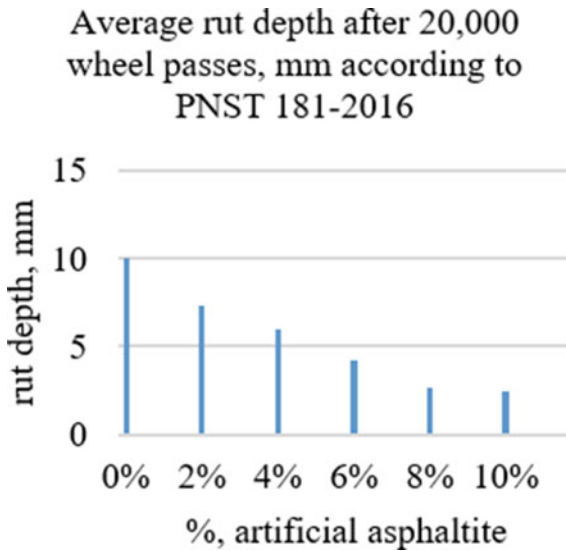


Fig. 4 Average rut depth after 20,000 wheel passes, mm according to PNST 181-2016

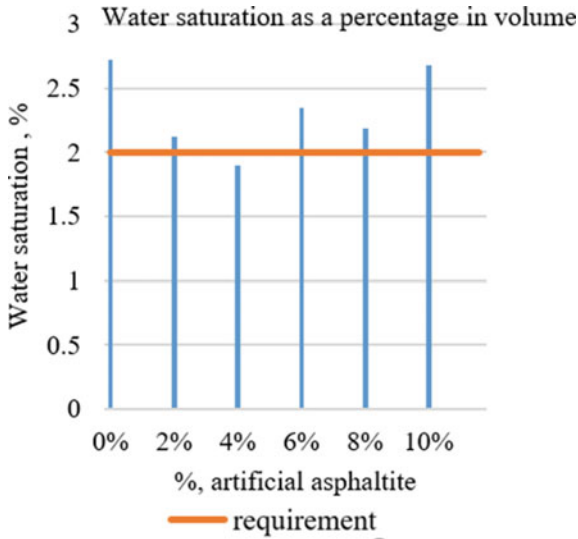


Fig. 5 Water saturation as a percentage in volume, State Standard 9128-2013

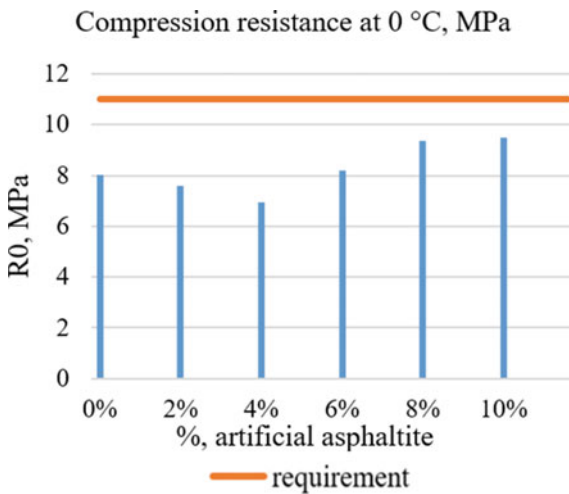


Fig. 6 Compression resistance at 0 °C, MPa, State Standard 9128-2013 (no more than 11.0, MPa)

7. The shear resistance coefficient of internal friction decreases by 3% from 0.92 to 0.9°.
8. The shear resistance of the coupling under shear at a temperature of 50 °C, MPa increases by 33% from 0.3 to 0.45 MPa at the required 0.25 MPa.
9. The Splitting stretch at 0 °C, MPa increases by 17% from 3.48 to 4.23 MPa with the required 3.5 MPa and not more than 6.0 MPa.

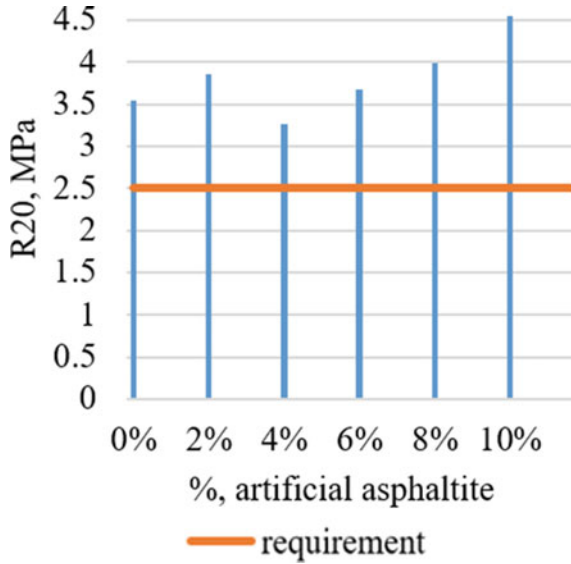


Fig. 7 Compression resistance at 20 °C, MPa, State Standard 9128-2013 (no more than 2.5, MPa)

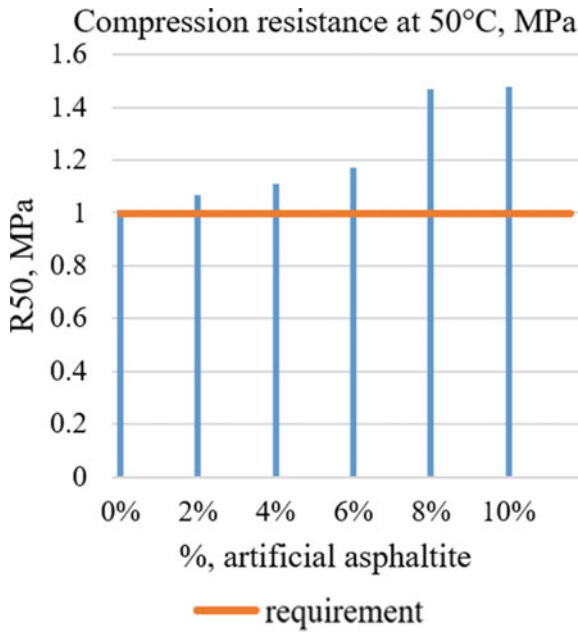


Fig. 8 Compression resistance at 50 °C, MPa, State Standard 9128-2013 (no more than 1.0, MPa)

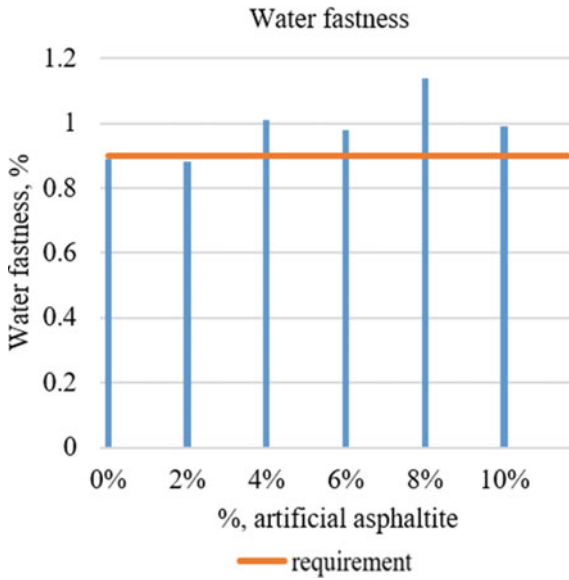


Fig. 9 Water fastness, State Standard 9128-2013 (not less than 0,9)

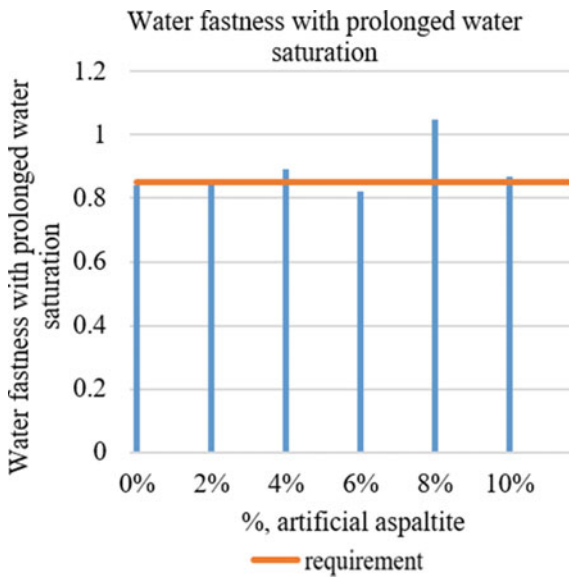


Fig. 10 Water fastness with prolonged water saturation, State Standard 9128-2013 (not less than 0,85)

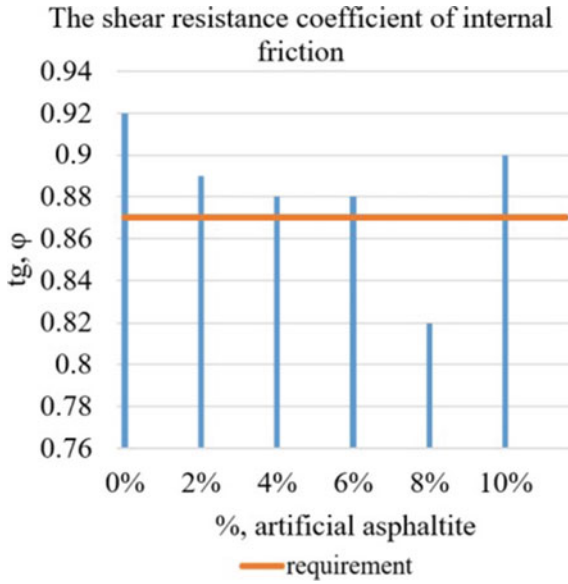


Fig. 11 The shear resistance coefficient of internal friction, State Standard 9128-2013 (not less than 0,87)

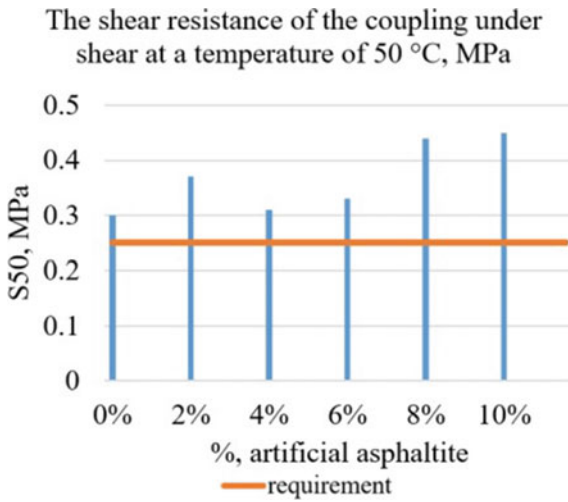


Fig. 12 The shear resistance of the coupling under shear at a temperature of 50 °C, MPa, State Standard 9128-2013 (not less than 0,25)

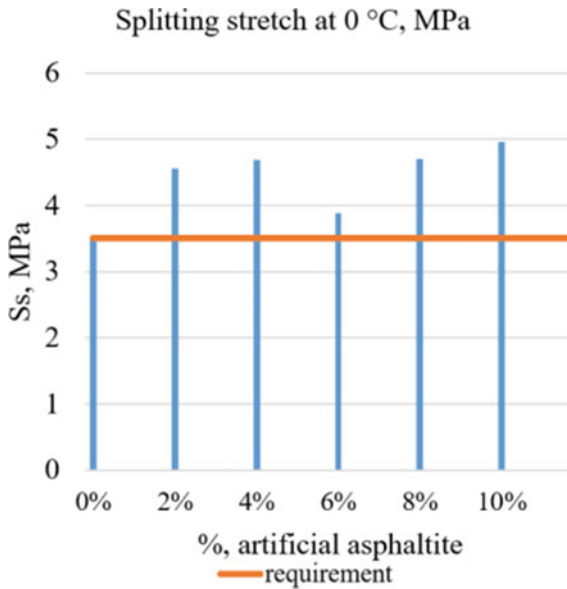


Fig. 13 Splitting stretch at 0 °C, MPa, State Standard 9128-2013 (not less than 3,5, no more than 6,0)

The homogeneity of the variance of parallel experiments is confirmed on the basis of the obtained the Cochran criterion after processing the experimental results in Tables 6 and 7, and it is less than the tabular value. Therefore, we can assume that this experiment is reproducible in laboratory conditions.

Table 6 Grain composition of the mineral part of the asphalt concrete mixture

Asphaltite amount, %	Experiment number			Experiment number			Average value		S1 ² , dispersion	S2 ² , dispersion
	1	2	3	1	2	3	The rate of rut for mat ion	Cohesion shear stability at 50 °C		
0	10.0	9.8	10.1	0.31	0.3	0.3	10.0	0.30	0.02333	0.00003
2	7.3	7.2	7.5	0.37	0.35	0.39	7.3	0.37	0.02333	0.00040
4	6.0	5.9	6.0	0.32	0.30	0.30	6.0	0.31	0.00333	0.00013
6	4.3	4.1	4.2	0.34	0.33	0.33	4.2	0.33	0.01000	0.00003
8	2.7	2.6	2.7	0.42	0.45	0.44	2.7	0.44	0.00333	0.00023
10	2.4	2.3	2.4	0.44	0.44	0.46	2.4	0.45	0.00333	0.00013

Table 7 Grain composition of the mineral part of the asphalt concrete mixture

For S1^2				For S2^2				
The Cochran criterion	G =	0.35		G =	0.41			
Number of degrees of freedom	d.f1(r - 1) =	2	d.f2(N) =	5	d.f1(r - 1) =	2	d.f2(N) =	5
Significance level	q =	0.05		q =	0.05			
Critical deviation	Gt =	0.6161		Gt =	0.41			
Comparison	G < Gt	True		G < Gt	True			

4 Discussion

Based on the analysis, it can be concluded that artificial asphaltite, when added to a bituminous binder, has a greater effect on rutting speed, shear resistance, and compressive strength. Therefore, this additive improves the performance characteristics of asphalt concrete mixture and extends its service life. This means that the turnaround time will increase to 14 years from the existing 4–8 years with the addition of 10% artificial asphaltite and the standard traffic intensity, taking into account the speed of rutting.

On the basis of the research in accordance with State Standard 33143-2014 “Automobile roads of general use. Viscous road petroleum bitumens. Method for determination of Fraas brittleness temperature”, after adding artificial asphaltite over 6% bitumen does not pass in terms of cracking resistance when exposed to negative temperatures and comparison with indicators according to State Standard 22245-90 “Viscous petroleum road bitumens. Specifications” [20, 21]. As a result, the most optimal amount of artificial asphaltite is 6%. To save money, and to avoid additional heating time, artificial asphaltite must be added using a screw method, or in hot melt bags. Before being added to the automated control system, artificial asphaltite must be cleaned from dust and dirt, then, it must be ground to a fine structure for better dissolution in bitumen. After grinding, artificial asphaltite must be immediately used for the production of asphalt concrete mixture, otherwise, when reused after long-term storage due to adhesion of particles, additional grinding is necessary, which will lead to unjustified labor costs. It is advisable to use this additive in the upper layers of pavement surfacing.

As a recommendation for further research of artificial asphaltite, it is necessary to study the freeze–thaw resistance of asphalt concrete mixture with asphaltite in order to confirm or deny the negative low-temperature effect of artificial asphaltite on bitumen in the composition of asphalt concrete mixture on asphalt concrete as an integral object, since the existing research on the Fraas brittle point does not accurately say how the low temperature will affect the asphalt concrete in general.

5 Conclusions

As a consequence of the experiment, the results of changes in the physical and mechanical characteristics of the asphalt concrete mixture were obtained depending on the amount of the added modifier asphaltite.

The experiment showed that with the addition of 6% artificial asphaltite, the rut formation rate decreases by 58% from 10 to 4.2 mm, the shear resistance increases by 10%, and the strength increases by 15% with compression at 50 °C.

Since the rate of rut formation decreases, and with the current turnaround time of 4–8 years, artificial asphaltite, with the addition of 6% to the asphalt mixing plant, will make it possible to achieve a turnaround time of 10 years at a standard traffic intensity and, if we assume that the dependence of the rut formation rate from time to time will be linear.

The disadvantage of this additive is the need to purchase additional equipment for dosing artificial asphaltite, adhesion during long-term storage at the open air, which subsequently requires repeated grinding and labor costs.

References

1. The use of natural asphalt and asphaltites to improve the quality of road bitumen and asphalt concrete. <http://www.abz-1.ru/download/publication/21.pdf>. Accessed 12 May 2019
2. Mavliev, L., Vdovin, E.: Structure of road soil cement compositions modified by complex additive based on organosilicon compounds and electrolytes. In: E3S Web of Conferences, vol. 140, p. 02016 (2019)
3. LenDor Group ABS cost. <http://ldgroup.spb.ru/sale/asphalt.html>. Accessed 23 Apr 2019
4. Vdovin, E., Stroganov, V., Kononov, N.: modification of road soil cement with activated fillers. In: Lecture Notes in Civil Engineering, LNCE, vol. 150, pp. 335–345 (2021)
5. State Standard 22245-90 Viscous oil road bitumens. Specifications (with Amdt No. 1)
6. State Standard 9128-2009 Mixes asphalt road, airfield and asphaltic-cement concrete
7. Vdovin, E.A., Stroganov, V.F.: Optimization of complex frost-resisting additives in line with operational requirements towards freezing temperature in road dressing constructions. IOP Conf. Ser. Mater. Sci. Eng. **832**(1), 012034 (2020)
8. Vdovin, E.A., Stroganov, V.F.: Modification of cement-bound mixtures with sodium formate additives for the construction of pavement bases at low air temperatures. In: IOP Conference Series: Materials (2020)
9. Asphalt concrete plant ABZ-1. <http://abz-asphalt.ru/catalog/pbv/>. Accessed 16 May 2018
10. Asphalt concrete mixtures Beaton group of companies ABS cost. <http://www.bea-tongroup.ru/price/asphalt>. Accessed 23 Apr 2019
11. Vdovin, E., Mavliev, L., Stroganov, V.: Interaction of clay soil components with portland cement and complex additive based on octyltriethoxysilane and sodium hydroxide. IOP Conf. Ser. Mater. Sci. Eng. **890**(1), 012031 (2020)
12. Ismailov, A.: Technological solutions to ensure the required storage quality of the initial components for the production of asphalt concrete mixtures. Basic Res. **11**, 67–75 (2017)
13. Ermoshin, N., Ismailov, A.: The qualimetric method for optimising the selection of components for making high quality asphalt-concrete mixes. In: Sustainable Energy Systems: Innovative Perspectives: Conference proceedings, Saint-Petersburg, 29–30 October 2020, pp. 339–350. Springer, Cham (2021). https://doi.org/10.1007/978-3-030-67654-4_37

14. Ismailov, A., Bokovaya, N., Averchenko, G.: The impact modifier will factorit-C on the physico-mechanical properties of asphalt mix. In: *Lecture Notes in Civil Engineering*. LNCE, vol. 150, pp. 525–534 (2021). https://doi.org/10.1007/978-3-030-72404-7_51
15. State Standard 33100-2014 Public automobile roads. Road design rules
16. State Standard 12801-98 Materials based on organic binders for road and airfield construction. Test methods (with Amendment No. 1)
17. Kolevatova, A., Lavrova, A., Romanenko, Yu., Maidanova, N., Vasiliev, V.: The use of asphaltites for the modification of bituminous binders. *Izvestia SPbGTI (TU)* **43**(69), 33–55 (2018)
18. Traffic intensity. <http://szdorogi.ru/obekty-upravleniya/dannye-ob-inten>. Accessed 13 Nov 2018
19. Rosenthal, D., Syroezhko, A., Ralis, R.: Production of bitumen of various brands by compounding tar with natural asphaltite. *Petrochemistry* **47**(4), 329–330 (2007)
20. Shestopalov, A., Boitsev, A.: Methods for evaluation structural anisotropy of asphalt. *Int. Rev. Mech. Eng.* **11**(5), 361–364 (2017)
21. State Standard 33143-2014 Motor roads for general use. Viscous road oil bitumens. Method for determination of brittleness temperature according to Fraas

Experimental Studies of the Endurance of Reinforced Concrete Beams



Ilizar Mirsayapov 

Abstract The object of research is reinforced concrete structures, under the action of cyclic loads; one of the types of destruction is the fatigue destruction of the working fittings. The mode of operation of steel reinforcement as a part of a reinforced concrete structure is non-stationary, regardless of the loading mode in these cases, determining the fatigue strength of the reinforcement requires a large number of experiments, which requires more financial and labor resources, developing an equation for changing the specific energy of steel destruction in the zones of formation and development of cracks; developing a methodology for calculating the durability of steel reinforcement with cracks.

Theoretical studies of fatigue strength of steel reinforcement were carried out. It is established that the fatigue destruction of steel reinforcement is characterized by the formation and development of micro and macro cracks in the structure of the metal to critical sizes, two main stages are derived: before the formation of micro and macro cracks of fatigue; development of macro cracks of fatigue to critical sizes. To simulate the operation of steel reinforcement during regime cyclic deformation, methods of mechanics of destruction of elastic plastic materials were used; equations for changing the mechanical characteristics of reinforcement under various cyclic loading modes were obtained.

The significance of the results obtained for the construction industry lies in the fact that the proposed calculation models can reduce the cost of conducting studies of fatigue strength of reinforcement up to two times, labor intensity up to three times compared to generally accepted traditional experimental studies.

Keywords Steel reinforcement · Stress structure profile · Fatigue crack · Damage · Plastic resource · Specific energy · Creep stress of concrete · Elastic operation of reinforcement

I. Mirsayapov (✉)

Kazan State University of Architecture and Engineering, Zelenaya Street 1, 420043 Kazan, Russia
e-mail: mirsayapov1@mail.ru

1 Introduction

The process of multi cycle fatigue of metals is conditionally divided into two main stages: before the appearance of the main crack (the stage of the emergence of the fatigue main crack); the period of development of the main crack before destruction. If durability in the 1st stage is designated N_t , and durability in the 2nd stage of N_{zh} , then the full durability from the first loading cycle to fatigue destruction will be: $N = N_t + N_{zh}$ [1–5]. At the stage of the emergence of a main fatigue crack, intensive plastic deformation of the metal in local volumes occurs, which leads to significant closed hysteresis loops, the area of which is equal to energy scattered over one cycle of loading. The total width of these hysteresis loops is equal to nonelastic deformation per cycle. After the exhaustion of the plastic resource, microscopic cracks are formed in local plastically deformed volumes, one of which can develop into a main crack [6–10]. Therefore, the first stage can be called the stage of scattered fatigue damage. The second stage characterizes the development of the main crack in critical sizes. The first main crack implies a crack, which, under a given loading mode, develops at a higher speed than all other cracks, and is a source of final fatigue destruction. Based on numerous numerical experimental data, it has been established that the velocity dependence of $\vartheta = dp/dt$ on the accumulation of fatigue damage to the number of loading cycles is significantly different in the 1st and 2nd stages of fatigue destruction. Therefore, it can be assumed that the mechanisms of accumulation of damage at these stages are different. This requires various representations to assess the durability of N_T and N_{Zh} . Studies carried out at the Central Research Institute of the MTS NIIZHB, NIS; the hydraulic project showed [11–15] that fatigue cracks originate mainly in one of the two stress concentration centers:

- 1) At the obtuse angles of the connection of longitudinal ribs with inclined with transverse protrusions (ribs).
- 2) At the base of the transverse protrusions (ribs) in the places of their interlinking with the body of the bar.

Therefore, the aim of the work is to develop a theory of the development of fatigue cracks of steel reinforcement to create design models of reinforcement with cracks. The objectives of the work are to establish a scheme for the formation of fatigue cracks in reinforcing bars for reinforced concrete structures; to develop an equation for changing the specific energy of steel destruction in the zones of formation and development of cracks; develop a methodology for calculating the durability of steel reinforcement with cracks.

2 Materials and Methods

To assess the local stresses in the main center of concentration, we determine the effective coefficients of concentration of loads. Local stresses in the zone of the first focus are determined by the equation:

$$\sigma_{SM} = 0,843 \cdot \sigma_s^{\max}(t) \cdot b \cdot a \cdot \frac{t \cdot h \cdot m}{\cos \beta} \quad (1)$$

where $\beta = \sqrt{\frac{k}{E f}}$; $k = 1.45 \cdot E \frac{h}{\sqrt{\frac{b_b}{\cos \beta}}}$;

$f = b \cdot h$;

h —The width of the transverse rib;

b —The height of the transverse ribs;

$r = 10 h$ —The radius of curvature of concentration;

$a = \frac{1}{h}$; $m = b \cdot a / 2 \cdot \cos \beta$,

The transition from local stresses to the concentration coefficient is made according to the equation:

$$\alpha_k = \frac{\sigma_{sh} + \sigma_M}{\sigma_{sh}} \quad (2)$$

The theoretical coefficient of concentration of stresses in the second focus is calculated in the next sequence. The radius of curvature r is determined in the second end of the rib with the core of the bar and the conditional calculated width of the protrusion, and equal to the distance between the points of the beginning of the interfacing on both sides of the transverse rib. For a circular filler width a' can be accepted equal to the width of the protrusion plus a doubled radius of conjugation r . With the ratio a'/r , the theoretical concentration coefficient is calculated:

The condition of the marginal equilibrium in endurance is (Fig. 1).

For preparation of concrete mixtures, Portland cement was used with an activity of 50 MPa, sand with a module of size 1.45; granite crushed stone, 5–15 mm fractions. The parameters of samples that differ within the series mechanical characteristics of concrete and reinforcement and test modes in series are given in Tables 1, 2 and 3.

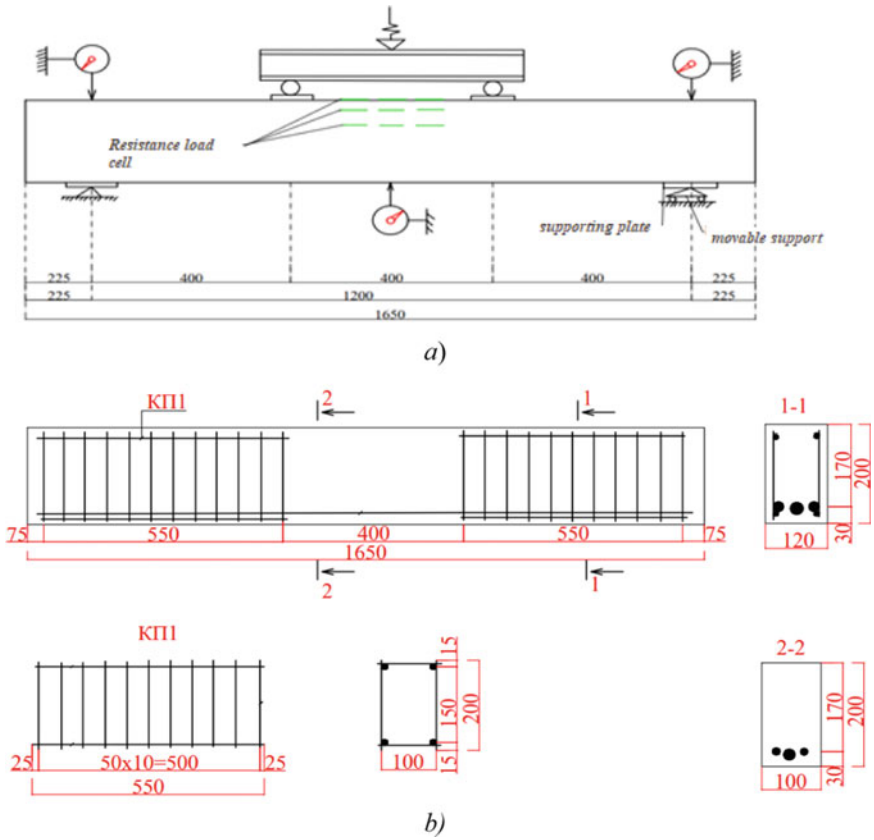


Fig. 1 a the test circuit of the beams; b reinforcement of reinforced concrete beams

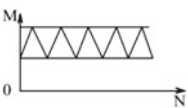
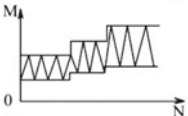
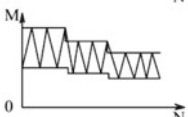
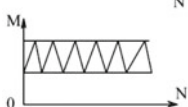
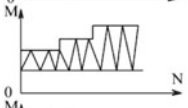
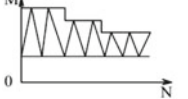
Table 1 Mechanical characteristics of concrete of experimental compositions

№ compositions	On day 28			Average during the test period				
	R, MPa	R _b , MPa	R _{bt} , MPa	E _b · 10 ⁻⁴ MPa	R, MPa	R _b , MPa	R _{bt} , MPa	E _b , MPa
1	50,0	33	2,0	3,3	55	36	2,2	34,800
2	50,0	34	2,0	3,4	55	36	2,2	35,000

Table 2 Mechanical characteristics of reinforcing steels

Reinforcement diameter, mm and class	A _S , cm ²	σ _y , MPa	σ _u , MPa	δ _p , %	E _b · 10 ⁻⁵ MPa
1 18 AIII	2,54	433,1	661,4	15,4	2,0
2 25 AIII	4,91	420	695,0	15,4	2,0
3 14 AIV	1,54	640	960	10,0	2,0

Table 3 Characteristics of prototypes and test modes

№ Series	Loading mode	Dimensions, mm		Strength, R_b , MPa	A_s , cm ²	E_b , MPa	No
		b	h				
B1		120	210	36	9.99	34800	6
B2		120	210	36	9.99	34800	9
B3		120	210	36	9.99	34800	9
B4-1		120	210	38	7.99	35000	9
B4-2		120	210	38	7.99	35000	6
B4-3		120	210	38	7.99	35000	6

3 Results

Reinforced concrete beams, tested as a model of the bending element of a static and repeated load, reached the limit from the action of bending moments. The destruction of the tested reinforced concrete beams occurred along the compressed part of the concrete in the following sequence: horizontal cracks were formed on the side surface of the beams at a distance of 1.0–2.5 cm from the extreme compressed part of the section on the area between the attached forces with a further increase in the length and width of the opening with the increase in the number of cycles of repeated loading. In addition, with an increase in the number of cycles, these cracks were connected to each other, forming a single plane of destruction. Then, after the length of the crack reached the critical value of $LCR = 25\text{--}30$ cm, separate pieces of concrete started to come off from the compressed part of the cross section. The maximum state occurred when the compressed part of the cross section became insufficient to perceive the load equal to the maximum value of the load of the cycle of the repeated load. Consequently, the destruction of the beams of the compressed part of the cross section occurred due to the layer-by-layer separation of concrete fibers due to the development of micro- and macro cracks in the process of repeated loading.

Analysis of the patterns of formation and development of fatigue cracks allows noting the nature of the development of longitudinal fatigue cracks in the compressed zone of beams under regime cyclic loads, which are confirmed by the results of theoretical studies. Under a block repeated loading, the development of cracks depends on the sequence of changes in the maximum loads. Inside each block, longitudinal cracks in the concrete of a compressed zone also develop as in constant cyclic loading mode. Distinctive features are manifested at the time of change of loading mode.

Under block loading with a sequential increase in maximum load, they developed at a higher speed than at the previous stage with a lower load value in the initial stage, and then the rate of development of cracks slows down.

The sequence and pattern of the development of cracks in the concrete of the compressed zone of the beams are shown in Fig. 2.

Under block cyclic loading with a decreasing level of maximum load of the cycle after a decrease in the load during a certain number of cycles, the crack does not develop; there is a slight decrease in the opening crack. After the “delay time”, the further development of a crack with significantly lower speeds begins. The patterns of the development of longitudinal cracks in the compressed zone coincide with

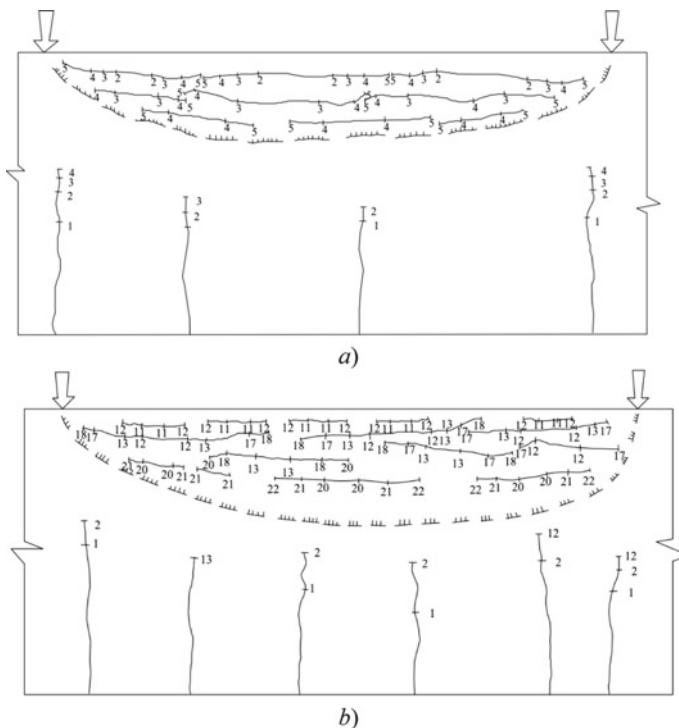


Fig. 2 Picture of the formation and development of normal cracks in the stretched area and horizontal cracks in the concrete of the compressed zone: **a** with stationary cyclic loading; **b** with a regime non-stationary cyclic load

the patterns of development of concrete deformations of the compressed zone, and characterize a decrease in concrete strength under multiple repeated loading.

It is known that the formation and development of micro- and macro cracks leads to a change in the shape of the power output of the compressed part of the cross-section from the triangular to the curved (approaching rectangular) at the destruction stage. The results of experimental studies confirm this provision that the development of longitudinal cracks leads to the transformation of the stress of concrete stresses of the compressed zone from the rectangular triangle. In the nature of the destruction of the beams according to the concrete of the compressed zone at a static and repeated load, there is a small difference, which consists in different values of the height of the compressed zone during destruction, under cyclic loading; the height of the compressed zone has a large value. Moreover, the lower the level of load during destruction, the greater the height of the destruction zone [11–15].

Under repeated loading, there was an increase in the deformations of concrete of the compressed zone throughout the tests. First, we consider the development of concrete deformations with constant values of loading parameters.

With stable characteristics of cyclic loading, the deformation of the compressed part of the cross-section developed during the tests. The main part of the deformations of compressed concrete was manifested in the initial loading cycles. The patterns of changes in the deformations of the compressed part of concrete with an increase in the number of loading cycles are shown in Fig. 3. According to these graphs, you can see an increase in deformations and the dependence of the development rate on the level of the maximum load of the cycle.

The final deformations of the compressed part of the concrete when the limit state is reached depend on the value of the maximum load of the cycle. In the case of high values of the maximum load of the cycle of concrete deformation of the compressed part of the cross-section and at the moment of reaching the fatigue limit of the beams had the limit values. So, for beams tested at the levels of maximum load $\gamma = 0.735; 0.653; 0.71; 0.9; 0.85$ final deformations reached $2.85 \cdot 10^{-3}; 2.78 \cdot 10^{-3}; 2.75 \cdot 10^{-3}; 2.65 \cdot 10^{-3}; 3.1 \cdot 10^{-3}$. The results obtained show that under repeated loads,

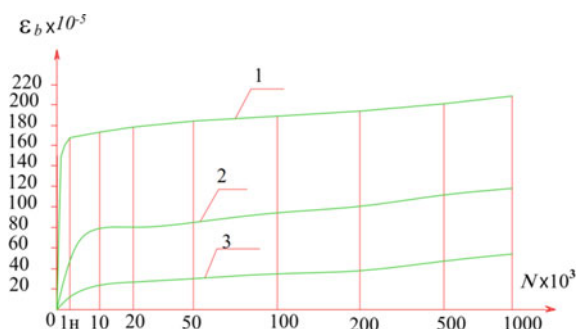


Fig. 3 The nature of the development of concrete deformations of the compressed zone on the upper fibers with constant parameters of cyclic loading. 1—with M_{max} ; 2—with M_{min} ; 3—at $m = 0$

the maximum condition of the beams along the compressed part of the cross section reaches the limit values of deformations for the compressed concrete zone. This is explained by a change in the shape of the stress diagram in the compressed zone due to the development of longitudinal micro and macro cracks and turning off part of the upper fibers from the work. After the formation of a continuous crack of separation, there is a slight decrease in the deformations of the extreme compressed fibers.

With low values of the maximum load of the cycle in the concrete of the compressed zone, the limit values of deformations are not achieved. For example, for beams, where $\gamma = 0.52$, $\gamma = 0.571$ deformations during the destruction are $186 \cdot 10^{-5}$ and $202 \cdot 10^{-5}$, which is significantly less than the limiting deformation for beams tested at high load values.

Under the action of repeated loads, the curves of deformations also change efficiently. The patterns of changes in the deformations of the upper fiber of concrete during load are shown in Fig. 4B. The specified dependencies are built on the basis of data of static step loads to the maximum load of the cycle after a certain amount of loading and unloading. So, for the deformation of the upper fiber of the beam at the first loading cycle, the diagram $M - \varepsilon$ convex, with $n = 104$ cycles—straightforward, and with $n = 105$ cycles it becomes concave. A change in convex dependence into straightforward occurs due to the fact that under repeated loading, most of the unprofitable deformations accumulate and concrete begins to deform elastically. The second change is the transition of the rectangular diagram of $M - \varepsilon$, into the concave associated with the development of the non-linear part of the deformations of the vibration creep of the compressed part of the cross-section.

These graphs show that an increase in the complete deformations of concrete of the compressed zone occurs due to the development of their unnecessary (irrevocable) component. Concrete deformations for one cycle from zero to the maximum load value with an increase in the amount of loads change slightly. In this case, an increase in nonelastic deformations occurs in the initial period of repeated loads. For example, after 104 loading cycles, the increase in nonelastic deformations decreases, however, an increase in these deformations with less intensity continues further.

The accumulation of non-linear deformations of concrete of the compressed part of the cross section in the initial stress stage is caused by the development of linear deformations of vibrational creep. An increase in nonlinear deformations of concrete of compressed part of the cross-section depends on the development of micro- and macro cracks in the compressed part of the cross section.

Based on the analysis of the dependencies of the development of concrete deformations of the compressed zone, it can be concluded that the change in the form of the graph $M - \varepsilon$ allows predicting the nature of the destruction of reinforced concrete beams.

With sequentially increasing and decreasing multiple-repeated cyclic loads, the graphs of deformations change quantitatively and qualitatively. The schedules of the deformations at the top of the compressed zone of the beam cross-section show that under the first static loading the diagram $M - \varepsilon$ convex relative to the axis of deformation, with $n = 20, 103$ cycles—straightforward, and with 105 cycles becomes concave.

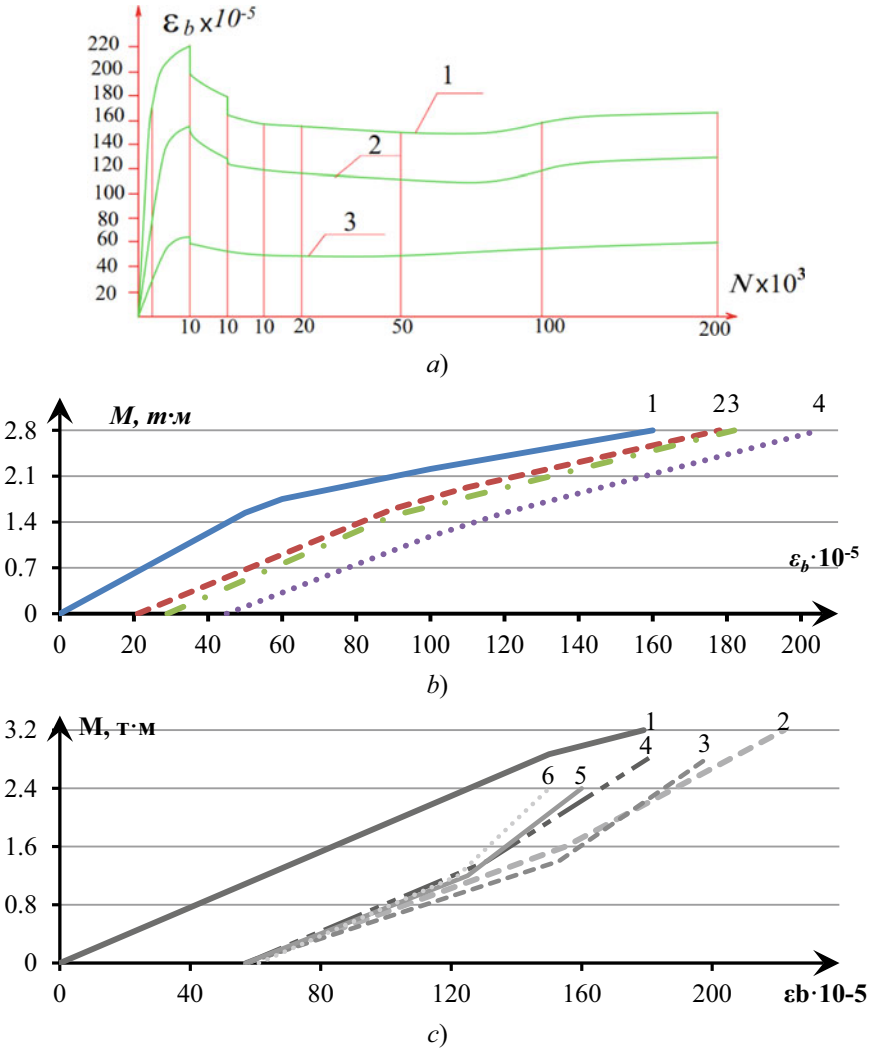


Fig. 4. a The patterns of changes in concrete deformations at the upper level with a sequential decreasing regime. 1—with M_{max} ; 2—with M_{min} ; 3—at $m = 0$; **b** the patterns of changes in the deformations of concrete of the compressed zone at various stages of loading: 1— $n = 1$; 2— $n = 104$; 3— $n = 5 \cdot 104$; 4— $n = 106$; **c** the patterns of the nature of the deformation of concrete of the compressed zone at various stages of loading: 1— $n = 1$; 2— $n = 104$; 3— $n = 1$; 4— $n = 104$; 5— $n = 1$; 6— $n = 2 \cdot 105$

4 Discussion

These graphic dependencies are consistent with the patterns of development of deformations in the coordinates $\varepsilon - N$. Within the limits of each block, an increase in complete deformations of concrete of the compressed zone occurs due to an increase in the nonelastic part. Elastic deformations within one cycle change little. An increase in nonelastic deformations is most noticeably manifested in the initial stages of loading within the first block, which is associated with the compression of the gel component of concrete, at the next stages there is a stabilization of deformations.

The accumulation of complete deformations of concrete of the compressed part of the cross section with a sequentially decreasing mode of block loading was observed at all stages of the test. The patterns of manifestation of concrete deformations of the compressed part of the cross section with an increase in the amount of loads are shown in Fig. 4c. Figure 4 shows that in the first loading unit, the development of concrete deformation of the compressed part of the cross section was similar to the development of deformations when loading with stable characteristics. At the time of reducing the load in subsequent blocks, relative stabilization of deformations is observed within the loading unit. These processes are repeated during subsequent blocks after the maximum load of the cycle is reduced.

The number of cycles during this period and the patterns of development of deformations depend on the load of the load and the number of cycles in this block: the larger the load difference, the greater the number of cycles without the development of deformations and the degree of decrease in deformations. Under the action of a multiple repeating load with decreased maximum load, a change in diagrams $m - \varepsilon$, associated with the nature of the deformation of concrete of the compressed zone. High-quality transformations of the deformation diagram in coordinates $M - \varepsilon$ on different loading blocks as the number of loading cycles increases, characterize the degree of consumption of the plastic resource of the material and the degree of development of micro- and macro cracks in the body of concrete of the compressed zone.

5 Conclusion

1. The experimental studies of 48 reinforced concrete beams on the action of repeated loads of the stationary and non-stationary modes made it possible to establish the following basic patterns of behavior of these structures under load:
2. When the parameters adopted by repeated load, the destruction of reinforced concrete beams using concrete of medium strength with high values of the reinforcement coefficient occurred along the concrete of the compressed zone due to the formation and development of micro- and macro crack of fatigue.
3. Repeated loading led to an increase in the deformation of concrete of the compressed zone during the tests regardless of the loading regime.

4. The loading mode affects the general development rate of complete concrete deformations after changing the maximum stress values in the loading blocks.

References

1. Atutis, E., Valivonis, J., Atutis, M.: Deflection determination method for BFRP prestressed concrete beams under fatigue loading. *Comp. Struct.* **226**, 111182 (2019)
2. Kim, G., Loreto, G., Kim, J.Y., Kurtis, K.E., Wall, J.J., Jacobs, L.J.: In situ nonlinear ultrasonic technique for monitoring microcracking in concrete subjected to creep and cyclic loading. *Ultrasonics* **88**, 64–71 (2018)
3. Li, Q., Liu, M., Lu, Z., Deng, X.: Creep model of high-strength high-performance concrete under cyclic loading. *J. Wuhan Univ. Technol. Sci. Ed.* **34**, 622–629 (2019)
4. Chen, P., Zhou, X., Zheng, W., Wang, Y., Bao, B.: Influence of high sustained loads and longitudinal reinforcement on long-term deformation of reinforced concrete beams. *J. Build. Eng.* **30**, 101241 (2020)
5. Bouziadi, F., Boulekbache, B., Haddi, A., Hamrat, M., Djelal, C.: Finite element modeling of creep behavior of FRP-externally strengthened reinforced concrete beams. *Eng. Struct.* **204**, 109908 (2020)
6. Mirsayapov, I.T.: Detection of stress concentration regions in cyclic loading by the heat monitoring method. *Mech. Solids* **45**, 133–139 (2010)
7. Song, L., Fan, Z., Hou, J.: Experimental and analytical investigation of the fatigue flexural behavior of corroded reinforced concrete beams. *Int. J. Concr. Struct. Mater.* **13**, 1–14 (2019)
8. Zamaliev, F.S., Zakirov, M.A.: Stress-strain state of a steel-reinforced concrete slab under long-term. *Mag. Civil Eng.* **7**, 12–23 (2018)
9. Tang, H., Chen, Z., Avinesh, O., Guo, H., Meng, Z., Engler-Pinto, C., Kang, H.: Notch insensitivity in fatigue failure of chopped carbon fiber chip-reinforced composites using experimental and computational analysis. *Compos. Struct.* **10**, 112280 (2020)
10. Mirsayapov, I.T., Garifullin, D.R.: Engineering methods for calculating elastic modulus deformations and limits of concrete endurance under cyclic loading. *News KSUAE* **53**, 15–26 (2020)
11. Mirsayapov, I.T., Garifullin, D.R.: Stress-strain state of normal sections of reinforced concrete elements under cyclic inelastic deformation of reinforcement. *News KSUAE* **54**, 44–53 (2020)
12. Augeard, E., Ferrier, E., Michel, L.: Mechanical behavior of timber-concrete composite members under cyclic loading and creep. *Eng. Struct.* **210**, 110289 (2020)
13. Trekin, N.N., Kodysh, E.N., Mamin, A.N., Trekin, D.N., Onana, J.: Improving methods of evaluating the crack resistance of concrete structures. *ACI Spec. Publ.* **326**, 93 (2018)
14. Liang, J., Nie, X., Masud, M., Li, J., Mo, Y.L.: A study on the simulation method for fatigue damage behavior of reinforced concrete structures. *Eng. Struct.* **150**, 25–38 (2017)
15. Zhang, G., Zhang, Y., Zhou, Y.: Fatigue tests of concrete slabs reinforced with stainless steel bars. *Adv. Mater. Sci. Eng.* (2018)

Bearing Capacity of a Glass Facade Systems, Including Stiffness of Nodes and Work of Filling



Alexander Galyamichev 

Abstract The paper presents a study made on the stress–strain state of mullion-transom glass facade under the action of uniformly distributed load simulating wind impact. Structural systems with various parameters were modeled and analyzed in Finite Element software package. Obtained results were compared with experimental investigation performed on full-size fragments of facade system. Dependencies allowed to evaluate the influence of changing parameters on the results and select the calculation scheme which reveals the operation of facade system in a more accurate way. The filling’s contribution to overall stiffness was described. The methods for determination of the joint stiffness of the connection between adjacent transoms and for analytical calculation of inner efforts and deflections were developed.

Keywords Glass · Facade · Mullion-transom · Hinge · Multi-span beam

1 Introduction

The use of translucent enclosing structures in civil and industrial construction is one of the most effective ways to create aesthetically attractive buildings. Nowadays glass facades have become indispensable part of contemporary architecture [1]. Such facades have many advantages, e.g., ensuring the required level of natural lighting, visual contact with the environment, ease of cleaning [2, 3]. Modern types of glass offer energy efficient properties, significantly decreasing an overall energy consumption of buildings [4].

Due to the aforementioned advantages, facade systems became extremely popular in Russian construction practice. However, their development and application are complicated by the discrepancy between existing regulatory documents and modern requirements together with construction technologies. The lack of research made on the calculation model’s interpretation complicates the designer’s task of providing and justifying a solid and stable system. For example, no open access guidelines or

A. Galyamichev (✉)

Peter the Great St. Petersburg Polytechnic University, Polytechnicheskaya 29, 195251 St. Petersburg, Russia
e-mail: gav@spbstu.ru

sufficient data on calculation of complex structures with facade cladding made of glass, such as translucent structures with a continuous scheme, are provided. The choice of a calculation scheme remains one of the critical factors for the correct calculations [5].

Structural issues of facade cladding are studied in [6]. Article [7] presents finite element modeling and experimental verification of glass curtain wall system. Many researches are dedicated to the studies on the influence of different types of fastening on the behavior of the glass structure [8–11].

The study [12] investigates methods of effective lighting and minimization of energy consumption through the use of facade glazing. The article provides an overview of high-performance glazing, adaptive electric and artificial lighting that can be used to reduce the energy demand of buildings. The potential of double-glazed facades is analyzed in [13].

Issues related to the use of glass in engineering play a significant role in the design process and therefore should be considered at all stages of a project [14]. Particularities of the material (e.g. high compressive strength, chemical resistance, hardness) make it preferential over more conventional options, however fragility, presence of material flaws and other factors limit its application. Fatigue crack behavior in tempered glass during microcrack growth is discussed in [15].

The review of numerous design documentation shows that existing methods for assessing the stress–strain state of the mullion-transom facade systems do not consider the stiffness of the joints. The relevance of this paper is justified by the need of assessment of the actual operation of the multi-span design scheme of the glass facade system, as well as comparative analysis with the design scheme commonly used in construction practice nowadays.

The lateral wind load in absence of thermal loading represents the predominant exposure on the members of facade system. Numerous papers represent the investigation of wind load effects on the building envelope [16–20].

This paper includes experimental and numerical investigations. The modeling of structure was performed by means of Finite Element Method, commonly used for the design of enclosing structures [21, 22].

The purpose of this research was a determination of the stress–strain state of the glass facade system subjected to lateral wind loading.

Following tasks were carried out:

- Development of testing procedure and test bench for mullion-transom system under the action of a uniformly distributed load;
- Measurement of deflections at characteristic points of a structure;
- Proposal of several numerical models for describing the behavior of a system;
- Comparison and analysis of static calculation results;
- Limit state analysis.
- Development of analytical method for determination of inner efforts.

The subject of the research was the stress–strain state of the full-size fragment of a mullion-transom facade under the action of a uniformly distributed load.

2 Methods

2.1 Experimental Study

The experiments were performed in order to access the deflections of characteristic points of structure. The test setup and experimental scheme were designed to simulate the most unfavorable type of impact corresponding to negative wind pressure. Horizontal arrangement of the bench was justified by low influence of in-plane loads on the stress–strain of the system.

Test samples with dimensions of 5730 × 1850 mm (two-span system) and 2730 × 1850 mm (one-span system) were subjected to testing. The distance between mullions was 900 mm, and the step of installation of the brackets and mullion’s fixators was 3000 mm (Figs. 1 and 2).

Brackets of the facade fragment were securely fastened to the supporting base in order to eliminate the influence of the fastening features on the experimental results. Supporting base consisted of load-bearing high-rigidity transverse frames.

Deflections in characteristic points of the system were measured at 6 points of the structure by mechanical dial indicators 6-PAO with following characteristics:

- Graduation: 0.01 mm;
- Maximum value of measurement: 100 ± 0.5 mm;
- Accuracy in the interval [0...1 mm]: ±0.03;
- Accuracy in the interval [0...10 mm]: ±0.3.

Characteristic points are shown in Figs. 1 and 2. The location was chosen in order to collect the data for the most unfavorable position of structural members.

Before the start of the test, an inspection control of the mounted structures was carried out and the position and the number of mounted fasteners were checked

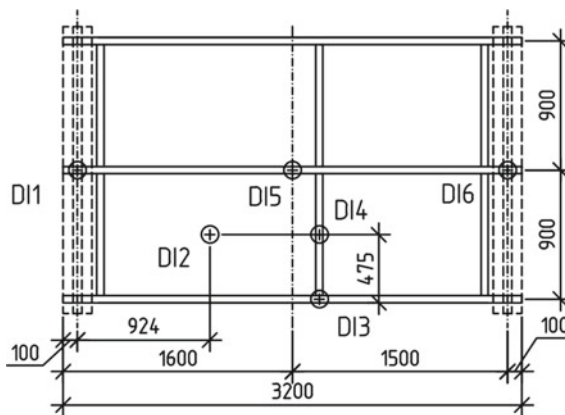


Fig. 1 Location of dial indicators installed on the one-span system

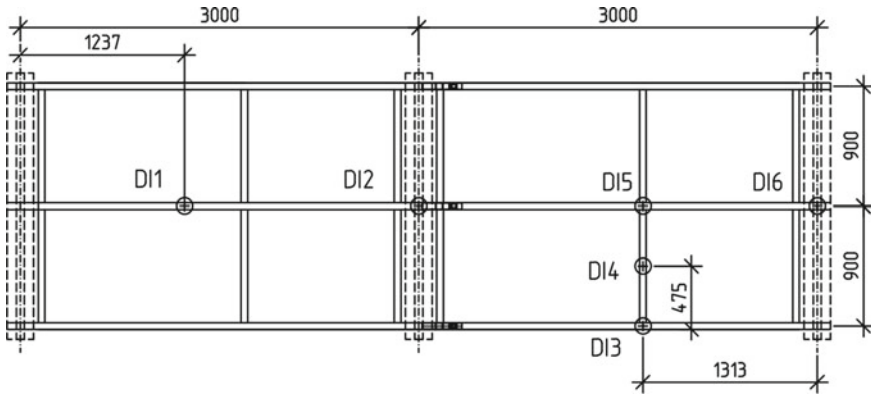


Fig. 2 Location of dial indicators installed on the two-span system

using measuring tools. The frame elements of the system were checked for initial deformations, defects, and dents.

A uniformly distributed load was applied by means of fine crushed stone packed in marked containers of 7.5 kg. The initial load of 80 kg/m² was applied in order to eliminate structural backlash, then the sample was unloaded, and subsequent stages were recorded together with readings of dial indicators. The maximum load step was assumed as 50 kg/m². The tests continued until the start of yield (Figs. 3 and 4).

The results of laboratory tests were processed, and the relative deflection in the central mullion was found as the difference between the deflection in the center of mullion and half-sum of the deflection in the supports.



Fig. 3 Distribution of unit loads over the fragment of facade system

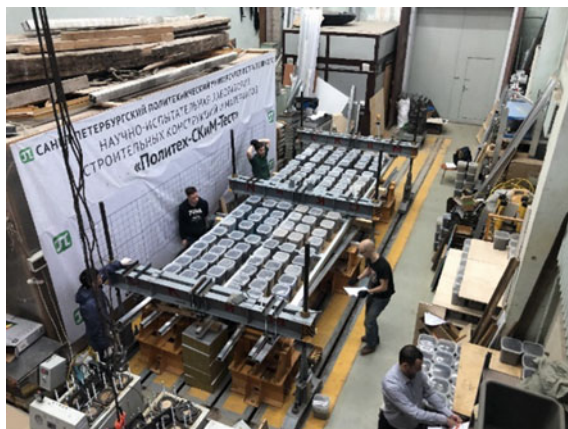


Fig. 4 Test set-up

2.2 Numerical Study

Fragments of the facade system were modeled in FEM-based SCAD Office 21.1 software package. Geometric characteristics of 1D finite elements were obtained in a satellite software SCAD Consul 21.1.

The frame of a system was composed of aluminum alloy AlMg0.7Si 6063 T6, which had characteristics as follows from Russian Standard GOST 22233-2018 «Extruded profiles from aluminum alloys for building envelopes. Technical conditions»:

- Design resistance: 135 MPa;
- Modulus of elasticity: 70 GPa;
- Poisson's ratio: 0.3.

According to Russian Standard GOST 30698-2014 «Tempered glass. Specifications», glass had the following properties:

- Design resistance: 120 MPa;
- Modulus of elasticity: 70 GPa;
- Poisson's ratio: 0.2.

The thickness of the glass panel in the given fragment of facade system was 6 mm.

The wind load acting on a mullion-transom facade is perceived by the mullion, which then transmits it to the load-bearing elements of a building. The wind load is applied perpendicularly to the glass filling, and it is uniformly distributed over its entire area.

The glass filling was simulated through 2D finite elements with thickness of 6 mm. In this case in numerical model the wind load was applied directly to glass panels.

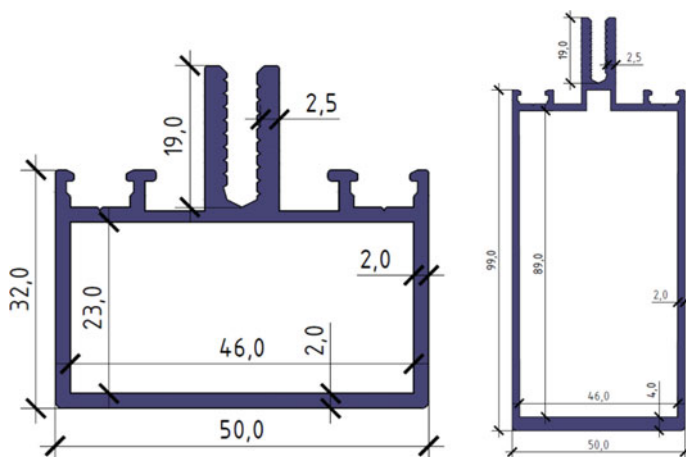


Fig. 5 Cross-sections of a transom (left) and mullion (right) profiles

When no glass filling was accounted in the finite element model, the load was at first recalculated in a form of linearly distributed and then applied to the aluminum members of a frame. The load application was done in accordance with [23] (Fig. 6).

One-Span System

The general view of the design model, with introduced boundary conditions and hinges, is shown in Figs. 7, 8 and 9.

Two-Span System

To assess the convergence of the results of laboratory tests and numerical modeling, several variants of simplified design schemes were considered (Figs. 10, 11, 12, 13, 14, 15, 16, 17 and Fig. 18).

In the design scheme no. 4, the connection of the profiles in vertical direction (at the expansion joint) was modeled by means of an embedded part, located at the junction of two profiles and at the distance of 25 mm from the central axis of the mullion. This embedded part was attached to the mullion using rigid bodies of two types, connecting the corresponding nodes of the transom profile and the embedded part. The bending stiffness of the embedded part was obtained as a result of several iterations: a model with certain value of stiffness was calculated, then the deflection of the central mullion was compared to the experimental study, and based on it the stiffness was adjusted. The operation was repeated until the convergence appeared (Fig. 19).

Limit State Requirements

According to Russian Set of Rules 128.13330.2012 «Aluminum Structures», ULS condition in considered case can be read as follows:

$$N/A_{ef} + M/W_{ef, x} \leq R \quad (1)$$

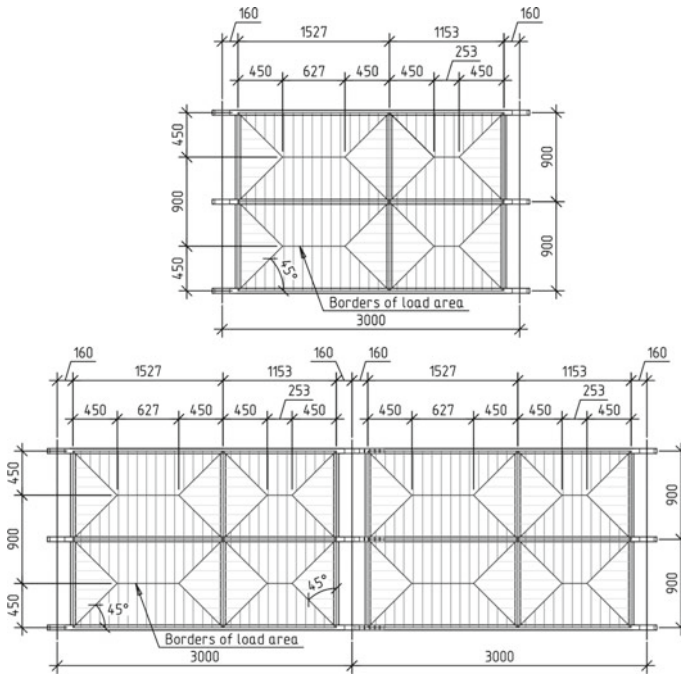


Fig. 6 Load distribution (left—one-span scheme; right—two-span scheme)

where

N is longitudinal force in the element;

M is a bending moment in the element;

A_{ef} is effective cross-section's area;

$W_{ef, x}$ is effective cross-section's moment of inertia;

R is a design resistance of aluminum to bending, compression, tension.

SLS condition was set in accordance with Russian Set of Rules 20.13330.2016 «Loads and actions»:

$$f \leq f_{limit} \tag{2}$$

where f is an actual deflection of element;

f_{limit} is a maximum allowable deflection:

$$f_{limit} = L/150$$

where L is a distance between the nearest supports.

However, Russian Set of Rules 426.1325800.2018 «The translucent facade of buildings and structures. Design rules» specifies maximum allowable deflection as:

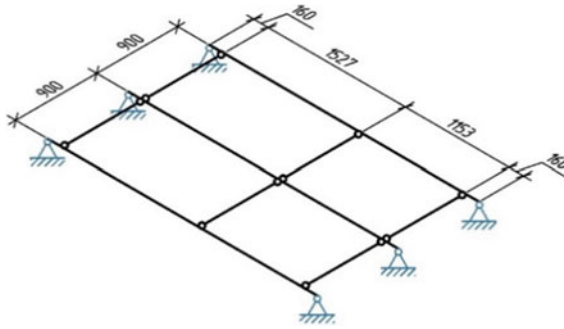


Fig. 7 Calculation scheme of a one-span scheme

$$f_{\text{limit}} = L/200$$

3 Results and Discussion

3.1 Experimental Study

Based on the readings of dial indicators, the following graphs of the dependences between deflection at characteristic points and corresponding value of uniformly distributed load were obtained.

One-Span System

See Figs. 20 and 21.

Two-Span System

See Fig. 22.

3.2 Numerical Study

On the basis of an experimental study of expansion joint, the bending stiffness of the embedded part for the **scheme without glass** was equal to:

$$EI_{y1} = 79.5 \text{ kg} \cdot \text{m}^2 \quad (3)$$

The bending stiffness of the embedded part for the **scheme with glass** was equal to:

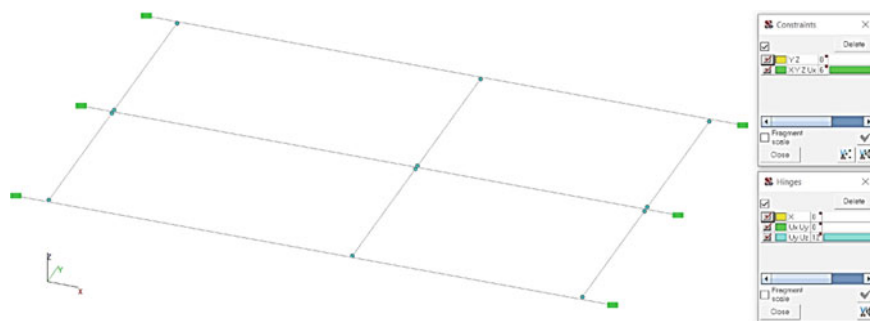


Fig. 8 Numerical model of a one-span scheme (without glass)

$$EI_{y2} = 70 \text{ kg} \cdot \text{m}^2 \quad (4)$$

As a result of the static calculation, the deflection values of the center of the central mullion were obtained. The graphs showing the dependencies between deflection of the central mullion of system and value of uniformly distributed load were processed for each type of considered structural schemes on the base of performed static calculation and laboratory tests (Figs. 23, 24 and 25).

It can be concluded that the results of numerical calculation lay below the experimental values for most of cases (except scheme no. 2), which makes it possible to apply the proposed models for practical calculations and to evaluate the stress–strain state of a given design solution using Finite Element Method.

It should be noted that the calculation results obtained when accounting the glass filling demonstrate increase of the rigidity of the system, however they also lead to higher labor costs. At the same time it allows to assess the stresses and deflections of the translucent filling itself; it can be needed at the stage of detailed design (Figs. 26 and 27).

Under loads corresponding to the onset of SLS, fragments of structures did not undergo the critical changes, also when the deflection reached the value of $L/150$. When the design is performed under the requirements of Russian Sets of Rules and Russian national building codes, for assessment of SLS assumption of a maximum allowable deflection equal to $L/200$ of the distance between the nearest supports is preferable. The value of $L/150$ of the distance between the nearest supports can be used if necessary justification of design solution for a specific project is provided.

3.3 Methodology of Analytical Calculation

For the purpose of analytical calculation of the considered design solution and determination of the maximum inner efforts and deflections in one-span and multi-span

(from 2 to 5 spans) design schemes, taking into account the previously given rigidity of the expansion joint, specific coefficients for the classical formulas were obtained.

In Fig. 28 q refers to linearly distributed load.

The expansion joint of the mullions was located at a distance:

$$a = 0.053L = 0.158 \text{ m} \tag{5}$$

The final bending stiffness of the embedded part was taken equal to:

$$EI_y = 70 \text{ kg} \cdot \text{m}^2 \tag{6}$$

Thus, the deflections of the adjusted numerical model were equal to ones obtained during tests. At the same time, the deflections of the mullion in each span can be found by the formula:

$$f = \chi_3 \cdot q^n \cdot L^4 / EI_x \tag{7}$$

The bending moment can be calculated by the following expression:

$$M = \chi_1 \cdot q \cdot L^2 \tag{8}$$

The transverse forces in the guide profile can be read as:

$$Q = \chi_2 \cdot q \cdot L \tag{9}$$

Coefficients χ_1, χ_2, χ_3 depend on the position of the section under consideration and on the span in which the inner effort (moment or transverse force) is located. The geometrical characteristics of cross-section of mullion and embedded part, the introduction of glass filling into calculation also directly contribute to values of coefficients, and, therefore, to the values of moments, loads and deflections. For the profiles shown in Fig. 5, the coefficients are shown in Table 1.

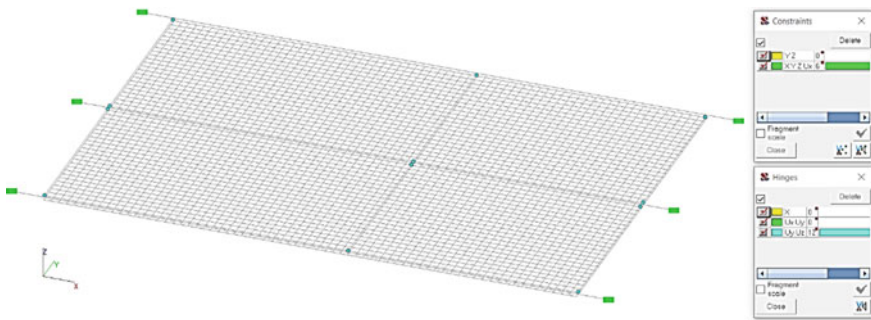


Fig. 9 Numerical model of a one-span scheme (with glass)

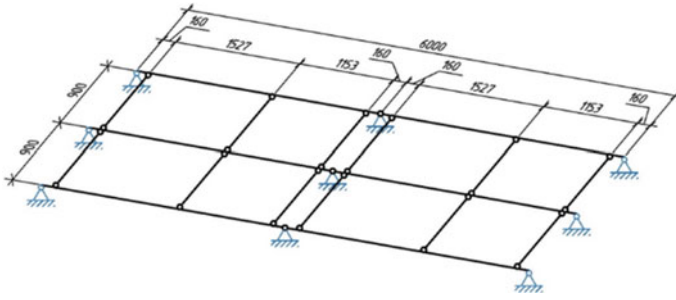


Fig. 10 Calculation scheme no. 1 of a two-span scheme (with central hinge)

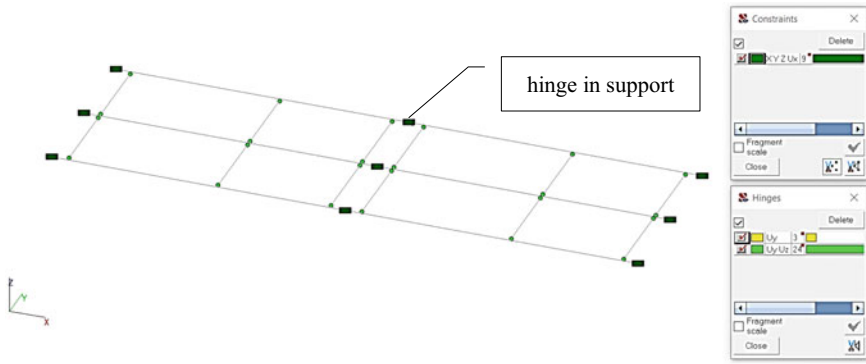


Fig. 11 Numerical model no. 1 of a two-span scheme (with central hinge)

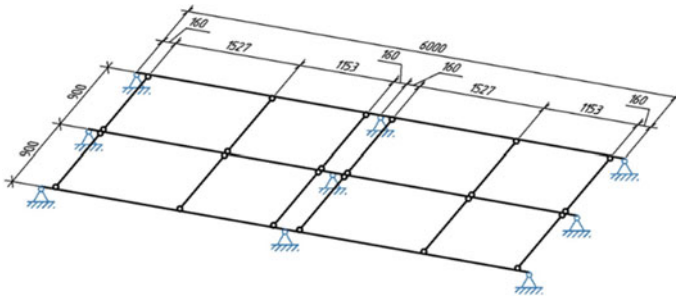


Fig. 12 Calculation scheme no. 2 of a two-span scheme (without central hinge)

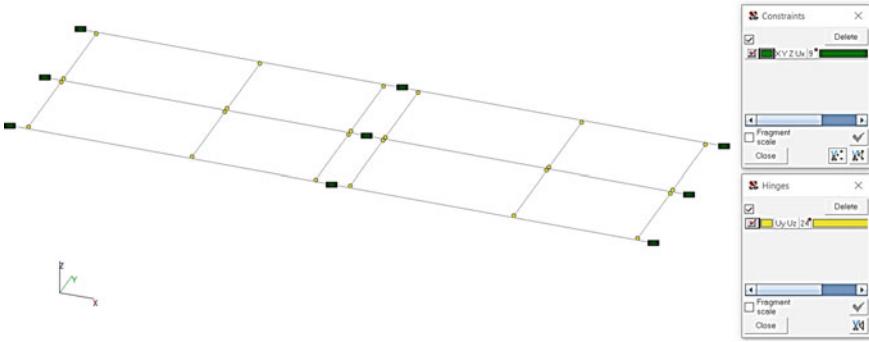


Fig. 13 Numerical model no. 2 of a two-span scheme (without central hinge)

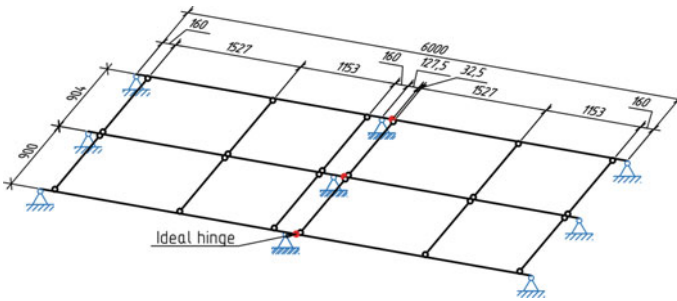


Fig. 14 Calculation scheme no. 3 of a two-span scheme (with an ideal linear and angular hinge in the connector)

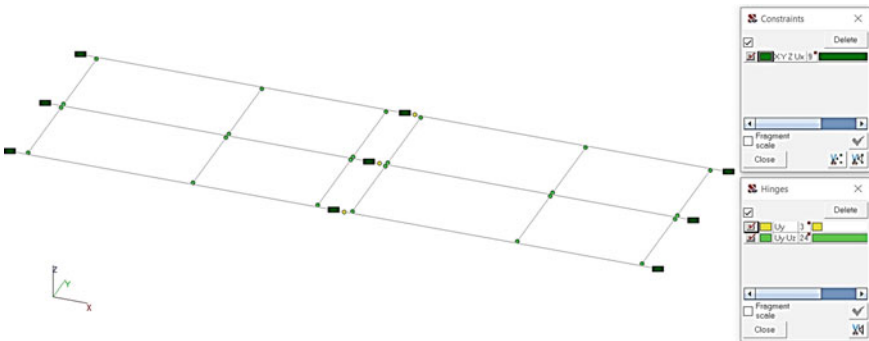


Fig. 15 Numerical model no. 3 of a two-span scheme (with an ideal linear and angular hinge in the connector)

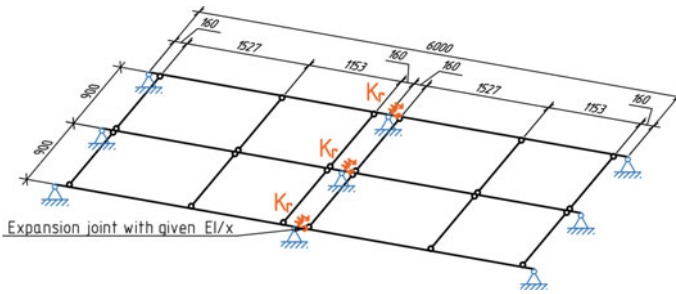


Fig. 16 Calculation scheme for no. 4 and no. 5 of a two-span scheme (with embedded part simulating the stiffness of expansion joint)

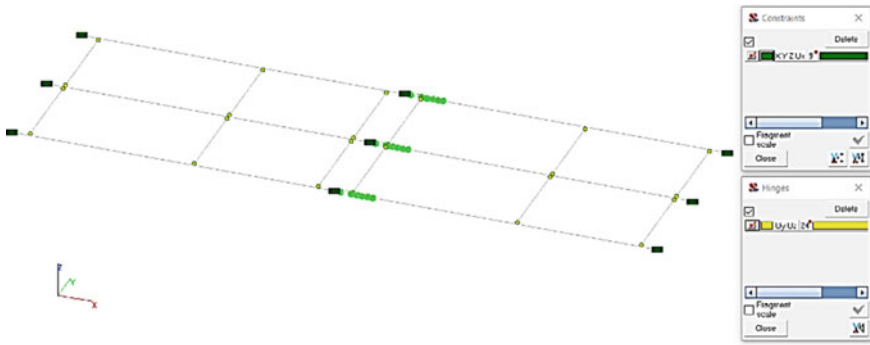


Fig. 17 Numerical model no. 4 of a two-span scheme (without glass and with embedded part simulating the stiffness of expansion joint)

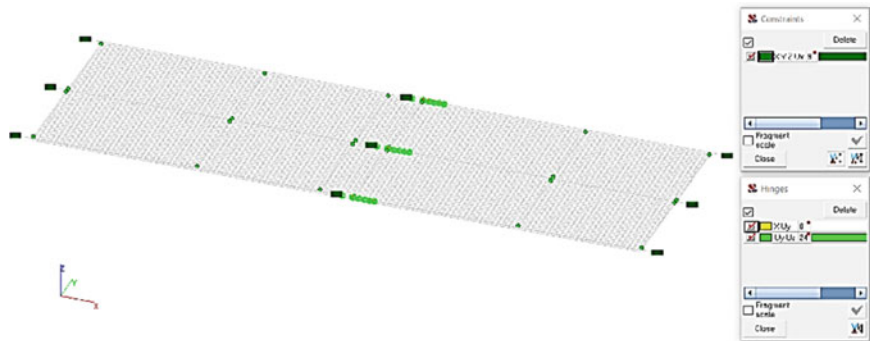


Fig. 18 Numerical model no. 5 of a two-span scheme (with glass and embedded part simulating the stiffness of expansion joint)

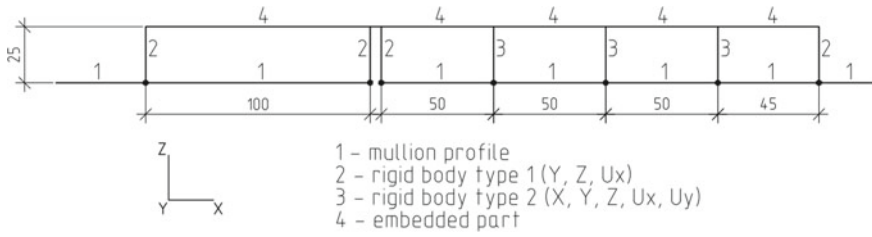


Fig. 19 Simulation of the expansion joint

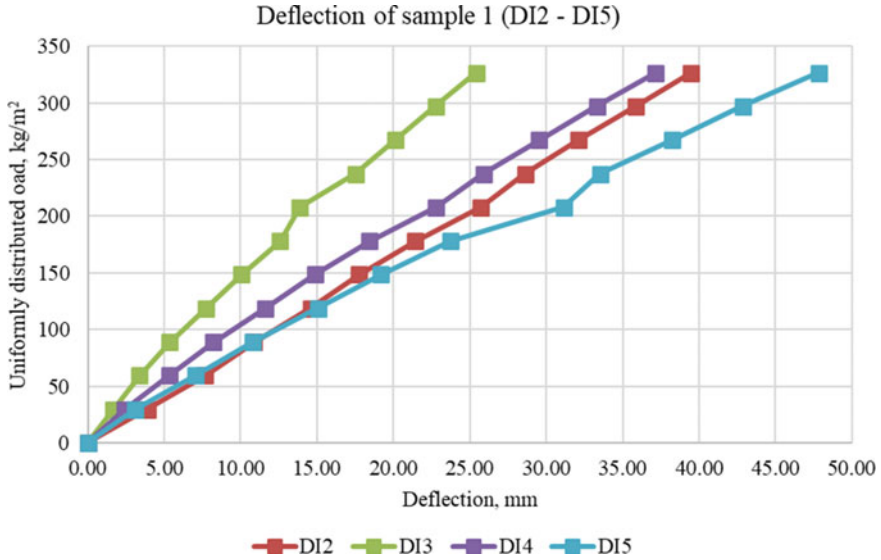


Fig. 20 Deflection of characteristic points (DI2–DI5) of one-span system

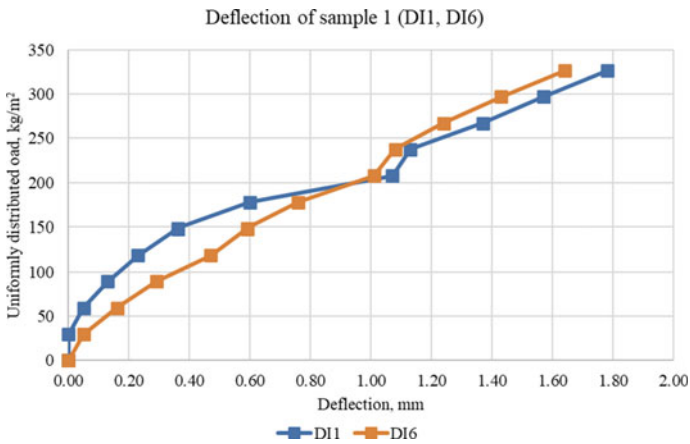


Fig. 21 Deflection of characteristic points (DI1, DI6) of one-span system

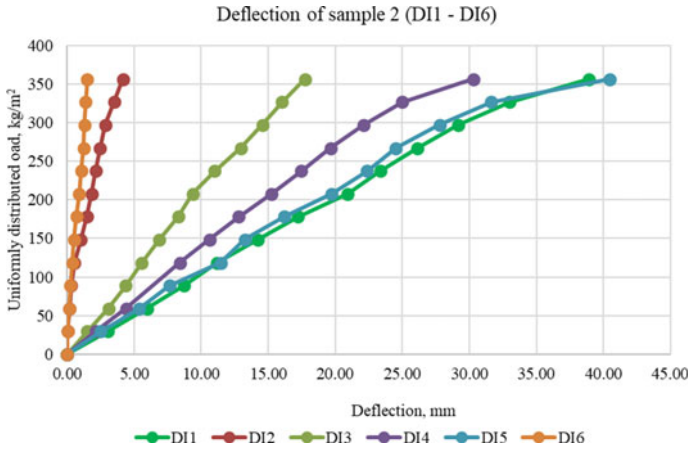


Fig. 22 Deflection of characteristic points (DI1–DI6) of two-span system

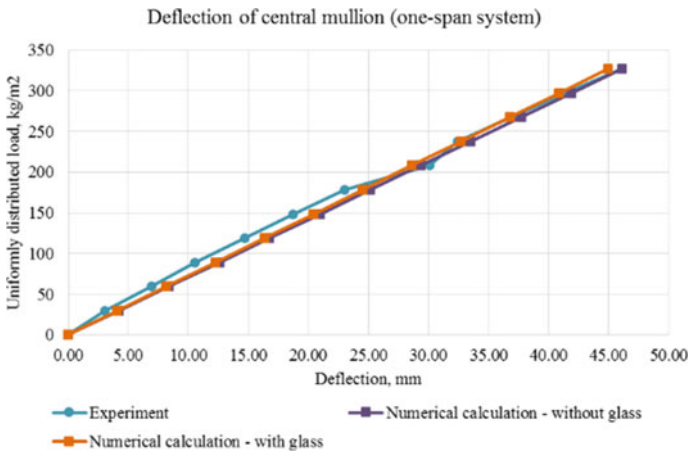


Fig. 23 Deflection of the central mullion (one-span system)

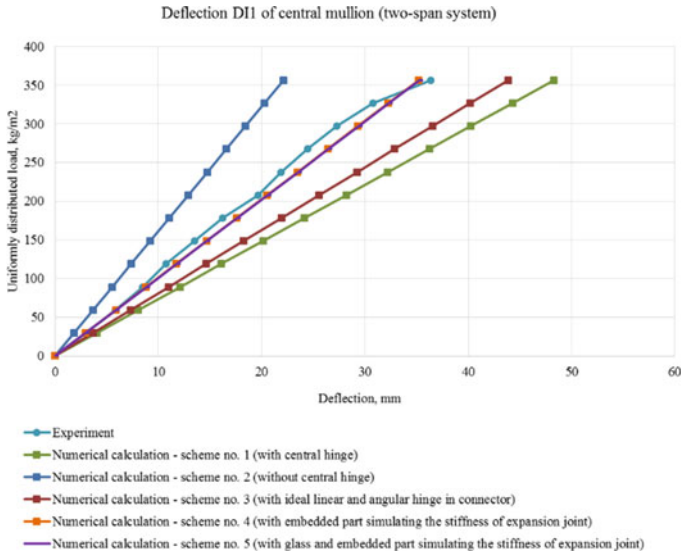


Fig. 24 Deflection DI1 of the central mullion (two-span system, without glass)

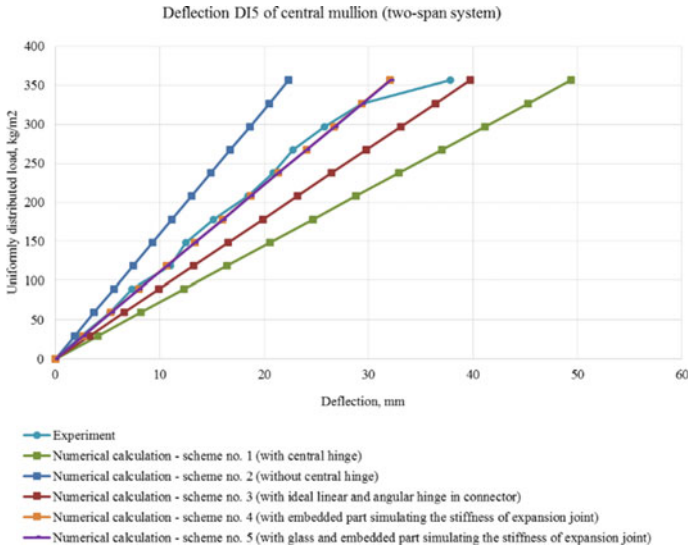


Fig. 25 Deflection DI5 of the central mullion (two-span system)

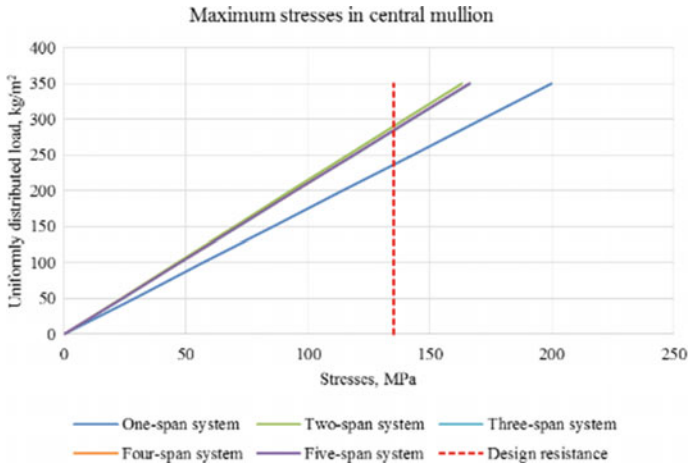


Fig. 26 Maximum stresses arising in central mullion

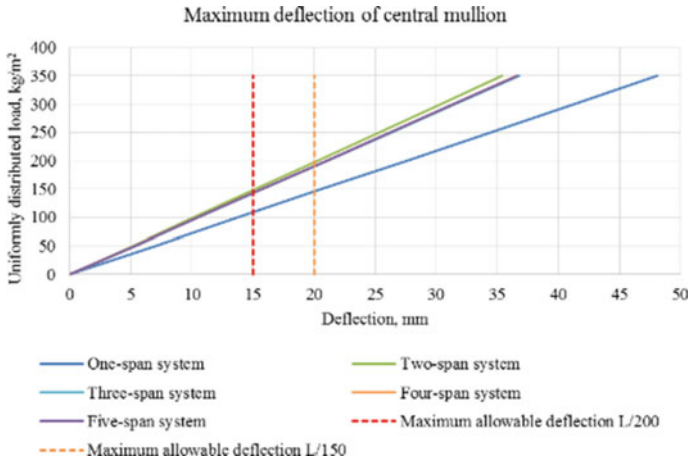


Fig. 27 Maximum deflections of central mullion

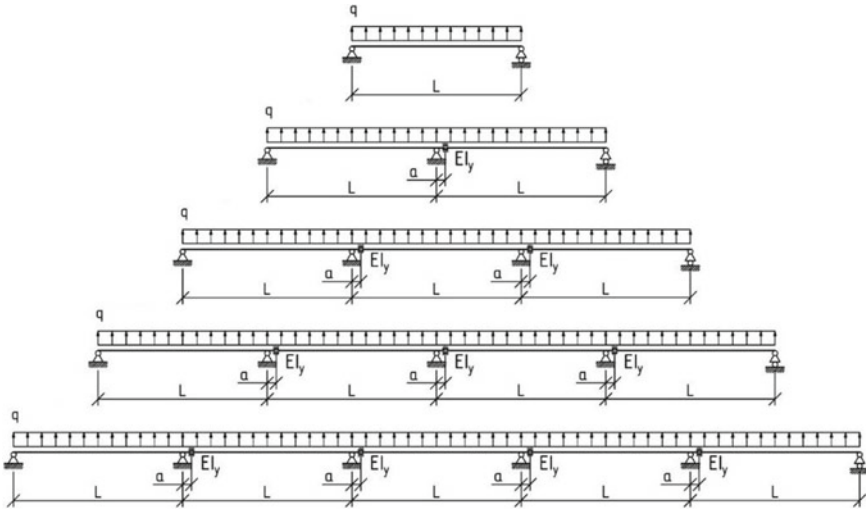


Fig. 28 Design diagrams of mullion profile (arranged horizontally for convenience)

4 Conclusions

The described methods of experimental and numerical investigation obtained in the course of this study can be used for design and calculation of transom-mullion glass facade systems. Following conclusions were drawn on the base of performed tests and calculations:

1. The method for determination of the joint stiffness of the connection between adjacent transoms was proposed.
2. Actual calculation scheme of mullion-transom glass facade system refers to the multi-span beam with joint of controlled rigidity in the location of expansion joint.
3. The stress–strain state of mullion-transom glass facade systems is directly influenced by the rigidity of the connection between bracket and transom profile, and expansion joint between adjacent transoms, as well as the glass filling of the system.
4. In mullion-transom facades it is recommended to locate the expansion joint in areas with a bending moment close to zero.
5. In order to increase the rigidity of the system, it is recommended to use two- or multi-bolt joint solutions for attachment of mullions to brackets to increase the system's rigidity as SLS is a determining factor for given design solution.
6. While designing the facade system, it is recommended to develop a mullion-to-bracket joint with controlled rigidity, as it will bring the system closer to the ULS and SLS criteria and thus minimize metal consumption due to the optimal design scheme of structural elements

Table 1 Coefficients χ_1, χ_2, χ_3

Span number	Value	Coefficient	Coefficients χ_1, χ_2, χ_3 depending on design scheme				
			1	2	3	4	5
Bending moments $M = \chi_1 \cdot q \cdot L^2, \text{kg/m}^2$							
1	$M_{left\ support}$	χ_1	0	0	0	0	0
	M_{span}		-0.125	-0.0965	-0.0995	-0.0991	-0.0992
	$M_{right\ support}$		0	0.0607	0.0539	0.0548	0.0546
2	$M_{left\ support}$		-	0.0607	0.0539	0.0548	0.0546
	M_{span}		-	-0.0965	-0.0706	-0.0737	-0.0733
	$M_{right\ support}$		-	0	0.0548	0.0479	0.0487
3	$M_{left\ support}$		-	-	0.0548	0.0479	0.0487
	M_{span}		-	-	-0.0991	-0.0733	-0.0763
	$M_{right\ support}$		-	-	0	0.0556	0.0486
4	$M_{left\ support}$		-	-	-	0.0556	0.0486
	M_{span}		-	-	-	-0.0987	-0.0729
	$M_{right\ support}$		-	-	-	0	0.0555
5	$M_{left\ support}$		-	-	-	-	0.0555
	M_{span}		-	-	-	-	-0.0988
	$M_{right\ support}$		-	-	-	-	0
Transverse force $Q = \chi_2 \cdot q \cdot L, \text{kg}$							
1	Q_{left}	χ_2	0.5	0.439	0.446	0.445	0.445
	Q_{right}		-0.5	-0.561	-0.554	-0.555	-0.555
2	Q_{left}		-	0.559	0.498	0.505	0.504
	Q_{right}		-	-0.439	-0.501	-0.493	-0.494
3	Q_{left}		-	-	0.553	0.491	0.499
	Q_{right}		-	-	-0.445	-0.508	-0.500
4	Q_{left}		-	-	-	0.554	0.492
	Q_{right}		-	-	-	-0.444	-0.507
5	Q_{left}		-	-	-	-	0.554
	Q_{right}		-	-	-	-	-0.444
Span number	Value	Coefficient	Coefficients χ_1, χ_2, χ_3 depending on design scheme				
			1	2	3	4	5
Deflection $f = \chi_3 \cdot q_n \cdot L^4/EI_x, \text{mm}$							
1	-	χ_3	0.01302	0.00926	0.00968	0.00963	0.00963
2	-		-	0.00817	0.00519	0.00557	0.00553
3	-		-	-	0.00870	0.00571	0.00608
4	-		-	-	-	0.00863	0.00565
5	-		-	-	-	-	0.00864

7. Coefficients of empirical formulas for analytical calculation of inner efforts and deflections in the aluminum frame of a mullion-transom glass facade were proposed for specific profiles shown in Fig. 5.

Acknowledgements The research group would like to thank company Casting-Extrusion Plant «Segal» for providing the samples of SIAL mullion-transom glass facade system.

References

1. Roginska-Niesluchowska, M.: Use of daylight and aesthetic image of glass facades in contemporary buildings. In: IOP Conference Series: Materials Science and Engineering (2017). <https://doi.org/10.1088/1757-899X/245/8/082035>
2. Pariafsai, F.: A review of design considerations in glass buildings. *Front. Archit. Res.* **5**, 171–193 (2016). <https://doi.org/10.1016/j.foar.2016.01.006>
3. Laufs, W., Luible, A.: Introduction on use of glass in modern buildings. *Rapp. ICOM.* (2003)
4. Jin, Q., Overend, M.: A comparative study on high-performance glazing for office buildings. *Intell. Build. Int.* **9**, 181–203 (2017). <https://doi.org/10.1080/17508975.2015.1130681>
5. Galyamichev, A.: Comparative analysis of the classical and structural ways of fastening the glazing to the aluminium facade substructure. *Svetoprozrachnye Konstr.* **3**, 44–51 (2017)
6. Mazzucchelli, E.S., Angelo, L., Tattoni, S., Stefanazzi, A.: Analysis and control of façade claddings structural issues. *Tema Technol. Eng. Mater. Archit.* **3**, 88–100 (2017). <https://doi.org/10.17410/tema.v3i1.120>
7. Memari, A.M., Shirazi, A., Kremer, P.A.: Static finite element analysis of architectural glass curtain walls under in-plane loads and corresponding full-scale test. *Struct. Eng. Mech.* **25**, 365–382 (2007). <https://doi.org/10.12989/sem.2007.25.4.365>
8. Bernard, F., Daudeville, L.: Point fixings in annealed and tempered glass structures: modeling and optimization of bolted connections. *Eng. Struct.* **31**, 946–955 (2009). <https://doi.org/10.1016/J.ENGSTRUCT.2008.12.004>
9. Bedon, C., Amadio, C.: Buckling analysis and design proposal for 2-side supported double Insulated Glass Units (IGUs) in compression. *Eng. Struct.* **168**, 23–34 (2018). <https://doi.org/10.1016/j.engstruct.2018.04.055>
10. Sivanerupan, S., Wilson, J., Gad, E., Lam, N.: Drift performance of point fixed glass façade systems. *Adv. Struct. Eng.* **17**, 1481–1495 (2014). <https://doi.org/10.1260/1369-4332.17.10.1481>
11. Sivanerupan, S., Wilson, J.L., Gad, E.F., Lam, N.T.K.: Analytical study of point fixed glass façade systems under monotonic in-plane loading. *Adv. Struct. Eng.* **19**, 611–626 (2016). <https://doi.org/10.1177/1369433216630192>
12. Raj, N., Charde, D.: Smart Technology used for active daylighting techniques mainly based on smart windows, artificial lighting and daylight harvesting. Presented at the (2018)
13. Pérez-Grande, I., Meseguer, J., Alonso, G.: Influence of glass properties on the performance of double-glazed facades. *Appl. Therm. Eng.* **25**, 3163–3175 (2005). <https://doi.org/10.1016/j.applthermaleng.2005.04.004>
14. Honfi, D., Reith, A., Vigh, L.G., Stocker, G.: Why glass structures fail? - Learning from failures of glass structures. In: Proceedings of the Challenging Glass 4 and Cost Action TU0905 Final Conference, pp. 791–800 (2014)
15. Tokunaga, H., Ikeda, K., Kaizu, K., Kinoshita, H.: The fatigue crack growth behavior in thermally tempered glass by the growth of indentation-induced microcracks. *J. Solid Mech. Mater. Eng.* **1**, 577–583 (2007). <https://doi.org/10.1299/jmmp.1.577>

16. Bedon, C., Zhang, X., Santos, F., Honfi, D., Kozłowski, M., Arrigoni, M., Figuli, L., Lange, D.: Performance of structural glass facades under extreme loads – design methods, existing research, current issues and trends. *Constr. Build. Mater.* **163**, 921–937 (2018). <https://doi.org/10.1016/j.conbuildmat.2017.12.153>
17. Zolotareva, L., Lebedinskaya, A., Komarova, S.: Analysis of wind load impact on the high-rise buildings glass facade. *IOP Conf. Ser. Mater. Sci. Eng.* **698** (2019). <https://doi.org/10.1088/1757-899X/698/2/022046>
18. Lu, W., Wang, Y., Chen, H., Jiang, L., Duan, Q., Li, M., Wang, Q., Sun, J.: Investigation of the thermal response and breakage mechanism of point-supported glass facade under wind load. *Constr. Build. Mater.* **186**, 635–643 (2018). <https://doi.org/10.1016/j.conbuildmat.2018.07.114>
19. Nijssse, R.: Glass walls carrying the roof and withstanding the wind load on the façade: conservatory of the museum in Dordrecht and Raaks glass cube in Haarlem. In: *Challenging Glass 3: Conference on Architectural and Structural Applications of Glass, CGC 2012*, pp. 111–120 (2012). <https://doi.org/10.3233/978-1-61499-061-1-111>
20. Lou, W., Zhang, M.: Test of wind load characteristics of cylindrical building with double-skin facade. *Huazhong Keji Daxue Xuebao (Ziran Kexue Ban)/J. Huazhong Univ. Sci. Technol. (Natural Sci. Ed.)* **37**, 90–93 (2009)
21. Lalin, V.V., Rybakov, V.A.: The finite elements for design of building walling made of thin-walled beams. *Mag. Civ. Eng.* **8**, 69–80 (2011). <https://doi.org/10.5862/MCE.26.11>
22. Maskaleva, V., Rybakov, V.: The analysis of convergence of finite element method for a foundation slab on the bilinear subgrade. *Appl. Mech. Mater.* 842–847 (2015)
23. Gerasimova, E., Galyamichev, A., Dogru, S.: Stress-strain state of insulated glass unit in structural glazing systems. *Mag. Civ. Eng.* **98**(9808) (2020). <https://doi.org/10.18720/MCE.98.8>

Regularities for Resistance of Supply and Exhaust Ventilation Cross Junctions



Arslan Ziganshin , Timur Karimullin , Emil Yagfarov ,
and Konstantin Logachev 

Abstract Today the problem of designing and constructing of energy efficient ventilation system is relevant. One of the ways to decrease energy consumption of such system is to use the outlines of vortex zones to create shaped fitting elements. To develop this idea, a study of numerical models of supply and exhaust crosses is being carried out. The dependences of their local drag coefficients (for the passage in the forward direction and for the side branch) are determined when the ratio of the air flow through the side branch to the total flow rate is in the range from 0.1 to 0.45. The study is carried out numerically, with a detailed comparison with known experimental data on the resistance of such crosses. For diverging (supply) crosses, well-known sources recommend using data on the resistance of tees. For converging (exhaust) crosses, there are data on local drag coefficients for crosses. A qualitative agreement was obtained for the behavior of the local drag coefficients, but at the same time, a quantitative difference in the determined dependencies was also obtained. Next, a study of the outlines of the vortex zones will be carried out and the resulting numerical model will be used to determine them in the entire range of changes in the air flow ratio, as well as to develop designs for energy-efficient shaped crosses.

Keywords Ventilation cross junctions · Numerical study · Local drag coefficient · Validation

1 Introduction

Today, the issue of reducing the energy consumption of engineering systems of buildings, including ventilation systems, which account for 11–14% in the total share of energy costs in buildings [1–3], is topical. Therefore, much attention is

A. Ziganshin (✉) · T. Karimullin · E. Yagfarov
Kazan State University of Architecture and Engineering, Zelenaya Street, 1,
420043 Kazan, Russia
e-mail: ziganshin.arslan@gmail.com

K. Logachev
Belgorod State Technological University named after V.G. Shukhov, Kostyukov Street, 46,
308012 Belgorod, Russia

paid to improving the efficiency of ventilation systems, both in terms of creating the most efficient air distribution [4–6], and when transporting air through ventilation ductworks. It is important as well as for the civil as for the industrial buildings where the numerous kind of ventilation systems, and its efficiency had straight influence to the efficiency of pollutant capture [7] and cleaning [8, 9] devices operating.

There are various ways to reduce the aerodynamic resistance of fitting elements of ventilation systems. For example, for ventilation elbows, tees and diffusers, bionic (biomimetic) structures are being developed, where the walls of fitting elements are shaped according to outlines taken from wildlife—the attachment of a branch to a plant trunk [10], river bends [11, 12] and the human larynx [13]. The possibility of reducing the resistance in this way is shown. However, the resulting design leads to an increase in the size of the fitting element. Another direction is the installation of guiding and separating vanes [14–17], which also lead to some reduction in resistance, but this complicates the design and, accordingly, increases the cost of the fitting element. Such shortcomings are deprived of a method for reducing resistance by shaping the wall of a fitting element along the outlines of the vortex zones.

This method showed a significant reduction in resistance for such fittings as tees [18], elbows [19, 20] and exhaust openings of various configurations [21–23], but for its use it is necessary to determine the outlines of the vortex zones and their dependence on the regime and design parameters for the improved fitting element.

The article presents the results of the continuation of the study, the beginning of which is described in [24] and which shows the stages of verification and validation of the flow in the supply and exhaust equilateral cross junctions (Fig. 1). Here, a study is made of the effect on the resistance of the crosses of a change in the ratio of air flow rates flowing along the side branch (G_B) to the total air flow rate (G_T).

In [25], data on the change of the local drag coefficients (LDC) for supply and exhaust crosses are given when G_B/G_T changes in the range from 0 to 1. For the supply diverging crosses, it is indicated that data for the supply tee can be used approximately. At the same time, it should be noted that the data for the LDC on the side branch (ζ_B) for the tee are indicated depending on the ratio of not the flow rates, but the velocities u_B/u_T , and for the LDC on the straight direction passing through the cross (ζ_S) are given in the usual form—depending on the ratio of flow rates, moreover, it is the flow rate in the side branch to the total flow rate— G_B/G_T . This leads to some uncertainty, since, for example, with $G_B/G_T = 0.5$, for a tee it means $G_S/G_T = 0.5$ and $G_B = G_S$, that is, equal flow rates for branches during diverging. At the same time, for the cross $G_B/G_T = 0.5$ means that $G_S/G_T = 0$, that is, the absence of flow in the straight direction. Therefore, the case $G_B/G_T = 0.5$ for a tee, apparently, corresponds to the case $G_B/G_T = 1/3$ for a cross, when the cross also has the equality of flows in a side branch and to the passage in a straight direction $G_B = G_S$.

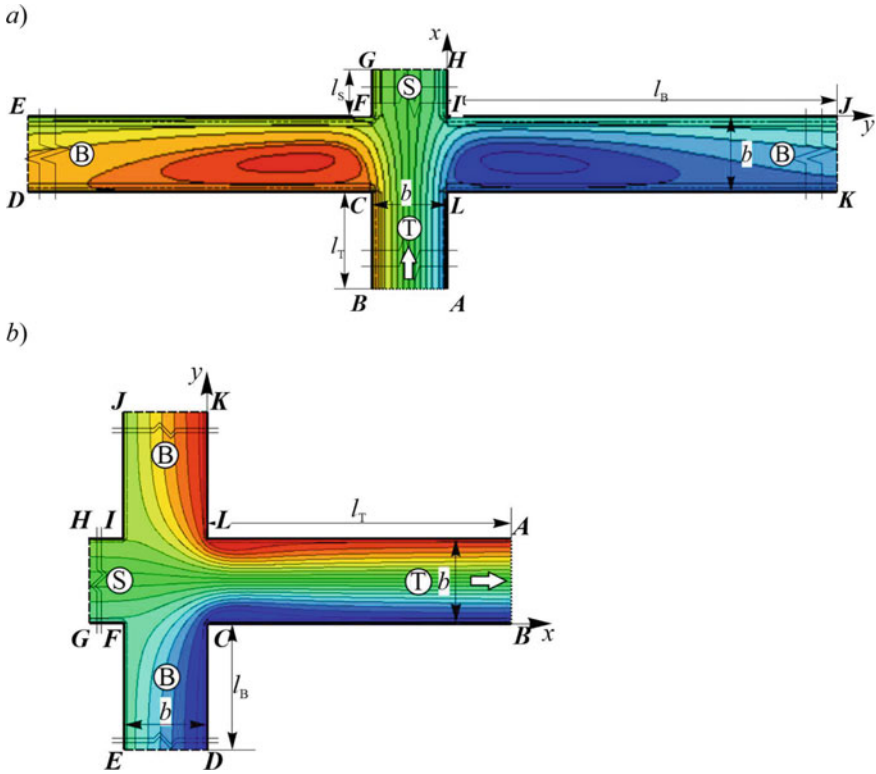


Fig. 1 The geometry of the studied problem and the flow streamline at $G_B/G_O = 0.275$ for supply **a** and at $G_B/G_O = 0.356$ for exhaust crosses **b**

2 Methods

The problem was solved numerically using the Ansys Fluent software package in a two-dimensional turbulent formulation. The previously found combination of the standard $k - \epsilon$ turbulence model and enhanced wall treatment for near-wall modeling [24] was used for the study. The boundary conditions (BC) of the problem are defined as follows: section **AB** is the inflow (Fig. 1a) or the exhaust (Fig. 1b) boundary with a flow velocity value $u_0 = 30$ m/s (BC “velocity-inlet”), sections **DE**, **GH** and **JK**—free boundaries through which air flows out of the supply cross (Fig. 1a) or flows into the exhaust cross (Fig. 1b)—BC “pressure-outlet” or “pressure-inlet” respectively, with excess pressure set to zero, the remaining boundaries are impermeable walls—BC “wall”. The geometry was constructed using the Gambit software. The main dimensions of the cross: $b = 0.1$ m; $l_T = 2$ m; $l_B = l_S = 8$ m for the supply and $l_B = l_S = 2$ m; $l_T = 8$ m for the exhaust.

In the numerical solution of all solved problems, all stages of the study of the grid dependence were carried out, the dimensions of the computational grid accepted

as final were 4.76×10^{-5} m, and their total number was about 5.3 million, the dimensionless distance y^+ according to this method of near-wall modeling [26] was about 1.

Determination of the LDC values was carried out according to the previously developed and tested method [27]. For this, cross sections were built in all channels every 0.05 m (0.5b). Based on the results of the numerical solution, further in these sections, the values of the total pressure averaged over the flow rate were determined— P_B , P_S , P_T , (respectively, in the branches and in the straight channel). Using this pressure distribution along the length, the values of the average specific pressure drop R were determined. With its help, the pressure drop due to friction in the corresponding channel was found: $\Delta P^{fr} = R \cdot l$, where R and l are the specific pressure losses and the lengths of the corresponding channels [28].

The values of the local drag coefficient (LDC) were determined by the formulas:

$$\zeta_B = \frac{P_B - P_S - \Delta P_B^{fr} - \Delta P_S^{fr}}{(\rho u_0^2/2)} - \text{for the branch}; \quad (1)$$

$$\zeta_S = \frac{P_S - P_T - \Delta P_S^{fr} - \Delta P_T^{fr}}{(\rho u_0^2/2)} - \text{for the straight direction}. \quad (2)$$

Since a symmetric flow was modeled in the cross junction, the LDC values of two side branches were equal to each other up to the third decimal place; $\rho = 1.225 \text{ kg/m}^3$ —air density.

3 Results and Discussion

It is interesting to analyze the dependence of ζ_S for a tee. In [29], a numerical study was carried out using a previously validated computer model [30]. The obtained LDC values were compared with known reference data [25] and experiments [31]. These results, together with the LDC data for the cross, are shown in Fig. 2.

It can be seen that in the handbook [25] with $G_B/G_T < 0.5$, $\zeta_S < 0$, which is explained by the separation of the boundary layer slowly flowing along the solid wall, and, accordingly, the increase in the specific energy of the flow passing in the forward direction. In this case, for $G_B/G_T > 0.5$, ζ_S is already greater than zero and, accordingly, it is assumed that the point of transition ζ_S through zero corresponds to $G_B/G_T = 0.5$.

However, it is clear that for a tee that has the same dimensions for all legs, flow going in the forward direction and losing half the flow in the side branch will experience impact losses as the flow expands. Therefore, the data [29, 31] seem more plausible, where $\zeta_S = 0$ at $G_B/G_T < 0.5$. The change in ζ_B for all three authors is similar, although the data of the handbook [25] here again differ from the data of

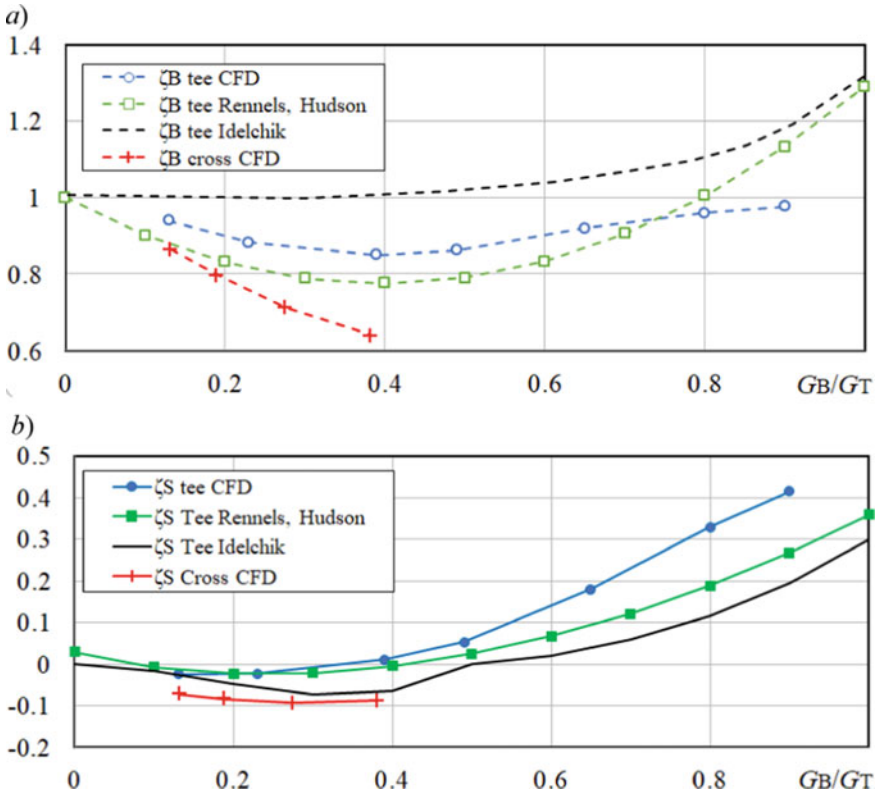


Fig. 2 Dependence of ζ_S and ζ_B on G_B/G_T for diverging (supply) cross

[29, 31], which agree well with each other. Which may indicate a difference in the conduct of experiments.

Obtained numerically and shown in Fig. 2 values of ζ_S and ζ_B for the diverging (supply) cross at different ratios G_B/G_T were obtained by changing the excess static pressure at the boundaries of the channels of the cross and are given in Table 1. Since symmetrical cases are studied when the both of side branches have the same conditions—pressure (P) and therefore, the flow rates (G), then the corresponding values are marked with a subscript “B”—a lateral branch (for both branches), and a channel with a common (total) flow rate (before separation in the supply cross, or after merging in the exhaust cross) is marked with the index “T”. The direct channel, where the flow is located before the merging in the exhaust cross or after diverging in the supple cross, is indicated by the index “S”. The superscript “st” indicates a static pressure.

Based on the results of a similar study, the dependences of the change in ζ_S and ζ_B for the converging (exhaust) cross were obtained. Here, in contrast to the supply one, in [25] the corresponding dependences for the resistance of the cross are given, which

Table 1 The pressure values at the boundaries of the crosses and G_B/G_O , ζ_{II} , ζ_B

Converging cross (exhaust)					Dividing cross (supply)				
P_B^{st} , Pa	P_S^{st} , Pa	G_B/G_T	ζ_S	ζ_B	P_B^{st} , Pa	P_S^{st} , Pa	G_B/G_T	ζ_S	ζ_B
-450	0	0.0813	0.229	-0.467	0	0	0.132	-0.0714	0.865
-300	0	0.153	0.357	-0.116	-15	0	0.189	-0.0836	0.799
-135	0	0.249	0.457	0.243	-35	0	0.275	-0.0924	0.714
0	0	0.356	0.474	0.466	-55	0	0.381	-0.0876	0.641
60	0	0.426	0.459	0.538	-	-	-	-	-

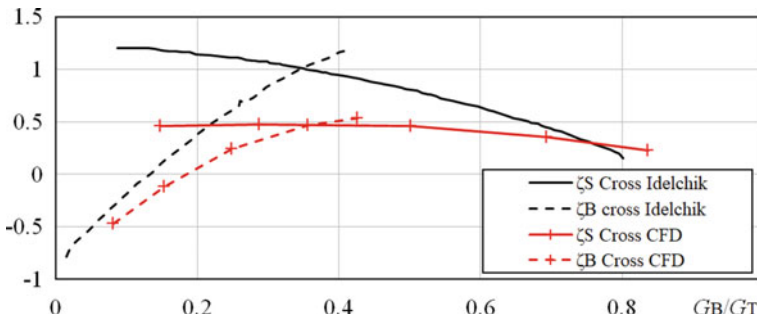


Fig. 3 Dependence of ζ_S and ζ_B on G_B/G_T for converging (exhaust) cross

are shown in Fig. 3 together with those obtained from the results of the numerical study.

It can be seen that although the general form of the dependences obtained numerically corresponds qualitatively to the data of the handbook [25], the quantitative difference varies from 10 to 50%. This can also, as in the case of the supply cross (tee), indicate a difference in the conditions of the experiment.

4 Conclusions

The results obtained indicate a fairly good qualitative agreement between the obtained numerical results and the known experimental data on the resistance of the supply and exhaust crosses. Some quantitative difference, apparently, is due to the difference in the conditions of the experiment. The constructed computer models will be further used to determine the outlines of the vortex zones, their dependencies on the flow rate ratio, with the aim of further development and research of the energy-efficient shaped designs of the supply and exhaust ventilation crosses.

Acknowledgements The research was carried out under the joint grant of the Russian Science Foundation (#23-49-00058) and NSFC (#5221101677), project “Flow Characteristics with Multiple

Vortex and Ventilation Efficiency Improvement Mechanism in the Environment of Low Carbon Building”.

References

1. LaRose, A., Cogan, J.: Annual Energy Outlook
2. Lecamwasam, L., Wilson, J., Chokolich, D.: Guide to Best Practice Maintenance & Operation of HVAC Systems for Energy Efficiency. <https://www.environment.gov.au/system/files/energy/files/hvac-factsheet-energy-breakdown.pdf>
3. Schild, P.G., Mysen, M.: Technical Note AIVC 65. Recommendations on Specific Fan Power and Fan System Efficiency. Sint-Stevens-Woluwe (2009)
4. Kareeva, J., Zakieva, R., Bliznjakova, K.: Numerical study of the influence of the inlet geometric parameters on the jet characteristics. Presented at the (2021). https://doi.org/10.1007/978-3-030-80103-8_39
5. Cao, Z., Zhang, C., Zhai, C., Wang, Y., Wang, M., Zhao, T., Lv, W., Huang, Y.: Evaluation of a novel curved vortex exhaust system for pollutant removal. *Build. Environ.* **200**, (2021). <https://doi.org/10.1016/j.buildenv.2021.107931>
6. Kareeva, J.R., Zakieva, R.R.: Verification of the numerical model of the process of jet outflow from the inlet at an angle. *News KSUAE*, 82–89 (2021). https://doi.org/10.52409/20731523_2021_4_82
7. Logachev, K.I., Ziganshin, A.M., Popov, E.N., Averkova, O.A., Kryukova, O.S., Gol'tsov, A.B.: Experiment determining pressure loss reduction using a shaped round exhaust hood. *Build. Environ.* **190**, 107572 (2021). <https://doi.org/10.1016/j.buildenv.2020.107572>
8. Belyaeva, G.I., Zamalieva, A.T., Ziganshin, M.G.: Experimental and calculated testing of the efficiency of cyclone filtering devices. *IOP Conf. Ser. Mater. Sci. Eng.* **972**, (2020). <https://doi.org/10.1088/1757-899X/972/1/012067>
9. Zamalieva, A.T., Ziganshin, M.G.: Improving energy and environmental efficiency of flue gas cleaning at thermal power plants. *IOP Conf. Ser. Earth Environ. Sci.* **288**, (2019). <https://doi.org/10.1088/1755-1315/288/1/012073>
10. Gao, R., Liu, K., Li, A., Fang, Z., Yang, Z., Cong, B.: Biomimetic duct tee for reducing the local resistance of a ventilation and air-conditioning system. *Build. Environ.* **129**, 130–141 (2018). <https://doi.org/10.1016/j.buildenv.2017.11.023>
11. Gao, R., Zhang, H., Li, A., Liu, K., Yu, S., Deng, B., Wen, S., Li, A., Zhang, H., Du, W., Deng, B.: A novel low-resistance duct tee emulating a river course. *Build. Environ.* **144**, 295–304 (2018). <https://doi.org/10.1016/j.buildenv.2018.08.034>
12. Gao, R., Wang, M., Guo, W., Zhang, S., Wen, S., Wu, D., Zhou, H., Li, A.: Study of the shape optimization of a variable diameter in a ventilation and air-conditioning duct based on the Boltzmann function. *J. Build. Eng.* **43**, (2021). <https://doi.org/10.1016/j.job.2021.102833>
13. Goeke, S., Wunsch, O.: Adjoint based topology optimization of a duct bend. *Pamm.* **19**, 2–3 (2019). <https://doi.org/10.1002/pamm.201900438>
14. Yin, Y., Li, A., Wen, X., Zhang, J., Zhang, X., Guo, J., Li, J., Zhang, W., Che, J.: Resistance reduction of an elbow with a guide vane based on the field synergy principle and viscous dissipation analysis. *J. Build. Eng.* **54**, (2022). <https://doi.org/10.1016/j.job.2022.104649>
15. Ziganshin, A., Eremina, S., Safiullina, G., Logachev, K.: Numerical study of the flow in a symmetrical ventilation junction tee with a Baffle Vane. In: *Proceedings of STCCE 2021, STCCE 2021. Lecture Notes in Civil Engineering*, pp. 213–222. Springer, Cham (2021). https://doi.org/10.1007/978-3-030-80103-8_23
16. Zhang, W., Li, A.: Resistance reduction via guide vane in dividing manifold systems with parallel pipe arrays (DMS-PPA) based on analysis of energy dissipation. *Build. Environ.* **139**, 189–198 (2018). <https://doi.org/10.1016/j.buildenv.2018.04.010>

17. Shopayeva, A., Safiullin, R.: CFD-modeling of flow in confluence nodes of ventilation units of multi-storey buildings. *IOP Conf. Ser. Mater. Sci. Eng.* **890**, (2020). <https://doi.org/10.1088/1757-899X/890/1/012157>
18. Ziganshin, A.M., Badykova, L.N.: Numerical investigation of flow in profiled ventilation tee at junction. *News High. Educ. Inst. Constr.* **702**, 41–48 (2017)
19. Ziganshin, A.M., Beljaeva, E.E., Sokolov, V.A.: Pressure losses reduction with profiling of sharp elbow and elbow with dead-end. *News High. Educ. Inst. Constr.* **697**, 108–116 (2017)
20. Ziganshin, A.M., Ozerov, A.O., Solodova, E.E.: Numerical study of flow in U-shaped elbow and reduction of its resistance. *News High. Educ. Inst. Constr.* **1**, 82–93 (2019)
21. Logachev, K.I., Ziganshin, A.M., Averkova, O.A.: On the resistance of a round exhaust hood, shaped by outlines of the vortex zones occurring at its inlet. *Build. Environ.* **151**, 338–347 (2019). <https://doi.org/10.1016/j.buildenv.2019.01.039>
22. Averkova, O.A., Logachev, I.N., Logachev, K.I., Uvarov, V.A., Ziganshin, A.M.: Features of the settlement scheme aspiration of elevator overloads. In: *Proceedings of the 6th European Conference on Computational Mechanics: Solids, Structures and Coupled Problems, ECCM 2018 and 7th European Conference on Computational Fluid Dynamics, ECFD 2018*, pp. 2638–2649 (2020)
23. Ziganshin, A.M., Batrova, K.E., Gimadieva, G.A., Logachev, K.I., Averkova, O.A.: Increase of energy efficiency of ventilation systems by means of profiling phason elements. *Constr. Ind. Saf.* **67**, 111–123 (2019)
24. Ziganshin, A.M., Karimullin, T.L., Yagfarov, E.I.: Setting a numerical solution to the problem of air flow in ventilation cross junctions. *News High. Educ. Inst. Constr.* **752**, 42–49 (2021). <https://doi.org/10.32683/0536-1052-2021-752-8-42-49>
25. Idel'chik, I.E., Steinberg, M.O.: *Handbook of Hydraulic Resistance*. CRC Press, Boca Raton (1994)
26. *Near-Wall Treatments for Wall-Bounded Turbulent Flows*. <http://www.sharcnet.ca/Software/Fluent12/html/th/node97.htm>. Accessed 03 Mar 2021
27. Logachev, K.I., Ziganshin, A.M., Averkova, O.A.: Simulations of dust dynamics around a cone hood in updraft conditions. *J. Occup. Environ. Hyg.* **15**, 715–731 (2018). <https://doi.org/10.1080/15459624.2018.1492137>
28. Posohin, V.N., Ziganshin, A.M., Mudarisov, D.I.: The influence zones of disturbing elements in pipeline systems. *News KSUAE.* **28**, 121–126 (2014)
29. Ziganshin, A.M., Safiullina, G.R., Valiullov, R.R.: The tee local drag coefficient determination: experimental for symmetric at junction and numerical for asymmetric at division. In: *Engineering Systems and Urban Economy: Materials of the 2nd Regional Scientific and Practical Conference, Saint-Petersburg*, pp. 248–256 (2020)
30. Ziganshin, A.M., Valiullov, R.R., Ibragimova, A.R.: Flow in a dividing tee - symmetric and asymmetric. In: *Materials of the International Scientific and Practical Conference of Students, Graduate Students and Young Scientists, Ekaterinburg*, pp. 155–159 (2019)
31. Rennels, D.C., Hudson, H.M.: Pipe flow. In: *Pipe Flow: A Practical and Comprehensive Guide*, p. 320. Wiley, Hoboken (2012). <https://doi.org/10.1002/9781118275276>

Load-Bearing Capacity of Raft-Pile Foundations, Taking into Account the Redistribution of Forces Between Piles During Cyclic Loading



Ilizar Mirsayapov 

Abstract The aim of the work is to study the load-bearing capacity of the raft-pile foundation under cyclic loading, taking into account the redistribution of forces between the piles. The load-bearing capacity of a raft-pile foundation under cyclic loading consists of three components: piles, soil under the raft and soil under the lower end of the piles. The sediment of pushing through the raft-pile foundation significantly changes the distribution of loads on the piles, especially on the extreme and corner ones, which are overloaded. In this article, this process is considered in three-dimensional mode, taking into account the joint deformation of all elements of the system “pile cap—piles—soil between piles—soil below the toe”. It takes into account the redistribution of forces between the elements of the system under cyclic loading due to the occurrence of deformations of the soil, pile grillage and piles in the appropriate conditions. The load-bearing capacity of the raft-pile foundation is determined for the stage when tangential stresses along the side surface are absent in the upper and middle parts of the pile as a result of reaching the maximum shear resistance. The soil is forced under the tip when the stress under the fifth pile and under the plate exceeds the fatigue strength and maximum deformations of the soil under three-axis cyclic compression. Theoretical studies are carried out and the redistribution of forces between the main elements of the raft-pile foundation is considered. The change in the stress–strain state of the base of the raft-pile foundation under cyclic loading due to the redistribution of forces between the corner, extreme and ordinary piles is considered. The significance of the results obtained for the construction industry is that for the first time the proposed method allows us to assess the load-bearing capacity of the raft-pile foundation.

Keywords Raft-pile foundation · Pile · Settlement · Soil · Cyclic loading

I. Mirsayapov (✉)
Kazan State University of Architecture and Engineering, 420043 Kazan, Russia
e-mail: mirsayapov1@mail.ru

1 Introduction

In raft-pile foundations, the side and corner piles are overloaded compared to the average piles [1–5]. At the same time, the forces of the corner piles are up to 4 times greater, and in the side piles are up to 2 times more than in the middle piles.

Cyclic loading forces are being redistributed between the piles and the surrounding soil of the pile space [6–10]. The performed studies show that with increasing loading cycles, the ultimate resistance of the soil to shear along the lateral surface of the pile decreases, which leads to an increase in stress in the soil under the pile toe and, as a consequence, to deformations increase and fatigue strength of the soil under the pile toe decrease [11–14]. If the stress in the soil exceeds the maximum resistance of the soil to the triaxial stress state in the case of cyclic loading, the soil is forced under the lower plane of the pile and the pile is moved within the conditional foundation. Then the limit state is firstly reached under the corner piles and part of the force is transferred both to the other piles by loading them and onto the soil under the raft. That means that the limit state reaches on the soil below the toe (if connection of the pile with the pile cap is not a rigid) and under the raft at the same time (if the connection of the pile with the raft is rigid). Then the limit state reaches in the side rows of piles, while there is the redistribution of forces between the corner and side piles. After piercing the soil of the conditional foundation with side and angular piles under the lower end, these piles begin to move without increasing the load on them, which leads to overloading of the average ordinary piles and an increase in their vertical movements (settlement). Such piles are called creeping. This process continues until the forces between all the piles are aligned (become the same).

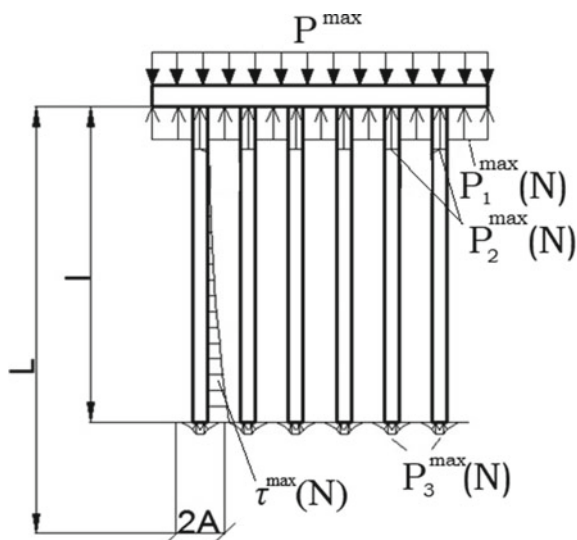
The creep of the side and corner piles leads to a change in distribution of forces on all piles of the raft-pile foundation. For an analytical description of the process of redistribution of forces between corner, side and ordinary piles of a raft-pile foundation in the process of cyclic loading it is necessary to consider the process in a spatial formulation, taking into account the joint deformation of all elements of the system because of the rigid connection of the pile and the raft.

2 Materials and methods

The creep of the side and angular piles significantly changes the distribution of loads on all piles of the raft-pile foundation. This process is considered in a spatial formulation, taking into account the joint deformation of all elements of the system “pile cap—piles—soil of the pile space—soil below the pile toe” due to the rigid connection of the pile and the pile cap (Fig. 1).

The redistribution of forces between piles within the pile cap is taken into account by jointly solving 4 quasi-static equations [15]. At the same time, the proposals of Ter-Martirosyan [16] for static loading are taken as a basis. These equations were modified by the author to take into account the effect of changes in the stress–strain

Fig. 1 The scheme of the raft-pile foundation under cyclic loading



state of the system under cyclic loading, as well as the process of redistribution of forces during the pushing of edge and corner piles. At the same time, the force in the middle piles increases by K times:

$$K(F) = \frac{4F_1 + 2F_2(n_1 + n_2)}{n_3 F_3}, \quad (1)$$

where F_1 —efforts in corner piles, F_2 —efforts in edge piles, F_3 —efforts in middle (ordinary) piles, n_1 , n_2 are the number of edge piles in the sides of the raft-pile foundation, n_3 is the number of middle (ordinary) piles in the raft-pile foundation.

The stresses in certain specific zones of the system “pile cap—piles—soil of the pile space—soil below the pile toe” are determined by jointly solving four equations depending on the number of loading cycles and cyclic loading parameters [15]. When solving the above equations, the change in the stress–strain state and forces in individual elements of the raft-pile foundation and the zone of ultimate equilibrium of the soil along the lateral surface of the piles is taken into account (Fig. 2).

The soil shear strength between the pile and the soil is calculated based on the Mohr–Coulomb law:

$$\tau^*(N) = \gamma z \cdot \tan \varphi(N) + C(N) + \Delta \sigma_x^{ad} \cdot \tan \varphi(N), \quad (2)$$

where $C(N)$ is the cohesion between soil particles under cyclic loading conditions, $\Delta \sigma_x^{ad}$ is the additional horizontal stress on the pile from the soil due to the joint deformation of the system (influence of the pile cap), $\varphi(N)$ is the angle of internal friction of soil under cyclic loading.

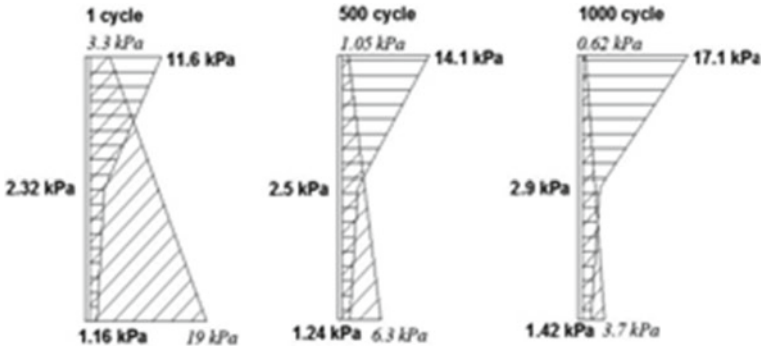


Fig. 2 Plots of mobilized shear stress and ultimate shear stress in soil along piles

The cohesion between soil particles under cyclic loading conditions is calculated based on the results of the author’s study (Mirsayapov et al. 2012, Mirsayapov and Shakirov 2016) according to the dependence:

$$c(N) = c_0 \cdot m(t_1 \tau_1) \cdot \lambda(t_1 \tau_1) \cdot \sqrt{\frac{k(\tau_1)}{k(t)} + \frac{1}{1 + k(\tau_1)}} \cdot c(t_1 \tau), \quad (3)$$

where c_0 is the adhesion between soil particles under short-term static loading.

Tangential stresses are calculated as follows:

$$\tau_0^{\max}(N) = \frac{a \cdot b(p_3(N) - p_2(N)) \cdot K(F)}{(a + b) \cdot l \cdot \frac{1}{\alpha} \cdot (4e^{-\alpha l} - 1)}. \quad (4)$$

The equations system [1] is solved for each cycle under consideration, taking into account the change in all system parameters due to the redistribution of forces between the pile cap, piles, soil in the process of cyclic loading, and taking into account the change in the ultimate equilibrium zone in the space between piles.

Stresses in the soil under the raft are calculated by the formula:

$$p_1^{\max}(N) = \frac{p^{\max} \cdot AB - p_2^{\max}(N) \cdot ab \cdot K(F)}{(AB - ab)}. \quad (5)$$

The stress in the pile section at the level of the head under cyclic loading is determined by the formula:

$$\begin{aligned}
 p_2^{\max(N)} &= [P \cdot G_{\Gamma P}(N) \cdot AB(AB - ab) \cdot L \cdot \beta_{gr} \left(1 - \frac{l}{L}\right) + 0,33 \cdot \tau_0(N) \\
 &\cdot E_{gr}(N) \cdot (A - a)(AB - ab) \cdot k_1 + 0,33 \cdot \tau_0(N) \cdot E_{gr}(B - b)(AB - ab) - 4 \\
 &\cdot \frac{K(F) \cdot \tau_0(N)}{\alpha} \cdot E_{gr}(N) \cdot l(AB - ab) \cdot \omega(1 - v_{gr}) \cdot k(l) + \frac{K(F) \cdot \tau_0(N)}{\alpha} \cdot E_{gr}(N) \cdot \frac{a + b}{b} \\
 &\cdot l(AB - ab) \cdot e^{\alpha l} \cdot \omega(1 - v_{ar}) \cdot k(l)] \cdot \\
 &\left[a \cdot \omega \cdot (1 - v_{gr}) \cdot k(l) \cdot (AB - ab) \cdot E_{gr}(N) + \right. \\
 &\left. + ab \cdot \beta_{gr} \cdot L \cdot \left(1 - \frac{l}{L}\right) \cdot G_{gr}(N) \right]^{-1}
 \end{aligned}
 \tag{6}$$

where G is the soil shear modulus under cyclic loading, $k(l)$ is the dimensionless coefficient taking into account the effect of depth application of a rigid die, l is the pile length.

The stresses in the soil under the lower end of the pile can be calculated using the formula:

$$p_3^{\max(N)} = \frac{K(F) \cdot p_2(N) \cdot 4ab + 4(a + b) \cdot l \cdot \frac{\tau_0(N) \cdot K(F)}{\alpha}}{4ab} - \frac{4(a + b) \cdot l \cdot \frac{\tau_0(N)}{\alpha} \cdot e^{-\alpha l}}{4ab}
 \tag{7}$$

The bearing capacity of the subgrade of the raft-pile foundation under cyclic loading at the calculated time ($t = N$) depending on the ratio $\tau_0(N) \leq \tau^*(N)$ is estimated based on the conditions for two zones (Fig. 3):

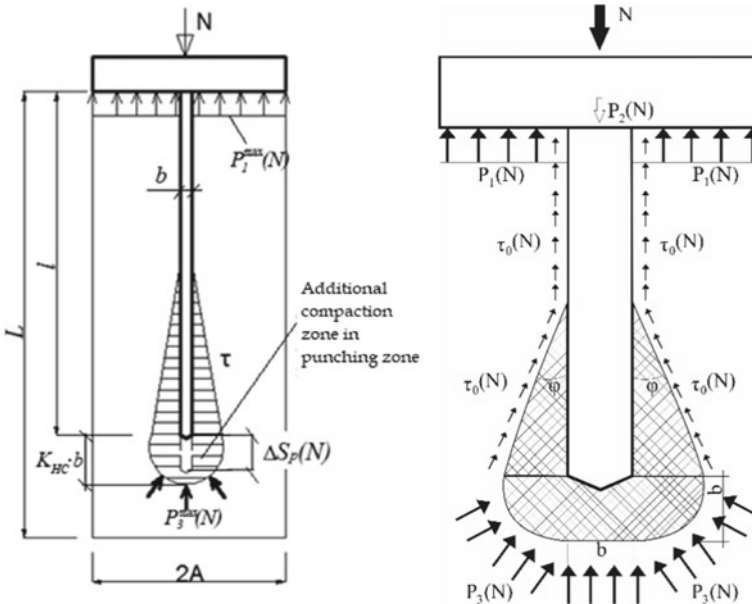


Fig. 3 The scheme of the pile—soil system for calculation the settlement of the penetration

– in the soil under the raft:

$$p_1^{max}(N) \leq \sigma_{1u}(N); \quad (8)$$

– in the soil under the lower end of the pile:

$$p_3^{max}(N) \leq \sigma_{1u}(N); \quad (9)$$

3 Results and Discussions

The results of the experimental and theoretical studies show that triaxial compression is realized in the soil under the toe and destruction (punching) occurs with the formation and development of many shear cracks in the ultimate equilibrium surfaces. The ultimate stresses in the soil of an additional compressible thickness in the zone of punching by a pile or under a raft under triaxial cyclic loading are determined using a design soil model under regime spatial compression.

Cyclic loading leads to a decrease in strength and an increase in soil deformability due to the formation and development of micro-macrocracks in the structure, as well as degradation of the structure in local potentially dangerous areas of limiting equilibrium. In the calculation model, these processes are taken into account by analytical equations for changes in the specific cohesion and the angle of internal friction between particles.

Cyclic deviatoric loading is accompanied by the formation and development of plastic shear zones and soil ruptures in the planes of ultimate equilibrium. Soil failure in a spatially stressed state occurs when the number and length of fatigue microcracks reach a critical value in the limiting equilibrium planes.

The position of the limit equilibrium planes in space changes during cyclic loading with an increase in the number of cycles. The destruction of the soil in the local volume of the additional compressible thickness of the punching zone occurs along the limit equilibrium area on which there will be a minimum value of the potential energy of destruction.

This process will be abrupt depending on the fulfillment of conditions (8) and (9), the processes of crack development and stopping will alternate, and, as a result, bearing capacity will decrease.

According to the calculated model of the soil (Mirsayapov and Koroleva 2015), with inelastic triaxial cyclic deformation, the Coulomb friction forces do not act on the ultimate equilibrium surfaces, but are applied to the sliding surface of the soil particles. To determine the orientation of these surfaces, it is necessary to establish the deformed state of the soil under cyclic loading.

Considering that the destruction of the soil under cyclic loading occurs in the space of the main stresses (Mirsayapov and Koroleva, 2015), it is assumed that Coulomb's law relates the projection of forces acting on the ultimate equilibrium surfaces and the slip surface normal. Then the condition of the soil flow under conditions of triaxial compression under cyclic loading can be represented as:

$$|t| = S \cdot t g \phi(t, t_1, N, \tau) + c_0(t, t_1, N, \tau), \quad (10)$$

where $S = \sigma_1 \cdot l \cdot l' + \sigma_2 \cdot m \cdot m' + \sigma_3 \cdot n \cdot n'$, $t = ((\sigma_1 \cdot l \cdot m' - \sigma_2 \cdot m \cdot l')^2 + (\sigma_2 \cdot m \cdot n' - \sigma_3 \cdot n \cdot m')^2 + (\sigma_3 \cdot n \cdot l' - \sigma_1 \cdot l \cdot n')^2)^{1/2}$.

The spatial orientation of the marginal equilibrium area is determined by the formulas (Mirsayapov and Koroleva 2011):

$$l^2 = \frac{\bar{I}_3}{I_2 \cdot \bar{\sigma}_1}; m^2 = \frac{\bar{I}_3}{I_2 \cdot \bar{\sigma}_2}; n^2 = \frac{\bar{I}_3}{I_2 \cdot \bar{\sigma}_3}; \quad (11)$$

where l is the length of the pile, a_c is the size of the cross-section of the pile.

Then taking into account (1), (4), (11) the expression of pushing pressure is taking the form:

$$\sigma_{lu}(N) = \frac{4}{A_1} [\sigma_v(t, t_1, N) \cdot \cos \alpha_1(t, t_1, N) + \tau_v(t, t_1, N) \cdot A_{sh} \cdot \sin \alpha_1(t, t_1, N)] \quad (12)$$

The regularities of changes in the stress–strain state of the elements of the raft-pile foundation under cyclic loading were established, taking into account the redistribution of forces between the side, angular and ordinary piles. A volumetric stress–strain state is realized in the considered zone. The loss of the bearing capacity of the raft-pile foundation during cyclic loading occurs under the condition that the maximum stress state is reached in 2 zones: in the soil under the raft and in the soil under the lower end of the pile.

Defined regularities of soil deformation under the raft, along the lateral surface of piles and under the lower plane of piles refer to non-water-saturated soils under the action of cyclic loads, for which no account of inertial forces is required.

In cases where raft-pile foundations are based on water-saturated soils, it is necessary to take into account the influence of vibration creep deformations of primary consolidation associated with the squeezing of bound and loosely bound water from the pores of the soil. In addition, it will also be necessary to clarify the effect of the rate of application of the load on the rate of deformation of the primary consolidation.

4 Conclusions

1. The performed analytical studies allowed us to define the main regularities of deformation, taking into account the redistribution of forces between extreme, angular and ordinary piles. According to them, the main reason for the redistribution is the penetration sediment, which is determined for the stage when tangential stresses along the lateral surface are absent in the upper and middle parts of the pile due to the achievement of the maximum shear resistance. The penetration of the soil under the tip of the pile occurs when the stress under the fifth pile and under the plate grillage exceeds the fatigue strength of the soil under triaxial cyclic compression.
2. The equations of the bearing capacity of the raft-pile foundation under cyclic loading have been developed. The obtained equation of the mechanical state of the raft-pile foundation describes the basic laws of the behavior of such foundations observed in experiments at various loading stages. It allows assessing the settlement of raft-pile foundations during cyclic loading reliably.
3. A computational model describing the redistribution of forces between angular, extreme and ordinary piles of a raft-pile foundation has been developed. Comparison of the calculation results with the data of experimental studies of pile foundations showed good convergence between the calculated and experimental values (deviation of no more than 15%).

References

1. Katzenbach, R., Leppla, S.: Environment-friendly and economically optimized foundation systems for sustainable high-rise buildings. In: 19th International Conference on Soil Mechanics and Geotechnical Engineering (2011)
2. Katzenbach, R., Leppla, S.: Optimised design of foundation systems for high-rise structures. In: Proceedings of the 6th International Conference on Structural Engineering, Mechanics and Computation, pp. 2042–2047 (2016). <https://doi.org/10.1201/9781315641645-338>
3. Bokov, I.A., Fedorovskii, V.G.: On the calculation of groups of piles using mutual influence coefficients in the elastic half-space model. *Soil Mech. Found. Eng.* **54**, 363–370 (2018). <https://doi.org/10.1007/s11204-018-9482-8>
4. Bokov, I.A., Fedorovskii, V.G.: On the applicability of the influence function obtained from single-pile calculations for the calculation of pile groups. *Soil Mech. Found. Eng.* **55**, 359–365 (2019). <https://doi.org/10.1007/s11204-019-09549-y>
5. Hirai, H.: Assessment of cyclic response to suction caisson in clay using a three-dimensional displacement approach. *Mar. Georesources Geotechnol.* **36**, 805–817 (2018). <https://doi.org/10.1080/1064119X.2017.1386743>
6. Harichkin, A.I., Shulyatev, O.A., Kurillo, S.V., Fedorovsky, V.G.: Features of interaction of piles with each other and with the ground as part of groups. Issues of design and construction of aboveground and underground structures of buildings and structures, pp. 56–67 (2018)
7. Travush, V.I., Shulyatev, O.A., Shulyatev, S.O., Shakhramanyan, A.M., Kolotovichev, Yu.A.: Analysis of the results of geotechnical monitoring of the Lakhta center tower. *Subgrades Found. Soil Mech.* **2**, 15–21 (2019)

8. Shulyatev, O.A.: New set of rules for designing foundations and foundations of high-rise buildings. *Subgrades Found. Soil Mech.* **6**, 37–40 (2016)
9. Kayumov, R.A., Tazyukov, B.F., Mukhamedova, I.Z.: Identification of mechanical characteristics of a nonlinear-viscoelastic composite by results of tests on shells of revolution. *Mech. Compos. Mater.* **55**, 171–180 (2019). <https://doi.org/10.1007/s11029-019-09802-3>
10. Mirsayapov, I.T.: Punching settlement of raft-pile foundation under cyclic loading. *News KSUAE* **4**(54), 6–14 (2020)
11. Mirsayapov, I.T., Koroleva, I.V.: Studies of the water migration effect on changes in the clay soil physicommechanical characteristics under triaxial loading conditions. *News KSUAE* **2**(48), 168–174 (2019)
12. Mirsayapov, I.T., Shakirov, M.I.: Combined plate-pile foundations settlement calculation under cyclic loading. In: *IOP Conference Series: Materials Science and Engineering*, vol. 890, p. 012069 (2020). <https://doi.org/10.1088/1757-899X/890/1/012069>
13. Mirsayapov, I.T., Shakirov, M.I.: Bearing capacity and settlement of raft-pile foundations under cyclic loading. In: *Energy Geotechnics – Proceedings of the 1st International Conference on Energy Geotechnics*, pp. 423–428 (2016)
14. Mirsayapov, I.T., Koroleva, I.V., Ivanova, O.A.: Low-Cycle endurance and deformation of clay soils under three-axis cyclic loading. *Housing Constr. Moscow* **9**, 6–8 (2012). 18083643/0044-4472
15. Mirsayapov, I.T., Koroleva, I.V.: Bearing capacity of foundations under regime cyclic loading. In: *15th Asian Reg. Conf. Soil Mech. Geotech. Eng. ARC*, pp. 1214–1217 (2015)
16. Ter-Martirosyan, Z.G., Sidorov, V.V.: Interaction of a long barreta with a single-layer and double-layer base. *Housing Constr.* **1**, 36–39 (2010)

Improvement of Technology and Quality Control of 3DCP



Rustem Mukhametrakhimov  and Liliya Ziganshina 

Abstract Relevance of the problem being solved is caused by the imperfection of 3DCP products, which is expressed in the formation of defects and deviations, one of the reasons for which is the lack of a quality control system for 3DCP. The purpose of the research is to develop the sequence of operations and control tools for the additive manufacturing (3DCP). Influence of the features of CAD-model preparation, rheological and technological characteristics of the mixture (mobility and yield strength) on the quality of construction products printed on a 3D printer has been studied. It is necessary to take into account the features in the formation of the G-code of a CAD-model to obtain products on a 3D printer with the required length: elongation of the sample by an amount caused by the spreading of the raw mixture, as well as elongation of the sample by the distance from the center of gravity of the extruded raw mixture to its face in the initial and end positions of the nozzle. Non-mobile mixtures are characterized mainly by the formation of defects in the form of geometry violation, violation of linearity, gaps between layers and along the layer length, thickness variation, and the absence of spreading. More mobile mixtures are characterized by a greater degree of formation of defects in the form of geometry violations, violation of linearity, thickness variation, spreading, however, there are no defects as gaps between layers and along the length of the layer. The dependence of the geometric deviations of the length of printed sample, which is a multilayer strip, on the yield strength of the mixture, under constant 3D printing modes, is expressed by a linear function $\Delta l = -0.5276 \cdot \tau_0 + 168.31$. Based on the identified features of 3DCP, the main provisions for the organization and implementation of quality control of 3DCP are proposed, which establish the sequence of operations and means of control during the production of works. Significance of the obtained results for the construction industry is to reduce the defects in 3DCP products by improving the quality control system in additive manufacturing, taking into account the influence of the features of CAD-modeling, rheological and technological characteristics of the mixture, as well as the sequence of operations and control tools during incoming, operational and acceptance control.

R. Mukhametrakhimov (✉) · L. Ziganshina
Kazan State University of Architecture and Engineering, Kazan 420043, Russia
e-mail: muhametrakhimov@mail.ru

Keywords Concrete · Rheology · 3D printing · 3DCP · Additive technologies · Construction technology and management · Quality control

1 Introduction

Various industries, in particular construction, include wide application of innovative technologies aimed at the development and implementation of automation and robotization in production [1–7].

One of such actively developing innovative technologies in construction is the use of additive technological processes that make it possible to produce items, structures, frames of buildings and facilities based on the creation of a physical object from a CAD-model by adding material, usually layer by layer, in contrast to subtractive production (mechanical processing) and traditional molding production (casting, stamping) [8].

The prospects for superiority of additive technologies in the construction industry as compared with traditional approaches are noted by many authors [9–13] due to the significant reduction of construction time and labor costs, the possibility of manufacturing products of different configurations, the absence of significant waste during production, economic benefits, ensuring environmental protection and improved life safety during the production process.

3DCP technologies are studied at various scientific schools, the main of which are Eindhoven University of Technology [14–16], Swinburne University of Technology [17–19], Singapore Centre for 3D Printing [20–22] Moscow State University of Civil Engineering [23–25], Belgorod State Technological University named after V.G. Shukhov [4, 26–33], Voronezh State Technical University [34–36], Kazan State University of Architecture and Engineering [37–45] and others.

According to the Russian State Standard GOST 57590-2017 [46], there are seven major categories of additive manufacturing (photopolymerization in a bath, material jetting, binder jetting, synthesis on a substrate, material extrusion, directed energy deposition, and sheet lamination). The layered extrusion of material using raw mixtures based on mineral binders, mainly Portland cement, is most widespread in construction [23, 40, 41, 47–51].

The technology of concrete molding by layered extrusion is a set of interrelated processes and methods for processing of raw components. The key elements of the technology are raw materials, energy and equipment, which are closely interrelated and conditioned by economic and scientific and technical aspects [52].

The works of V.I. Telichenko, O.M. Terentyev, A.A. Lapidus [53] show that the technology of additive construction manufacturing from the scientific point of view considers the theoretical foundations, methods and techniques of construction processes that ensure the processing of semi-finished products (mortar and concrete mixtures) with qualitative changes in their conditions, physical and mechanical properties, geometric dimensions to obtain products of the desired quality.

Several works indicate a significant expansion of the applications of additive manufacturing in construction. However, it should be noted that the construction products are characterized by defects and deviations, manifested in mixture spreading, the presence of gaps, bends, voids, reduced cracking resistance, etc. [38, 40, 54–56], one of the reasons for which is imperfect quality control system in 3D printing.

Moreover, some requirements to quality control methods for products obtained by additive manufacturing technologies (including construction 3D-printing) are presented in [57], but these requirements are general, and the scope of the standard applies to a wide range of the existing additive manufacturing technologies, without considering the technological features of each of them.

Thus, of particular relevance are the studies on the peculiarities of production technology and work quality control in additive manufacturing of construction products by the layered extrusion (3D-printing).

This work aims to develop the set of operations and controls for additive manufacturing of construction products by layered extrusion (3D-printing).

The following tasks should be solved:

- To study the influence of raw mixture mobility on the quality of construction products produced by layered extrusion (3D-printing);
- To determine the peculiarities of G-code formation of three-dimensional digital model and the mixture spreading in the process of extrusion on geometric deviations of cured composites;
- To establish the relationship between the geometric deviations of the printed product length in a form of multilayer strips, and the yield strength of the mixture at constant modes of 3D-printing;
- To develop the basic provisions for the organization and implementation of quality control during the erection of construction products by 3D-printing, establishing the sequence of operations and means of control during the production of work.

The object of the research is the processes of additive construction manufacturing.

The subject of research is controlled operations, methods, scope and means of control of additive construction manufacturing.

2 Materials and Methods

The research was performed in the laboratory of additive technologies of construction manufacturing at the Kazan State University of Architecture and Engineering.

During creation of construction products by layered extrusion (3D-printing) the following sequence of technological operations was carried out:

1. Creation of digital three-dimensional model of the object;
2. Dividing the model into layers in the cross section;

3. Converting the model into digital data in the G-code programming language that allows modeling, code generation and 3D printer control;
4. Preparation of the raw mixture with the specified properties and its feeding into the removable storage hopper of the construction 3D-printer;
5. Transfer of the developed code to the print head extruder;
6. Layered extrusion of the raw mixture in accordance with the set digital 3D model;
7. Material curing until object (product) formation is completed;
8. Post-processing: removal of supporting structure (if necessary).

For 3D-printing, a raw mixture with the following initial components was used:

- a) Portland cement: CEM I 42,5 H produced by Sukholozhskcement (SLK Cement holding) which meets the Russian State Standard 31108-2016;
- b) Fine aggregate: quartz sand with particle size modulus $M_k = 2.3$ which meets the Russian State Standard 8736-2014;
- c) Tap drinking water that meets the requirements of the Russian State Standard 23732-2011.

Mixing of the components of the raw mixture was carried out in a compulsory concrete mixer for 10 min until a homogeneous mass was obtained.

Mobility of the mixture was determined in accordance with the requirements of the Russian State Standard 5802-86 by the depth of the reference cone immersion.

The yield strength of the mixture was determined at the boundary of gravity flowability using a simple viscometer, which is a hollow cylinder of polypropylene with a height of 200 mm and an inner diameter of 105 mm, in accordance with [58].

3D-printing of samples from the raw mixture was carried out by layered extrusion using the portal shop building "AMT S-6044" 3D-printer (LLC "SPEC AVIA", Yaroslavl), by printing it using a predesigned three-dimensional digital model (G-code).

The printed samples were cured for 28 days in natural conditions at a temperature of (20 ± 2) °C, relative humidity of $(50 \pm 20)\%$.

Quality control of the 3D-printed product included visual and measuring methods. The measuring control was carried out with a metal ruler according to the Russian State Standard 427-75, a metal tape measure according to the Russian State Standard 7502-98, and a magnifying glass according to the Russian State Standard 25706-83.

3 Results and Discussions

The products created using a construction 3D printer must meet the requirements of design and regulatory documents, deviation from which can lead to low-quality products with various defects that can be caused by non-optimal composition of concrete mixtures and technological parameters (mobility).

At the first stage, studied were the role of preparation of digital model and the influence of mobility and yield strength of the mixture on the quality of construction products printed on a 3D printer.

The quality of 3D-printed products of three compositions with various mobilities was studied:

Composition No. 1 had excessive mobility and low yield strength,

Composition No. 2 had insufficient mobility and high yield strength,

Composition No. 3 had mobility and yield strength close to the optimal values.

The test results of the 3D-printed bench are shown in Fig. 1 and Table 1.

Figure 1 shows that the most optimal mixture for extrusion on the examined 3D printer is the mixture of composition No. 3, while its use does not exclude the formation of defects in 3D-printing. The detected defects of the 3D-printed product from the raw mixture of composition No. 3 are shown in Fig. 2.

Table 1 and Figs. 1 and 2 show that the mobility and yield strength of the mixture have a significant impact on the quality of construction products printed on a 3D printer. The mixture with excessive mobility and the lowest yield strength has the highest degree of defect formation in the form of geometric defects, violation of linearity, thickness variation, and spreading, while there are no defects in the form of gaps between layers and along the layer length. Mixture composition No. 2 with insufficient mobility and high yield strength compared to the composition No. 2 is characterized by the presence of defects in the form of violations of geometry,

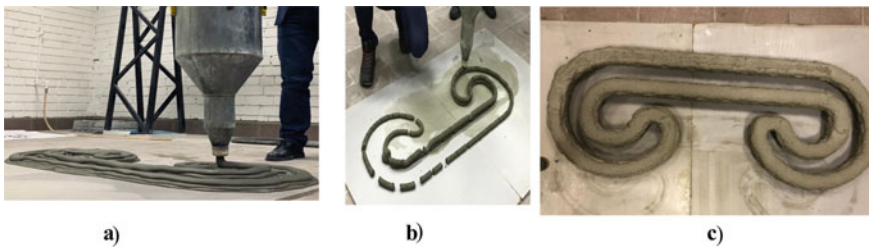


Fig. 1 3D printing of the product with raw mixtures of various mobilities: **a** mixture of composition No. 1; **b** mixture of composition No. 2; **c** mixture of composition No. 3

Table 1 Results of visual and measuring control of products printed using the 3D printer

Defect type	Defect characteristics		
	Composition No. 1	Composition No. 2	Composition No. 3
1	2	3	4
Geometry violation	More significant	Significant	Significant
Violation of linearity	More significant	Significant	Significant
Gaps between layers	Not detected	Significant	Insignificant
Gaps along the layer length	Not detected	Significant	Not detected
Thickness variation	More significant	Significant	Not detected
Spreading	More significant	Not detected	Significant

Note—The defects were characterized by the criteria: more significant/significant/insignificant



a) increased porosity



b) widespread influxes



c) deviation of the height of the product layers from the design value



d) deviation of the product length and width from the design value, the influx in the starting point



e) blowholes at local areas



f) shrinkage cracks at local areas

Fig. 2 Defects of a 3D-printed product

violation of linearity, gaps between layers and the layer length, thickness variation, while spreading was not detected. Mixture composition No. 3 with mobility and yield strength close to the optimal values is the least susceptible to the formation of these types of defects.

At the second stage, the influence of features of the modeling of the digital model of the product on the quality of construction products printed on a 3D printer was investigated.

It was found that the formation of defects in the form of deviations of geometric parameters of the printed product was associated not only with the mobility of the concrete mixture, but also with some features of G-code generation of three-dimensional digital model of the sample and the process of its 3D-printing (Fig. 3, expression 1): 1) the design (set) length of the sample (L_d) is the distance between the points of the center of gravity of the extruded raw mixture at the initial and final positions of the 3D printer nozzle during printing; 2) the actual sample length is the sum of the design (set) sample length (L_d), the lengths ($L_{s.m.}$) caused by the spreading of the raw mixture, and the distance from the center of gravity of the extruded raw mixture to its edge ($a/2$) at the initial and final nozzle positions. In this case, with increasing mobility, the length ($L_{s.m.}$) caused by the spreading of the raw material mixture increases.

$$L_d = L_n - \left(\frac{a}{2} \cdot 2 + L_{s.m.} \cdot 2 \right) \tag{1}$$

The deviation of the length (Δl) of the printed product in this case will be as follows:

$$\Delta l = \frac{a}{2} \cdot 2 + L_{s.m.} \cdot 2 \tag{2}$$

In practice, the first term of expression (2) can be adjusted when creating the control program of the printed object (i.e. by adjusting the G-code of the digital model), so it can be neglected. Then the expression (2) will be described by the following function (3):

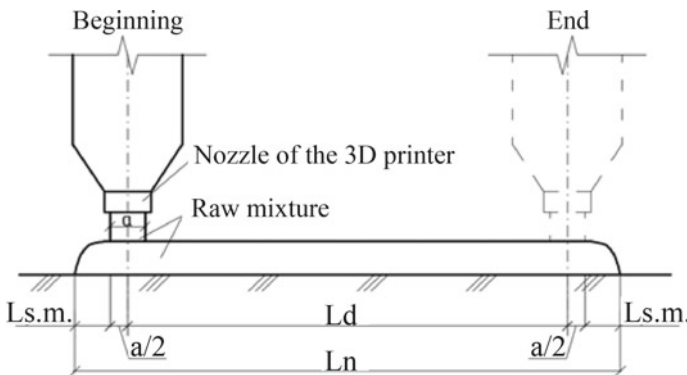


Fig. 3 The scheme to determine the actual length of 3D-printed samples [38]

$$\Delta l = f(L_{s.m.}) \tag{3}$$

To determine the equation of the revealed function (3), the effect of the yield strength of the mortar mixture on the deviation of the printed product length was studied. The G-code of the sample was a 400 mm long strip, the number of printed layers was 4. The yield strength of mixture was taken as the variable factor X, and the deviation of the printed product length was taken as the response function Y. The results obtained are shown in Fig. 4.

Figure 4 shows that for the sample in a form of a 4 layers strip, the printed product length linearly depends on the yield strength according to the following Eq. (4):

$$\Delta l = -0.5276 \cdot \tau_0 + 168.31 \tag{4}$$

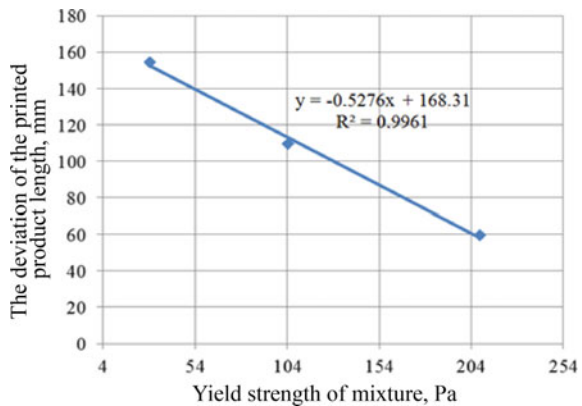
The deviation of the printed sample length is higher for the lower yield strength of mixture. The obtained equation will make it possible to predict the deviation of the printed product length on the mixture mobility, the yield strength, and to print products with the design length.

At the third stage, based on the analysis of available data, the sequence of operations and means of control during the manufacturing of construction products by layered extrusion (3D-printing) during incoming, operational and acceptance inspections were systematized.

Incoming inspection provides control of the used construction materials, products, structures, semi-finished products and equipment by checking their compliance with the quality indicators of materials, products and equipment of the requirements of regulatory documents specified in the design documentation and (or) the contract for the contractor, as well as the availability of supporting documents confirming this quality. The incoming inspection is performed by the builder and the person who carries out the construction.

The results of incoming inspection should be documented in the logs of incoming inspection and laboratory tests.

Fig. 4 Relationship between the printed product length deviation and the yield strength of mixture



The readiness and serviceability of the control program of the printed object is checked for its uninterrupted reproduction by the 3D printer, excluding the occurrence of errors that lead to failures during 3D-printing.

Where appropriate, supporting structures in the form of laminated plywood substrates, temporary bonding elements, etc. can be used during the 3D printing process. The working surfaces of these structures must be free of chips, blowholes, voids and other defects and must be cleaned of dirt and dust before use. They must be designed to ensure their removal without damaging the printed product upon completion of 3D-printing, i.e. the surfaces of supporting structures that are in contact with concrete must have minimal adhesion to the printed concrete.

In addition, the marking of the extrusion start point on the surface of the base, supporting structure (if any) is subject to control to ensure 3D-printing of the object within the working area of the 3D printer.

The sequence of operations and means of control during the manufacturing of construction products by layered extrusion (3D-printing) for the incoming quality control are shown in Table 2.

Table 2 The sequence of operations and means of control during the manufacturing of construction products by layered extrusion (3D-printing) for the incoming quality control

Processes under control	Operations to be controlled	Inspection (method, volume)	Documents
Preparation works	– Readiness and operability of the control program of the printed object;	Visual	Passports (certificates), general work log
	– Availability of quality documents for the components of the raw mixture (ready-made dry mixtures), supporting structure (if applicable);	The same	
	– Quality of the base preparation;	Visual, Measuring	
	– Readiness of all mechanisms and devices that ensure the production of works with the construction 3D printer;	Visual	
	– Marking of the extrusion starting point on the surface of the base, supporting structure (if any)	Visual, Measuring	

Measuring tools: tape measure, plumb line, metal ruler

Operational Inspection. Operational quality control is carried out by the builder (technical customer) and the person who carries out the construction.

The technological process should be organized based on the technical capabilities and characteristics of the equipment used (CAD units), modes of 3D-printing, duration of technological operations and pauses during 3D-printing of the product based on the technological and rheological characteristics of the concrete mixture used.

The sequence of operations and means of control during the manufacturing of construction products by layered extrusion (3D-printing) for the operational quality control are shown in Table 3.

Acceptance Control. During the acceptance control of construction products erected by layered extrusion (3D-printing), it is necessary to check the quality of performed construction and erection works as well as of hidden works and separate structural elements with drawing up the acts of certification of hidden works and the act of intermediate acceptance of critical structures.

Table 3 The sequence of operations and means of control during the manufacturing of construction products by layered extrusion (3D-printing) for the operational quality control

Processes under control	Operations to be controlled	Inspection (method, volume)	Documents
Concrete mixture preparation, extrusion (3D printing), concrete hardening	– Dosing accuracy of the concrete mixture components;	Laboratory	General work log, concrete work log
	– Properties of the prepared concrete mixture (mobility, yield strength, stability of properties, etc.);	The same	
	– Specified extrusion modes (extrusion speed, the speed of the 3D printer’s print head motion);	Technical inspection	
	– Length, height and width of printed layers;	Visual, measuring	
	– Temperature and humidity conditions of concrete hardening according to the requirements of the work program	Measuring	

Measuring tools: tape measure, plumb line, metal ruler, level, laser level, pocket penetrometer

Operational control is carried out by master (foreman), laboratory post engineer, surveyor

Table 4 The sequence of operations and means of control during the manufacturing of the erected construction products by the layered extrusion (3D-printing) when performing the quality acceptance inspection

Processes under control	Operations to be controlled	Inspection (method, volume)	Documents
Acceptance of completed work	– Compliance of geometric parameters with the design parameters;	Visual, Measuring	General work log, geodetic executive scheme
	– Quality of the concrete surface, including after its post-treatment;	The same	
	– The actual concrete strength;	Laboratory	
	– Compliance with the design position of the erected structures (deviation from the coaxiality of vertical structures, deviations from linearity and flatness)	Visual, Measuring	
Measuring tools: tape measure, plumb line, metal ruler, level, laser level			
Acceptance control is carried out by master (foreman), laboratory post engineer, surveyor during the work, representatives of the technical supervision of the customer			

Technical criteria of the quality acceptance inspection of the erected construction products by the layered extrusion (3D-printing) when performing the quality acceptance inspection are given in Table 4.

4 Conclusions

1. The influence of raw mixture mobility on the quality of construction products obtained by layered extrusion (3D-printing) was established. Low-mobility mixtures are mainly characterized by formation of defects in the form of violation of geometry, violation of linearity, gaps between the layers and along the length of the layer, thickness variation, lack of spreading. More mobile mixtures are characterized by a greater degree of defect formation in the form of geometric defects, violation of linearity, thickness variation, spreading, but defects in the form of gaps between layers and along the length of the layer were not detected.
2. It was found that to obtain products with the required geometric dimensions, it is necessary to consider the features during the formation of the G-code of the 3D digital model and the mixture spreading in the process of extrusion. It was

found that the actual length of the 3D-printed product consists of 1) the designed (set) length of the sample (L_d)—the distance between the points of the center of gravity of the extruded raw mixture in the initial and the final positions of the 3D-printer nozzle; 2) distances from the center of gravity of the extruded raw mixture to its edge ($a/2$) in the initial and final positions of the nozzle; 3) the length ($L_s.m.$) caused by the spreading of the raw mixture. To some extent, these features can be compensated by adjusting the technological parameters of 3D-printing (nozzle diameter, spindle speed, feed rate, etc.).

3. A product printed by layered extrusion using a portal-type 3D printer with an uncontrolled form of the extruded layer (without nozzle guides) in a form of multilayer strips of cement-sand mortar was found to have the geometric deviations of the length from the design value. For the nozzle diameter of 25 mm, extrusion speed of 20,000 units, extruder speed of 7000 units these deviations are expressed as a linear dependence on the yield strength of a fine-grained concrete mixture $\Delta l = -0.5276 \cdot \tau_0 + 168.31$. Reducing the yield strength from 208 to 29 Pa leads to a decrease in geometric deviations of the length of the printed samples by 23.75%.
4. Developed were the basic provisions for the organization and implementation of quality control in the manufacturing of building products by 3D-printing, which establish the sequence of operations and means of control during the production of works.

Acknowledgements This work was supported by 3D-Stroy LLC (Kazan, Russia), the Russian Federation Presidential Scholarship for Young Scientists and Postgraduate Students (SP-1051.2021.1).

References

1. Vatin, N., Chumadova, L., Goncharov, I., Zykova, V., Karpenya, A., Kim, A., Finashenkov, E.: 3D printing in construction. *Constr. Unique Build. Struct.* **52**, 27–46 (2017). <https://doi.org/10.18720/CUBS.52.3>
2. Klyuev, S.V., Klyuev, A.V., Vatin, N.I., Shorstova, E.S.: Technology of 3-D printing of fiber reinforced mixtures. Presented at the (2021). https://doi.org/10.1007/978-3-030-67654-4_25
3. Khozin, V., Khokhryakov, O., Nizamov, R.: A carbon footprint» of low water demand cements and cement-based concrete. In: *IOP Conference Series: Materials Science and Engineering*, vol. 890, p. 012105 (2020). <https://doi.org/10.1088/1757-899X/890/1/012105>
4. Chernysheva, N.V., Lesovik, V.S., Volodchenko, A.A., Glagolev, E.S., Drebezgova, M.Y.: Composite materials using energy-saving technogenic raw materials for 3D additive technologies. In: “Science-Intensive Technologies and Innovations” Collection of Reports of the International Scientific-Practical Conference, pp. 452–456 (2016)
5. Vdovin, E.A., Stroganov, V.F.: Properties of cement-bound mixes depending on technological factors. *Mag. Civ. Eng.* **93**, 147–155 (2020). <https://doi.org/10.18720/MCE.93.12>
6. Khozin, V., Khokhryakov, O., Nizamov, R.: A «carbon footprint» of low water demand cements and cement-based concrete. In: *IOP Conference Series: Materials Science and Engineering* (2020). <https://doi.org/10.1088/1757-899X/890/1/012105>

7. Stroganov, V.F., Amel'chenko, M.O., Mukhametrakhimov, R.K., Vdovin, E.A., Tabaeva, R.K.: Increasing the adhesion of styrene–acrylic coatings modified by Schungite filler in protection of building materials. *Polym. Sci. Ser. D* **15**, 162–165 (2022). <https://doi.org/10.1134/S1995421222020277>
8. GOST R 57558-2017/ISO/ASTM 52900:2015 Additive manufacturing processes. Basic principles. Part 1. Terms and definitions
9. Gorbach, P.S., Shustov, P.A., Levchuk, S.S.: Additive production methods in the construction industry. *Bull. Angarsk State Tech. Univ.* **10**, 174–177 (2016)
10. Zolotareva, S.V.: Development and application of 3D technologies in construction. In: Proceedings of the VII International Youth Forum “Education, Science, Production;” pp. 1033–1037 (2016)
11. Gutorov, N.Y., Chepenko, A.S., Naumenko, N.A., Pavlenko, O.A.: Additive technologies and modern construction technologies. In: Collection of Reports of the X International Scientific and Practical Conference of Students, Graduate Students and Young Scientists: In 4 Volumes, pp. 85–87 (2017)
12. Matyukhina, A.A., Nikiforova, N.A., Nikulina, A.S., Dementieva, Y.A. Lesnichenko, E.N.: Advantages of additive technologies and ways to improve 3D construction. In: Technical Conference of Young Scientists of BSTU, pp. 2185–2189 (2017)
13. Luneva, D.A., Kozhevnikova, E.O., Kaloshina, S.V.: 3D printing technology using layer-by-layer extrusion in construction. *Mod. Technol. Constr. Theory Pract.* **2**, 251–261 (2017)
14. Bos, F.P., Menna, C., Pradena, M., Kreiger, E., da Silva, W.R.L., Rehman, A.U., Weger, D., Wolfs, R.J.M., Zhang, Y., Ferrara, L., Mechtcherine, V.: The realities of additively manufactured concrete structures in practice. *Cem. Concr. Res.* **156**, 106746 (2022). <https://doi.org/10.1016/j.cemconres.2022.106746>
15. van Overmeir, A.L., Figueiredo, S.C., Šavija, B., Bos, F.P., Schlangen, E.: Design and analyses of printable strain hardening cementitious composites with optimized particle size distribution. *Constr. Build. Mater.* **324**, 126411 (2022). <https://doi.org/10.1016/j.conbuildmat.2022.126411>
16. Mechtcherine, V., Bos, F.P., Perrot, A., da Silva, W.R.L., Nerella, V.N., Fataei, S., Wolfs, R.J.M., Sonebi, M., Roussel, N.: Extrusion-based additive manufacturing with cement-based materials – production steps, processes, and their underlying physics: a review. *Cem. Concr. Res.* **132** (2020). <https://doi.org/10.1016/j.cemconres.2020.106037>
17. Marchment, T., Sanjayan, J.: Lap joint reinforcement for 3D concrete printing. *J. Struct. Eng.* **148** (2022). [https://doi.org/10.1061/\(ASCE\)ST.1943-541X.0003361](https://doi.org/10.1061/(ASCE)ST.1943-541X.0003361)
18. Jayathilakage, R., Sanjayan, J., Rajeev, P.: Comparison of rheology measurement techniques used in 3D concrete printing applications (2021). https://doi.org/10.1007/978-981-15-7222-7_23
19. Muthukrishnan, S., Ramakrishnan, S., Sanjayan, J.: Effect of microwave heating on interlayer bonding and buildability of geopolymer 3D concrete printing. *Constr. Build. Mater.* **265** (2020). <https://doi.org/10.1016/j.conbuildmat.2020.120786>
20. Geng, Z., Pan, H., Zuo, W., She, W.: Functionally graded lightweight cement-based composites with outstanding mechanical performances via additive manufacturing. *Addit. Manuf.* **56**, 102911 (2022). <https://doi.org/10.1016/j.addma.2022.102911>
21. Andrew Ting, G.H., Noel Quah, T.K., Lim, J.H., Daniel Tay, Y.W., Tan, M.J.: Extrudable region parametrical study of 3D printable concrete using recycled glass concrete. *J. Build. Eng.* **50**, 104091 (2022). <https://doi.org/10.1016/j.jobe.2022.104091>
22. Weng, Y., Li, M., Zhang, D., Tan, M.J., Qian, S.: Investigation of interlayer adhesion of 3D printable cementitious material from the aspect of printing process. *Cem. Concr. Res.* **143** (2021). <https://doi.org/10.1016/j.cemconres.2021.106386>
23. Korolev, E.V., Zuong, T.K., Inozemtsev, A.S.: A method for providing internal care for cement hydration in 3D printing expressions. *Vestn. MGSU* **6**, 834–846 (2020). <https://doi.org/10.22227/1997-0935.2020.6.834-846>
24. Inozemtsev, A.S., Korolev, E.V., Zuong, T.K.: Analysis of existing technological solutions for 3D printing in construction. *Vestn. MGSU* **7**, 863–876 (2018). <https://doi.org/10.22227/1997-0935.2018.7>

25. Zuong, T.: High-strength lightweight fiber-reinforced concrete for structural purposes: Thesis, Moscow (2020)
26. Poluektova, V.A.: Patterns of surface phenomena and modification of polymer-mineral dispersions for additive technologies: Thesis (2022)
27. Novosadov, N.I., Poluektova, V.A.: Strength characteristics of a polymer-cement composite for additive technologies. In: III International Scientific and Practical Conference, pp. 133–137 (2017)
28. Lesovik, V.S., Zagorodnyuk, L.K., Glagolev, E.S., Chernysheva, N.V., Drebezgova, M.Y., Kucherova, A.S., Kaneva, E.V.: Modern three-dimensional technologies and factors restraining them. *Bull. BSTU* **1**, 22–30 (2016). <https://doi.org/10.12737/23011>
29. Klyuev, S.V., Khezhev, T.A., Pukhareno, Y.V., Klyuev, A.V.: Experimental study of fiber-reinforced concrete structures. *Mater. Sci. Forum.* **945**, 115–119 (2019). <https://doi.org/10.4028/www.scientific.net/MSF.945.115>
30. Klyuev, S.V., Khezhev, T.A., Pukhareno, Y.V., Klyuev, A.V.: Fibers and their properties for concrete reinforcement. *Mater. Sci. Forum.* **945**, 125–130 (2019). <https://doi.org/10.4028/www.scientific.net/MSF.945.125>
31. Klyuev, S.V., Bratanovskiy, S.N., Trukhanov, S.V., Manukyan, H.A.: Strengthening of concrete structures with composite based on carbon fiber. *J. Comput. Theor. Nanosci.* **16**, 2810–2814 (2019). <https://doi.org/10.1166/jctn.2019.8132>
32. Klyuev, S.V., Khezhev, T.A., Pukhareno, Y.V., Klyuev, A.V.: Fiber concrete for industrial and civil construction. *Mater. Sci. Forum.* **945**, 120–124 (2019). <https://doi.org/10.4028/www.scientific.net/MSF.945.120>
33. Klyuev, S.V., Khezhev, T.A., Pukhareno, Y.V., Klyuev, A.V.: To the question of fiber reinforcement of concrete. *Mater. Sci. Forum.* **945**, 25–29 (2019). <https://doi.org/10.4028/www.scientific.net/MSF.945.25>
34. Slavcheva, G.S., Artamonova, O.V.: Rheological behavior of 3D printable cement paste: criterial evaluation. *Mag. Civil Eng.* **8**, 97–108 (2018). <https://doi.org/10.18720/MCE.84.10>
35. Slavcheva, G.S., Britvina, E.A., Ibrayeva, A.I.: 3D construction printing: an operational method for controlling the rheological characteristics of mixtures. *Bull. Eng. Sch. Far East. Fed. Univ.* **41**, 134–143 (2019)
36. Slavcheva, G.S., Artamonova, O.V.: Rheological behavior of dispersed systems for building 3D printing: a control problem based on the capabilities of the Nano arsenal. *Nanotechnol. Constr. Sci. Internet J.* **3**, 107–122 (2018). <https://doi.org/10.15828/2075-8545-2018-10-3-107-122>
37. Mukhametrakhimov, R.K., Gorbunova, P.S.: The role of dispersed reinforcement in the formation of technological properties and rheological properties of concrete mixtures for building 3D printing. In: *Actual Problems and Prospects for the Development of the Construction Complex*, pp. 270–274 (2019)
38. Mukhametrakhimov, R., Lukmanova, L.: Influence of cement-sand mortar mobility on the quality of 3D printed hardened composite. *Constr. Unique Build. Struct.* **94**, 9404 (2021). <https://doi.org/10.4123/CUBS.94.4>
39. Mukhametrakhimov, R., Lukmanova, L.: Structure and properties of mortar printed on a 3D printer. *Mag. Civ. Eng.* **102** (2021). <https://doi.org/10.34910/MCE.102.6>
40. Mukhametrakhimov, R., Lukmanova, L.: Influence of the technological properties of cement-sand mortar on the quality of 3D printed products. In: *IOP Conference Series: Materials Science and Engineering* (2020). <https://doi.org/10.1088/1757-899X/890/1/012082>
41. Mukhametrakhimov, R., Lukmanova, L.: Investigation of portland cement in 3d concrete printing. *Lect. Notes Civ. Eng.* **169**, 1–13 (2021). https://doi.org/10.1007/978-3-030-80103-8_1
42. Mukhametrakhimov, R.K., Ziganshina, L.V.: Technology and quality control of 3DCP. *News KSUAE* **59**, 64–79 (2022). https://doi.org/10.52409/20731523_2022_1_64
43. Khaliullin, M., Dimieva, A.: Composite gypsum binder under introducing thermally activated clay as a pozzolanic component and adding ground limestone. In: *IOP Conference Series: Materials Science and Engineering* (2020). <https://doi.org/10.1088/1757-899X/890/1/012093>
44. Khaliullin, M., Gilmanshina, A.: The effect of additives of mechanically activated mineral fillers on the properties of composite gypsum binders. Presented at the (2021). https://doi.org/10.1007/978-3-030-80103-8_36

45. Khaliullin, M., Gilmanshina, A.: The effect of ground limestone on the properties of composite gypsum binder using thermally activated clay as a pozzolanic component. *E3S Web Conf.* **274**, 04006 (2021). <https://doi.org/10.1051/e3sconf/202127404006>
46. GOST R 57590-2017: Additive technological processes. Basic principles - Part 3. General requirements
47. Jianchao, Z., Zhang, T., Faried, M., Wengang, C.: 3D printing cement based ink, and it's application within the construction industry. In: *ASCMCES 2017, MATEC Web of Conferences*, p. 02003 (2017)
48. Pshtiwan, S., Shami, N., Gavin, P.: A study into the effect of different nozzles shapes and fibre-reinforcement in 3D printed mortar. *Materials (Basel)* **12** (2019). <https://doi.org/10.3390/ma12101708>
49. Slavcheva, G.S.: Drying and shrinkage of cement paste for 3D printable concrete. *IOP Conf. Ser. Mater. Sci. Eng.* **481** (2019). <https://doi.org/10.1088/1757-899X/481/1/012043>
50. Klyuev, S.V., Klyuev, A.V., Shorstova, E.S.: Fiber concrete for 3-D additive technologies. *Mater. Sci. Forum.* **974**, 367–372 (2019). <https://doi.org/10.4028/www.scientific.net/MSF.974.367>
51. Kruger, P.J.: Rheo-mechanics modelling of 3D concrete printing constructability (2019). <https://doi.org/10.13140/RG.2.2.16259.04649>
52. Rybiev, I.A.: *Building Materials Science*. Higher School, Moscow (2004)
53. Telichenko, V.I., Terentiev, O.M., Lapidus, A.A.: *Technology of building processes: In: 2 hours. Part 1*. Higher School, Moscow (2008)
54. Buswell, R.A., Leal de Silva, W.R., Jones, S.Z., Dirrenberger, J.: 3D printing using concrete extrusion: a roadmap for research. *Cem. Concr. Res.* **112**, 37–49 (2018). <https://doi.org/10.1016/j.cemconres.2018.05.006>
55. Marchment, T., Sanjayan, J., Xia, M.: Method of enhancing interlayer bond strength in construction scale 3D printing with mortar by effective bond area amplification. *Mater. Des.* 107684 (2019). <https://doi.org/10.1016/j.matdes.2019.107684>
56. Le, T.T., Austin, S.A., Lim, S., et al.: Hardened properties of high-performance printing concrete. *Cem. Concr. Res.* **42**, 558–566 (2012). <https://doi.org/10.1016/j.cemconres.2011.12.003>
57. GOST R 57587-2017: Products obtained by the method of additive technological processes. Methods of control and testing
58. Bazhenov, Y.M., Demyanova, V.S., Kalashnikov, V.I.: *Modified High-Quality Concretes*. Publishing House of the Association of Construction Universities (2006)

Clay Soil Deformations Under Regime Long-Term Triaxial Compression Taking into Account Initial Defects



Ilizar Mirsayapov  and Niyaz Aysin 

Abstract The arrangement of deep pits leads to a change in the stress–strain state of the soil mass within the radius of the zone of influence. This is caused by the unloading of the base during excavation, horizontal movement of the walls of the pit, technological factors. When entering the zone of existing buildings, there is a need for an assessment and geotechnical forecast of the behaviour of the soils of the foundations of existing buildings and structures. At the same time, it is necessary to take into account existing and newly arisen defects and damage to soils. The purpose of the study is to determine, based on laboratory studies, the dependences of the main deformation characteristics of clay soil with existing defects, for this it is necessary: to conduct an experimental study with triaxial compression of clay samples with cracks and without cracks; to establish the features of the development of cracks in the structure of the clay sample; to establish the features of the development of deformations of clay soil with cracks with triaxial compression. Based on the results of the study, new data on the affect of defects in soil samples were obtained. Based on the research results, the dependences of the main deformation characteristics of clay soil are constructed. The significance of the results obtained for the construction industry lies in the fact that they make it possible to more accurately assess the settlement of foundations when constructing deep pits near existing buildings.

Keywords Clay soil · Deformations · Microcracks · Macrocracks · Bearing capacity · Rheology of soils

1 Introduction

The process of destruction and development of nonlinear deformations of clay soil under triaxial compression is accompanied by the formation and development of

I. Mirsayapov (✉) · N. Aysin
Kazan State University of Architecture and Engineering, 420043 Kazan, Russia
e-mail: mirsayapov1@mail.ru

micro- and macro-cracks in the planes of ultimate equilibrium. Micro- and macro-cracks in the soil structure affect the deformation and strength of the soil under prolonged loading.

Libin Gong et al. [1] studied the modeling of rocky soil, the cracks of which are filled with a weaker type of soil, in which the degree of water saturation of the filler significantly affects the shear strength and the stability of the soil. For the first time using Fast Lagrangian Analysis of Continua (FLAC) numerical software, a series of direct shear tests with constant water content was carried out on unsaturated filled butt soil using numerical software. According to the literature review, the initial water saturation of the filler and shear rate, joint roughness, filling thickness and normal stress affect the shear strength of the joint.

Emil Soból et al. [2, 3] studied 15 different Warsaw clays. The collected data allowed the authors to create empirical models describing the characteristics of rigidity with high reliability. Combined empirical models allow us to estimate the value of the shear modulus of a connected soil in a wide range of shear deformations with high accuracy. As a result of the study, it was found that the maximum shear modulus increases with the average effective pressure. The plasticity number had a negligible effect on the G_{MAX} value, and depends on the effective stress p' and the void ratio e . Shear deformation had the greatest impact on the shear modulus and normalized shear modulus degradation curves. With an increase in both plasticity and effective stress, the nonlinear threshold strain shifted to a higher shear strain. However, the average effective stress (p') had a noticeably smaller effect on the elastic range of shear deformation than the plasticity index (P_1).

Clay soils have pronounced rheological properties, which vary depending on the degree of damage to the structure with initial defects and damages. A relatively small number of works study the influence of defects in the form of micro- and macro-cracks on the rheological properties of soils. The issues of changing the strength and deformability of clay soils with initial defects and damages under prolonged regime static loading have not been practically studied [4–8].

When designing and building, it is necessary to avoid uneven precipitation. In the article by Heng Zhang et al. [9], an analytical solution based on the Laplace integral transformation method has been developed for predicting long-term uneven precipitation of buildings on non-rock soil foundations. The methodology is based on Laplace integral transformation and the theory of viscoelasticity. It combines an analytical solution with a finite element method for a solution taking into account the sequence of construction and loading. The accuracy of the analytical solution based on the integral Laplace transform is confirmed by the monitoring results.

In clay soils under triaxial compression, stresses and deformations vary depending on the stress level, the ratio of vertical and horizontal stresses, the duration of the load, the trajectory and the size of the initial structural defects [10–13]. Therefore, the stress to strain ratio is not constant, and changes, even if one of these quantities does not change over time and the other (stress or strain) changes.

In connection with the above, it becomes necessary to establish patterns of changes in the strength and deformability of soils, taking into account changes in long-term loading modes and the influence of existing defects and damages, for this it is necessary to solve a number of tasks:

1. To conduct an experimental study with triaxial compression of clay samples with cracks and without cracks;
2. To establish the features of the development of cracks in the structure of the clay sample;
3. To establish the features of the development of deformations of clay soil with cracks during triaxial compression.

2 Materials and Methods

The tests were carried out on a true triaxial compression device with rigid walls. The device was developed at the department [14, 15]. Loads are transferred to the soil sample using mechanical levers, which ensures constant pressure when the sample is deformed. The tests were carried out at the same lateral pressure. Vertical σ_1 stresses were applied to the sample with a given step.

Artificially prepared samples of clay soil were used for testing, having the shape of a cube with dimensions of $10 \times 10 \times 10$ cm, with the specified characteristics: density $\rho = 1.91 \text{ g/cm}^3$; humidity $W = 0.2$. To determine the effect of the formation and development of defects on the strength and deformation of clay soil, artificial cracks of two types were created (see Fig. 1): 1—one crack in the assumed plane of the ultimate equilibrium of the soil; 2—in the form of two intersecting cracks in two planes of ultimate equilibrium.

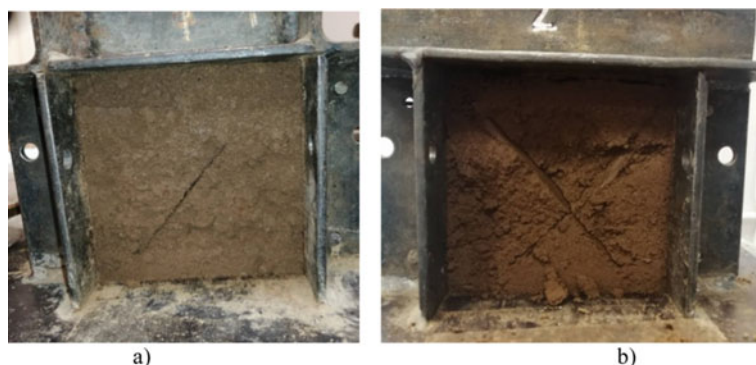


Fig. 1 Samples with cracks in the equilibrium planes: **a** with one crack; **b** with two intersecting cracks in two equilibrium planes

To establish the regularities of the development of deformations under regime long-term triaxial loads, three series of soil samples were tested at a given value of all-round pressure.

Movements, coaxial with the applied loads, were measured by hour-type indicators. The values of deformations were determined by calculation. At the initial stage, the soil sample was subjected to comprehensive compression $\sigma_1 = \sigma_2 = \sigma_3 = 160$ kPa. After stabilization of axial deformations at constant values of lateral stresses $\sigma_2 = \sigma_3 = 160$ kPa, a vertical load was applied to the sample. Each loading stage was sustained then the next load level was applied until the ultimate strength was reached.

The deformations of the sample were recorded at certain time intervals for the accepted loading time in this block.

3 Results

Within each block of regime long-term static loading there was an increase in linear vertical deformations, shear deformations, as well as a change in the intensity of shear deformations, the modulus of vertical deformations and the shear modulus, indirectly characterizing the change in the strength and deformation characteristics of soils during loading.

Graphs based on the results of triaxial long-term regime loads show that at the stage of comprehensive compression, lateral deformations grow more intensively than vertical ones (see Fig. 2). The maximum value of lateral deformations is reached at the moment when vertical deformations make up 25–30% of the maximum deformations during fracture. A noticeable increase in vertical linear deformations begins at $\sigma_z > 0.3 \sigma_{ult}$.

In the blocks of regime long-term loading there was an increase in vertical deformations both at the stage of comprehensive and at the stage of deviator loading. Analysis of the development schedule of vertical deformations shows that they develop throughout the tests with varying intensity. The most intensive development of vertical deformations occurs at the stage of deviator loading in the range of vertical stresses from 300 to 880 kPa. At this interval of deviator loading, the maximum vertical deformations were in samples with two cracks, the minimum deformations were in samples without cracks (see Fig. 3a). This is explained by the fact that samples without cracks resisted the formation of a shear plane along the face of the compacted pyramids, and in samples with cracks, the stress deviator causes only the displacement of the compacted pyramids.

Horizontal deformations ϵ_x and ϵ_y also developed throughout the long-term deviator loading with different intensity. As the charts show (see Fig. 3b), the highest value of horizontal deformations is observed in samples with two cracks, the minimum deformations are observed in samples without cracks. The analysis of the graphs

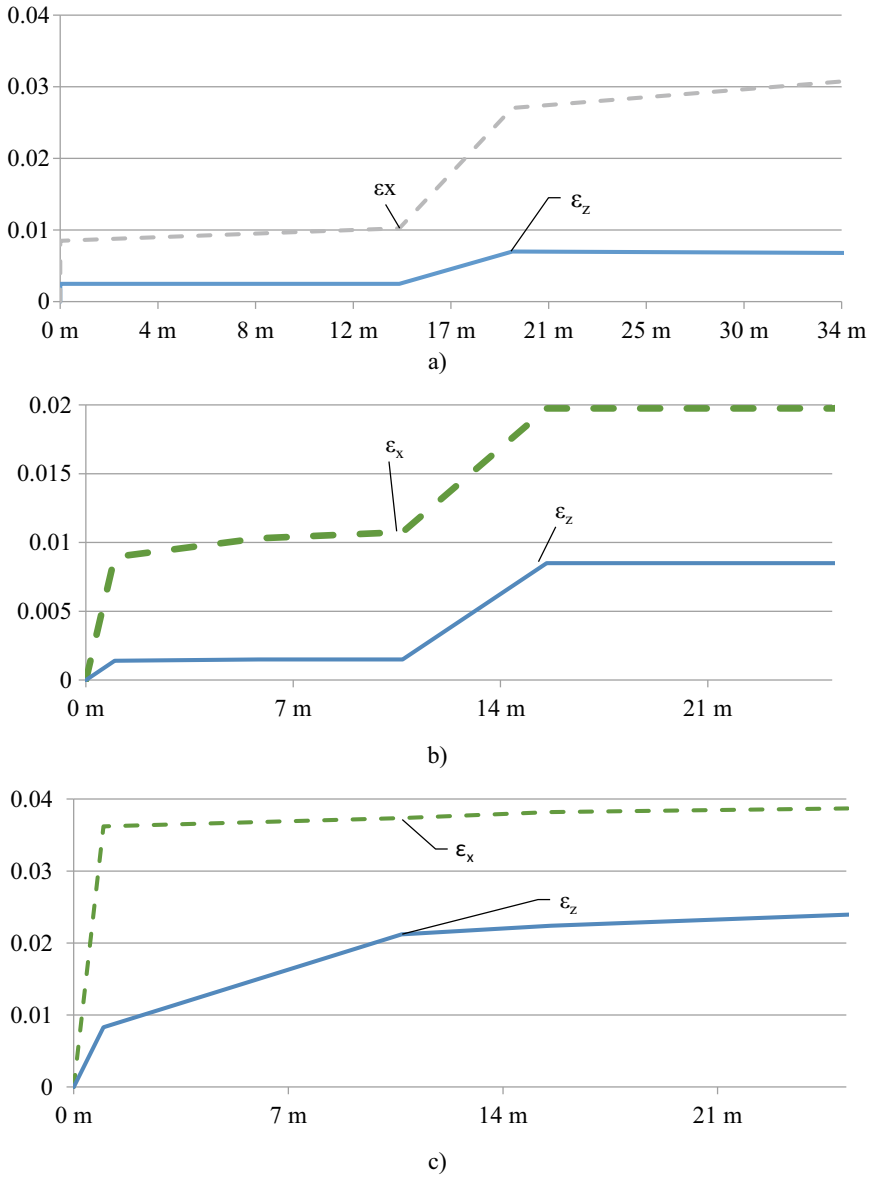


Fig. 2 Deformation of samples: **a** without cracks; **b** with one crack; **c** with two cracks

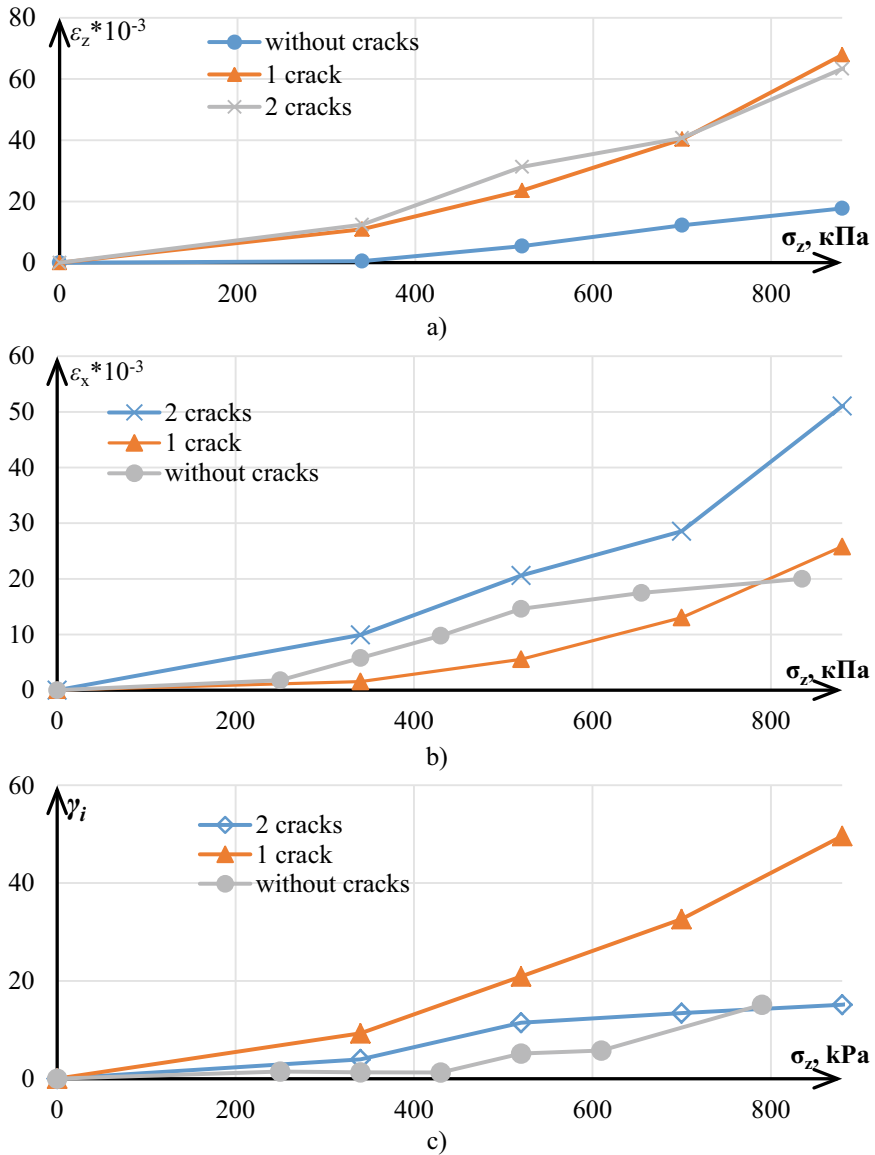


Fig. 3 Deformations of samples at the stage of deviant loading: **a** vertical; **b** transverse; **c** intensity of shear deformations

of the development of horizontal deformations shows that the most intensive development of horizontal deformations occurs in the stress range of 500–800 kPa of deviator loading.

The results of experimental studies show that the greatest values of the intensity of shear deformations were in samples with one crack and the minimum values of the intensity of shear deformations in samples without cracks (see Fig. 3c).

At the stage of deviator loading, the linear modulus of vertical deformations, the shear modulus and the volumetric modulus of deformations decreased on all blocks of regime loading (see Fig. 4). The most intensive decrease in the modulus of vertical deformations occurred in samples without cracks. In the samples with one and two cracks, the decrease in the modulus of vertical deformations occurred more smoothly than in the samples without cracks. The same situation can be seen with the volumetric modulus of deformations. Due to the fact that the initial cracks led to a more intensive growth of all components of deformations, the decrease in the volume modulus of deformations was smooth with an increase in the stress deviator.

4 Discussions

Analysis of the graphs of the development of vertical deformations shows that the most intensive development of deformations occurred at the initial stage within the first loading block (approximately $t = 0$, hour), then there was a relative stabilization of the development of deformations, but complete stabilization did not occur. It should be noted that the most intensive development of deformations was observed in samples with two cross artificial cracks and less intensive development of deformations was observed in samples without initial cracks, and in samples with one artificial crack deformations were about two times less than in samples with two artificial cracks. During the transition to the next loading block, at the time of the change (increase) of the deviator, an increase in the total vertical deformations occurred, then, as in the first loading block, the most intense loading and stabilization of deformations occurred within the second block. In subsequent loading blocks, the above patterns were repeated. At the same time, in each subsequent block, in general, the intensity of deformation development was less than in the previous block.

Linear horizontal deformations had approximately the same patterns of development within each block. At the same time, the following pattern should be noted: at the time of the deviator increase, the transverse deformations decreased by an amount up to $3.25 \cdot 10^{-4}$. Then the initial value was restored during $t = 24$ h, and a further increase in horizontal deformations occurred.

The development of shear deformations had its own characteristics:

1. At the initial stage, there was an increase in shear deformations as horizontal linear deformations also increased.
2. At the time of the increase in the stress deviator, there was an abrupt decrease in shear deformations similar to transverse deformations.

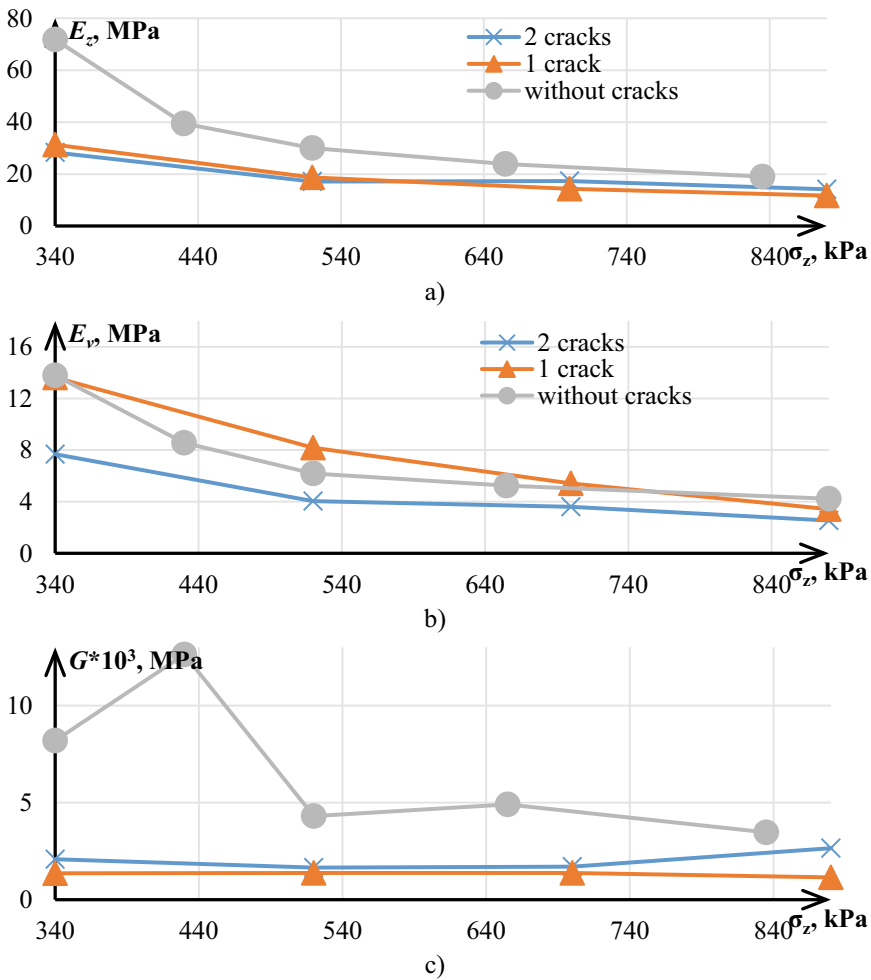


Fig. 4 Deformation modules: **a** vertical; **b** volumetric; **c** shear

- Then there was a stabilization of shear deformations and their further growth. Then they exceeded the shear deformations in the previous block. The main reason for this is the degradation of the soil structure, the rotation of the equilibrium plane and the deviation of the resultant tangential stresses from the plane of ultimate equilibrium.

The results of these experimental studies make it possible to increase the accuracy of calculations up to two times, compared with other methods. The need for such calculations is confirmed by the demand for such cases in the construction field [16].

5 Conclusions

The performed experimental studies of three series of clay samples in a cubic stabilometer under conditions of long-term regime static loading allowed us to establish the following basic patterns of behaviour of clay soils under load:

1. The main regularities of changes in the basic physical and mechanical properties of soils under triaxial loading are that under such loads, cracks develop along the planes of ultimate equilibrium and leads to a decrease in the strength characteristics of the soil.
2. During the test, the main regularities of the development of initial defects in the form of cracks in the planes of ultimate equilibrium both in length and width were established. The rate of crack development depends on the rate of change of the vertical stress deviator and the change in the lateral pressure.
3. The initial defects of clay soil samples in the form of one or two cracks located in the planes of extreme equilibrium led to an increase in vertical, horizontal deformations and the intensity of shear deformations, regardless of the loading mode, compared with samples without initial defects.

References

1. Gong, L., Nemcik, J., Ren, T.: Numerical simulation of the shear behavior of rock joints filled with unsaturated soil. *Int. J. Geomech.* **18**, 04018112 (2020). [https://doi.org/10.1061/\(ASCE\)GM.1943-5622.0001253](https://doi.org/10.1061/(ASCE)GM.1943-5622.0001253)
2. Sobol, E., Gabryś, K., Zabłocka, K., Šadzevičius, R., Skominas, R., Sas, W.: Laboratory studies of small strain stiffness and modulus degradation of Warsaw mineral cohesive soils. *Minerals* **10**, 1127 (2020). <https://doi.org/10.3390/min10121127>
3. Gluchowski, A., Sas, W.: Long-term cyclic loading impact on the creep deformation mechanism in cohesive materials. *Materials* **13**, 3907 (2020). <https://doi.org/10.3390/ma13173907>
4. Xianzhang, L., Peng, L., Feng, Zh., Yingying, Zh., Yan, L., Lingshi, A.: Permanent deformation characteristics of coarse grained subgrade soils under train-induced repeated load. *Hindawi Adv. Mater. Sci. Eng.* **15**, 15 (2017). <https://doi.org/10.1155/6241479.2017.15>
5. Kutergin, V.N., Pankov, K.V., Kalbergenov, R.G., Karpenko, F.S., Manukin, V.B.: Assessment of soil strength changes under cyclic loads simulating the impact of storm waves on the structure. *Geocol. Eng. Geol. Hydrogeol. Geocryol.* (5), 450–459 (2015)
6. Hussein, H.K., Zeena, W.S., Adel, H.J.: Behaviour of soft clayey soil improved by fly ash and geogrid under cyclic loading. *Civil Eng. J.* **6**, 225–237 (2020). <https://doi.org/10.28991/cej-2020-03091466>
7. Mirsayapov, I.T.: Punching settlement of raft-pile foundation under cyclic loading. *News KSUAE* **4**(54), 6–14 (2020)
8. Mirsayapov, I.T., Koroleva, I.V.: Studies of the water migration effect on changes in the clay soil physicommechanical characteristics under triaxial loading conditions. *News KSUAE* **2**(48), 168–174 (2019)
9. Zhang, H., Su, C., Bai, J., Yuan, R., Ma, Y., Wang, W.: The rheological analytical solution and parameter inversion of soft soil foundation. *Symmetry* **13**, 1228 (2021). <https://doi.org/10.3390/sym13071228>

10. Hicher, P.Y.: Experimental study of viscoplastic mechanisms in clay under complex loading. *Geotechnique* **66**, 661–669 (2016). <https://doi.org/10.1680/jgeot.15.p.203>
11. Hu, C., Liu, H.: A new bounding-surface plasticity model for cyclic behaviors of saturated clay. *Commun. Nonlinear Sci. Numer. Simul.* **22**, 101–119 (2015). <https://doi.org/10.1016/j.cnsns.2014.10.023>
12. Wang, Y.: Cyclic response of natural soft marine clay under principal stress rotation as induced by wave loads. *Ocean eng.* **129**, 191–202 (2017). <https://doi.org/10.1016/j.oceaneng.2016.11.031>
13. Kayumov, R.A., Tazyukov, B.F., Mukhamedova, I.Z.: Identification of mechanical characteristics of a nonlinear-viscoelastic composite by results of tests on shells of revolution. *Mech. Compos. Mater.* **55**, 171–180 (2019). <https://doi.org/10.1007/s11029-019-09802-3>
14. Mirsayapov, I.T., Koroleva, I.V., Ivanova, O.A.: Low cycle endurance and deformation of clay soils under triaxial cyclic loading. *Housing Constr.* **9**, 6–8 (2012). 18083643/0044-4472. 6–8 September 2012
15. Mirsayapov, I.T., Koroleva, I.V.: Bearing capacity of foundations under regime cyclic loading. In: 15th Asian Reg. Conf. Soil Mech. Geotech. Eng. ARC, pp. 1214–1217 (2015)
16. Pronozin, Y.A., Kaygorodov, M.D., Karaulov, A.M.: Analytical determination of well parameters while eliminating uneven settlement of foundations by drilling soil. *Constr. Geotech.* **11**, 40–48 (2020). <https://doi.org/10.15593/2224-9826/2020.2.04>

Special Aspects of Stress–Strain Analysis of Combined Piled-Raft Foundation Under Performance Static and Cyclic Loading



Mirsayapov Ilizar Talgatovich  and Garaev Almaz Ilgamovich

Abstract Purpose of the study consists in consideration of different special aspects of stress–strain analysis of combined piled-raft foundation (CPRF) under various kinds of loading. Central objective of the present study is analysis of current methods of calculation combined piled-raft foundation under various kinds of loading. Topicality of this problem is conditioned by the absence of calculation methodology that would be reliable to give an account of collaborative work of combined piled-raft foundation and subsoil surrounding it under performance cyclic loading. With that current calculation methodologies are developed for the case of cyclic loading with characteristics constant in time. Meanwhile under actual usage conditions of various buildings characteristics of cyclic loading change on different process steps.

We undertook theoretical study of varied calculation methodologies of load capacity and settlement of combined piled-raft foundation depending on different kinds of stress–strain state interaction and change that happens between basic elements of combined piled-raft foundation and soil in-situ surrounding it, and also between elements with one another under various kinds of loading.

Significance of findings for construction industry lies in the fact that analysis of varied calculation methods of stress–strain state of combined piled-raft foundation under different kinds of loading helps to give an appraisal of different authors' approaches to these calculations and determine what conditions of system "foundation–soil in-situ" are still open and under what kinds of loading.

Keywords Combined piled-raft foundation · Pile · Foundation slab · Settlement · Load capacity

M. I. Talgatovich (✉) · G. A. Ilgamovich
Kazan State University of Architecture and Engineering, Kazan, Russian Federation
e-mail: mirsayapov1@mail.ru

© The Author(s), under exclusive license to Springer Nature Switzerland AG 2023
N. Vatin (ed.), *Proceedings of STCCE 2022*, Lecture Notes in Civil Engineering 291,
https://doi.org/10.1007/978-3-031-14623-7_9

109

1 Introduction

One of the most valid methods of load capacity increase at large load levels and negative soil conditions is usage of CPRF. During civil and structural design an important objective consists in load capacity appraisal and projected growth of foundation settlement. Determination of stress–strain state of CPRF represents a task with several unknowns because there are materials with different structural and stress-related properties at subfoundation, and all of these deformations round into conditions [1–4].

Special aspects of CPRF calculation consists in system “foundation—soil in-situ” solution. In solving of this system it is necessary to answer such questions as determination of foundation settlement (settlement of slab foundation and pile group), determination of stress pattern and deformations development at collaborative work of combined piled-raft foundation and subsoil surrounding it, and also elements of CPRF with one another under performance cyclic loading [5, 6].

Methodology for CPRF settlement determination is offered at existing specification document SP 24.13330.2011 and at the papers of such authors as Mirsayapov I. T. and SHakirov M.I. [7–10], Mangushev R. A. and Fadeev A. B. [11], Ter-Martirosyan Z. G., CHin’ T. V. [12], Samorodov A.V. [13]. For all these methodologies it is significant that for CPRF calculation consideration must be given to various kinds of the interaction between pile and subsoil, slab and subsoil, the effect of piles against each other through subsoil and mutual influence of piles and the mat.

Methodology for CPRF load capacity determination is offered at the papers of such authors as Mirsayapov I. T. and SHakirov M.I. [7, 8], Artem’ev D. A. [14], Samorodov A.V. [13].

Behavior of CPRF elements with surrounding soil mass during stress–strain analysis of combined piled-raft foundation was observed by many authors. For example, during CPRF settlement determination different effects and special aspects are taken into account, one of these aspects is additional CPRF settlement at the expense of pile shaft deformation. By such authors as Ter-Martirosyan Z. G. and CHin’ T. V. at the study [15], at the study [16] by authors Utkin V. S., Sushev L. A., Solov’ev S. A. methodology of pile settlement determination at the expense of pile shaft compression with account for friction forces at approach surface was offered. Based on experimental investigations in the study [17] by Gotman A. L. and Gavrikov M. D. the methodology of pile shaft settlement determination with arising of additional settlements of pile shaft with load increase was developed. At the study by Gotman N. Z., Alekhin V. S. Sergeev F. V. [18] determination method of soil load capacity under pile base of pile group content is observed. The way of stress–strain state determination is based on research results carried out for the pile in content of pile group and for one pile.

Findings of calculation methodology helps to observe stress–strain state change of system “combined piled-raft foundation—soil in-situ” under short-time static loading and constant cyclic loading and do not observe loading changes that vary on different steps of buildings and structures operation, which is an important problem today. In

connection with this the purpose of the research is methodology development of stress–strain state of combined piled-raft foundation calculation under performance cyclic loading. In the furtherance of this goal it is necessary to:

- study calculation methodology of stress–strain state of combined piled-raft foundation under static loading;
- study calculation methodology of stress–strain state of combined piled-raft foundation and soil basement performance cyclic loading;
- study calculation methodology of load capacity and settlement of combined piled-raft foundation with account for stress–strain state change under performance cyclic loading.

2 Materials and Methods

In determining stress–strain state of combined piled-raft foundation under various loadings it is necessary to consider different kinds of interaction that appear in process of their combined deforming. These special aspects were observed by the authors during settlement and load capacity determination of combined piled-raft foundation by the way of “combined piled-raft foundation—soil in-situ” system observing.

Calculation Methodology of Combined Piled-Raft Foundation Settlement. Calculation methodology offered in SP 24.13330.2011 consists in definition of three parts:

$$s = s_{ef} + \Delta s_p + \Delta s_c \quad (1)$$

where

s_{ef} —relative foundation settlement;

Δs_p —additional settlement based on pile piercing;

Δs_c —additional settlement based on pile shaft compression.

Calculation of relative foundation settlement s_{ef} is carried out by summing up deformations layer-by-layer of line-deformed foundation with relative limitation of compressed width in according with SP 22.13330.2016.

Ground distortion of piercing Δs_p is an inconstant value and depends on pile step in combined piled-raft foundation. Calculation is carried out by the cellular method in elastic–plastic position.

Settlement computation at the expense of pile shaft compression lies in the fact that pile shaft compression takes place under the influence of external load by linear deformation relation.

In the studies [7–10] the model consisting of raft foundation rigidly connected with piles and soil mass surrounding it was accepted as a computational model.

Settlement of combined piled-raft foundation under multitime repeat cyclic loading is calculated from formula:

$$S(N) = S_{ef}(N) + \Delta S_p(N) + \Delta S_c(N) \quad (2)$$

where

$S_{ef}(N)$ —deformation under multitime repeat cyclic loading of relative foundation;
 $\Delta S_p(N)$ —deformation under multitime repeat cyclic loading at the expense of pile piercing;

$\Delta S_c(N)$ —deformation under multitime repeat cyclic loading at the expense of pile shaft compression.

Settlement of relative foundation is calculated from the formula:

$$S_{ef}(N) = \sum_{i=1}^n [\varepsilon_{z,i}(t, t_0)] * h_i \quad (3)$$

where

h_i —height of i-soil layer;

n —number of soil layers of compressed width;

t —timespan that depends on the beginning moment of reviewing and cycle numbers of loading N ;

$\varepsilon_{z,i}(t, t_0)$ —deformations of i-soil layer under cyclic loading;

t_0 —timespan equal to the period of 1st cycle of loading.

Settlements under repeat loading at the expense of deformation of foot of pile are determined from the formula:

$$\Delta S_c(N) = \frac{\sigma_c^{max}(N_1)(l-a)}{E_b(N_1)} + \frac{\varepsilon_{pl}^{fp}(N) * (l-a)}{\left[1 + \frac{E_b(N)}{E_{rp}(N)} * \frac{A_{cb}}{A_{rp}}\right]} \quad (4)$$

where

$E_b(N)$ —coefficient of proportionality between normal stress and relative dilatational momentary-elastic deformation of a pile corresponding to it under multitime repeat loading;

A_{cb} —pile square made by crossing oblongated body with virtual plane that are situated perpendicular to each other;

$E_{rp}(N)$ —characteristic of soil changes that appear under various kinds of loading during multitime repeat loading effect;

$\varepsilon_{pl}^{fp}(N)$ —deformations in dispersive soils under continuous dynamic loading because of interparticle interaction weakening and their mutual repacking;

$G_v(N)$ —characteristic of deformability determined by the ratio of shear stress bent to soil and to shearing angle under multitime repeat loading;

$K_v(N)$ —volume modulus of ground distortion under multitime repeat loading;
 σ_c^{max} —maximum pressure in pile shaft;
 A_{zp} —soil square of the cell;
 l —longitudinal size of pile.

Settlement under repeat loading at the expense of pile shaft deformation is determined by formula:

$$\Delta S_p(N) = \alpha_{cb} \left[\frac{P_3(N)}{G_v(N)} - \left(\frac{P_3(N) + 2P_3(N) \cos B}{3} \right) * \frac{3K_v(N) - G_v(N)}{3K_v(N) - G_v(N)} \right] \quad (5)$$

where

$P_3(N)$ —pressure in foot of pile;
 α_{cb} —pile size made by crossing oblongated body with virtual plane that are situated perpendicular to each other.

In the study by Fadeev A. B. and Mangushev R. A. [11] settlement of combined piled-raft foundation (CPRF) is determined by two components:

$$S_{n-c} = S_1 + S_2 \quad (6)$$

First component of settlement S_1 represents settlement of raft foundation and depends on load share passed to soil basement by raft foundation:

$$S_1 = (1 - \alpha) S_{\Pi} \quad (7)$$

where

α —load share applied to the pile;
 S_n —settlement of raft foundation.

Second component of settlement S_2 represents settlement of a pile and depends on load share passed by pile and determined by contractility of soil column under pile:

$$S_2 = \alpha S_c \quad (8)$$

where S_c —settlement of a pile.

In the study [12] for CPRF settlement determination the objective about quantitative estimate of stress–strain state of CPRF cell is observed. Settlement of a pile in composition of CPRF is observed depending on three augends: friction forces T , loadings at raft foundation P and forces that appear at pile field foundation R . In connection with high values of pile material rigidity settlements in all three cases are considered to be identical, videlicet:

$$S_c = S_1(T) = S_2(P) = S_3(R) \quad (9)$$

Pile settlement $S_1(T)$ because of friction forces effect is determined by formula:

$$S_1(T) = S_c = S_b + \frac{\tau_a}{3G}(b - a) \quad (10)$$

where

- G —shear modulus;
- τ_a —value of shear strength operated to pile skin;
- b —a half of width of CPRF cell;
- a —a half of width of a pile section.

Depending on loading R at piled footing foundation settlement of a pile $S_3(R)$ is calculated from formula:

$$S_3(R) = S_{cb} = \frac{R(1 - \nu)K_1}{4aG} = \frac{R(1 - \nu)K_1}{2aE} \quad (11)$$

where

- K_1 —coefficient taking into account pile length;
- ν —Poisson's ratio;
- R —a stress arises under pile foot.

In depending on loading P under raft foundation settlement of a pile $S_2(P)$ is calculated from formula:

$$S_2(P) = \frac{PL}{E}\beta(\nu) \quad (12)$$

where

- L —height of soil column;
- $\beta(\nu) = 0.8$;
- E —modulus of soil deformation.

In the study by Samorodov A. V. [13] generalized Hooke's law for uniformly loaded soil layer formed the basis for CPRF settlement determination. Constraint for settlement of combined piled-raft foundation determination is written as:

$$S_{n,r} + S_N \leq S_u \quad (13)$$

where

- $S_{n,r}$ —settlement of raft foundation;
- S_N —settlement of pile field;
- S_u —maximum allowable settlement.

Calculation Methodology of Load Capacity of Combined Piled-Raft Foundation. In the studies [7, 8] methodology of load capacity determination of CPRF

under multitime repeat cyclic loading is represented. The model composed of raft foundation rigidly connected with piles and soil mass surrounding it is taken to be computational model (Fig. 1c).

Load capacity of CPRF was determined according to the conditions that strain under the foot of pile $P_{3,i}(N)$ and strain on the level of pile head $P_{2,i}(N)$ do not exceed

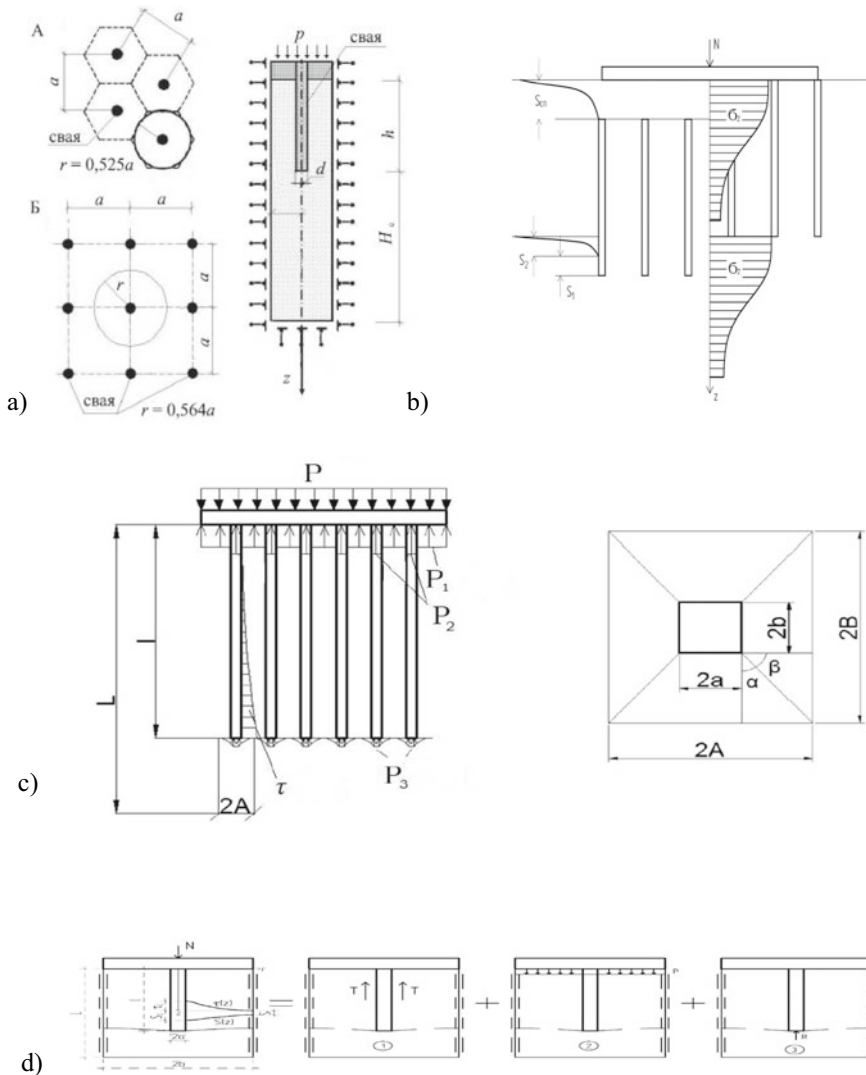


Fig. 1 Computational models: **a** cellular method [SP 24.13330.2011]; **b** Model to settlement of combined piled-raft foundation determination [11]; **c** collaboration diagram of combined piled-raft foundation with soil basement [7]; **d** Model for determination of settlement of single cell of combined piled-raft foundation [12]

ultimate strain in soil $\sigma_{lu}(N)$:

$$P_{2,i}(N) \leq \sigma_{lu}(N) \quad (14)$$

$$P_{3,i}(N) \leq \sigma_{lu}(N) \quad (15)$$

Strains arising under multitime repeat loading were determined from four equations of quasi-static and there were received the following equations:

Ground stress under raft foundation is calculated from the formula:

$$P_1(N) = \frac{P * AB - p_2(N) * ab}{(AB - ab)} \quad (16)$$

where

P —uniformly distributed load;
 A, B —sizes of the cell;
 a, b —sizes of pile section.

The pressure on the level of pile head is expressed in the formula:

$$P_2(N) = \frac{P * G_{gr}(N) * AB * (AB - ab) * L * \beta_{gr} * \left(1 - \frac{1}{L}\right) + 0.33 * \tau_0(N) * E_{gr}(N) * (A - a) * (AB - ab) * k_1}{\alpha * \omega * (1 - \nu_{gr}) * k(l) * (AB - ab) * E_{gr}(N) + ab * \beta_{gr} * L * \left(1 - \frac{1}{L}\right) * G_{gr}(N)} + \frac{0.33 * \tau_0(N) * E_{gr}(N) * (B - b) * (AB - ab) * k_2 - 4 * \frac{\tau_0(N)}{\alpha} * E_{gr}(N) * l * (AB - ab) * \omega * (1 - \nu_{gr}) * k(l)}{\alpha * \omega * (1 - \nu_{gr}) * k(l) * (AB - ab) * E_{gr}(N) + ab * \beta_{gr} * L * \left(1 - \frac{1}{L}\right) * G_{gr}(N)} + \frac{\frac{\tau_0(N)}{\alpha} * E_{gr}(N) * \frac{a+b}{b} * l * (AB - ab) * e^{-\alpha l} * \omega * (1 - \nu_{gr}) * k(l)}{\alpha * \omega * (1 - \nu_{gr}) * k(l) * (AB - ab) * E_{gr}(N) + ab * \beta_{gr} * L * \left(1 - \frac{1}{L}\right) * G_{gr}(N)} \quad (17)$$

where

G —physical value characterizing material's ability to oppose shear deformation;
 $k(l)$ —value considering depth of press-tool application on its length;
 ω —characteristic depending on the form of the cell;
 ν —elastic constant, ratio of relative constraint to relative longitudinal tension value;
 $\alpha = 5/l$, where l —length of a pile.

Pressure under a pile foot is calculated from the formula:

$$P_3(N) = \frac{P_2(N) * 4ab + 4(a + b) * l * \frac{\tau_0(N)}{\alpha} - 4(a + b) * l * \frac{\tau_0(N)}{\alpha} * e^{-\alpha l}}{4ab} \quad (18)$$

where $\tau_0(N)$ pressure arising at the expense of lateral abrasion at pile surface under multitime repeat loading.

In the study [14] based on the range of bench tests hypothesis about puddled zones formation was put forward, and on the ground of this hypothesis the methodology of determination of combined piled-raft foundation load capacity was composed:

$$R_{o\delta\Omega} = \sum_{i=0}^n R_{CB} + R_{\Pi J} \quad (19)$$

$R_{n,i}$ —maximal load accepted by a pile;

$$R_{CB\ i} = R_{\delta o\kappa\ i} + R_{J o\delta\ i} \quad (20)$$

where $R_{\delta o\kappa, i}$ —loading rate accepted by a pile at the expense of lateral abrasion, $R_{J o\delta, i}$ —loading rate accepted by foot of a pile, $R_{n,i}$ —loading rate accepted by raft foundation.

$$R_{\Pi J} = \int_0^{A_p} f(x) \sigma_{rp} dA_p \quad (21)$$

where

$f(x)$ —characteristic of pressure profile in soil;

σ_{rp} —pressure in soil under raft foundation;

A_p —square of raft foundation without including cross section of piles.

In the study [13] load capacity of CPRF $P_{n,i}$ is determined from constraint of maximum allowable settlement of raft part of foundation $S_{n,i}$ and expressed in the formula:

$$R_{\Pi J} = \int_0^{A_p} f(x) \sigma_{rp} dA_p \quad (22)$$

where

d_J —size of the cross section of a pile;

$S_{n,i}$ —settlement of raft foundation;

k —coefficient accepted in depending on width of foundation base;

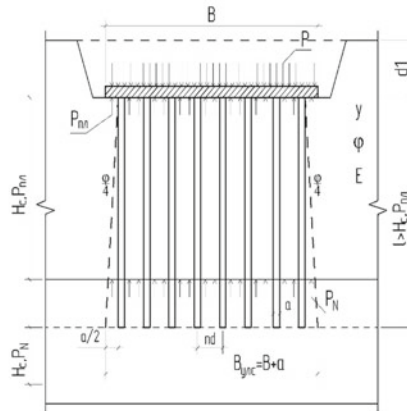
γ —unit weight of soil;

β —nondimensional factor equal to 0.8;

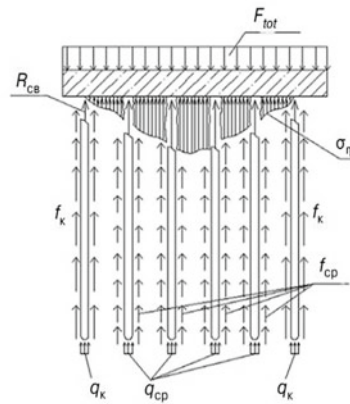
E —modulus of deformation of soil (Fig. 2).

Calculation Methodology of Stress–Strain State of Components of Combined Piled-Raft Foundation with Surrounding Soil Mass. In the study [15] methodology of settlement determination of a pile at the expense of material contractility is observed. Represented methodology helps to determinate settlement of pile from strain effect σ_x , σ_z , τ_z (Fig. 3).

Fig. 2 Computational models: **a** Computational model of cooperation of combined piled-raft large-sized foundation with soil mass [13]; **b** Computational model of cooperation of combined piled-raft foundation [14]



a)



b)

In the study [16] settlement of a pile consists of the following components (Fig. 3):

$$\Delta S_c = \Delta_p + \Delta_G + \Delta_{f,otp} - \Delta_f \tag{23}$$

where

Δ_p —deformations as a result of pile shaft deforming from action of external forces;

Δ_G —deformations as a result of pile shaft deforming from action of proper weight of pile;

$\Delta_{f,otp}$ —additional settlement as a result of negative friction forces arising;

Δ_f —negative settlement as a result of action of friction forces.

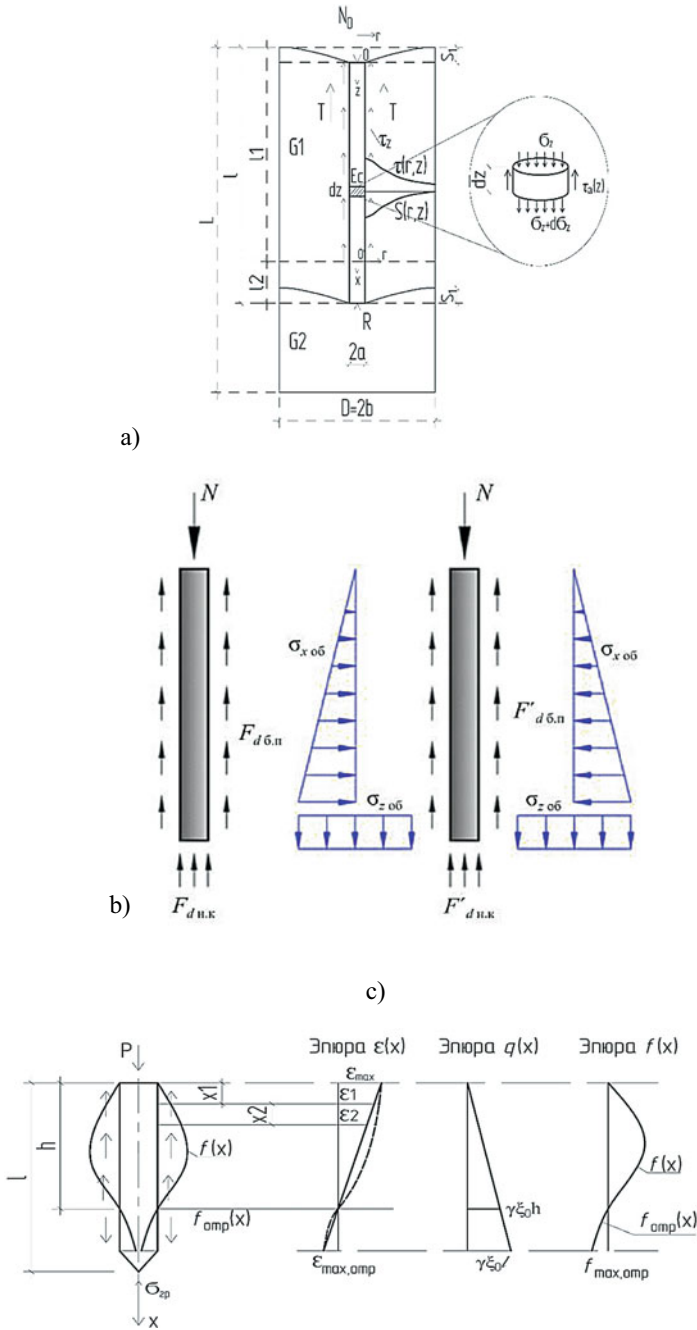


Fig. 3 a Computational model of compressible pile and two-layered soil in-situ cooperation [15]; b Computational model for ultimate stress definition for single pile and pile in composition of a pile group [17]; c Computational model of pile action in homogeneous ground of foundation [16]

In the study [17] the following formulas for additional settlement determination were received:

–deformation as a result of pile shaft compression S_p :

$$S_p = \frac{l(2N_{03} - N_f)}{2EA} \quad (24)$$

where

l —longitudinal size of a pile;

E —coefficient of proportionality between normal stress and relative dilatational momentary-elastic deformation of a pile corresponding to it;

A —pile square made by crossing oblongated body with virtual plane that are situated perpendicular to each other;

N_f —maximal load accepted by a pile by the effect of soil friction on lateral surface;

N_{03} —value of applied load.

– deformation as a result of compression under pile foot S_l :

$$S_l = \frac{(1 - \mu^2)\omega d P}{E_0 A} \quad (25)$$

where

E_0 —addition of mechanical stress bringing unit incrementation of soil relative deformation under pile foot;

μ —elastic constant, ratio of relative constraint to relative longitudinal tension value;

d —size of a pile;

ω —shape coefficient accepted for circular section equal to 1.

P —load rate under pile foot.

Total settlement of a pile:

$$S = \frac{l(2N_{03} - N_f)}{2EA} + \frac{(1 - \mu^2)\omega d P}{E_0 A} + S_g \quad (26)$$

In the study [18] determination method of stress–strain state takes into account the effect of “crimping”, at that time load capacity of foundation is expressed in a formula:

$$F_{d.r.c} = F_{d \text{ ucn}} * \frac{F'_{d.r.c}}{F'_{d.o.c}} \quad (27)$$

where

$F_{d.z.c}$ —maximal load accepted by a pile foot in composition of pile field;

$F_{d.ucn}$ —maximal load accepted by a pile foot according to the data from field tests;

$F'_{d.z.c} = (R + \Delta R) * A + u \sum (f_i + \Delta f_i) h_i$ and $F'_{d.o.c} = R * A + u \sum f_i h_i$ —maximal load accepted by a pile in composition of piles group and single pile.

3 Results and Discussion

As a result of consideration of different methodologies of stress–strain state determination of combined piled-raft foundation there were found the formulas that help to determine load capacity and settlement of combined piled-raft foundation in result of static and cyclic loadings.

In that way, settlement of combined piled-raft foundation under short-time static loading can be determined considering deformations of linearly deformed foundation and additional settlements that depend on pile step, deformations of pile shaft and external load action by the formula (28); considering mutual influence and load distribution between raft foundation and piles (29), and also with the consideration of resulting friction forces, strains under raft foundation and under pile foot.

$$s = s_{ef} + \Delta s_p + \Delta s_c \quad (28)$$

$$S_{n,c} = S_{CB} + S_{nII} \quad (29)$$

$$S_c = S_1(T) = S_2(P) = S_3(R) \quad (30)$$

Settlement of combined piled-raft foundation under cyclic loading can be determined by the formula (31) due to the specifics of fatigue endurance limit approach in one of the elements of system “combined piled-raft foundation–soil in-situ” considering performance of soil vibrocreep deformations and concrete of a pile in confined spaces.

$$S(N) = S_{ef}(N) + \Delta S_p(N) + \Delta S_c(N) \quad (31)$$

Load capacity of combined piled-raft foundation under cyclic loadings is determined in reliance on fatigue limit load decrease and cyclic creep of soil foundation increase according to the arrangement of development limitation of vertical deformations in it and is estimated from constraints:

$$P_{2,i}(N) \leq \sigma_{1u}(N) \quad (32)$$

$$P_{3,i}(N) \leq \sigma_{1u}(N) \quad (33)$$

The methodology that helps to determine load capacity of combined piled-raft foundation at the expense of definition of its maximum allowable settlement is also exposed:

$$P_{nл} = \frac{d_1 + \sqrt{d_1^2 + \frac{4 * S_{nл} * E}{k * \gamma * \beta}}}{2} k * \gamma \quad (34)$$

By the methodologies of stress–strain state determination of single elements forming part of CPRF under static loadings settlement with increase of loading rate appears due to the deformation of surrounding soil S_g , additional settlement at the expense of pile shaft compression S_p and compression under pile foot S_l and is expressed by a formula:

$$S = S_p + S_l + S_g \quad (35)$$

Settlement as a result of pile shaft compression with the consideration of friction forces action and arising negative friction is also determined by the formula (36):

$$\Delta S_c = \Delta_p + \Delta_G + \Delta_{f,отр} - \Delta_f \quad (36)$$

Considered calculation methodologies of stress–strain state determination of combined piled-raft foundation and single elements forming part of CPRF under static and cyclic loadings show that during calculation system “foundation–soil in-situ” was observed. Under static and cyclic loadings calculation methodologies considering mutual influence of pile field components with one another in subsoil, influence of resistance appearing at lateral surface of pile and earth back pressure under pile toe on pile deformation value, dependences of load sharing accrue to CPRF between raft foundation and pile field, development of soil foundation and pile shaft deformation according to its loading by vertical load were found out.

4 Conclusion

Summarizing analysis of carried out calculation methodologies of stress–strain state of combined piled-raft foundation, one can conclude as follows:

1. Base quantity of calculation methodologies of stress–strain state of combined piled-raft foundation are developed for static loading in the way that loading data is unchanged during all life cycle of building or structure.
2. Current calculation methodologies of combined piled-raft foundation cannot take into account stress–strain state appearing in piles, raft foundation, soil between

- piles and surrounding soil mass as a result of collaborative work of system “raft foundation pile soil between piles soil under pile foot” under performance cyclic loading.
3. In connection with the above it is long past time to develop calculation methodology of determination of CPRF load capacity and settlement taking into account the alterations of stress–strain state under performance cyclic loadings.

References

1. Katzenbach, R., Leppla, S.: Environment-friendly and economically optimized foundation systems for sustainable high-rise building. In: ICSMGE 2017 – 19th International Conference on Soil Mechanics and Geotechnical Engineering/19th ICSMGE Secretariat, Seoul, pp. 3381–3384 (2017)
2. Katzenbach, R., Leppla, S.: Optimised design of foundation systems for high-rise structures: Insights and Innovations in Structural Engineering. In: Mechanics and Computation - Proceedings of the 6th International Conference on Structural Engineering, Mechanics and Computation, pp. 2042–2047. CRC Press, Balkema (2016). <https://doi.org/10.1201/9781315641645-338>
3. Bokov, I.A., Fedorovskii, V.G.: On the calculation of groups of piles using mutual influence coefficients in the elastic half-space model. *Soil Mech. Found. Eng.* **6**(54), 363–370 (2018). <https://doi.org/10.1007/s11204-018-9482-8>
4. Bokov, I.A., Fedorovskii, V.G.: On the applicability of the influence function obtained from single-pile calculations for the calculation of pile groups. *Soil Mech. Found. Eng.* **6**(55), 359–365 (2019). <https://doi.org/10.1007/s11204-019-09549-y>
5. Mirsayapov, I., Khorkov, E., Minzianov, R.: Research of the stress-strain state of a reinforced concrete beamless floor In: 2nd International Scientific Conference on Socio-Technical Construction and Civil Engineering (STCCE 2021); E3S Web Conf., vol. 274. <https://doi.org/10.1051/e3sconf/202127403031>
6. Mirsayapov, I., Minzianov, R.: Rebar movement in seals under static loading. In: IOP Conference Series: Materials Science and Engineering, Volume 890, International Scientific Conference on Socio-Technical Construction and Civil Engineering (STCCE 2020), Kazan, Russian Federation, 29 April–15 May 2020. <https://doi.org/10.1088/1757-899X/890/1/012073>
7. Mirsayapov, I.T., Shakirov, M.I.: Deformation features of raft-pile foundations models under the action of cyclic loading. In: Socio-Technical Construction and Civil Engineering: IOP Conf. Series: Materials Science and Engineering, Kazan, Russia, pp. 1–9 (2021)
8. Mirsayapov, I.T.: Punching settlement of raft-pile foundation under cyclic loading. *News KSUAE* **4**(54), 6–14 (2020)
9. Mirsayapov, I.T., Koroleva, I.V.: Studies of the water migration effect on changes in the clay soil physicochemical characteristics under triaxial loading conditions. *News KSUAE* **2**(48), 168–174 (2019)
10. Mirsayapov Ilizar, T., Shakirov, M.I.: Combined plate-pile foundations settlement calculation under cyclic loading. In: IOP Conference Series: Materials Science and Engineering, vol. 890, no. 012069. <https://doi.org/10.1088/1757-899X/890/1/012069>
11. Fadeev, A.B., Mangushev, R.A.: Determination of combined piled-raft foundation. *Vestnik grazhdanskih inzhenerov* **2**, 64–67 (2007)
12. Ter-Mirtirosyan, Z.G., Chhin', T.V.: Cooperation of long piles with soil mass in composition of piled-raft foundation. *Vestnik MGSU* **3**(7), 74–78 (2012)
13. Samorodov, A.V.: New structure of piled-raft foundation. *Vestnik Pridneprovskoj gosudarstvennoj akademii stroitel'stva i arhitektury* **1**, 61–68 (2016)

14. Mirsayapov, I.T., Artem'ev, D.A.: Modeling of stress-strain state of piled-raft foundation with combined deformation with surrounding soil mass. *Vestnik grazhdanskih inzhenerov* **2**, 121–123 (2009)
15. Ter-Martirosyan, Z.G., V'et, C.T.: Cooperation of single long pile with two-layered foundation under compressibility of pile shaft. *Vestnik MGSU* **4**(7), 28–34 (2012)
16. Utkin, V.S., Sushev, L.A., Solov'ev, S.A.: Developing of calculation methods of pile foundations by settlement. *Vestnik MGSU* **3**(16), 331–339 (2021). <https://doi.org/10.22227/1997-0935.2021.3.331-339>
17. Gotman, A.L., Gavrikov, M.D.: Investigation of work features of long-bladed vertically loaded insitu piles and their calculation. *Constr. Geotech.* **3**(12), 72–83 (2021). <https://doi.org/10.15593/2224-9826/2021.3.08>
18. Gotman, N.Z., Alekhin, V.S., Sergeev, F.V.: Determination of ultimate resistance of pile foundation in a group of piles. *Vestnik PNIPU. Constr. Archit.* **3**(8), 13–21 (2017). <https://doi.org/10.15593/2224-9826/2017.3.02>

Physical and Mechanical Characteristics of Modified Soil Cement with Polycarboxylate Superplasticizers



Evgenii Vdovin , Pavel Bulanov , Victor Stroganov ,
and Lenar Mavliev 

Abstract We studied basic physical properties and mineral composition of polymineral clays with different index of plasticity, common in the Volga region, whose clay components are represented by mixed-layered (mica–montmorillonite) minerals, hydromicas and chlorites in different quantities. The modification effect of studied soil cement with polycarboxylate superplasticizers on compressive strength, tensile strength in bending and frost resistance has been established. The polycarboxylate modifiers optimal content and effectiveness on soil cement have been determined. It is shown that the modification by polycarboxylate superplasticizers of soils with clay minerals and Portland cement content up to 10% makes it possible to achieve grade levels for strength—M40, frost resistance—F15 and the cement soils usage in bases and coatings structural layers of various pavement types, depending on road and climatic conditions.

Keywords Soil cement · Polycarboxylate superplasticizer · Portland cement · Polymineral clay · Modifier

1 Introduction

It is known that the soil cement is a kind of building material obtained as a result of mixing and subsequent compaction of soils, Portland cement and water (and additives as needed) [1, 2]. Compared to conventional cement concrete, they have some advantages: economy, reduction of negative impact on environment and manufacturability (workability) during construction [3]. Soil cement is widely used as the pavements base, strengthening materials of highways slopes and foundations, etc. [4, 5].

The increase of traffic intensity, traffic load and tire pressure made it necessary for engineers and scientists to develop more advanced technologies that increase the pavements bearing capacity [6, 7]. Various types of clay soils and local materials are

E. Vdovin (✉) · P. Bulanov · V. Stroganov · L. Mavliev
Kazan State University of Architecture and Engineering, Kazan, Russia
e-mail: vdovin007@mail.ru

used in foundations and highway pavements construction, especially in areas with a lack of durable stone materials [8, 9]. However, in wet conditions these materials [10] are susceptible to the climatic factors effects. This fact contributes to the development of damage processes in the structural pavements layers and reduction the roads life [11].

It is known that the various binders introduction improved the properties of clay soils and local materials. These binders are divided into traditional and non-traditional [1, 11]. Traditional include both mineral (cement, lime, fly ash) and various organic binders (bitumen, tar, etc.), and non-traditional—various types of enzymes, liquid polymers, resins, silicates, lignin derivatives and so on. Clay soils and Portland cement are the most effective since cement soils have a sufficiently high strength [12, 13].

Russian and foreign experience indicates that it is advisable to use modifiers [14–17] in order to increase the level of structural and technical characteristics and durability of soils with a high content of clay minerals, strengthened by Portland cements, in pavement layers, as well as to reduce the mineral binder consumption. In addition, the soil cement mixtures modification improves the operational and technological (workability) characteristics [6]. Ones of the most promising modifiers of cement-mineral systems are polycarboxylates, which, unlike known superplasticizers, according to J. Plank and C. Hirsch [18], contribute to a positive change in hydrated newgrowths morphology and a decrease of ettringite crystals size. It is also noted [19, 20] that it was possible to form stable organomineral phases due to the polymeric modifier integration into the lamellar calcium hydroaluminate structure.

Superplasticizers increase the cement floccules peptization as a result of adsorption on surfaces of particles and binder hydrated phases and the formation of an electrostatic charge upon immobilized water release [21]. The advantage of superplasticizers based on polycarboxylate esters is due to the presence of both acrylate groups in the main chain and side chains directed towards the pore solution from cement floccules, which provide the steric effect [22, 23].

According to J. Plank, E. Sakai, C.W. Miao, C. Yu, J.X. Hong polycarboxylate superplasticizers are classified into 9 types [24, 25]: esterification products of poly(methacrylic acid) with methoxy poly(ethylene glycol) in the presence of an acid catalyst (e.g. p-toluol sulfonic acid) and an azeotropic solvent or vacuum to remove the water, including products of copolymerization of ω -methoxy poly(ethylene glycol) methacrylate ester macromonomer with methacrylic acid; products of free radical copolymerization in an aqueous solution of α -allyl- ω -methoxy- or ω -hydroxy poly(ethylene glycol) and maleic anhydride or acrylic acid; products of free radical copolymerization of 4-hydroxy-butyl-poly(ethylene glycol) vinyl ether and maleic anhydride or acrylic acid; copolymerization products of α -metallyl- ω -methoxy- or ω -hydroxy poly(ethylene glycol) as a macromonomer with acrylic acid; copolymerization products of isoprenyl oxy poly(ethylene glycol) ether as a macromonomer with acrylic acid; zwitterionic polycarboxylate superplasticizers having mixed side chains and consisting of polyamidamine and poly(ethylene glycol) segments; silylated polycarboxylate superplasticizers; synthesized into non-crosslinked polycarboxylate molecules using diesters (e.g. poly(ethylene glycol) and methacrylic acid or maleic

anhydride); phosphate polycarboxylates obtained by esterification of hydroxyethyl methacrylate with phosphoric acid.

Based on analysis of reviewed scientific research in the plasticizers usage field in cement-mineral road materials, it has been established that polycarboxylate superplasticizers were interesting as it is the most promising way to modify soil cement based on soils with a high content of clay minerals.

According to studies [26], polymineral clays containing mixed-layered (mica-montmorillonite) minerals, hydromicas and chlorites are common in the Volga region.

In this regard, the aim of the work is to study the physical and mechanical characteristics of soil cement based on polymineral clays modified by polycarboxylate superplasticizers for road pavements.

To achieve this aim, the following tasks were solved:

- 1) to study the basic physical properties and mineral compositions of polymineral soils with different content of clay minerals;
- 2) to determinate the polycarboxylate superplasticizers effect on physical and mechanical characteristics of soil cement based on polymineral clays with different plasticity index.

2 Materials and Methods

For the research, clay soils of the Sakharovsk and Koshchakovsk deposits with polymineral composition were used, which are among the most common in the Volga region. The content of Portland cement (PC) CEM I 42.5 N JSC “Volskement” in the studied cement soils was varied in amounts of 6.0; 8.0 and 10.0% (by weight of soil).

The mineral composition of clays was determined on a Bruker D8 Advance automatic X-ray diffractometer with a Vario attachment and a Vantec linear coordinate detector. We used $\text{CuK}\alpha$ radiation, monochromatized ($\lambda(\text{Cu-K}) = 1.54184 \text{ \AA}$) by a bent Johanson germanium monochromator, X-ray tube operating mode 40 kV, 40 mA. The experiments were carried out at room temperature in the Bragg–Brentano geometry with a flat sample.

The soils plasticity index was determined according to the standard GOST 5180 as the difference between soil moisture at the liquidity limit using the balance cone method and soil moisture at the plasticity limit. The soils granulometric composition was determined in accordance to the standard GOST 12,536.

The following grades were used as polycarboxylate superplasticizers: Odolit-K (Russia), Hyperlit (Russia), Remicrete SP-10 (Germany), Relamix PK (Russia). Polycarboxylate superplasticizers were introduced in amounts of 0.025, 0.050, 0.075, 0.100 and 0.125% (by weight of the soil).

Determination of the ultimate compressive strength (R_{str}) and ultimate tensile strength in bending (R_{bend}) of soil cement was carried out after the samples were water saturated during 2 days. The samples age at the testing time was 28 days.

The freeze–thaw durability (K_{freeze}) was determined as the ratio of the soil cement strength after 15 freeze–thaw cycles to the water-saturated samples strength after 28 days of hardening under normal conditions. Physical and mechanical properties tests of soil cement were carried out according to the standard GOST 23,558.

3 Results and Discussion

Analysis of results of the studied clay soils mineral composition determining showed that these soils belong to polymineral clays in accordance to the standard GOST 9169. The studied clay soils according to the standard GOST 25,100 are divided into the following varieties: Sakharovsk deposit soil which is light silty loam (plasticity index—11.62, sand particles content—9.14%); the Koshchakovsk deposit soil which is heavy silty loam (plasticity index—14.59, sand particles content—8.32%).

In the Sakharov deposit soil the relict minerals content is more than 85% (52.49% quartz), and the clay minerals amount is 10.66%. In the Koshchakovsk deposit soil the relict minerals content is 73.9% (35.8% quartz), and the clay minerals amount is 26.1%. The clay components of the studied soils are represented by mixed-layered (mica–montmorillonite) minerals, hydromicas and chlorites.

It was established that when soil cement based on the Sakharovsk deposit soil has been modified by polycarboxylate superplasticizers: the ultimate compressive strength increased by 38–71%; ultimate tensile strength in bending—39–63%, freeze–thaw durability—42–77% (Fig. 1). When the soil cement based on Koshchakovsk deposit soil has been modified by polycarboxylate superplasticizers: the ultimate compressive strength increased by 30–75%; ultimate tensile strength in bending—23–66%, freeze–thaw durability—16–37%.

Study results analyzing (Figs. 1 and 2) shows that the optimal content of modifiers was:

- for soil cement based on the Sakharovsk deposit soil: Odolit-K and Hyperlit—0.05%, Remicrete SP-10 and Relamix PK—0.075%.
- for soil cement based on the Koshchakovsk deposit soil: Odolit-K, Hyperlit, Remicrete SP-10 and Relamix PK—0.1%.

The most effective polycarboxylate modifier to improve the physical and mechanical characteristics of the studied cement soils is Odolit-K (Fig. 2).

It was established that when soil cement based on the Sakharovsk deposit soil has been modified by Portland cement content of 10% and Odolit-K polycarboxylate superplasticizer (0.05% by weight of the soil), the M40 strength grade and the F15 freeze–thaw durability grade are achieved. It makes possible to use modified strengthened soils in structural layers of bases and coatings of transitional and lightweight pavement types, depending on road and climatic conditions. When the soil cement based on Koshchakovsk deposit soils was modified by polycarboxylate superplasticizers, the strength grade M40 and the freeze–thaw durability grade F15

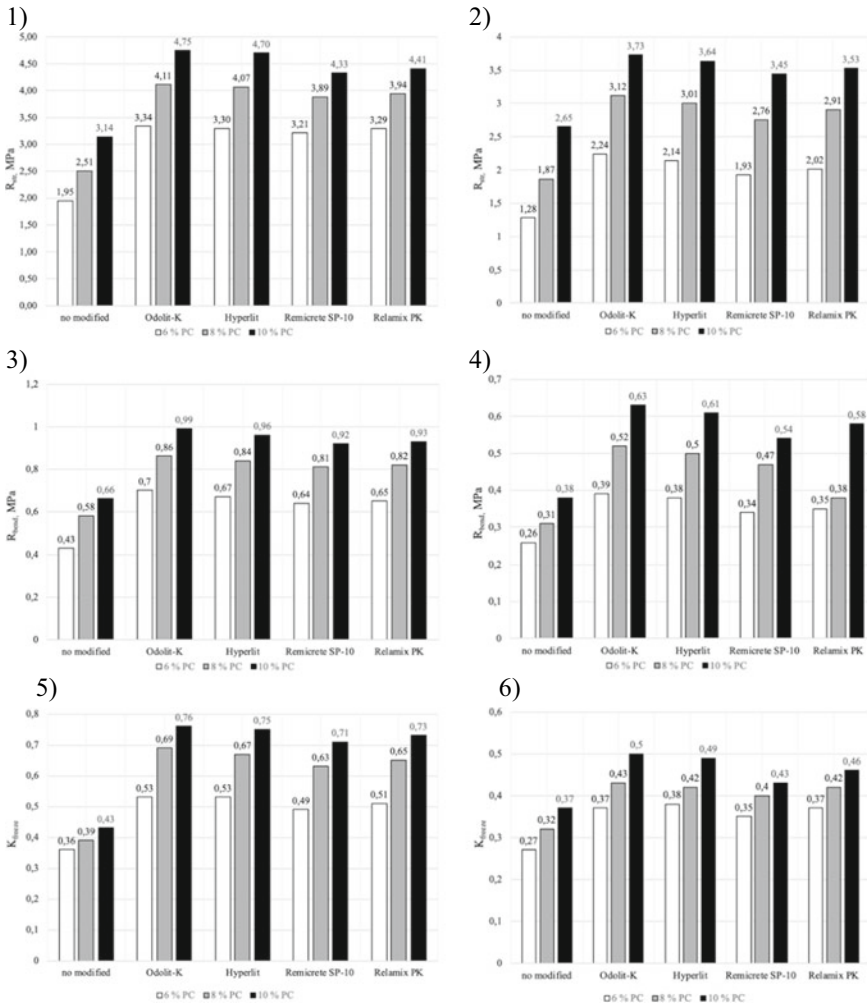


Fig. 1 Physical and mechanical characteristics of modified soil cement with the optimal content of polycarboxylate superplasticizers: 1, 3, 5—soil cement based on the Sakharov deposit soil; 2, 4, 6—soil cement based on the Koshchakovsk deposit soil

are not achieved, which is associated with a high content of clay minerals (2,4 times) and plasticity index increased (1,3 times) compared to Sakharov deposit clay soil. The increased clay minerals content in soils and the levels of plasticity index limit the scope of soil cement in pavements. In this regard, to ensure the required levels of physical and mechanical characteristics, additional solutions are needed for the modification process.

Many authors explained the positive modification results by polycarboxylate plasticizers with the impact effect on soils clay minerals and cement system.

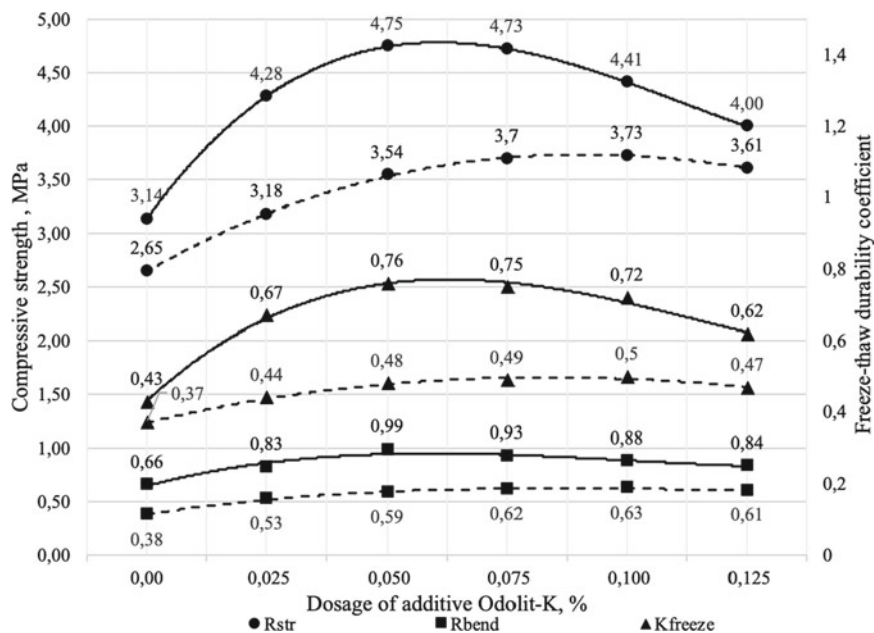


Fig. 2 Dependences of physical and mechanical characteristics of soil cement modified by polycarboxylate superplasticizer Odolit-K, with 10% Portland cement ——— soil cement based on the Sakharov deposit soil; - - - - soil cement based on the Koshchakovsk deposit soil

Theoretically, the existence of two main interactions types of clay minerals with polycarboxylates is assumed [27, 28]:

- electrostatic penetration between positively charged areas of the clay surface and negatively charged plasticizer groups in the cement pore solution;
- plasticizer side chains intercalation in aluminosilicate layers of clay minerals, using hydrogen bonds.

In studies [29, 30], it was found that in the acidic environment of clay minerals, the aggregation proceeds by the electrostatic attraction of negatively charged basal planes with positively charged mineral cleavages, and when polycarboxylate polymer is present in small amounts, small aggregates were formed due to hydrogen bonds between the side chains polyethylene glycol and clay surfaces. At a higher content, the polycarboxylate molecules can completely cover the self-aggregated clay particles and thereby help to increase the repulsive effect between these aggregates.

In an alkaline soil environment and a polycarboxylate superplasticizer low content, the polymer is able to retain clay mineral particles as long as close distance between clay and polymer particles was maintained. Under these conditions, the polycarboxylate polymer is fully stretched due to repulsive forces between the negatively charged carboxylate groups in the backbone and steric interactions between the highly hydrated polyethylene glycol side chains of the clay minerals. As a result,

polycarboxylate molecules are able to bind particles of clay minerals and form a physical network of hydrogen bonds between polycarboxylate molecules and active centers of clay mineral surfaces, which significantly increases the strength of soil cement. With an increased content of polycarboxylate in the soil, the possibility of modifying clay particles increases due to an increase in steric repulsion forces due to the complete coverage of the surface of clay mineral particles. As a result of these processes, the soil viscosity decreases which increased the maximum density and decreased the optimal moisture content of clay soil modified by polycarboxylate superplasticizer [29, 30].

In soil cement acidic pH changes to an alkaline. In this case, clay minerals acquire a completely negative charge, and part of the hydrated hydroxyl groups will be deprotonated into an oxy group. This allows the polyethylene glycol side chains to penetrate into the aluminosilicate mineral layers and bind to the clay minerals surface. The implementation of these processes contributes to decrease the optimal moisture level and to increase the maximum density index of the soil cement mixture [31].

4 Conclusions

- Based on analysis of reviewed scientific research in the field of plasticizers usage in cement-mineral systems, it has been established that one of the most promising methods of modifying road soil cement is the polycarboxylate superplasticizers usage.
- Results analysis of determining the studied clay soils mineral composition showed that the studied soils belonged to polymineral clays common in the Volga region, the clay components of which were represented by mixed-layered (mica-montmorillonite) minerals, hydromicas and chlorites in the amount of 10.7 and 26.1%.
- When the studied soil cement is modified by polycarboxylate superplasticizers, the ultimate compressive strength was increased by 30–75%; ultimate tensile strength in bending—23–66%, freeze–thaw durability—16–77%. The most effective polycarboxylate modifiers for improving the physical and mechanical characteristics of the studied soil cement is Odolit-K.
- When soils with clay minerals content of 10.7% and Portland cement of 10% is modified by polycarboxylate superplasticizer Odolit-K, the strength level grade M40 and freeze–thaw durability grade F15 were achieved, which made it possible to use modified strengthened soils in structural layers of bases and coatings transitional and lightweight pavement types depending on road and climatic conditions.
- It should be noted that the increased clay minerals content (26.1%) in soils and levels of plasticity index indicators (14.6) limits the scope of soil cement in pavements. To ensure the required levels of physical and mechanical characteristics, additional solutions are needed for the modification process.

References

1. Abbey, S.J., Eyo, U.E., Okeke, C.A.U., Ngambi, S.: Experimental study on the use of RoadCem blended with by-product cementitious materials for stabilisation of clay soils. *Constr. Build. Mater.* **280**, 122476 (2021)
2. Jiang, N.-J., Du, Y.J., Liu, K.: Durability of lightweight alkali-activated ground granulated blast furnace slag (GGBS) stabilized clayey soils subjected to sulfate attack. *Appl. Clay Sci.* **161**, 70–75 (2018)
3. Behnood, A.: Soil and clay stabilization with calcium-and non-calcium-based additives: a state-of-the-art review of challenges, approaches and techniques. *Transp. Geotech* **17**, 14–32 (2018)
4. Eyo, E.U., Abbey, S.J.: Machine learning regression and classification algorithms utilised for strength prediction of OPC/by-product materials improved soils. *Constr. Build. Mater.* **284**, 122817 (2021)
5. Ayeldeen, M., Kitazume, M.: Using fiber and liquid polymer to improve the behaviour of cement-stabilized soft clay. *Geotext. Geomembr.* **45**(6) (2017)
6. Chong, S.H.: Development of constitutive model for simulation of cemented soil. *Geotech. Geol. Eng.* **37**(5), 4635–4641 (2019)
7. Gayfutdinov, R.F., Khafizov, E.R.: Research of abrasive wear of crushed stone for highways. *News KSUAE* **31**(51), 128–137 (2020)
8. Amiri, M., Sanjari, M., Porhonor, F.: Microstructural evaluation of the cement stabilization of hematite-rich red soil. *Case Stud. Constr. Mater.* **16**, e00935 (2022)
9. Zhang, Y., Zhong, X., Lin, J., Zhao, D., Jiang, F., Wang, M.-K., Ge, H., Huang, Y.: Effects of fractal dimension and water content on the shear strength of red soil in the hilly granitic region of southern China. *Geomorphology* **351**, 106956 (2020)
10. Cai, Y., Xu, L., Liu, W., Shang, Y., Su, N., Feng, D.: Field test study on the dynamic response of the cement-improved expansive soil subgrade of a heavy-haul railway. *Soil Dyn. Earthq. Eng.* **128**, 105878 (2020)
11. Roshan, K., Choobbasti, A., Soleimani, K., Fakhrabadi, A.: The effect of adding polypropylene fibers on the freeze-thaw cycle durability of lignosulfonate stabilised clayey sand. *Cold Reg. Sci. Technol.* **193**(3), 103418 (2021)
12. Wang, D., Wang, H., Larsson, S., Benzerzour, M., Maherzi, W., Amar, M.: Effect of basalt fiber inclusion on the mechanical properties and microstructure of cement-solidified kaolinite. *Constr. Build. Mater.* **241**, 118085 (2020)
13. Salik, T., Gandomi, A.H.: Improvement of shear strength of cohesive soils by additives: a review. *Basics Comput. Geophys.* 189–211 (2021)
14. Konovalova, N.A., Dabizha, O.N.I., Pankov, P.P., Rush, E.A.: Utilization of hydrolytic lignin in cement soil compositions. *Ekologicheskaya promyshlennost' Rossii* **11**(23), 32–37 (2019)
15. Kuyukov, S.A., Genze, D.A., Shmatok, V.V., Zhigailov, A.A.: An integrated approach to improving the durability of a cement-soil base. *Transp Transportnyye sooruzheniya Ekologiya* **4**, 80–89 (2019)
16. Zhigailov, A.A., Kuyukov, S.A., Testeshev, A.A., Shmatok, V.V.: Feasibility study of the method for improving the physical and mechanical characteristics of the modified road cement soil. *Putevoy Navig.* **42**(68), 24–29 (2020)
17. Vdovin, E.A., Bulanov, P.E., Mavliev, L.F.: Modification of cement-sand-gravel mixtures with waste from road construction industries. *News KSUAE* **3**(57), 32–41 (2021)
18. Liu, Q., Chen, Zh., Yang, Y.: Model of the charged mosaic surface of the cement particle based on the adsorption behavior of surfactants using ATR-FTIR spectroscopy. *Mater. Sci.* **215**, 108802 (2021)
19. Kanchanason, V., Plank, J.: Effect of calcium silicate hydrate – polycarboxylate ether (C-S-H-PCE) nanocomposite as accelerating admixture on early strength enhancement of slag and calcined clay blended cements. *Cem. Concr. Res.* **119**(1), 44–50 (2019)

20. Kanchanason, V., Plank, J.: Effectiveness of a calcium silicate hydrate – polycarboxylate ether (C-S-H-PCE) nanocomposite on early strength development of fly ash cement. *Constr. Build. Mater.* **169**, 20–27 (2018)
21. Ig, M., Plank, J.: Non-adsorbing small molecules as auxiliary dispersants for polycarboxylate superplasticizers. *Colloids Surf. A Physicochem. Eng. Aspects* **587**, 124307 (2019)
22. Akhlaghi, O., Menciloglu, Y.Z., Akbulut: Non-adsorbing small molecules as auxiliary dispersants for polycarboxylate superplasticizers. *Colloids Surf. A Physicochem. Eng.* **587**, 124307 (2019)
23. Schmid, M., Plank, J.: Interaction of individual meta clays with polycarboxylate (PCE) superplasticizers in cement investigated via dispersion, zeta potential and sorption measurements. *Appl. Clay Sci.* **207**(5), 106092 (2021)
24. Plank, J., Sakai, E., Miao, C.W., Yu, C., Hong, J.X.: Chemical admixtures – chemistry, applications and their impact on concrete microstructure and durability. *Cem. Concr. Res.* **78**, 81–99 (2015)
25. Meier, M.R., Lei, L., Rinkenburger, A., Plank, J.: Crystal growth of $[\text{Ca}_3\text{Al}(\text{OH})_6\cdot 12\text{H}_2\text{O}]_2\cdot (\text{SO}_4)_3\cdot 2\text{H}_2\text{O}$ (Ettringite) studied under microgravity conditions. *J. Wuhan Univ. Technol. Mater. Sci. Ed.* **35**(5), 893–899 (2020)
26. Valitov, N.V., Zorina, S.O., Afanas'yeva, N.I., Antonov, V.A., Sabirov, A.A., Chaykin, V.G., Meskhi, A.M., Glebashev, S.G., Zakirova, F.A., Luzhbina, I.V.: Minerageny of the upper permian and meso-cenozoic complexes of the Republic of Tatarstan. *Kazan' : Izd-vo Kazansk. gos. universiteta, Kazan* (2007)
27. Zhang, Y., Wang, P., Sun, G., Yang, J., Gao, R.: Synthesis and performance characterization of a low adsorption clay-resistant polycarboxylate superplasticizer. *J. Wuhan Univ. Technol. Mat. Sci. Edit.* **36**, 446–455 (2021)
28. Lei, L., Palacios, M., Plank, J., Jeknavorian, A.: Interaction between polycarboxylate superplasticizers and non-calcined clays and calcined clays: a review. *Cem. Concr. Res.* **154**, 106717 (2022)
29. Xu, H., Sun, Sh., Yu, Q., Wei J.: Effect of β -cyclodextrin pendant on the dispersion robustness of polycarboxylate superplasticizer toward kaolin. *Polymer Comp.* **39**(3), 755–761 (2018)
30. Zhang, L., Lu, Q., Xu, Zh., Liu, Q., Zeng, H.: Effect of polycarboxylate ether comb-type polymer on viscosity and interfacial properties of kaolinite clay suspensions. *J. Colloid Interface Sci.* **378**, 222–231 (2012)
31. Ng, S., Plank, J.: Interaction mechanisms between Na montmorillonite clay and MPEG-based polycarboxylate superplasticizers. *Cem. Concr. Res.* **42**, 847–854 (2012)

Theoretical Foundations of Fatigue Destruction of Steel Reinforcement of Reinforced Concrete Structures



Iizar Mirsayapov 

Abstract In reinforced concrete structures under cyclic loads one of the types of failure is fatigue failure of working reinforcement. Operation mode of steel reinforcement in reinforced concrete constructions is non-stationary irrespective of loading conditions. In these cases determination of fatigue resistance of reinforcement requires a great number of experiments which requires a great number of financial and manpower resources. The aim of the work is to develop a theory of fatigue cracking of steel reinforcement and to create design models of reinforcement with cracks. For this purpose it is necessary: to establish the scheme of fatigue crack formation in reinforcement rods for reinforced concrete structures; to develop the equation of change in specific energy of steel fracture in the zones of crack formation and development; to develop a methodology for calculating the durability of steel reinforcement with cracks.

Theoretical research of fatigue strength of steel reinforcement has been carried out. It is established, that fatigue failure of steel reinforcement is characterized by formation and development of micro and macro cracks in metal structure up to critical dimensions; two basic stages are derived: to the formation of micro and macro fatigue cracks; development of macro-fatigue cracks to critical dimensions. The methods of fracture mechanics of elastic–plastic materials were used for modeling of steel reinforcement operation under cyclic mode of deformation and the equations of mechanical characteristics change of reinforcement under different modes of cyclic loading were obtained using these methods. On the basis of theoretical research the equations of change of basic force parameters of steel reinforcement, allowing developing analytical formulas for evaluation of fatigue strength under cyclic loading, have been obtained.

Keywords Steel reinforcement · Stress structure profile · Fatigue crack · Damage · Plastic resource · Specific energy · Creep stress of concrete · Elastic operation of reinforcement

I. Mirsayapov (✉)

Kazan State University of Architecture and Engineering University, Zelenaya Street 1, 420043
Kazan, Russia

e-mail: mirsayapov1@mail.ru

1 Introduction

The process of multi cycle fatigue of metals is conditionally divided into two main stages: before the appearance of the main crack (the stage of the emergence of the fatigue main crack) and the period of development of the main crack before destruction. If durability in the first stage is designated N_t , and durability in the second stage of N_{zh} , then the full durability from the first loading cycle to fatigue destruction will be: $N = N_t + N_{zh}$ [1–5]. At the stage of the emergence of a trunk fatigue crack, intensive plastic deformation of the metal in local volumes occurs, which leads to significant closed hysteresis loops, the area of which is equal to energy scattered over one cycle of loading. The total width of these hysteresis loops is equal to nonelastic deformation for the cycle. After the exhaustion of the plastic resource, microscopic cracks are formed in local plastically deformed volumes, one of which can develop into a main crack [6–10]. Therefore, the first stage can be called the stage of scattered fatigue damage. The second stage characterizes the development of the main crack in critical sizes. The first main crack is implied by a crack, which, with a given loading mode, develops at a higher speed than all other cracks, and is a source of final fatigue destruction. A lot of numerical experimental data found that the velocity dependence of $\vartheta = dp/dt$ on the accumulation of fatigue damage to the number of loading cycles is significantly different in stages I and II of fatigue destruction. Therefore, it can be assumed that the mechanisms of accumulation of damage at these stages are different. This requires attracting various representations to assess the durability of N_{TI} N_{Zh} . Studies carried out at the Central Research Institute of the MTS NIIZHB, N_{IS} , the hydraulic project showed [11–15] that the cracks of fatigue are born mainly in one of the two foci of stress concentration:

- 1) In the obtuse angle of the connection of longitudinal ribs with inclined with transverse protrusions (ribs).
- 2) At the base of the transverse protrusions (ribs) in the places of their interfaces with the body of the rod.

Therefore, the aim of the work is to develop a theory of the development of fatigue cracks of steel reinforcement to create design models of reinforcement with cracks. The objectives of the work are: to establish a scheme for the formation of fatigue cracks in reinforcing bars for reinforced concrete structures; to develop an equation for changing the specific energy of steel destruction in the zones of formation and development of cracks; develop a methodology for calculating the durability of steel reinforcement with cracks.

2 Materials and Methods

To assess the local stresses in the main foci of concentration, we determine the effective coefficients of concentration of loads. Local stresses in the zone of the first

focus are determined by the formula:

$$\sigma_{SM} = 0,843 \cdot \sigma_s^{\max}(t) \cdot b \cdot a \cdot \frac{t \cdot h \cdot m}{\cos \beta} \quad (1)$$

where $\beta = \sqrt{\frac{k}{E f}}$; $k = 1.45 \cdot E \frac{h}{\sqrt{\frac{b h}{\cos \beta}}}$; $f = b \cdot h$;

h —The width of the transverse rib;

b —The height of the transverse ribs;

$r = 10h$ —The radius of curvature of concentration;

$a = \frac{1}{h}$; $m = b \cdot a / 2 \cdot \cos \beta$,

The transition from local stresses to the concentration coefficient is made according to the formula:

$$\alpha_k = \frac{\sigma_{sh} + \sigma_M}{\sigma_{sh}} \quad (2)$$

The theoretical coefficient of concentration of stresses in the second focus is calculated in the following sequence. The radius of curvature r is determined the second -end of the rib (rib) with the core of the rod and the conditional calculated width of the protrusion, and equal to the distance between the points of the beginning of the interfacing on both sides of the transverse rib. For a circular filler width a' , it can be accepted equal to the width of the protrusion plus a doubled radius of conjugation r . With the ratio a'/r , the theoretical concentration coefficient is calculated:

$$\alpha_k = 1 + 0,21 \cdot \sqrt{\frac{a'}{r}} \cdot \cos^2 \beta \quad (3)$$

where β is the angle of elevation of the oblique part of the transverse rib. In addition, in the longitudinal working reinforcement of the bending elements, an uneven stretching occurs with a large plot at the more stretched face of the element. Consider the stress state of the rod in the first loading cycle. Let the bending element be affected by such a bending moment M that the resulting stress field causes micro damage in the zone of influence of the above-mentioned concentrator (Fig. 1).

The total stresses in this zone are calculated as:

$$\sigma_{sk}^{\max} = \sigma_s^{\max}(t_0) + \sigma_{SM} + \Delta \sigma_S, \quad (4)$$

where $\sigma_s^{\max}(t_0)$ are the initial nominal stresses in the reinforcement without taking into account the concentration of stresses; σ_{SM} - local stresses in the concentration zone; $\Delta \sigma_S$ is the increment of stresses due to bending.

When determining the durability of N_T , first of all, it is necessary to establish the dimensions of the initial zone of damage in places of stress concentration, i.e. the dimensions of the zone of influence of the stress concentrators on the surface of the reinforcing rod.

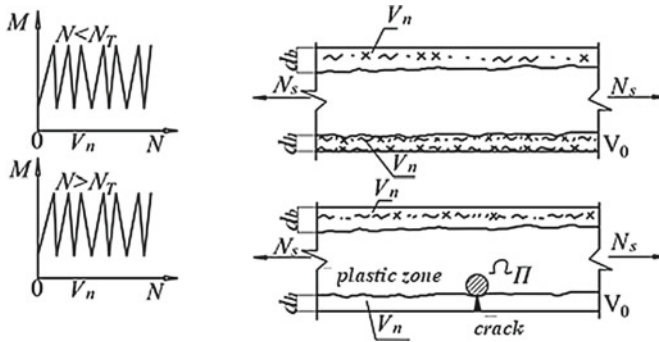


Fig. 1 Schematization of the development of damage in the reinforcement rod with an increase in the number of loading cycles

For this, the stresses in the main foci of concentration are first determined, based on formulas (1) and (3). In the zones of stress concentration, in the general case, a volumetric tense state occurs. When evaluating a stress-deformed state in the concentrator zone, the same criteria can be used as in the absence of stress concentration. A comprehensive stress state leads to an increase in the concentration of the first main stresses of σ_{1k}^{max} , which leads to the coaching of elastic deformations.

3 Results

To determine the size of the zone of influence of the stress concentrator, it is necessary to calculate the relative gradient of the first main stress σ_{1k}^{max} .

$$\sigma = \frac{\sigma}{\sigma_{max}} = \frac{1}{\sigma_{max}} \left[\frac{\partial \sigma}{\partial x} \right]_{x=a} \tag{5}$$

A gradient characterizes the rate at which stresses decrease as the distance from the concentrator increases. To simplify the calculation process, we use the real plot of the stress distribution in the integration zone, which is tangent to the plot at the point $x = a$. The equation of this line is:

$$\sigma_s = u + \sigma(x - a_0). \tag{6}$$

When describing the regularities of cyclic deformation of the material in the local zone of stress concentration, the following prerequisites and assumptions are taken:

- 1) within the initial zone of plastic damage, a rigid load is realized, $\Delta \varepsilon_s = const$ i.e.;
- 2) at a distance Δl_n from the focus of concentration, the magnitude of the stresses $\Delta \sigma_{sk}^{max}$ and the scope of plastic deformation $\Delta \varepsilon_{pl,sk}^{max}$ are constant;

- 3) The formation of micro cracks in the concentration zone occurs, a_k , at a distance from the focus of concentration, the accumulated energy of inelastic deformation, taking into account its dispersion within the damage zone $\alpha_t (\alpha_t > \Delta l_n)$ reaches the value of W (.

Specific energy of inelastic deformation per cycle:

$$\Delta W_i = \int_0^{\Delta \varepsilon} \Delta \sigma d(\Delta \varepsilon) = \sigma_{sh}^{max} \cdot k_\sigma \cdot \bar{\varepsilon} \cdot \alpha_\sigma^{\frac{2}{1+m}} \cdot \bar{\sigma}_h^{\frac{1-m}{1+m}} \cdot \frac{\sigma_y}{E_s}. \quad (7)$$

The energy of inelastic deformation in the zone of concentration of stresses, corresponding to the limit of endurance, is determined by the equation:

$$\Delta W_{BbIH} = \int_0^{\Delta \varepsilon_{\Pi\Pi\Pi}^{\text{II}}} \Delta \sigma d(\Delta \varepsilon) \quad (8)$$

where is $\Delta \varepsilon_{\Pi\Pi\Pi}^{\text{II}} = \frac{1}{2} \ln \frac{1}{1-\psi} \cdot N_{BbIH}^{-1/2}$.

N_{BbIH} – the number of loading cycles corresponding to the endurance limit; ψ – coefficient of transverse narrowing of the material;

$\Delta \sigma_{BbIH} = \sigma_{spBbIH} \cdot (1 - \rho_{si})$; σ_{spBbIH} – limit of endurance of reinforcement for a given ρ_s . Then we determine the loss of energy per cycle due to the manifestation of plastic deformations in local volumes ΔW_r :

$$\begin{aligned} \Delta W_r &= \Delta W_i - \Delta W_{BbIH} = \int_0^{\Delta \varepsilon} \Delta \sigma d(\Delta \varepsilon) - \int_0^{\Delta \varepsilon_{\Pi\Pi\Pi}^{\text{II}}} \sigma_{BbIH} \cdot d(\Delta \varepsilon) \\ &= (\sigma_{sh}^{max}) \cdot k_\sigma \bar{\varepsilon} \cdot \alpha_\sigma^{\frac{2}{1+m}} \cdot \sigma_{sh}^{-\frac{1-m}{1+m}} \cdot \frac{\sigma_y}{E_s} - \int_0^{\Delta \varepsilon_{\Pi\Pi\Pi}^{\text{II}}} \sigma'_{sp BbIH} \cdot (1 - \rho_{si}) \cdot d(\Delta \varepsilon). \end{aligned} \quad (9)$$

After determining the ΔW_r assuming that the energy loss in each cycle has the same value, we calculate the number of loading cycles until the plastic resource of the initial plastically damaged zone is exhausted:

$$N_{T1} = \frac{0, 5 \varepsilon_b^n (\sigma_y + \sigma_u) \cdot \vartheta}{(\sigma_{sh}^{max}) \cdot k_\sigma \bar{\varepsilon} \cdot \alpha_\sigma^{\frac{2}{1+m}} \cdot \sigma_{sh}^{-\frac{1-m}{1+m}} \cdot \frac{\sigma_y}{E_s} - \int_0^{\Delta \varepsilon_{\Pi\Pi\Pi}^{\text{II}}} \sigma'_{sp BbIH} \cdot (1 - \rho_{si}) \cdot d(\Delta \varepsilon)} \quad (10)$$

The advantage of Eq. (10) is that here it is possible to take into account the background of loading and various designs and technological features that lead to a decrease ε_b^n and, as a consequence N_T .

When moving from one block to another, the plastic resource changes ε_b^n and ΔW_r . Therefore, when calculating the endurance limit, it is possible to take into account the change in the loading mode, if $N_1 > N_{T1}$; otherwise the mode variability does not affect the duration of the initial damage zone.

The condition is then checked:

$$N_m > N_1. \quad (11)$$

If condition (11) is met, then the durability of the initial zone is greater than or equal to the duration of the first stage, and at this stage the development of cracks does not occur. Otherwise, it is necessary to determine the increment of the length of the micro crack during the $\Delta N = N_1 - N_{11}$. Consider the development of the initial micro crack with the length formed in the concentrator zone. Numerous experimental studies have established that the development of micro cracks during cyclic loading is significantly uneven. In this case, it is necessary to distinguish the incubation period and the period of continuous development of cracks, which alternate until the complete destruction of the sample.

To describe the development of micro cracks at this stage, we use a model for the development of a fatigue crack, proposed and based on the consideration of the specific energy of inelastic deformation, at a distance of x^* from the top of the crack, taking into account the energy that is not reversibly dissipated within the plastic zone of damage.

The distribution of deformations and stresses at the top of a fixed crack under static loading for reinforcing steel can be represented as the following dependencies:

$$\sigma_{ij}(r, \theta) = A \left(\frac{\mathcal{J}}{AIm} \right)^{\frac{m}{1+m}} \cdot \frac{1}{r^{\frac{m}{1+m}}} f_{ij}(\theta) \quad (12)$$

$$\varepsilon_{ij}(r, \theta) = \left(\frac{\mathcal{J}}{AIm} \right)^{\frac{m}{1+m}} \cdot \frac{1}{r^{\frac{m}{1+m}}} \varphi_{ij}(\theta), \quad (13)$$

where \mathcal{J} is j-integral introduced by Cherepanov and Rais;

Im —dimensionless function of deformation hardening index m of crack opening type.

For the most common values m and for flat tensile deformation $Im = 5/282$. For normal rupture cracks, normalized functions from the angle (θ).

$$f_{ij}(\theta) = \varphi_{ij}(\theta) = \begin{cases} I(i = j) \\ 0(i \neq j) \end{cases}, \quad (14)$$

where m is the hardening index;

r —the distance from the top of the crack to the point in question,

θ is the angle between the continuation of the crack and the point in question at its apex.

In this case, the relationship between stresses and plastic deformation is presented in the form of power dependence:

$$\sigma_{\vartheta} = A \cdot \varepsilon_{p\vartheta}^m, \quad (15)$$

Here σ_s , ε_{ps} is the equivalent stress according to the energy theory of strength and equivalent plastic deformatin. For the case of cyclic loading, Eqs. (13) and (13) are given as follows:

$$\Delta \varepsilon = \left(\frac{1 - v^2}{A' I_m} \right)^{\frac{m}{1+m}} \cdot \left(\frac{\Delta k^2}{E} \right)^{\frac{1}{1+m}} \cdot \frac{1}{r^{\frac{1}{1+m}}} \cdot \varphi_{ij}(\theta) \quad (16)$$

$$\Delta \sigma = \left(\frac{1 - v^2}{A' I_m} \right)^{\frac{m}{1+m}} \cdot \left(\frac{\Delta k^2}{E} \right)^{\frac{m}{1+m}} \cdot \frac{1}{r^{\frac{1}{1+m}}} \cdot f_{ij}(\theta) \quad (17)$$

Basic assumptions of the adopted model.

- 1) At the top of the fatigue crack within the plastic zone of fatigue damage, a hard load is realized, i.e. $\Delta \varepsilon_s = \text{const}$;
- 2) $\Delta \sigma_s^{\text{max}}$ and the scope of plastic deformation $\Delta \varepsilon_{pl}^{\text{max}}$ are constant;
- 3) distribution of stresses and inelastic deformations at the top of the crack $R_m \geq r \geq x^*$ is described by (16) and (17) equations;
- 4) The increase in length by the size of x^* occurs when at a distance of x^* from the top of the crack, the accumulated energy of inelastic deformation, taking into account its scattering within the damage zone $\dot{\alpha}_m(\alpha_m \geq x^*)$ reaches the size W_R .

The dimensions of the plastic zone of damage at the top of the micro -cutter are determined in the form:

$$\alpha_i = \frac{k_I^{\text{max}}}{\sigma_{BbIH}^2 \cdot Y^2(l) \pi} \quad (18)$$

$$k_I^{\text{max}} = \sigma_s^{\text{max}}(t) \cdot \sqrt{a_1} \cdot Y(l) \quad (19)$$

It should be noted that k_I^{max} calculated according to (19), maybe less then k_{th} . Nevertheless, the development of micro cracks will occur, since it is known that surface micro cracks up to 0.5 mm long develop at $k_I^{\text{max}} \leq k_{th}$.

Specific energy of inelastic deformation for the cycle:

$$\Delta W = \int_0^{\Delta \varepsilon} \Delta \sigma d(\Delta \varepsilon). \quad (20)$$

Substituting in values $\Delta \varepsilon$ and $\Delta \sigma$ from (12) and (13) we get:

$$\Delta W_i = \frac{(1 - v^2)}{I_m E_s} \cdot \frac{1}{m + 1} \cdot \frac{\Delta k^2}{r} \cdot \varphi_{ij}(\theta) \cdot f_{ij}(\theta). \quad (21)$$

The size of the first micro-element of the plastic zone x^* can be found from the condition that at a distance of x^* there is no accumulation of damage, and the energy of nonelastic deformation for the cycle ΔW^* at a distance of the crack is equal to

the energy of nonelastic deformation beyond the cycle with stresses corresponding to the endurance limit ΔW_{BbIH} . Then, based on (21) we have:

$$x^* = \frac{\mathcal{J}}{I_m \Delta W_{BbIH}} = \frac{\Delta k_i^2 (1 - \nu^2)}{E \cdot I_m \cdot \Delta W_{BbIH}} \cdot \frac{1}{1 + m}. \tag{22}$$

The energy of inelastic deformation during hard loading corresponding to the endurance limit is determined by the formula:

$$\begin{aligned} \Delta W_{BbIH} &= \int_0^{\Delta \varepsilon_{III}^I} \Delta \sigma_{BbIH} \cdot d(\Delta \varepsilon), \\ \Delta \varepsilon_{III}^I &= \frac{1}{2} \ln \frac{1}{1 - \Psi} \cdot N_{BbIH}^{-1/2} \end{aligned} \tag{23}$$

where Ψ —The transverse narrowing coefficient, for reinforcing steels, it changes from 0.41 to 0.69; on average, you can accept it;

N_{BbIH} —The number of loading cycles corresponding to the endurance limit;

$\Delta \sigma_{BbIH} = \sigma_{BbIH} (1 - \rho_s(t))$; $\Delta \sigma_{BbIH}$ —Endurance limit for the given $\rho_s(t)$.

The plastic zone of damage at the top of the micro crack is divided into separate trace elements by the width. The trace elements are simultaneously subjected to cyclical loading of various intensity. The distribution of specific energy of ineffective deformation for the cycle within the plastic zone described by the Eq. (21) is schematically shown in (Fig. 2).

In accordance with the adopted assumptions at a distance of ΔL of the top of the micro crack, the specific energy of inextricable steel deformation has constant value, i.e. $\Delta W_i = \Delta W_k = \text{const}$.

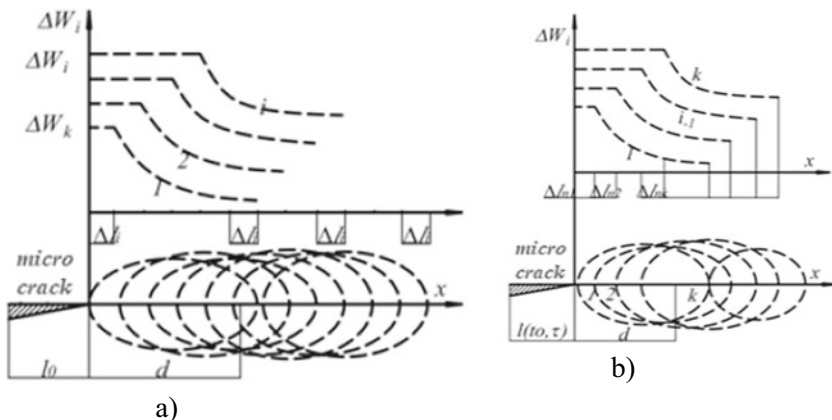


Fig. 2 a A scheme for accumulation of specific energy of inextricable deformation of steel within the plastic zone at the top of the micro crack b scheme for moving the plastic zone during the development of macro crack and accumulation of specific energy of inextricable deformation within the plastic zone of pre-development

The development of micro cracks begins with the destruction of the micro element I. The complete fatigue destruction of the trace element I occurs when the energy of the inhuming hysteresis of the critical value is achieved.

$$W_p = \sum_{i=1}^{N_R} \left[\Delta W_i - \Delta W_r \left(\frac{\Delta W_i}{\Delta W_r} \right)^\beta \right] = \text{const} = W_{pl} \tag{24}$$

where ΔW_r —specific energy of nonelastic deformations for the cycle at equal limit of endurance;

ΔW_i —specific energy of nonelastic deformation of steel in the loading cycle “i” is calculated according to (21).

At the same time, the length of the micro crack increases by ΔL , and the plastic zone moves to ΔL along the front of the micro crack (Fig. 2). As described above, the micro cracks increase, and the plastic zone in front of the developing micro cracks moves. It should also be noted that this process is abolished, since the periods of continuous development of micro cracks alternate with periods of delay.

The condition of destruction of the “i-th” element is described by Eq. (24) passing to the sum, from the Eq. (24) we will receive:

$$\sum_{j=1}^i \Delta \bar{W}_{ij} \cdot N_j = W_p. \tag{25}$$

Given (21) and (23) Eq. (25) for the case of steel reinforcement in the form:

$$\begin{aligned} \Delta \bar{W}_{ij} = \Delta W_{ij} - \Delta W_r &= \frac{1 - v^2}{I_m E_s} \cdot \frac{1}{m'} \cdot \frac{\Delta k^2}{r_1} \cdot \varphi_{ij}(\theta) \cdot f_{ij}(\theta) \\ &- \int_0^{\Delta \varepsilon_{III}^H} \Delta \sigma_{BbIH} \cdot d(\Delta \varepsilon) \end{aligned} \tag{26}$$

where $r_1 \cong x^*$ Distance from the top of the micro crack to the right border of the i-the microelements.

Taking into account (22) and (26), from (25) we find the durability of the i-th microelement in cycles:

$$N_1 = \frac{0,5 \cdot \varepsilon_b^H \cdot (\sigma_y + \sigma_u)}{\frac{1-v^2}{I_m \cdot E_s} \cdot \frac{1}{m'+1} \cdot \frac{\Delta k^2}{r} \cdot \varphi_{ij}(\theta) \cdot f_{ij}(\theta) - \int_0^{\Delta \varepsilon_{III}^H} \Delta \sigma_{BbIH} \cdot d(\Delta \varepsilon)}. \tag{27}$$

Similarly, the durability of the second, and “i-th” elements are determined. At the same time, it must be borne in mind that the durability of conditioned microelements decreases with the removal of the micro-element in question from the top of the micro crack, since the farther from the top of the micro crack, the trace element is located, the more additional energy the nonelastic deformation will be accumulated in it due to preliminary loading with its renovations.

Conducting similar calculations, we compose a general equation of durability for any microelement of the plastic zone.

$$N_i = \frac{0,5 \cdot \varepsilon_b^n \cdot (\sigma_y + \sigma_u) - \sum_1^{k-1} \Delta W_{i-1}}{\frac{1-\nu^2}{l_m \cdot E_s} \cdot \frac{1}{m'+1} \cdot \frac{\Delta k^2}{r} \cdot \varphi_{ij}(\theta) \cdot f_{ij}(\theta) - \int_0^{\Delta \varepsilon_{III}^{II}} \Delta \sigma_{BbIH} \cdot d(\Delta \varepsilon)} \quad (28)$$

Next, stage II of fatigue damage begins the stage of development of the main crack of Fig. 3. Schematically this crack is shown in (Fig. 2).

At this stage, the distribution of stresses and deformations at the top of the macro crack is determined by the coefficient of intensity of the stresses, which is the function of applying the load, body geometry and the location of the crack.

It was experimentally established that macro cracks are formed on both sides of the reinforcement in the places of connection of the longitudinal and transverse ribs. Then the loading scheme of the reinforcing rod will have the form of Fig. 4.

At the same time, we accept that at a distance Δl_n from the top of the macro crack:

Fig. 3 The dependence of the accumulation of fatigue damages on the number of loading cycles

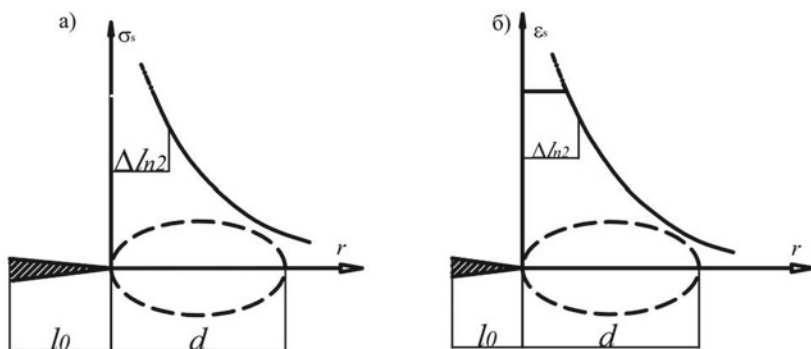
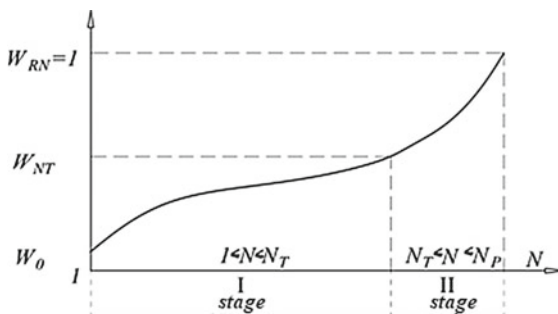


Fig. 4 The plastic zone at the top of the macro crack and the discharge of stresses **a** and deformations **b** within the plastic zone and perpendicular to the direction of the crack

$$\sigma_{s1} = \sigma_{sr} = \text{const}, \quad \varepsilon_{s1} = \varepsilon_{sR} = \text{const}, \quad \Delta W_1 = \Delta W_R. \quad (29)$$

$$\sum_{j=1}^i \Delta W_{ij} \cdot N_j = W_p$$

Taking into account the equation for the case of steel reinforcement, we can conclude:

$$\Delta \bar{W}_{ij} = \Delta W_{ij} - \Delta W_r = \frac{1 - \nu^2}{I_m E_s} \cdot \frac{n'}{1 + n'} \cdot \frac{\Delta k^2}{r_i} \cdot \bar{\sigma}(n') \cdot \varepsilon(n')$$

$$- \int_0^{\Delta \varepsilon_{\text{III}}} \Delta \sigma_{\text{BbIH}} \cdot d(\Delta \varepsilon) \quad (30)$$

where r_i is the distance from the top of the macro crack to the point in question.

Based on mentioned above, we determine the durability of the i -th micro crack in cycles:

$$N_1 = \frac{0,5 \cdot \varepsilon_b^n \cdot (\sigma_y + \sigma_u) - \sum_1^{k-1} \Delta W_{i-1}}{\frac{1-\nu^2}{I_m E_s} \cdot \frac{n'}{1+n'} \cdot \frac{\Delta k^2}{r_i} \cdot \bar{\sigma}(n') \cdot \varepsilon(n') - \int_0^{\Delta \varepsilon_{\text{III}}} \Delta \sigma_{\text{BbIH}} \cdot d(\Delta \varepsilon)} \quad (31)$$

4 Discussion

Similarly the durability of the 2nd, i -th trace elements are determined. It must be borne in mind that the durability of conditioned microelements decreases with the removal of the microelements in question from the top of the macro crack, Since, the farther from the top of the macro crack, the trace element will be located, the more additional energy nonelastic deformation will accumulate in it due to preliminary loading with its stresses $\Delta \sigma \cdot \varphi(\xi)$, where $\varphi(\xi)$ is the coefficient of decrease in stretching stresses as it moves from the top of the macro crack.

Taking the foregoing and the equations into consideration we write the general formula for calculating the durability of the i -th element within the plastic zone when $l_0 < l \leq l_0 + d$.

$$N_i = \frac{0,5 \cdot \varepsilon_b^n \cdot (\sigma_y + \sigma_u) - \sum_1^{k-1} \Delta W_{i-1}}{\frac{1-\nu^2}{I_m E_s} \cdot \frac{n'}{1+n'} \cdot \frac{\Delta k^2}{r_i} \cdot \bar{\sigma}(n') \cdot \varepsilon(n') - \int_0^{\Delta \varepsilon_{\text{III}}} \Delta \sigma_{\text{BbIH}} \cdot d(\Delta \varepsilon)} \quad (32)$$

The energy of preliminary ineffective deformation is calculated in the equation:

$$\Delta W_{np(i-1)} = \frac{1 - \nu^2}{I_m E_s} \cdot \frac{n'}{1 + n'} \cdot \frac{\Delta k_{\xi i+1}^2}{l_0 + nd + (i - 1) \Delta l_n} \cdot \bar{\sigma}(n') \cdot \varepsilon(n')$$

$$- \int_0^{\Delta \varepsilon_{\text{III}}^{\text{II}}} \Delta \sigma_{\text{BbIH}} \cdot d(\Delta \varepsilon). \quad (33)$$

where $\Delta k_{\varepsilon_{i+1}}^2$ —range of stress intensity factor for macrocrack length $l(t) = l_0 + nd + (i - 1)\Delta l_n$.

Based on the Eqs. (32) and (33), we determine the durability of the i -th micro crack within the plastic zone for the case when $l(t) > l_0 + d$.

$$N_i = \frac{0,5 \cdot \varepsilon_b^n \cdot (\sigma_y + \sigma_u) - \sum_1^{k-1} \Delta W_{np(i-1)}}{\frac{1-v^2}{1_m E_s} \cdot \frac{n'}{1+n'} \cdot \frac{\Delta k^2}{l_0+nd+(i-1)\Delta l_n} \Delta \bar{\sigma}(n') \cdot \varepsilon(n') - \int_0^{\Delta \varepsilon_{\text{III}}^{\text{II}}} \Delta \sigma_{\text{BbIH}} \cdot d(\Delta \varepsilon)} \quad (34)$$

The number of loading cycles to increasing macro crack $l(t) = l_0 + 2d$ will be:

$$N_{k1} = N_1 + N_2 + N_3 + \dots + N_{k-1} + N_{k1} = \sum_{i=1}^{k1} N_i \quad (35)$$

According to the above mechanism, an abrupt development of the macro crack occurs until:

$$l(t_i) < l_u \quad (36)$$

After a violation of the condition (36), if a decrease in the level of load does not occur, the dynamic unstable development of the macro crack begins, which, in the end, leads to a fatigue rupture of the reinforcing bar.

Existing methods for determining the durability of reinforcing steels of reinforced concrete structures, unlike the method developed by the author, are based on the method of linear accumulation of fatigue damage. For this reason, the actual values differ from the estimates ten times towards the reserve. The proposed method allows you to calculate durability with an accuracy of 15% towards the reserve.

5 Conclusion

The theoretical studies of the fatigue strength of the steel reinforced concrete reinforcement structures with regime loading made it possible to establish the following basic patterns of fatigue destruction of the reinforcement:

1. The main reason for the fatigue destruction of the steel reinforcement in the reinforced concrete structures is the formation and development of micro- and macro cracks of fatigue in the structure of the metal in the joints of the longitudinal and transverse ribs of the reinforcement.
2. A new theory has been developed, describing the development of micro- and macro cracks of fatigue and established schemes for the formation of fracture cracks in the reinforcement bars of reinforced concrete structures.

3. For the first time, an equation of changes in the specific energy of the destruction of steel in the areas of formation and development of cracks was developed.
4. Two equations have been developed: for the durability of reinforcement until the plastic resource of the initial plastically damaged zone is exhausted and for durability until the plastic resource of the damaged zone before the macro crack tip is exhausted.
5. Analytical equations of changes in the basic power parameters have been obtained that characterize the resistance of the reinforcement by the development of fatigue cracks.

References

1. Atutis, E., Valivonis, J., Atutis, M.: Deflection determination method for BFRP prestressed concrete beams under fatigue loading, p. 226 (2019)
2. Kim, G., Loreto, G., Kim, J.Y., Kurtis, K.E., Wall, J.J., Jacobs, L.J.: In situ nonlinear ultrasonic technique for monitoring microcracking in concrete subjected to creep and cyclic loading. *Ultrasonics* **88**, 64–71 (2018)
3. Li, Q., Liu, M., Lu, Z., Deng, X.: Creep model of high-strength high-performance concrete under cyclic loading. *J. Wuhan Univ. Technol. Sci. Ed.* **34**, 622–629 (2019)
4. Chen, P., Zhou, X., Zheng, W., Wang, Y., Bao, B.: Influence of high sustained loads and longitudinal reinforcement on long-term deformation of reinforced concrete beams. *J. Build. Eng.* **30** (2020)
5. Bouziadi, F., Boulekbache, B., Haddi, A., Hamrat, M., Djelal, C.: Finite element modeling of creep behavior of FRP-externally strengthened reinforced concrete beams. *Eng. Struct.* **204** (2020)
6. Mirsayapov, I.T.: Detection of stress concentration regions in cyclic loading by the heat monitoring method. *Mech. Solids* **45**, 133–139 (2010)
7. Song, L., Fan, Z., Hou, J.: Experimental and analytical investigation of the fatigue flexural behavior of corroded reinforced concrete beams. *Int. J. Concr. Struct. Mater.* **13** (2019)
8. Zamaliev, F.S., Zakirov, M.A.: Stress-strain state of a steel-reinforced concrete slab under long-term. *Mag. Civ. Eng.*, 12–23 (2018)
9. Mirsayapov Ilizar, T., Garifullin, D.R.: Engineering methods for calculating elastic modulus deformations and limits of concrete endurance under cyclic loading. *News KSUAE* **53**, 15–26 (2020)
10. Mirsayapov Ilizar, T., Garifullin, D.R.: Stress-strain state of normal sections of reinforced concrete elements under cyclic inelastic deformation of reinforcement. *News KSUAE* **54**, 44–53 (2020)
11. Gambarelli, S., Ožbolt, J.: Interaction between damage and time-dependent deformation of mortar in concrete: 3D FE study at meso-scale. *IOP Conf. Ser. Mater. Sci. Eng.* **615**, 012013 (2019)
12. Augeard, E., Ferrier, E., Michel, L.: Mechanical behavior of timber-concrete composite members under cyclic loading and creep. *Eng. Struct.* **210** (2020)
13. Trekin, N.N., Kodysh, E.N., Mamin, A.N., Trekin, D.N., Onana, J.: Improving methods of evaluating the crack resistance of concrete structures. *ACI Spec. Publ.* **326**, 93.1–93.6 (2018)
14. Liang, J., Nie, X., Masud, M., Li, J., Mo, Y.L.: A study on the simulation method for fatigue damage behavior of reinforced concrete structures. *Eng. Struct.* **150**, 25–38 (2017)
15. Zhang, G., Zhang, Y., Zhou, Y.: Fatigue tests of concrete slabs reinforced with stainless steel bars. *Adv. Mater. Sci. Eng.*, 1–5 (2018)

Unmanned Aerial Vehicle – An Element of Technology for Obtaining Spatial Data



Vladimir Bezmenov , Kamil Safin , and Sergey Stepanov 

Abstract The article discusses the possibilities of using unmanned aerial vehicles to obtain spatial data. A brief overview of the unmanned aerial vehicles market and the main areas of their application is performed. An assessment of the effectiveness of the use of unmanned aerial vehicles to obtain spatial data is given.

To assess the possibility of using an unmanned aerial vehicles for mapping and solving engineering problems, numerical modeling of the accuracy of determining spatial coordinates under the shooting conditions characteristic of this task and the equipment used is performed. Aerial photography of engineering structures and determination of soil volumes are considered as engineering tasks.

A feature of the use of unmanned aerial vehicles in solving engineering tasks is the position of the camera, which differs from the classical case of aerial photography at the time of taking images, which has a significant impact on the accuracy of the obtained spatial coordinates of the points of the object under study. Based on numerical modeling data, the contribution of errors in determining the orientation elements of images to the accuracy of determining spatial coordinates in mapping and solving engineering problems is determined. Recommendations are given on the accuracy of determining the orientation elements of the image to achieve the required accuracy of materials without the need to create ground control points on the object being photographed.

Keywords Unmanned aerial vehicle · Multicopter · Aerial photo survey · Spatial coordinates · Mapping · Engineering task · Image orientation elements

The effectiveness of the use of unmanned aerial vehicles UAVs for aerial photography is quite obvious and well studied [1]. Currently, UAVs, in addition to aerial photography, are used in a variety of fields of practical and research activities. Vivid examples of this are the use of UAVs for the study of glacial cracks [2], monitoring

V. Bezmenov · K. Safin
Kazan Federal University, Kazan, Russian Federation

S. Stepanov (✉)
Kazan State University of Architecture and Engineering, Kazan, Russian Federation
e-mail: bvm-zenit@mail.ru

of forest fires [3, 4], high-voltage power lines [5], to search for earthquake-damaged buildings [6]. The technology of obtaining spatial data based on the use of unmanned aerial vehicles is aimed at minimizing human participation in it. The effectiveness of this technology and the reliability of the results obtained may be unreasonably reduced due to the use of classical approaches in processing aerial photography materials and evaluating the accuracy of the final results, especially in the cases where the elements of external orientation will be arbitrary, corresponding to perspective photography.

UAVs are different in their design, size, weight, type of takeoff, landing. These qualities are the basis for the classification of UAVs [7]. It is noted that the most developed are mini-UAVs (international classification): take-off weight 5–150 kg, flight range up to 10 km, flight altitude 150–300 m, and flight duration up to 2 h. These UAVs do not require a runway [7]. Almost 68% of UAVs are small drones purchased for professional purposes. At the same time, the share of UAVs used for monitoring and mapping (including GIS), for architecture, construction and design, real estate (cadastre) is 16% [8].

Among the UAVs, we can distinguish a class of devices called multicopters (UAV-multicopter). This group includes multi-rotor helicopters with more than two rotors. The UAV-multicopter has a number of useful qualities that give it certain advantages over the UAV of the classical (airplane) scheme. The advantages of multicopters include: vertical takeoff and landing, the ability to move in any direction (in horizontal and vertical planes), the ability to “hover” – being at a certain point in space for a given time. That is why the UAV-multicopter is the most acceptable for solving engineering tasks. The interest in hardware and software systems for generating spatial data (coordinates, etc.) from images obtained from a multicopter UAV is also explained by the fact that the products of such systems are characterized by a lower cost compared to aerial laser scanning systems based on a multicopter UAV [9]. Some of these systems have been certified [10].

Nevertheless, the solution of some engineering problems is possible based on the materials of aerial photography obtained using both a multi-copter UAV and an airplane-type UAV [11]. For these reasons, the article discusses numerical experiments on the example of solving both topographic and engineering problems.

The approach to accuracy estimation used in numerical modeling is described in the article [12]. Table 1 shows the results of numerical modeling of the accuracy of determining the spatial coordinates of terrain points during mapping for various shooting heights with cameras with focal lengths f equal to 20, 35 and 50 mm for the case of aerial photography for mapping purposes. Data on the influence of errors of angular elements of external orientation on the final accuracy of determining spatial coordinates are also given.

Table 2 shows the results of numerical modeling of the accuracy of determining the spatial coordinates of terrain points during aerial photography of engineering objects at distances D to the object being shot 46 and 65 m with cameras with focal lengths f equal to 20, 35 and 50 mm. Data on the influence of errors of angular elements of external orientation on the final accuracy of determining spatial coordinates are also given.

Table 1 The accuracy of determining the spatial coordinates: the mapping

f , mm	$H = 100$ m			$H = 200$ m			$H = 300$ m		
	M_X , m	M_Y , m	M_Z , m	M_X , m	M_Y , m	M_Z , m	M_X , m	M_Y , m	M_Z , m
20	0.04	0.04	0.12	0.08	0.09	0.13	0.18	0.21	0.56
35	0.03	0.03	0.11	0.06	0.08	0.12	0.13	0.16	0.52
50	0.02	0.03	0.11	0.05	0.07	0.12	0.12	0.15	0.50
Contribution of error in angular elements of external orientation, %									
20	52	65	80	57	72	83	54	65	88
35	70	83	85	76	87	92	75	83	95
50	77	90	87	85	93	94	85	91	97

Table 2 The accuracy of determining the spatial coordinates: an engineering task

f , mm	$D = 46$ m $H_1 = 80$ m, $H_2 = 110$ m			$D = 65$ m $H_1 = 80$ m, $H_2 = 125$ m		
	M_X , mm	M_Y , mm	M_Z , mm	M_X , mm	M_Y , mm	M_Z , mm
20	16.0	31.7	21.0	23.5	40.7	28.7
35	12.2	28.6	16.2	18.1	35.5	22.2
50	11.0	27.8	14.8	16.5	34.1	20.3
Contribution of error in angular elements of external orientation, %						
20	56	57	61	60	63	63
35	73	63	79	77	72	81
50	81	64	87	85	75	89

Figures 1 and 2 show the results of numerical modeling of the effect of errors of linear elements of external orientation on the accuracy of determining spatial coordinates during aerial photography for mapping purposes and solving engineering tasks, respectively. The simulation results show that the accuracy of determining spatial coordinates is mainly influenced by errors of angular elements of external orientation. Increasing the accuracy of determining linear elements of external orientation does not significantly increase the accuracy of determining spatial coordinates.

Table 3 shows the results of calculations for a shooting camera close in its characteristics to the Sony Alpha A5000, installed on unmanned aerial vehicles. Camera specifications: focal length $f = 20$ mm, matrix dimensions (y and x axes) 5456×3632 pixels, pixel size $\text{pix} = 4.25$ microns. Flight altitude $H = 150$ m, the longitudinal overlap of the stereo pair images is 60%. The errors in determining the linear and angular elements of the external orientation of the camera are assumed to be equal to the characteristics of the GNSS-inertial solution Trimble APX-15 EI UAV for real-time mode (RTK) and post-processing mode (Post) [12]. Measurement errors: $m_x = m_y = 0.5$ pixels, $m_p = 0.3$ pixels. Calculations are made for ideal and arbitrary shooting cases. The orientation angles ω , φ , κ for the first and second images of the

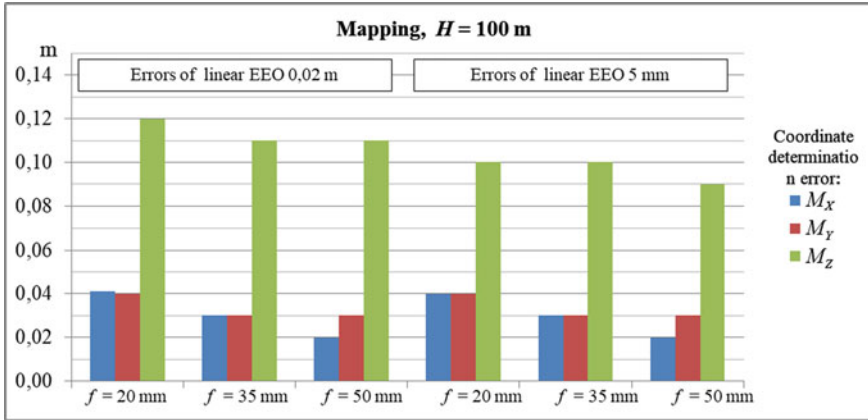


Fig. 1 Comparison of errors in determining spatial coordinates with constant accuracy of determining the angular elements of external orientation (EEO)

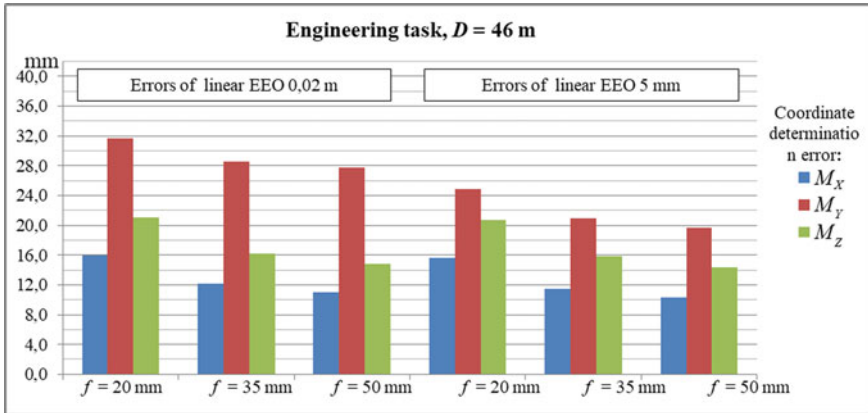


Fig. 2 Comparison of errors in determining spatial coordinates with constant accuracy of determining angular elements of external orientation (EEO)

stereo pair for an arbitrary case, respectively, were 50, 40, 5° and 40, 30, 5°, and the angle of inclination of the shooting base relative to the horizon was 32°.

A fairly common engineering task performed based on the results of aerial photography from a UAV is to determine the volume of soils. Studies of the possibility of using UAVs to solve this problem were carried out using a control area (polygon), for which a digital terrain model (DEM) was built – a control DEM. The control DEM was built based on the materials of the total station survey – the basic method for performing such work (Trimble M3 DR 5''). The coordinates of the reference points for aerial photography processing were determined using GNSS in Stop and Go mode (Trimble R8). The discrepancy between the volume of aerial photography

Table 3 The accuracy of determining the spatial coordinates: an engineering task

Calculation method	M_X , m	M_Y , m	M_Z , m	Errors in determining the angular elements of external orientation
The classical approach	0,01	0,01	0,02	No errors
General shooting case: formulas (4)–(6), $N = N_4$ [12]	0,20	0,17	0,11	RTK mode: 0,02–0,05 m; 0,03°; 0,18°
	0,14	0,12	0,09	Post mode: 0,02–0,05 m; 0,025°; 0,080°

from the UAV and the volume obtained from the control DEM was 9.5%. It should be noted that these results were achieved with a significant number of reference points, the coordinates of which were determined with high accuracy: 0.02 m in plan and 0.03 m in height.

1 Conclusion

The article presents the results of numerical experiments simulating aerial photography from UAVs for the case of mapping and solving an engineering problem. The determination of errors in the spatial coordinates of the points of the object under study was carried out using a method that allows taking into account errors in the elements of the external and internal orientation of the shooting camera, errors in measuring the coordinates of points in the image, in relation to an arbitrary shooting case [13, 14]. Numerical experiments show that under conditions corresponding to an arbitrary shooting case, when solving engineering problems, it is possible to determine spatial coordinates with an accuracy of at least 15 mm (the focal length of the shooting camera is 20–50 mm, the distance to the object under study is 45–100 m). At the same time, the accuracy of determining the linear elements of external orientation should be 2–5 mm, the angular elements 10–20”.

The effective use of UAVs to solve engineering problems without using reference points on the object under study may require, in addition to the standard onboard GNSS equipment, other solutions for determining the elements of the external orientation of the UAV and integrating these solutions with onboard GNSS equipment [15].

References

1. Babashkin, N.M., Kadnichansky, S.A., Falkov, E.Y.A.: Comparison of the effectiveness of aerial photography using unmanned and manned aviation systems. *Geoprofi* **64**(1), 15–19 (2017)
2. Blyakharsky, D.P., Ishalina, O.T., Tyurin, S.V.: Decoding of hidden glacial cracks based on the materials of unmanned aerial photography near the Progress station (East Antarctica). *Izvestia vuzov «Geodesy and Aerophotosurveying»* **64**(1), 45–53 (2020)

3. Sherstjuk, V., Zharikova, M., Dorovskaja, I., Sheketa, V.: Assessing forest fire dynamics in UAV-based tactical monitoring system. *Adv. Intell. Syst. Comput.* **1246**(2021), 285–301 (2021)
4. Hossain, F.M.A., Zhang, Y.M., Tonima, M.A.: Forest fire flame and smoke detection from UAV-captured images using fire-specific color features and multi-color space local binary pattern. *J. Unmanned Veh. Syst.* **8**(4), 285–309 (2020)
5. Lebedev, I., Izhboldina, V.: Method for inspecting high-voltage power lines using UAV based on the RRT algorithm. *Smart Innov. Syst. Technol.* **232**, 179–190 (2022)
6. Zhang, R., et al.: Automatic detection of earthquake-damaged buildings by integrating UAV oblique photography and infrared thermal imaging. *Remote Sens.* **12**(16), 2621 (2020)
7. Fetisov, V.S., Neugodnikova, L.M., Adamovsky, V.V., Krasnoperov, R.A.: Unmanned aviation: terminology, classifications, current state. *Photon, Ufa* (2014)
8. 2017 Drone Market Sector Report Prospectus. <https://droneanalyst.com/wp-content/uploads/2017/09/Skylogic-Research-2017-Drone-Market-Sector-Report-PROSPECTUS.pdf>. Accessed 08 May 2022
9. Consumer Drone Shipments to Exceed 90 Million Units and Generate \$4.6 Billion in Revenue by 2025. <https://www.abiresearch.com/press/consumer-drone-shipments-exceed-90-million-units-a/>. Accessed 08 May 2022
10. Kadnichansky, S.A., Kurkov, M.V., Kurkov, V.M., Chibunichiev, A.G.: On certification tests of a software and hardware complex based on an unmanned aircraft Geoscan 401. *Geodesy Cartogr* **3**, 32–38 (2020)
11. Kurkov, V.M., Valdez, M.D.J.P., Blyakharsky, D.P.: Creation of three-dimensional models of objects of monuments of historical and cultural heritage using unmanned aerial vehicles of airplane and multirotor types. *Izvestia vuzov «Geodesy and Aerophotosurveying»* **60**(2), 94–99 (2016)
12. Bezmenov, V.M., Safin, K.I.: Photogrammetric intersection. Accuracy estimation for an arbitrary case of aerial survey. *Izvestia vuzov «Geodesy and Aerophotosurveying»*. *Izvestia vuzov* **63**(4), 400–406 (2019)
13. APX-15 UAV version 3: single board inertial solution datasheet. https://www.applanix.com/downloads/products/specs/APX15_UAV.pdf. Accessed 08 May 2022
14. Barkov, R.R., Chitalova, E.S.: Shooting of building facades with a budget unmanned aerial system. *Appl. Test. Geoprofi* **3**, 25–29 (2020)
15. Bezmenov, V.M., Bezmenov, V.S., Garaev, N.N., Safin, K.I.: A method for determining the spatial coordinates and angular position of a remote object. Patent RF No. 2681836 (2019)

Performance Characteristics of Styrene-Acrylic Polymer Compositions and Coatings Filled with Dispersive Components



Victor Stroganov , Evgenii Vdovin , Maxim Amel'chenko ,
and Radmilla Tabaeva

Abstract The object of the study is kaolin activated in the vortex layer apparatus, which is used as a filler for styrene-acrylic paint coatings. A comparative analysis of the performance characteristics of coatings filled with initial and activated kaolins was performed. Dispersion analysis was chosen as the research method, which allowed the authors to establish that the processing of the filler in the vortex layer apparatus caused an increase in its dispersion to 6 microns. In filled paint coatings, changes in the indicators of washability, water/moisture absorption, adhesive strength, as well as resistance to aggressive media, including model ones simulating the process of biological corrosion, were determined. Coatings and the condition of their surfaces after exposure to liquid media were fixed by the CIELab method by changing the color characteristics. It was found that filling with activated kaolin provides an increase in the level of performance characteristics of coatings – washability by 3.5 times, water absorption by 2.5 times and adhesive strength by 1.5 times, as well as resistance to aggressive media.

Keywords Styrene-acrylic copolymer · Coatings · Vortex layer apparatus · Activation

1 Introduction

Styrene-acrylic paint coatings (PC) are one of the most common materials for protecting building materials, structures from external factors and corrosion [1–3]. The level of protective characteristics of coatings is largely determined by both the properties of the polymer matrix of the composition and its filling [4–6].

It is known [7–9] that one of the most common fillers of PWM is kaolin, which serves as a substitute for an expensive pigment—titanium dioxide [7, 10, 11] and contributes to the uniform distribution of dispersed mineral particles of other components of the composition [7, 12]. However, along with providing the above functions,

V. Stroganov (✉) · E. Vdovin · M. Amel'chenko · R. Tabaeva
Kazan State University of Architecture and Engineering, 420043 Kazan, Russian Federation
e-mail: svf08@mail.ru

kaolin filling makes it possible to reduce the level of protective characteristics of coatings. In this regard, it is urgent to find a solution for leveling the negative effect of the filler-kaolin on the properties of polymer coatings.

The protective characteristics of coatings are largely determined by intermolecular interactions between mineral components and the polymer matrix [13–15], an increase in the level of which can be provided by the activation of the filler. Among the popular activation methods, dispersion in various apparatuses is noted [16, 17], however, the most effective should include processing in a vortex layer apparatus [18–21].

Thus, the aim of the article is to study the effect of kaolin activation in the vortex layer apparatus on the properties of styrene-acrylic polymer paint and varnish protective coatings.

2 Methods

2.1 Obtaining Filler and Paint Composition

Activated kaolin was obtained in a vortex layer apparatus (ABC) Vortex297 (Fig. 1). The filler was loaded into a sealed container of the apparatus together with grinding bodies (cylindrical ferromagnetic particles with a diameter of 2 mm) and dispersed for 5 min.

The preparation of the paint composition was carried out on a dissolver according to the method [22, 23], consisting of the following stages:

- pre-mixing—distilled water and functional additives were added to the dry components with the specified ratios;

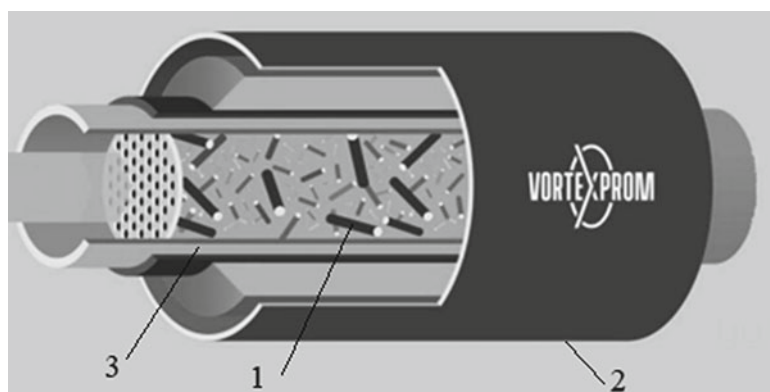


Fig. 1 Reactor of the vortex layer apparatus Vortex297: 1—ferromagnetic grinding bodies; 2—the body of the device; 3—sealed container

- preparation of pigment paste—the resulting mixture was placed in a dissolver and stirred at a speed of $n = 2000$ rpm for 30 min.;
- preparation of the composition—pigment paste was mixed with styrene-acrylic film-forming agent in a ratio of 1:0.5 (pigment paste: film-forming agent) and mixed (~30 min.) until a homogeneous lump containing no aggregates and air bubbles is obtained.

An aqueous dispersion of the homacryl 101 M brand (Homa Company) was used as a styrene-acrylic copolymer.

2.2 Preparation of Paint Coatings Samples for Testing

Free films were obtained by applying a paint composition to a fluoroplast substrate (the time of coating formation is up to 7 days at 20 ± 2 °C). The formation was controlled by changing the state of the surface to “aftertack”. Ready-made free films were used in determining the moisture absorption and action of the model medium.

To determine the values of the indicators of washability and water absorption of paint coatings, a composition was applied to a preweighed fat-free glass plate until it was completely covered and dried for 24 h at a temperature of 20 ± 2 °C.

Cement-sand samples (CSS) were cubes with dimensions of $10 \times 10 \times 10$ cm. The material of the samples is M400 grade cement, sand up to 1.5 mm in size, water. Samples were obtained by simultaneously mixing these materials in a water-cement ratio of 0.32, and pouring the resulting mixture into metal molds lubricated with a separating liquid (oil). The process of hardening the samples was completed in 7 days, after which they were removed from the mold.

Determination of water absorption and resistance to aggressive media was carried out on glass plates with paint and varnish coatings applied to their surfaces. The composition was applied to the plate until it was completely covered and then dried for 7 days.

2.3 Determination of the Characteristics of the Filler and Protective Coatings

The dispersion of the kaolin activated in the vortex layer apparatus was determined using the HORIBA LA-950 device, the principle of operation of which is based on scattering and detection of reflected/refracted laser light, red and blue spectra (650 and 405 nm), in accordance with ISO 13320-1.

One of the main protective characteristics of paint coatings are the following indicators: washability, resistance to aggressive media, water and moisture absorption.

The washability (X) of paint coatings was determined as follows. The painted glass plate was fixed in a holder and a three-row brush with natural bristles 11 ± 2 mm long, including a stopwatch, was driven in a circular motion (over the plate area). At the same time with the movement of the brush, 25 cm^3 of water was supplied to the upper part of the plate from the burette for 30 s. The flushing water was collected in a pre-weighed bowl located under the plate. After 30 s, the brush was stopped and washed with small portions of water until the paint coating particles were completely removed. The washing water was collected in the same cup and evaporated in a thermal shock to a constant mass. Then the bowl was cooled to room temperature and weighed again.

The washability value (g/m^2) of the paint coating was determined by the formula (1):

$$X = \frac{m - m_0}{S}, \quad (1)$$

m – the mass of the bowl, g;

m_0 – the mass of the bowl after drying, g;

S – the surface area of the coating, m^2 .

The arithmetic mean of three parallel definitions was taken as the test result, the absolute discrepancy between which did not exceed the permissible discrepancy equal to 0.3 g/m^2 .

Water absorption (W_p) of coatings was carried out on glass painted plates immersed in water for 24 h.

A glass plate with a cured coating was weighed and placed in a bath filled with distilled water at a temperature of 20 ± 2 °C. Air bubbles that appeared on the coating after the sample was immersed in water were removed with a soft brush. After 24 h after immersion, the plate was removed from the water, dried with filter paper, weighed and water absorption (%) was calculated according to the formula (2):

$$W_{\Pi} = \frac{m_2 - m_1}{m_1 - m_0} \cdot 100\% \quad (2)$$

m_0 – weight of a clean plate, g;

m_1 – weight of the coated plate, g;

m_2 – weight of the coated plate after the experiment, g.

Moisture absorption (W_{pl}) of coatings was determined on free films. The free films of the composition were immersed in a pre-weighed beaker with a tightly closed lid and the mass (film + cup) was determined. Moreover, the free films were placed in a desiccator, in which the relative humidity of $95 \pm 2\%$ was constantly maintained, and kept in it for 24 h. Then the samples were taken out and weighed in a tightly closed cup. The moisture absorption value (%) was determined by the formula (3):

$$W_{\Pi} = \frac{m_3 - m_2}{m_2 - m_1} \cdot 100\% \quad (3)$$

m_1 – empty cup weight, g;

m_2 – weight of a cup with a film, g;

m_3 – the mass of the cup with the film after the test, g.

The adhesive strength of paint coatings to the cement-sand surface was determined on the PSO-10MG4S adhesive meter device. Paint compositions were applied to the pre-cleaned surfaces until they were completely covered, which were further dried for 24 h. A 50×50 mm steel plate with a ball shank, an adhesive consisting of ED-20 epoxy resin (10 wt. h.) and a diethylenetriamine hardener (1 wt. h.) was glued to the formed coating. After curing of the adhesive layer, the shank was fixed in the fork grip of the adhesive meter and then a force was applied using the handle, the vector of which is directed perpendicular to the coated surface. When the arm is loaded, the strain gauge converter of the device generates an electrical signal that varies in proportion to the applied load, which is registered by the electronic unit and converted into force. The adhesion strength was calculated as the ratio of the force expended on the separation of the steel plate to its area.

The determination of changes in the quality indicators of coatings was carried out on free films, and tests of their resistance to aggressive media were carried out in acidic, alkaline and neutral media, which are—3% sulfuric acid solution; 0.1n sodium hydroxide solution and distilled water.

The presence of possible microcracks and defects on the surface of paint coatings before and after their exposure in aggressive environments was determined using a Levenhuk DTX90 digital microscope (magnification $\times 280$).

The color characteristics of the free films were changed in accordance with GOST 52,490–2005. In the graphical light model, the “lightness” is given by the L coordinate, and the chromatic component of the color is given by two Cartesian coordinates a and b (Fig. 2).

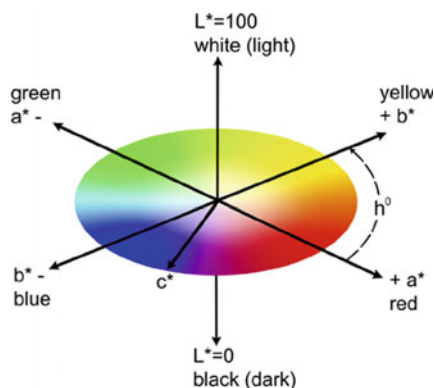


Fig. 2 Graphical representation of the lab color model

Processing of the results obtained by measuring the coordinate data of the comparison samples and the tested paint coatings, and subsequent calculations of the parameters of the difference in their color characteristics, was carried out according to the formulae (4–7):

– total color difference:

$$\Delta E_{ab}^* = [(\Delta L^*)^2 + (\Delta a^*)^2 + (\Delta b^*)^2]^{1/2} \quad (4)$$

$$\Delta L^* = L_T^* - L_R^* \quad (5)$$

$$\Delta a^* = a_T^* - a_R^* \quad (6)$$

$$\Delta b^* = b_T^* - b_R^* \quad (7)$$

где:

$\Delta L^*_T, \Delta a^*_T, \Delta b^*_T$ – color coordinates of the test sample;

$\Delta L^*_R, \Delta a^*_R, \Delta b^*_R$ – color coordinates of the comparison sample.

$\Delta L^*, \Delta a^*, \Delta b^*$ – the difference between the color coordinates of the test sample and the comparison sample.

2.4 Testing in Model Media

Determination of the biostability of paint coating samples was carried out in a laboratory kinetic plant [24]. The tests were carried out for 7 days at a medium temperature of 40 ± 2 °C, which, according to the Van't Hoff rule, is equivalent to 28 days at 20 ± 2 °C with automatic regulation of the main parameters of the medium – temperature and pH (3.45).

The laboratory plant consists of a test tank in which the test samples immersed in the model medium are installed, a make-up tank, a drain tank, as well as a measuring tank for determining the pH of the model medium and pH electrode calibration, an electronic control unit that performs the functions of measuring the pH, temperature of the model medium and maintaining them at a given level.

A mixture of carboxylic acids was used as a model medium: oxalic, tartaric, malic, lactic, citric and acetic acids, the choice of which is due to their presence in the metabolites of bacteria isolated in public and residential premises [25, 26].

3 Results and Discussion

It is known [13, 14] that filling with a highly dispersed filler causes not only an increase in contact between the filler particles and the film-forming agent, but also ensures a uniform distribution of dispersed components in the volume of the polymer coating. According to the results of the dispersion analysis, it was found that its processing in the vortex layer apparatus contributes to an increase in the degree of dispersion of the filler to 6 microns (Fig. 4), compared with the initial kaolin (Fig. 3).

The high dispersion of activated kaolin contributes to a more equal distribution of components in the coating volume, which leads to an increase in operational characteristics (Table 1). It was found that the washability of paint coatings, when filled with activated kaolin, decreases by 3.5 times, and water absorption by more than 2.5 times. It should also be noted that the moisture absorption index decreased to 4.4%.

The analysis of the adhesive strength results showed that the filling with activated kaolin provides a high level of adhesion of the protective coating with a cement-sand substrate—3.22 MPa, compared with an inactive filler.

The high level of adhesive strength can also be explained by an increase in the contact area of the PC with the protected surface due to the high dispersion of the

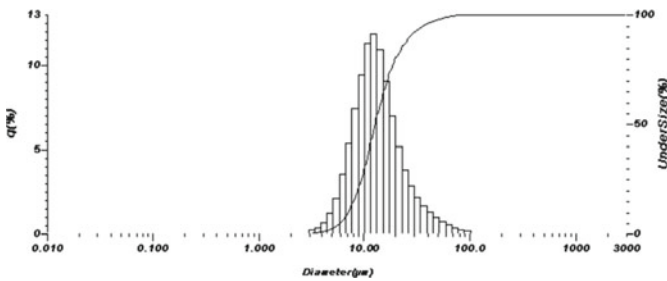


Fig. 3 Dispersed particle distribution of the initial kaolin

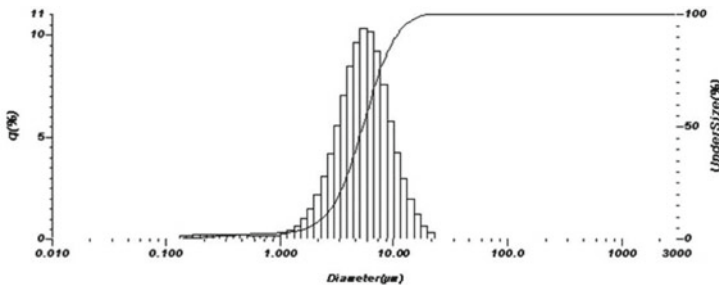
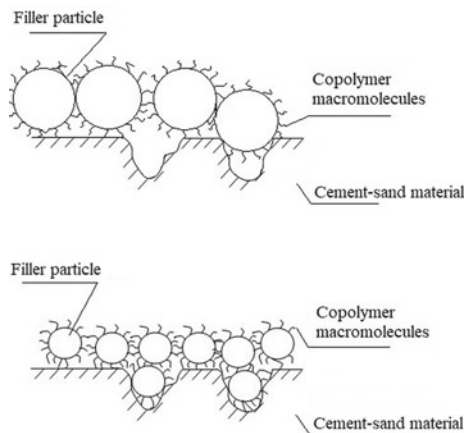


Fig. 4 Dispersed distribution of kaolin particles activated in the vortex layer apparatus

Table 1 Results of determining the performance characteristics of paint coatings

Parameters	The parameter values of the filled paint coatings	
	Initial kaolin	Activated kaolin
Washability, g/m ²	17,8	4,8
Water sorption, %	15,1	5,2
Moisture sorption, %	5	4,4
Adhesion strength, MPa	2,01	3,22

**Fig. 5** Schematic representation of the effect of high dispersion of activated kaolin on increasing the contact area between the substrate and the composition

filler—activated kaolin, which is schematically shown in Fig. 5 and confirmed by the increased area of separation of the “mushroom” from the surface of the CSS (Fig. 6).

Resistance to aggressive media is a parameter that allows judging the durability of the paint coatings. The change in the color characteristics of the PC surface before and after their exposure, as well as the state of the appearance of the coating surface (Fig. 7) were selected as the determined and controlled parameters.

It was found that filling the composition with the initial kaolin causes partial destruction of the film under the influence of an alkaline medium and the removal of its upper (non-exposed) parts (Fig. 8a).

The introduction of activated kaolin into styrene-acrylic coatings increases their resistance to aggressive media and the absence of defects and destruction on the surface of the PCs under the action of alkaline and neutral media (Fig. 8b).

In the comparative analysis of the initial color characteristics of coatings (Table 2) it was found that the kaolin filling has a negligible effect on the value of the chromaticity coordinates (L, a, b) when they are compared with each other.

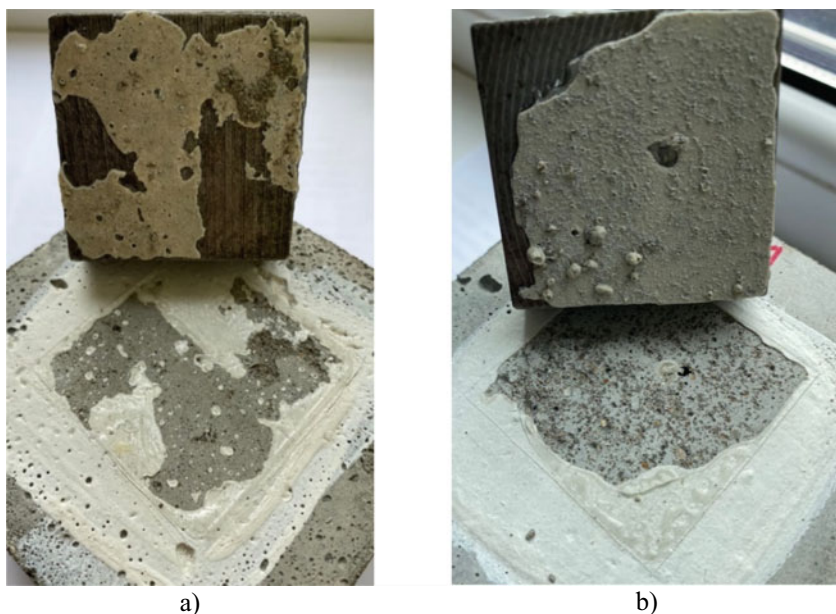


Fig. 6 The result of cleavage of paint coatings filled with the original **a** and activated **b** kaolin from the cement-sand substrate

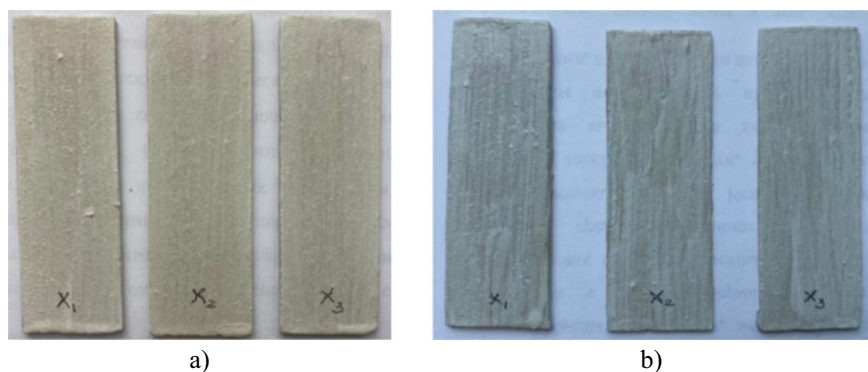


Fig. 7 Surface appearance of paint coatings samples filled by initial **a** and activated **b** kaolin

When exposing PCs samples in aggressive environments (Table 3) it was found that the greatest change in color characteristics occurs in coatings filled with activated kaolin, which is expressed in higher values of the total color difference (ΔE_{ab}^*), compared with the PCs on the original filler. It should also be noted that the coordinates of the coatings shift towards yellow tones (Δb^*), which may indicate chemical aging processes of the styrene component of the film-forming agent [26–28].

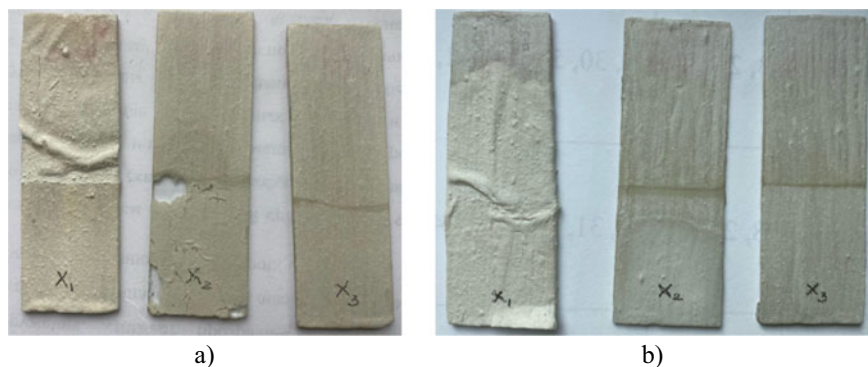


Fig. 8 Appearance of the surface of paint coatings samples filled by initial **a** and activated **b** kaolin after their exposure in aggressive media: x_1 —3% sulfuric acid; x_2 —0.1n sodium hydroxide, x_3 —water

Table 2 The value of the coordinates of the color characteristics of the coating

Exposure media	The value of the coordinates of the color characteristics of the filled coating					
	Initial kaolin			Activated kaolin		
	L	a	b	L	a	b
Initial sample	90	2	2	88	1	0
H ₂ SO ₄	87	3	4	94	1	2
NaOH	87	2	2	86	1	2
H ₂ O	88	2	2	83	2	2

Table 3 The results of calculating the parameters of the color difference of paint coatings after their exposure in aggressive media

Exposure media	Parameter values			
	ΔL^*	Δa^*	Δb^*	ΔE_{ab}^*
Coatings filled by initial kaolin				
H ₂ SO ₄	-3	1	2	3,74
NaOH	-3	0	0	3,00
H ₂ O	-2	0	0	2,00
Coatings filled by activated kaolin				
H ₂ SO ₄	6	0	2	6,32
NaOH	-2	0	2	2,83
H ₂ O	-5	1	2	5,48

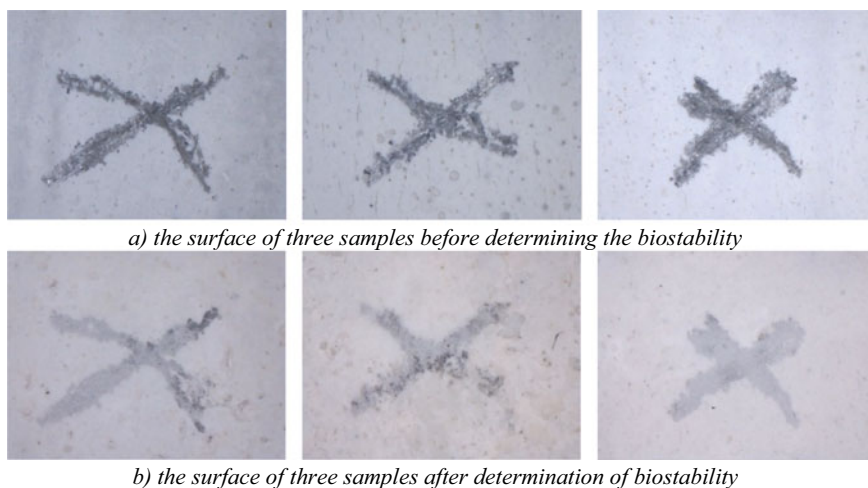


Fig. 9 Photos of the surface of paint coatings samples filled with the initial kaolin before **a** and after **b** determination of their biostability

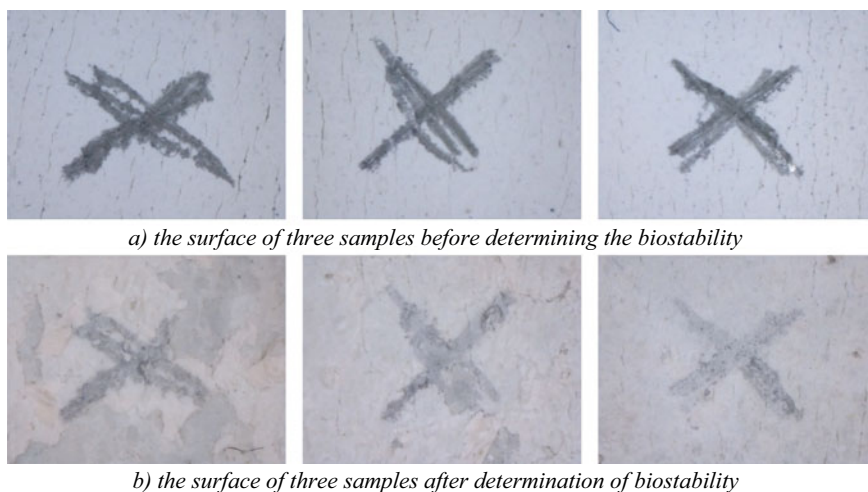


Fig. 10 Photos of the surface of paintwork samples filled with activated kaolin before **a** and after **b** determination of their biostability

One of the urgent problems of building materials science is biocorrosion. Dozens of buildings and structures are destroyed and lose their functionality every year due to the action of metabolites of microorganisms and mold, which are a mixture of organic acids [29–31]. In this regard, the determination of the resistance of coatings to the action of metabolites of microorganisms—the model medium—was carried out.

It was found that the effect of a model mixture of organic acids contributes to the appearance of microcracks on the surface of the films and their partial destruction, both in PCs samples filled with the initial kaolin (Fig. 9) and activated (Fig. 10).

However, when analyzing the results on the change in the mass of films after their exposure in the model medium, it was found that activated kaolin helps to reduce the sorption of the coating medium by up to 18%, compared with the initial—26%, which, apparently, can be explained by the compacted structure of the formed LPCs.

4 Conclusion

Thus, filling the PCs with kaolin activated in the vortex layer apparatus causes an increase in the level of interaction between the components of the paint composition and their uniform distribution over the coating volume. The formed PCs structure provides an increase in the level of operational indicators: washability—by 3.5 times, water absorption—by 2.5 times and adhesive strength—by 1.5 times. In addition, the introduction of activated kaolin provides an increase in the resistance of coatings to aggressive media and bio-resistance.

The results obtained confirm the effectiveness of the vortex layer apparatus and the prospects of research on the use of the method of activation of fillers in the composition of protective polymer coatings.

References

1. Ivaschenko, Y., et al.: Analysis of styrene-acrylic dispersions as binders for paints for construction purposes. *Bull. Belgorod State Technol. Univ. V. G. Shukhov* **3**, 6–11 (2018). https://doi.org/10.12737/article_5a5dbd2d492241.03354026
2. Benali, Y., Ghomari, F.: Latex influence on the mechanical behavior and durability of cementitious materials. *J. Adhes. Sci. Technol.* **31**, 219–241 (2017)
3. Li, Z.: Investigation of properties of styrene-acrylic copolymer containing imidazole for protection of HRB400 steel in atmospheric environment. *Int. J. Electrochem. Sci.* **17** (2022). <https://doi.org/10.20964/2022.04.11>
4. Film Formation in Modern Paint Systems. *Pigment & Resin Technology*, vol. 39, pp. 23–30 (2010). <https://doi.org/10.1108/prt.2010.12939cac.003>
5. Kopeć, M., et al.: Influence of TiO₂ pigment particles on chromate ion transport in epoxy films. *npj Mater. Degrad.* **5** (2021). <https://doi.org/10.1038/s41529-021-00156-7>
6. Silaeva, A., et al.: Influence of reinforcing filler sizes on technological and functional properties of paint and varnish materials. *Mater. Sci.* 32–38 (2022). <https://doi.org/10.31044/1684-579x-2022-0-2-32-38>
7. Gysau, D.: Fillers for Paints, Vincentz Network, 2019. <https://doi.org/10.1515/9783748600312>
8. Ahmed, N.M.: Comparative study on the role of kaolin, calcined kaolin and chemically treated kaolin in alkyd-based paints for protection of steel. *Pigm. Resin Technol.* **42**, 3–14 (2013). <https://doi.org/10.1108/03699421311288715>
9. Vesely, D., Kalendova, A., Manso, M.V.: Properties of calcined kaolins in anticorrosion paints depending on PVC, chemical composition and shape of particles. *Prog. Org. Coat.* **74**, 82–91 (2012). <https://doi.org/10.1016/j.porgcoat.2011.11.017>

10. Ahmed, N.M., Selim, M.M.: Innovative titanium dioxide-kaolin mixed pigments performance in anticorrosive paints. *Pigm. Resin Technol.* **40**, 4–16 (2011). <https://doi.org/10.1108/03699421111095883>
11. El-Sawy, S.M.: Egyptian kaolin as a filler and extender pigment for anti-corrosive paints. *Corr. Prev. Control* **41**, 31–35 (1994)
12. Shakrani, S.A., Ayob, A., Ab Rahim, M.A., Alias, S.: in *J. Phys.: Conf. Ser.* (Institute of Physics Publishing, 2020) **1529** (2020). <https://doi.org/10.1088/1742-6596/1529/4/042099>
13. Rother, R.: *Fillers for Polymer Applications*, p. 489. Springer, Berlin (2017). <https://doi.org/10.1007/978-3-319-28117-9>
14. Müller, B., Poth, U.: *Coatings Formulation* (Vincentz Network, 2019). <https://doi.org/10.1515/9783748600268>
15. Stoye, D., Freitag, W.: *Paints, Coatings and Solvents: Second, Completely Revised Edition*, Wiley Blackwell, Hoboken (2007). <https://doi.org/10.1002/9783527611867>
16. Stroganov, V.F., Amel'chenko, M.O.: The effect of the mechanical activation of silicate nature fillers on the properties of styrene—acrylic polymer coatings. *Polym. Sci. Ser. D* **12**, 227–230 (2019). <https://doi.org/10.1134/S1995421219030225>
17. Vorsina, I.A., Grigorieva, T.F., Udalova, T.A., et al.: Mechanical activation of the mixtures of kaolinite and polymer. *Chem. Sustain. Dev.* **22**, 17–22 (2014)
18. Voitovich, V.A., Shvarev, R.R., Zacharichev, E.A.: The effectiveness of the vortex layer apparatus in the processes of grinding powder materials *Nov. Ogneup* **10**, 48–53 (2017)
19. Vdovin, E., Stroganov, V., Konovalov, N.: Modification of road soil cement with activated fillers. In: Vatin, N., Borodinecs, A., Teltayev, B. (eds.) *Proceedings of ECEE 2020*. ECEE 2020. LNCE, vol. 150, pp. 335–345. Springer, Cham (2021). https://doi.org/10.1007/978-3-030-72404-7_33
20. Shcherban, E.M., et al.: Improvement of strength and strain characteristics of lightweight fiber concrete by electromagnetic activation in a vortex layer apparatus. *Appl. Sci. (Switzerland)* **12** (2022). <https://doi.org/10.3390/app12010104>
21. Ibragimov, R.A., Potapova, L.I., Korolev, E.V.: Investigation of structure formation of activated nanomodified cement stone by IR spectroscopy. *News KSUAE* **3**(57), 41–49 (2021). https://doi.org/10.52409/20731523_2021_3_41
22. Talbert, R.: *Paint Technology Handbook*. Paint Technology Handbook. CRC Press, Boca Raton (2007). <https://doi.org/10.1201/9781420017786>
23. Strehmel, B., Groteklaes, M., Mischke, P.: *Lehrbuch der Lacktechnologie*, Vincentz Network, 2019. <https://doi.org/10.1515/9783748600220>
24. Patent of the Russian Federation No 170410, publ. 04/24/2017, bull. № 12
25. Yakovleva, G., et al.: Metabolic activity of micromycetes affecting urban concrete constructions. *Sci. World J.* **2018** (2018). <https://doi.org/10.1155/2018/8360287>
26. Yakovleva, G.Y., et al.: Assessment of biodamage resistance of various concrete grades. *Int. J. Pharm. Technol.* **8**, 24291–24299 (2016)
27. Prokopchuk, N.R., Krut'ko, E.T., Globa, A.I.: *Chemical modification of polymer binders*, BGTU (2012)
28. Bociąga, E., Trzaskalska, M.: Influence of ageing on the gloss, color, and structure of colored ABS. *Color Res. Appl.* **41**, 392–398 (2016). <https://doi.org/10.1002/col.21971>
29. *Modern Styrenic Polymers: Polystyrenes and Styrenic Copolymers* (2003). <https://doi.org/10.1002/0470867213>
30. Ilinskaya, O., Bayazitova, A., Yakovleva, G.: Biocorrosion of materials and sick building syndrome. *Microbiol. Aust.* **39**, 129–132 (2018). <https://doi.org/10.1071/MA18040>
31. Sanchez-Silva, M., Rosowsky, D.V.: Biodeterioration of construction materials: state of the art and future challenges. *J. Mater. Civ. Eng.* **20**, 352–365 (2008). [https://doi.org/10.1061/\(asce\)0899-1561\(2008\)20:5\(352\)](https://doi.org/10.1061/(asce)0899-1561(2008)20:5(352))

Activation of Fillers for Cement-Mineral Systems



Evgenii Vdovin , Victor Stroganov , and Nikita Konovalov 

Abstract This work studies the activated mineral fillers used to modify cement-mineral materials. Modification of cement-mineral systems by activated fillers provides an opportunity to increase the level of strength indicators of composite road-building material, as well as to reduce the content of the main binder. Dolomite, zeolite-containing rock, lime and their mixtures were used as mineral fillers. Mechanical activation of fillers was carried out in the Vortex 297 vortex layer apparatus with different exposure times. To ensure effective activation, the optimum filling factor of the grinding chamber and the size of ferromagnetic particles were determined. The laser analyzer was used to study the character of dispersity distribution of mineral filler particles as a function of the activation time. The surface state of mineral fillers after activation was assessed by the acid–base interactions. The free surface energy was evaluated, which characterizes the surface ability to interphase interaction. The effects of activation time and the content of mineral filler components on compressive strength of cement paste samples were established. The optimum activation time of mineral filler components in the vortex layer apparatus and their ratio were determined.

Keywords Mineral filler · Mechanical activation · Vortex layer apparatus · Free surface energy · Dispersity

1 Introduction

1.1 Mineral Fillers

In construction and road material science, the main objective of research is to improve the physical and mechanical properties of materials by modifying them [1]. Modification is the interrelation between changes in the physical and chemical structure and properties of materials. Various examples of modifications are considered in

E. Vdovin (✉) · V. Stroganov · N. Konovalov
Kazan State University of Architecture and Engineering, Kazan, Russia
e-mail: vdovin007@mail.ru

works of Yu.M. Bazhenov, V.B. Ratinov, Yu.M. Butt, V.I. Solomatov and others. The modification process is driven by the following main factors:

- the creation of artificial crystallization centers by direct introduction of impurity components into the mixture (inoculation);
- the introduction of surfactants that slow down grain growth and promote the formation of stable fine crystalline germs (inhibition);
- the application of several technological operations, in particular heat treatment, intensive mixing, causing the formation of a sufficient number of active centers.

Portland cement is known to be the main hydraulic binder used in construction. When modifying the properties of composite materials based on Portland cement, it is relevant to use active mineral additives [2–4]. This is the way to get binders and materials based on them with a given set of special properties, including the improved sulfate, corrosion, acid and water resistances, late hardening strength, lower heat of hydration, better workability [5–7]. The use of active mineral fillers also makes it possible to reduce the content of Portland cement in mixtures and the volume of the clinker part in the production of cement, which reduces the pollution of the environment with man-made emissions.

Zeolite-containing rock and dolomite are mineral fillers used to modify the structure and properties of cement-mineral systems. Dolomite can participate in the reaction of cement hydration with the formation of carbonate-AFm phases and increase its strength [8–10]. Natural zeolite is a mineral material containing large amounts of reactive SiO_2 and Al_2O_3 , like other pozzolanic materials. It contributes to the increase in the concrete strength through a pozzolanic reaction with $\text{Ca}(\text{OH})_2$. Several studies [11–13] have shown that the optimum amount of natural zeolite replacement is about 10–20%. It is noted that concretes with zeolite content of 10% have increased compression and bending strength, frost resistance, including under the action of chlorides. The efficiency of the modifying effect of mineral fillers can be enhanced by their activation.

1.2 Filler Activation

The activation can be divided into several types: mechanical (when material is grinded in various grinding devices); mechanical-chemical (when material is grinded together with various chemical additives); thermal; electro-magnetic; ultrasonic; activation by ionizing radiation; chemical (when material is etched with acid or alkaline solutions to create microrelief of particles). The most technologically advanced and effective way to increase the activity of fillers is mechanical activation [14, 15]. The theory of Juhasz and Rebinder (the founders of mechanochemistry) states that under the influence of mechanical activation, the primary and secondary processes take place. Primary processes (accumulation of defects, amorphization, formation of metastable polymorphic forms, increase in internal and surface energy, increase in surface area, decrease in coherence energy of solids) in general increase the reactivity of

matter. Secondary processes (aggregation, adsorption, recrystallization) occur spontaneously in active systems and can appear even during milling or after its completion. The multi-stage nature of mechanical activation requires the use of high-energy mills with different operating modes (compression, shear, impact). The most effective mechanical activation takes place in electromagnetic mills, such as the vortex layer apparatus, which is designed for effective mixing and grinding of various materials and mixtures to intensify technological processes [15–17]. The milling process is affected by several factors, namely the atmosphere of the milling media, particle size and volume ratio of ferromagnetic elements and milling material, degree of filling of the milling chamber, milling speed and time [18, 19]. During the milling process, the surface condition of fillers changes, which should be assessed in terms of increasing the activity.

1.3 Surface Condition Assessment

Qualitative and quantitative methods for assessing the surface state after activation include determination of the specific surface and total surface of particles, sedimentation analysis, determination of the median particle size and distribution pattern, potentiometric titration, assessment of acid–base interactions, etc. The method of acid–base interactions is used to determine the free surface energy (FSE), which characterizes the ability of interphase interaction [20]. These interactions are of a special type, in which one of the particles is a donor and the other is an acceptor of a pair of electrons. The free surface energy is the most informative characteristic of this approach. It is generally accepted that FSE has a complex thin structure, additively containing several components of different nature [21]. The values of these components can be used to judge about the potential ability of a surface to interphase interaction. These components include dispersity interaction (γ_{LW} , Van der Waals forces), acid parameter (γ^+), base parameter (γ^-), acid–base component (γ_{AB}), total FSE (γ_s). The interphase boundary has a surplus of uncompensated energy. This excess per surface unit is the specific free surface energy [22]. It is not a special form of energy, but is associated with the position of the molecules at the interphase. The energy aspect of the free surface energy is determined by the work of isothermal and reversible change of the surface layer area per 1 m². The free surface energy is regarded as the work for the transportation of molecules from the volume of the body to the surface [23]. The stronger are the intermolecular bonds in a given body, the greater the level of FSE at the boundary with the gas phase is. The free surface energy of objects is one of the most fundamental parameters in its meaning and content, which is a function of the response of the criteria and conditions of adhesion bonding and serves as a physical and chemical equivalent of the characteristics of resistance of adhesion bonds to external influences [24]. The literature data show that the influence of activation of mineral fillers in the electromagnetic field [25] on the structure and properties of cement-mineral building materials and their assessment techniques are not sufficiently investigated.

1.4 Purpose and Objectives of the Research

This work aims at studying the effect of activation parameters of mineral fillers in the vortex layer apparatus on the behavior of dispersity, free surface energy, and compressive strength of samples of modified cement-mineral materials.

The following tasks were solved:

- To determine the optimal sizes of ferromagnetic particles during the activation of mineral fillers in a vortex layer apparatus;
- To study the change in the dispersity of fillers based on dolomite, cement chipboard and their mixtures as a function of the activation time in the vortex layer apparatus;
- To determine the free surface energy and its components in activated mineral fillers;
- To study the influence of activation time and content of activated fillers on the level of compressive strength of the modified cement-mineral paste.

2 Materials and Methods

Activation of mineral fillers was carried out for 2, 4, 6 min in the ABC Vortex 297 vortex layer apparatus under the influence of ferromagnetic particles moving in the magnetic field of the reactor (Fig. 1). The length of the working zone of the inductor was 330 mm, the voltage at the vortex layer inductor varied from 30 to 380 V, current was 20–180 A, the inductor frequency was up to 400 Hz.

The ferromagnetic particles for the activation of fillers in ABC were selected by assessing the optimal ratio of length (l) and diameter (d) (Table 1).

The degree of dispersity was determined using the laser particle size analyzer HORIBA LA-950 after a fixed time of the filler activation. The particle sizes varied from 0.1 to 1000 microns. Laser diode with a wavelength of 650 nm and LED with a wavelength of 405 nm were used as the sources of optical radiation.



Fig. 1 Reactor of the ABC Vortex 297 vortex layer apparatus

Table 1 Technical characteristics of ferromagnetic particles

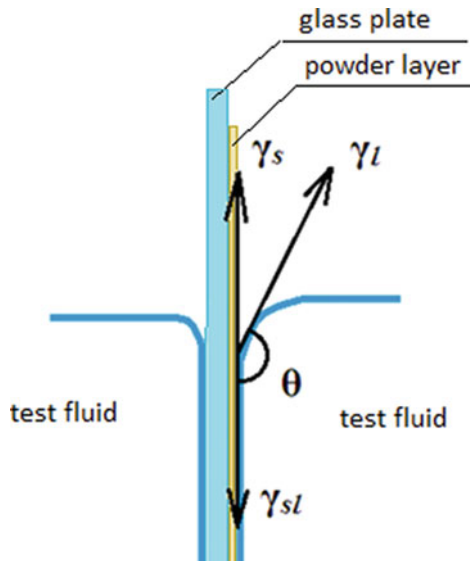
l, particle length, mm	d, particle diameter, mm
19.8	5.0
21.8	3.0
19.8	2.0
15.8	1.5

The constituents and parameters of the free surface energy of activated fillers were determined by the contact angle. The selective wetting was carried out in the presence of test (distilled water, glycerin, formamide) and neutral (n-hexane) liquids. When a solid is immersed in a liquid, it takes some finite time for the meniscus shape to acquire an equilibrium position. The equilibrium is achieved by the simultaneous interaction of three surface tensions: surface energy of the filler (γ_s), interphase energy (γ_{sl}), and surface tension of the liquid at the boundary with the gas medium (γ_l) (Fig. 2). The surface energy γ_l acts at a certain angle θ , which is called the contact angle.

Dolomite and zeolite-containing rock (cement chipboard) were used as mineral fillers. Dolomite was from the “Bima” deposit, with $\text{CaCO}_3 + \text{MgCO}_3$ content of 93.8% and moisture content of 0.2%, the average median particle size was 19.9 μm (Fig. 3).

Zeolite-containing rock was of the Tatarsko-Shatrashanskoe deposit with clinoptilolite content of 20–30%, SiO_2 content of 57.2–66.3% (amorphous SiO_2 content of 31.6%), CaO content of 14.6–18.8%. The median particle size was 4.9 μm (Fig. 4).

Fig. 2 A scheme to determine the contact angle



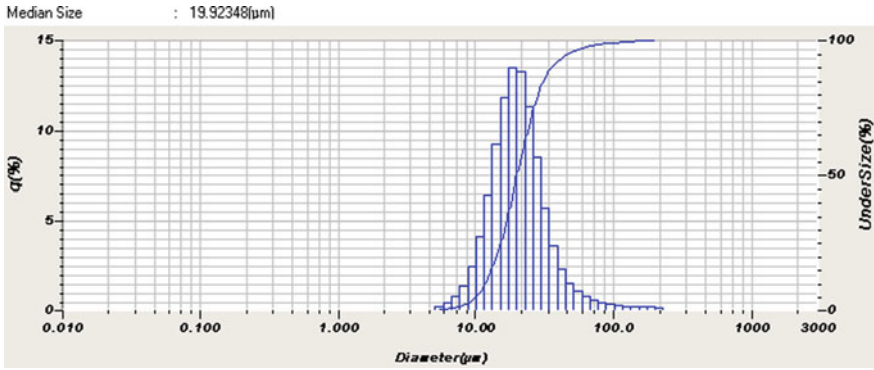


Fig. 3 Particle distribution of dolomite powder

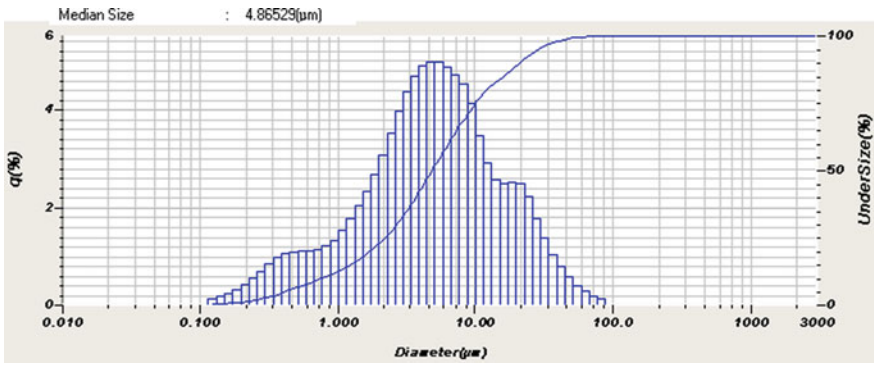


Fig. 4 Particle distribution of powder of cement chipboard

To obtain the cement-mineral paste samples, the common-hardening plain CEM I 42,5H Portland cement was used as a binder (Tables 2 and 3).

Table 2 Chemical composition of cement

Chemical composition, %						
CaO	SiO ₂	Al ₂ O ₃	Fe ₂ O ₃	MgO	SO ₃	Na ₂ O
66.41	22.06	4.89	4.35	1.6	3.11	0.71

Table 3 Mineralogical composition of cement

Content of major minerals			
C ₃ S	C ₂ S	C ₃ A	C ₄ AF
63.6	15.3	5.6	13.2

The strength of the cement paste was determined on the samples cubes, with the size of faces of 40×40 mm, at the age of 28 days.

The effect of activation time and filler composition on the compressive strength of cement paste was evaluated by optimizing a three-factor rotatable planning experiment. The activated filler content, zeolite to dolomite ratio, and activation time were used as the independent variables. The content of activated filler varied from 10 to 30% of the Portland cement amount, the ratio of filler components varied from 20 to 80%.

3 Results and Discussion

According to the studies [18], the optimum ratio of ferromagnetic particle size values (l/d) are in the range $10 \div 13$, and the loading factor of the grinding chamber is in the range $0.5 \div 0.7$. When these conditions are met, the number of impacts, the impulse value and the impact frequency are the maximum. The research data also shows that, when affecting mineral materials, the optimum particle diameter should be in the range of $1.4 \div 1.9$ mm. Using this approach, the optimum size of ferromagnetic particles was determined: 15.8×1.5 mm, with a length (l) to diameter (d) ratio of 10.53 (Table 4). The coefficient of filling the milling chamber during activation is taken 0.6.

Changes in the dispersity of fillers after activation for 2, 4, 6 min were assessed. When activating dolomite in ABC up to 6 min, the median particle size decreased from 19.9 to 9.7 μm (Figs. 5, 6 and 7). Activation of dolomite for more than 4 min reduced the rate of increase in dispersity by 12% as a result of coagulation of filler particles, which reduces the efficiency of treatment.

The median size and character of the normal distribution of zeolite-containing rock particles did not change significantly after activation.

The characteristics of the free surface energy of mineral fillers after activation during the optimum time interval were determined (Table 5, Fig. 8). Dolomite is characterized by a low polarity (γ^{AB}) of 0.4 mJ/m^2 , and its total FSE is determined mainly by the dispersity components (γ_s and γ^{LW}) of 52.3 and 51.9 mJ/m^2 , respectively. The surface of the dolomite filler is generally neutral. The polarity of the cement chipboard is quite high, as the acid–base component of the FSE (γ^{AB}) is 12.2 mJ/m^2 . The cement chipboard has a predominance of acid surface properties ($\gamma^+ = 7.3 \text{ mJ/m}^2$) over the base properties ($\gamma^- = 5.1 \text{ mJ/m}^2$).

Table 4 Technical characteristics of ferromagnetic particles

l, particle length, mm	d, particle diameter, mm	l/d
19.8	5.0	3.96
21.8	3.0	7.27
19.8	2.0	9.9
15.8	1.5	10.53

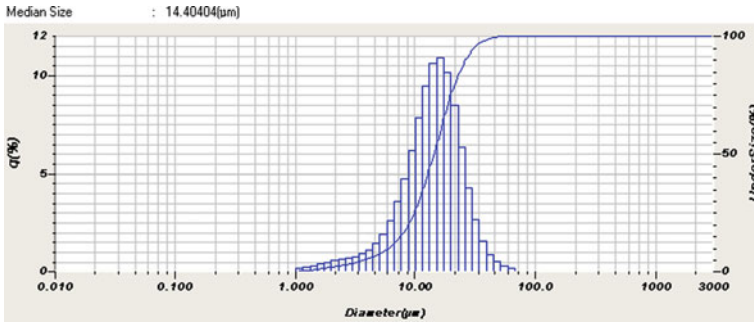


Fig. 5 Distribution of dolomite powder particles during activation for 2 min

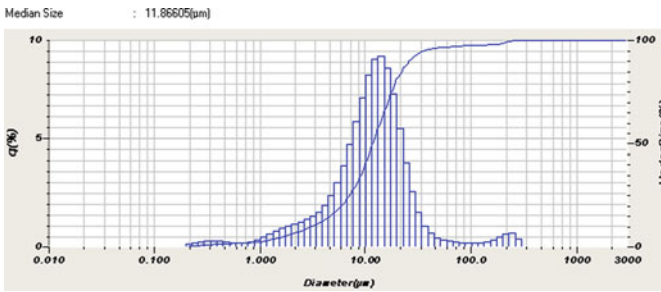


Fig. 6 Distribution of dolomite powder particles during activation for 4 min

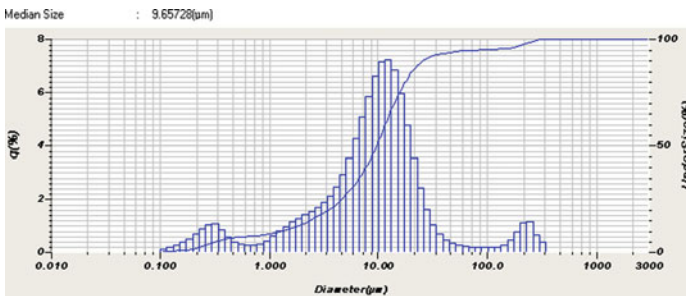


Fig. 7 Distribution of dolomite powder particles during activation for 6 min

Table 5 FSE Parameters of activated fillers

Activated filler	FSE parameters of activated fillers, mJ/m^2				
	γ^{LW}	γ^+	γ^-	γ^{AB}	γ_s
Dolomite	51.9	0.05	0.7	0.4	52.3
Cement chipboard	45.0	7.3	5.1	12.2	57.2

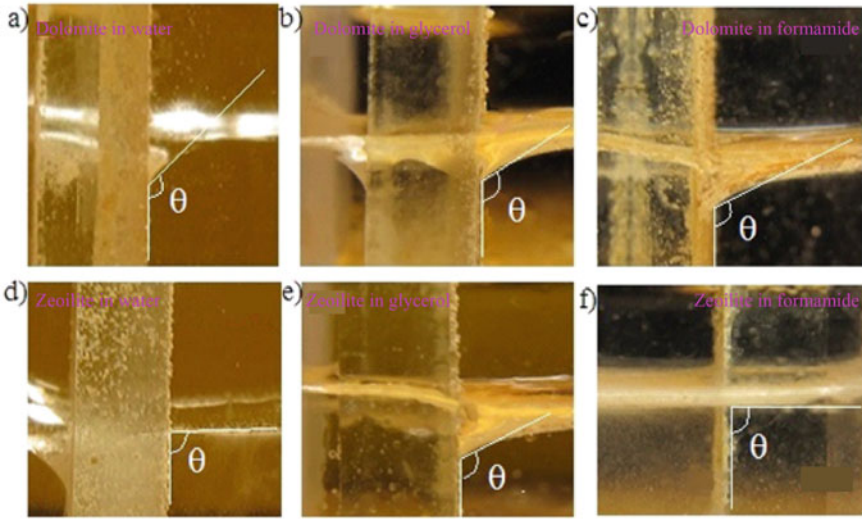


Fig. 8 Evaluation of surface properties of powders of dolomite — **a, b, c**; zeolite — **d, e, f** in test liquids: **a, d** — water; **b, e** — glycerol; **c, f** — formamide

Total FSEs of samples of activated fillers (γ_s) are of the same order, but for the cement chipboard, it is 4.9 mJ/m^2 higher (Table 5). Thus, a comparison of the obtained results shows a more pronounced polarity of activated cement chipboard in comparison with dolomite, which indicates its increased activity in interphase interactions and is consistent with the studies [12].

The experimental data was used to determine the optimum ratio of mineral filler components (Fig. 9). The maximum compressive strength of modified cement paste samples (53.12 MPa) is achieved for the content of cement chipboard of 66% and dolomite of 34%. The strength increase is 28% in comparison with the strength values for the dolomite content of 20%.

The analysis of strength indicators (Fig. 10) revealed the optimal content of activated filler, which was 17% of the weight of Portland cement. The activation time in ABC, at which the maximum compressive strength of cement paste samples is achieved, is 4 min (Figs. 9 and 10), which agrees with the results of the study of dispersivity of activated fillers.

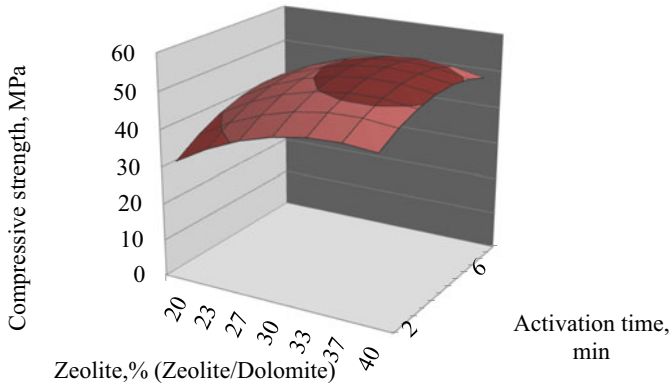


Fig. 9 The relationship between compressive strength of cement paste and the activation time and filler ratio

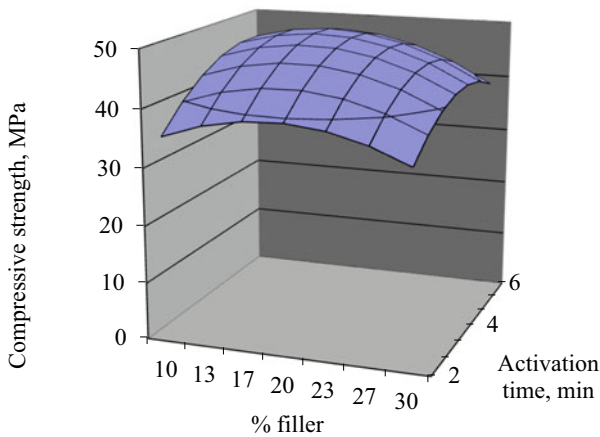


Fig. 10 Relationship between compressive strength of cement paste and the activation time and filler content

4 Conclusions

1. The optimum size of ferromagnetic particles based on the maximum exposure energy and frequency in the vortex layer apparatus was established, which was 15.8×1.5 mm for the studied mineral fillers and grinding ferromagnetic elements.
2. The possibility of reducing the median size of dolomite particles by 17.3% was revealed at the optimal activation time of 4 min. Dispersivity of zeolite-containing rock particles is stable under the studied activation modes.

3. The surface characteristics of activated fillers and the parameters of free surface energy were determined. Acid–base component of free surface energy of activated zeolite-containing rock was 12.2 mJ/m^2 , which is an order of magnitude higher than that of activated dolomite (0.4 mJ/m^2) and indirectly affects the increased activity in interphase interactions.
4. The optimal parameters of mineral fillers activation in a vortex layer apparatus for modification of cement-mineral systems were determined: filler content of 17% of Portland cement weight, zeolite/dolomite percentage ratio of 66/34, activation time of 4 min.

References

1. Liu, Y., Wang, J., Hu, S., Cao, S., Wang, F.: Enhancing the mechanical behaviour of concretes through polymer modification of the aggregate-cement paste interphase boundary. *J. Build. Eng.* 104605 (2022). <https://doi.org/10.1016/j.jobe.2022.104605>
2. Wang, Y., et al.: Alumina-rich Pozzolan modification on Portland-limestone cement concrete: hydration kinetics, formation of hydrates and long-term performance evolution. *Constr. Build. Mater.* **258**, 119712 (2020). <https://doi.org/10.1016/j.conbuildmat.2020.119712>
3. Sharma, R., Jang, J.G., Bansal, P.P.: A comprehensive review on effects of mineral admixtures and fibers on engineering properties of ultra-high-performance concrete. *J. Build. Eng.* **45**, 103314 (2022). <https://doi.org/10.1016/j.jobe.2021.103314>
4. Deng, S., Ren, P., Jiang, Y., Shao, X., Ling, T.-C.: Use of CO₂-active BOFS binder in the production of artificial aggregates with waste concrete powder. *Resour. Conserv. Recycl.* **182**, 106332 (2022). <https://doi.org/10.1016/j.resconrec.2022.106332>
5. Gupta, M., Raj, D.R., Kumar Sahu, D.A.: Effect of rice Husk Ash, silica fume & GGBFS on compressive strength of performance based concrete. *Mater. Today Proc.* **55**, 234–239 (2022). <https://doi.org/10.1016/j.matpr.2021.06.343>
6. Nie, Y., Shi, J., He, Z., Zhang, B., Peng, Y., Lu, J.: Evaluation of high-volume fly ash (HVFA) concrete modified by metakaolin: technical, economic and environmental analysis. *Powder Technol.* **397**, 117121 (2022). <https://doi.org/10.1016/j.powtec.2022.117121>
7. Alqarni, A.S.: A comprehensive review on properties of sustainable concrete using volcanic pumice powder ash as a supplementary cementitious material. *Constr. Build. Mater.* **323**, 126533 (2022). <https://doi.org/10.1016/j.conbuildmat.2022.126533>
8. Xu, J., Lu, D., Zhang, S., Xu, Z., Hooton, R.: Reaction mechanism of dolomite powder in Portland-dolomite cement. *Constr. Build. Mater.* **270**, 121375 (2021). <https://doi.org/10.1016/j.conbuildmat.2020.121375>
9. Tian, W., Liu, Y., Wang, M., Wang, W.: Performance and economic analyses of low-energy OHMIC curing sustainable reactive powder concrete with dolomite powder as fine aggregates. *J. Clean. Prod.* **329**, 129692 (2021). <https://doi.org/10.1016/j.jclepro.2021.129692>
10. Xu, J., Chen, J., Lu, D., Xu, Z., Hooton, R.D.: Effect of dolomite powder on the hydration and properties of calcium sulfoaluminate cements with different gypsum contents. *Constr. Build. Mater.* **225**, 302–310 (2019). <https://doi.org/10.1016/j.conbuildmat.2019.07.050>
11. Kazemian, M., Shafei, B.: Internal curing capabilities of natural zeolite to improve the hydration of ultra-high performance concrete. *Constr. Build. Mater.* **340**, 127452 (2022). <https://doi.org/10.1016/j.conbuildmat.2022.127452>
12. Rahul, P., Prasad Ravella, D., Chandra Sekhara Rao, P.V.: Durability assessment of Self-Curing high performance concretes containing zeolite admixture. *Mater. Today Proc.* (2022). <https://doi.org/10.1016/j.matpr.2022.01.352>

13. Zolghadri, A., Ahmadi, B., Taherkhani, H.: Influence of natural zeolite on fresh properties, compressive strength, flexural strength, abrasion resistance, Cantabro-loss and microstructure of self-consolidating concrete. *Constr. Build. Mater.* **334**, 127440 (2022). <https://doi.org/10.1016/j.conbuildmat.2022.127440>
14. Ibragimov, R., Fediuk, R.: Improving the early strength of concrete: Effect of mechanochemical activation of the cementitious suFSEnsion and using of various superplasticizers. *Constr. Build. Mater.* **226**, 839–848 (2019). <https://doi.org/10.1016/j.conbuildmat.2019.07.313>
15. Stroganov, V., Sagadeev, E., Ibragimov, R., Potapova, L.: Mechanical activation effect on the biostability of modified cement compositions. *Constr. Build. Mater.* **246**, 118506 (2020). <https://doi.org/10.1016/j.conbuildmat.2020.118506>
16. Vdovin, E., Stroganov, V., Konovalov, N.: Modification of road soil cement with activated fillers. In: Vatin, N., Borodinecs, A., Teltayev, B. (eds.) *Proceedings of EECE 2020. EECE 2020. LNCE*, vol. 150. Springer, Cham (2021). https://doi.org/10.1007/978-3-030-72404-7_33
17. Khaydarov, B., et al.: Efficient method of producing clinker-free binding materials using electromagnetic vortex milling. *Mater. Lett.* **226**, 13–18 (2018). <https://doi.org/10.1016/j.matlet.2018.05.016>
18. Zhang, D.J., Tian, X.F., Hou, H.B., Liu, H., Tan, S.K.: Mechanical behavior and mechanism of stabilizing soft soil by slag cementitious material. *Yantu Lixue/Rock Soil Mech.* **28** (2007)
19. Vdovin, E.A., Stroganov, V.F., Konovalov, N.V. Mavliev, L.F.: Analysis of the possibilities of modification and the choice of rational methods and technologies for strengthening the soil by activated fillers for road construction. *News KSUAE* **4**(46), 274–282 (2018). ISSN: 2073-1523, eISSN: 2073-154X
20. Lobel, B.T., Robertson, H., Webber, G.B., Ireland, P.M., Wanless, E.J.: Impact of surface free energy on electrostatic extraction of particles from a bed. *J. Colloid Interphase Bound. Sci.* **611**, 617–628 (2022). <https://doi.org/10.1016/j.jcis.2021.12.117>
21. Huang, T., Luo, J., Luo, R., Tu, C.: Investigation on the relationship between the surface texture index and the surface free energy of aggregate. *Constr. Build. Mater.* **325**, 126759 (2022). <https://doi.org/10.1016/j.conbuildmat.2022.126759>
22. Çıtak, A., Yarbaş, T.: Using contact angle measurement technique for determination of the surface free energy of B-SBA-15-x materials. *Int. J. Adhes. Adhes.* **112**, 103024 (2022). <https://doi.org/10.1016/j.ijadhadh.2021.103024>
23. Kuznetsov, G.V., et al.: Influence of roughness on polar and diFSErsed components of surface free energy and wettability properties of copper and steel surfaces. *Surf. Coat. Technol.* **422**, 127518 (2021). <https://doi.org/10.1016/j.surfcoat.2021.127518>
24. Starostina, I.A., Kolpakova, M.V., Stoyanov, O.V.: An estimation of adhesive interaction of polymer coatings with metals using the van Oss–Chaudhury–good equation. *Polym. Sci. Ser. D.* **14**, 8–12 (2021). <https://doi.org/10.1134/S1995421221010238>
25. Ibragimov, R.A., Potapova, L.L., Korolev, E.V.: Investigation of structure formation of activated nanomodified cement stone by IR spectroscopy. *News KSUAE* **3**(57), 41–49 (2021). https://doi.org/10.52409/20731523_2021_3_41

Adiabatic Efficiency of Monoblock Air Supply Unit with Humidification Module Based on Porous Rotating Atomizers



Nazir Sibgatullin and Rinat Safiullin 

Abstract The paper presents the characteristics of a monoblock air supply unit with a heat and mass transfer module based on porous rotating nozzles, which create an almost monodisperse spray with a controlled droplet size. These qualities of the sprayer allow creating smaller washing chambers with controlled heat and mass transfer processes. The dispersion of the spray was experimentally determined for multilayer rotating atomizers with an outer layer of radial synthetic fibers developed for compact chambers. It has been established that with the help of such devices it is possible to obtain droplets of $25 \div 40$ microns in size, which will be effective in humidifying the air.

Experiments to determine the adiabatic efficiency of the new design of a monoblock supply unit have shown that its humidifying module belongs to low-intensity washing chambers, in which the spray ratio ranges from 0.1 to 0.2, and the humidification efficiency reaches 80% at a spray ratio near 0.2.

Keywords Washing chamber · Porous rotating atomizers · Droplet dispersion · Adiabatic efficiency

1 Introduction

According to the parameters of the internal air in the air-supply centers for ventilation and air conditioning systems (ACS) an appropriate heat and humidity treatment of the external air is carried out, which includes the processes of heating, cooling, humidifying or dehumidifying the air [1, 2]. In many cases, the main device for carrying out these processes is a washing chamber, where air interacts with a torch of sprayed water droplets, which form a significant interfacial contact surface [3–5].

The spray plume dispersion characteristics have a significant effect on the energy efficient course of heat and moisture exchange processes [5–7] and on the conditions of air jets in premises [8, 9]. Most industrial washing chambers have nozzles in their

N. Sibgatullin · R. Safiullin (✉)
KazanStateUniversity of Architecture and Engineering, Kazan, Russia
e-mail: safiullin_rinat@mail.ru

design, which create an extremely polydisperse spray [10–12]. Small droplets, having a smaller mass, quickly acquire a higher temperature in the process of contact with air, as a result they completely evaporate within the free space of the chamber and the air is intensively humidified. Large drops contained in the spray plume of nozzle evaporate slowly, easily reach the walls and pan of the chamber, are impacted and merged on a liquid film and have practically no effect on the intensity of humidification or cooling of the air, although their share in the spray reaches 30–40% [13, 14].

In addition to the polydispersity of the spraying plume, the nozzles have a number of other disadvantages. It is indicated in [15–17] that the nozzles make “passing” flows of droplets (drops fly along the airway), which force the designers to take a large length of the washing chambers. Due to the low productivity on water, the number of nozzles in the chamber can reach several hundred pieces [18]. It determines the high metal consumption and large overall dimensions of the nozzle chambers in width, and, accordingly, requires large rooms for ventilation equipment. It is also well known that droplets spread from the nozzle in the form of a hollow cone [4], and the intersection of droplet plumes sharply increases the degree of their polydispersity and the overall efficiency of heat and mass transfer process decreases.

It follows from the foregoing that the designers of climatic technology are faced with the task of developing more advanced and compact ACS which ensure the rational use of areas, volumes of buildings and energy resources. Today, new designs of chambers with transverse spraying [19, 20] and without intersections of spray flares are needed, that will allow more efficient control of the heat and mass transfer process with different spray intensities depending on the volume and parameters of the air being treated. First of all, it is necessary to develop and use a high-performance atomizer capable of creating a spray plume close to monodisperse with droplets of the optimal size (for example, droplets with a diameter of $20 \div 40 \mu\text{m}$ are needed for humidification purposes).

The technical basis for the creation of an energy efficient washing chamber for the heat and humidity treatment of air can be porous rotating atomizers (PRA) [21, 22]. They create a volumetric and practically monodisperse plume of droplets, allow spraying water of any volume, and chambers based on them are characterized by a high intensity of formation of an interfacial surface [23]. Research works promoting the widespread use of PRA in heat and mass transfer devices are relevant and promising.

2 Materials and Methods

This paper studies the characteristics of a new design of a monoblock air supply unit with a humidification module, in which only one PRA is installed. It is capable of creating a thin volumetric spray plume of practically monodisperse droplets with a diameter of $25 \div 35 \mu\text{m}$ (Figs. 1 and 2). The purpose of the work is to experimentally determine the effectiveness of such a humidifying module at different intensities of spraying the air stream with water.



Fig. 1 External view of a monoblock air supply unit with a humidification module **a** and a spraying unit with the PRA **b**

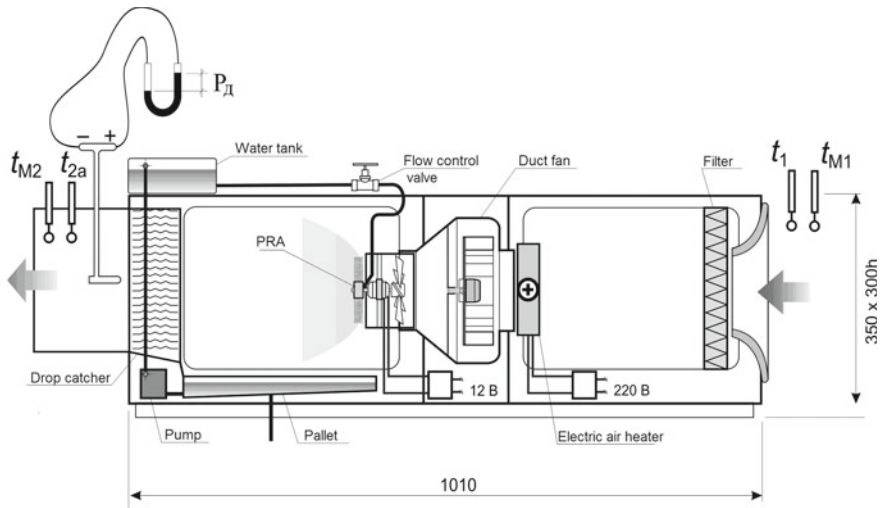


Fig. 2 Scheme of an experimental air supply unit with a humidification module

As an atomizer for the new monoblock unit, we used and investigated 7 variants of PRA designs, three of them are shown in Fig. 3. Figures 3a and 3b show examples of samples No. 3 and 4 in the form of cylinders with an outer diameter $D_{ext} = 17$ mm and $D_{ext} = 25$ mm made, which were made of porous filtering ceramics (PFC) and micro-powder abrasive mark M10. An outer annular layer consisting of synthetic fibers $12 \div 14 \mu\text{m}$ in diameter and 5 mm long, directed along the formation and detachment of drops, was used as a spraying surface in such complex PRA. Figure 3c shows a variant of a complex sample of PRA No. 7, in which the role of the basis (frame) is played by a cylinder made of abrasive mark M10, and the uniform distribution of water over the surface of the fibrous “coat” was carried out due to an additional intermediate porous layer with a thickness of 8 mm and an outer diameter $D_{ext} = 35$ mm.

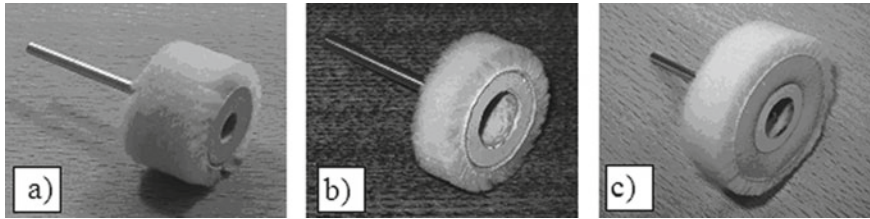


Fig. 3 Samples of complex PRA with a fibrous spraying layer

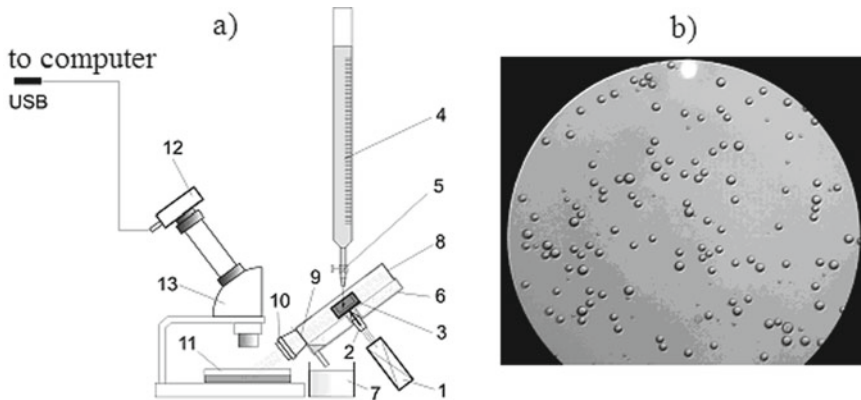


Fig. 4 Experimental setup for determining the dispersing ability of complex PRA: **a** — setup scheme; **b** — a typical photo of droplets trapped in an immersion medium (droplets in a spray are practically monodisperse)

The study of the disperse characteristics of the PRA's samples were carried out on an experimental setup (Fig. 4), which made it possible to capture droplets in an immersion medium. The installation included an electric drive (1) with five fixed values of shaft revolutions $n = 15,000, 20,000, 25,000, 30,000,$ and $35,000$ rpm. Sprayer (3) was rigidly mounted on a substrate and attached to the motor shaft (1) with a collet (2). Water was supplied to atomizer (3) from a 100-ml supplying measuring container (4). The water consumption in the experiments varied from 0.5 to 2.8 l/h. The flow rate was controlled by valve (5). The sprayed water was directed through the receiving hopper (6) into the collecting tank (7).

The sampling of the required set of droplets for recording their disperse composition was carried out using a sampling device (8) through a passage window (9). The exposure time for the flow of drops through the sampling window was set using an iris diaphragm (10). Water droplets were captured in a cuvette (11) with an immersion medium having the same density as water. Here the droplets acquired a spherical shape and were photographed in transmitted light using a camera (12) mounted on the eyepiece of a microscope (13) having a 56-x magnification. The image from camera

(12) was transmitted in real time directly through the USB input of the computer, and then to the monitor screen.

The study of the efficiency of a humidification module with a PRA of a new monoblock air supply unit was carried out at several mass air flows from 80 to 150 kg/h, determined at five positions of the dimmer. The dynamic pressure in the outlet of the installation was determined using a pneumometric tube and a differential micromanometer TESTO 445. The water consumption for the atomizer was 1.0–2.8 kg/h and was set according to the notches on the regulator, set by the volumetric method.

The spraying coefficient B , kg/kg, was taken as a value for characterizing the intensity of air spraying. It means the ratio of the amount of sprayed water G_W to the amount of air G passing through the chamber:

$$B = \frac{G_W}{G}. \quad (1)$$

The efficiency of the humidification process was estimated by the heat transfer coefficient E_a for the adiabatic process

$$E_a = 1 - \frac{t_2 - t_{m1}}{t_1 - t_{m1}} \quad (2)$$

where t_1 and t_2 are the dry bulb temperature before and after the washing chamber; t_{m1} – temperature of the wet thermometer of the processed air, °C.

3 Results and Discussion

In the experiments with the capture of droplets in an immersion medium it was found that the dispersion of the spraying plume, produced by the complex samples, significantly depended on the flow rate of water. Figure 5 shows the distribution histograms for samples PRA No. 3 and No. 4, obtained at flow rates $Q = 2.0$ and 2.8 kg/h. It can be seen that with an increase in the flow rate through the atomizer, the spread of droplet sizes in the spraying plume becomes wider.

Figure 6 shows the dependence between the average diameter of droplets in the spraying plume of the PRA and the peripheral speeds of rotation $v = 2 \div 40$ m/s, which were achieved in experiments with the samples of PRA No. 3 – 7. It follows from the Fig. 6 that the diameter of the droplets in the spray does not depend on the material of the framework layers of the complex PRA, but is determined by the size of the fibers on the outer (spraying) surface, as well as by the ratio of the peripheral velocity v and the flow rate Q .

The results obtained in the experiments with samples of various PVR designs show that this type of atomizers makes it possible to obtain a very thin ($25 \div 40 \mu\text{m}$) and rather uniform spraying plume. It is an illustrative example of the fact that

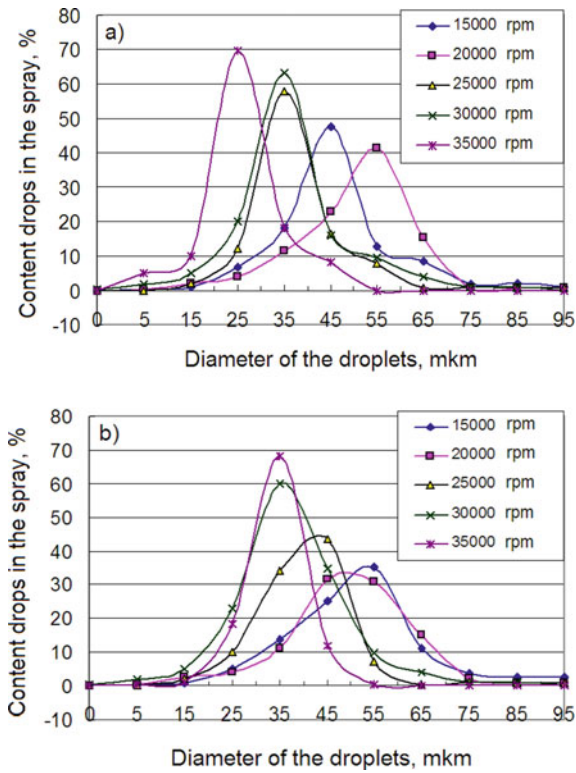


Fig. 5 Spray dispersion of complex PRA: a — $Q = 2.0$ kg/h; b — $Q = 2.8$ kg/h

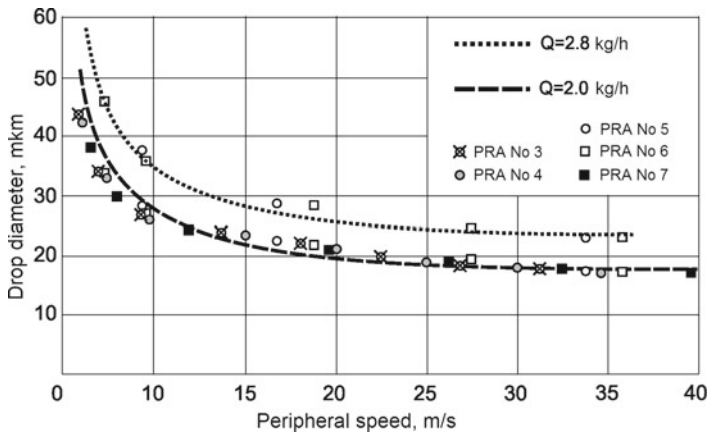
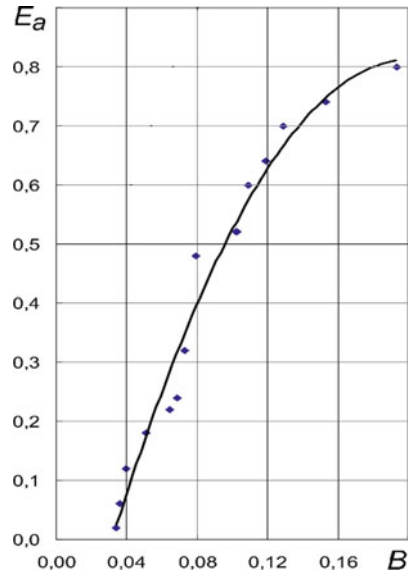


Fig. 6 Influence of the speed of rotation for PRA with an outer layer of fibers on average droplet size in spraying plume

Fig. 7 Dependence of the adiabatic humidification coefficient E_a on the coefficient B , for a monoblock air supply unit with a humidifying module based on a PRA



the use of a PRA can significantly increase the range of operation of the washing chambers with the receipt of drops characteristic of fine atomization. PRA will create a volumetric torch of a homogeneous monodisperse droplet structure when spraying water in quantities suitable for industrial use in humidifiers.

Figure 7 shows the dependence of the adiabatic efficiency coefficients E_a of the humidifying module on the spray coefficient B . It can be seen from the figure that the developed humidifying module belongs to low-intensity washing chambers, in which the coefficient B lies in the range of $0.1 \leq B \leq 0.2$. It can be seen that due to the small droplet size (less than 40 microns), the humidification efficiency is quite high (up to 80%) even with a small spray ratio. Therefore, PRA is recommended to be used in low-intensity chambers for adiabatic air humidification in the winter season in small monoblock air supply units.

4 Conclusion

The analysis of research works aimed at studying the characteristics of different types of sprayers shows that there are many areas of application for washing chambers based on PRA, in which they have technological advantages over other types of heat and mass transfer apparatus. First of all, these are objects in which it is necessary to stably and accurately maintain the relative humidity of the air, create an atmosphere of stable fine-dispersed fog, quickly respond to signals from automatic control devices - to have low inertia and the ability to change the characteristics of the humidification and cooling process; consume a rational amount of energy, to have good weight and

dimensions. The optimal solution is the use of humidifiers with PRA also in large rooms with a design capacity of a single unit of hundreds of kilograms per hour.

The paper investigates the technical capabilities of a new design of a monoblock air supply unit with a humidification module, in which a porous rotating atomizer plays the main role. An experimental determination of the effectiveness of such a humidifying module was carried out at different intensities of air spraying with water. In experiments to determine the dispersion of a PRA with an outer layer of synthetic fibers, which are recommended for a humidifying module, it was found that the diameter of droplets in the spray does not depend on the material of the framework layers of complex PRA, but is determined only by the size of the fibers on the outer (spraying) surface. The fineness of the spray is significantly affected by the ratio of the peripheral rotation speed of the atomizer and the flow rate of sprayed water. The results of experiments with samples of various designs of PRA show that this type of atomizers allows creating a very thin ($25 \div 40 \mu\text{m}$) and rather uniform spray plume.

Experiments to determine the adiabatic efficiency of the new design of a monoblock supply unit have shown that its humidifying module belongs to low-intensity washing chambers, in which the spraying coefficient ranges from 0.1 to 0.2, and the humidification efficiency reaches 80% even with a small irrigation coefficient.

References

1. ASHRAE: American Society of Heating, Refrigeration and Air conditioning. Handbook: Equipment. Atlanta, Ga.: ASHRAE (2008)
2. Johri, A.K.: Experimental studies on air–water spray interaction. M. Tech. Thesis. Department of Mechanical Engineering, Indian Institute of Technology Delhi (1996)
3. Fonseca, N., Cuevas, C.: Experimental and theoretical study of adiabatic humidification in HVAC&R applications. *Ingeniare. Rev. Chil. Ing.* (2010). <https://doi.org/10.4067/s0718-33052010000200011>
4. Sureshkumar, R., Kale, S.R., Dhar, P.L.: Heat and mass transfer processes between a water spray and ambient air–I. Experimental data. *Appl. Therm. Eng.* (2008). <https://doi.org/10.1016/j.applthermaleng.2007.09.010>
5. Sureshkumar, R., Kale, S.R., Dhar, P.L.: Heat and mass transfer processes between a water spray and ambient air–II. Simulations. *Appl. Therm. Eng.* (2008). <https://doi.org/10.1016/j.applthermaleng.2007.09.015>
6. Tissot, J., Boulet, P., Trinquet, F., Fournaison, L., MacChi-Tejeda, H.: Air cooling by evaporating droplets in the upward flow of a condenser. *Int. J. Therm. Sci.* (2011). <https://doi.org/10.1016/j.ijthermalsci.2011.06.004>
7. Broidam, V., Dorofenko, N.: Efficiency of direct free cooling in an air conditioning system for rooms with heat supply and recovery. *News KSUAE* **4**(50), 279–287 (2019)
8. Kareeva, J., Varsegova, E., Zakieva, R., Bliznjakova, K.: Research of the geometrical parameters of air inlet hole influence on the characteristics of jet. *News KSUAE* **4**(54), 104–111 (2020)
9. Kareeva, J., Zakieva, R., Bliznjakova, K.: Numerical study of the influence of the inlet geometric parameters on the jet characteristics. In: Vatin, N. (eds.) *Proceedings of STCCE 2021*. STCCE 2021. LNCE, vol. 169. Springer, Cham (2021). https://doi.org/10.1007/978-3-030-80103-8_39. <https://iopscience.iop.org/journal/1757-899X>
10. Nuyttens, D., Baetens, K., De Schamphelleire, M., Sonck, B.: Effect of nozzle type, size and pressure on spray droplet characteristics. *Biosyst. Eng.* (2007). <https://doi.org/10.1016/j.biosystemseng.2007.03.001>

11. Sadafi, M.H., Ruiz, J., Lucas, M., Jahn, I., Hooman, K.: Numerical and experimental study on a single cone saline water spray in a wind tunnel. *Int. J. Therm. Sci.* (2017). <https://doi.org/10.1016/j.ijthermalsci.2017.06.011>
12. Xia, L., Gurgenci, H., Liu, D., Guan, Z., Zhou, L., Wang, P.: CFD analysis of pre-cooling water spray system in natural draft dry cooling towers. *Appl. Therm. Eng.* (2016). <https://doi.org/10.1016/j.applthermaleng.2016.03.096>
13. Alkhedhair, A., Jahn, I., Gurgenci, H., Guan, Z., He, S.: Parametric study on spray cooling system for optimizing nozzle design with pre-cooling application in natural draft dry cooling towers. *Int. J. Therm. Sci.* (2016). <https://doi.org/10.1016/j.ijthermalsci.2016.02.004>
14. Hung, D. V., Tong, S., Nakano, Y., Tanaka, F., Hamanaka, D., Uchino, T.: Measurements of particle size distributions produced by humidifiers operating in high humidity storage environments. *Biosyst. Eng.* (2010). <https://doi.org/10.1016/j.biosystemseng.2010.07.001>
15. Alkhedhair, A., Gurgenci, H., Jahn, I., Guan, Z., He, S.: Numerical simulation of water spray for pre-cooling of inlet air in natural draft dry cooling towers. *Appl. Therm. Eng.* (2013). <https://doi.org/10.1016/j.applthermaleng.2013.08.012>
16. Alkhedhair, A., Jahn, I., Gurgenci, H., Guan, Z., He, S., Lu, Y.: Numerical simulation of water spray in natural draft dry cooling towers with a new nozzle representation approach. *Appl. Therm. Eng.* (2016). <https://doi.org/10.1016/j.applthermaleng.2015.10.118>
17. Xie, J.L., Gan, Z.W., Duan, F., Wong, T.N., Yu, S.C.M., Zhao, R.: Characterization of spray atomization and heat transfer of pressure swirl nozzles. *Int. J. Therm. Sci.* (2013). <https://doi.org/10.1016/j.ijthermalsci.2012.12.015>
18. Sun, Y., Guan, Z., Gurgenci, H., Li, X., Hooman, K.: A study on multi-nozzle arrangement for spray cooling system in natural draft dry cooling tower. *Appl. Therm. Eng.* (2017). <https://doi.org/10.1016/j.applthermaleng.2017.05.157>
19. Jiang, J.J., Liu, X.H., Jiang, Y.: Experimental and numerical analysis of a cross-flow closed wet cooling tower. *Appl. Therm. Eng.* (2013). <https://doi.org/10.1016/j.applthermaleng.2013.08.043>
20. Tarabanov, M., Prilepskiy, D.: Energy efficient air washing chambers for ventilation and air conditioning systems. *Ventilation, heating, air conditioning, heat supply and building thermal physics*, No. 5, pp. 24–33 (2012)
21. Kinnersley, P.: Atomizers for the aerial application of pesticides in Tsetse (Glossinasp) and Armyworm (Spodopteraexempta) Control (Cranfield University, 1992–07). PhD thesis
22. Bayvel, L., Orzechowski, Z.: *Liquid Atomization*. Taylor and Francis, London (1993). <https://doi.org/10.1201/9780203748787>
23. Safullin, R., Kareeva, J.: Formation and motion of droplets in gas cleaning devices with porous rotating atomizers. *IOP Conf. Ser. Mater. Sci. Eng.* **890**, 012159. STCCE-2020 (2020). <https://doi.org/10.1088/1757-899X/890/1/012159>

Polyvinyl Chloride Compounds for Construction Industry



Karina Khuziakhmetova , Lyaylya Abdrakhmanova , Rashit Nizamov , and Anvar Islamov 

Abstract The work is devoted to the development of formulations intended for the production of profiled molding products of various functional purposes. Polymer mixtures based on polyvinyl chloride were widely used for production of profiles. Different concentrations (from 7 to 40 parts per hundred parts of polyvinyl chloride resin) of acrylonitrile butadiene styrene copolymer were used as an additive polymer. Experimental samples were made in the form of flat profiles by extrusion. The technological and structural parameters of the polymer mixture based on polyvinyl chloride were considered. It was found that the presence of acrylonitrile butadiene styrene in the entire concentration range leads to easier recyclability, which is confirmed by high melt flowability. In the region of low concentrations of elastomer (7 and 10 parts per hundred parts of polyvinyl chloride resin) a synergistic effect on expanding is observed, and increase of acrylonitrile butadiene styrene concentration up to 40 parts per hundred parts of polyvinyl chloride resin results in higher elasticity, thermal stability and decrease of microhardness. To explain the results obtained, the supramolecular structure of the composites was evaluated by scanning electron microscopy.

Keywords PVC · ABS · Modification · Polymer blends · Moulded parts

1 Introduction

The operation of polymer building products depends on their functional purpose, as well as technical requirements imposed on them at the stage of production [1–5]. An important factor here is not only the large-tonnage nature of the polymers [6–11], but also their ability to be modified to create impact-, cold-, and heat-resistant polymeric materials [12–16].

One of the more problematic polymers at the processing stage is polyvinyl chloride (PVC), because in the area of processing temperatures its tendency to thermal

K. Khuziakhmetova (✉) · L. Abdrakhmanova · R. Nizamov · A. Islamov
Kazan State University of Architecture and Engineering, 1 Zelenaya Street, Kazan 420043, Russia
e-mail: karina261996@mail.ru

degradation manifests itself [17–20]. This peculiarity can lead to deterioration of the basic mechanical properties. In this regard, the reduction of processing temperature can be achieved by using technological additives from among elastomers. One common elastomeric additive is acrylonitrile butadiene styrene (ABS) [21, 22].

ABS is characterized by a wide variety of composition, molecular structure, production and processing methods [23–25]. As a rule, it consists of two phases: butadiene rubber and styrene-acrylonitrile plastic (SAN). Butadiene is evenly distributed in the rigid SAN matrix [26, 27]. ABS due to the combination of strength properties and non-flammability of butadiene, as well as elasticity and thermal stability of SAN matrix, is widely used as a modifier of physical, mechanical and thermal properties of PVC, which can improve the manufacturability and impact strength of PVC [28, 29]. At the same time PVC interacts more with SAN than with rubber. It follows that the interaction between SAN and PVC is decisive in the creation of PVC/ABS blends [30–33].

Studies are mainly focused on ABS-based mixtures in which the dispersed phase is PVC [34–36]. However, polymer mixtures based on PVC with a high concentration of ABS have special properties [37]. Due to its structure, ABS form a mesh of meshing macromolecules with PVC medium, which causes both changes in the melt flow patterns in the molding machines, and changes in the dispersed structure of composites and their functional properties. Therefore, the main interest is the consideration of structural and technological peculiarities when changing concentrations of ABS in PVC medium.

2 Materials and Methods

Suspension PVC of S-6359-M grade (100 phr), complex stabilizer - bicarbonate lead stearate (5 parts per hundred parts of PVC resin (phr)), stabilizer-lubricant - calcium stearate (3 phr) were used for research. ABS-20P (JSC Plastik, Russia), the concentration of which was 7, 10, 20, 30 and 40 phr. was chosen as impact strength and recyclability modifier. Softening point and melt flow index (at 220 °C and 10 kgf) of ABS was 97 °C and not less than 5–12 g/10 min, respectively. The average particle size of ABS was 199.5 μm with a characteristic bimodal particle size distribution.

Preparation of mixtures of different compositions was carried out in a laboratory mixer LDU-3 MPR with a propeller nozzle for 4 min at 700 rpm.

Film samples were prepared by thermoplasticizing method on laboratory rollers LB 200 100/100 E at temperature of rolls 160–170 °C for rigid samples for 3–4 min depending on the composition. Each series of samples was prepared simultaneously at the same temperature regime at the same thickness of the gap between the rolls 0.010–0.020 cm.

A LabTechScientific LTE 16–40 laboratory twin-screw extruder with a flat-slot die shape was used to produce flat profiles of 2 × 30 mm or larger (depending on the swelling coefficient of the melt) and 20–25 cm in length. Temperature mode was

adjusted by ten-cylinder zones with screw rotation speed of 16–30 rpm (depending on the formulation), the optimum engine load was 30–50% of the maximum.

The melt fluidity index (MFI) was determined on a Franck plastometer. Pre-prepared film samples weighing 3 g were heated to 185 °C and loaded with 21.6 kg. MFI value was determined by the mass of six samples that came out of a 2 mm diameter capillary and reached a stable flow.

The thermostability was determined on film samples ground to a size of 2 × 2 mm weighing 2–4 g and was characterized by the induction time from the beginning of tube immersion in the thermal oven to the color change of the indicator during HCl release during PVC dehydrochlorination at 180 °C.

Changes in linear dimensions were determined by «risks» on two extruded samples 220 ± 0.2 mm long, cut lengthwise and placed in a desiccator 2B-151, heated to 100 ± 2 °C, for 60 min.

Vickers microhardness was performed on an HVS-1000 digital display hardness tester. The test was performed by indenting a pyramidal diamond indenter with an opposing angle of 136° with a defined test force into the surface of the extruded sample.

The expansion of the extrudate was determined on three samples by measuring the geometric dimensions with a thickness gauge and a caliper, the values of which were compared with the dimensions of the die opening.

Thermomechanical analysis was carried out on the device, working on the principle of constant loading under the conditions of compression at a load of 1 N and a constant heating rate of 3 °C/min up to 220 °C on samples with a diameter of 8 ± 0.5 mm and a thickness of 3 ± 0.1 mm.

Scanning electron microscopy (SEM) was performed on a CarlZeiss Merlin high-resolution scanning electron microscope at a 5 kV primary electron accelerating voltage and a 300 pA probe current to minimize exposure to the test object. Samples were placed in liquid nitrogen, followed by chipping. The chipped samples were fixed on a holder and placed in a chamber of Quorum Q 150TES vacuum unit. The conductive layer was applied by cathodic spraying with Au/Pd alloy in an 80/20 ratio. The thickness of the applied layer was 15 nm.

Using an energy dispersion spectrometer the elemental composition of the samples at different sections of the composite with nitrogen fixation as a reference element in the composition of ABS and chlorine showing the presence of PVC was investigated.

3 Results and Discussion

The indicators of the main technological parameters of the compositions are presented in Table 1. With the increase of ABS concentration up to 40 phr the tendency to increase of technological parameters is observed. At that, MFI increases by 45.81%, thermal stability by 20.18% and change of linear dimensions, starting from 10 phr, by 66.67%.

Table 1 Technological parameters of the samples

ABS concentration, phr	MFI, g/10 min	Thermal stability, min	Changes in linear dimensions, %
7	2.362	91	0.25
10	2.676	92	0.05
20	3.233	93	0.06
30	3.767	102	0.11
40	4.359	114	0.15

MFI demonstrates that the introduction of ABS concentration up to 40 phr is accompanied by a uniform increase in the index. This may be due to the formation of a more homogeneous structure as a result of destruction of PVC agglomerates, in the absence of which the melt fluidity increases.

Compositions with the highest ABS concentration proved to be more stable to temperature influences. Increase of ABS concentration is accompanied by linear increase of this index.

The greatest change in linear dimensions was observed in the composition with 7 phr ABS. At the same time, the value in question begins to increase insignificantly from 10 phr ABS.

Suspension PVC of S-6359-M grade (100 phr), complex stabilizer - bicarbonate lead stearate (5 parts per hundred parts of PVC resin (phr)), stabilizer-lubricant - calcium stearate (3 phr) were used for research. ABS-20P (JSC Plastik, Russia), whose concentration was 7, 10, 20, 30 and 40 phr was chosen as impact strength and recyclability modifier. Softening point and melt flow index (at 220 °C and 10 kgf) of ABS was 97 °C and not less than 5–12 g/10 min, respectively. The average particle size of ABS was 199.5 μm with a characteristic bimodal particle size distribution.

Figure 1 shows that an increase in the concentration of ABS copolymer up to 40 phr leads to an increase in the swelling value by 14.20% compared to the minimum concentration of ABS. At the same time, the microhardness of the compositions (Fig. 2) decreases linearly to 8.40%, which may be due to a decrease in the density of the physical meshing knots according to Table 2.

Figure 3 shows the thermomechanical curves of the PVC samples. As can be seen, the introduction of small doses of ABS (7 and 10 phr) leads to an overlap of the curves. A further increase in concentration leads to a narrowing of the region of high elasticity.

The processing data of the thermomechanical curves are presented in Table 2. It shows that with increasing concentration of ABS, the region of the beginning and the end of the glass transition temperature (T_g) begins to decrease, while the initial T_g increases, which is important in terms of increasing the heat resistance of the samples. In turn, the region of high elasticity begins to decrease and goes faster to the flowing state at lower temperatures, as evidenced by the flowing temperature (T_f). This leads to an increase in the value of high elasticity (ε). This fact causes a

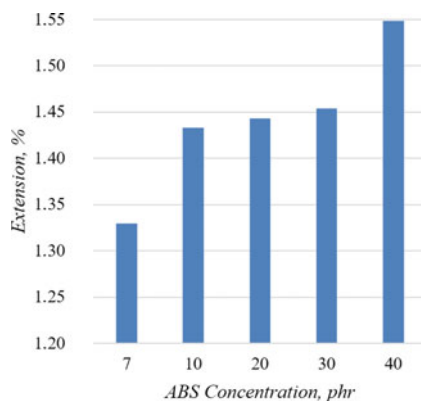


Fig. 1 Dependence of expanding on ABS concentration

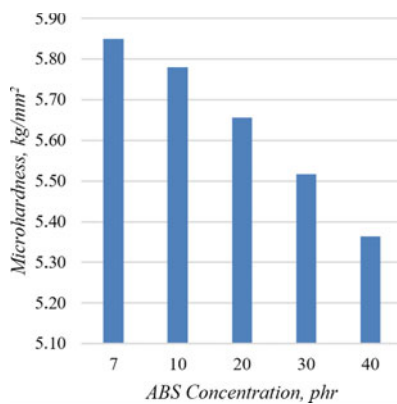


Fig. 2 Dependence of microhardness on ABS concentration

Table 2 Processing data of thermomechanical curves of samples

ABS concentration, phr	Temperature, °C		Area of high elasticity, °C	E , N/cm ²	ϵ , %	ν , mol/g $\times 10^{-6}$
	$T_g^{initial} - T_g^{final}$	T_f				
7	92 – 130	188	58	9.77	20	7.21
10	95 – 130	188	58	8.77	22	6.51
20	96 – 133	186	53	6.13	32	4.64
30	100 – 133	185	52	5.81	34	4.50
40	110 – 133	180	47	5.31	37	3.87

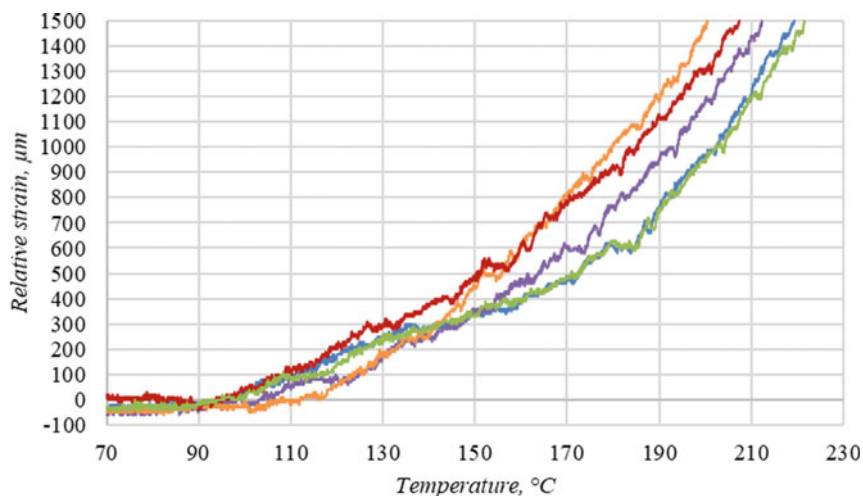


Fig. 3 Thermomechanical curves of PVC samples with different concentrations of ABS (phr): ■ – 7; ■ – 10; ■ – 20; ■ – 30; ■ – 40

decrease in the high elasticity modulus (E) and, accordingly, a decrease in the density of physical meshing knots (ν).

To analyze the data obtained, the morphology was analyzed using SEM (Fig. 4). Microphotographs of brittle chip samples with different concentrations of ABS are shown at a scale division price of 200 nm. The morphology of the PVC/ABS mixture is mainly represented as inclusions of different sizes, which indicates phase separation and indicates heterogeneity between the PVC and ABS components. It can be seen that at low doses of ABS (Fig. 4a, b) the heterogeneity is less pronounced with larger inclusion sizes. A further increase in concentration leads to greater heterogeneity at small inclusion sizes (Fig. 4c, d). However, at the maximum ABS content (Fig. 4e), the surface inclusions begin to disappear and transition to continuous phase structures. Since ABS belongs to the intermediate group of elastomers in which particle sizes tend to vary depending on processing parameters [38], the decrease in the size of ABS inclusions can be explained by a change in the rotation speed of the extruder screws with an increase in elastomer concentration.

The solubility of SAN results in an active interaction with the butadiene core, which in turn leads to structural changes in the mixture. The structural changes of the mixture in the dispersed phase and dispersion medium were examined using energy dispersive spectra according to Table 3. As can be seen, an increase in ABS concentration leads to the fact that the element nitrogen, which is characteristic of

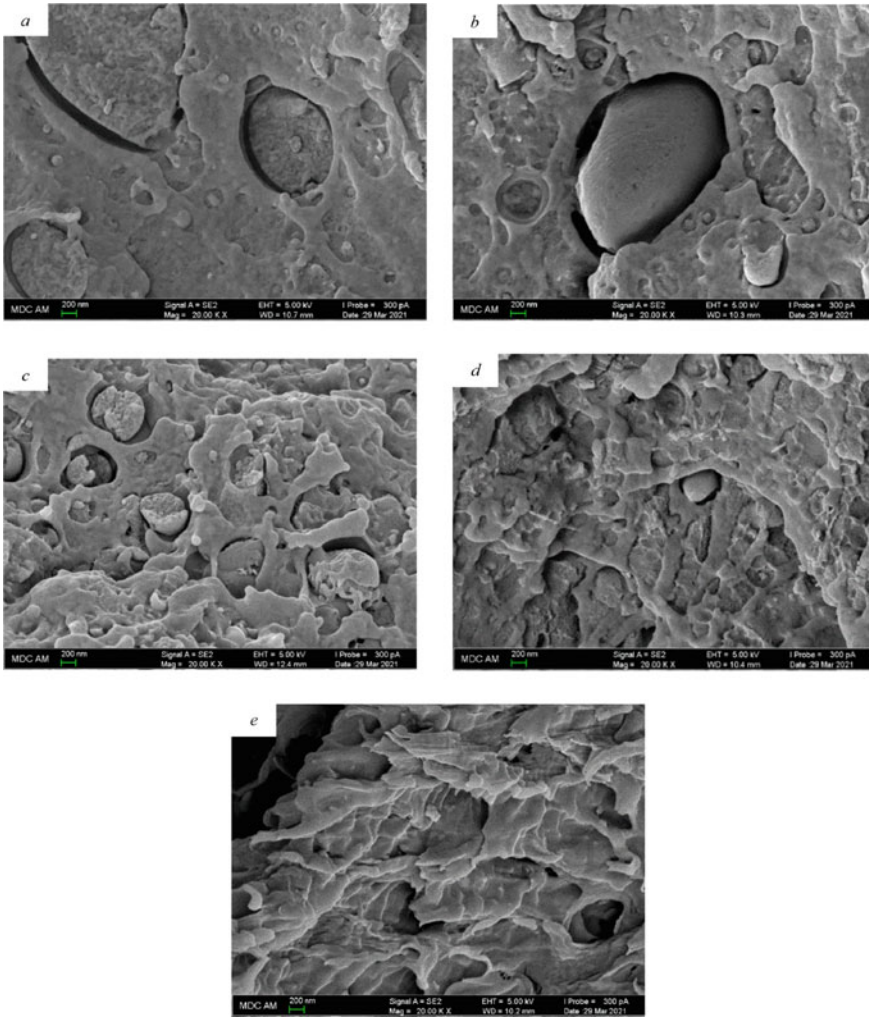


Fig. 4 SEM micrographs with different concentrations of ABS (phr): **a** – 7; **b** – 10; **c** – 20; **d** – 30; **e** – 40

ABS, appears not only on the surface of the dispersed phase, but also in the dispersion medium. This suggests that the dispersed phase in the form of various inclusions begins to combine with the dispersion medium, resulting in the interpenetration of the two structures. A further increase in ABS concentration can lead to a phase inversion between the components of PVC and ABS.

Table 3 Content of nitrogen atoms in the elements of the structure

ABS concentration, phr	% weight/% atomic	
	Cl	N
7:	–	1.91/2.03
In the dispersed phase	24.39/10.27	–
In the dispersed medium		
10:	–	3.05/3.15
In the dispersed phase	14.40/5.85	–
In the dispersed medium		
20:	20.19/8.35	1.47/1.53
In the dispersed phase	20.24/8.05	–
In the dispersed medium		
30:	21.70/8.83	1.14/1.17
In the dispersed phase	18.26/5.85	–
In the dispersed medium		
40:	24.65/10.58	8.16/8.58
In the dispersed phase	25.49/10.30	2.29/2.50
In the dispersed medium		

4 Conclusion

Thus, the range of ABS concentrations can form different effects on the structure of PVC-based mixture. Increasing the ABS concentration leads to a linear increase in MFI, thermal stability, an insignificant change in linear dimensions and swelling compared to the minimum elastomer concentration. The microhardness of the compositions decreases linearly, which may be due to a decrease in the density of the physical meshing knots. Increasing the ABS concentration leads to a narrowing of the area of high elasticity. The morphology of the PVC/ABS mixture is represented in the form of different sizes of elastomer inclusions, which begin to decrease and tend to continuous phase structures when the ABS concentration is entrained. This can be evidenced by the presence of nitrogen in the dispersion medium of PVC at the maximum concentration of ABS.

References

1. Ellen MacArthur Foundation/World economic forum: The New Plastics Economy: Catalysing Action. World Econ. Forum. (2017)
2. Liu, Y., Zhou, C., Li, F., Liu, H., Yang, J.: Stocks and flows of polyvinyl chloride (PVC) in China: 1980–2050. *Resour. Conserv. Recycl.* **154** (2020). <https://doi.org/10.1016/j.resconrec.2019.104584>
3. Ashrapov, A.K., Abdrakhmanova, L.A., Nizamov, R.K., Khozin, V.G.: Research of PVC compound with carbon nanotubes. *Nanotekhnologii v Stroit. nauchnyy internet-zhurnal* **3**, 13–24 (2011)

4. Nizamov, R.K.: Multifunctional fillers for construction polyvinyl chloride composites. *Stroit. Mater.* 68–70 (2006)
5. Galeev, R., Abdrakhmanova, L., Nizamov, R.: Nanomodified organic-inorganic polymeric binders for polymer building materials. In: *Solid State Phenomena* (2018). <https://doi.org/10.4028/www.scientific.net/SSP.276.223>.
6. Karaś, R.: The technology of designing plastic windows and their transport from Poland since 1990. *Polimery* **66** (2021). <https://doi.org/10.14314/polimery.2021.1.3>
7. Gholizadeh, H., Fazlollahabbar, H., Khalilzadeh, M.: Reliability computation for an uncertain PVC window production system using a modified Bayesian estimation. *J. Intell. Fuzzy Syst.* **40** (2021). <https://doi.org/10.3233/JIFS-190718>.
8. Putrawan, I.D.G.A., Azharuddin, A., Adityawarman, D., Ar Rahim, D.: Sintesis Merkaptotetil Karboksilat sebagai Bahan Baku Stabiliser Termal Polivinil Klorida: Variasi Sumber Asam Lemak. *J. Tek. Kim. Indones.* **18** (2020). <https://doi.org/10.5614/jtki.2019.18.2.3>
9. Jemii, H., Bahri, A., Boubakri, A., Hammiche, D., Elleuch, K., Guermazi, N.: On the mechanical behaviour of industrial PVC pipes under pressure loading: experimental and numerical studies. *J. Polym. Res.* **27** (2020). <https://doi.org/10.1007/s10965-020-02222-1>
10. Fu, Z., Yang, Z., Rong, Y., Deng, L., Wu, J.: A zinc Schiff base complex as high-efficiency stabilizer for flexible poly (vinyl chloride) against thermal degradation. *J. Vinyl Addit. Technol.* (2021). <https://doi.org/10.1002/vnl.21812>
11. Allen, N.S., Edge, M.: Perspectives on additives for polymers. 1. Aspects of stabilization. *J. Vinyl Addit. Technol.* **27** (2021). <https://doi.org/10.1002/vnl.21807>
12. Joshi, P.S., Marathe, D.S.: Experimental investigation of mechanical properties of impact modified polyvinyl chloride-fly ash composites. *J. Miner. Mater. Charact. Eng.* **07** (2019). <https://doi.org/10.4236/jmmce.2019.71003>
13. Islamov, A., Fakhrutdymova, V.: Surface modification of PVC by silica sol. In: *IOP Conference Series: Materials Science and Engineering* (2020). <https://doi.org/10.1088/1757-899X/890/1/012083>
14. Galeev, R., Nizamov, R., Abdrakhmanova, L., Khozin, V.: Resource-saving polymer compositions for construction purposes. In: *IOP Conference Series: Materials Science and Engineering* (2020). <https://doi.org/10.1088/1757-899X/890/1/012111>
15. Nizamov, R., Abdrakhmanova, L.: Influence of fillers on polyvinyl chloride materials thermal resistance. In: *Solid State Phenomena* (2016). <https://doi.org/10.4028/www.scientific.net/MSF.871.84>
16. Ivanova, S.R., Minsker, K.S., Nagumanova, E.I., Nizamov, R.K., Kazar'yans, S.A.: The stabilizing properties of synthetic zeolites in plasticized polyvinyl chloride compounds. *Plast. Massy Sint. Svoystva Pererab. Primen.* (2005)
17. Ciacci, L., Passarini, F., Vassura, I.: The European PVC cycle: in-use stock and flows. *Resour. Conserv. Recycl.* (2017). <https://doi.org/10.1016/j.resconrec.2016.08.008>
18. Abbas-Abadi, M.S.: The effect of process and structural parameters on the stability, thermo-mechanical and thermal degradation of polymers with hydrocarbon skeleton containing PE, PP, PS, PVC, NR, PBR and SBR (2020). <https://doi.org/10.1007/s10973-020-09344-0>
19. Galeev, R., Nizamov, R., Abdrakhmanova, L.: Influence of dispersed fillers on properties and processability of polyvinyl chloride compositions. In: *E3S Web of Conferences* (2020). <https://doi.org/10.1051/e3sconf/202016414018>
20. Kopotilova, A.: Features of construction in conditions of dense urban development. *Young Sci.* 59–61 (2017)
21. Gilbert, M., et al.: Chapter 24—thermoplastic elastomers. In: Gilbert, M. (ред.) *Brydson's Plastics Materials* (Eighth Edition), pp. 631–652. Butterworth-Heinemann (2017)
22. Lavrov, N.A., Belukhichev, E.V.: Polyvinyl chloride-based polymer blends (overview). *Plast. massy.* 55–59 (2020). <https://doi.org/10.35164/0554-2901-2020-3-4-55-59>
23. Sabah, F., En-Naji, A., Wahid, A., El Ghorba, M., Chakir, H.: Study of damage of the specimens in acrylonitrile butadiene styrene (ABS), based on a static damage study and damage by unified theory to predict the life of the material. *Key Eng. Mater.* (2019). <https://doi.org/10.4028/www.scientific.net/KEM.820.40>

24. Hu, D., Zhou, Q., Zhou, K.: Combined effects of layered nanofillers and intumescent flame retardant on thermal and fire behavior of ABS resin. *J. Appl. Polym. Sci.* **136** (2019). <https://doi.org/10.1002/app.48220>
25. Bano, S., Ramzan, N., Iqbal, T., Mahmood, H., Saeed, F.: Study of thermal degradation behavior and kinetics of ABS/PC blend. *Pol. J. Chem. Technol.* **22**, 64–69 (2020). <https://doi.org/10.2478/pjct-2020-0029>
26. Lu, G., et al.: Surface laser-marking and mechanical properties of acrylonitrile-butadiene-styrene copolymer composites with organically modified montmorillonite. *ACS Omega* **5**, 19255–19267 (2020). <https://doi.org/10.1021/acsomega.0c02803>
27. Simionescu, T.M., Spiridon, I., Varganici, C.D., Darie-Nita, R.N., Minea, A.A.: An experimental study on mechanical and thermal behavior of acrylonitrile butadiene styrene enhanced with fire retardants. *Environ. Eng. Manag. J.* **19** (2020)
28. Khuziakhmetova, K.R., Abdrakhmanova, L.A., Nizamov, R.K., Khozin, V.G.: Influence of fiber filler on the structure and properties of polyvinyl chloride/acrylonitrile-butadiene-styrene blends. *Image J. Adv. Mater. Technol.* **6** (2021). <https://doi.org/10.17277/jamt.2021.04.pp.291-298>
29. Khuziakhmetova, K., Abdrakhmanova, L., Nizamov, R.: Polymer mixtures based on polyvinyl chloride for the production of construction materials. In: Vatin, N. (eds.) *Proceedings of STCCE 2021. STCCE 2021. LNCE*, vol. 169. Springer, Cham (2021). https://doi.org/10.1007/978-3-030-80103-8_2
30. Kurek, A.P., Dotto, M.E.R., de Araújo, P.H.H., Sellin, N.: Evaluation of the etching and chrome plating on the ABS, PVC, and PVC/ABS blends surface. *J. Appl. Polym. Sci.* **134** (2017). <https://doi.org/10.1002/app.44571>
31. Li, Y., et al.: Effects of chlorinated polyethylene and antimony trioxide on recycled polyvinyl chloride/acryl-butadiene-styrene blends: flame retardancy and mechanical properties. *Polymer (Guildf)* **190**, 122198 (2020). <https://doi.org/10.1016/j.polymer.2020.122198>
32. Jaidev, K., Suresh, S.S., Gohatre, O.K., Biswal, M., Mohanty, S., Nayak, S.K.: Development of recycled blends based on cables and wires with plastic cabinets: an effective solution for value addition of hazardous waste plastics. *Waste Manag. Res.* **38**, 312–321 (2020). <https://doi.org/10.1177/0734242X19890918>
33. Ehsan Kianfar: (PVC/ABS) and Nanocomposite (CAU-10-H) Composite Membrane for Separation of C₂H₆ from CH₄. *Fine Chem. Eng.* (2020). <https://doi.org/10.37256/fce.122020476>
34. Matseevich, A., Matseevich, T., Askadskii, A.: Study of the abrasion resistance of wood-polymer composites and mixtures of ABS-plastic with polyvinyl chloride. In: *MATEC Web of Conferences* (2018). <https://doi.org/10.1051/mateconf/201819604069>
35. Chen, F., Liang, H., Yin, S., Huang, S., Tang, Q.: Fabrication of novel resinous diamond composites with acrylonitrile butadiene styrene/polyvinyl chloride/dioctyl phthalate/diamond by hot pressing molding. *J. Mater. Res.* **34** (2019). <https://doi.org/10.1557/jmr.2019.79>
36. Xiong, C.W., Ho, C.Y., Qiao, D.: Analytical study on pulsed-laser processing for acrylonitrile butadiene styrene/polyvinyl chloride. *Medziagotyra* **26** (2020). <https://doi.org/10.5755/j01.ms.26.1.20310>
37. Zhou, L.L., Lin, Y.S., Yang, J.Y., Wu, Q.Y.: Morphological structure and toughening mechanism of ABS toughened rigid PVC. *Zhongguo Suliao China Plast* **15**, 27 (2001)
38. Wilkes, C.E., Daniels, C.A., Summers, J.W., Krauskopf, L.G., Godwin, A.: *PVC handbook 6 processing aids and impact modifiers* (2005)

Modification of Wood-Polymer Composites with Silica Sols of Different Nature



Ayaz Khantimirov , Lyaylya Abdrakhmanova , Vadim Khozin ,
and Rashit Nizamov 

Abstract At the present time the actual task in the development of compositions for profile molding products made of wood-polymer composites is the search for effective binding agents for the system wood filler - polymer. In this work, we investigated the influence of different types of silica as binding agents on the properties of wood-polymer composites based on polyvinyl chloride. Silica sols had different stabilizing media, pH values and silica content. Tests were carried out on film samples obtained by rolling. Both technological and operational properties of the studied composites were considered. It was found that the introduction of silica, regardless of their type, increases the tensile strength. At the same time composites modified with silica with higher SiO₂ content (about 30%), have increased values of strength characteristics. It was also found that silica sols stabilized with sodium ions (Na⁺) do not lead to an increase in melt viscosity.

Keywords Polyvinyl chloride · Wood-polymer composites · Coupling agent · Silica sol · Profile mouldings

1 Introduction

Wood-polymer composites (WPC) are modern composite materials that combine the advantages of both wood and polymer materials [1, 2]. The most popular WPC polymers among thermoplastic resins are polyethylene (PE), polypropylene (PP) and polyvinyl chloride (PVC). However, among them, PVC is the most advantageous in terms of operational characteristics [3, 4].

At the present time in the field of modification of wood-polymer composites a research is conducted on the use of wood-mineral fillers in their composition, as well as the search for effective binder agents on the interface of wood filler - polymer.

A. Khantimirov (✉) · L. Abdrakhmanova · V. Khozin · R. Nizamov
Kazan State University of Architecture and Engineering, 1, Zelenaya Street,
Kazan 420043, Russia
e-mail: khantimirov94@mail.ru

Binding agents based on clay minerals [5–12], carbon [13–18] and silica [19–28] showed the greatest effectiveness. Silica-based substances have also shown their effectiveness as fillers [29–34].

For example, in [29] PVC composite with silica-lignin filler up to 10 wt.% was obtained. Compared to the composition without silica, the new composite has an increased value of Young's modulus without reducing the tensile strength. The silica-lignin filler also decreased the composite processing temperature, due to which the thermal stability increased.

In [30] wood-polymer composites based on PVC with gradual replacement of the organic filler with highly dispersed silicon oxide powder were investigated. The initial content of wood flour was 48.5 wt%. The replacement of wood flour with silicon oxide powder in the composition of WPC led to a significant increase in the Brinell hardness and water resistance of the material, but at the same time, the bending strength and impact toughness decreased.

Often WPCs are modified with nanosilica both in dry powder form and in the form of aqueous dispersion. For example, in [25] the effect of micro- and nanosilica on the properties of WPCs based on high-density polyethylene was studied. The particles were included in WPC in the form of dry and aqueous dispersion. Compositions with dry dispersions of microsilica had a reduction in mechanical strength of more than 30%, but the introduction of nanosilica increased the strength. Aqueous dispersions improved mechanical strength by up to 30%. Thus, the authors conclude that silica particles can reinforce WPC to a moderate degree if they are in the nanometer range and uniformly distributed in the composite volume.

Also earlier [24] we studied in detail the effect on the properties of PVC composites of silica sol, which is a 30% colloidal solution of silicon oxide particles with $\text{pH} = 10.3$. Composites with a complex of improved properties were obtained; the optimal concentration of silica sol was 0.35% of the weight of wood flour.

Thus, the analysis of the literature allows us to draw conclusions about the need for research with new types of silica as binding agents in PVC-based WPC.

2 Materials and Methods

Composites structures contained PVC mark C-7059-M (100 m.p.), impact strength modifier FM-50 (7 m.p.), stabilizer-lubricant calcium stearate (3 m.p.), thermal stabilizer double-base lead stearate (5 m.p.), silica-modified wood flour 180 (50 m.p.). Preparation of mixtures of different compositions was carried out in a laboratory mixer LDU-3 MPR with a propeller nozzle for 5 min at 700 rpm.

As a nano-modifier we used different silica sols of “Laxil” company LLC “STC “KOMPAS” (Kazan, Russia). The characteristics of the used silica sols are shown in Table 1.

Introduction of nanomodifiers was carried out as follows: wood flour was mixed with the modifier diluted to the required concentrations with distilled water. The resulting mixture was thoroughly mechanically mixed for 5–7 min at 500–700 rpm

Table 1. Characteristics of used silica sols

Parameter	Silica sols grades			
	Laxil 15	Laxil 30	Laxil 30-A	Laxil 30-AL
pH, units. pH	10,49	9,93	8,14	2,15
Mass concentration of SiO ₂ , % wt	15,3	33,75	32	33,1
Viscosity, cSt, not more	5	10	12	10
Density, g/cm ³	1,105	1,239	1,224	1,234
Sol stabilizer	Na ⁺	Na ⁺	NH ₄ ⁺	Al ⁺

in a laboratory mixer. Then the wood flour was pre-dried in a thermal chamber at 100° C for 10–12 h, after which the modified wood flour was used to fill the compositions.

Foil samples were obtained to study PVC compositions. The foils were made on laboratory rollers LB 200 100/100E at a roller temperature of 160...170 °C for 5 min.

Tensile strength was determined with the help of tensile machine PM-250 at a tensile speed of 100 mm/min on five prepared samples 150 × 15 mm in size (according to the standard: GOST 14,236–81). The melt flow rate *i* (MFR) was determined on the Franck plastometer at 190 °C and a load of 21.6 kg (according to the standard: GOST 11,645–73). Thermal stability time τ was determined by the method “kongo red” at 180 °C (according to the standard: GOST 14,041–91).

3 Results and Discussion

Experimental studies are aimed at studying the main technological and operational properties of WPC-PVC using different types of ashes with different physical and chemical parameters. Earlier [19] it was established that the maximum operational and technological parameters of building PVC materials based on modified wood flour are provided at the optimum concentration of silica ashes, equal to 0.35 wt.% of the weight of wood flour. Exactly such compositions were studied in this work.

When creating filled WPCs, we carried out the modification of the surface of wood flour with ashes as binder agents to ensure compatibility of polymer matrix and wood particles. Treatment of the wood flour surface has a positive effect on enhancing the interaction at the PVC-wood filler interface. To explain the obtained data, the analysis of possible mechanisms of influence of silicic acid sols of different nature on the properties of WPC-PVC was carried out taking into account such indicators as acidity, silicate modulus, viscosity, which differ depending on the nature of the stabilizing ion in the sol.

The test results are shown in Figs. 1, 2 and 3.

It follows from the data presented that the greatest changes are observed in the melt flowability index of the compositions. Mechanical properties with almost all types of ashes are noticeably higher than for the control sample. The thermal stability index is approximately at the same level for all investigated compositions.

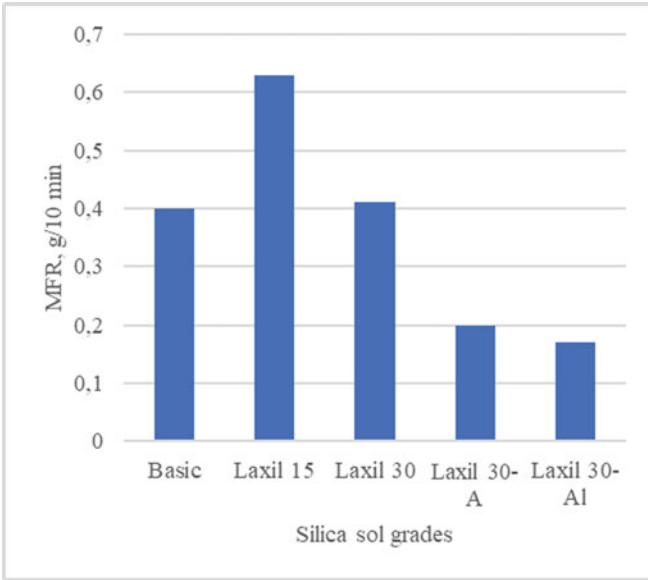


Fig. 1 Dependence of MFR of WPC-PVC on silica sol grades

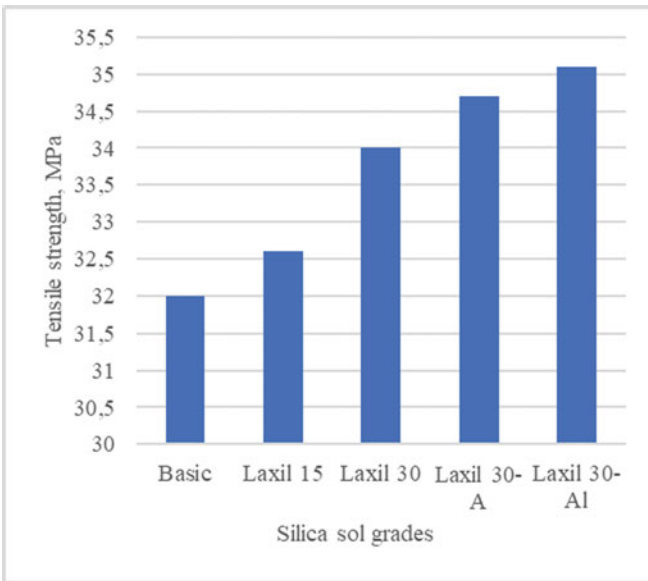


Fig. 2 Tensile strength dependence of WPC -PVC samples on silica sol grades

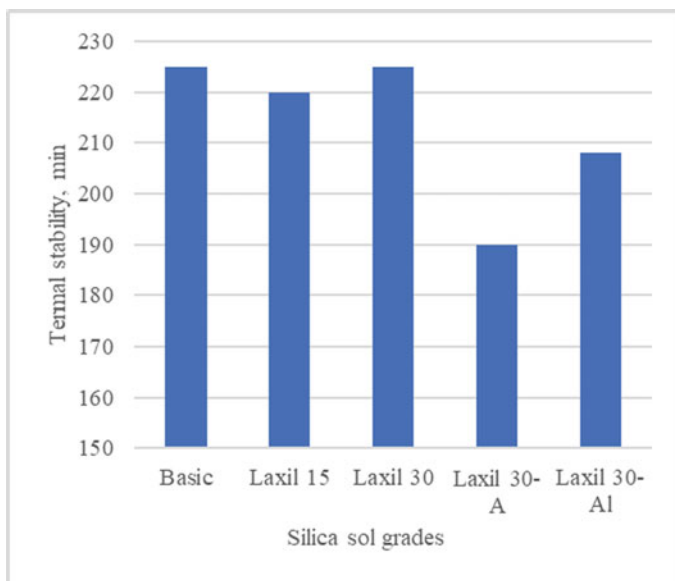


Fig. 3 Dependence of thermal stability of WPC-PVC on silica sol grades

The silica sol can be divided into two groups according to the nature of the stabilizing ion and, accordingly, their pH value: alkaline nature (Laxil 15, Laxil 30 and Laxil 30-A) and acidic nature (Laxil 30-Al).

Let us first consider the regularities of modification with alkaline silica. They should be effective binding agents due to the acidic nature of both the basic polymer - PVC, and wood particles. At almost equal pH values, Laxil 15 has the most positive effect on recyclability, showing the maximum PTR value (Fig. 1). Apparently, the lower viscosity of the colloidal solution Laxil 15 contributes to a greater degree of formation of a glass-like film on the porous surface of wood particles, resulting in reduced capillarity of the fibrous structure of wood flour. This facilitates processing by reducing sorption of the polymer by the filler, improving wall slip and reducing frictional resistance.

The strength properties increase with the introduction of Laxil (Fig. 2). It can be noted that the degree of increase is directly related to the amount of SiO_2 . The highest values are inherent when using Laxil 30-A and Laxil 30-Al.

As for the value of the thermal stability index (Fig. 3), it is at the level of the unmodified composition. The lowest values are inherent when using Laxil 30-A, the alkaline nature of which is expressed to a lesser extent, and therefore to a lesser extent the possibility of its acceptance of hydrogen chloride released during thermal degradation of PVC.

The use of silica sol stabilized with aluminum ions, having $\text{pH} = 2.15$, i.e. a clearly pronounced acid character of aqueous solutions, has its own features in the patterns of modification of WPC-PVC. With regard to changes in thermostability, it would

be logical to expect a decrease in this index in the presence of acidic agents that catalyze the degradation of PVC [35]. However, the thermal stability time decreases slightly compared to the unmodified composition. Probably aluminum due to the large number of free p- and d-orbitals can actively interact with chlorine atoms in the PVC macromolecule and form chemical bonds, which prevents the elimination of hydrogen chloride, and, accordingly, increase the stability of the polymer.

The increased tensile strength (Fig. 2) with Laxil 30-AI is caused by the formation of a more “monolithic” composite structure.

The same facts are due to the lower MFR (Fig. 1) compared to alkaline silica sol (0.17 g/10 min compared to 0.63 g/10 min for Laxil 15).

4 Conclusion

Thus, the results presented in the work expand the range of effective binder agents for WPC-PVC from the number of silica sols. It is shown that the introduction of silica sols regardless of the chemical nature leads to an increase in the tensile strength, with the determining factor being the SiO₂ content (about 30%). The recyclability of melt compositions is facilitated in the presence of low-viscosity and low-modulus silica sols.

Acknowledgements The authors express their gratitude to LLC “STC” KOMPAS” for the silica sol samples provided.

References

1. Klyosov, A.A.: Wood-Plastic Composites (2007). <https://doi.org/10.1002/9780470165935>
2. Wilkes, C.E., Summers, J.W., Daniels, C.A.: PVC handbook (2007)
3. Matseevich, T., Askadskiy, A.: Mechanical properties of decking on the base of polyethylene, polypropylene and polyvinylchloride. *Stroit. stvo Nauk. i Obraz* **3**, 49–59 (2017). <https://doi.org/10.22227/2305-5502.2017.3.4>
4. Fayzullin, I.Z., Volfson, S.I., Musin, I.N., Fayzullin, A.Z., Nikiforov, A.A.: Influence of the type of wood flour and nanoadditives on the structure and mechanical properties of polypropylene-based wood-polymer composites. In: AIP Conference Proceedings, pp. 309–306 (2016). <https://doi.org/10.1063/1.4967155>
5. Saieh, S.E., Eslam, H.K., Ghasemi, E., Bazyar, B., Rajabi, M.: Physical and morphological effects of cellulose nano-fibers and nano-clay on biodegradable WPC made of recycled starch and industrial sawdust. *BioResources* **14**, 5278–5287 (2019). <https://doi.org/10.15376/biores.14.3.5278-5287>
6. Rangavar, H., Taghiyari, H.R., Oromiehie, A., Gholipour, T., Safarpour, A.: Effects of nanoclay on physical and mechanical properties of wood-plastic composites. *Wood Mater. Sci. Eng.* **12**, 211–219 (2017). <https://doi.org/10.1080/17480272.2016.1156743>
7. Yadav, S.M., Yusoh, K.: Bin: preparation and characterization of wood plastic composite reinforced by organoclay. *J. Indian Acad. Wood Sci.* **13**, 118–131 (2016). <https://doi.org/10.1007/s13196-016-0175-5>

8. Yadav, S.M., Yusoh, K.: Bin: modification of pristine nanoclay and its application in wood-plastic composite. *E-Polymers* **16**, 447–461 (2016). <https://doi.org/10.1515/epoly-2016-0217>
9. Galeev, R., Abdrakhmanova, L., Nizamov, R.: Nanomodified organic-inorganic polymeric binders for polymer building materials. In: *Solid State Phenom.*, vol. 276 SSP, pp. 223–228 (2018). <https://doi.org/10.4028/www.scientific.net/SSP.276.223>
10. Nizamov, R.K., Galeev, R.R., Abdrakhmanova, L.A., Khozin, V.G., Naumkina, N.I., Lygina, T.Z.: Grounding of efficiency of filling the polyvinyl-chloride compounds with finely dispersed wastes of metallurgical production. *Stroit. Mater.* (2005)
11. Stroganov, V.F., Amel'chenko, M.O., Mukhametrakhimov, R.K., Vdovin, E.A., Tabaeva, R.K.: Increasing the adhesion of styrene–acrylic coatings modified by schungite filler in protection of building materials. *Polym. Sci. Ser. D.* **15**, 162–165 (2022). <https://doi.org/10.1134/S1995421222020277>
12. Ivanova, S.R., Minsker, K.S., Nagumanova, E.I., Nizamov, R.K., Kazar'yans, S.A.: The stabilizing properties of synthetic zeolites in plasticized polyvinyl chloride compounds. *Plast. Massy Sint. Svoystva Pererab. Primen.* 39–43 (2005)
13. Shieh, Y.T., Hsieh, K.C., Cheng, C.C.: Carbon nanotubes stabilize poly(vinyl chloride) against thermal degradation. *Polym. Degrad. Stab.* **144**, 221–230 (2017). <https://doi.org/10.1016/j.polydegradstab.2017.08.017>
14. Silvano, L.T., Vittorazzo, J., Atilio, L., Araujo, G.R.: Effect of preparation method on the electrical and mechanical properties of PVC/carbon nanotubes nanocomposites. *Mater. Res.* **21** (2018). <https://doi.org/10.1590/1980-5373-mr-2017-1148>
15. Saatchi, M.M., Shojaei, A.: Effect of carbon-based nanoparticles on the cure characteristics and network structure of styrene-butadiene rubber vulcanizate. *Polym. Int.* **61**, 664–672 (2012). <https://doi.org/10.1002/pi.4132>
16. Hatthapanit, K., Sae-Oui, P., Sombatsompop, N., Sirisinha, C.: Enhancement of rubber-carbon black interaction by amine-based modifiers and their effect on viscoelastic and mechanical properties. *J. Appl. Polym. Sci.* **126**, 315–321 (2012). <https://doi.org/10.1002/app.36969>
17. Baccaro, S., Cataldo, F., Cecilia, A., Cemmi, A., Padella, F., Santini, A.: Interaction between reinforce carbon black and polymeric matrix for industrial applications. *Nuclear Instruments Methods Phys. Res.* 191–194 (2003). [https://doi.org/10.1016/S0168-583X\(03\)00638-4](https://doi.org/10.1016/S0168-583X(03)00638-4)
18. Nizamov, R.K., Nagumanova, E.I., Abdrakhmanova, L.A., Khozin, V.G.: Polyvinyl chloride materials filled with finely dispersed wastes of wood processing. *Str.pdf. Stroit. Mater.* 14–17 (2004)
19. Ghorbani, M., Biparva, P., Hosseinzadeh, S.: Effect of colloidal silica nanoparticles extracted from agricultural waste on physical, mechanical and antifungal properties of wood polymer composite. *Eur. J. Wood Wood Prod.* **76**, 749–757 (2018). <https://doi.org/10.1007/s00107-017-1157-z>
20. Jiang, J., Mei, C., Pan, M., Cao, J.: Improved mechanical properties and hydrophobicity on wood flour reinforced composites: incorporation of silica/montmorillonite nanoparticles in polymers. *Polym. Compos.* **41**, 1090–1099 (2020). <https://doi.org/10.1002/pc.25440>
21. Sun, L., et al.: Effects of sio2 filler in the shell and wood fiber in the core on the thermal expansion of core–shell wood/polyethylene composites. *Polymers (Basel)* **12**, 1–11 (2020). <https://doi.org/10.3390/polym12112570>
22. Islamov, A., Fakhruudmova, V.: Surface modification of PVC by silica sol. In: *IOP Conference Series: Materials Science and Engineering* (2020). <https://doi.org/10.1088/1757-899X/890/1/012083>
23. Saied, M.A., Ward, A.A.: Physical, dielectric and biodegradation studies of PVC/silica nanocomposites based on traditional and environmentally friendly plasticizers. *Adv. Nat. Sci. Nanosci. Nanotechnol.* **11** (2020). <https://doi.org/10.1088/2043-6254/ab9d17>
24. Abdrakhmanova, L.A., Nizamov, R.K., Burnashev, A.I., Khozin, V.G.: Nanomodification of wood flour by sols of silicic acid. *NANOTECHNOLOGIES Constr.* 56–67 (2012)
25. Zhou, H., Hao, X., Wang, H., Wang, X., Liu, T., Xie, Y., Wang, Q.: The reinforcement efficacy of nano- and microscale silica for extruded wood flour/HDPE composites: the effects of dispersion patterns and interfacial modification. *J. Mater. Sci.* **53**, 1899–1910 (2018). <https://doi.org/10.1007/s10853-017-1650-0>

26. Abdelghany, A.M., El-Damrawi, G., ElShahawy, A.G., Altomy, N.M.: Structural investigation of PVC/PS polymer blend doped with nanosilica from a renewable source. *SILICON* **10**, 1013–1019 (2018). <https://doi.org/10.1007/s12633-017-9564-7>
27. Purcar, V., et al.: Preparation and characterization of some sol-gel modified silica coatings deposited on polyvinyl chloride (PVC) substrates. *Coatings* **11**, 1–13 (2021). <https://doi.org/10.3390/coatings11010011>
28. Nizamov, R.K., Nagumanova, E.I., Trofimova, F.A., Lygina, T.Z.: Efficiency of application of fillers on basis of glauconite-containing rocks for polyvinyl chloride compounds. *Stroit. Mater.* 14–17 (2005)
29. Klapiszewski, L., Pawlak, F., Tomaszewska, J., Jesionowski, T.: Preparation and characterization of novel PVC/Silica-lignin composites. *Polymers (Basel)* **7**, 1767–1788 (2015). <https://doi.org/10.3390/polym7091482>
30. Shkuro, A.E., Matonin, A.N.: Wood-plastic composites with silica powder. *Vestn. Kazan. Tehnol. Univ.* **23**, 73–77 (2020)
31. Abdullah, N.A., Tahiruddin, N.S.M., Othaman, R.: Effects of silica content on the formation and morphology of ENR/PVC/Silica composites beads. In: *AIP Conference Proceedings* (2017). <https://doi.org/10.1063/1.4983901>
32. Galeev, R., Nizamov, R., Abdrakhmanova, L., Khozin, V.: Resource-saving polymer compositions for construction purposes. In: *IOP Conference Series: Materials Science and Engineering* (2020). <https://doi.org/10.1088/1757-899X/890/1/012111>
33. Galeev, R., Nizamov, R., Abdrakhmanova, L.: Influence of dispersed fillers on properties and processability of polyvinyl chloride compositions. In: *E3S Web of Conferences* (2020). <https://doi.org/10.1051/e3sconf/202016414018>
34. Nizamov, R., Abdrakhmanova, L.: Influence of fillers on polyvinyl chloride materials thermal resistance (2016). <https://doi.org/10.4028/www.scientific.net/MSF.871.84>
35. Minsker, K.S., Zaikov, G.E.: Achievements and challenges of research in the field of aging and stabilization of PVC. *Plast. Massy.* 27–35 (2001)

Solution of the Problem of Modeling Acid Hydraulic Fracturing with a Planned Technological Stop During the Pumping Process Using Standard Software



Irik Fattakhov , Alexander Kochetkov , and Julia Kareeva 

Abstract This work aims to complement the technique of standard modeling of the acid hydraulic fracturing with the fracture height limiting technology using a technological stop. This technology involves pumping stopping during the main hydraulic fracturing until the fracture closes and then resuming the pumping. Thus, a secondary fracture with a shift along the azimuthal angle is created, and the fracture network is redistributed: the increase in the coverage height changes to the fracture network branching along the lateral. This technology is not considered in the standard acid HF simulators, while the modification of commercial simulators is technically complicated and associated with increased costs. The proposed solution makes it possible to perform calculations using a standard simulator without its modification.

The scientific novelty of the work consists in the correct and suitable for further analysis modeling of the acid fracturing with a technological stop and calculation of the properties of the created fractures using the standard HF simulator. For the first time, a technique has been developed which makes it possible to perform the calculations correctly, obtain a set of indicators, and compare them with that obtained during the standard acid fracturing. So the proposed technique makes it possible to replicate the acid fracturing technology with a planned stop without additional costs for a software upgrade.

Keywords Hydraulic fracturing · Acid fracturing · Fracture height limitation · Acid fracturing of carbonate reservoirs · Acid fracturing simulator · Secondary fracture · Fracture conductivity

I. Fattakhov · A. Kochetkov
PJSC TATNEFT named after V.D. Shashin, Almetyevsk, Russia

I. Fattakhov
Ufa State Petroleum Technical University (Oktyabrsky Branch), Oktyabrsky, Russia

J. Kareeva (✉)
Kazan State University of Architecture and Engineering, Kazan, Russia
e-mail: jkareeva2503@gmail.com

1 Introduction

In carbonate reservoirs with close location of watered zones [25], the task of vertical limitation of hydraulic fracturing (HF) is often complicated by the absence of restriction barriers [17]. If the mechanical stress contrast is insufficient, the fracture continues to increase in height throughout the pumping process [9]. This is especially typical for acid fracturing, which does not involve the fracture packing with a propping agent [24]. It is possible to limit the vertical development of acid hydraulic fracture by reducing volume, viscosity and speed of acid pumping [18], and these processes can be simulated using the standard software [20]. At the same time, viscosity affects the fracture geometry not directly but in response to differences in the rheological parameters (consistency factor, critical shear stress, and degree n in the stepped fluid model) [1]. On the other hand, the listed approaches can cause a significant reduction of additional oil production, both in the average daily values at the start of the well, and in the duration of the effect of acid fracturing [19]. In general, to create an effective fracture, the sufficient volume, viscosity [21] and pumping rate are required. During acid HF of carbonate rocks, the reactions with limestone (CaCO_3) and dolomite ($\text{CaMg}[\text{CO}_3]_2$) mainly occur, the reaction products of which are soluble in water or are carbon dioxide, and do not reduce rock conductivity [2]. Laboratory analysis makes it possible to select the acid composition, upon the interaction with which the reaction products that reduce the rock conductivity are not produced [13]. Thus, after conducting the appropriate tests, the hydraulic fracturing plan involves finding an optimum solution in terms of treatment volume, pumping rate, and rheology of acid compositions [6].

2 Materials and Methods

In some cases, the standard search for an optimum solution results in the use of relatively low volumes of acid compositions, which limits the cost-effectiveness of hydraulic fracturing [7]. One additional solution to limit fracture height is a technological stop during pumping of the main acid fracturing. Figure 1 shows changes in the stress field of the reservoir by stages of the process. The initial state with a certain direction σ_{min} (a) conditions the formation of the first fracture during pumping before the stop (b) [10]. At the same time, after the stop, the first fracture is closing, the mechanical stresses in the zone of its closing increase and the direction of the minimum horizontal stress σ_{min} is shifted (c) [11]. This creates conditions in which, when pumping resumes, the second fracture with displaced direction is initiated (d) [28], the height growth of which begins from a new reference point, thereby the final vertical interval covered by fractures is reduced relative to the standard pumping without a technological stop with the same total volume of acid compositions and pumping parameters [12]. The distribution of acid over the two fractures makes it possible to limit the vertical spread of the fracture while maintaining the conductivity

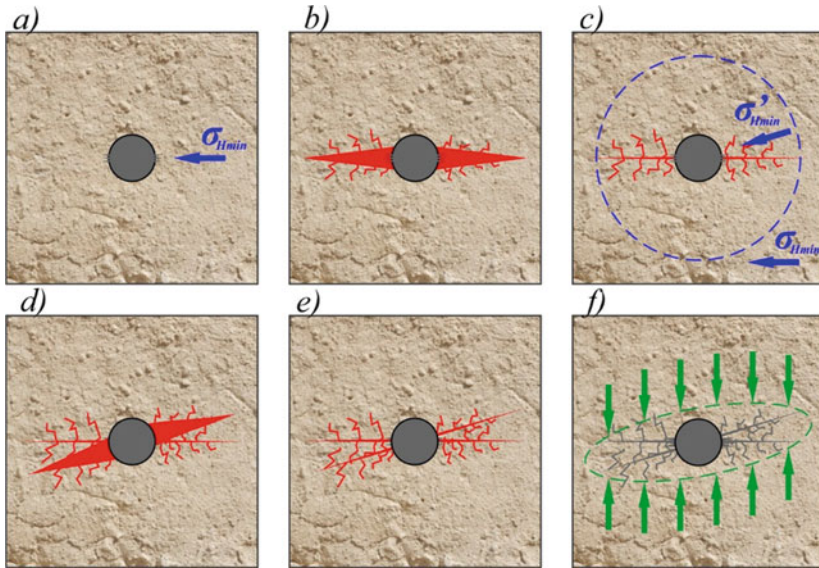


Fig. 1 Changes in the stress state of the stratum

created by the given volume of acid composition [14]. A limited in height but more developed network of man-made fractures is created (e), which provides additional fluid flow into the area with artificially increased conductivity after the reactions are completed and the well is put into operation (f) [8].

When modeling acid HF with a technological stop in the standard simulator, an error occurs related to the operation of the standard hydraulic fracturing simulation software. As shown in Fig. 2, if the fracture closes after the first stage of acid fracturing, depending on the acid-rock reaction settings, the simulator either completes the calculation (a) or nullifies the accumulated fracture parameters and performs calculations only for the second stage of acid fracturing (b). Thus, if the acid reaction is turned on for all stages, the calculation of the second stage will not be performed (a). Disabling the acid reaction for the first stage will make it possible to model all stages of acid fracturing, but the geometry of the first stage will not be taken into account (b), which will distort the result obtained.

To calculate the first and second stages of HF using this technology, it is proposed to calculate the first and second stages separately, with subsequent merging of the obtained data [15]. It is necessary to combine the results so that the technology features (total conductivity of created fractures and total coverage in height and length) are correctly taken into account [16]. The combined data will be suitable for subsequent analysis, if the following conditions are met:

1. It is assumed that after the technological stop, the previously created fracture is closed and designated as the primary one, and after the resumption of pumping, the secondary fracture is formed.

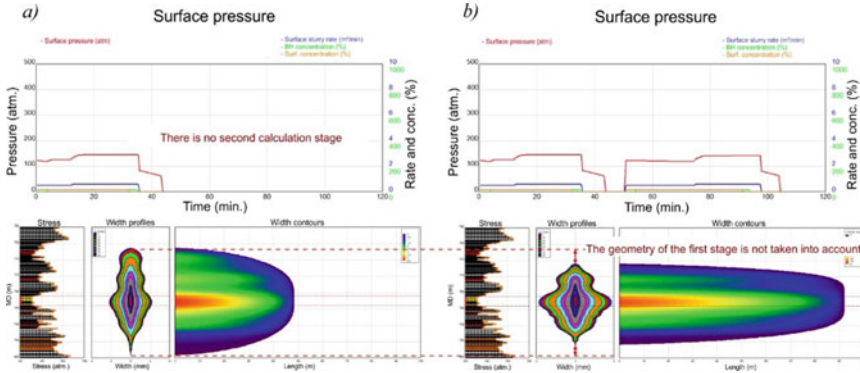


Fig. 2 Distortion in calculations when using standard approaches

2. Modeling, including calibration of pressures of the primary and secondary fracture, is performed separately.
3. Volumes of acid compositions and other stages of acid HF are represented as the sum of the stages corresponding to the primary and secondary fracture.
4. The geometry of the analyzed fracture is represented as a system of primary and secondary fracture, limited to the greatest coverage in height and length.
5. The conductivity of the analyzed fracture is represented as the sum of the conductivities of the primary and secondary fracture.
6. For the prediction of pressures at the design stage, the calculation is performed separately, with the acid reaction for the first stage turned off, as shown in Fig. 2 (b).

Below are the generalized formulas applied to the results of the simulation before and after a technological step:

$$\begin{cases} V_{AC1} = V_{AC1}^1 + V_{AC1}^2 \\ \dots \\ V_{ACN} = V_{ACN}^1 + V_{ACN}^2 \end{cases}$$

$$H_f = \max(H_{bottom}^1; H_{bottom}^2) - \min(H_{top}^1; H_{top}^2)$$

$$L_f = \max(L_{acid}^1; L_{acid}^2)$$

$$w_f = \frac{w_{acid}^1 + w_{acid}^2}{2}$$

$$k_f = k_f^1 + k_f^2$$

where V_{AC} is the volume of N acid composition, V_{AC1}^1, V_{AC1}^2 are the volumes of acid compositions in the calculation results before and after the technological stop, H_f is the fracture network height, $H_{bottom}^1, H_{bottom}^2, H_{top}^1, H_{top}^2$ are the calculated fracture bottom and top (TVD) before and after the technological stop, L_f is the lateral distribution of the fracture network,, L_{acid}^1, L_{acid}^2 is the calculated etched length before and after the stop, w_f is the etched width, k_f is the calculated fracture conductivity.

Thus, the primary and secondary fracture parameters determined independently are combined to enable subsequent analysis and comparison with the standard acid HF technique [27].

3 Results and Discussion

Calculations taking into account the listed conditions were performed for 9 wells, where acid fracturing with technological stop was applied. Table 1 shows the comparison with calculated values for the case of acid fracturing without a technological stop, while maintaining the amount of treatment.

The influence of the technological stop on the obtained parameters of acid hydraulic fracture system differs depending on peculiarities of the lithological

Table 1 The results of modeling

No. of well	Acid volume, m ³	Fracture height, m		Fracture half-length, m		Fracture conductivity, mD·m	
		With stop	Without stop	With stop	Without stop	With stop	Without stop
1	45.8	29.0	34.0	81.5	58.6	214.8	286.1
2	57.6	26.4	33.8	88.0	94.1	169.9	153.3
3	51.6	30.5	43.5	53.9	56.8	246.4	208.5
4	52.4	21.1	25.6	69.0	77.1	193.8	161.1
5	72.6	22.9	34.1	102.0	107.3	47.4	32.9
6	53.6	24.6	23.0	111.6	121.7	127.8	153.8
7	49.8	21.8	17.7	71.4	88.5	624.0	501.1
8	51.9	13.7	15.7	119.0	171.6	292.8	346.4
9	49.8	29.8	33.8	20.8	53.0	517.1	177.8
Average values for 9 wells		24.4	29.0	79.7	92.1	270.4	224.6
Average values for the site		25.3		74.6*		249	

* - the average value of the half-length for the site is reduced due to the presence of a number of processes with increased leakage and etched length 2 or more times below the average value.

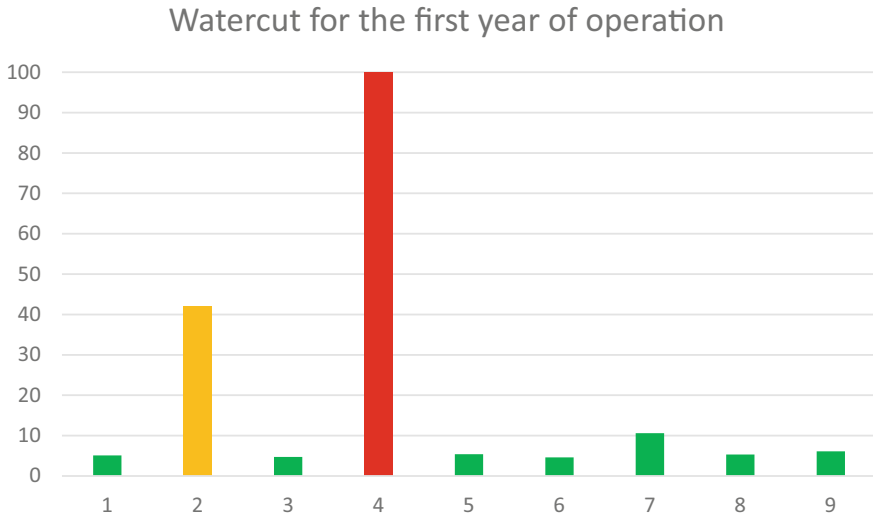


Fig. 3 The average watercut of production by wells

section, geomechanical properties of a stratum at the well site. At the same time, in most cases, for a given volume of acid, the following conclusions can be drawn:

1. The fracture height decreases in 7 cases out of 9 for an average of 4.6 m, which is 19%, upon that the height is 0.9 m lower than the average for the site;
2. The fracture length decreases in 8 cases out of 9 for an average of 12.4 m, which is 16%, and is 5.1 m greater than the site average;
3. The conductivity changes individually, with 6 cases out of 9 showing an average increase of 94 mD-m, which is 35%, 21.4 mD-m more than the site average.

The considered wells, where the technology of acid fracturing with technological stop was applied, were characterized by increased risks of undesirable growth of fracture height according to the results of the miniHF analysis; in particular, an increased fluid efficiency and decreased net fracture pressure was noted [2]. Under these conditions, the obtained fracture height 0.9 m lower than the average for the considered development area (as well as an increase in fracture length and conductivity) is a positive result. In some cases, the opposite effect was observed in the simulation, which can be explained, among other things, by the physicochemical and geomechanical instability of carbonate rocks [3], but in most cases, the trends persist [23].

At the considered wells, acid fracturing was carried out after drilling [22], without a preliminary putting into operation, which complicates the evaluation of potential of incremental oil flow rate [5]. However, for several dense fractured reservoirs with not strongly pronounced fracturing, acid fracturing is probably the only technological approach, which makes it possible to extract oil or gas with satisfactory flow rates for a long time [4]. Nevertheless, under the conditions of increased watercut risk,

the actual watercut of the well production is of interest [26]. The first 12 months of well operation after acid fracturing were taken for evaluation. In 7 out of 9 cases, the watercut did not exceed 10%, in one case the well was operating with an average watercut of 42%, and one well was re-injected. Details are shown in Fig. 3.

4 Conclusion

Thus, by taking into account the results obtained, the theoretical justification, and the proposed technique of modeling the process of acid fracturing with technological stop, the results of experimental works are considered successful. The following conclusions and recommendations are formulated based on the results of the conducted work:

1. When performing acid fracturing in conditions of close height proximity of watered stratum sites and the absence of stress barriers sufficient to slow down the growth of fracture height, it is advisable to conduct hydraulic fracturing with a technological stop and increased volume of acid compositions;
2. The proposed modeling technique using integrated data can be used to calculate the acid fracturing using the proposed technology, and no changes in specialized software are required;
3. It is recommended to conduct additional research, including determination of the actual fracture height after acid fracturing with technological stop, to calibrate models and determine the accuracy of calculations using the proposed technique;
4. It is also recommended to conduct experimental works on more wells, for different fields, in conditions of high and low natural fracturing, as well as in conditions of high and low solubility of rock in acid to specify criteria for technology applicability and determine the most promising objects for its application.

References

1. Cherniy, S.G., Lapin, V.N., Esipov, D.V., Kurnakov, D.S.: Methods for simulating the initiation and propagation of cracks. Publishing SB RAN, Novosibirsk (2016)
2. Jennings, Jr. A.R.: PE-Hydraulic Fracturing Applications, OGCI/PetroSkills, Enhanced Well Stimulation, Inc., Whitehouse (2003)
3. Kovalev, K.M.: Carbonate core: features, difficulties, research prospects, SPE-187872-RU (2017)
4. Glushenko, V.I., Silin, M.A., Mishenko, I.T.: Acid Treatment of Wells. Interkontakt Science, Moscow (2010)
5. Wang, L., Dong, Z., Li, X., et al.: A multi-scale flow model for production performance analysis in shale gas reservoirs with fractal geometry. *Sci. Rep.* **8**, 11464 (2018). <https://doi.org/10.1038/s41598-018-29710-1>

6. Quosay, A.A., Knez, D., Ziája, J.: Ziája Hydraulic fracturing: new uncertainty based modeling approach for process design using Monte Carlo simulation technique. *PLoS ONE* **15**(7), e0236726 (2020). <https://doi.org/10.1371/journal.pone.0236726>
7. Wang, M., Chen, S., Lin, M.: Enhancing recovery and sensitivity studies in an unconventional tight gas condensate reservoir. *Pet. Sci.* **15**, 305–318 (2018). <https://doi.org/10.1007/s12182-018-0220-7>
8. López-Comino, J.A., Cesca, S., Jarosławski, J., et al.: Induced seismicity response of hydraulic fracturing: results of a multidisciplinary monitoring at the Wysin site. *Pol. Sci. Rep.* **8**, 8653 (2018). <https://doi.org/10.1038/s41598-018-26970-9>
9. Torres, L., Yadav, O.P., Khan, E.: A review on risk assessment techniques for hydraulic fracturing water and produced water management implemented in onshore unconventional oil and gas production. *Sci. Total Environ.* **539**, 478–493 (2016). <https://doi.org/10.1016/j.scitotenv.2015.09.030>
10. Xiao, Y., Guo, J., Wang, H., Lu, L., Chen, M.: Elastoplastic constitutive model for hydraulic aperture analysis of hydro-shearing in geothermal energy development. *J. Indexing Metrics* **95**(9), 861–872 (2019). <https://doi.org/10.1177/0037549718793216>
11. Zhang, F., Ma, G., Liu, X., Tao, Y., Feng, D., Li, R.: Experimental analysis of multiple factors on hydraulic fracturing in coalbed methane reservoirs. *PLoS ONE* **13**(4), e0195363 (2018). <https://doi.org/10.1371/journal.pone.0195363>
12. Taherdangkoo, R., Tatomir, A., Anighoro, T., Sauter, M.: Modeling fate and transport of hydraulic fracturing fluid in the presence of abandoned wells. *J. Contam. Hydrol.* **221**, 58–68 (2019). Epub 2018 Dec 21. <https://doi.org/10.1016/j.jconhyd.2018.12.003>
13. He, L., Chen, Y., Zhao, H., Tian, P., Xue, Y., Chen, L.: Game-based analysis of energy-water nexus for identifying environmental impacts during Shale gas operations under stochastic input. *Sci. Total Environ.* **627**, 1585–1601 (2018). <https://doi.org/10.1016/j.scitotenv.2018.02.004>
14. Oetjen, K., et al.: Temporal characterization and statistical analysis of flowback and produced waters and their potential for reuse. *Sci. Total Environ.* **619–620**, 654–664 (2018). <https://doi.org/10.1016/j.scitotenv.2017.11.078>
15. Fattakhov, I.G., Kuleshova, L.S., Bakhtizin, R.N., Mukhametshin, V.V., Kochetkov, A.V.: Complexing the hydraulic fracturing simulation results when hybrid acid-propanol treatment performing and with the simultaneous hydraulic fracture initiation in separated intervals. In: *SOCAR Proceedings*, no. 2, pp. 103–111 (2021)
16. Fattakhov, I.G., Kuleshova, L.S., Kochetkov, A.V., Safiullina, A.R., Gizatullin, I.R.: The use of a liquid destructor with flow into the stream during the injection of the fracturing mixture. *IOP Conf. Ser. Mater. Sci. Eng.* **952**(1), 012044 (2020)
17. Nurgaliev, R.Z., Kozikhin, R.A., Fattakhov, I.G., Kuleshova, L.S., Gabbasov, A.K.H.: Prospects for the use of new technologies in assessing the impact of geological and technological risks. *IOP Conf. Ser. Earth Environ. Sci.* **378**(1), 012117 (2019)
18. Nurgaliev, R.Z., Kozikhin, R.A., Fattakhov, I.G., Kuleshova, L.S.: Application prospects for new technologies in geological and technological risk assessment. *Gornyi Zhurnal* (4), 36–40 (2019)
19. Bahtizin, R.N., Nurgaliev, R.Z., Fattakhov, I.G., Andreev, V.E., Safiullina, A.R.: On the question of the efficiency analysis of the bottom-hole area stimulation method. *Int. J. Mech. Eng. Technol.* **9**(6), 1035–1044 (2018)
20. Masoomi, P., Dolgov, S.V.: Comparison of different scenarios for hydraulic fracturing fluids (water-based gels and foams) using numerical simulation. *Bulatov readings. T. 2. C.*, pp. 150–155 (2017)
21. Shlyapkin, A.S., Tatosov, A.V.: Formation of a hydraulic fracture with a high-viscosity gel. *Geol. Geophys. Dev. Oil Gas Fields* **9**(345), 109–112 (2020)
22. Nurgaliev, O.T., Volchenko, Yu.A.: Radioisotope method and measuring complex rikp-01 for express determination of proppant concentration in working mixtures used in hydraulic fracturing of oil and gas reservoirs. *Autom. Telemekh. Commun. Oil Ind.* **8**, 24–28 (2016)
23. Bulgakova, G.T., Sharifullin, A.R., Sitdikov, M.R.: Mathematical modeling of heat and mass transfer in a vertical fracture of a hydraulic fracturing during injection and cleaning of a fracture. *Vestnik of Tyumen State University. Phys. Math. Model. Oil gas Energy* **6**(2(22)), 41–62 (2020)

24. Makhmueva, E.A.: Reagents and fluids for hydraulic fracturing. *Young Sci.* **33**(167), 8–10 (2017)
25. Fattakhov, I.G., Yusifov, T.Y.U., Baybulatova, Z. K.H., Yusifov, M.Y.U., Akimov, A.V., Kalinina, S.V.: Application of modern hydraulic fracturing technology in bottom water reservoirs. *Nauchnoe obozrenie* (17), 204–208 (2016)
26. Fattakhov, I.G., Malyshev, P.M., Shakurova, A.F., Shakurova, A.I.F., Safiullina, A.P.: Diagnostic analysis of the efficiency of hydraulic fracturing. *Basic Res.* (2–27), 6023–6029 (2015)
27. Yusifov, T.Y.U., Popov, V.G., Fattakhov, I.G., Safiullina, A.P., Ismailov, F.S.: Hydraulic fracturing and its effective application. *Nauchnoe obozrenie* (8), 23–28. (2015)
28. Yusifov, T.Y., Fattakhov, I.G., Ziyatdinov, A.M., Akhmetshin, D.I., Safiullina, A.P.: The influence of the stress state of the formation on the formation of a hydraulic fracture. *Nauchnoe obozrenie* (19), 97–102 (2015)

Optimization of Technological Solutions for Underground Space Construction of Existing Buildings



Leysan Zigangirova, Ilyas Galiev , and Ruslan Ibragimov 

Abstract The development of underground space is an important direction in the construction of new facilities and reconstruction of existing ones. The development of underground space frees up space above the ground, increases the economic efficiency of buildings, and preserves historical objects. To this end, the article discusses the basic principles of technology that enable the development of underground space. In this research, the main variable parameters are highlighted, an experimental matrix is proposed and a mathematical model of the dependence of the labor intensity on the pitch of the cross beams and the load on the foundation cutoff is developed. According to the results of the study, the dependence function of the parameters affecting the strengthening of an existing building designed to expand the underground space has been obtained. The optimal parameters of the weight of metal structures and labor intensity, in which the maximum economic efficiency of the technology used are achieved, have been found.

Keywords Underground space · Economic effect · Optimization of technological solutions

1 Introduction

The development of underground space in major metropolitan areas has become an integral part of the construction culture for the effective use and modernization of urban space [1, 2]. The prerequisites for the complex development of underground space are the system of creating comfortable pedestrian spaces and transport interchange communications, lack of parking spaces, climatic conditions (long off-season), the liberation of the ground area, the new quality of public spaces, the preservation of existing buildings, the high cost of land in the center, the urban development potential of the territory [3, 4].

L. Zigangirova · I. Galiev (✉) · R. Ibragimov
Kazan State University of Architecture and Engineering, Kazan, Russia
e-mail: galiev-ih@mail.ru

The construction of underground facilities requires a thorough study of the geological, hydrogeological conditions of the area, and often during the reconstruction of existing facilities it is necessary to strengthen the structures of the foundations and foundations of buildings or, if necessary, to transplant to new foundations. Without this stage, the construction of additional underground floors in existing buildings is impossible, since the structures of cultural heritages, in common, are in a state of significant physical wear and require careful inspection.

Currently, there are several technologies for the development of underground space:

1. A wall in the ground. The technology involves the construction of a foreshock, which is a guide for the future trench and to strengthen its walls. Then the soil is developed to the required depth with the help of a hydraulic grab and the excavation is carried out under the protection of clay mortar, where prefabricated reinforcement frames are arranged, after concreting which a solid monolithic wall is formed [5].
2. The caisson. It represents a complete figure of various shapes, which is lowered into the ground under its own weight, as well as with the help of the work of jacks. Similar structures of caissons serve simultaneously as a deep foundation for aboveground structures of the structure, as well as a wall for the underground part of the building [6].
3. «TOP-DOWN». This technology makes it possible to develop the underground space in tiers near the existing buildings. The technology involves the construction of a tongue-and-groove fence with the manufacture of piles around the perimeter or a “wall in the ground” device. Next, a tiered development of the soil with alternate concreting of floor slabs is carried out. This technology makes it possible to conduct construction work simultaneously both in the underground and aboveground parts [7–9].

The choice of technology to expand the underground space is associated with the category of the building condition, with possible risks. The fundamental factors are the condition of load-bearing structures, soil, the range of nearby objects, the conditions of groundwater occurrence. It is the expansion of the underground space under the existing buildings that makes it possible for the city to develop its territories efficiently and organically. Based on the data analysis, Fig. 1 is compiled [10].

The authors [11–15] have developed a technology for the development of underground space under existing buildings. But these studies lack an algorithm and an optimization approach to solving technological problems. The purpose of this article is to optimize technological solutions in which the cost of work performed and labor costs will be minimal. To solve this problem, a multifactorial experiment of stochastic dependence of one value Y on several other values is used X_i .

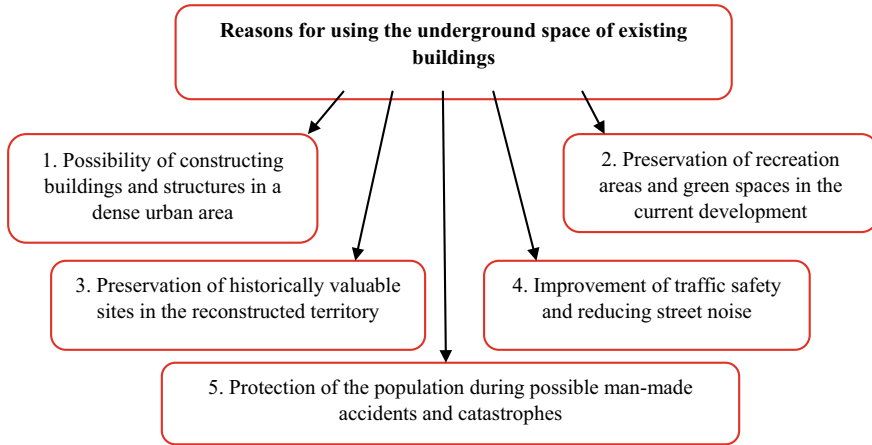


Fig. 1 Reasons for using the underground space of existing buildings

2 Materials and Methods

A Box central composite design was applied in the research. The Gradient 3.1 program was used to solve this problem. Design type: two-factor compositional (rotatable) experiment with a quadratic model.

A multifactorial experiment allows solving problems with high accuracy by choosing the number of experiments, the conditions for conducting. All parameters that affect the condition of the task set change with a certain step, set in advance, and the result of a multifactorial experiment is obtained in the form of a mathematical model of the function under study.

In order to obtain a function that describes the curve, it is necessary to correctly formulate the conditions of the problem: to choose a mathematical model, change factors with their specific step, choose optimality criteria and an experimental plan.

Problem statement: it is necessary to develop a multifactorial model of the dependence of weight and labor intensity on the location of the beam pitch and load.

The main factors for solving this problem are the pitch of the beams, the load transferring from all the structures of the existing building to the reinforcing elements. The levels of variation of these independent variables and the planning matrix are shown in Tables 1 and 2.

Table 1 Experiment planning matrix

No.	Planning Matrix		Natural values of variables	
	X1	X2	X1	X2
1	-1	-1	1	100
2	1	-1	2	100
3	-1	1	1	200
4	1	1	2	200
5	-1.4142	0	0.79289	150
6	1.4142	0	2.2071	150
7	0	-1.4142	1.5	79.289
8	0	1.4142	1.5	220.71
9	0	0	1.5	150

Table 2 Levels of variation

Factors	Name of factors	Levels of variation		
		- 1	0	+1
X1	Step of arrangement of reinforcement beams, m	1	1.5	2
X2	Load, kN/m ²	100	150	200

3 Results

To construct surfaces and output optimal values the Mathematica program was used. It serves to develop mathematical models, allows performing both numerical and symbolic calculations and has the ability to build surfaces with advanced graphics.

For the construction using this program, the combinations obtained in the Gradient 3.1 program were used, where we got 9 possible combinations of leading factors. These data were entered into the program in the form of the following combinations:

Data1 = {{1, 100, 20.97}, {2, 100, 23.34}, {1, 200, 31.32},{2, 200, 35.56},{0.79289, 150,27.73},{2.2071,150,31.64},{1.5, 79.289, 19.7}, {1.5, 220.71, 34.19}, {1.5, 150, 26.24}};

Data2 = {{1, 100, 394.07},{2, 100, 447.27},{1,200,619.96},{2,200,657.41}, {0.79289,150, 661.25}, {2.2071, 150, 559.23},{1.5, 79.289, 455.45},{1.5, 220.71, 656.19}, {1.5, 150, 486.14}};

Based on the results of calculations, the surfaces of the dependencies of the leading factors on the weight of metal structures and the labor intensity of reinforcing elements are constructed and optimal points are found (Figs. 2 and 3).

After excluding statistically insignificant coefficients, the form of mathematical dependence on the independent variables X1, X2 is the following:

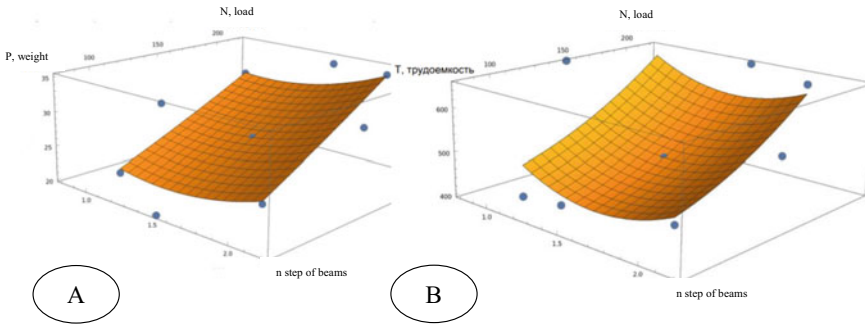


Fig. 2 The interpretation surface of the influence of the leading factors on: **A** the total weight of metal structures; **B** the total labor intensity

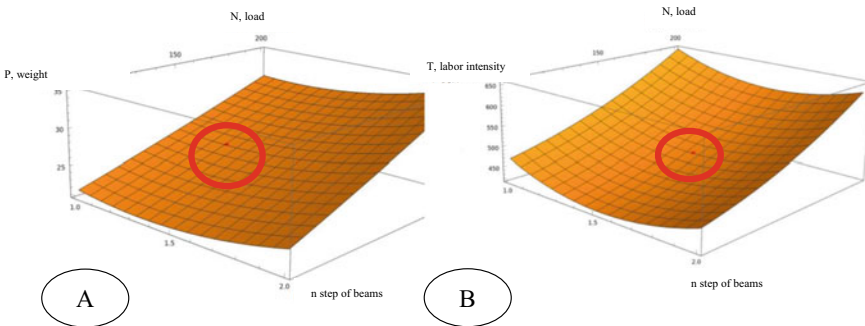


Fig. 3 The optimal point depending on the step of the location of the beams and the applied load: **A** the weight of metal structures; **B** the point of labor intensity

$$F_1 = 26,09 - 18,88X_1 + 0,053X_2 + 6,37X_1^2 + 0,000089X_2^2 + 0,0187X_1X_2; \tag{1}$$

$$F_2 = 832,78 - 574,33X_1 + 0,544X_2 + 194,85X_1^2 + 0,0086X_2^2 - 0,1575X_1X_2 \tag{2}$$

The optimal point equal to the step of the beams at a load of $N = 150$ kN is equal to $n = 1.26187$ m, with a total weight of metal structures $P = 25.8786$ kN/m.

The optimal point equal to the step of the location of the beams at a load of $N = 150$ kN is equal to $n = 1.5344$ m, with a total labor intensity of $T = 485.9$ people-h.

4 Conclusions

1. The function describing the curve of dependence of three parameters is obtained: the weight of metal structures used to strengthen the building, the complexity of mounting and the applied load from the existing building.
2. The optimal points of the studied parameters have been identified, at which the weight and labor intensity is minimal, which leads to a reduction in the total weight of the metal structures used to strengthen the existing building, respectively, reduces the total cost of the technology and lead to a positive economic effect. The minimum weight of metal structures for the surveyed building is observed with a beam step equal to 1.26 m, and the minimum labor intensity of the work performed is observed with a beam step equal to 1.53 m.

References

1. Bobylev, N.: Underground space as an urban indicator: measuring use of subsurface. *Tunn. Undergr. Space Technol.* **55**, 40–51 (2016)
2. Ibragimov, R.A., Korolev, E.V., Deberdeev, T.R., Leksin, V.V.: Efficient complex activation of Portland cement through processing it in the vortex layer machine. *Struct. Concr.* **20**(2), 851–859 (2019). <https://doi.org/10.1002/suco.201800008>
3. Nelson, P.P.: A framework for the future of urban underground engineering. *Tunn. Undergr. Space Technol.* **55**, 32–39 (2016)
4. Stroganov, V., Sagadeev, E., Ibragimov, R., Potapova, L.: Mechanical activation effect on the biostability of modified cement compositions. *Constr. Build. Mater.* **246** (2020). <https://doi.org/10.1016/j.conbuildmat.2020.118506>
5. Kadyrov, A.S., Zhunusbekova, ZhZh., Ganyukov, A.A.: Study and calculation of earth-moving machines for the construction by «wall in the ground» method. *Mater. Mech. Eng. Technol.* **1**(1), 3–8 (2021)
6. Lugina, K.A., Segaev, I.N.: Construction of structures by the method of a sinkhole. *Alley Sci.* **1**(4(20)), 519–522 (2018)
7. Tan, Y., Huang, R., Kang, Z., Bin, W.: Covered semi-top-down excavation of subway station surrounded by closely spaced buildings in downtown Shanghai: building response. *J. Perform. Constr. Facil.* **30**(6) (2016)
8. Wong, J.Y., Yip, C.C., Mugumya, K.L., Tan, B.H., Anwar, M.P.: Effectiveness of top-down construction method in Malaysia. *Int. J. Innov. Technol. Explor. Eng.* **8**(6 Special Issue 4), 386–392 (2019)
9. Jamsawang, P., Voottipruex, P., Tanseng, P., Jongpradist, P., Bergado, D.T.: Effectiveness of deep cement mixing walls with top-down construction for deep excavations in soft clay: case study and 3D simulation. *Acta Geotech.* **14**(1), 225–246 (2019)
10. Darina, M.A.: The use of the underground space of public buildings during their reconstruction. *Education and science in the modern world. Innovation* **1**(26), 125–131 (2020)
11. Galiev, I.H., Ashrapov, A.H., Ibragimov, R.A.: Scientific and technical support of the object of cultural heritage «Merchant Lisitsyn's house» during the construction works for its restoration and reconstruction. *News KSUAE* **1**(43), 211–218 (2018)
12. Galiev, I.H., Ibragimov, R.A.: Monitoring of reconstructed buildings using 3D scanners. *Constr. Prod.* **3**, 19–26 (2021)

13. Galeev, R.R., Nizamov, R.K., Abdrakhmanova, L.A.: Filling of epoxy polymers with chemically precipitated chalk from chemical water treatment sludge. In: Klyuev, S.V., Klyuev, A.V. (eds.) Proceedings of the International Conference Industrial and Civil Construction 2021. ICICC 2021. LNCE, vol. 147, pp. 93–97. Springer, Cham (2021). https://doi.org/10.1007/978-3-030-68984-1_14
14. Khuziakhmetova, K., Abdrakhmanova, L., Nizamov, R.: Polymer mixtures based on polyvinyl chloride for the production of construction materials. In: Vatin, N. (eds.) Proceedings of STCCE 2021. STCCE 2021. LNCE, vol. 169, pp. 14–21. Springer, Cham (2021). https://doi.org/10.1007/978-3-030-80103-8_2
15. Ibragimov, R., Bogdanov, R., Korolev, E.: The effect of metal and polypropylene fiber on technological and physical mechanical properties of activated cement compositions. Case Stud. Constr. Mater. **16** (2022). <https://doi.org/10.1016/j.cscm.2022.e00882>

Thermophysical Properties of Aerated Concrete Enclosing Structures



Olga Barysheva  and Alina Barysheva 

Abstract In construction, a transition to new effective enclosing structures that meet the requirements of modern standards in terms of heat engineering characteristics is underway. Multilayer enclosing structures are often used with the use of heat-insulating materials with a porous structure, which have good heat-shielding properties, and can reduce the thickness and weight of the enclosing structures. The operational properties of such structures and their durability are largely determined by the moisture conditions of the materials. The main goal was to determine heat and moisture transfer in aerated concrete enclosing structures in order to ensure a given temperature regime in the premises. The achievement of this goal was associated with the solution of the following tasks: conducting an experimental study, modeling heat transfer using the example of autoclaved aerated concrete based on the Elcut software package; calculation of the moisture state of structures made of autoclaved aerated concrete at various values of moisture content of aerated concrete blocks. Under various heat and humidity conditions, the characteristics of heat transfer in autoclaved aerated concrete have been experimentally found. Using the Elcut program, models of heat transfer in enclosing structures made of autoclaved aerated concrete were obtained using various brands of autoclaved aerated concrete. The computational substantiation of multilayer building envelopes made of aerated concrete with optimal design solutions to ensure a comfortable thermal and humidity regime in the premises has been carried out.

Keywords Thermophysical properties · Atmospheric moisture · Porous materials · Heat transfer · Thermal conductivity

O. Barysheva (✉)

Kazan State University of Architecture and Engineering, Kazan, Russian Federation

e-mail: obbars@gmail.com

A. Barysheva

Department of Secondary Vocational Education of the Institute of Computer Technology and Information Security (College of Information Technology), Kazan, Russian Federation

1 Introduction

Aerated concrete is a type of aerated concrete, a building material, an artificial stone with approximately spherical, closed, but communicating with each other, small pores with a diameter of up to 1...3 mm evenly distributed throughout the volume. Aerated concrete is a budget option, but despite this, it is a durable, fire-resistant and environmentally friendly material. This material has increased heat-shielding properties. It allows reducing the thickness and weight of the enclosing structures. For the manufacture of aerated concrete, quartz sand, cement and specialized gas formers and impurities are used: gypsum, lime, industrial waste [1–4], etc.

The growth of production capacities for the production of autoclaved aerated concrete blocks was determined by the increased demand for these products, which in turn was caused by the high quality and unique properties of the manufactured product. Obtaining aerated concrete with precise geometric dimensions and improved physical and mechanical properties became possible due to the emergence of new modern technological complexes [5–7].

The main products of autoclaved aerated concrete blocks remain small building blocks. Over the past two decades, the density of the produced aerated concrete has been steadily decreasing. If in 2012 products from autoclaved aerated concrete blocks were produced mainly with a density of 500 kg/m³, today aerated concrete of the D400 brand is gaining popularity. The brand of aerated concrete produced depends on the equipment used and the region in which the plants are located. The same factors have a significant impact on the price of aerated concrete [8–11].

The moisture regime of the enclosing structures affects their heat-shielding properties, since the thermal conductivity of the moistened materials increases, and the resistance to heat transfer of the entire structure decreases accordingly. A decrease in heat-shielding properties, in turn, causes even more intense humidification due to the intensification of the processes of diffusion and condensation of moisture. At high humidity of materials in the enclosing structures, corrosion of metal inclusions can also be observed, and the occurring phase transition processes reduce the durability of the structure and can cause its destruction. In addition, when the enclosing structures are moistened, conditions are created that are favorable for the formation of mold and fungi, which negatively affects the internal microclimate of the room. The situation is further aggravated by the introduction of new methods of work, new building materials and methods of thermal insulation devices. Instead of predominantly homogeneous external walls, mostly brick, multilayer systems began to be used, in the thickness of which, due to improper design and insufficient ventilation, condensate accumulates with the ensuing unfavorable consequences. The reason for the unfavorable moisture state of multilayer enclosing structures is often the absence of the forecast of their state, which is practically not carried out at the design stage, which leads to an increase in heat loss and to premature destruction of structures. In order to avoid the negative consequences of dampening structures, when designing them, it is necessary to determine the expected operational state by calculating the thermal and moisture regime. It should be borne in mind that the thermal and humidity

regime of enclosing structures made of porous building materials is determined, first of all, by the processes of heat and moisture transfer occurring in the materials. Thus, the calculations of the thermal and humidity regime of the building envelope must be performed taking into account the basic laws of the processes of heat and moisture transfer in porous materials [12–16].

Reasons for moisture in porous materials of enclosing structures [17–20] are:

1. Construction moisture that is introduced into the fence during the construction of the building. The amount of moisture introduced into the fence depends on its design and on the method of work, as well as on the building material used. The technological humidity of building materials usually has a great influence on the thermal and humidity regime of the enclosing structure only in the first years after the construction of the building.
2. Ground moisture, which can penetrate into the fence from the ground due to capillary suction through cracks, crevices and through the pores of materials. In the absence of reliable moisture insulation of the lower part of the wall, soil moisture can lead to significant moisture in the enclosing structures.
3. Atmospheric moisture, which can penetrate into the fence during rain, as a result of wetting the outer surface of the wall or as a result of damage to the roof and gutters. As a result, a large amount of moisture can enter the building envelope and cause serious damage after a while.
4. Operational moisture that enters the fence from various internal sources of moisture release because of human activity and production processes of the building. At the same time, moisture can get into the enclosing structure because of violations of operational processes, for example, with pipeline leaks. The intake of moisture from various operational processes can have a significant effect on the moisture regime of the enclosing structures.
5. Hygroscopic moisture, which is in the materials of the enclosing structure due to the sorption absorption of water vapor from the air. The intake of moisture into the enclosing structures is greatly influenced by the air regime of the premises. Water vapor can cause the same problems as liquid moisture entering structures directly, although the amount of moisture associated with this source is usually much less.
6. Condensation moisture that enters the fence due to condensation of water vapor on the inner surface of the fence and in its thickness. The process of condensation of moisture from the air is closely related to the heat technical mode of the enclosure. In the overwhelming majority of cases, condensation moisture is the main reason for increasing the moisture content of the fence.

In real conditions, it is almost impossible to eliminate all the causes of moisture in the enclosing structures. When designing a building, it is necessary to consider the potential for wetting materials in the building envelope. It is necessary to take into account various reasons for material moistening, including the peculiarities of the corresponding mechanisms and the patterns of heat and moisture transfer processes.

2 Method of Calculation

2.1 *The Mechanism of Moisture and Heat Ttransfer in Porous Materials*

In porous materials, moisture transfer is inseparable from heat transfer [7], and the phenomena of heat and moisture transfer must be considered in their inseparable connection. Therefore, to describe the processes of moisture transfer in porous materials, methods and approaches are used that are used in the study of heat transfer processes.

The basic law of heat transfer has the following form (Fourier's law):

$$q = -\lambda \cdot \nabla T, \quad (1)$$

where q —heat flux density, λ —coefficient of thermal conductivity, ∇T —temperature gradient.

In accordance with the thermodynamic analogy of the processes of heat and moisture transfer, the basic law of moisture transfer will have the following form [21–24]:

$$j = -k \nabla \theta T, \quad (2)$$

where j —moisture flux density, k —moisture conductivity coefficient, $\nabla \theta$ —moisture transfer potential gradient.

The moisture transfer potential is taken as the moisture concentration in the porous material (volumetric moisture content of the material). The law of moisture transfer in this case is described by an equation similar to Fick's law:

$$j = -D_w \nabla W, \quad (3)$$

where j —moisture flux density, D_w —moisture diffusion coefficient, ∇W —material moisture gradient.

In the practice of construction design, it is assumed that the process of moisture transfer occurs through vapor diffusion under the influence of the gradient of the partial pressure of water vapor in the air filling the pore of the material. Then the law of moisture transfer will be written in the following form:

$$j_v = -\mu \nabla p, \quad (4)$$

where j_v —vaporous moisture flow, μ —vapor permeability coefficient, ∇p —partial pressure gradient of water vapor in air.

Under isothermal conditions, there is an unambiguous relationship between the moisture content of the material and the relative humidity of the air, which is determined by the sorption isotherm. This makes it possible to make an equivalent replacement of the gradient of the partial pressure of vapor for the specific flow of vaporous moisture by the gradient of the moisture content of the material:

$$\nabla p = \frac{p_{sat}}{\xi} \nabla W, \quad (5)$$

where ξ —relative specific vapor capacity of the material, which is equal to the tangent of the slope of the tangent to the sorption isotherm, p_{sat} —maximum possible partial vapor pressure (saturated pressure) at a given temperature.

Substituting expression (5) into formula (4) and equating it with formula (3), we obtain the following relationship between the moisture diffusion coefficient and the vapor permeability coefficient for a given material:

$$D_w = \mu \frac{p_{sat}}{\xi} \nabla W, \quad (6)$$

Considering as the moisture transfer potential the moisture content of the air filling the pores of the material, and not the moisture content of the material itself [21, 22], a formula is proposed for recalculating the moisture diffusion coefficient:

$$D = \mu \frac{p_{sat}}{\gamma}, \quad (7)$$

where γ —specific gravity of water vapor in a material at a given temperature.

Thus, the vapor permeability coefficient used in construction is analogous to the moisture diffusion coefficient. At the same time, when recalculating the moisture diffusion coefficient, it is necessary to take into account that its value depends on what is taken as the moisture transfer potential. These formulas are applicable only within the sorption moisture content of the material.

At high material humidity, moisture transfer occurs mainly in the form of a liquid. In this case, the predominant mechanism of moisture transfer is capillary transfer. The capillary movement of liquid moisture in porous materials is caused by capillary suction forces, which are determined by the peculiarities of the porous structure of the material.

Thermal diffusion (movement of vaporous moisture in the material in the direction of decreasing temperature in the presence of a temperature gradient) is also observed under non-isothermal conditions at low material humidity, but experimental data show that its intensity is low, which gives grounds for further ignoring thermal diffusion in the calculations of enclosing structures. In capillary-porous materials at a certain humidity the movement of moisture can occur in the form of film and thermofilm transfer. Surface phenomena significantly affect the materials.

At high material humidity, moisture transfer occurs mainly in the form of a liquid. In this case, the predominant mechanism of moisture transfer is capillary transfer.

The capillary movement of liquid moisture in porous materials is caused by capillary suction forces, which are determined by the peculiarities of the porous structure of the material.

The movement of moisture in the pores of the material is considered. The moisture content of the material is taken as the moisture potential [7], therefore, the following equation is used for isothermal conditions:

$$j_w = -k \nabla W, \quad (8)$$

where j_w —liquid moisture flow, k —moisture conductivity coefficient, ∇W —material moisture gradient.

In Eq. (8), the moisture conductivity coefficient is a proportionality coefficient and is analogous to the diffusion coefficient of liquid moisture.

Boundary conditions have a significant effect on the processes of heat and moisture transfer in porous materials. Depending on the boundary conditions, moistening of materials can occur in the mode of capillary impregnation with direct contact of the material with water or in the mode of sorption moistening due to the absorption of water vapor from the air, as well as due to condensation of moisture from the air.

Extending the analogy between thermal conductivity and diffusion to non-stationary conditions, the following differential moisture transfer equation is solved:

$$\frac{\partial p}{\partial t} = \frac{\mu}{\xi \gamma} p_{sat} \frac{\partial^2 p}{\partial x^2}, \quad (9)$$

Taking into account the dependence of the sorption properties of building materials on temperature made it possible to increase the accuracy of calculating the partial pressure in the pores of the material:

$$\frac{\partial W}{\partial t} = \frac{p_{Hac} \partial}{\xi \gamma \partial x} \left(\mu \frac{\partial p}{\partial x} + k \frac{\partial W}{\partial x} \right), \quad (10)$$

However, the model does not take into account thermal, moisture conductivity, and the heat of phase transitions. In this case, in the calculation, the temperature field changes abruptly, that is, within one time step, it is constant [2–7, 9–13].

In the actual operating conditions of buildings, the outside and inside air temperatures are not constant, but change over time. Temperature changes can occur because of a change in cold and warm masses of outdoor air, during periodic heating of buildings, under the influence of solar radiation in summer, etc. Periodic changes in air temperatures cause changes in the temperature of the inner surface of the fence. In winter with low values of the R_0 , all that can lead to a decrease in the surface temperature below the dew point temperature and to the formation of condensation on it, and in summer - to an increase in the temperature of the indoor air in the room. These circumstances must be taken into account in heat engineering calculations and, therefore, in a number of cases, to consider the process of heat transfer in non-stationary conditions.

Reduced resistance to heat transfer of a fragment of the heat-protective envelope of a building R_0^r , ($m^2 \cdot ^\circ C$)/ W , determined by the formula:

$$R_0^r = \frac{1}{\frac{1}{R_0^c} + \sum l_j \Psi_j + \sum n_k \chi_k} = \frac{1}{\sum a_i U_i + \sum l_j \Psi_j + \sum n_k \chi_k}, \quad (11)$$

where R_0^c —area-average conditional resistance to heat transfer of a fragment of the heat-shielding shell of a building or a dedicated enclosing structure, ($m^2 \cdot ^\circ C$)/ W ;

l_j —the length of a linear heterogeneity of the j -th type, falling on 1 m^2 fragments of the heat-protective shell of a building, or a dedicated enclosing structure, m/m^2 ;

Ψ_j —specific heat losses through linear inhomogeneity of the j -th type, $W/(m \cdot ^\circ C)$; n_k —the number of point in homogeneities of the k -th type per 1 m^2 fragments of the heat-protective shell of a building, or a dedicated enclosing structure, pcs./ m^2 ;

χ_k —specific heat losses through a point inhomogeneity of the k -th type, $W/^\circ C$;

a_i —area of the planar element structure i -th species attributable to 1 m^2 fragment heat protective shell of the building, or a dedicated partition structure, m^2/m^2 :

$$a_i = \frac{A_i}{\sum A_i}, \quad (12)$$

where A_i —area of the i -th part of the fragment, m^2 ; U_i - heat transfer coefficient of the homogeneous i -th part of a fragment of the heat-protective shell of a building (specific heat losses through a flat element of the i -th type), $W/(m \cdot ^\circ C)$.

$$U_i = \frac{1}{R_{0,i}^c}, \quad (13)$$

where $R_{0,i}^c$ —conditional resistance to heat transfer of a homogeneous part of a fragment of a heat-protective envelope of a building of the i -th type, $1/W/(m \cdot ^\circ C)$, which is determined either experimentally or by calculation using the formula:

$$R_{0,i}^c = \frac{1}{\alpha_{in}} + \sum_s R_s + \frac{1}{\alpha_{out}}, \quad (14)$$

where α_{in} —heat transfer coefficient of the inner surface of the enclosing structure, $W/(m \cdot ^\circ C)$; α_{out} - heat transfer coefficient of the outer surface of the building envelope, $B_T/(M \cdot ^\circ C)$; R —thermal resistance of a layer of a homogeneous part of a fragment, $W/(m \cdot ^\circ C)$, determined by the formula:

$$R_s = \frac{\delta_s}{\lambda_s}, \quad (15)$$

where δ_s —layer thickness, m; λ_s —thermal conductivity of the layer material, $W/(m \cdot ^\circ C)$, taken on the basis of test results in an accredited laboratory.

Specific heat losses through a linear thermal inhomogeneity are determined from the results of calculating a two-dimensional temperature field of a structural unit at an internal air temperature t_{in} and an external air temperature t_{out} .

$$\Psi_j = \frac{\Delta Q_j^L}{t_{in} - t_{out}}, \quad (16)$$

where t_{in} —design indoor air temperature, $^\circ C$; t_{out} —design outdoor temperature, $^\circ C$; ΔQ_j^L —additional heat losses through linear heat engineering heterogeneity of the j -th type, per 1 r. m, W/m , defined by formulas:

$$\Delta Q_j^L = Q_j^L - Q_{j,1} - Q_{j,2} \quad (17)$$

where Q_j^L —heat loss through the computational domain with a linear thermal inhomogeneity of the j -th type, per 1 r.m of the joint, resulting from the calculation of the temperature field, W/m ; $Q_{j,2}$ —heat loss through areas of homogeneous parts of a fragment included in the computational domain when calculating the temperature field of a domain with a linear thermal inhomogeneity of the j -th type, W/m , defined by formulas:

$$Q_{j,1} = S_{j,1} \cdot \frac{t_{in} - t_{out}}{R_{0,j,1} \cdot 1 m}, \quad Q_{j,2} = S_{j,2} \cdot \frac{t_{in} - t_{out}}{R_{0,j,2} \cdot 1 m} \quad (18)$$

where $S_{j,1}$, $S_{j,2}$ —areas of homogeneous parts of a structure included in the computational domain when calculating the temperature field, m^2 . The quantity $S_{j,1} + S_{j,2}$ is equal to the area of the computational domain when calculating the temperature field, Ψ_j - specific linear heat losses through linear heat engineering heterogeneity of the j -th type, $W/(m \cdot ^\circ C)$.

It is necessary to monitor the processes of moisture accumulation and drying in order to avoid the negative consequences of humidification of material enclosing structures. At the design stage of enclosing structures, it is necessary to determine their expected operational state by calculating the thermal and humidity regime. The heat and moisture regime of the enclosing structures is largely determined by the processes of heat and moisture transfer occurring in porous building materials (aerated concrete), as well as their moisture and structural characteristics.

3 Results and Discussion

3.1 Experimental Study of Heat Transfer in Aerated Concrete Enclosing Structures

An example of the material under study was the sample of autoclaved aerated concrete.

Figure 1 shows the main options for wall fillings using masonry from autoclaved aerated concrete blocks in monolithic construction: 1 - Single-layer aerated concrete wall with brick cladding. Facing layer 120 mm, less often 250 mm. The cladding layer in buildings with a load-bearing frame either covers the ends of the floors, or is laid out flush with them. In low-rise construction, the cladding layer is usually self-supporting to the height of the building. Aerated concrete grades D300 – D500, 300–400 mm thick are used; 2 - Single-layer aerated concrete wall. The masonry performs a constructive and heat-insulating function. External finishing - surface leveling, painting. In low-rise construction, such a wall structure is widespread. In residential buildings with a supporting frame, it is used in the overwhelming majority of cases on glazed balconies and loggias, D300 – D400 300–375 mm; 3 - 4 - Aerated concrete masonry with external insulation. To protect the insulation from atmospheric influences, either a plaster facade with a thin plaster layer or a hinged facade system with a ventilated air gap is arranged. Aerated concrete mainly serves as a load-bearing base for insulation. Thickness in floor-by-floor supported walls - 200–250 mm, in load-bearing walls of low-rise buildings - according to the calculation of the bearing capacity (250–400 mm). Average density grade within D400 - D600.

Systems of external insulation on aerated concrete base are widely used.

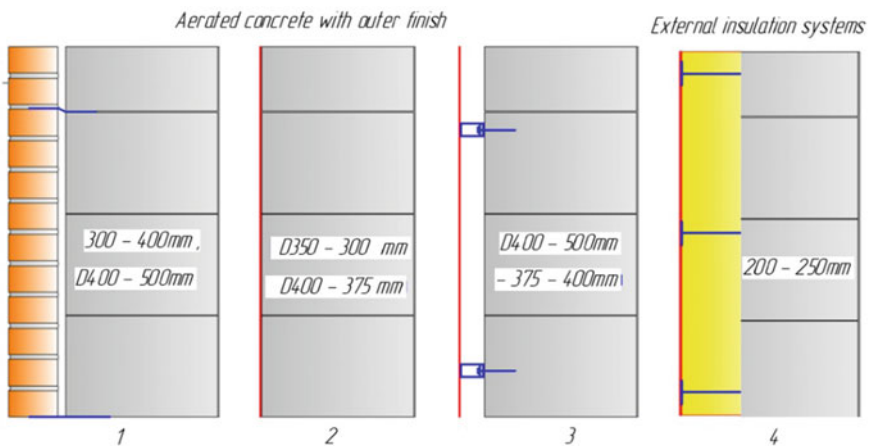
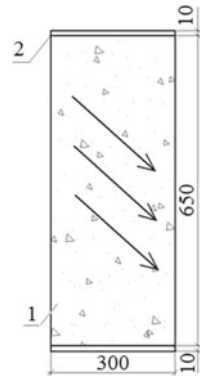


Fig. 1 Options for wall fillings

Fig. 2 Scheme of the element of walls



The most common options for construction in the northern regions of Russia are: 200–250 mm D400 - D600 wall blocks, mineral wool insulation and plastering or hinged facade systems for insulation. Internal finishing in most cases - grinding the surface with plaster compounds with a layer up to 5 mm thick.

Consider the most common variant of low-rise construction. The masonry of aerated concrete blocks sizes is: thickness 300 mm, thickness with external insulation of mineral wool slabs with a thickness of 100 mm, the thickness of the external plaster finish is 10 mm, the thickness of the internal plaster finish is 5 mm.

For the calculation, take aerated concrete blocks of the D400 brand, in which a 1 m³ of porous concrete contains 400 kg of solid components, which occupy about a third of the volume. Block size is: length 650, width 400, thickness 300 mm.

Figure 2 shows a diagram of a wall element made of aerated concrete with an average thickness of 10 mm masonry joints: 1 – aerated concrete blocks; 2 – mortar joints; → - the direction of the heat flow is perpendicular to the plane of the element under consideration.

There are two categories of aerated concrete wall masonry [9]: on glue (category 1) and on solution (category 2). Laying in solution (category 2) is performed on a conventional cement-sand mortar with thick masonry joints 10 ± 2 mm, masonry category 1 is performed on a special glue joints with a thickness of 2 ± 1 mm. The actual thickness of the thin-layer mortar in the structure must be at least 0.5 mm and not more than 3 mm.

The smaller the thickness of the masonry, the higher the coefficient of thermal uniformity and, consequently, the reduced resistance to heat transfer of the walls is R' . In this work, we will use a cement-sand mortar with thickness of 10 mm as a solution.

The solution of two-dimensional problems of linear heat conduction is considered using the finite element method in the Elcut program [1]. Table 1 shows the calculated thermal performance of aerated concrete.

Fragments of the model can be imported from AutoCAD or other design systems. The calculation results can be viewed in various forms of presentation: field lines, color maps, graphs of various values along arbitrary contours, etc. Various integral

Table 1 Calculated heat engineering parameters of cellular concrete

Concrete grade by average density	Coefficient of thermal conductivity of concrete in a dry state $\lambda_0, \frac{W}{m \cdot ^\circ C}$	Density, $\rho_0, kg/m^3$	Specific heat capacity, $c_0, \frac{J}{kg \cdot ^\circ C}$	Water vapor permeability coefficient of concrete $\mu, mg/m/h/Pa$	Calculated thermal conductivity coefficients $\lambda, \frac{W}{m \cdot ^\circ C}$ for conditions A, $W = 4\%$	Calculated thermal conductivity coefficients $\lambda, \frac{W}{m \cdot ^\circ C}$ for conditions B, $W = 5\%$
D400	0.096	400	840	0.23	0.113	0.117
D500	0.120	500	840	0.20	0.141	0.147
D600	0.140	600	840	0.16	0.170	0.183

Table 2 Calculated thermal and technical parameters of the materials used

Material name	Coefficient of thermal conductivity (B), $\lambda, \frac{W}{m \cdot ^\circ C}$	Density, $\rho_0, \frac{kg}{m^3}$	Specific heat capacity, $c_0, \frac{J}{kg \cdot ^\circ C}$
External and internal plaster from a complex solution (sand, lime, cement)	0.870	1700	840
Heat insulating material: mineral wool slabs	0.045	125	840
Cement sand mortar (for joints of aerated concrete slabs)	0.930	1800	840

values on user-defined lines, surfaces or volumes can be calculated. The postprocessor provides the output of tables and figures to files for further processing or high-quality graphic printing. Thermal performance of the materials used are given in Table 2.

In the Elcut program, a source specified at a specific point in the xy plane describes a part of the enclosing structure in the form of a string, followed by a given point of the plane, and is set by the power of heat release per unit length. The specified temperature condition sets the known temperature value t_0 on the edge or at the vertex of the model. The convection boundary condition can be specified at the outer boundary of the model, which describes convective heat transfer. After performing the calculations, the program displays a color map showing the distribution of the selected physical quantity, as well as the calculation results in graphical form. Thermal performance of the enclosing structure is determined for the grade of aerated concrete blocks D400.

Heat transfer coefficient of the inner surface of the enclosing structure is $\alpha_{in} = 8, 7 W(m^2 \cdot ^\circ C)$. It is assumed that the ceiling above the heating panels is ventilated with outside air, the heat transfer coefficient of the outer surface of the enclosing structure will be equal to $\alpha_{out} = 23 W(m^2 \cdot ^\circ C)$. We set the temperature of the

internal air in the room $t_0 = 20^{\circ}\text{C}$ and outside temperature $t_{out} = -24^{\circ}\text{C}$ for the northern region of Russia.

The Elcut program shows the distribution of the temperature field of a part of the enclosing structure made of aerated concrete blocks (product brand D400) (Fig. 3). It can be represented by the following graphical presentation formats: isotherms, vectors (temperature gradient, heat flux), color card (temperature, temperature gradient, heat flux and etc.). In the Elcut program, you can set an integration contour and present the temperature distribution along a given contour in the form of a table or a thermogram.

The thermal engineering calculation of a fragment of the enclosing structure made of D400 aerated concrete blocks, taking into account the use of mineral wool as an

Fig. 3 Picture of the field of a fragment of the enclosing structure

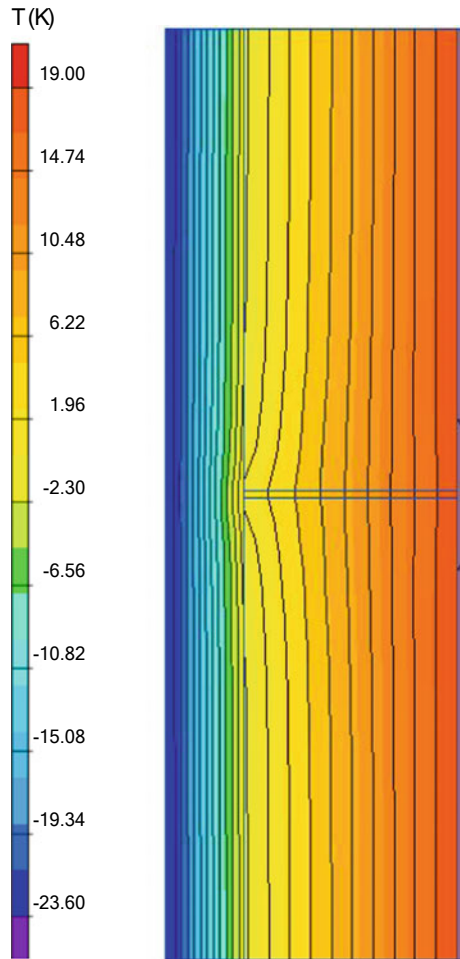


Table 3 Physical quantities of the investigated enclosing structure made of aerated concrete blocks (product brand D400) at the boundaries of the outer, inner walls and in the cross section

The part of the building envelope under consideration	Heat flow through the wall, Q, W	Specific heat flux $q, \frac{W}{m^2}$	Temperature difference $\Delta T, ^\circ C$	Average surface temperature $T_s, ^\circ C$	Integral of the heat flux density along the contour $X, W/m^2$	Surface integral of $\nabla T, m \cdot ^\circ C$
Outer wall	10.666	8.14	$3.27 \cdot 10^5$	-23.65	$2.84 \cdot 10^5$	12.259
Inner wall	10.665	8.14	0.0057	19.06	0.005	12.259
Cross section	0.005	0.012	42.35	3.96	17.296	0.119

insulating material, with external and internal finishing from a complex solution (sand, lime, cement), showed the results presented in Table 3.

The calculation of heat transfer through the enclosing structure is performed using the specific heat flux density. Specific heat flux per $1 m^2$ is calculated by the formula:

$$q = \frac{Q}{S}, W/m^2 \tag{19}$$

where Q —heat flow through the inner surface of the node, W ; S —area of a homogeneous part of a structure included in the computational domain when calculating the temperature field, m^2 .

According to the found values in the Elcut program, graphs of the temperature distribution, heat flux along the outer wall of the enclosing structure were plotted (product brand D400) (Figs. 4 and 5).

The graphs are obtained for the case along the inner wall of the enclosing structure (product brand D400) (Figs. 6 and 7). Based on the results, a graph of the temperature distribution of the cross-section falling on the “cold bridge” is constructed (Fig. 8). Using the graphs, it is possible to determine the temperature and heat flux on the surface at any selected point.

Thus, along the outer wall, the temperature is inhomogeneous, a disturbance arises near the seam between the aerated concrete blocks, in this area the temperature rises. Due to the presence of heat-insulating material, the heat flow is directed towards the heated room.

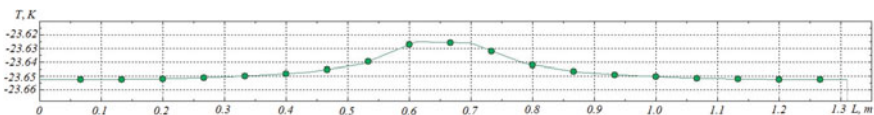


Fig. 4 Temperature distribution

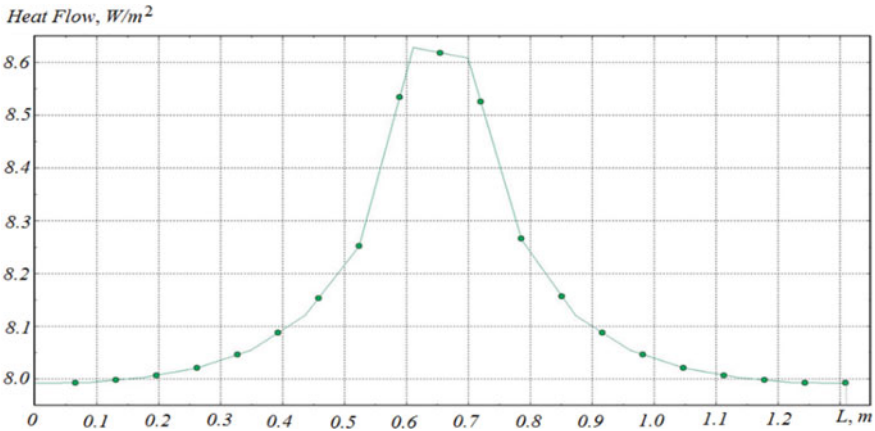


Fig. 5 Heat flux distribution

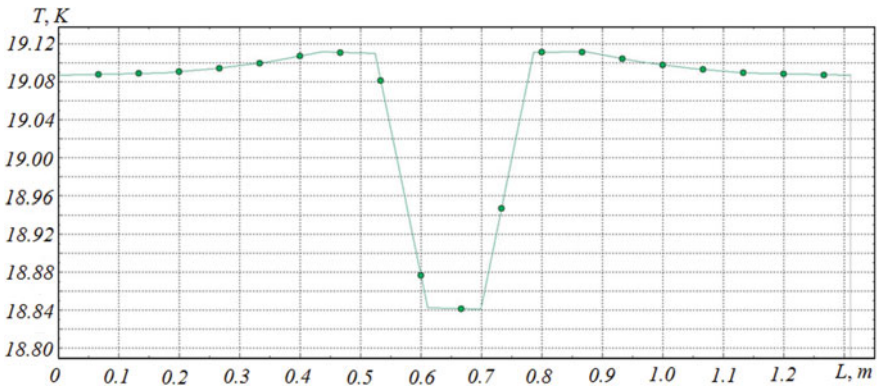


Fig. 6 Temperature distribution

The maximum value of the heat flux on the outer surface of the enclosing structure is observed near the seam between the aerated concrete blocks and is the 8.63 W/m^2 . The maximum value of the heat flux on the inner surface is also observed near the seam between the aerated concrete blocks and is the 10.2 W/m^2 .

Thus, when laying the enclosing structure using aerated concrete blocks and insulation, it is recommended to use D400 aerated concrete blocks.

External insulation of aerated concrete walls is more economically advantageous (in terms of the cost of the material) than the increase of the thickness of the aerated concrete wall. The use of external wall insulation made of aerated concrete is the dew point temperature output from aerated concrete to the insulation.

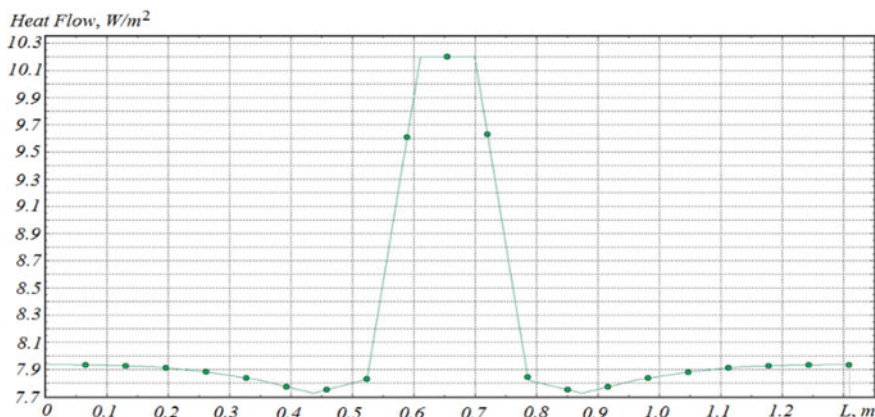


Fig. 7 Heat flow distribution

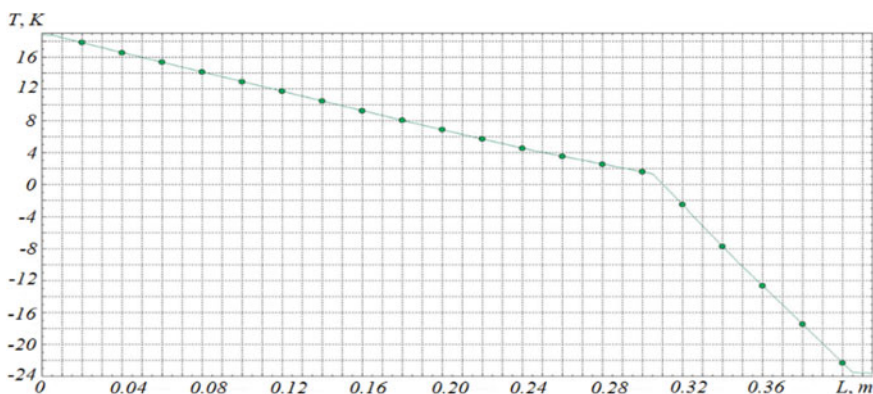


Fig. 8 The graph of the temperature distribution in the cross section

4 Conclusions

Mineral wool with a screen finish is not subject to significant moisture, regardless of the initial moisture content of the base masonry. The initial moisture contained in aerated concrete is a source of moisture for insulation in the first heating seasons.

Based on theoretical calculations, it was determined: the specific heat flux through the enclosing structure consisting of D400 aerated concrete blocks is the 10.43 W/m². The results of experimental calculations show similar dynamics. The numerical values are slightly lower than the results obtained theoretically. For example, the specific heat flux through the enclosing structure consisting of D400 aerated concrete blocks is the 8.63 W/m². When using aerated concrete blocks with a thickness of

300 mm, with an external insulation made of mineral wool slabs with a thickness of 100 mm and using facing plaster, the enclosing structure using autoclaved aerated concrete of the D400 brand showed the best thermophysical characteristics. When laying the enclosing structure using aerated concrete blocks and insulation, it is recommended to use D400 aerated concrete blocks. This is the most optimal design solutions to ensure a comfortable thermal and humidity conditions in the premises.

References

1. Simutkin, M., Tuzikova, V., Tlusty, J., Tulsy, V., Muller, Z.: in IOP Conf. Ser. Mater. Sci. Eng. (2017). <https://iopscience.iop.org/article/10.1088/1757-899X/189/1/012028>
2. K.V.A.: Int. J. Res. Eng. Technol. (2016). <https://doi.org/10.15623/ijret.2016.0512025>
3. Int. J. Eng. (2019). <https://doi.org/10.19072/ijet.521255>
4. Aadithiya, K.V.: Int. Res. J. Eng. Technol. (2017). <https://doi.org/10.15623/ijret.2016.0512025>
5. Geetha, S., Madhavan, S.: in Mater. Today Proc. (2015). <https://doi.org/10.1016/j.matpr.2015.07.255>
6. Li, Z., et al.: Eng. Struct. (2017). <https://doi.org/10.1016/j.engstruct.2017.03.033>
7. Su, Y., Li, J., Zhang, X.: Transp. Porous Media (2020). <https://doi.org/10.1007/s11242-019-01347-2>
8. Barysheva, O., Sadykov, R., Khabibullin, Y., Zheltukhina, E.: in E3S Web Conf. (2019). <https://doi.org/10.1051/e3sconf/201914008002>
9. Kashani, A., Ngo, T.D., Mendis, P., Black, J.R., Hajimohammadi, A.: J. Clean. Prod. (2017). <https://doi.org/10.1016/j.jclepro.2017.02.154>
10. Vardhan, R., Chandel, S., Sakale, R.: Int. J. Sci. Res. Dev. (2016). <https://ijsrd.com/articles/IJSRDV4I70009.pdf>
11. Nandi, S., Chatterjee, A., Samanta, P., Hansda, T.: Int. J. Eng. Res. (2016). <https://doi.org/10.17950/ijer/v5i1/009>
12. Hajimohammadi, A., Ngo, T., Mendis, P.: Cem. Concr. Compos. (2018). <https://doi.org/10.1016/j.cemconcomp.2017.12.014>
13. Chung, S.Y., Abd Elrahman, M., Kim, J.S., Han, T.S., Stephan, D., Sikora, P.: Constr. Build. Mater. (2019). <https://doi.org/10.1016/j.conbuildmat.2019.03.270>
14. Lee, H.K., Kim, H.K., Hwang, E.A.: Waste Manag. (2010). <https://doi.org/10.1016/j.wasman.2009.09.043>
15. Chica, L., Alzate, A.: Constr. Build. Mater. (2019). <https://doi.org/10.1016/j.conbuildmat.2018.12.136>
16. S.E.V., P.R.KH., T.M.K.: Am. J. Interdiscip. Innov. Res. (2020). <https://doi.org/10.37547/tajir/volume02issue12-01>
17. Kapustin, F., Vishnevsky, A.: in Solid State Phenom. (2020). <https://doi.org/10.4028/www.scientific.net/SSP.309.8>
18. Krot, A., Ryazanova, V.A., Gabitov, A.I., Gaisin, A.M., Chernova, A.R.: in Mater. Sci. Forum (2019). <https://doi.org/10.4028/www.scientific.net/MSF.968.317>
19. Yarmakovskiy, V.N., Kadiev, D.Z.: in IOP Conf. Ser. Mater. Sci. Eng. (2020). <https://doi.org/10.1088/1757-899X/896/1/012087>
20. Kazaryan, R., Belyaev, K.: in E3S Web Conf. (2019). <https://doi.org/10.1051/e3sconf/20199102024>
21. Dregalin, A.F., Barysheva, O.B., Cherenkov, A.S.: Russ. Aeronaut. (2007). <https://doi.org/10.3103/S1068799807030117>
22. Barysheva, O.B.: Russ. Aeronaut. (2007). <https://doi.org/10.3103/S1068799807040058>

23. Kareeva, J., Gabdrafiqov, R., Chukhlova, M.: in E3S Web Conf. (2021). <https://doi.org/10.1051/e3sconf/202127408013>
24. Krutova, I.A., Zolotonosov, Y.A.D.: Computer simulation of fluid flow and heat transfer in conical coiled heat exchangers of the «pipe-in-pipe» type. News KSUAE 3(53), 65–73 (2020)

Investigation of Polymer Composite Cage for Reinforcement of Concrete Columns



Dmitriy Erohin, Tagir Zinnurov , and Ilia Grishin

Abstract The authors proposed an innovative solution for strengthening reinforced concrete columns made of polymer composite materials: fiberglass reinforcement and polymer concrete. Investigation of the operation of a cage made of polymer composite materials includes: full-scale compression test of samples of round cross-section racks reinforced with a cage made of polymer composite materials; numerical modeling of a reinforced concrete column strengthened with a spiral of fiberglass reinforcement using three-dimensional models in the ANSYS software package. Within the framework of the studied theory of elasticity and mechanics of a solid body, a method for calculating the reinforcement structure from fiberglass reinforcement together with a concrete cylinder in a linear formulation is proposed. As a result, a comprehensive analysis of the data obtained was carried out and recommendations were developed for the design and calculation of the cage for reinforcing reinforced concrete columns made of polymer composite materials.

Keywords Cage · Column · Reinforced concrete · Polymer concrete · Fiberglass reinforcement

1 Introduction

The condition of the bridges, overpasses, flyovers and other engineering and technical structures to ensure traffic flow with increased traffic is due to the high quality of the road network indicators and requires special attention. According to the Ministry of Transport of the Russian Federation, there are more than 70,000 bridge observations in the Russian Federation, of which more than 7% are in disrepair. In addition there are side effects in the form of aggressive environments, with a particularly significant increase in the load on vehicles [1, 2]. There is a problem that more than half of all the bridges in Russia were designed according to the old regulatory documents and need to be strengthened [3].

D. Erohin (✉) · T. Zinnurov · I. Grishin
Kazan State University of Architecture and Engineering, 1 Zelenaya Street, Kazan 420043,
Russian Federation
e-mail: erokhin1604@mail.ru

An urgent task is fast and high-quality strengthening of columns with low economic costs. The problem of is solved when using a cage, usually made of steel or reinforced concrete. However, these materials have significant drawbacks compared to modern polymer composite materials, which are described in [4–8]. Therefore, it is proposed to strengthen the bridge columns with a spiral of fiberglass reinforcement, which is included in the work due to the local tension of the rod, and joint work and mechanical protection is ensured by applying the polymer concrete mixture using the thixotropic method (Fig. 1). Due to the chemical resistance, hydrophobicity and high adhesion of polymer concrete, the support structure is protected from the effects of aggressive media, and the power spiral of fiber-reinforced plastic rebar is securely fixed on the support body [9–11].

The technology of reinforcing columns of bridge structures with polymer composite materials has a number of advantages:

- reduction of economic costs for repair work;
- increase in the durability of the columns of bridge structures;

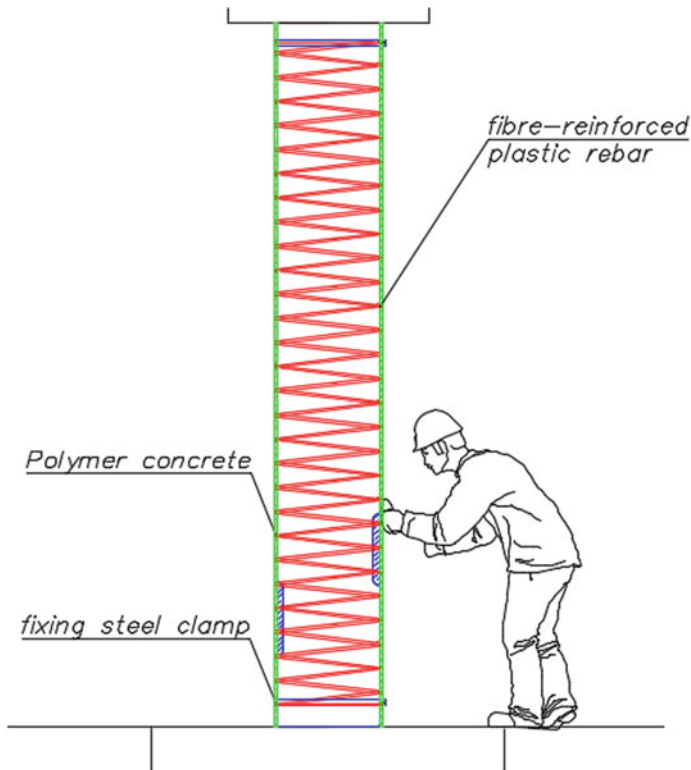


Fig. 1 The design of the polymer composite reinforcement cage

- no need for protection from aggressive environments, especially at the level of the watercourse;
- reduction of terms of construction and installation works to strengthen the columns of bridges;
- low weight of the reinforcement cage structure, so there is no need to strengthen the foundation.

The aim of the reinforcement structure work is quite simple and consists in constraining the transverse deformations of concrete due to the outer shell. Research in this direction is carried out by both domestic and foreign scientists. There are works of V.A. Rosnovsky and D. Kendal in the area of pipe-concrete structures [12, 13]. Today, with the introduction of polymers in the construction, a large number of works are aimed at studying hybrid shells in the fiberglass (GFRP)-concrete-steel (DSTC) joint, in the cage when the shell becomes a permanent formwork for the construction of columns [14–17]. However, such structures cannot be used when strengthening the operated columns, therefore, it is necessary to provide a technological process for placing such cages [18].

2 Materials and Methods

Strengthening of reinforced concrete compressible columns, in order to increase their bearing capacity, is usually carried out in case of increasing the temporary load or extension of service life during repair work.

The polymer composite material creates a constant radial pressure on the element to be reinforced, elastically deforms until its fracture, and therefore exerts an increasing passive radial pressure on the concrete specimen under axial load. This process is well described in [18].

Due to the pretension and adhesion of fiberglass reinforcement with concrete, their joint work is ensured. In theory, it is possible to establish an identity between the relative deformations of concrete ε_c and reinforcement ε_k [19].

The equilibrium equations in a concrete sample can be written as follows:

$$\varepsilon_z = \frac{-\sigma_z}{E_1} + \frac{\sigma_p \cdot \mu_1}{E_1}, \quad (1)$$

$$\varepsilon_p = \frac{-\sigma_p}{E_1} + \frac{\sigma_z \cdot \mu_1}{E_1}, \quad (2)$$

E_1, μ_1 – the elasticity modulus and Poisson's ratio of concrete, respectively;

E_2, μ_2 – the elasticity modulus and Poisson's ratio of the polymer composite casing, respectively;

σ_z, ε_z – stresses and strains in the material of the compressible sample, in the direction of the z axis, respectively;

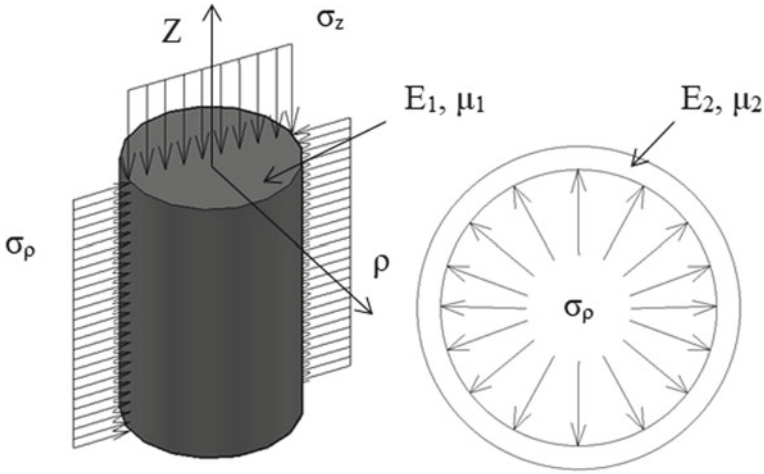


Fig. 2 3D calculation scheme of a column in a holder made of polymer composite materials

$\sigma_\rho, \varepsilon_\rho$ – radial stresses and strains in the material of the compressible concrete sample, numerically equal to the pressure exerted by the concrete sample on the cage, respectively.

Radial deformations can be represented as:

$$\varepsilon_p = \frac{\Delta r}{r_1} = \frac{r_2 - r_1}{r_1}, \tag{3}$$

where r_1 is the radius of the central axis of the holder before deformation, r_2 is the radius of the central axis of the cage after deformation. If $l_1 = 2\pi r_1$ then the length of the circle running along the central axis of the cage before deformation; if $l_2 = 2\pi r_2$ then the length of the circle running along the central axis of the cage after deformation. Then the deformations along the fibers of the cage, in accordance with the scheme, can be expressed as:

$$\varepsilon_p = \frac{l_2 - l_1}{l_1} = \frac{2\pi(r_2 - r_1)}{2\pi r_1} = \frac{\Delta r}{r_1} = \varepsilon_p, \tag{4}$$

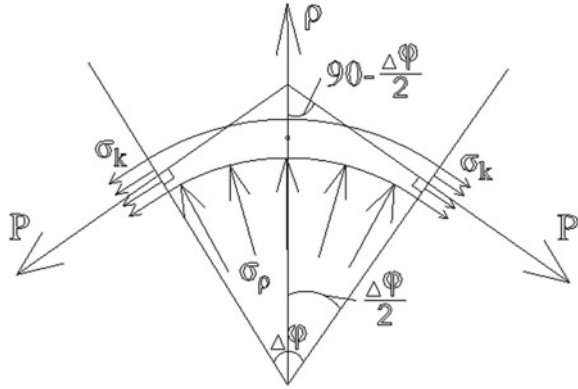
According to Hooke's law $\sigma_k = E_2 \cdot \varepsilon_k$.

Let us determine the radial stresses of the sample. We replace the stresses σ_k with the resulting force P (Fig. 3).

$$P = \sigma_k \cdot b \cdot h, \tag{5}$$

b and h are the width and height of the cage, respectively. Let us assume that at small angles $\varphi \rightarrow 0$, then $\sin \varphi \approx \varphi$ can be counted.

Fig. 3 Calculation model of a sample with a cage in a horizontal plane



The equilibrium equation, in accordance with the model in Fig. 3, will look like:

$$\sigma_p \cdot \Delta\varphi \cdot b \cdot R = P \cdot \cos(90^\circ - \varphi/2) \cdot 2, \tag{6}$$

Following that it converts to:

$$\sigma_p = \sigma_k \cdot \frac{h}{R}. \tag{7}$$

As it has already been noted, we accept the equality of the deformation in the contact zone of the cage and the reinforced concrete sample $\varepsilon_p = \varepsilon_k$ we have:

$$\sigma_k = E_2 \cdot \varepsilon_p, \tag{8}$$

We get

$$\sigma_k = h \cdot E_2 \cdot \frac{\varepsilon_p}{R}, \tag{9}$$

Using Eq. (9) we express ε_p in terms of σ_p , and we get:

$$\varepsilon_p = \frac{\sigma_p \cdot R}{E_2 \cdot h}. \tag{10}$$

We substitute Eq. (10) into Eq. (1) and express in terms of:

$$\sigma_p = \frac{\sigma_z \cdot \mu_1}{\left(\frac{E_1 \cdot R}{E_2 \cdot h} + 1\right)}. \tag{11}$$

Tensions σ_z are given as an external load distributed over the cross-sectional area of the sample, σ_p are calculated by formula (10). To determine the dependence σ_k , we use the following dependence:

$$\sigma_p = \frac{\sigma_z \cdot \mu_1 \cdot R}{\left(\frac{E_1 \cdot R}{E_2} + h\right)}. \quad (12)$$

Formula (12) allows analyzing the dependence of the tensions in the cage σ_k on the parameters σ_z , E_1 , E_2 , R , h .

It is reasonable to assume that the greater the pitch of the power spiral turns and the larger the diameter of the reinforcement, the greater the increase in the bearing capacity of the sample. The diameter of the reinforcement and the pitch of the turns should be set based on the design requirements for the twisting of the reinforcement around the column according to the formula:

$$d_a = \frac{d_k \cdot R_f}{E_f}, \quad (13)$$

where d_a is the diameter of fiberglass reinforcement, mm; d_k is the diameter of the column, mm; R_f is the tensile strength fiberglass reinforcement, MPa; E_f is the tensile modulus fiberglass reinforcement, MPa.

3 Results and Discussion

In order to confirm the operation of a polymer composite cage and further study of its the stress–strain state, 10 samples with a diameter of 105 mm and height of 470 mm were made from fine-grained heavy concrete class B30, with working reinforcement of a periodic profile class A400, with a diameter of 6 mm. Five samples of the total number had reinforcement in the form of a spiral of glass fiber reinforced polymer (GFRP) with a diameter of 2.5 mm, located at a pitch of 20–25 mm and covered with polymer concrete 4 mm thick. (Fig. 4). Upon reaching the age of 28 days, the strength of the concrete was tested by a non-destructive ultrasonic method and using a hydraulic press. Load cells were installed on the samples with polymer composite cage to record the stresses in the concrete and fiberglass reinforcement.

The test results have shown that the reinforcement cage made of polymer composite materials operates together with the compressible sample and engages immediately after the load is applied to the sample. Polymer concrete reliably fixes the power spiral on the sample and redistributes stresses among all the turns of fiberglass reinforcement. The fracture of polymer concrete has a cohesive nature, and occurs along the material of the compressed sample (Fig. 4).

Comparing the two variants of samples, we noted a significant increase in the breaking load for samples with a polymer composite cage, which amounted to 60%

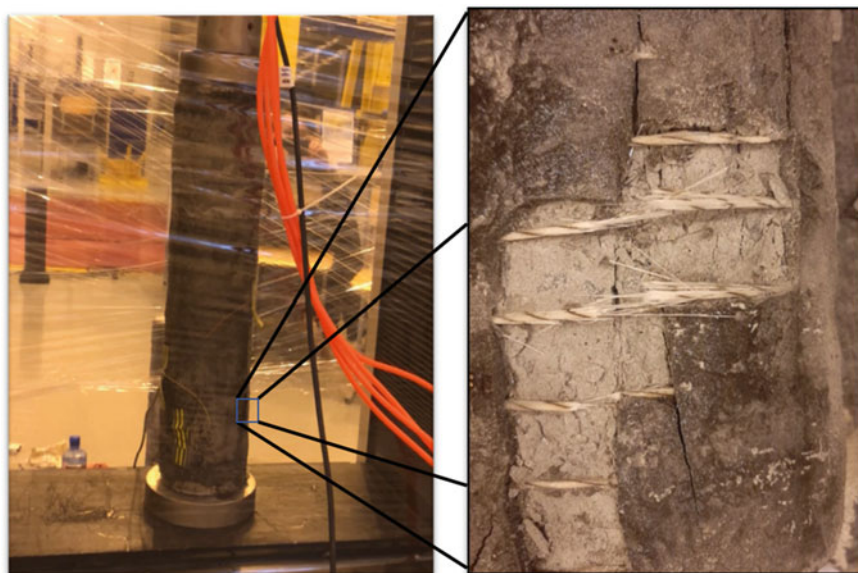


Fig. 4 Testing a sample reinforced with a polymer composite cage

relative to unreinforced samples. The results of testing the samples are presented in Table 1. The authors have found that changing the pitch and diameter will affect the bearing capacity of the sample, which is proved using numerical simulation. It is also planned to use glass fiber reinforced polymer with sand dressing for better mechanical engagement with polymer concrete, as well as a decrease in the amount of hardener in the composition of polymer concrete for greater stress relaxation and less brittle destruction of the reinforcement cage. Analyzing the graph of the dependence of vertical deformations on the load during full-scale tests of compressible samples (Fig. 5), we note the appearance of a zone of plastic deformation, which demonstrates the ductile fracture of the sample reinforced by the cage.

Table 1 Sample test results

Sample №	With cage					Without cage				
	1	2	3	4	5	1	2	3	4	5
P_{max} – breaking load, κN	232.9	208.4	245.2	269.6	236.8	403.1	378.5	359.8	378.1	381.2
Average breaking load, κN	238.6					380.1				

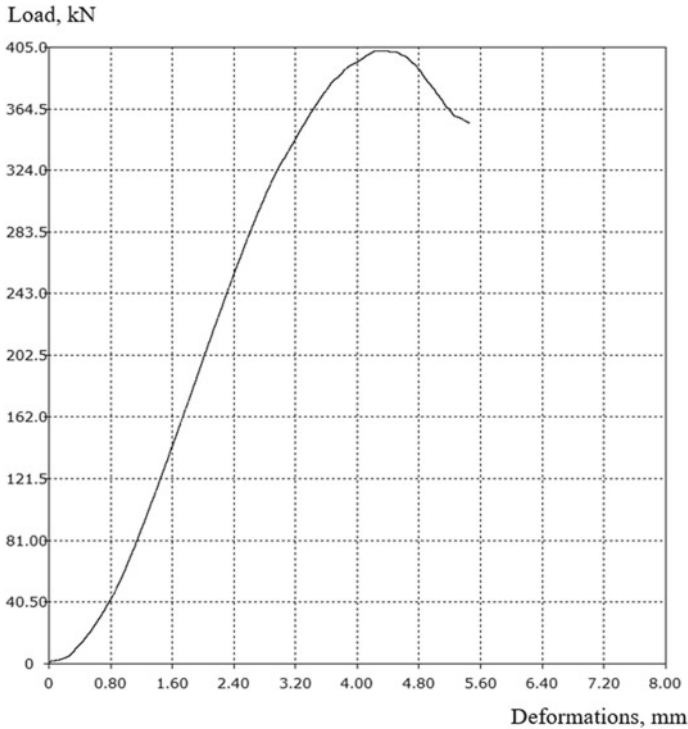


Fig. 5 «Deformations – load» during full-scale tests of compressible samples

The problem of numerical study of the stress–strain state of a reinforced concrete cylinder in a polymer composite casing was solved by making and analyzing three-dimensional models of bridge columns created using the ANSYS software package. The numerical model of the sample is shown in Fig. 6.

In the sample model, the lower nodes have movement restrictions in all directions, to simulate the embedding of the rack in the grillage, and the upper nodes do not move along the Z axis. The applied longitudinal compressive force is implemented over the entire cross-sectional area of the sample.

The general results of numerical simulation and full-scale testing of samples demonstrate the adequacy of the model, since the vertical displacements have discrepancies of no more than 6%. In Fig. 6, one can see a clear distribution of stresses in the contact zone of concrete with fiberglass reinforcement, namely, the inclusion of only the outer fibers of the helix in the tensile work. Therefore, it is not recommended to take the diameter of the glass composite reinforcement more than 8 mm, due to the incomplete use of the reinforcement section. Another reason for limiting the diameter of the rod is the difficulty in winding the helix onto the column. The surface of interaction of fiberglass reinforcement and old reinforced concrete is a stress concentrator, therefore, there is a destruction of the protective layer of concrete at the points

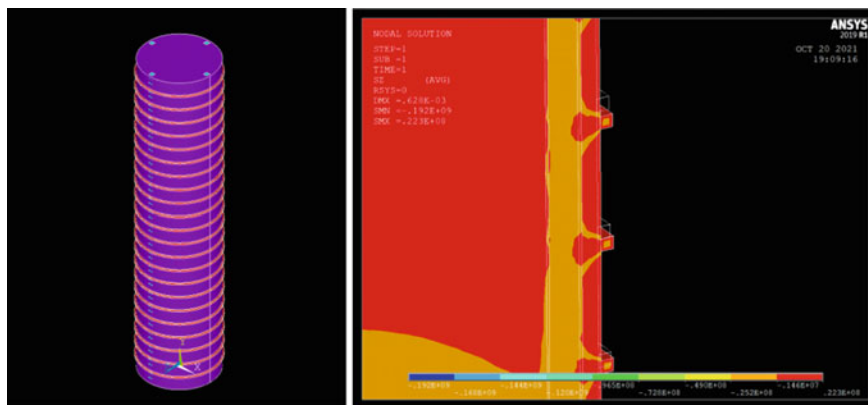


Fig. 6 Tension distribution in a 3D model of a compressible sample

of contact and a redistribution of stresses in the power spiral. The numerical model made it possible to reveal an increase in radial displacements in the sample, which were observed along the outer face in the interval of 0.1–0.3 of the sample height, which was well substantiated by the momentless theory of thin shells. When testing samples reinforced with a cage in this zone, crack development was observed and a break in the power spiral occurred.

4 Conclusions

The design solutions developed for the abutment reinforcement caging demonstrated good resistance to compressive forces. The breaking load of samples with a polymer-composite holder increased on average by 60%. The conducted studies prove that the developed reinforcement method can significantly increase the bearing capacity of a compressible structure, protect it from atmospheric and other types of influences. The developed calculation method takes into account the influence of the pitch of the turns of the power spiral and the diameter of the fiber-reinforced plastic rebar on the bearing capacity of the structure. The diameter of the reinforcement and the pitch of the turns are set based on the design requirements and the complexity of the work.

An analysis of numerical simulation results and full-scale testing of samples shows the true operation of the cage. Only the outer fibers of the fiberglass reinforcement of the spiral work in tension, therefore the diameter of the rebar for the power spiral must be limited to 8 mm. The helix pitch should be increased at an interval of 0.1–0.3 of the sample height from the embedment, in order to absorb the maximum tensile stresses in the rebar.

References

1. Provotorov, I., Gasilov, V., Anisimova, N.: Problems of increased transport load as a result of implementation of projects of high-rise constructions. In: E3S Web of Conferences, vol. 33, no. 18, p. 03019. (2018). <https://doi.org/10.1051/e3sconf/20183303019>
2. Solovev, B.V.: Features of the design and operation of reinforced concrete road bridges, taking into account the increased loads from transport. Vestnik Yuzhno-Ural'skogo State Univ. Constr. Arch. **35**(168), 14–15 (2009)
3. Drobishevskiy, B.A.: Problems of small bridge building. Transp. Constr. **11**, 22–24 (2005)
4. Miroshnik, V.A.: Problems of accident rate of bridge structures. Bridges Tunn. Theory Res. Pract. **1**, 55–59 (2012)
5. Ivancev, I.I.: Reinforced Concrete Road Bridges, p. 278. Association of Construction Universities, Moscow (2008)
6. Ono, K: Structural materials: Metallurgy of bridges. In: Kaufman, B., Briant, C., (eds.) Metallurgical Design and Industry. Prehistory to the Space Age, 1st edn, pp. 193–269. Springer, Cham (2018)
7. Park, R.: Concrete, reinforced. In: Meyers, R.A. (ed.) Encyclopedia of Physical Science and Technology, 3rd edn., pp. 583–602. Academic Press, Cambridge (2003)
8. Ovchinnikova, T.S.: Corrosion and anti-corrosion protection of reinforced concrete bridge structures. Internet J. «Naukovedenie» **5**(24), 1–25 (2014)
9. Chitty, W.J., Dillmann, P., Hostis, V., Lombard, C.: Long-term corrosion resistance of metallic reinforcements in concrete - a study of corrosion mechanisms based on archaeological artefacts. Corros. Sci. **47**(6), 1555–1581 (2005). <https://doi.org/10.1016/j.corsci.2004.07.032>
10. Abbood, I.S., Odaa, S.A., Hasan, K.F., Jasim, M.A.: Properties evaluation of fiber reinforced polymers and their constituent materials used in structures: a review. Mater. Today Proc. **43**, 1003–1008 (2021)
11. Smits, J.: Fiber-reinforced polymer bridge design in the netherlands: architectural challenges toward innovative, sustainable, and durable bridges. Engineering **2**, 518–527 (2016)
12. Rosnovskiy, V.A.: Pipe Concrete in Bridge Building, p. 110. Transdorjilisdat, Moscow (1963)
13. Kendall, D.: Developments in FRP bridge design. Reinforced Plast. **54**, 13–20 (2010)
14. Shendrik, V., Druzhinin, P., Bobobekov, O.: Evaluation of the effectiveness of the method for calculation of composite materials in the construction of the bridges in terms of their safety and reliability. Transp. Res. Procedia **20**, 596–601 (2017)
15. Li, X., Wang, L.G., Gao, H.Y., Zhang, N.: Experimental investigation on behavior of splicing glass fiber-reinforced polymer-concrete-steel double-skin tubular columns under axial compression. Adv. Struct. Eng. **25**(6), 1357–1368 (2022)
16. Zeng, L., Li, L., Chen, G., et al.: Experimental study on mechanical behavior of GFRP-recycled concrete-steel tubular columns under axial compression. Chin. Civil Eng. J. **47**(2), 21–27 (2014)
17. X. Zou, H. Lin, P. Feng, Y. Bao, J. Wang A review on FRP-concrete hybrid sections for bridge applications. Comp. Struct. **262**, 113336 (2021)
18. Shilin, A.A., Zaicev, M.V., Kartuzov, D.V.: A guide to strengthening reinforced concrete structures using composite materials, Moscow, p. 226 (2017)
19. Zinnurov, T.A., et al.: Numerical modeling of composite reinforcement with concrete. J. Phys. Conf. Ser. **1158**, 042046 (2019). <https://doi.org/10.1088/1742-6596/1158/4/042046>
20. Zinnurov, T.A., Majstrenko, I.Y., Erokhin, D.I., Zamilova, A.K., Umarov, B.S.: Investigation of the effect of thickenings in fiberglass reinforcement (FRP) on adhesion to concrete. News KSUAE **2**(56), 84–93 (2021). https://doi.org/10.52409/20731523_2021_2_84
21. Mukhametrakhimov, R.K., Lukmanova, L.V.: Influence of Portland cements with different mineralogical composition on basic properties of 3D-printed composites. News KSUAE **2**(56), 37–49 (2021). https://doi.org/10.52409/20731523_2021_2_37

Processing of Thermal Power Waste into Composite Materials Using Coke Waste



Galina Medvedeva , Alsu Yusupova, Kamilya Giniyatova, and Kamilla Minikaeva

Abstract At the current stage of construction, the basic trend in resource saving is the use of secondary materials, i.e., waste products. The most recent energy-efficiency standards require higher thermal resistance of exterior enclosing structures. These characteristics are difficult or impossible to achieve by means of traditional building materials used in domestic production. Therefore, new technologies of multilayered structures involving the use of efficient insulation materials are being created. This article describes a new composite material made on the basis of waste from coke production (Kemerovo, Russia). The production of the samples of this material is described, as well as its physical and mechanical properties. Specified composite material is cement containing coke waste, with or without a protective coating (obtained by impregnation in sulfur melt). The study showed that the material made from coke waste and impregnated with sulfur has satisfactory parameters in terms of the main aspects, specifically, energy conservation, strength, cost-effectiveness and increased thermal insulation properties, resulting in expanding the scope of considered materials and using them as thermal insulation in exterior walls.

Keywords Thermal insulation material · Coke waste · Composite material · Energy conservation

1 Introduction

Today, a huge amount of industrial waste has accumulated in the Russian Federation, polluting the environment and taking up a lot of land. Consequently, the problem of collection and disposal of production and consumption waste is one of the oldest in human history. The main purpose of waste management is the prevention of harmful impact of industrial waste on human health and the environment. The conditions of

G. Medvedeva (✉) · K. Giniyatova · K. Minikaeva
Kazan State University of Architecture and Engineering, Kazan, Russia
e-mail: medvedevaga79@mail.ru

A. Yusupova
Kazan National Research Technological University, Kazan, Russia

existence and development of life on Earth are determined by environmental factors, i.e., elements of the environment that significantly affect living beings. The use of technogenic products in the production of building materials contributes to the solution of the following main tasks: energy and raw material conservation, waste management, environmental improvement in the regions [1, 2].

Thermal insulation materials are one of the most common groups of materials. They are used for the manufacture of building structures in conjunction with structural materials that resist loads resulting from the process of operation due to high strength, and cladding materials that protect insulating and structural materials from external impacts due to resistance to various factors (mechanical actions, aggressive chemicals, ultraviolet, etc.). For their part, thermal insulation materials provide a comfortable temperature condition due to the low thermal conduction coefficient. In addition, the materials provide energy efficiency of buildings and technological processes when used in construction and technical insulation [3].

The use of industrial waste provides an opportunity to meet up to 40% of the construction requirements of raw materials. Furthermore, this allows to reduce the costs associated with production of building materials by 10–30% compared to production from natural raw material. In addition, industrial waste can be used to create new building materials with high technical and economic characteristics [4–9].

Sulfur composite materials with high waterproof strength properties are known [10–12], as well as technologies for obtaining waterproof coatings by impregnation in a sulfur melt [13–15]. From this perspective, the water-resistant and strength properties of concrete can be improved. However, there is no information in the literature about the sulfur impregnation of cement concrete modified with coke waste. We are of the opinion that this surface treatment would significantly improve the water-resistant and strength properties of the modified composite materials and, thereby, expand the field of management of coke waste and sulfur waste from the oil refining complex.

2 Main Body

This composite material is a cement containing coke dust, with or without a protective coating (obtained by sulfur impregnation).

The basic materials are:

- 1) Cement M500 (GOST 31,108–2020);
- 2) Sulfur, which is a waste product of the Nizhnekamsk refinery (GOST 127- 03);
- 3) Silica sand (GOST 8736–2014);
- 4) Coke dust, which is a waste product of the Industrial Metallurgical Holding «Koks» (Kemerovo, Russia). TU 0763–199-00,190,437–2004 «Coke dusts. Technical specifications».

Elemental composition of dry ash-free coke mass (%): 96–98 of carbon, 0.5–1.2 of hydrogen, 0.3–1.1 of oxygen (Table 1).

Table 1 Main characteristics of coke dust

Parameter name	Altai-Koks	Test method
Piece size, mm	0–10	
Ash content %, max	20.0	GOST R 55,661–2013
Mass fraction of total moisture, %, max	24.0	GOST 27,588–91
Mass fraction of total sulfur, %, max	4.2	GOST 8606–93 or GOST 2059–95
Mass fraction of pieces over 10 mm, %, max	8	GOST 5954.2–91

The composition samples were made by mixing the following initial components: cement, sand and coke in various proportions:

- 1st batch – 1:3 ratio;
- 2nd batch – 1:2:1 ratio;
- 3rd batch – 1:1:2 ratio;
- 4th batch – 1:3 ratio (without adding sand).

In terms of the mechanical strength characteristics, the favorable ratio is as follows: cement: filler (sand and coke dust) ratio of 1:3. Therefore, this mixture ratio was maintained in the work. Samples were made from the resultant mixtures by pouring into molds $2 \times 2 \times 6$ cm in size.

The adding of coke waste to the cement concrete composition allows to improve the thermal insulation properties of concrete.

With an increase in coke dust in the composition, the thermal conductivity of the samples decreases due to the formation of a porous structure.

With an increase in coke waste in the filler, the strength decreases by 2.7 times. Samples in which coke waste is the only component of the filler have extremely low strength and fall to pieces when under light load. The reason for this is the formation of a porous structure of the samples and the lack of adhesion between the binder and the filler. The density decreases due to the low-specific density of the coke filler and a large number of pores and voids in the material. Open pores in samples with coke waste arise from high water absorption.

Test beams with a protective coating were made by loading the obtained samples into a container with molten sulfur at a temperature of 120–130 °C and treated with molten sulfur for 30 min. Following that, the resulting products were removed from the impregnation chamber and cooled to ambient temperature. The cooling process was followed by crystallization of the melt in the pore space. Consequently, the properties of the material changed.

The results of physical and mechanical testing of the obtained materials are presented in the figures below.

Figure 1 shows a graph of the dependence of the ultimate compressive strength of the initial compositions with and without sulfur impregnation. The strength of the samples impregnated with the sulfur melt increased compared to the initial samples.

Thus, samples of a composite material based on coke waste of the tailored composition had a compressive strength of 14 MPa. The material impregnated with sulfur had a compressive strength of 74 MPa, i.e., the strength increased by 6 times after impregnation. Compressive strength of cement: coke dust samples became higher after impregnation (compressive strength increased by 4 times).

Figure 2 shows a graph of the dependence of the water absorption of initial samples with or without sulfur impregnation.

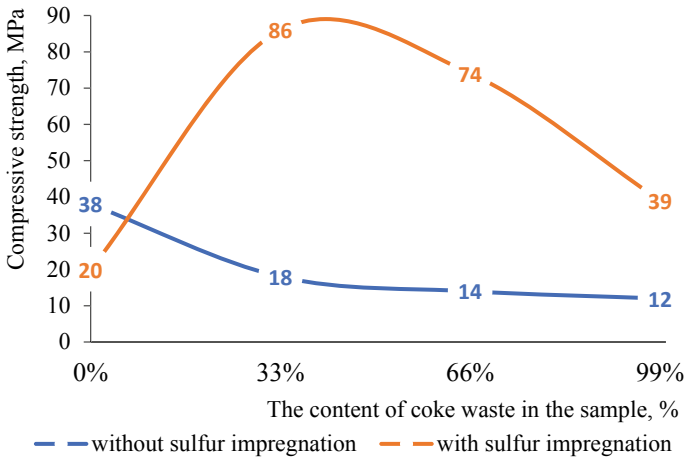


Fig. 1 Compressive strength of composite material samples with different content of coke waste and with or without sulfur impregnation

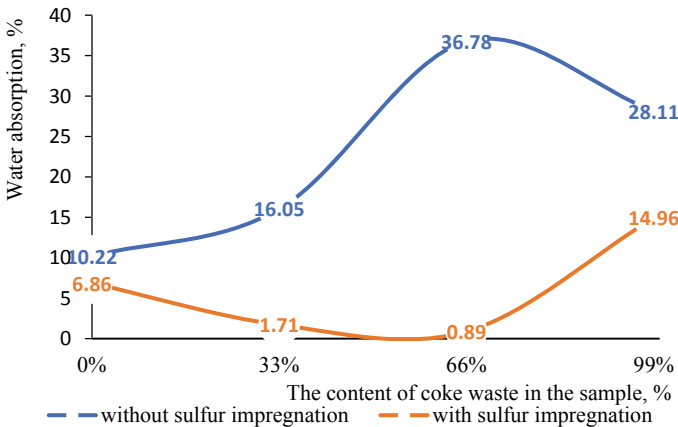


Fig. 2 Dependence of water absorption of composite material samples with different content of coke waste with or without sulfur impregnation

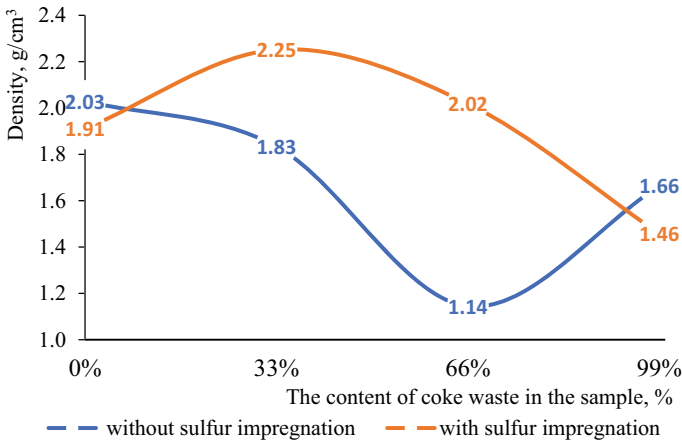


Fig. 3 Dependence of the density of composite material samples with different content of coke waste with or without sulfur impregnation

It can be seen that sulfur impregnation increases the water resisting property of building composite materials. Water absorption decreased up to 40% in composite material samples with coke waste impregnated with sulfur melt.

The density of the composite material modified with coke waste also increases after impregnation (Fig. 3).

The micrographs of the samples treated by sulfur impregnation method show a light layer on the surface due to the formation of a dense protective layer of sulfur. In the near-surface layer, a slightly green color is observed, which is specific to sulfides. This can be explained by partial chemical interaction of sulfur and cement components (e.g., calcium hydroxide) with the formation of calcium sulfide. The samples have a coating with a greater depth of impregnation (up to 1 cm in thickness), as a result, they have increased strength, density and low water absorption.

On the basis of X-ray phase analysis, it was found that the surface coating consists mainly of crystalline quartz, orthorhombic sulfur, and calcium sulfide.

In summary, the strength of the samples increased significantly after treatment with sulfur impregnation. The compressive strength also increased by almost 6 times. The material based on coke waste of the tailored composition had a compressive strength of 14 MPa, the material impregnated with sulfur had a compressive strength of 74 MPa. Additionally, their density increased from 1.14 to 2.02 g/cm³; water absorption decreased to 0.8%.

3 Conclusion

Summing up what has been said, the study showed that the material made from coke waste and impregnated with sulfur has satisfactory characteristics in terms of the main parameters, specifically:

- energy conservation, since the material has a low thermal conduction coefficient and can be used as a thermal insulation material;
- strength, the material acts as a structural material, as it has satisfactory strength characteristics;
- cost-effective for structural application.

That is, this material preferably combines the characteristics of an insulating material and a structural wall material.

One of the major considerations for using this material is the environmental aspect. A viable option for recycling coke dust can offer an opportunity to solve a great many of the environmental problems associated with the disposal of this waste.

References

1. Pichugin, A.P., Denisova, A.S., Hritankov, V.F.: Environmental problems of efficient use of waste and local raw materials in construction. *Build. Mater.* **3**, 73–75 (2005)
2. Medvedeva, G.A., Akhmetova, R.T., Grigorievich, L.A.: Use of wastes from thermal power industry in manufacturing of high-strength sulfur concrete. *Res. J. Pharmaceut. Biol. Chem. Sci.* **7**(1), 1969–1981 (2016)
3. Kolosova, A.S., Pikalov, E.S.: Modern effective heat-insulating materials on organic basis. *Int. J. Appl. Fund. Res.* **4**, 74–85 (2021)
4. Shishelova, T.I., Samuseva, M.N.: Directions of using ash and slag materials (ZShM) of thermal power plants of the Irkutsk region as secondary raw materials. *Progr. Mod. Nat. Sci.* **2**, 24–26 (2007)
5. Sulejmanova, L.A., Pogorelova, I.A., Marushko, M.V.: The use of composite binders in the technology of aerated concrete. *Bull. Belgorod State Technol. Univ. Named After. V. G. Shukhov* (2), 10–16 (2018)
6. Bazhenov, Yu.M.: *Technology of concrete*. Higher School, Moscow (1987)
7. Siddique, R.: Waste materials and by-products in concrete. In: *Waste Materials and By-Products in Concrete* (2008)
8. Kareeva, J., Gabdrafikov, R., Chukhlova, M.: Selection of model for the numerical study of the convective jet problem. In: *E3S Web of Conferences*, vol. 274 (2021)
9. Akhmerova, G.M., Fedorov, A.V.: The influence of soil moisture on heat losses of pipes in the impassable channels. *Proc. Kazan State Univ. Arch. Civil Eng.* **2**(36), 117–121 (2016)
10. Korolev, E.V., Proshin, A.P., Erofeev, V.T.: *Building materials based on sulfur*. Penza (2003)
11. Yusupova, A.A., Akhmetova, R.T., Treshchev, A.A.: Sulfur composite technology from oil refinery waste. *IOP Conf. Ser. Mater. Sci. Eng.* **5**, 3057–3061 (2019)
12. Fomin, A.Y., Khozin, V.G.: New sulfur-containing materials. *World Road* **S1**, 61–63 (2018)
13. Medvedeva, G.A., Ahmetova, R.T., Pyatko, Yu.N.: Utilization of thermal energy waste into composite heat-insulating materials. *J. Ecol. Ind. (J. Tatar Branch Russ. Ecol. Acad.)* **1**(45–46), 47–50 (2012)

14. Medvedeva, G.A., Ahmetova, R.T., Stroganov, V.F.: Technology of waterproof heat-insulating materials by the impregnation method. *Bull. Technol. Univ.* **21**, 18–20 (2012)
15. Medvedeva, G.A., Ahmetova, R.T., Safin, I.S.: Utilization of waste heat power in the production of heat insulating materials impregnated with a melt of sulfur. *News KSUAE* **2**(28), 310–315 (2014)

Economic Efficiency Substantiation of the Use of a Sectional Coil Exchanger in an Individual Heating Point System



Elvira Shagiakhmetova , Anna Romanova , Yakov Zolotonosov , Pavel Martynov , and Ella Biktemirova 

Abstract The environmental problem associated with the concentration of greenhouse gases and the consequent global warming of the climate should be addressed in an integrated manner. The authors propose the calculation of economic efficiency of a fundamentally new design of a heat exchanger based on intensification of processes of hydrodynamics and heat exchange. Switching to a new type of heat exchange equipment will save operating costs in residential apartment buildings, reducing CO₂ concentration. When performing economic calculations, the methods of calculating the net present value of the project (NPV), discounted payback period (PBP), as well as the method of calculating the expected monetary result (EMV) for the risk insurance budget were used. Calculations were performed for two scenarios: basic and strategic. The discounted payback period from the replacement of one heat exchanger unit for the base scenario was 5.66 years, and for the strategic scenario – 2.73 years. The heat exchangers in question have a wide range of industrial applications, including: chemistry and petrochemicals, power engineering, household appliances, food and medical industries, shipbuilding and a number of related industries. Market analysis has shown that 4,000 units of new heat exchange equipment can be installed in the Republic of Tatarstan by 2033. At the same time, the reduction of greenhouse gas emissions in 2033 will amount to 81,160 tons of carbon dioxide equivalent.

Keywords Hot water services · Carbon footprint · Energy consumption · Economic efficiency

1 Introduction

According to the assessment of the Intergovernmental Panel of Experts of the Russian Federation on Climate Analysis, since the 1970s there has been a global change

E. Shagiakhmetova (✉) · A. Romanova · Y. Zolotonosov · P. Martynov · E. Biktemirova
Kazan State University of Architecture and Engineering, Kazan, Russian Federation
e-mail: elvirale@mail.ru

in climatic conditions in the world. It is caused by an increase in air temperature and is associated with the concentration of greenhouse gases in the atmosphere. These processes are directly related to the increase in energy consumption with 40% of buildings. Many modern scientists are considering the possibility of reducing energy costs. For example, Małgorzata Fedorczyk-Cisak, Anna Kotowicz, Elżbieta Radziszewska-Zielina, Bartłomiej Sroka, Tadeusz Tatar and Krzysztof Barnas believe that the energy consumption of a building depends not only on the installation solutions and materials, but also on the location of the object relative to others. Therefore, a proper urban layout is necessary [1]. Herie Park considers it necessary to create a building energy management system (BEMS) to balance energy production and consumption [2]. According to Rishi K. Jane, Kevin M. Smith, Patricia J. Callaghan, John E. Taylor, the ability to predict a building's energy consumption using sensors using machine learning techniques is vital to reducing the carbon footprint of buildings [3]. Arvind's paper notes that energy saving by increasing energy efficiency in a building has become of paramount importance all over the world [4], Antti Kosonen, as well as Maria Herrando, Antoniom. Pantaleo, Kaywang, Kristosn. Markides, Hayreldin faraj, Mahmudhaled, Jalalfaraj, Faruahem, Katicasteline, that renewable energy sources and technical solutions are needed to reduce greenhouse gas emissions from buildings [5–7]. Romanova A. and the co-authors consider environmental building and prove in their article. Sustainable development of the field of operational services on innovative basis of smart technologies [8, 9].

Scientists do not ignore the issues and social effects. The development of energy poverty, according to Maria Mrówczyńska, Marta Skibaa, Anna Bazan-Krzywoszanska, Małgorzata Sztubecka is due to the fact that the group of households with the lowest income consumes more electricity due to the fact that these households are unable to equip themselves with newer household appliances and lighting with lower energy consumption. [10]. Hu S, Yan D, Azar E, Guo F believe that the reduction of greenhouse gas emissions and the global shift to clean energy in buildings is primarily influenced by the behavior of residents themselves [11].

Some studies have focused on climate change and the impact of these changes on building performance, in particular on energy consumption. Francesco Mancini and Gianluigi Lo Basso, based on the example of Italy, substantiate that climate warming leads to a decrease in the need for heating much higher than an increase in the need for cooling. The annual savings in primary energy in a year can even be higher than 20% [12]. Seleshi G. Yalew, Michelle T. H. vanVliet, David E. H. J. Gernaat and others also believe that on a global scale, one can expect a potential increase in the need for cooling and a decrease in the need for heating [13].

Other authors focus on different building elements. Mario Maiolo Behrouz Pirouz, Roberto Bruno, Stefania Anna Palermo, Natale Arcuri and Patrizia Piro consider the role of a green roof in the Mediterranean climate in mitigating internal temperature fluctuations [14]. K I Logachev, A M Ziganshin, O A Averkova and A B Goltsov solve energy consumption problems by developing energy efficient local ventilation systems [15]. Ettore Zanetti, Marcello Aprile, Dongsuk Kum, Rossano Scoccia, Mario Motta offer a hybrid PV heating system with 20% reduction in

energy consumption and 10% reduction in CO₂ emissions [16]. Studies conducted in Switzerland by Portia Murray, Julien Marquant, Mathias Niffeler, Georgios Mavromatidis, Kristina Ore-hounig show that the most cost-effective measures to achieve future emission targets should include roof upgrades and substitution. The windows together with the photovoltaic unit [17]. Taimarov M. A., Lavirko Yu. V. Provide urban gas with secondary heat resources to address energy conservation and reduce the cost of natural gas [18]. That heating systems, with the development of thermal processes, efficient cooling technologies with the possibility of removing heat from areas with high heat flow are in demand. According to M. M. Sarafraz, Mohammad Reza Safaei, Zhe Tian, Marjan Goodarzi, Enio Pedone Bandarra Filho and M. Arjomandi heat exchangers of the new configuration are small but provide higher thermal efficiency and longer service life [19].

Thus, in order to reduce the energy consumption of buildings and thereby reduce their carbon footprint, it is possible to implement various measures, including by replacing heat exchange equipment with new models. The aim of the study is to prove the economic viability of a new type of heat exchange equipment developed by a group of scientists headed by Professor Zolotonosov Y [20–24].

2 Methods

The following methods were used:

1. Methods of statistical analysis of data;
2. Method of calculation of the net present value of the project [26, 26]:

$$NPV = \sum_{t=1}^T \frac{C_t}{(1+d)^t} - \sum_{t=1}^T \frac{I_t}{(1+d)^t} - I_0 \quad (1)$$

where d – is a discounting rate;

C_t – it is the economic effect of the introduction of heat exchange equipment in the period t ;

I_t – operating costs in the period t ;

I_0 – initial investment в приобретение и монтаж теплообменного оборудования in the project.

Method of Calculation of the Expected Monetary Result (EMV) to quantify project risks by phase of implementation and risk budgeting:

$$EMV = \sum_{n=1}^N Pr_n \times I_n \quad (2)$$

where P_m – probability of project risk at step n ;

I_n – the effect of risk on a project if it occurs in a period of n .

4. Method of Calculation of the Net Present Value of the project, taking into account the development and EMV.

$$NPV(1) = \sum_{t=1}^T \frac{C_t}{(1+d)^t} - \sum_{t=1}^T \frac{I_t}{(1+d)^t} - I_0 - I - EMV, \quad (3)$$

where I- development work costs

5. Graphical method of presenting the final results of the study.

3 Results and Discussion

Heat exchange equipment accounted for more than 70 per cent of the production structure of important industries in the Russian Federation. An analysis of their design has shown that in industry and housing and communal services, mainly surface heat exchangers with a high level of moral and physical wear (up to 80%) are mainly used [23].

At the moment, there are acute issues related to the improvement of heat exchange equipment, its reconstruction and modernization to increase the efficiency of power plants.

In order to solve these problems, a series of innovative heat exchange equipment proposed by Professor of the Kazan State University of Architecture and Engineering Y.D. Zolotonosov is offered [24]. The heat exchange equipment in question can be used to replace imports of a plate heat exchange apparatus.

It should be noted that the class of foreign plate heat exchangers is designed for operating conditions where the water recharge is less than 0.1 mg - eq/l. While for Russia's heat networks the water supply is fixed at 0.7 mg - eq/l.

The increased stiffness of the of the recharging water in the Russian Federation causes an active growth of salt deposits on the heat exchange surface of the apparatuses and requires frequent extraction of the sheaf of their sheath and its washing using chemical means. At the same time, numerous rubber sealing gaskets suffer, which are not subject to reuse in the future. The price of the purchased gasket material is about 30% of the total cost of a new plate heat ex-changer.

The constructions of innovative heat exchange equipment include: small-bar sectional heat exchange units of conical and spherical shape, the internal heat exchange elements of which are in the form of smooth pipes or spring twisted channels, the coils of which are rigidly fastened by laser welding, or in the form of screw pipes of the "confuser-diffuser" type made by the method of rotational forging. Also proposed are tubular heat exchangers of a non-rigid structure, tubular beams of which are composed of elements of the type «pipe in a pipe», and in the bases thereof floating heads [24].

Tests of a prototype sectional coil heat exchanger were carried out in a 14-storey single-entrance residential building in Kazan, which showed the prospects of its use

Fig. 1 General view of the IHP with a sectional coil heat exchanger during testing in a 14-storey single-entrance residential building in Kazan



as a water heater of an individual heating point (IHP) for a hot water supply system (Fig. 1).

During the five-day winter tests, its estimated capacity of 5 m³/h was confirmed. The thermal load for the entire study period was 17.8 Gcal, the water temperature for the needs of hot water supply fell within the normative values of + 58 ...62°C. In addition, 2.26 Gcal of thermal energy was saved for heating cold water (the initial temperature of which was +5°C) for 5 days of testing, which in monetary terms in terms of a year will amount to about 170,036 rubles.

Saving thermal energy will reduce CO₂ emissions, which, among other things, will allow the Russian Federation to move into a low-greenhouse-gas-emitting development trajectory. The reduction of the carbon footprint with the use of one heat exchanger of the new sample will amount to 20.29 tons. If the cost of 1 ton of carbon unit is 20 euros, the savings per year will be equal to 35,516 rubles (Table 1).

It should be noted that the heat exchangers described in the works of Y.D. Zolotonosov [20–24] have a wide range of industrial applications, including: chemistry and petro chemistry, energy, housing and communal services, food and medical industry, shipbuilding and a number of related industries. Market analysis has shown that 4,000 units of new heat exchange equipment can be installed in the Republic of Tatarstan by 2033. At the same time, the reduction of green-house gas emissions in 2033 will amount to 81,160 tons of carbon dioxide equivalent (Fig. 2).

When performing calculations to substantiate the economic efficiency of the introduction of new heat exchange equipment, two calculation options were considered: basic and strategic. The basic scenario takes into account only the reduction in the cost of Gcal consumption of thermal energy, operating costs and metal consumption during production. While the strategic option, in addition to the basic data, takes into account the reduction of the carbon footprint of enterprises and apartment buildings that have installed new heat exchange equipment (Table 2).

Table 1 Table captions should be placed above the tables

Number	Name	Value	Unit of measurement
1	Saving thermal energy for 5 days of use	2.26	Gcal
2	Thermal energy savings during the year	94.92	Gcal
3	Converting Gcal to kW	110,372.093	kW
4	Coefficient of thermal energy conversion (fuel-natural gas)	0.1838	–
5	Reduction of CO2 emissions per year	20.29	T
6	Average cost per ton of carbon unit	20	
7	Rate of the euro against the ruble	90	rub./eur
8	Savings in CO2 emissions per year	36 516	rub.

(Source Calculated by authors based on <https://www.carbonfootprint.com/calculator.aspx>)

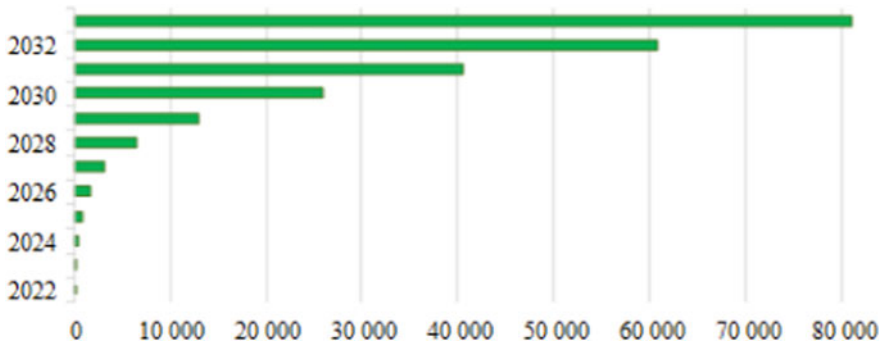


Fig. 2 Reduction of greenhouse gas emissions, tonnes carbon dioxide equivalent. (Source Calculated by authors)

The calculated discounted payback period for the project at a discount rate of 20 per cent would be 5.66 years for the base scenario and 2.73 years for the strategic related scenario (Fig. 3).

The EMV value has been determined for the formation of the risk insurance budget in the event of risky events such as: postponement of the timing of the selection of structures and the development of drawings of a full-scale sample, postponement of the development of drawings of technological equipment of machine equipment, non-compliance of the temperature of the heated medium with the required values for various variants of heat exchange equipment, etc. The final value was 3.99 million rubles.

The final performance indicators of the project of installing heat exchange equipment of a new sample at 4000 enterprises and apartment buildings of the Republic of Tatarstan are presented in Table 3.

The discounted cash flow values by year for the NPV value are shown in Fig. 4.

Table 2 Basic data for calculating the cost of hot water services (per unit of heat exchange equipment)

Number	Name	Value		Unit of measurement
		Basic scenario	Strategic scenario	
1	The cost of heat exchange equipment	70 000		rub.
2	The cost of installation and commissioning works	140 000		rub.
3	Operating costs per year	120 000		rub.
4	Reduction of the cost of consumption of Gcal of thermal energy, operating costs and metal consumption in production per year	170 036		rub.
5	Reduction of the carbon footprint per year	–	36 516	rub.

(Source Calculated by authors)

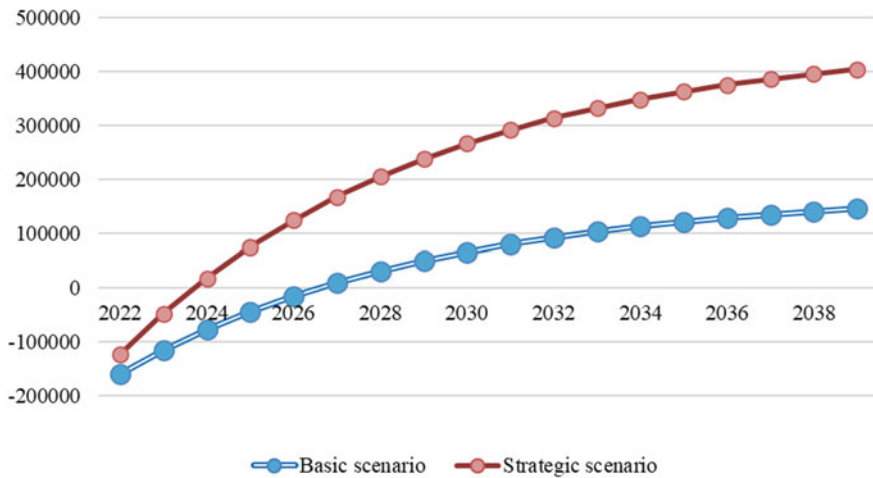
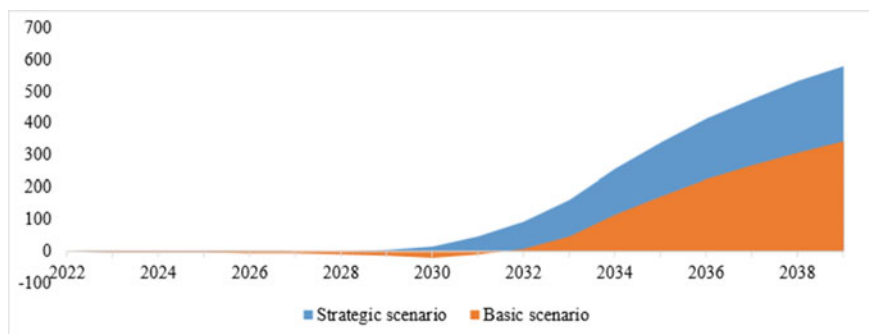


Fig. 3 The calculated discounted payback period for the project at a discount rate of 20 per cent would be 5.66 years for the base scenario and 2.73 years for the strategic related scenario (Source Calculated by authors)

Table 3 Efficiency indicators (per 4000 units of heat exchange equipment)

Number	Name	Value		Unit of measurement
		Basic scenario	Strategic scenario	
1	Annual discount rate, d	20		%
2	NPV	344.29	581.93	mln. rub.
3	EMV	3.99	3.99	mln. rub.
4	I	27.51	27.51	mln. rub.
5	NPV (1)	312.79	550.43	mln. rub.

**Fig. 4** Discounted cash flow (for NPV). (Source Calculated by authors)

4 Conclusions

A new type of modernized heat exchanger surfaces improves the efficiency of heat transfer reducing the cost of hot water supply and thus reducing the carbon footprint of buildings. In addition, the elements of the heat exchanger, which are made in the form of spring-rolled pipes, lead to a decrease in the metal consumption during the production thereof, in turn, affect the final cost of the product. The base scenario, which takes into account reduced heat consumption costs, operating costs and metal capacity, is 5.66 years, with a reduced carbon footprint of 2.77 years for one unit of heat exchanger. The accumulated value of the net cash flow for 4000 items of the equipment under consideration will be the minimum (base scenario) 312, 79 million rubles, maximum (strategic scenario) 550.43 million rubles. with an 18-year planning horizon.

Further research involves the creation of semi-industrial samples of the heat exchangers, the conduct of experimental research on their heat Hydrodynamic characteristics with monitoring of the temperature of the heated medium to the required values. This will make it possible to start their industrial production and implementation at enterprises and apartment buildings of the Republic of Tajikistan.

The proposed series of heat exchange equipment, taking into account the efficiency, the complex of consumer properties and the modern organization of its production, can compete significantly with foreign analogues.

References

1. Fedorczyk-Cisak, M., Kotowicz, A., Radziszewska-Zielina, E., Sroka, B., Tatara, T., Barnaś, K.: Multi-criteria optimisation of an experimental complex of single-family nearly zero-energy buildings. *Energies* **13**(7), 1541 (2020). <https://doi.org/10.3390/en13071541>
2. Park, H.: Human comfort-based-home energy management for demand response participation. *Energies* **13**(10), 2463 (2020). <https://doi.org/10.3390/en13102463>
3. Jain, R.K., Smith, K.M., Culligan, P.J., Taylor, J.E.: Forecasting energy consumption of multi-family residential buildings using support vector regression: Investigating the impact of temporal and spatial monitoring granularity on performance accuracy. *Appl. Energy* **123**, 168–178 (2014). <https://doi.org/10.1016/j.apenergy.2014.02.057>
4. Chel, A., Kaushik, G.: Renewable energy technologies for sustainable development of energy efficient building. *Alexandria Eng. J.* **57**, 655–669 (2017)
5. Kosonen, A., Keskiisaari, A.: Zero-energy log house – Future concept for an energy efficient building in the Nordic conditions. *Energy Build.* **228**, 110449 (2020)
6. Herrando, M., Pantaleo, A.M., Wang, K., Markides, C.N.: Solar combined cooling, heating and power systems based on hybrid PVT, PV or solar-thermal collectors for building applications. *Renew. Energy* **143**, 637–647 (2019). <https://doi.org/10.1016/j.renene.2019.05.004>
7. Faraj, K., Khaled, M., Faraj, J., Hachem, F., Castelain, C.: Phase change material thermal energy storage systems for cooling applications in buildings: a review. *Renew. Sustain. Energy Rev.* **119**, 109579 (2020). <https://doi.org/10.1016/j.rser.2019.109579>
8. Romanova, A.I., Berval, A.V., Burkeev, D.O., Ilyina, E.V., Egorov, D.A.: Evaluation of savings on operational services from innovative energy-saving materials. *IOP Conf. Ser. Mater. Sci. Eng.* **786**(1), 012029 (2020)
9. Romanova, A., Ilina, E.: Sustainable development of the field of operational services on innovative basis of smart technologies. In: *E3S Web of Conferences*, vol. 274, p. 10012 (2021)
10. Mrówczyńska, M., Skibaa, M., Bazan-Krzywoszańska, A.: MałgorzataSztubeckab Household standards and socio-economic aspects as a factor determining energy consumption in the city. *Appl. Energy* **264**, 114680 (2020). <https://doi.org/10.1016/j.apenergy.2020.114680>
11. Shan, H., Yan, D., Azar, E., Guo, F.: A systematic review of occupant behavior in building energy policy. *Build. Environ.* **175**, 106807 (2020). <https://doi.org/10.1016/j.buildenv.2020.106807>
12. Mancini, F., Basso, G.L.: How climate change affects the building energy consumptions due to cooling, heating, and electricity demands of italian residential sector. *Energies* **13**(2), 410 (2020). <https://doi.org/10.3390/en13020410>
13. Yalaw, S.G., van Vliet, M.T.H., Gernaat, D.E.H.J., Ludwig, F., Miara, A., Park, C., Byers, E., De Cian, E., Piontek, F., Iyer, G., Mouratiadou, I., Glynn, J., Hejazi, M., Dessens, O., Rochedo, P., Pietzcker, R., Schaeffer, R., Fujimori, S., Dasgupta, S., Mima, S., da Silva, S.R.S., Chaturvedi, V., Vautard, R., van Vuuren, D.P.: Impacts of climate change on energy systems in global and regional scenarios. *Nat. Energy* **5**, 794–802 (2020). <https://doi.org/10.1038/s41560-020-0664>
14. Maiolo, M., Pirouz, B., Bruno, R., Palermo, S.A., Arcuri, N., Piro, P.: The role of the extensive green roofs on decreasing building energy consumption in the mediterranean climate. *Sustainability* **12**(1), 359 (2020). <https://doi.org/10.3390/su12010359>
15. Logachev, K.I., Ziganshin, A.M., Averkova, O.A., Gol'stov, A.B.: Reducing power consumption of local exhaust ventilation systems. *J. Phys. Conf. Ser.* **1683**(4), 042015 (2020). <https://doi.org/10.1088/1742-6596/1683/4/042015>

16. Zanetti, E., Aprile, M., Kum, D., Scoccia, R., Motta, M.: Energy saving potentials of a photo-voltaic assisted heat pump for hybrid building heating system via optimal control. *J. Build. Eng.* **27**, 100854 (2020). <https://doi.org/10.1016/j.jobe.2019.100854>
17. Murray, P., Marquant, J., Niffeler, M., Mavromatidis, G., Orehounig, K.: Optimal transformation strategies for buildings, neighbourhoods and districts to reach CO2 emission reduction targets. *Energy Build.* **207**, 109569 (2020). <https://doi.org/10.1016/j.enbuild.2019.109569>
18. Taimarov, M.A., Lavirko, Yu.V.: Gas supply to residential and industrial facilities using energy-saving technologies. *News KSUAE* **3**(57), 50–60 (2021). https://doi.org/10.52409/20731523_2021_3_50
19. Sarafraz, M., Safaei, M., Tian, Z., Goodarzi, M., Filho, E.B., Arjomandi, M.: Thermal assessment of nano-particulate graphene-water/ethylene glycol (WEG 60:40) nano-suspension in a compact heat exchanger. *Energies* **12**(10), 1929 (2019). <https://doi.org/10.3390/en12101929>
20. Zolotonosov, Y.D., Gorskya, T.Y., Martynov, P.O.: A mathematical model of the heat exchanger with a spring-twisted channel made of elements of ovoid. *News KSUAE.* **1**(43), 171–178 (2018)
21. Gorskaya, T., Zolotonosov, Y., Martynov, P., Khabibullina, A., Krutova, I.: Heat exchangers with spring-twisted heat-exchange elements made of wire with sections of various geometries. *IOP Conf. Ser. Mater. Sci. Eng.* **890**(1), 012143 (2020). <https://doi.org/10.1088/1757-899X/890/1/012143>
22. Zolotonosov, Y., Krutova, I., Vachagina, E.: Geometric modeling of coil heat exchanger based on spring-twisted channel. In: Vatin, N. (ed) *Proceedings of STCCE 2021*. STCCE 2021. *Lecture Notes in Civil Engineering*, vol 169. Springer, Cham (2021). https://doi.org/10.1007/978-3-030-80103-8_21
23. Martynov, P.O., Akhmerova, G.M., Zolotonosov, Ya.D., Bagautdinova, A.G.: Efficiency and prospects of using a sectional coil water heater in the system of an individual heating point. *News Univ. Constr.* **9**(717) (2018)
24. Zolotonosov, Ya.D., Vachagina, E.K., Zolotonosov, A.Ya., Varsegova, E.K.: Innovative heat exchangers. *Constru. Calcul.*, **192** (2021)
25. Romanova, A.I., Lukmanova, E.I.: Methodology for determining the economic feasibility of the project. *Izvestia High. Educ. Inst. Constr.* **12**, 68 (2000)
26. Shagiakhmetova, E., Burkeev, D., Fedorova, S., Shaikhutdinova, D.: Improving energy efficiency of rental housing. In: *Web of Conferences, 2nd International Scientific Conference on Socio-Technical Construction and Civil Engineering (STCCE - 2021)*, France, 2021, vol. 274, p. 5001 (2021)

A Study of the Structure and Properties of a Fine Bitumen Emulsion via an Anionactive Emulsifier



Aidar Garipov, Dmitry Makarov , Vadim Khozin ,
and Sergey Stepanov 

Abstract Careful selection of an emulsifier is crucial in the process of obtaining anionactive bitumen emulsions (BE) featuring the required properties. Any emulsifier selected to produce an emulsion of high quality should be affordable, commercially feasible and easy to work with. Emulsifiers face special requirements when bitumen emulsions are being obtained since the former are instrumental in determining the structure and properties of the resulting bitumen emulsion. The mechanism of action of an emulsifier is that it reduces the surface tension at the boundary between the bitumen phases and the water phase while also building up a protective shell around the bitumen particles.

Stearic and oleic acids serve as the feedstock for the production of anionactive surfactants. However, lack of raw materials and high costs make their production quite difficult. The chemical composition of flotation asphaltic bitumen is similar to anionactive emulsifiers which are composed of higher fatty acids. Flotation asphaltic bitumen is a mixture of secondary tars which are obtained via distillation of fatty acids or from isolated tars of primary vegetable oils.

This paper outlines the optimal formulation and technology of combined emulsification used to produce a finely dispersed bitumen emulsion. It has been identified that a bitumen emulsion with two percent of flotation asphaltic bitumen obtained via the combined method is more structured and features a smaller size of bitumen particles. It is proven that from the point of view of uniformity, a bitumen emulsion obtained by combined emulsification is five times better than a bitumen emulsion produced by conventional methods.

Keywords Bitumen emulsion · Anionactive emulsifier · Surfactant · Relative viscosity · Uniformity · Stability · Optical microscopy

A. Garipov · D. Makarov (✉) · V. Khozin · S. Stepanov
Kazan State University of Architecture and Engineering, Kazan, Russian Federation
e-mail: makarov@kgasu.ru

1 Introduction

Mixtures of higher fatty acids are used as an emulsifier in the production of fine bitumen emulsions. The concentration of acids varies from 0.5 to 5% of the mass of the emulsion [1–3]. The ratio of water and bitumen depends upon the intended field of application of the emulsion. In this study, the concentration of bitumen in the emulsion is 55%.

The quantitative proportion and appearance of bitumen, water, emulsifier and alkali, as well as the degree of separation of bitumen serve to determine the operational, technical and physico-chemical properties of the bitumen emulsion [4–6]. Various methods are applied to evaluate the physico-chemical properties of bitumen emulsions [7, 8].

The dispersion which is characterized by the distribution of the mass of the dispersed phase in fractions - droplets of various sizes - can be used as the criterion to assess the effectiveness of the emulsification process and the stability of emulsions itself [9, 10]. Bitumen emulsions are characterized by high polydispersity. The polydispersity is influenced by the molecular nature of its constituent components [11, 12]. When forming a dispersed phase in direct-type emulsions, bitumen shows different ways of emulsification. This is due to the physico-chemical nature of bitumen along with its composition and properties. Paraffin-naphthene hydrocarbons coagulate asphaltenes while aromatic hydrocarbons peptize them. There is a certain ratio of aromatic and paraffin-naphthene hydrocarbons where the dispersion of asphaltenes and their emulsifying effect on water reach their maximum point.

The emulsifiability of bitumen can be characterized by the quantitative ratio of resins and asphaltenes found in their composition [13]. Furthermore, bitumen manifests an increased ability of emulsification with a ratio of the number of resins to asphaltenes from 0.5 to 2. The surface activity of bitumen that is due chiefly to asphaltogenic acids and their anhydrides found in the composition of bitumen, produces a considerable impact on the process of emulsification. The emulsifiability of bitumen is characterized by the acid index which should be no less than 0.8 – 1 mg KOH/g. However, the dispersion of emulsions depends not only upon the amount of acids and their anhydrides in bitumen, but also upon the content of asphaltenes which serve as oleophilic emulsifiers. A number of studies [8, 14] have established a criterion for emulsifiability of bitumen by the ratio of the content of acidic compounds of bitumen and asphaltenes.

It is not only the properties of emulsions that determine the particle size, but also the presence of a boundary surface where the phase interacts with the medium. Concentrated emulsions are known for particles of the dispersed phase interacting with each other. Therefore, microheterogenic systems such as these can be qualified as connected-dispersed where particles are bound to each other by intermolecular forces which, in turn, forms a spatial structure in the dispersion medium. The integrity of this structure is determined by the molecular cohesion of dispersed-phase particles reflecting the viscosity of the emulsion which is determined by internal friction that is the resistance to mechanical mixing or flowage at a given velocity of shear [7, 15].

The mutual influence of phase particles on each other must be taken into account. It is not only free water but also bound water that should be factored in as the dependence of the viscosity of the emulsion on the concentration of the dispersed phase is being established. It has been proven that the viscosity of an emulsion is contingent upon the drop in osmotic pressure where bitumen droplets serve as osmotic particles. The viscosity of the emulsion is also in large part affected by the alkaline balance of soaps, which is accounted for by hydration and the presence of a double electric layer which is formed through the interaction of the adsorption layers of the emulsifier with the dispersion medium [16].

A comparative analysis of the available technologies used to produce bitumen emulsions has revealed that combined emulsification is the most effective way to obtain anionactive emulsions where the emulsifier is introduced both into bitumen and into the aqueous phase prior to preparing the emulsion [17, 18]. This approach allows for obtaining finely dispersed emulsions on bitumens, even low-active ones.

Below the combined technology employed to churn out bitumen emulsions is described. First, an aqueous solution (of the resulting emulsifier) is put together by introducing NaOH into water heated to 80 °C that is being stirred at a rate of 150–200 rpm., in the amount required to achieve a saponification reaction and to create a pH of the medium of at least 11 [19]. Half of the total amount of flotation asphaltic bitumen is added to the obtained alkaline solution, and the other half is introduced into bitumen heated up to 140 °C.

This study aims to obtain finely dispersed, stratification-resistant bitumen emulsions via an anionactive emulsifier.

2 Materials and Methods

The chemical enterprise “Nefis Cosmetics” (Kazan, Russia) produces flotation asphaltic bitumen as a technical product. The physical and chemical parameters of flotation asphaltic bitumen are listed in the table below (Table 1);

Table 1 Physical and chemical parameters of flotation asphaltic bitumen

Indicator name	Characteristics and norms	Actual value
Appearance	Thick ointment-like mass	Complies
Color	dark brown to black	Complies
Acid index, mg KOH/g	50–70	64.2
Solidification temperature of fatty acids (titer), °C max	23	22.8
Mass fraction of water and volatile substances, % max	5	4.0
Saponification value, mg KOH/g, min	140	144
Mass fraction of ash, % max	1	0.9

This study relies upon the following standard regulatory methods of the Russian Federation used to assess the structure and properties of bitumen emulsions:

- relative viscosity was determined by measuring the expiration time of 50 ml of emulsion from a viscosity gage through a hole with a diameter of 4 mm at an emulsion temperature of 40 °C;
- the content of bitumen with an emulsifier was determined by evaporation of water from the emulsion after which the residue was weighed. The mass fraction of bitumen with emulsifier (V_e) in percentage terms was calculated by a formula (1) with an accuracy of 0.1%:

$$B_{\%} = \frac{M_3 - M_1}{M_2} * 100\% \quad (1)$$

where:

M_1 —mass of the cup, g;

M_2 —mass of the emulsion, g;

M_3 —mass of the sample cup after evaporation, g;

- uniformity was determined by the bitumen residue on the sieve No. 014 which has a cell size of 140 microns (0.14 mm) after the emulsion had been filtered through it which was expressed as a percentage of the mass of the emulsion. Uniformity was calculated by a formula (2) with an accuracy of 0.1%.

$$M_{014} = \frac{M_5 - M_1}{M_3 - (M_4 - M_2)} * 100\% \quad (2)$$

M_1 —mass of the sieve under the No. 014 and the porcelain cup (metal pan), g;

M_2 —mass of a laboratory glass cup, g;

M_3 —mass of the emulsion in a laboratory glass cup (the mass of the cup is not taken into consideration), g;

M_4 —mass of a laboratory glass cup with emulsion residue, g;

M_5 —mass of the sieve No. 014 and the porcelain cup (metal pan) with the emulsion residue following drying, g;

- the storage stability of the bitumen emulsion was determined by filtering the emulsion after seven days of storage at a temperature of (21 ± 4) °C through a sieve with a metal mesh No. 014 and recording the mass of the emulsion residue which remained on the sieve;
- optical microscopy was applied in order to determine the mechanism of influence of the developed emulsifiers upon various characteristics of bitumen emulsions. An Axioskop40 microscope was employed to investigate the microstructure of

the bitumen emulsion. The bitumen emulsion was observed in transmitted light at a magnification of 1000X.

3 Results and Discussion

It is critical to ensure an accurate determination of the percentage of alkali in the emulsion in order to obtain finely dispersed, stable bitumen emulsions. The works by P. Rebinder [3] demonstrate the kinetics behind the decomposition of bitumen emulsion when it interacts with mineral materials depending on the presence of free alkali in the system. An increase in the content of alkali in the system causes a rise in dispersion, which, once it reaches its maximum point, decreases as the concentration of alkali in the emulsion keeps increasing.

Besides, an overabundance of alkali, adsorbed on the surface of stone material, causes passivation of the latter which in turn results in the processes of interaction of the bitumen emulsion with mineral materials slowing down significantly while reduces the adhesion of bitumen to them [20–22]. Together with slowing down the decomposition of emulsions, an overabundance of alkali impacts their properties as well as the properties of the bitumen extracted from them thereby decreasing the adhesion of the stone material which is the result of the adsorption of alkali on its surface. It explains why the optimal content of alkali must be calculated correctly.

The amount of caustic soda A needed for saponification of one gram of an emulsifier was calculated by the following formula (3):

$$A = \frac{a * 0.714}{1000} + C \quad (3)$$

a - saponification number of emulsifiers (mg. KOH per 1 g);

0.714 - Conversion Ratio of Molecular Weight from caustic soda to caustic potassium;

C - excessive caustic soda in an aqueous solution of the emulsifier, in percentage terms (30%).

The calculation determined that 0.13 g should be introduced for a full saponification reaction to take place. NaOH is necessary for a complete emulsification of 1 gr of flotation asphaltic bitumen. The quality and completeness of the reaction impacts such properties of a bitumen emulsion as relative viscosity, uniformity and stability.

The primary technological and operational properties of bitumen emulsions were investigated depending on the concentration of an emulsifier from 0.5 to 5% in order to establish the optimal content of flotation asphaltic bitumen in the bitumen emulsion.

The theory of dispersed systems [23–27] says that a decrease in the particle size of a bitumen emulsion results in an increase in the relative viscosity of the emulsion provided that the concentration of bitumen in the emulsion stays unchanged.

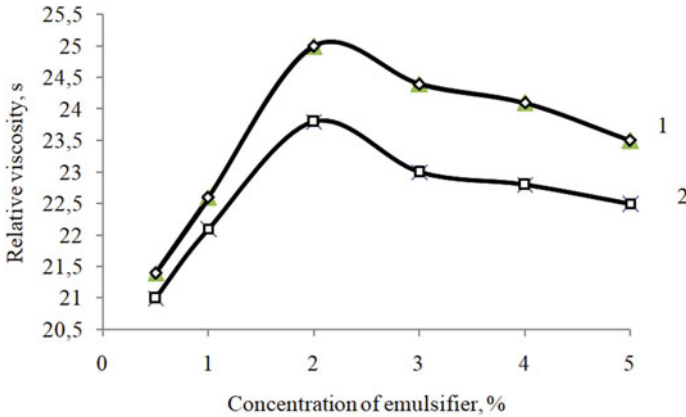


Fig. 1 Dependence of the relative viscosity of bitumen emulsions upon the concentration of an emulsifier and the method of emulsion preparation: 1 – a bitumen emulsion on flotation asphaltic bitumen (combined method); 2 – bitumen emulsion on flotation asphaltic bitumen (conventional method)

Figure 1 shows the dependence of the relative viscosity of bitumen emulsions on the concentration of flotation asphaltic bitumen from 0.5 to 5%.

Figure 1 demonstrates that the curves have the same extreme values with a content of 2% up to 25 s with a combined emulsification technology (curve 1) and up to 23.8 s in the instance of conventional emulsification (curve 2), where the emulsifier is injected only into an aqueous alkaline solution. It can thus be assumed that a bitumen emulsion with 2% of flotation asphaltic bitumen obtained via the combined method is more structured and features a smaller size of bitumen particles.

The uniformity of bitumen emulsions is determined by sending bitumen particles through a sieve with a hole size of 0.14 mm. Figure 2 shows changes in the uniformity of a bitumen emulsion depending upon the concentration of the emulsifier and the method of preparation used. The bitumen emulsion obtained by combined emulsification, with a concentration of flotation asphaltic bitumen of 2% (curve 1) demonstrates minimum values of residue on the sieve while the absolute value of the residue does not exceed 0.05% of the mass of the bitumen emulsion that is it passes almost completely through the sieve. The bitumen emulsion obtained by the conventional method shows minimal values with a content of emulsifier of 3% (curve 2) and is marked by much residue on the sieve equaling 0.25%.

Therefore, from the point of view of uniformity, a bitumen emulsion obtained by combined emulsification is five times better than a bitumen emulsion produced by conventional methods. The uniformity results are completely in line with the relative viscosity indicators of the emulsion. The higher the viscosity of a bitumen emulsion, the higher its uniformity.

Figure 3 highlights the change in the stability of emulsions which is established by having bitumen particles pass through a sieve with a hole size of 0.14 mm. after seven days of storage.

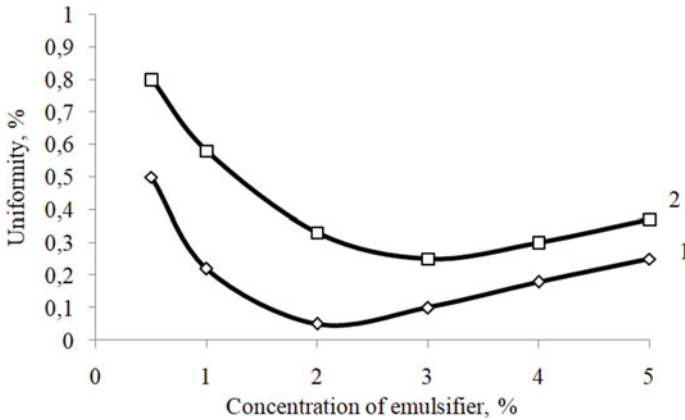


Fig. 2 Dependence of the uniformity of bitumen emulsions upon the concentration of an emulsifier and the method of emulsion preparation: 1 – a bitumen emulsion on flotation asphaltic bitumen (combined method); 2 – bitumen emulsion on flotation asphaltic bitumen (conventional method)

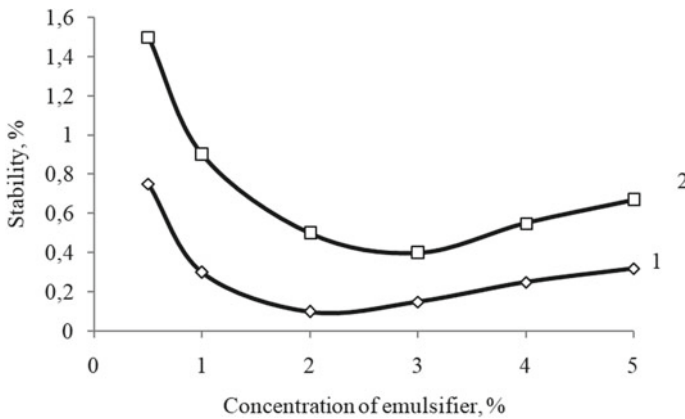


Fig. 3 Dependence of the stability of bitumen emulsions when in storage after seven days upon the concentration of an emulsifier and the method of emulsion preparation: 1 – a bitumen emulsion on flotation asphaltic bitumen (combined method); 2 – bitumen emulsion on flotation asphaltic bitumen (conventional method)

The curves also show an extreme nature with minimum values at the same concentrations of emulsifiers as was seen during the study of uniformity (Fig. 2). The stability of an emulsion with an optimal content of emulsifier of 2% has undergone little change which is 0.1% of the residue of bitumen particles on the sieve where it is prepared by a combined method (curve 1). A bitumen emulsion prepared by the conventional method has less stability (curve 2). At an optimal concentration of 3%, it shows a stability value of 0.4% of residue of bitumen particles on the sieve. The stability value of these emulsions is completely in line with the values of uniformity.

It must be mentioned that an emulsion containing smaller particle sizes happens to more structured and is known to have high stability when in storage. What also merits mention is that the combined emulsification technology has proven itself well as after seven days, the growth of residue on the sieve was insignificant meeting the requirements of regulatory standards with the exception of the composition with a content of flotation asphaltic bitumen of 5%.

The results obtained were used to determine the optimal compositions of bitumen emulsions (Table 2).

Table 3 shows comparative characteristics of the properties of bitumen emulsions.

Optical microscopy is one of the primary methods used to study the structure and properties of bitumen emulsions. A bitumen emulsion obtained by a combined method with a content of emulsifier of 2% – flotation asphaltic bitumen – was selected for the study.

Figure 4 shows a micrograph (with a magnification of 1000x) of the initial bitumen emulsion. The fig. shows a dense grid of bitumen particles of various sizes - the

Table 2 Optimal compositions of bitumen emulsions

Components	Bitumen emulsion on flotation asphaltic bitumene (combined method), in percentage terms	Bitumen emulsion on flotation asphaltic bitumene (traditional method), in percentage terms
Paving bitumen BND 70/100	55.0	55.0
Flotation asphaltic bitumen	2.0	3.0
Alkali (NaON)	0.26	0.39
Water	42.74	41.61

Table 3 Properties of bitumen emulsions

Properties	Bitumen emulsion on flotation asphaltic bitumen (combined method), in percentage terms	Bitumen emulsion on flotation asphaltic bitumen (traditional method), in percentage terms	Standard requirements
The content of a binder with emulsifier, in percentage terms	57.3	58.4	55–65
Relative viscosity (50 ml, 40 °C, 4 mm), s, max	25	23	40
Residue on a sieve - 0.14 mm, %, max	0.05	0.25	0.4
Residue on the sieve is 0.14 mm, after storage for seven days, in percentage terms, max	0.1	0.4	0.5

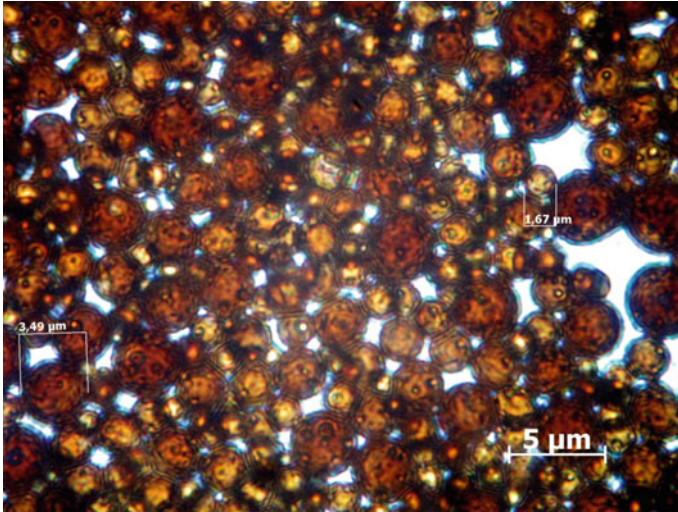


Fig. 4 Optical micrography of a bitumen emulsion (a magnification of 1000X)

dispersed phase which constitutes 55% of the emulsion. Also shown is an image of bitumen particles which in reality performs chaotic movements.

An emulsion represents a polydisperse system which is comprised of particles of various sizes as determined by the extreme values of their magnitude varying from 2 to 5 microns in size. This proves that the entire bitumen emulsion i.e. 100% of it passes through the sieve under the No. 014 which is used to evaluate the homogeneity and stability of emulsions during storage.

4 Conclusion

The study has determined the optimal formulation and technology of combined emulsification to prepare a fine bitumen emulsion: the concentration of alkali (NaOH) per 1 g. of emulsifier is 0.13 g. while the optimal content of emulsifier is 2% of flotation asphaltic bitumen.

It has been proven that bitumen emulsions produced by the combined method are much more superior in uniformity and stability to emulsions produced by the conventional method meeting the requirements of the standard regulations of the Russian Federation in full.

Methods of optical microscopy were used to highlight the polydisperse structure of the developed fine-dispersed emulsion and the size of bitumen particles (from 2 to 5 microns) was established.

References

1. Abramzon, A.A.: Properties and Application, 2nd edn. Chemistry, Leningrad (1981)
2. Kuchma, M.I.: Surfactants in Road Construction. Transport, Moscow (1980)
3. Rebinder, P.A.: Surfactants. Znanie, Moscow (1961)
4. Esfahani, M.A., Khoddami, S.M.N.: Evaluation and identification of parameters affecting the penetration of emulsion bitumen on aggregates. *Aust. J. Civil Eng.* **20**(1), 195–207 (2022). <https://doi.org/10.1080/14488353.2021.1945258>
5. Esfahani, M.A., Khatayi, A.: Effect of type and quantity of emulsifier in bitumen polymer emulsion on microsurfacing performance. *Int. J. Pavement Eng.* **4**(23), 957–971 (2022). <https://doi.org/10.1080/10298436.2020.1784416>
6. Murafa, A.V., Makarov, D.B., Nuriev, M.A., Khozin, V.G.: Nanomodified bitumen emulsions for construction purposes notes. *News of KSUAE* **2**(14), 245–249 (2010)
7. Kovalev, V.M., Petrenko, D.S.: Technology of Production of Synthetic Detergents. Chemistry, Moscow (1992)
8. Kolbanovskaya, A.S., Mikhailov, V.V.: Road Bitumen. Transport, Moscow (1973)
9. Antonova, I., Ayupov, D.: Anionic bitumen emulsions for waterproofing. In: E3S Web of Conferences, vol. 274. EDP Sciences (2021). <https://doi.org/10.1051/e3sconf/202127404007>
10. Ayupov, D.A., Hakimullin, Y.N., Makarov, D.B., Kazakulov, R.I.: Theoretical aspects of delamination of bituminous polymer binders. *Vestnik Tekhnologicheskogo universiteta* **19**(23), 50–52 (2016)
11. Gong, Y., Shao, T., Chen, L.: Preparation and characterization of fluorine-containing soap-free acrylic emulsion. *Pigm. Resin Technol.* **50**, 41–47 (2021). <https://doi.org/10.1108/PRT-02-2020-0015>
12. Wu, Y. F., Qu, X.: Influence of different types of emulsifiers on properties of emulsified asphalt binder and its evaporation residue by molecular dynamics simulation. *Adv. Mater. Sci. Eng.* **2021** (2021). <https://doi.org/10.1155/2021/3313460>
13. Nikishina, M.F., et al.: Road Emulsions. Transport, Moscow (1964)
14. Rosenthal, D.A., Bereznikov, V.P., Kudryavtseva, I.N.: Bitumen: Obtaining and Methods of Modification. LTI, Leningrad (1979)
15. Mittel, K.L., Mukerden, P.: The Wide World of Micelles: Micelle Formation, Solubilization and Microemulsions. Mir, Moscow (1980)
16. Ouyang, J., Cao, P., Tang, T., Meng, Y.: Investigation on maximum packing fraction of bitumen particles during emulsion drying. *Mater. Struct./Materiaux et Constr.* **5**(54) (2021). <https://doi.org/10.1617/s11527-021-01784-w>
17. Al-mohammedawi, A., Mollenhauer, K.: Current research and challenges in bitumen emulsion manufacturing and its properties. *Materials* **15**, 2026 (2022). <https://doi.org/10.3390/ma15062026>
18. Yaacob, H., et al.: Bitumen emulsion in malaysia-a conspectus. *Jurnal Teknologi (Sci. Eng.)* **65**, 97–104 (2013). <https://doi.org/10.11113/jt.v65.2153>
19. Zhao, P.H., Fan, W.Y., Dong, S., Nan, G.Z., Zhang, S.J.: Relationship between stability of anionic asphalt emulsion and oil-water interfacial tension. *Zhongguo Shiyou Daxue Xuebao (Ziran Kexue Ban)/J. China Univ. Petrol. (Ed. Nat. Sci.)* **36**, 175–179 (2012). <https://doi.org/10.3969/j.issn.1673-5005.2012.03.030>
20. Ignatavicius, S., et al.: Experimental investigation of optimum adhesion properties for anionic emulsions in road maintenance applications. *Constr. Build. Mater.* **304** (2021). <https://doi.org/10.1016/j.conbuildmat.2021.124678>
21. Meknaci, L., Graziani, A., Mignini, C., Henni, A. D., Miljković, M.: Influence of bitumen emulsion on the curing behaviour of standardised cold bitumen emulsion mortars. *Road Mater. Pav. Des.* (2021). <https://doi.org/10.1080/14680629.2021.2017329>
22. Garipov, A., Makarov, D., Khozin, V., Stepanov, S.: Modification of harsh cement pavement concretes with bitumen emulsion. In: Lecture Notes in Civil Engineering, vol. 169, pp. 351–363. Springer, Deutschland GmbH (2021). https://doi.org/10.1007/978-3-030-80103-8_38

23. Savvin, S.B., Chernova, R.K., Shtykov, S.N.: Surfactants. Nauka, Moscow (1991)
24. Iliopolov, S.K., et al.: Organic binders for road construction: Study guide. Izdatelstvo «Yg», Rostov-on-Don (2003)
25. Frolov, Yu.G.: Course of colloidal chemistry: Surface phenomena and dispersed systems. Chemistry, Moscow (1988)
26. Galeev, R., Abdrakhmanova, L.A., Nizamov, R.: Nanomodified organic-inorganic polymeric binders for polymer building materials. *Solid State Phenom.* **276**, 223–228 (2018). <https://doi.org/10.4028/www.scientific.net/SSP.276.223>
27. Galeev, R., Nizamov, R., Abdrakhmanova, L., Khozin, V.: Resource-saving polymer compositions for construction purposes. *IOP Conf. Ser. Mater. Sci. Eng.* **890**(1), 012111 (2020). <https://doi.org/10.1088/1757-899X/890/1/012111>

The Use of Surface Laser Scanning as a Standard Operating Procedure for Assessing the Quality of Construction and Installation Work



Andrey Bogdanov and Sergey Stepanov

Abstract In recent years, surface laser scanning (hereinafter referred to as SLS) has been increasingly used when performing geodetic surveys in the construction of buildings and structures. In this regard, it is relevant to consider the implementation of SLS method as a standard operating procedure when conducting executive surveys as part of construction control along with digital and BIM technologies during the construction and subsequent monitoring of the condition of building structures. This paper shows the sequence of work and the methodology for evaluating scan results when using surface laser scanning as a standard operating procedure for assessing the quality of construction and installation work. The use of this method when constructing structures allows to: significantly reduce the time and simplify the procedure of construction control; speed up decision-making on construction objects structures when critical deviations from the project targets being detected; carry out continuous monitoring when erecting building structures during construction and further operation.

Keywords Construction control · Surface laser scanning · 3D model · BIM technology · Point cloud

1 Introduction

Urban Planning Code of the Russian Federation is the core document in construction control and engineering supervision in Russia, according to which the regulatory framework is regulated by laws and other legal acts of the federal and regional level and those of local self-government. In 2010, Provision on construction control was approved.

In accordance with the Urban Planning Code of the Russian Federation, engineering supervision or construction (production) control is a set of expert verification measures carried out with optimal regularity and strict compliance with the entire

A. Bogdanov · S. Stepanov (✉)
Kazan State University of Architecture and Engineering, Kazan, Russian Federation
e-mail: gold04@mail.ru

process of construction and repair work, the current rules and regulations in place, as well as with project documentation carried out by the customer and other specified persons. Construction control is aimed at solving a multi-level integrated system that includes a number of measures and procedures that are mandatory at all steps (stages) of construction, reconstruction, overhauls of capital construction facilities. One of the crucial stages of construction control is conducting an executive survey, which is subject to production at all stages of facility construction, starting from excavation.

The purpose of the executive survey is to confirm whether the facility or the stage of its construction completed complies with the parameters reflected in the project documentation, and to detect possible discrepancies between the actual values and those stipulated in the initial project. The primary task of the executive survey is to develop documentation containing facilities location and route of communication. The requirements for the content and accuracy of the survey are directly proportional to the requirements for the final document.

Executive survey is the basis for making dimensional drawings and three-dimensional models, which will later serve as official documents, based on which one should decide to start the next stage of construction, or to fix identified discrepancies with the original values. Executive surveys may be repeated. Executive surveys can and may be conducted several times if needed during the construction of a building or a structure, the installation of equipment or any other structure, as well as the execution of various stages of construction and installation work. When conducting an executive survey, one should pay careful attention to such elements of a building or a structure that, once construction or installation is completed, will be inaccessible (e.g. concreted, covered with soil, laid with bricks or other building materials) for subsequent measurements. Hence the name of this survey – “executive”. Facilities are marked as “Asbuilt” at various stages of construction since the survey should be carried out following the actual completion of the specified building volume.

Executive survey must be conducted at all stages of construction: at the excavation stage, when erecting load-bearing structures [1, 2], fitting facade systems [3], building the roof, making expansion joints [4], when designing interiors, for inspecting and arranging utility lines, etc. Engineering surveys of this type can also be the following: space geodesic survey, architectural and construction surveys, production volume scaling, facade survey, buildings, structure and interior measurement surveys. Separately, one could single out the executive survey of communications carried out during and after the completion of construction. However, it should be performed before backfilling of underground utilities with earth and doing the survey of existing communications.

Facilities should always be built according to the agreed and approved project documentation. In recent years, BIM design systems have been increasingly used in the development of project documentation [5, 6]. Such programs as AVEVA, Autodesk, Intergraph, Bentley and others are used when designing. Designer supervision by the designer and engineering supervision by experts should be delivered when conducting construction. For construction control, to ensure compliance of the erected object with design data, to identify deviations, errors and their actual values, it is essential that the information on the status of construction is reliable and up-to-date.

All this allows to identify and correct critical errors in real time during construction in a timely manner, rather than trying to identify deviations after construction and installation work is completed, with the facility having already been erected, which would make it challenging, expensive or even impossible to fix anything.

Laser scanning is used for collecting and preserving parametric information on architectural heritage facilities [7–11], when constructing buildings and structures [12–14], when creating management models for existing buildings based on BIM [15]. To increase the efficiency and productivity of construction control, designer and technical supervision, executive survey of a construction object can also be carried out using the laser scanning method. In the process of processing the obtained 3D laser scanning data, the final cross-linked point cloud should be integrated into the coordinate system of the first initial design model. Such an opportunity is provided by binding the facility to the coordinate system according to construction benchmarks. As a result of the executive survey performed, the resulting point model is superimposed on the design 3D model in a single coordinate space. As a result of the two models overlaid on top of another, one can visually compare and measure the resulting discrepancies, study deviations of the actual situation fixed in the point cloud of laser scanning from the original ideal design model. Errors and violations identified at the current stage of construction are promptly corrected. Thus, loading the executive point model according to 3D scanning data makes it possible to accurately detect non-compliance with the design model, assess the significance and degree of negative impact, and most importantly to eliminate possible consequences of these errors.

The use of the SLS method for carrying out measurement work, in particular the executive survey, reduces the time required to perform the measurement work. To obtain accurate information, during construction control and engineering supervision, it is possible to obtain survey results in real time, as well as to quickly carry out reference measurement using the combined visual simulation of design and executive models. As a result, the construction process is monitored and controlled in a prompt manner and it becomes possible to carry it out by a flow line method, making sure one covers all stages of work.

The following types of finished products can act as records based on the executive survey results for the purposes of construction control and engineering supervision using laser scanning technology:

- point models of construction objects (stitched point clouds);
- point clouds overlaid with design models of facilities;
- floor plans with the real status fully reflected;
- dimensional drawings of facades of buildings and structures;
- dimensional drawings of the roof and ceilings with the elements of underground utilities fully reflected;
- dimensional drawings of objects with deviations from the design values fully reflected;
- three-dimensional executive models of construction objects;
- three-dimensional executive models overlaid with design models.

Table 1 Main technical characteristics of the Leica ScanStation 2 scanner

Specification name	Indicator
Type of scanner	Pulse type with built-in two-axis tilt compensator
Range	300 m
Accuracy of distance measurement	4 mm at 50 m
Scanning rate	Up to 50,000 points/sec
Field of view	270/360° (vertical/horizontal)
Object finder	Built-in digital camera
Dimensions	265 × 370 × 510 mm
Weight	18.5 kg
Operating temperature	0° ± 40 °C
Running time	up to 3 h

Some of the challenges of using the SLS method in action include the difficulties of survey in insufficient visibility, scanning glass or totally smooth surfaces and weather conditions.

2 Materials and Methods

To assess the advantages of the SLS method when performing executive surveys, the following equipment was used:

- Leica ScanStation 2 laser scanner – high-speed, high-precision pulse type instrument (Table 1);
- FARO Focus 3D laser scanner - laser scanner for short, medium and long range (Table 2);
- RIEGL VZ-400 laser scanner (Table 3);
- Trimble TX5 laser scanner (Table 4);

The results were processed via the following software: Leica Cyclone, Autodesk Auto CAD, Autodesk Re Cap, Navisworks, Autodesk Revit, Autodesk Point Layout.

Table 2 Main technical characteristics of the FARO Focus 3D scanner

Specification name	Indicator
Type of scanner	Phase type, surface laser scanner
Range	130 m
Accuracy of distance measurement	2 mm at 50 m
Scanning rate	Up to 983,000 points/sec
Field of view	300/360° (vertical/horizontal)
Object finder	Built-in digital camera
Dimensions	240 × 200 × 100 mm
Weight	5.2 kg
Operating temperature	5° ± 40 °C
Running time	up to 5 h

Table 3 Basic specifications of the RIEGL VZ-400 scanner

Specification name	Indicator
Type of scanner	Pulse type surface laser scanner
Range	Up to 800 m
Accuracy of distance measurement	5 mm by 500 m
Scanning rate	Up to 500,000 dots/sec
Field of view	100/360° (vertical/horizontal)
Object finder	Removable digital camera
Dimensions	206 × 308 mm
Weight	9.7 kg
Operating temperature	0 ± 40 °C
Running time	up to 5 h

Table 4 Basic specifications of the RIEGL VZ-400 scanner

Specification name	Indicator
Type of scanner	3R surface laser scanner
Range	120 m
Accuracy of distance measurement	2 mm by 25 m
Scanning rate	Up to 976,000 dots/sec
Field of view	305/360° (vertical/horizontal)
Object finder	Built-in digital camera
Dimensions	240 × 200 × 100 mm
Weight	5.0 kg
Operating temperature	5° ± 40 °C
Running time	up to 5 h

3 Results and Discussion

The analysis that was performed proved the use of the SLS method an effective one in the implementation of construction control. The work [16] demonstrates the effectiveness and efficiency of the use of the SLS method in the implementation of construction control based on the example of the facility called “Shukhov Radio Tower” (the city of Moscow).

A pre-construction survey, including measurements as part of construction control, was conducted using the example of works performed earlier at the Radio Tower facility on Shabolovka [16, 17]. The radio tower on Shabolovka Street located in Moscow (Fig. 1) is an internationally acclaimed monument of architecture of Russian avant-garde [18]. Another name is the Shukhov Tower which derives its roots from the name of its creator, an outstanding Russian engineer Vladimir Shukhov (1853–1939). The tower was built between 1919 and 1922.

Structure-wise, the tower is comprised of six hyperbolic sections. The original superstructure finished in 1922 underwent reconstruction in 1937. In 1991 it was taken down and replaced with a new one. According to the measurements taken, the



Fig. 1 The Shabolovka radio station in Moscow

total height of the six hyperboloid sections was 144.16 m. Without the superstructure, the upper section shrank by 0.36 m in 1991.

In 2011, a laser scan of the Shukhov Tower was carried out by Leica Scan Station 2 and FARO Focus3D scanners. Seven stations were used during the scanning. Four stations were placed on the ground in the immediate vicinity of the tower (one inside and three outside). The other three stations were located at the technological sites at 100, 125 and 141 m. [19].

Leica Cyclone was used to process the results and to sew together the model with the accuracy of mutual orientation of the scans of 7 mm. The final result was shown in the computer-aided design system Autodesk Auto CAD. The authors achieved the accuracy of about 1 cm for the constructed 3D model of the tower in a single coordinate system.

In the same year of 2011, other authors also performed laser scanning and 3D modeling of the load-carrying structures of the tower [20]. These works were done in order to develop design documentation for the reconstruction of the tower. The scan was carried out by a Riegl VZ-400 pulse scanner in the long-range mode. The works were carried out from seven stations at a distance of 100–200 m. from the tower. The accuracy of the mutual orientation of the scans was 3–4 cm. The tower structure was also scanned in order to provide general access to information about the historical and architectural monument. The goal was to scan the tower structures via a Trimble TX5 laser scanner to further combine working and design models in order to identify possible deviations from the design documentation, to determine the presence or absence of individual tower elements on the real object and to determine their configuration.

Prior to the scanning, the fastening points of round black-and-white connecting marks are determined which are positioned at a minimum visibility of two marks (Fig. 2) and later the point clouds are unified. Where the scanning results are obtained one after the other based on a certain route, one needs to provide a minimum of four connecting marks in the field of view of the scanner which comes down to the need to orient each system as per two corresponding marks. Where an extension is required, objects and elements of the situation can serve as connecting marks. To that end, spherical objects (street lights, etc.) can be used.

All structures feature a fair amount of small or large parts and components which means that one should pay special attention to choosing the location of a scanner. A corner, a canopy, or, for example, a protruding part of a facade, may obstruct the scanner and cause “shadows” (areas not covered by a cloud of dots), which may adversely affect the purity and integrity of the data collected. In order to avoid shadows, sometimes it is recommended to increase the number of scanner locations (Fig. 3).

The scanning process must have a given density. In order to cover the surface with dots while maintaining a sufficient degree of density, scans must be conducted from different positions so one should walk around the object and move the scanner from location to location. The process of simple objects scanning takes from several hours to several days for complex objects.

Fig. 2 Selection of scanner locations [21]

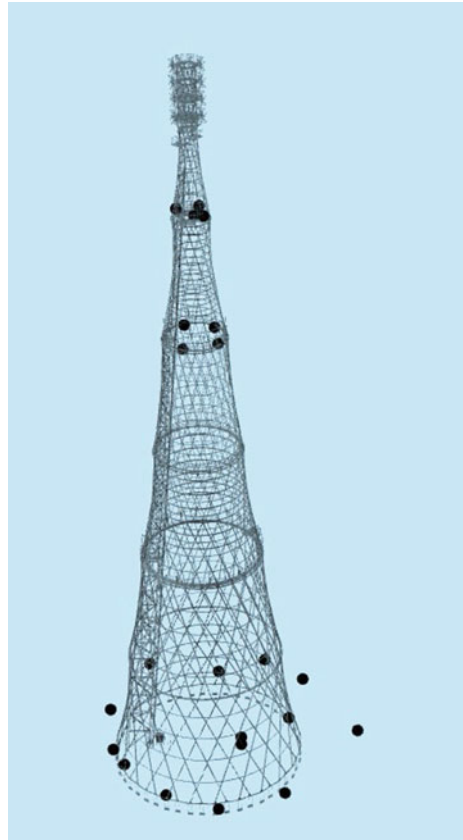
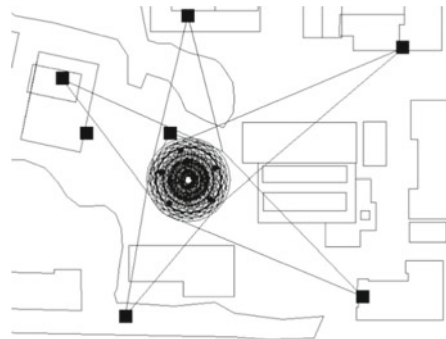


Fig. 3 Selection of scanner locations (top view) [21]



- - scanner station
- - scanner cylindrical stamp

Once a scan was over, the data stored by the device on a memory stick was loaded into AutoDesk Re Cap. Then point clouds are registered and combined into a single data array (Figs. 4 and 5). In order to register or link point clouds in manual mode, it is sufficient to mark three common points or three special targets on overlapping scans. Together with these works, the results of the scan are evaluated, accepted or rejected. Where necessary, the registration procedure is repeated. Based on the results, a report can be made and then the works on the project can be initiated. Time-wisely, the entire process of downloading data for eight stations takes about an hour and a half.

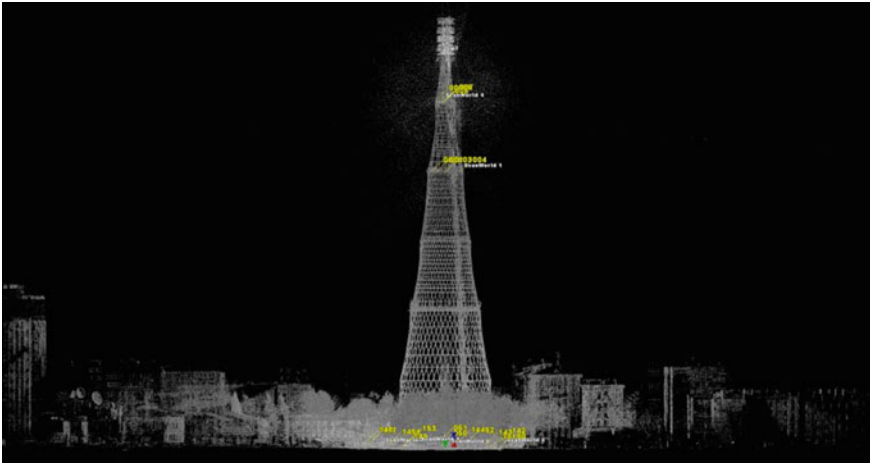


Fig. 4 Initial data obtained by the SLS (front view) [17]

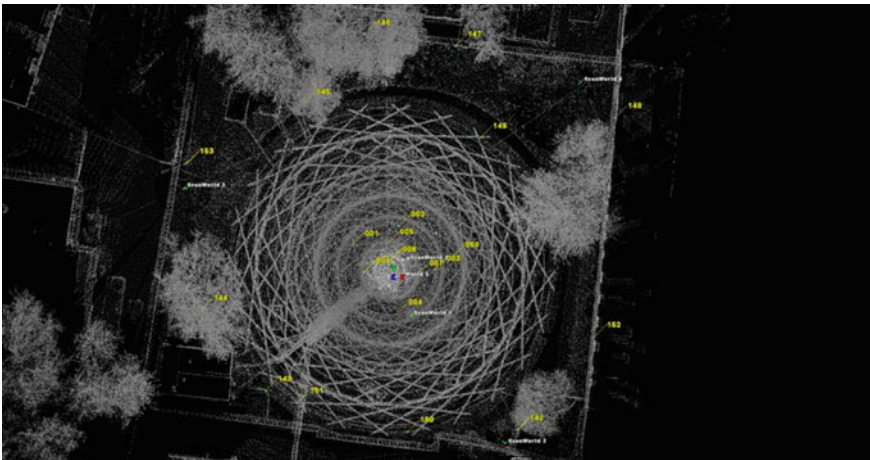


Fig. 5 Initial data obtained by the SLS (top view) [17]

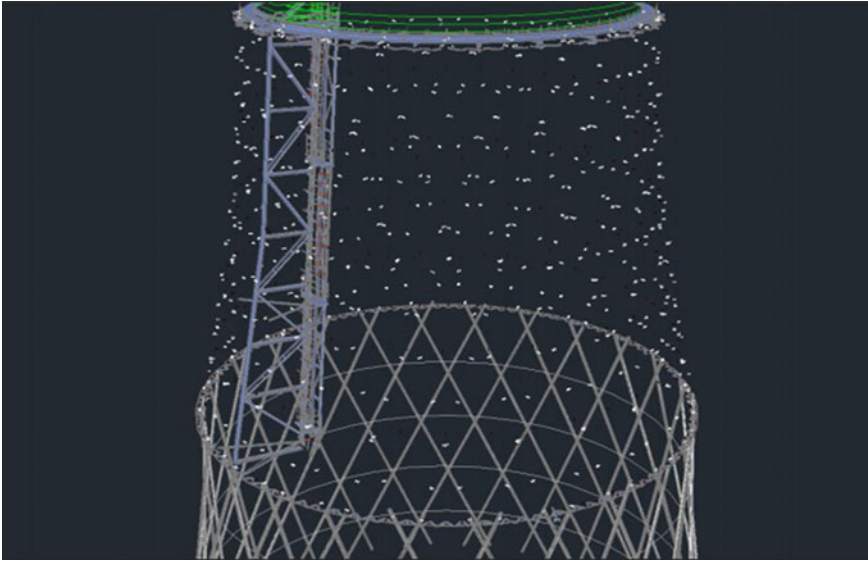


Fig. 6 The model after cleaning [22]

Aside from combining scans into a single model (registration), one must clean the point clouds from artifacts (Fig. 6 and 7).

A point cloud can be superimposed on an existing design model in Navisworks. The correspondence of the two models can be visually evaluated and the amount of deviations of individual elements can be instrumentally measured (Fig. 8).

The tools of the Autodesk Revit application, together with Autodesk Point Layout help carry out a quantitative analysis of the deviations of two models. The magnitude of deviations is estimated and reports which are used to make decisions on necessary changes are generated.

The first calculation of the tower with a height of 250 m was performed on January 27, 1919 [16]. The radii of the support rings coincide with the calculation for the four lower sections. The results of the survey demonstrated that the outer contour of the outline diverges from the calculations in the upper part of the tower: in the case of the ring, the actual radius is 10% larger than the calculated one at the level of 100 m, at the level of 125 m – by 29%, and at the level of 141 m – by 95%. The drawing of the 350-m tower does not conform to the design documentation. The outer outline of the tower’s contour as shown in the drawing visually corresponds only to a tower with a height of 150 m. (Fig. 9).

The results of the survey serve to show that the actual design of the sections of the “Shukhov Radio Tower” considerably diverges from the calculations made based on the detailed documentation. The number of intermediate stiffening rings in the four upper sections as shown in the drawing also does not correspond to the actual number which is nowadays not acceptable.

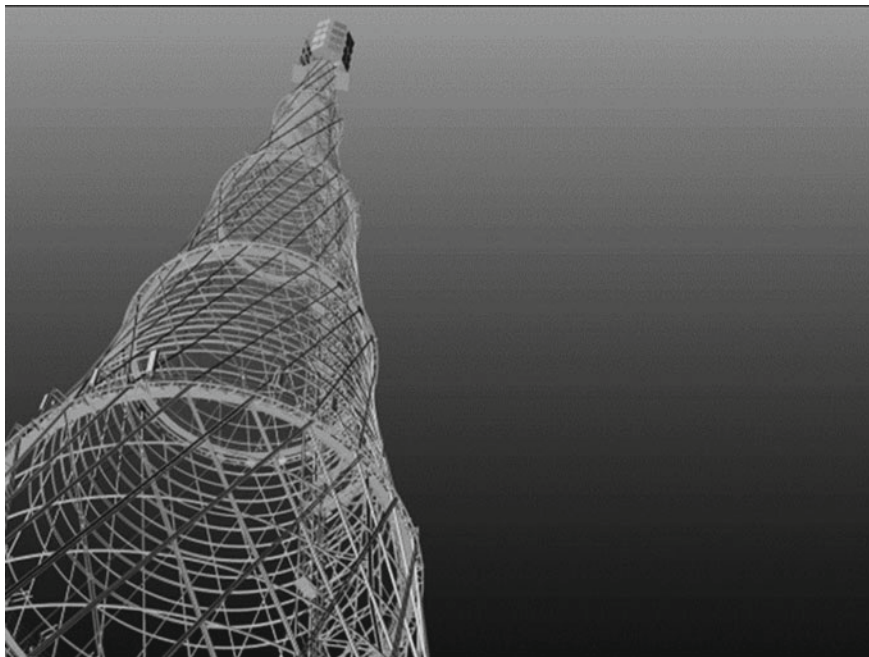


Fig. 7 The model after cleaning [22]

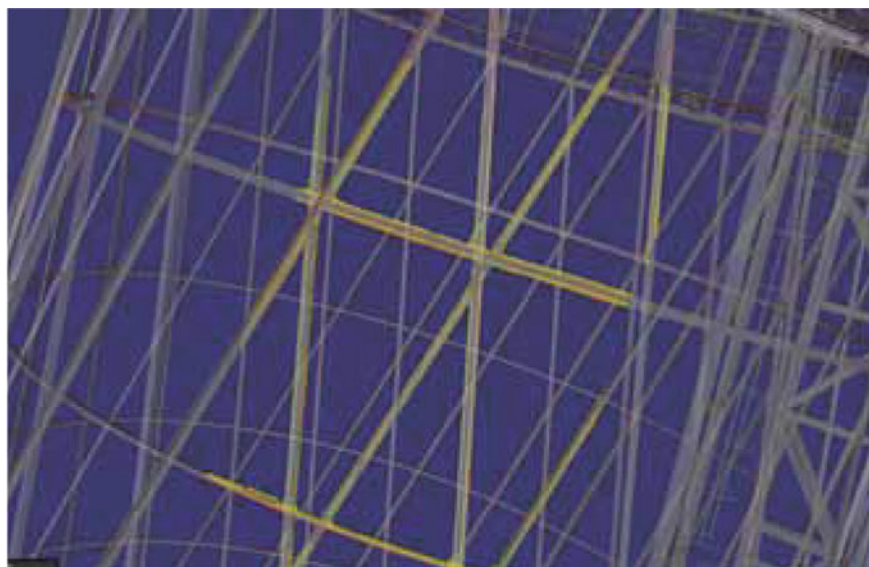


Fig. 8 A point cloud superimposed on a design model [23]

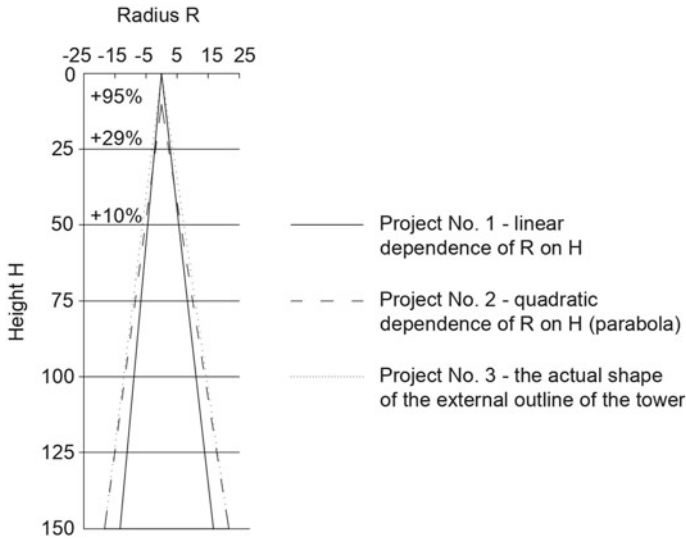


Fig. 9 Analysis of project deviations [16]

4 Conclusion

It was revealed that the application of the SLS method for construction control purposes considerably reduces the complexity of measurements, including that of executive surveys. It makes it possible to analyze quickly the compliance of design documentation with the actual facility under construction, to introduce timely changes, both in the detailed documentation and in the construction of the facility. Improved quality of control increases the reliability of the buildings and structures under construction while also saving materials during construction.

References

1. Mukhametrakhimov, R., Khuzin, A., Khamidullina, D.: Technology of device and quality control of monolithic steel-fiber concrete slabs using emptiness-formers. *News KSUAE* 3(45), 228–235 (2018)
2. Bogdanov, A., Listratov, J.: Construction control by ground laser scanning. *News KSUAE* 4(50), 401–409 (2019)
3. Mukhametrakhimov, R., Lukmanova, L., Kamaliev, M.: Features of the quality control system of the installation of hinged ventilated facade systems. *News KSUAE* 1(43), 234–240 (2018)
4. Mukhametrakhimov, R., Aliullova, I.: Construction technology and quality control of expansion joints with rubber compensators. In: *E3S Web Conferences*, Tashkent, vol. 264, 02066 (2021). <https://doi.org/10.1051/e3sconf/202126402066>.
5. Ibem, E.O., Laryea, S.: Survey of digital technologies in procurement of construction projects. *Autom. Constr.* 46, 11–21 (2014). <https://doi.org/10.1016/J.AUTCON.2014.07.003>

6. Herr, C.M., Fischer, T.: BIM adoption across the Chinese AEC industries: an extended BIM adoption model. *J. Comput. Des. Eng.* **2**(6), 173–178 (2019). <https://doi.org/10.1016/J.JCDE.2018.06.001>
7. Yin, Y., Antonio, J.: Application of 3D laser scanning technology for image data processing in the protection of ancient building sites through deep learning. *Image Vis. Comput.* **102**, 103969 (2020). <https://doi.org/10.1016/J.IMAVIS.2020.103969>
8. Hu, Y., Chen, X., Tang, Z., Yu, J., Chen, Y., Wu, Z., Yang, D., Chen, Y.: Collaborative 3D real modeling by multi-view images photogrammetry and laser scanning: the case study of Tangwei Village, China. *Digital Appl. Archaeol. Cult. Herit.* **21**, e00185 (2021). <https://doi.org/10.1016/J.DAACH.2021.E00185>
9. Chen, J.: Research on restoration of ancient buildings based on BIM technology. In: *Lecture Notes in Civil Engineering*, LNCE, vol. 226, pp. 479–486 (2020). https://doi.org/10.1007/978-3-030-94514-5_48
10. Karagkounis, D.L., Tsanaksidou, S.D.: Digital documentation and 3d modelling in the restoration of the first ancient theatre of Larissa, Greece. In: *Lecture Notes in Civil Engineering*, LNCE, vol. 209, pp. 586–593 (2022). https://doi.org/10.1007/978-3-030-90788-4_46
11. Bezmenov, V., Safin, K., Stepanov, S.: Application of unmanned aerial vehicles for solving engineering tasks. In *IOP Conference Series: Materials Science and Engineering*, vol. 890, no. 1. IOP Publishing Ltd (2020). <https://doi.org/10.1088/1757-899X/890/1/012135>
12. Aryan, A., Bosché, F., Tang, P.: Planning for terrestrial laser scanning in construction: a review. *Autom. Constr.* **125**, 103551 (2021). <https://doi.org/10.1016/J.AUTCON.2021.103551>
13. Tuttas, S., Braun, A., Borrmann, A., Stilla, U.: Validation of BIM components by photogrammetric point clouds for construction site monitoring. *ISPRS Ann. Photogram. Remote Sens. Spat. Inf. Sci.* **2**(3W4), 231–237 (2015). <https://doi.org/10.5194/ISPRSANNALS-II-3-W4-231-2015>
14. Omar, H., Mahdjoubi, L., Kheder, G.: Towards an automated photogrammetry-based approach for monitoring and controlling construction site activities. *Comput. Ind.* **98**, 172–182 (2018). <https://doi.org/10.1016/J.COMPIND.2018.03.012>
15. Soliman, K., Naji, K., Gunduz, M., Tokdemir, O. B., Faqih, F., Zayed, T.: BIM-based facility management models for existing buildings. *J. Eng. Res. (Kuwait)* **10**(1), 21–37 (2022). <https://doi.org/10.36909/JER.11433>
16. Leonov, A.V.: The analysis of differences between historical design documents and the real structure of the Shabolovka radio tower based on using 3D model. *Struct. Mech. Eng. Constr. Build.* **6**, 15–22 (2014)
17. Leonov, A.V., Anikushkin, M.N., Ivanov, A.V., Ovcharov, S.V., Bobkov, A.E., Baturin, Y.M.: Laser scanning and 3D modeling of the Shukhov hyperboloid tower in Moscow. *J. Cult. Herit.* **16**(4), 551–559 (2015). <https://doi.org/10.1016/J.CULHER.2014.09.014>
18. Graefe, R., Gappoev, M., Pertschi, O., Shukhov V.G.: (1853–1939): *The Art of Structure*. Mir, Moscow (1995)
19. Anikushkin, M., Leonov, A.: 3D modeling of the Shukhov radio tower based on laser scanning. *Ind. Civil Eng.* **4**, 56–58 (2013)
20. Vinogradov, D., Stepanov, D.: 3D portrait of the Shukhov tower. *Arch. Restorat. Des. Constr.* **3**(49), 74–75 (2011)
21. Val'kov, V.A., Mustafin, M.G., Makarov G.V.: Application of terrestrial laser scanning for creation of three-dimensional models of Shukhov tower. *J. Mining Inst.* **204**, 58 (2013)
22. <https://con-fig.com/wp-content/uploads/2019/02/Anikushkin-Nazemnoe-lazemoe-skanirovani-i-3D-modelirovanie-SHuhovskoj-bashni-na-SHabolovke-SPB-fevral-2013.pdf>
23. Korchukov, A.S., Leonov, A.V.: Using the laser scanning technology at 3d's models creation and monitoring of monuments of architecture. *Tehnologija i Organizacija Stroitel'nogo Proizvodstva* **1**, 49–51 (2013)

Increasing the Energy Efficiency of Ventilated Facades Using Different Insulators



Dmitriy Kraynov , Galina Medvedeva , Renat Sadykov ,
and Aigul Ibragimova

Abstract The goal of this research is to investigate a ventilated facade, its energy efficiency and applicability in combination with different types of insulation. The major advantage of a ventilated facade is an increase in thermophysical properties achieved due to an air gap between the facade part of the enclosing structure and the main wall «pie». However, a significant weakness of such a multilayered enclosing structure is an increase in the cost of materials and installation work. The authors performed a thermotechnical calculation of the hinged facade system, taking into account the impact of a bracket. After completing the calculation, the following values were compared: heat resistance and coefficients of thermal heterogeneity. A class of thermal efficiency of elements of the structure was determined. The article concludes the effectiveness of ventilated facade, both in physical and economic terms.

Keywords Ventilated facade · Thermal insulation · Energy efficiency · Air gap · Heat loss

1 Introduction

Today, various multi-layer enclosing structures with effective thermal insulation materials are widely used. Therefore the pressing issue is improvement of the energy efficiency of buildings and reduction in expenses for their operation. Such structures include hinged facades with a ventilated air gap. The main elements of the enclosing structure of the wall with a ventilated air gap are the following: a structural layer, a thermal insulation layer, a substructure for fixing the cladding layer and the cladding layer [1].

D. Kraynov (✉) · G. Medvedeva · R. Sadykov
Kazan State University of Architecture and Engineering, Kazan 420043, Russia
e-mail: dmitriy.kraynov@gmail.com

A. Ibragimova
Department of Urban Planning Permits of the Executive Committee of Kazan, Kazan 420043,
Russia

Ventilated facade is a structure consisting of bearing (structural) and thermal insulation layers. A wide range of thermal insulation materials, located on the outer side of the enclosure, is used [2]. The type of composition solves the problem of steam condensation, as a result of which the wall materials do not get wet. The accumulated moisture is released in the ventilated facade, but due to the gap where the air flows circulate, no condensation occurs [3]. The air conditions in the ventilated layer of a hinged facade system are formed under convective mass transfer and wind [3].

Energy efficient building envelopes are, first of all, structures with the required thermal and technical characteristics [4]. One of the most widespread ways to achieve the required characteristics is the use of various insulation materials with a low heat transfer coefficient [2].

One of the best ways to increase thermal resistance is to increase the thermal uniformity coefficient, which is achieved by using corrosion-resistant steel brackets, thermal conductivity of which is substantially lower than thermal conductivity of galvanized steel or aluminum alloys [5]. Facades with the use of supporting systems made of corrosion-resistant steel are considered expensive but have longer service life. The other most economically acceptable way is the choice of optimal thickness of insulation [6].

Studies of thermal fields of enclosing structures with a ventilated air gap have a long history. However, it is not always possible to take into account the complex nature of thermal transfer within the air gap, which should not be considered independently of the thermal insulation and the structural layer. A comprehensive approach to improving individual system elements and design solutions in general is an important factor in increasing the effectiveness of their use [7].

The main problem of hinged ventilated facades is the influence of metal brackets on the heat loss of the wall. Brackets pass through the insulation, leading to a decrease in the coefficient of thermal uniformity due to the difference in the thermal conductivity coefficients of the materials of the bracket and insulation. All existing solutions to the problem suggest reducing the number of brackets per unit area or increasing the thickness of the thermal insulation layer [3].

One advantage of using hinged ventilated facades is a significant reduction in construction costs. The improvement of the efficiency of ventilated facades is possible by choosing the most efficient and inexpensive option for insulating the exterior walls of buildings [3].

Thus, the priority tasks today are improving the energy efficiency of buildings, reducing the operation costs, the rational choice of insulation material and walling material in the design of the hinged ventilated facade design [8].

The research objective is to calculate the thermal technical characteristics of the wall envelope with a ventilated layer and analyze the use of different thermal insulation materials in ventilated facades [9].

In the furtherance of this goal, the following tasks were addressed: substantiation of the possibility of using ventilated facades with one of the considered insulators; determination of specific heat losses through the brackets of the ventilated facade; comparison of thermal insulation options in the construction of exterior walls in

terms of thermal characteristics and economic feasibility. The choice of insulation is based on a comparative analysis of the properties that are important for the structure.

2 Materials and Methods

2.1 Mathematical Model

The process of heat and moisture transfer in a flat enclosing structure is modeled as follows from the stated methodology [11].

To describe the heat transfer in a multi-layer enclosing structure of a one-dimensional problem, the heat conductivity equation is used:

$$T_\tau = [a(x)T_x]_x \pm F(x, \tau) \tag{1}$$

where $F(x, \tau)$ is a function describing heat sources or sinks. Equation (1) can be written as:

$$\frac{\partial T}{\partial \tau} = \frac{\partial}{\partial x} \left[a(x) \frac{\partial T}{\partial x} \right] \pm F(x, \tau) \tag{2}$$

where $a(x) = \lambda(x) / (C_p(x) \cdot \rho(x))$ is a temperature diffusivity coefficient of the material.

Air circulation in the layer occurs due to gravity (thermal) head and wind pressure. If the air inlets and outlets are located on different walls, the air velocity in the layer V_{gap} can be determined by the following equations [12]:

$$V_{gap} = \sqrt{\frac{K(K_f - K_b)V_{ext}^2 + 0.08h(t_{gap} - t_{ext})}{\sum \xi}} \tag{3}$$

If the air gap is located on the same side of the building, it is possible to take $K_f = K_b$. In this case, if we neglect the variation in wind speed with height, Eq. (3) is as follows [12]:

$$V_{gap} = \sqrt{\frac{0.08h(t_{gap} - t_{ext})}{\sum \xi}} \tag{4}$$

The temperature of the air entering the air gap τ_0 is determined from the formula [15]:

$$\tau_0 = t_{ext} + \frac{t_{int} - t_{ext}}{m \cdot \alpha_v (\sqrt{B_w} + 23B_o)} \tag{5}$$

where m is a coefficient equal to 0.26;

It is allowed to determine the air temperature entering the layer from the formula:

$$\tau_0 = 0.95 \cdot t_{ext} \quad (6)$$

The air temperature along the length of the layer is determined from the formula:

$$t_y = \frac{(k_{int} \cdot t_{int} - k_{ext} \cdot t_{ext}) + [\tau_0(k_{int} + k_{ext}) - (k_{int} \cdot t_{int} + k_{ext} \cdot t_{ext})] \cdot e^{-B(k_{int}+k_{ext})h/WC}}{k_{int} + k_{ext}} \quad (7)$$

where k_{int} and k_{ext} are the heat transfer coefficients of the internal and external parts of the wall up to the middle of the layer.

The relative influence of the effective thermal resistance of the air gap is of greater importance for calculation the heat loss through the enclosure, as it determines how much heat loss will be reduced [16]. Notwithstanding that the greatest absolute value of $R_{eff}^{(gap)}$ is achieved at the maximum R_0^{pr} of construction, the effective thermal resistance of the air gap has the greatest impact on heat loss at the minimum value of R_0^{pr} of construction.

In determining the thermal resistance of the layer R_{gap} the following formulae are used [14]:

$$R_{gap} = \frac{1}{\alpha_{gap}} \quad (8)$$

$$\alpha_{gap} = 5.5 + 5.7V_{gap} + \alpha_r \quad (9)$$

The calculation is further based on the representation of a part of the thermal envelope of the building as a set of independent elements, each of which affects the heat loss through the fragment. The specific heat losses due to each element are on the basis of comparison of the heat flow through the point containing the element [10].

1. The heat transfer resistance of the fragment of the building envelope R_0^{pr} , ($m^2 \cdot ^\circ C$)/W, should be determined from the formula [13]:

$$R_0^{pr} = \frac{1}{1/R_0 + \sum l_j \Psi_j + \sum n_k \chi_k} = \frac{1}{\sum a_i U_i + \sum l_j \Psi_j + \sum n_k \chi_k} \quad (10)$$

$$a_i = \frac{A_i}{\sum A_i} \quad (11)$$

$$U_i = \frac{1}{R_{0,i}} \quad (12)$$

2. The coefficient of thermal homogeneity r is an auxiliary value that characterizes the efficiency of insulation of the structure, determined by the formula [14]:

$$r = \frac{R_0^{pr}}{R_0} \quad (13)$$

The R_0 value is determined by averaging over the area of the values of conditional resistance to heat transfer of all parts of the fragment of the thermal envelope of the building, which is determined by the formula [13]:

$$R_0 = \frac{\sum A_i}{\sum \frac{A_i}{R_{0,i}}} = \frac{1}{\sum a_i U_i} \quad (14)$$

$$R_0 = \frac{1}{\alpha_{int}} + \sum R_s + \frac{1}{\alpha_{ext}} \quad (15)$$

$$R_s = \frac{\delta_s}{\lambda_s} \quad (16)$$

- Specific heat losses through linear thermal heterogeneity are determined by calculating the two-dimensional temperature field of the structural unit at internal air temperature t_{int} and external air temperature t_{ext} [16].

$$\Psi_j = \frac{\Delta Q_j^L}{t_{int} - t_{ext}} \quad (17)$$

$$\Delta Q_j^L = Q_j^L - Q_{j,1} - Q_{j,2} \quad (18)$$

where $Q_{j,1}$ and $Q_{j,2}$ are heat losses through areas of homogeneous fragment parts, included in the computational domain when calculating the temperature field of the area with linear thermal heterogeneity of the j -type, W/m, determined by the formulae:

$$Q_{j,1} = \frac{t_{int} - t_{ext}}{R_{0,j,1} \cdot 1} S_{j,1}; \quad Q_{j,2} = \frac{t_{int} - t_{ext}}{R_{0,j,2} \cdot 1} S_{j,2} \quad (19)$$

where $S_{j,1}$, $S_{j,2}$ are areas of homogeneous parts of the structure, included in the computational domain when calculating the temperature field, m^2 .

The $S_{j,1} + S_{j,2}$ value is equal to the area of the computational domain when calculating the temperature field.

- Specific heat losses through the point thermal heterogeneity of the k -type are determined by calculating the three-dimensional temperature field of the section of the structure containing the point thermal heterogeneity, according to the formula [13]:

$$\chi_k = \frac{\Delta Q_k^K}{t_{\text{int}} - t_{\text{ext}}} \quad (20)$$

where ΔQ_k^K is additional heat losses through the point heat heterogeneity of the k-type, W, determined by the following equation [13]:

$$\Delta Q_k^K = Q_k^K - Q_k \quad (21)$$

5. The result of calculating the temperature field of the structural node is the temperature distribution in the cross section of the node, including the internal and external sides.

The heat flow through the inner surface of the node is determined by the formula [13]:

$$Q_{\text{int}} = \alpha_{\text{int}} (t_{\text{int}} - t_{\text{int}}^{\text{surf}}) S_{\text{int}} \quad (22)$$

$$Q_{\text{ext}} = \alpha_{\text{ext}} (t_{\text{ext}} - t_{\text{ext}}^{\text{surf}}) S_{\text{ext}} \quad (23)$$

2.2 Numerical Solution

According to the considered methodology, the thermal calculation for a ventilated facade with the use of different insulators was carried out. For the calculation, three types of insulation were selected: mineral wool, cellular glass, polystyrene foam (Table 1). The thickness of insulation is 0.1 m. The thickness of the air layer is taken 0.05 m.

Table 1 Characteristics of the building envelope

Name	ρ , kg/m ³	δ , m	λ , W/(m·°C)	μ , mg/(m·h·Pa)	R_s , (m ² ·°C)/W
Plaster	1600	0.015	0.81	0.12	0.02
Cellular concrete blocks	600	0.3	0.18	0.28	1.67
Mineral wool	50	0.1	0.048	0.55	2.08
Cellular glass	110	0.1	0.052	0.02	1.92
Polystyrene	40	0.1	0.038	0.05	2.63
Air gap	–	0.05	–	–	
Ceramic tile	1700	0.016	0.4	–	0.04

The temperatures inside and outside are +20 and -31 °C, respectively. The heat transfer coefficient of the inner and outer shell was assumed to be $\alpha_{int} = 8.7 \text{ W}/(\text{m}^2 \cdot \text{°C})$ and $\alpha_{ext} = 23 \text{ W}/(\text{m}^2 \cdot \text{°C})$, respectively.

The temperature entering the layer is determined by the initial parameters $\tau_0 = -29.45 \text{ °C}$. Then the air velocity according to Eq. (4) is $v_{pr} = 0.106 \text{ m/s}$. The thermal resistance of the air layer is determined by Eq. (8) $R_{pr} = 0.12 \text{ (m}^2 \cdot \text{°C)/W}$.

These values are necessary to calculate the specific resistance of the heat loss of a point element.

The specific losses were calculated using numerical modeling methods that make allowance for the nonlinear parameter relationships and complex geometry of thermal inclusions when calculating the temperature fields.

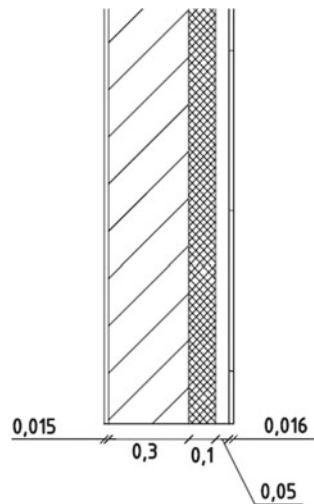
2.3 Numerical Modeling Using Software

The following ventilated facade construction is considered. A bracket is attached to the wall of the building with a thermal insulation gasket between the wall and the bracket [17]. The vertical rail is made of aluminum alloy. The brackets are made of aluminum alloy and are mounted with facade metal expansion anchors (Fig. 1).

For a comparative assessment of efficiency, the thermal calculation of three insulators of ventilated facade systems was performed numerically in the software package. Solving the problem using software allows taking into account all the geometric features of the structure and the thermal heterogeneity.

In order to determine the coefficient of thermal homogeneity of the systems under study, we calculated the reduced heat transfer resistance of a similar structure without brackets that introduce heterogeneity into the insulation layer.

Fig. 1 Scheme of the enclosing structure with an air gap



There is a distortion of initial conditions at the point where the bracket crosses the boundary of the calculation zone. This is explained by the fact that high heat flows pass through the bracket and the unaccounted influence of substructure and the outer facing layer, which are in direct contact with the bracket. Taking into account heat loss of the bracket in the air layer due to heat transfer with air leads to a balance scheme with one heat supply (an attachment point of the bracket to the wall) and two heat output points (an air gap and the guide rail with cladding). The process is described by the axisymmetric stationary equation of thermal conductivity, which is easily solved. The air temperature in the air gap is determined numerically (Fig. 2).

The obtained values of heat losses through the junction with different insulators are summarized in Table 2.

Table 3 provides a comparative analysis of the thermal characteristics obtained with the software and those given in SP 230.1325800.2015.

Fig. 2 Isotherms along the section of the node of the hinged ventilated facade with a bracket pass in increments of 0.1

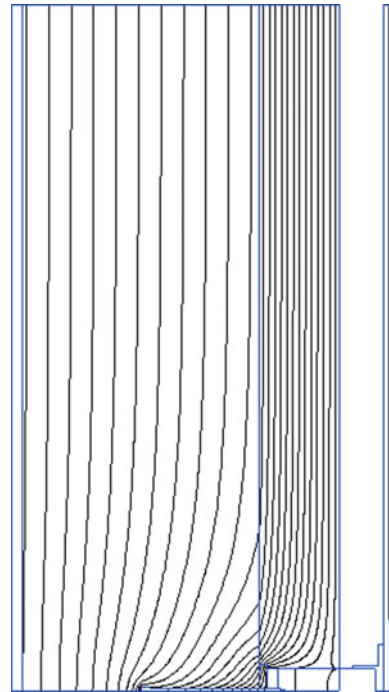


Table 2 Heat loss through the node

Insulation	Q, W	χ , W/°C	t_{\min} , °C
Mineral wool	30.902	0.025	18.32
Cellular glass	32.17	0.027	18.27
Polystyrene	27.251	0.022	18.48

Table 3 Specific heat loss through the bracket χ , W/°C for $\lambda_o = 0,18$ W/(m·°C)

Insulation	R_s , (m ² ·°C)/W	Software calculation	SP 230.1325800.2015
Mineral wool	2.08	0.025	0.0139
Cellular glass	2.63	0.027	0.0157
Polystyrene	1.92	0.022	0.0134

Table 4 The value of the reduced resistance with the use of different insulators

Insulation	R_0 , (m ² ·°C)/W	R_0^{Pr} , (m ² ·°C)/W	r
Mineral wool	4.05	3.23	0.798
Cellular glass	3.89	3.08	0.792
Polystyrene	4.60	3.67	0.798

Table 5 Energy efficiency class

Insulation	δ , m	U, W/(m ² ·°C)	Cost, rub/m ²	Ω , rub/(kW·h/year)	Energy efficiency class
Mineral wool	0.1	0.48	350	14.236	5
Polystyrene	0.1	0.38	473	60.082	7
Cellular glass	0.1	0.52	1200	96.153	8

Effect of brackets on the heat transfer resistance of a wall with a ventilated layer (Table 4).

The results show that polystyrene foam has the highest value of resistance to heat transfer of the fragment of the considered enclosing structure.

Let the class of thermal efficiency of the structural element be determined, i.e., the insulation in terms of the specific one-time cost of saving an energy unit Ω , rub/(kW·h/year) according to SP 345.1325800.2017 and tabulate it (Table 5).

To conclude, we can say that mineral wool is the most suitable insulation, both thermophysically and economically.

The feasibility of using a system with one of the heat insulation is shown on the basis of thermal engineering calculation of building envelopes.

3 Results and Discussions

Increasing the energy efficiency of buildings by increasing the characteristics of external enclosures involves the use of multi-layer structures with a layer of effective insulation [18]. The thermal insulation material should be chosen not only on the basis of material costs for its production, but taking into account the environmental protection as well. Therefore, the economic efficiency of energy-saving solutions is of

great interest. When choosing a thermal insulation for a system of hinged ventilated facades, it is necessary to be guided by physical and technical characteristics, fire safety and environmental friendliness.

Mineral wool heat insulation can modify energy efficiency properties on exposure to moisture. The facts of significant reduction of the thermal and technical properties are known [14]. Therefore the air gap and a waterproofing membrane are the important elements of the construction of the hinged ventilated facade. Waterproofing membrane should be mounted in a single and continuous layer, which cannot be achieved in practice [19]. Subsequently, the insulation gets wet and loses its insulating properties.

Polystyrene foam has special properties such as environmental and thermal stability. This is one of the main reasons why it is used for ventilated facade insulation [20, 21]. The closed-cell structure of the material does not collect moisture [16], hence the thermal performance remains unchanged and there is no need to use a waterproofing membrane.

The insulation based on polystyrene foam is not economical, has no moisture vapor transmission. That is why insulation with this material does not allow the walls to pass the air. The flammable material emits toxic substances during combustion [22, 23]. The advantage is the relative ease of installation at height, as the material has a small self-weight.

Thus, we defined the concept of reduced heat transfer resistance of a fragment of the enclosing structure and obtained calculated values of the reduced resistance. Furthermore, we concluded that when considering the hinged facade system, taking into account point heterogeneity, polystyrene foam has the highest value of the reduced resistance, which is the most relevant condition for improving energy efficiency. However, the low degree of environmental friendliness limits the use of polystyrene foam.

All the considered options of heat insulation meet the requirements of thermal protection of the building. But the essential requirement when choosing the material for the insulation layer is its non-combustibility, as the design of the hinged system implies its increased fire hazard. From this we can conclude that an account must be taken of many parameters when choosing a thermal insulation that is why it is impossible to decide on a particular insulation.



References

1. Sazankova, K.A.: Problems of energy efficiency of hinged ventilated facade systems. *Arch. Des.* **4**, 31–36 (2018)
2. Nemova, D.V.: Energy efficient technologies in enclosing structures. *Constr. Unique Build. Struct.* **3**, 77–82 (2012)
3. Tushina, V.M.: To the problem of bearing capacity and operational reliability of suspended ventilated facade. *Procedia Eng.* **153**, 799–804 (2016)

4. Pujadas-Gispert, E., Alsailani, M., van Dijk, K., Rozema, A.D., ten Hoop, J.P., Korevaar, C., Moonen, S.: Design, construction, and thermal performance evaluation of an innovative bio-based ventilated facade 2020. *Front. Arch. Res.* **9**(3), 681–696 (2020)
5. Petrichenko, M.R., Koto, E.V., Nemova, D.V., Tarasova, D.S., Sergeev, V.V.: Numerical modeling of ventilated facades in extreme climatic conditions. *Maga. Civil Eng.* **1**(77), 130–140 (2018)
6. Bolgarskiy, A.V., Muhachev, G.A., Shukin, V.K.: *Thermodynamics and Heat Transfer*, 2nd edn. High school, Moscow (1975)
7. Bogoslovskiy, V.N.: *Building Thermal Physics*, 2nd edn. High school, Moscow (1982)
8. Hackl, R., Harvey, S.: Framework methodology for increased energy efficiency and renewable feedstock integration in industrial clusters. *Appl. Energy* **112**, 1500–1509 (2013)
9. Sapacheva, L., Goreglyad, S.: Foam glass for green building in Russia. *Constr. Mater.* **1**, 30–31 (2015)
10. Sadykov, R., Kupriyanov, V., Kraynov, D., Safin, I., Ivancov, A.: *Calculation of the Reduced Resistance to Heat Transfer of External Building Envelopes*. Publisher KSUAE, Kazan (2018)
11. Fokin, K.: *Construction Heat Engineering of Enclosing Parts of Buildings*. AVOK-Press, Moscow (2006)
12. Nikolaev, S., Granik, Y., Starovskiy, G., Ziyranov, V., Belyaev, V.: *Design and application recommendations for building construction and renovation*. Moscow (2003)
13. SP 230.1325800.2015 Construction enclosing of buildings characteristics of thermal conductive of inclusions (2015)
14. SP 50.13330.2012 Thermal performance of the buildings (2012)
15. Gaisin, A., Samokhodova, S., Paimetkina, A., Nedoseko, I.: Comparative assessment of specific heat losses through the elements of the outer walls of residential buildings, determined by various methods. *Housing Constr.* **5**, 36–39 (2016)
16. Gagarin, V., Kozlov, V., Lushin, K., Plyuschenko, N.: Accounting for heat-conducting inclusions and a ventilated layer when calculating the heat transfer resistance of a wall with a hinged facade system (HFS). *Constr. Mater.*, 32–35 (2016)
17. Shahrestani, M., Runming, Y., Essah, E., Shao, L., Oliveira, A., Hepbasli, A., Biyik, E., Canod, T., Rico, E., Lechon, J.: Experimental and numerical studies to assess the energy performance of naturally ventilated PV facade systems. *Sol. Energy* **147**, 37–51 (2017)
18. Sanjuan, C., Suárez, M., González, M., Pistono, J., Blanco, E.: Energy performance of an open-joint ventilated facade compared with a conventional sealed cavity facade. *Sol. Energy* **85**, 1851–1863 (2011)
19. Giacone, E., Manco, S.: Energy efficiency measurement in industrial processes. *Energy* **38**(1), 331–345 (2012)
20. Nizovtsev, M., Letushko, V., Borodulin, V., Sterlyagov, A.: Experimental studies of the thermo and humidity state of a new building facade insulation system based on panels with ventilated channels. *Energy and buildings* **206**, 109607 (2020)
21. Khabibulina, A.: To the choice of designs of front systems taking into account heat-shielding characteristics at reconstruction of objects of cultural heritage. *News Kazan State Univ. Arch. Eng.* **3**(45), 62–71 (2018)
22. Kozlov, V.: Issues of accuracy in calculating the reduced resistance to heat transfer and temperature fields. *Constr. Renov.* **3**, 62–74 (2018)
23. Petrov, A., Kupriyanov, V.: On the influence of a computer model of structures with thermotechnical heterogeneity on the accuracy of thermotechnical calculations. *Privolzhsky Sci. J.* **1**(49), 32–39 (2019)

Planning Field Development Using Optimization Algorithms



Alexander Semanov, Aigul Semanova, Irik Fattakhov , Farit Iangirov, and Juliya Kareeva 

Abstract The ultimate oil recovery rate is affected by both the geological properties of strata and the technological parameters of field development. The key indicators when choosing a development system are well grid density, the ratio of production and injection wells, technological modes of operation. Under the conditions of complex geological structure of fields, this problem cannot be solved without the use of tools of geological and hydrodynamic modeling. This work considers three options of planned well count arrangement with the distances between the wellbores of 150, 250, and 350 m within the limits of the external contour of the object oil bearing. The inverse five-point system has been chosen as an arrangement scheme. Calculations have been made using the hydrodynamic model. The results obtained showed that different options for the development of the object can be implemented (with different withdrawal rates, strategy performance, oil recovery rates), depending on the company's development strategy and allocated investments. Another important factor in choosing the option of object development is the operation modes of wells. For this purpose, we propose to use optimization algorithms built into the simulator. These algorithms make it possible to find the best solutions, observing the given conditions. The following algorithms were used in iterative calculations to find the optimal operation modes: differential evolution, particle swarm method, simplex method. The calculation results show that the optimization algorithms can be used to select a wide range of solutions for field development.

Keywords Modeling · Development planning · Optimization algorithms · Multivariate calculations · Well grid · Well operation mode

A. Semanov · A. Semanova · I. Fattakhov
PJSC TATNEFT Named After V.D. Shashin, Almetyevsk, Russia

I. Fattakhov
Ufa State Petroleum Technical University (Oktyabrsky Branch), Oktyabrsky, Russia

F. Iangirov
Ufa State Petroleum Technical University, Ufa, Russia

J. Kareeva (✉)
Kazan State University of Architecture and Engineering, Kazan, Russia
e-mail: jkareeva2503@gmail.com

1 Introduction

Standard field development practice involves drilling in several stages. The first stage is drilling of the main well count, usually according to a strictly geometric grid. Parameters of drilling are defined according to the exploration data. Further, the object is consecutively re-drilled with infill wells. Location and density of the additional drilling grid are determined based on the information on the drilled well count, volume of areas not involved in development, necessary rates of reserves withdrawal [1]. The ultimate oil recovery rate is affected by both the geological properties of strata and technological parameters of field development. The geology was formed millions of years ago and cannot be changed, but the main technological parameter affecting the ultimate oil recovery rate and withdrawal rates, the development system, can and should be selected based on the geological features of the object structure [11, 12].

The key indicators when selecting the development system are the density of the well grid, the ratio of production and injection wells, technological modes of well operation. The optimum density of wells is selected by calculating several options and choosing the best one in terms of technological and economic parameters. Under the conditions of complex geological structure of fields, this problem cannot be solved without the use of tools of geological and hydrodynamic modeling [2, 3].

2 Materials and Methods

In this work, we consider the object formed by the Tula depositions. In the section of the Tula horizon at the territory of the field, there are Stl-2, Stl-3 and Stl-4 strata, with which several oil deposits are associated. Tula strata are composed of siltstones and sandstones of fine and fine-grained monomineral composition, mainly quartz. In all wells that penetrated the Tula stratum, porous-permeable interlayers are bordered by compacted rocks. In the stratum section, one, less frequently two or three (typical for Stl-2) separate porous-permeable interlayers are distinguished, the total oil-saturated thicknesses vary from 0.5 to 8.2 m. The average thickness is 2 m. Sandiness and partition coefficients are 0.756 and 1.218, respectively.

The analysis of oil samples showed the saturation pressure of 2.2 MPa, the volume factor of 1.025 fractions of a unit, the average gas content of 7.33 m³/t. The analysis of downhole samples showed that the average density of oil in the stratum was 888 kg/m³ and in standard conditions, it was 900 kg/m³. According to the density, oil belongs to the group of bituminous. According to viscosity, oil also belongs to the group of bituminous, the average dynamic viscosity is 22.53 mPa·s.

To carry out calculations using the hydrodynamic model within the outer contour of oil bearing capacity, three options of arrangement of wells of the planned count with the distance between the bores of 150, 250 and 350 m have been developed. In addition, the limiting minimum distance to the drilled fund (150 m) has been introduced. The inverse five-point system was chosen as an arrangement scheme [4]. Graphical visualization of the planned wells arrangement is shown in Figs. 1, 2 and 3.

The arrangement schemes used are determined by the search for the most optimal location of wells for maximum reserves depletion at different withdrawal rates [15]. The forecast calculation period was 100 years. Compensation is set equal to 1 to prevent premature watering and maintain the stratum pressure. In addition, economic limitations were set on the production wells operation (oil flow rate not less than 0.5 t/day, water cut not more than 98%). If these limits are exceeded, the wells are shut down [13].

Another important point when selecting options for object development is to determine the operation modes of wells. For this purpose, this paper proposes to use optimization algorithms built into the simulator. These algorithms make it possible to find the best solutions, observing the given conditions. In the process of calculations, the set of possible options is enumerated until the value of the target function

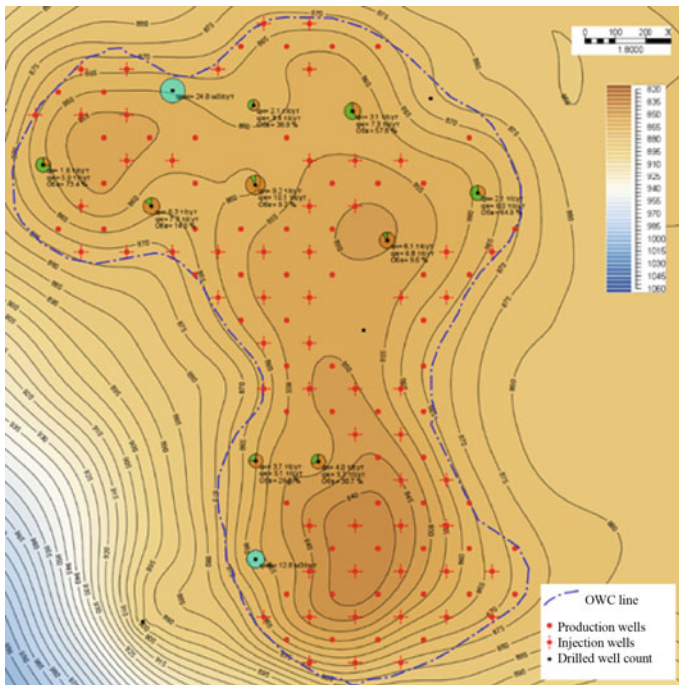


Fig. 1 Distance between wells of 150 m

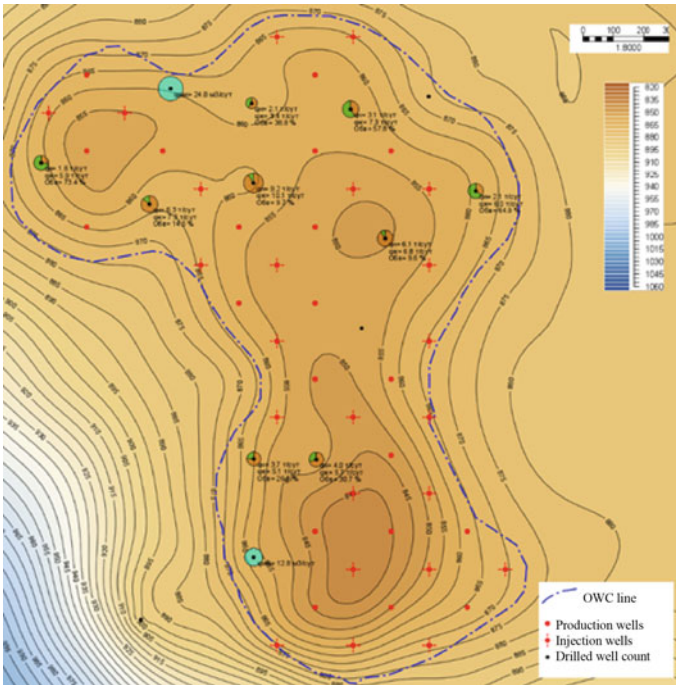


Fig. 2 Distance between wells of 250 m

reaches the given conditions. The options of calculations are formed by changing the parameters predetermined by the user [5, 6].

The following algorithms were used in iterative calculations to find the optimal modes of operation:

- Differential evolution;
- Particle swarm method;
- Simplex method.

Differential evolution is a stochastic optimization algorithm aimed at minimizing the target function in a given search space. The maximum number of iterations is set for this algorithm. One iteration of the algorithm involves one simulation run. When preparing the calculation, the target function must be set. The algorithm operates with some set of vectors from the search space. This set is called a population. The larger is the population size, the better the algorithm feels the target function. At the first iterations the algorithm fills the initial population with random vectors from the search space. The vector corresponding to the basic model is always included in the population. After the initial population is populated, the algorithm makes a trial vector at each iteration and computes the target function for it by running the simulator. The trial vector is compiled by randomly mixing the components of the target vector and the mutant vector (1). The parameter Cr corresponds to the probability of substitution

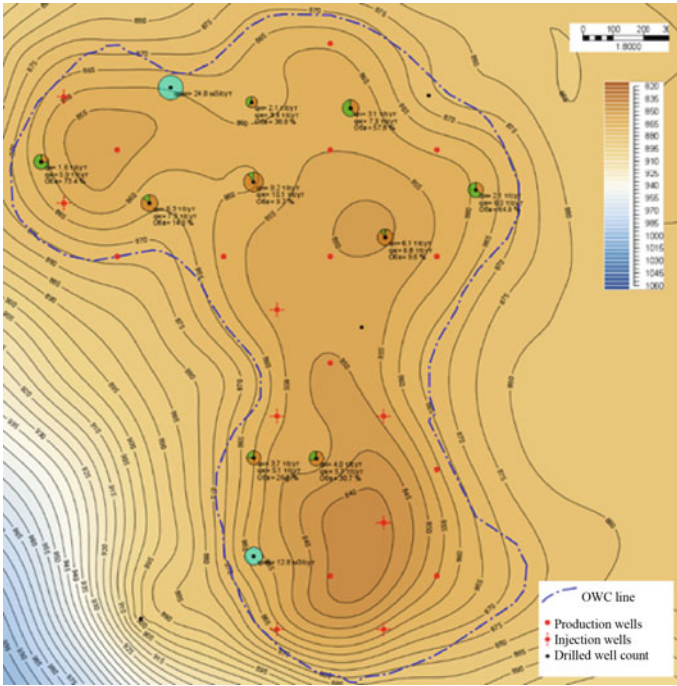


Fig. 3 Distance between wells of 350 m

of the target vector component by the mutant vector component. The choice of the target vector from the population can be changed by the user.

$$V_{\text{trial}} = M_{\text{ixingCr}}(V_{\text{target}}, V_{\text{mutant}}) \tag{1}$$

The mutant vector is compiled as a sum of the basic vector and several differences of random vectors from the population, multiplied by the parameter F. The choice of the basic vector from the population and the number of differences are also adjustable.

Below is an example of a formula for the number of differences equal to two (2):

$$V_{\text{mutant}} = V_{\text{basic}} + F \times (V_{\text{random1}} - V_{\text{random2}}) + F \times (V_{\text{random3}} - V_{\text{random4}}) \tag{2}$$

When the target function is calculated on the trial vector, its value is compared to the value of the target function on the target vector (3).

$$f_{\text{target}}(V_{\text{trial}}) ? f_{\text{target}}(V_{\text{target}}) \tag{3}$$

If the trial vector provides the best value of the target function, it replaces the target vector in the population. And so the algorithm keeps iterating until the number of iterations exceeds the value set by the user [14].

The Nelder-Mead algorithm (or simplex method) solves the classical problem of minimizing a function of n variables. This method has the following features:

- It uses the function value only at some points;
- It does not construct approximate values of the gradients at each of these points.

It belongs to the class of direct search methods. For this algorithm, it is also necessary to specify the target function. The Nelder–Mead method is based on a simplex. A simplex $S \subset \mathbb{R}^n$ is a convex hull of $n + 1$ points $x_0, x_1, \dots, x_n \in \mathbb{R}^n$. For example, a simplex in \mathbb{R}^2 is a triangle, in \mathbb{R}^3 it is a tetrahedron.

The simplex-based direct search method works with a simplex $S = x_0, \dots, x_n \in \mathbb{R}^n$ and corresponding values of function f in its vertices $f_i = f(x_i)$, $i = 0, \dots, n$. The initial simplex must be non-singular, i.e. consist of points not lying in one plane. Further the method performs a sequence of transformations of the simplex S , aimed at decreasing the values of the function in its vertices. At each step, the transformation is determined by calculation of one or more test points and function values at these points, and comparing these function values with its values at the vertices of the simplex. The process is completed when in some sense either the simplex S becomes sufficiently small or the values of f_i are close (if f is continuous).

The Nelder–Mead algorithm requires one or two calculations of function values, unlike other direct search methods that require n or more calculations.

The Particle Swarm Optimization (PSO) is a stochastic optimization algorithm aimed at minimizing the target function in a given search space. The algorithm was originally developed to simulate social behavior. Further, this algorithm has been remarked to be suitable for optimization problems.

The maximum number of iterations is set for this algorithm. One iteration of the algorithm includes a single simulation run. The target function must be set for this algorithm.

The algorithm works with some set of particles, called a swarm. Each particle is described by its position in the search space and its velocity vector. In addition, each particle stores its local best position. The swarm, in turn, stores the global best position. The larger is the swarm size, the better the search space will be explored.

At the first iterations, the algorithm fills the swarm with particles with random positions and velocity vectors. The positions corresponding to the basic model are always included in the swarm. After calculating the target function, the global and local best positions are updated at the points of the search space corresponding to the positions of the swarm particles. So, the velocity vector of the particle changes. The particle moves along the obtained velocity vector to a new position. Thus a swarm of particles explores a given search space, optimizing the target function [7].

3 Results and Discussion

The calculations results are presented in Fig. 4 and Table 1. The options with 150, 250 and 350 m distance between wells have 60, 20, and 12 production wells on the object, respectively. As expected, the maximum oil recovery rate has been received in the first option with minimum specific oil production per well (3,4 thousand tons per well). The maximum technological oil recovery rate was 0.49.

To perform test calculations on selection of well operation modes, a grid with a 250 m distance between wells was used. Fluid flow rates and well injectivity were used as variables. In addition, upper and lower limitations on bottomhole pressure were set. The target function is the maximum cumulative oil production [7, 8, 16]. The calculations have been carried out for 15 years. The results are shown in Figs. 5, 6 and 7.

The maximum cumulative indicators for the object are presented in Table 2. The calculation results show that optimization algorithms can be used to select a wide

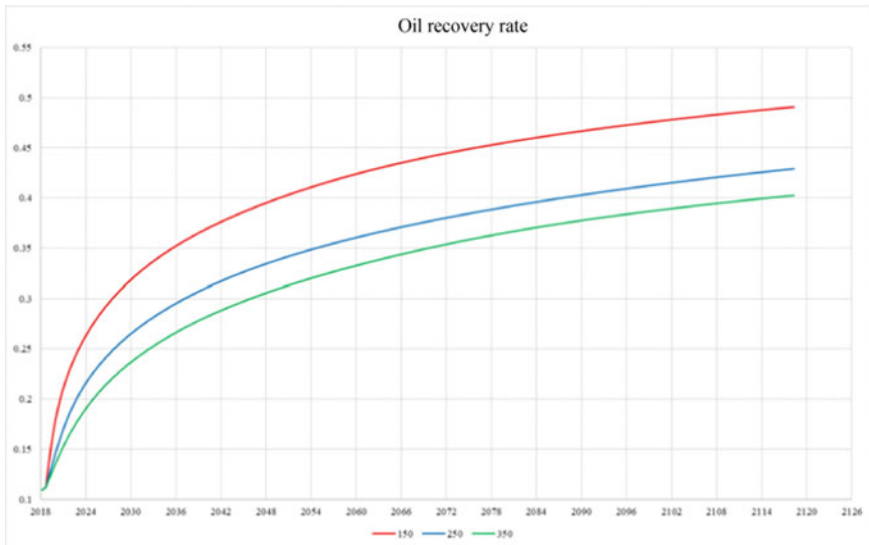


Fig. 4 The dynamics of oil recovery rate

Table 1 Calculation results

	150 m	250 m	350 m
Oil recovery rate	0.490	0.429	0.403
Number of production wells	60	20	12
Number of injection wells	57	23	8
Specific additional production per well (15 years), thousand m ³ /well	3.4	6.4	10.5

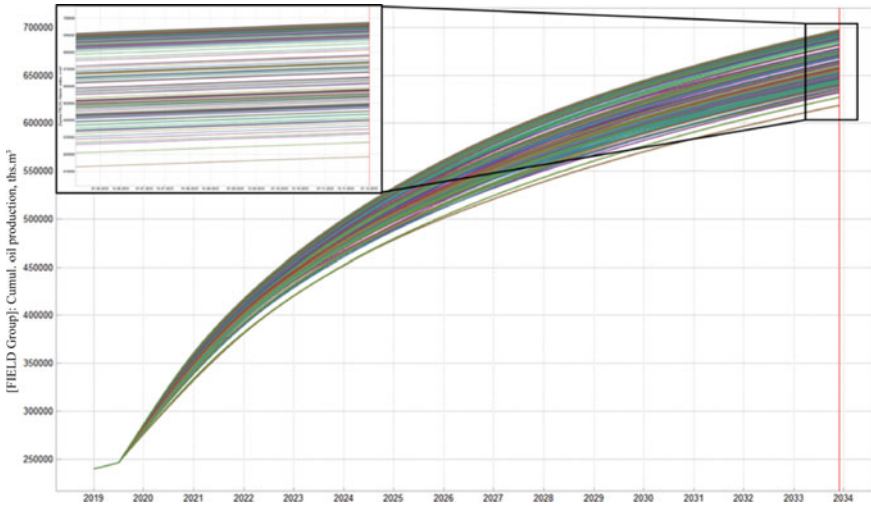


Fig. 5 The results obtained by the differential evolution

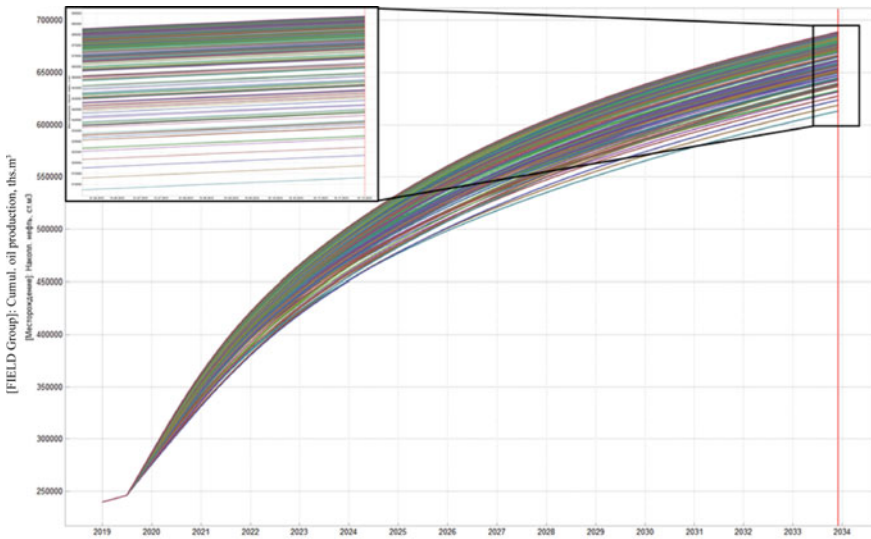


Fig. 6 The results obtained by particle swarm method

range of field development solutions. For example, according to differential evolution method, the difference between options with maximum and minimum cumulative oil production is 8.8%.

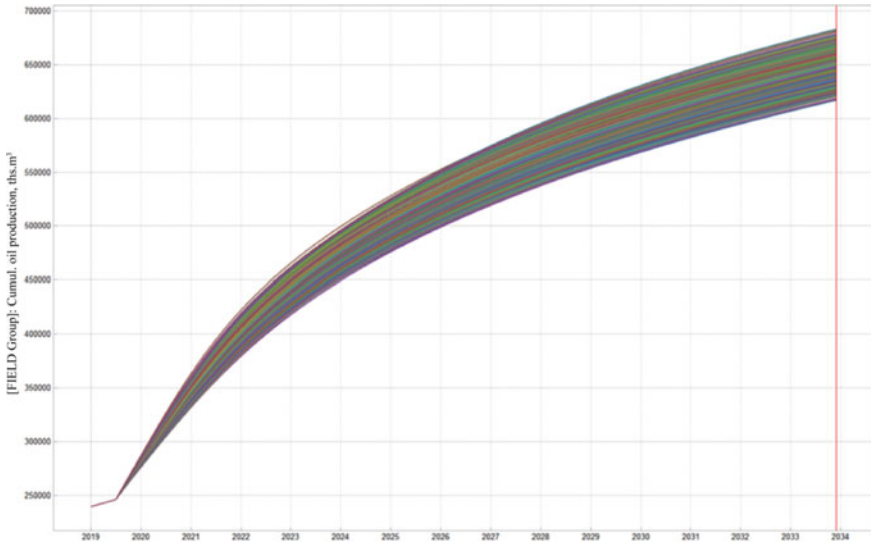


Fig. 7 The results obtained by the simplex method

Table 2 Comparison of results obtained by various optimization algorithms

	Diff. evolution	Particle swarm method	Simplex method
Cumulative oil production, thousand m ³	697.6	688.7	683
Cumulative fluid production, thousand m ³	1926.3	1900.6	1816

4 Conclusion

Thus, the maximum cumulative oil production was obtained using differential evolution method. Similar approaches can be used to select wellbore type, pumping type, development system pattern, and application of well interventions [17, 18]. Additionally, it is possible to select the optimal length and trajectory of horizontal wells. Optimization models make it possible to increase the accuracy of quantitative analysis and improve the current development system [9, 10]. The use of modeling simplifies and expands possibilities to find the optimal development option with different withdrawal rates and capital costs. To choose the appropriate option, it is necessary to perform economical calculations and determine the relationship between NPV and the density of the well grid. The results obtained showed that it is possible to implement different options of object development (with different withdrawal rates, strategy performance, oil recovery rates) depending on the company development strategy and allocated investments [19, 20].

References

1. Abyzbaev, I.I., Fazleeva, D. R., Abyzbaev, N. I., Yanchenko, S.V.: On the issue of integrated design of oil field development. *Prob. Gathering Treat. Transp. Oil Oil Prod.* **3**(119), 82–88 (2019)
2. Prokop'ev-Rotermil, A.A.: Designing the optimal option of the field development project. *Enigma* **27**(1), 109–115 (2020)
3. Antonov, O.G., Nasybullin, A.V., Lifantiev, A.V.: Improvement of methods of regulation of oil reservoir development. *Neftyanaya Provintsiya* **3**(7), 87–100 (2016)
4. Titov, V.E.: Tasks of modeling of filtration processes in designing the development of hydrocarbon fields. *Ashirovskie hteniya* **2**(18), 49–51 (2016)
5. Brilliant, L.S., Dulkarnaev, M.R., Danko, M.Y., et al.: Management of oil production on the basis of neural network optimization of well operation modes at the pilot operations site of reservoir YV1 of Vatyeganskoye field of TPP "Povkhneftegaz". *Georesursy* **24**(1), 3–15 (2022)
6. Brilliant, L.S., Zavyalov, A.S., Danko, M.Y., et al.: Integration of machine learning methods and geological and hydrodynamic modeling in field development design. *Neftyanoe Khozyaystvo* **3**, 48–53 (2022)
7. Mozhchil, A.F., Dmitriev, D.E., Bazyleva, N.Z., et al.: Application of optimization algorithms to solve engineering problems in conditions of high uncertainty. *Neftyanoe Khozyaystvo* **11**, 149–152 (2019)
8. Vaganov, L.A., Sencov, A.Y., Ankudinov, A.A., Polyakova, N.S.: Calculation of optimal injection rate for dispersed waterflooding system. *Oil Gas Stud.* (6), 63–67 (2017). <https://doi.org/10.31660/0445-0108-2017-6-63-67>
9. Bakhtizin, R.N., Fattakhov, I.G., Gimaev, R.G.: Study of unsteady water flooding production state. *Oil Gas Bus.* **11**(4), 68–72 (2013)
10. Fattakhov, I.G.: The consideration of the cyclic injection through the example of Stakhanovskiy oil field. *Mod. Fund. Appl. Res.* **4**(7), 70–73 (2012)
11. Dada, M.A., et al.: A field development strategy for the joint optimization of flow allocations, well placements and well trajectories. *Energy Explor. Exploit.* **39**, 502–527 (2020)
12. Nurgaliev, R.Z., Kozikhin, R.A., Fattakhov, I.G., Kuleshova, L.S.: Application prospects for new technologies in geological and technological risk assessment. *Gornyi Zhurnal* (4), 36–40 (2019)
13. Lushpeev, V.A., Margarit, A.: Optimization of oil field development process based on existing forecast model (2018)
14. Chen, S.Y., et al.: An analysis on the effect of selection on exploration in particle swarm optimization and differential evolution. In: 2019 IEEE Congress on Evolutionary Computation (CEC) (2019), pp. 3037–3044 (2019)
15. Feng, X., Liao, X.-W.: Study on well spacing optimization in a tight sandstone gas reservoir based on dynamic analysis. *ACS Omega* **5**, 3755–3762 (2020)
16. Fattakhov, I.G., Kuleshova, L.S., Yakubova, D.I., Murdasheva, L.V., Gafarov, R.R., Shaidullin, R.R.: Evaluation of the effectiveness of waterproofing based on model research. In: *Materials of the 45th Scientific and Technical Conference of Young Scientists, Graduate Students and Students*, pp. 180–182. USPTU Publishing House, Ufa (2018)
17. Bahtizin, R.N., Nurgaliev, R.Z., Fattakhov, I.G., Andreev, V.E., Safullina, A.R.: On the question of the efficiency analysis of the bottom-hole area stimulation method. *Int. J. Mech. Eng. Technol.* **9**(6), 1035–1044 (2018)
18. Babichev, I.N., Fattakhov, I.G., Kuleshova, L.S., Zaripov, L.F., Morozov, M.A.: Potential for the wellbore zone development using the dynamic impact. *IOP Conf. Ser. Earth Environ. Sci.* **378**(1), 012111 (2019)
19. Ramazanov, R., Kharlamov, K.A., Letko, I., Martsenyuk, R.: Analysis of injection wells operation at Srednebotuobinskoye field. *Neftyanoe khozyaystvo - Oil Industry* (2019)
20. Mahmood, F., Al-Hadrami, H., Pourafshary, P., Vakili-Nezhaad, G., Mosavat, N.: Optimization of smart water flooding in carbonate reservoir. In: *Paper presented at the Abu Dhabi International Petroleum Exhibition & Conference, Abu Dhabi, UAE* (2018)

Method of Assessing the Pressure Generated by the Water Packer Saturated Packer



Alfred Suleymanov , Rashit Kayumov , Denis Smirnov , Ilya Grishin ,
and Kamilya Belayeva

Abstract For today, the simplest and most reliable way to isolate geological beds when pumping wells is to use packers, which are elastomers capable of increasing in volume when in contact with certain formation fluids. The most significant indicator for the elastomers used in packers is the degree of their swelling, which provides layer isolation during construction and operation of wells. In this case, considerable pressure is applied on the wall of the tubing string, which can lead to its deformation. The purpose of this work is to create a method for determining the stresses caused by swelling of the packer for further assessment of the possibility of deformations in the tubing string. This article describes design of the device, which is used to assess the amount of deformation of the momentless shells caused by swelling of the elastomer samples used in the production of packers. The magnitude of the shell displacements was used to estimate the pressure that caused these displacements. In this case, the equations of the theory of momentless shells were used. It was assumed that the working conditions of the elastomer created by the device correspond to the working conditions of the packer, when its deformations along the pipe axis are almost absent, and the greatest radial pressure on the pipe occurs. An important condition is the choice of the shell material, for which a grid with a mesh size of 0.056 mm was proposed. The choice of such a material, on the one hand, is due to the need for unhindered access of water to the elastomer samples, and on the other hand, the need to exclude the possibility of blocking the cells as a result of its swelling. Obtained pressure values can be used for choosing one or another type of elastomer for the packer, taking into account the geometric parameters and mechanical properties of the tubing string.

Keywords Water-swellaable packers · Waterproofing joints · Tubing string · Momentless shells

A. Suleymanov · R. Kayumov · D. Smirnov · I. Grishin (✉) · K. Belayeva
Kazan State University of Architecture and Engineering, Kazan, Russia
e-mail: il6357grishin@yandex.ru

1 Introduction

Water-swellaable packers are designed for reliable and irreversible isolation of geological beds during the construction and operation of wells. The elastomer used for the packer manufacture can have wider applications and can be used, for example, in hydraulic engineering, for waterproofing joints at industrial, civil and transport construction sites [1–4].

When water-swellaable packers come into contact with wellbore fluids, the elastomer swells due to liquid absorption and seals the annular space in an open or cased well both during construction and well workover [5–7].

These packers have no moving parts. No special equipment is required for their installation in the annulus, and therefore the possibility of failure of such equipment is excluded. The use of water-swellaable packers to isolate geological beds in a well provides a safe and simplified alternative to cementing and perforating [3, 4, 8, 9]. The most likely place for geological bed water leakage is the area where the elastomer contacts the borehole wall [8–10]. Therefore, the provision of high stresses arising from the swelling of the elastomer in water is a prerequisite for its operation in the well [11–14]. However, excessive stress can deform the tubing string. In this connection, it becomes necessary to determine the pressure created by the swellaable packer on the tubing string wall during operation.

There is a known method for evaluating the efficiency of packers [1, 15], which consists in their prolonged thermal conditioning in water in special steel boxes and subsequent extrusion under load simulating the pressure of reservoir fluids. However, this method does not allow us to determine the magnitude of stresses arising directly in the elastomer during its swelling. The method of bench testing of water-swelling packers [15], developed by limited company Kvant together with TatNIPIneft, also does not make it possible to determine the value of internal stresses in the material.

2 Research Methods

2.1 *Experimental Methods*

The main goal of the study was to determine the maximum pressure that a packer can generate during water saturation in confined conditions. At the same time, it was required to limit its volumetric expansion so that the main volumetric expansion deformations would be directed for creating a measurable pressure. In addition, it was necessary to fulfill such conditions under which a continuous inflow of water would be ensured to the packer. The tested samples were cylinders 27 mm in height and 28 mm in diameter made of the same material from which the packer is made. Based on the required test conditions, a device design was proposed. It is schematically shown in Fig. 1. The scheme of using the device is as follows: seven cylindrical packer samples are placed in main ring 2, mesh 3 is applied above and below, then clamping

rings 1 are applied to the upper and lower mesh, tightened with bolts passing through holes 5. After that, the device is immersed in water, the packer samples become saturated with water resulting in swelling. When swelling, the samples expand in all directions, however, horizontally (radially) the volume increase is prevented by main ring 2, which has a significantly higher strength and rigidity compared to mesh 3. Thus, the expansion deformations are directed towards stretched mesh 3, according to the displacements of which the applied pressure is estimated. In the process of testing, the following should be considered. Mesh 3 should be selected so as to: 1) be strong enough to contain the packer swelling; 2) the mesh size should provide water access to the packer; 3) the cell size of the mesh should not be too small so that the packer material does not clog them when swelling and softening. For these purposes, a mesh was used according to TR 14-1-1702-76, with a cell of 0.056 mm and a wire diameter of 0.04 mm.

In addition, the size of the gap d is of some importance (Fig. 1). It should be minimum sufficient for free placement of samples into main ring 2. If the gap d is too large, part of the expansion deformation of the packer will go to overcome this distance until it touches the walls of the main ring. Since the main goal is to create a unidirectional expansion that causes the greatest pressure, the gap d should be minimized as much as possible.

The general view of the device in working condition is shown in Fig. 2, where a horizontal plate with a deformation indicator installed in it can be observed. The

Fig. 1 Device scheme: 1 - clamping rings; 2 - main ring; 3 - stretched mesh; 4 - sample packer; 5 - clamping bolt holes

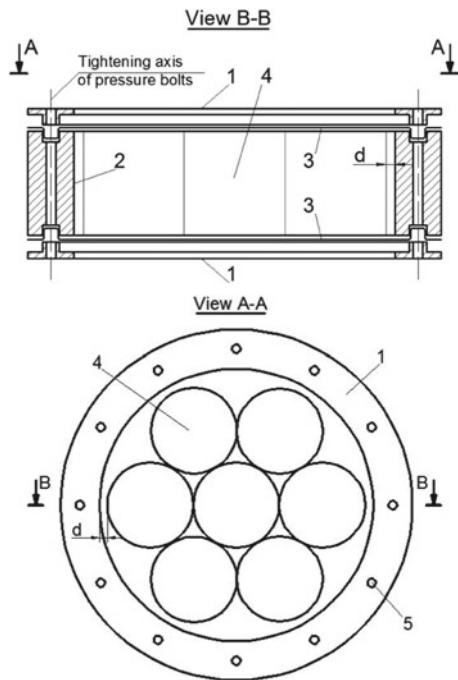


Fig. 2 The device after assembly with the plate installed on it



plate was installed in such a way that, after immersing the device in water, it remained above its surface. The hole pattern and numbering is shown in Fig. 3.

2.2 Theoretical Methods

To estimate the packer pressure on the mesh, the following computational scheme was used [19]:

- 1) It was assumed that the mesh, upon deformation, takes the shape of a surface of revolution, being rigidly fixed along its edge.
- 2) It was assumed that the pressures p_1 and p_2 shown in Fig. 4a are equal to p .
- 3) the surface of revolution was described by a function in the coordinate axes shown in Fig. 5b, where: $h = 0.0131$ m is the mesh thickness; A_1 is the lowest point of the surface of revolution, i.e. $y_1 = 0$; A_2 is an arbitrary point of the surface of revolution, with coordinates (x_2, y_2) ; θ_1 and θ_2 are angles of inclination of tangents to the horizontal at points A_1 and A_2 , respectively; $f(x)$ is a function describing the surface of revolution; x_c is a coordinate along the x -axis of the vertex of the surface of revolution, corresponds to the point where the displacements will be greatest; $N_1 = \sigma_1 \cdot h$ - where σ_1 are stresses acting inside the mesh, i.e. N_1 is taken as a uniformly distributed load tangential to the surface at a given point.

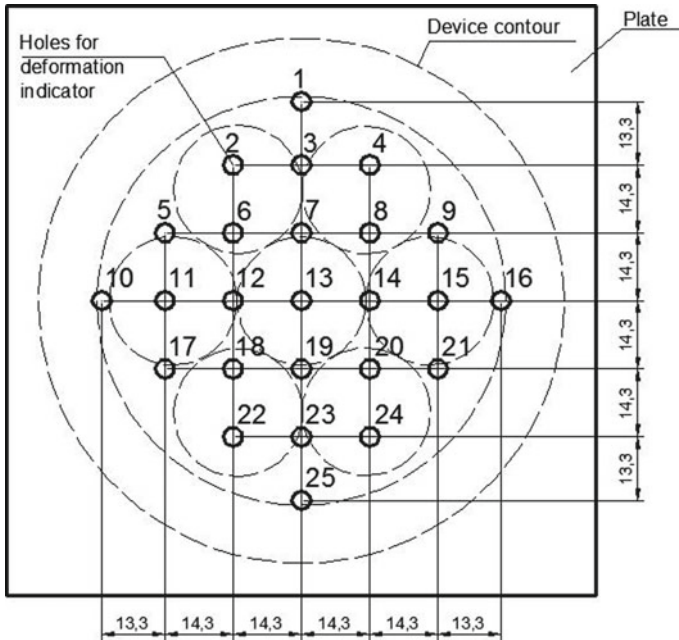


Fig. 3 Plate for measuring the movement of the mesh with hole numbering

Considered in Fig. 4b, the computational scheme corresponds to the part of the mesh cut along the lower point A_1 . Solving the problem of mechanical properties identification in this case [16–19], the equilibrium equation, compiled by summing the projections of all efforts on the y -axis, gives:

$$p \cdot \pi \cdot |x_1 - x_c| - \sigma_1 \cdot h \cdot 2\pi \cdot \sin(\theta_1) = 0 \tag{1}$$

When deriving Eq. (1), it has been assumed that the pressure p does not depend on the surface coordinate. Then, expressing p in terms of σ_1 , we get:

$$p = (\sigma_1 \cdot h \cdot 2 \cdot \sin(\theta_1)) / |x_1 - x_c| \tag{2}$$

3 Results and Discussions

In accordance with this numbering scheme shown at Fig. 3, the measurements of the mesh displacements caused by the packer pressure, shown in Tables 1 and 2, have been taken, which show the displacement results (in millimeters) at the points corresponding to holes 1–25 for 17 days of testing.

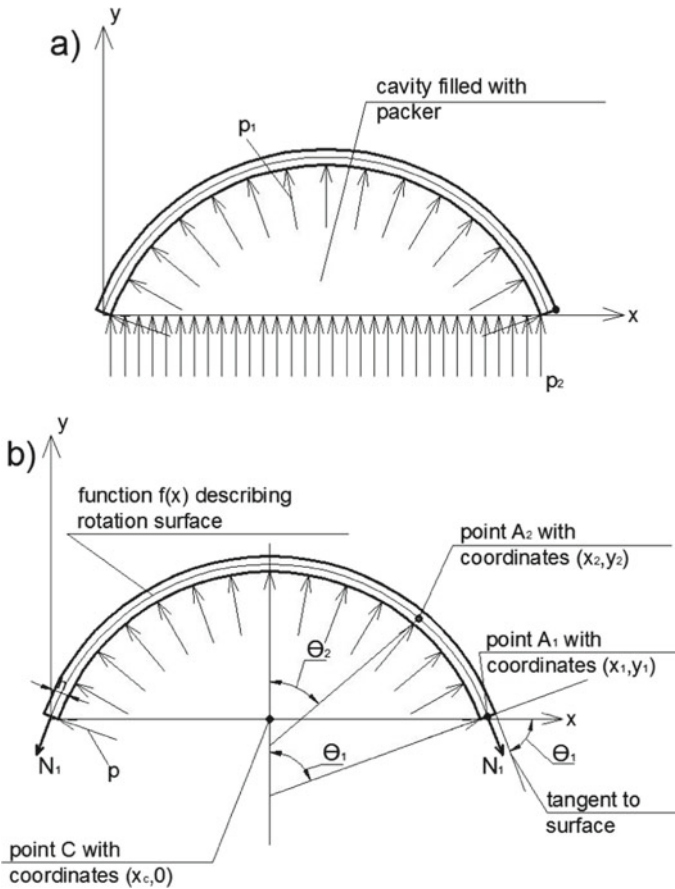


Fig. 4 Mesh computational scheme under packer pressure

Analyzing the data presented in Tables 1 and 2, it can be seen that the swelling rate decays over time. Approximately 18 days after the start of water saturation, the critical pressure was reached and the mesh broke, as shown in Fig. 5.

In general, each point on the surface will have its own pair of numbers x and θ according to Fig. 4b. Obviously, the pressure p can be variable, i.e. different for different points on the surface. This dependence will have the form shown in Fig. 6, where the abscissa shows the x coordinate of the surface point, and the ordinate shows the predicted pressure in MPa. Based on the initial hypotheses, we can conclude that the predicted pressure will, in any case, not exceed the value that is obtained for point A_1 , i.e. 0.35 MPa. In general, it can be assumed that the pressure of the packer on the mesh is equal to the average value in the area $x \in [0, 30]$, where the predicted pressures do not change very much. Then the preliminary estimate of the packer pressure on the mesh is about 0.32 MPa.

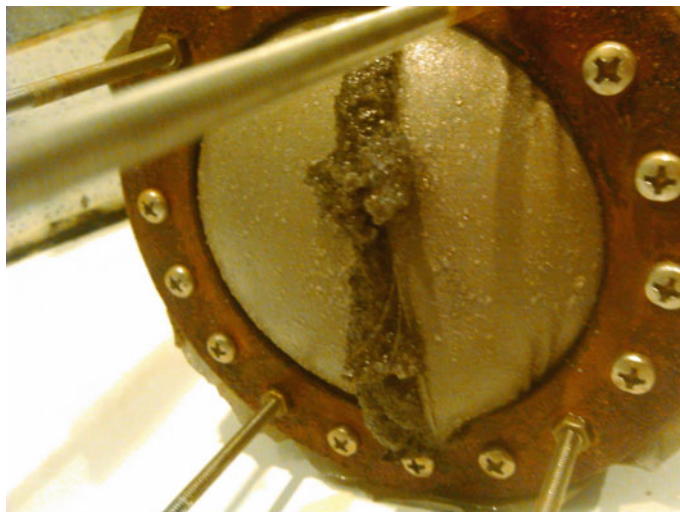


Fig. 5 Device after breaking the mesh

It should be noted that since the mesh broke, the packer did not develop the maximum possible pressures. Therefore, additional tests are necessary.

Finally following conclusions could be made:

1. Apparently, the pressure of the packer working under the conditions created by the device is not evenly distributed over the grid.
2. A preliminary estimate of the pressure applied by the packer on the grid, assuming its uniform distribution, is about 0.32 MPa.
3. Based on the data obtained at the moment, there is no reason to believe that the pressures developed by the packer lead to deformation of the tubing string.
4. Since the mesh broke during the test, and packer pressure was estimated using the equations of the theory of momentless shells as unevenly distributed, further testing is necessary to clarify the results.
5. The following measures should be taken to clarify the assessment of pressures developed by packer: it is necessary to increase the thickness or strength of the mesh used in the tests, for example, introducing a number of additional layers of it; it is necessary to clarify the elastic modulus, strength and breaking strain of the mesh, which will help to assess the value of the pressure developed by the packer; in case of measures to clarify the strength and deformative characteristics of the mesh will be insufficient to clarify the pressure, it is necessary to apply the theory of flexible momentless shells [19, 20].

Table 1 Grid movements

	1	3	7	13	19	23	25
1 day Time: 12:40	-0.13	0	0	0	0	0	0
1 day Time: 23:05	0.36	2.38	3.59	3.36	3.33	2.00	0.13
2 day Time: 12:20	0.87	3.30	4.79	5.24	4.61	2.85	0.27
3 day Time: 01:34	1.20	3.01	5.92	6.33	5.50	3.66	0.42
3 day Time: 12:20	1.56	4.28	6.61	6.75	6.15	3.78	0.42
4 day Time: 01:45	1.71	5.27	7.46	8.02	7.05	4.42	0.55
4 day Time: 11:25	2.01	5.67	8.01	8.18	7.50	4.74	0.65
5 day Time: 02:35	2.10	6.14	8.78	9.19	8.28	4.99	0.71
5 day Time: 13:10	2.10	6.58	9.34	9.72	8.74	5.31	0.73
6 day Time: 02:00	2.40	6.38	9.83 (1.35)	10.52 (2.01)	9.23	5.76	0.73
7 day Time: 01:51	2.40	7.40	10.56 (2.03)	11.1	10.01 (1.52)	6.05	0.90
8 day Time: 11:50	2.73	8.04	11.63	12.48	11.07	6.59	0.93
10 day Time: 00:00	3.15	8.78	12.79	13.61	12.3	7.28	1.10
12 day Time: 12:50	3.15	9.50 (1.02)	13.89	14.84	13.47	8.02	1.10
15 day Time: 00:19	3.33	1.90	15.01	16.11	14.09	8.74	1.17
18 day Time: 00:53	3.33	2.43	16.01	17.37	16.28	9.31	1.22

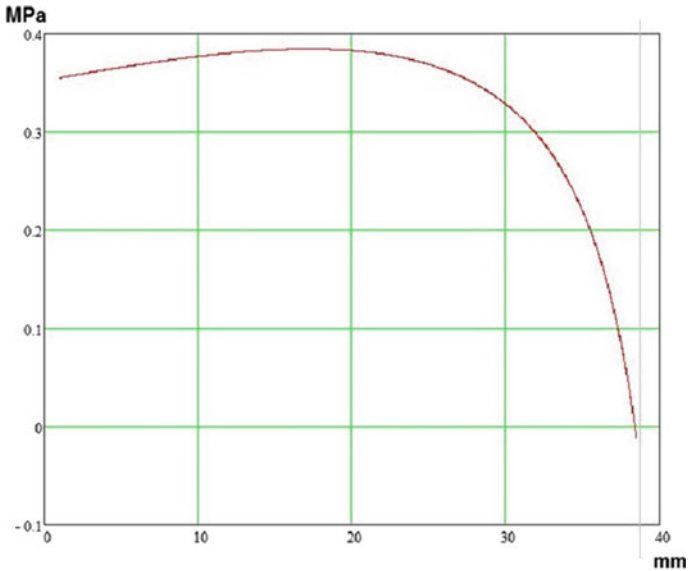
Table 2 Grid movements

	10	11	12	13	14	15	16
1 day Time: 12:40	0	0	0	0	0	0	0
1 day Time: 23:05	1.21	2.31	3.39	3.36	2.80	1.81	0.09
2 day Time: 12:20	0.9	3.07	4.71	5.24	4.27	2.94	0.20
3 day Time: 01:34	1.00	3.36	5.72	6.33	5.42	3.94	0.48
3 day Time: 12:20	1.13	3.72	6.38	6.75	6.22	4.52	0.52
4 day Time: 01:45	1.28	4.61	7.31	8.02	7.00	5.18	0.62
4 day Time: 11:25	1.39	4.78	2.74	8.18	7.62	5.62	0.63
5 day Time: 02:35	1.40	4.78	8.51	9.19	8.40	6.19	0.73
5 day Time: 13:10	1.40	5.11	9.03	9.72	8.91	6.56	0.73
6 day Time: 02:00	1.48	5.78	9.55 (1.05)	10.52 (2.01)	9.15	6.84	0.83
7 day Time: 01:51	1.54	5.85	10.28	11.1	10.21 (1.60)	7.26	0.93
8 day Time: 11:50	1.58	6.01	11.32	12.48	11.18	8.30	0.93
10 day Time: 00:00	1.67	7.45	12.47	13.61	12.23	8.30	0.93
12 day Time: 12:50	1.80	8.24	13.52	14.84	10.21	9.61 (1.28)	1.18
15 day Time: 00:19	2.18	8.52	14.56	16.11	14.47	10.18	1.20

(continued)

Table 2 (continued)

	10	11	12	13	14	15	16
18 day Time: 00:53	2.18	8.88	15.72	17.37	15.52	10.94	1.27

**Fig. 6** Predicted packer pressure on the mesh

References

1. Suleymanov, A., Smirnov, D., Lobanova, A.: Method of assessing durability of swelling rubber for packers. *News KSUAE* **4**(50), 376–385 (2019)
2. Smirnov, D.: Method for evaluating rubber durability. In: 67th All-Russian Scientific Conference, vol. 17. KGASU (2015)
3. Ivanova, S., Minsker, K., Nagumanova, E., Nizamov, R., Kazar'yans, S.: The stabilizing properties of synthetic zeolites in plasticized polyvinyl chloride compounds. *Plast. Massy Sint. Svoystva Pererab. Primen.* **12**, 39–43 (2005).
4. Vdovin, E., Stroganov, V.: Properties of cement-bound mixes depending on technological factors. *Mag. Civil Eng.* **93**(1), 147–155 (2020)
5. Karmanova, O., Shutilin, Y., Moskalev, A., Podvalnyi, E., Petrenko, V., Safonov, S.: Elastomer seals for oil production equipment. *Chem. Pet. Eng.* **53**(9–10), 642–646 (2018)
6. Ahmed, S., Salehi, S., Ezeakacha, C., Teodoriu, C.: Experimental investigation of elastomers in downhole seal elements: implications Safety. *Polym. Test.* **76**, 350–364 (2019)
7. Mitchell, C., Urquhart, N.: Development of an extended delayed oil swell packer for deployment in extended reach drilling oil wells. In: Abu Dhabi International Petroleum Exhibition & CONFERENCE 2017, SPE-188912-MS, Abu Dhabi, UAE (2017)
8. Nasyrov, A., Maslennikov E., Nagumanov, M.: Technological Aspects of Environmental protection in Oil Production. LLC Paracelsus Print, Izhevsk (2013).

9. Hasanov, A.: Emergency recovery work in oil and gas wells. Nedra, Moscow (1987)
10. Hyne, N., Norman, J.: Nontechnical Guide to Petroleum Geology, Exploration, Drilling and Production, 2nd edn. Pennwell Books, Tulsa (2001)
11. Qamar, S., Al-Hiddabi, S., Pervez, T., Marketz, F.: Mechanical testing and characterization of a swelling elastomer. *J. Elastomers Plast.* **41**(5), 415–431 (2009)
12. Qamar, S.: Numerical investigation of tubular expansion and swelling elastomers in oil wells. *J. Polym. Eng.* **41**(10), 883–892 (2021)
13. Khan, R.: Design and optimization of multistage tubular–mandrel system for down-hole expandable tubular. *Arab. J. Sci. Eng.* **46**, 2083–2095 (2021)
14. Pervez, T., Qamar, S., Al-Abri, O., Khan, R., Al-Abri, B.: Experimental and numerical simulation of in-situ tube expansion for deep gas wells. *J. Manuf. Mater. Process.* **27**, 727–732 (2012)
15. Azizova, A., Gabbasova, A., Kateev, R., Ishakov, A., Kadyrov, R.: Development of water-swollen packers for separation of reservoirs and reduction of water inflow of oil-producing wells. *Bureniye y neft* **7**(8), 60–62 (2015)
16. Urazakov, K., Nagumanov, M., Zdolnik, S.: Reference Book on Oil Production. Nedra, Saint-Petersburg (2012)
17. Kayumov, R.: Extended problem of the identification of mechanical characteristics of materials on the basis of testing of structures. *Mech. Solids* **39**(2), 74–81 (2004)
18. Kayumov, R., Tazyukov, B., Muhamedova, I.: Identification of the mechanical characteristics of a nonlinear-viscoelastic composite based on the test results for shells of revolution. *Mech. Compos.* **22**(2), 171–180 (2019)
19. Aleksandrov, A., Potapov, V.: Basics of Elasticity and Plasticity Theory. High school, Moscow (1990)
20. Truesdell, C.: On Sokolovsky's «Momentless Shells». *Trans. Am. Math. Soc.* **61**(1), 128–133 (1947)

Dry Plaster Mixes Using Local Mineral Components



Marat Khaliullin  and Alsu Gilmanshina

Abstract The objective of this paper is to investigate the effect produced by a set of modifying additives, including expanded clay dust ground down to a specific surface area of $300 \text{ m}^2/\text{kg}$ as that serves as a pozzolanic additive and high-molecular polyethylene oxide PEO-S with a molecular weight of 4×10^6 that performs the function of a water-retaining additive as part of the composition of dry plaster mixtures upon the indexes of the basic physical and mechanical properties of mortar mixes and solutions in order to identify the effectiveness of the application of this set of additives. The studies carried out have yielded the following results. The mathematical dependences which indicate the impact of the set of modifying additives in question upon the compressive strength and the bonding strength to the base of dry plaster mixture-based solutions have been established. It has been found that the set of modifying additives in question, when introduced in optimal quantities, results in a rise in compressive strength and bonding strength to the base of dry plaster mixture-based solutions. The effectiveness of introduction of a ground expanded clay dust additive shows that high pozzolan activity is due to its chemical interaction with portlandite $\text{Ca}(\text{OH})_2$ and other hydration products of Portland cement clinker minerals which yields newly formed phases that are engaged in structure formation and contribute to a rise in the strength of the solution. It has been established that high-molecular polyethylene oxide PEO-S is an effective and efficient water-retaining additive. The dependencies that were established have served as the basis for developing optimal compositions of dry plaster mixes which conform to regulatory requirements and are competitively viable as compared to other industrial counterparts owing to a reduction in the consumption of expensive Portland cement achieved through replacing a portion of it with ground expanded clay dust - industrial waste - and also thanks to the application of a water-retaining additive of locally produced high-molecular polyethylene oxide PEO-S instead of more expensive imported water-retaining additives.

Keywords Dry plaster mixes · Expanded clay dust · High-molecular polyethylene oxide · Pozzolan additive · Water-retaining additive

M. Khaliullin (✉) · A. Gilmanshina
Kazan State University of Architecture and Engineering, Kazan 420043, Russia
e-mail: khaliullin@kgasu.ru

1 Introduction

Growing housing construction in the Republic of Tatarstan and increasing prices of building materials seen in recent years have shone the light on the urgent need to provide the construction industry with inexpensive modern construction materials. Local production is one of the primary ways that can come into play to help cut down costs of building materials through lower shipping costs. A reduction in the production costs of building materials can be achieved in large part by putting to use industrial waste as initial components for manufacturing building materials which would also take care of environmental issues around waste disposal.

One of the known techniques to cut down costs of building materials and building products consists in introduction of well-selected mineral fillers based on ground natural raw materials or industrial waste into the composition of building materials and products which preserve their physical and mechanical properties at the same time decreasing the consumption of binders which are more expensive [1–5]. By interacting with other raw materials and their products which result from hardening due to newly formed phases a finely dispersed mineral additive can play a major part in the formation of the structure of the hardening composition which yields an increase in basic physical and mechanical properties as compared to additive-free compositions [6–8].

Production of expanded clay gravel is faced with the serious challenge of disposal of expanded clay dust which builds up in dust-cleaning systems such as dust-collecting chambers, cyclones and filters. Large plants which produce expanded clay may generate up to 7–8 tons of expanded clay dust daily. This waste then goes back to production and is added to raw clay. However, it more often ends up on the dump site.

The composition of expanded clay dust features an amorphous silicon-containing phase which demonstrates high chemical activity in binding calcium hydroxide which forms strong and difficult-to-dissolve products. The studies carried out by NIICeram-site and the Samara State University of Architecture and Civil Engineering [9] have found that expanded clay dust introduced into a foam concrete mixture which serves as an active micro-filler, considerably reduces the shrinkage of foam concrete products along with their density and thermal conductivity. The chemical and mineral composition of expanded clay dust makes it somewhat similar to ground thermally activated clay which has been proven by some studies to be highly efficient when applied as an active pozzolan additive to lime or Portland cement [10–12].

These days, expensive imported products based on cellulose esters are primarily used as water-retaining additives in the production of dry building mixes [13]. The works [14, 15] demonstrate the effective application of some domestic water-soluble polymers, for instance, high-molecular polyethylene oxide (PEO) with a molecular weight of 1.52×10^6 as water-retaining additives.

The objective of this paper is to investigate the effect that a set of modifying additives, including ground expanded clay dust used as a pozzolan additive and high-molecular polyethylene oxide used as a water-retaining additive in the composition

of dry plaster mixes produces on the indicators of the basic physical and mechanical properties of mortar mixtures and solutions in order to establish the effectiveness of the set of additives in terms of ensuring the performance standards of basic physical and mechanical properties and possibilities to reduce the prices of dry plaster mixes by decreasing consumption and having more expensive components of these mixes replaced.

2 Materials and Methods

The following components were applied in this paper to obtain dry plaster mixes.

The Portland cement CEM 0 52.5 N produced by the Novoroscement plant in compliance with GOST 31108 (Russian Federation National Standard) was used as the binder.

The quartz sand from a quarry operated by the Combine Plant of Non-metallic Materials (based in Kazan) was used as the filler according to GOST 8736 (Russian Federation National Standard). Pre-dispersed standard fractions of the initial sand served as the basis of the specified grain composition of the aggregate (Table 1). The content of pulverized and clay impurities in the initial sand remains within the tolerable limits as per GOST 8736 (Russian Federation National Standard).

Expanded clay dust acted as a fine-dispersed pozzolan mineral additive; the former being the waste coming from the production of expanded clay by Kamenergostroyprom (based in Nizhnekamsk). Expanded clay dust was previously ground to a specific surface of 300 m²/kg. The pozzolan activity of expanded clay dust which is determined by the absorption of lime from a lime solution [16] was 336 mg/g. The chemical composition of expanded clay dust is the following (in percentage terms by weight): SiO₂ – 59.12; Al₂O₃ – 17.85; Fe₂O₃ – 9.7; MgO – 3.01; CaO – 1.74; K₂O – 2.26; SO₃ – 0.93; TiO₂; Na₂O – 0.81; P₂O₅ – 0.22; MnO – 0.2; losses at calcination – 3.11. The mineralogical composition is presented in percentage by weight: non-dehydrated and dehydrated clay minerals – 53; quartz – 15; feldspar – 5; anhydrite – 3; X-ray amorphous phase – 27. The tests performed in compliance with GOST 8735 (Russian Federation National Standard) showed that 9.5% of undehydrated clay was present in the composition of expanded clay dust.

High-molecular polyethylene oxide PEO-S produced by Kazanorgsintez with a molecular weight of 4 × 10⁶ as per TU 6–05-231–341-88 (Corporate Standard) served as a water-retaining additive.

Table 1 Grain composition of quartz sand used to produce dry plaster mixes

Residue on sieves (in percentage terms) with holes (mm)					
2.5	1.25	0.63	0.315	0.16	<0.16
–	34	24	17	12	13

Esapon 1214 manufactured by Lamberti (Italy) was used as an air-retaining substance which is a non-ionic surfactant - sodium lauryl sulfate.

Tests of dry plaster mixes, mortar mixtures and solutions based on them were performed as per GOST 33083 (Russian Federation National Standard), GOST 31357 (Russian Federation National Standard), GOST R 58277 (Russian Federation National Standard). The mobility of adhesive mortar mixtures was 8–9 cm along the depth of immersion of the cone of a StroyTSNIIL device.

The adhesion of the solutions was established via an adhesion measuring device.

PSO-5-MG4 produced by Stroypribor (based in Chelyabinsk).

The multicomponent composition of dry plaster mixes was optimized via the method of central composite rotatable design during experiments [17].

3 Results and Discussions

The method of central composite rotatable design during experiments has allowed to explore the joint effect of modifying additives i.e. a pozzolan mineral additive, expanded clay dust and a water-retaining additive - PEO-S polyethylene oxide - upon the basic physical and mechanical properties of mortar mixtures and solutions in order to obtain optimal compositions of dry plaster mixes. These plaster dry mixes contained 75% of quartz sand by weight as part of a dry mix collected from the quarry of Combine of Non-metallic Materials. In addition, Esapon 1214 air-retaining substance was introduced into all mixtures in an amount of 0.01% by weight of the dry mixture.

The percentages of modifying additives in the composition of dry plaster mixes were used as variable factors:

x_1 – a water-retaining additive of PEO-S polyethylene oxide, in percent by weight of the dry mix (planning interval limit values from 0 to 4%);

x_2 – expanded clay dust with a specific surface area of 300 m²/kg, in percent by weight as part of the dry mix (planning interval limit values from 0 to 10%).

The following optimization parameters were adopted:

y_1 – compressive strength of solutions based on dry plaster mixes, MPa.

y_2 – bonding strength to the base of solutions based on dry plaster mixes, MPa;

The results of the experiment plan yielded mathematical models for the functions of y_1 and y_2 (formulas (1), (2)) which established the relationship between the content of modifying additives and the primary properties – the bonding strength to the base and the compressive strength of solutions based on dry plaster mixes.

$$y_1 = 2.6064 + 1.2638x_1 + 0.4098x_2 - 0.0168x_1x_2 - 0.446x_1^2 - 0.04676x_2^2 \quad (1)$$

$$y_2 = 0.2177 + 0.3568x_1 - 0.0073x_2 - 0.005x_1x_2 - 0.0841x_1^2 - 0.0007x_2^2 \quad (2)$$

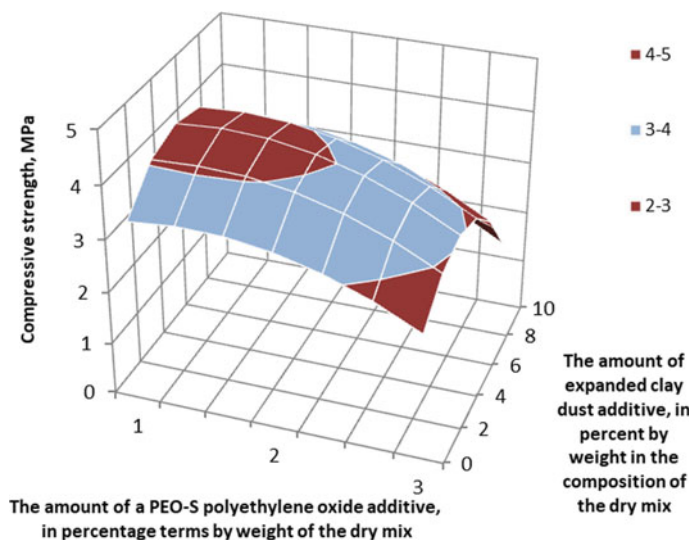


Fig. 1 The effect of a set of modifying additives on the compressive strength of solutions based on dry plaster mixes

The Fisher criterion calculated for the obtained models demonstrates that they adequately describe the results of the experiment.

An analysis of dependencies constructed based upon the obtained mathematical models of functions y_1 and y_2 presented in Figs. 1 and 2 indicates the following.

The introduction of expanded clay dust into the composition of dry plaster mixes ground to a specific surface of 350 kg/m^2 to optimal values of 4–6% by weight in the dry mix serves to build up the compressive strength of solutions by 21–33.8% as compared to compositions in which no such additive has been introduced (Fig. 1), which, due to the high pozzolan activity of ground expanded clay dust, may be accounted for by its chemical interaction with portlandite ($\text{Ca}(\text{OH})_2$) and other hydration products of Portland cement clinker minerals producing newly formed phases which are engaged in structure formation and contributing to a rise in the strength of the solution [18–20].

A rise in the content of the ground expanded clay dust additive above the optimal values results in a decrease in the strength of solutions associated with an increase in the water demand of mortar mixtures. An introduction of ground expanded clay dust into the composition of dry plaster mixes up to 8% in weight keeps the strength of the solutions at the level of the compositions without the introduction of this additive.

An introduction of high-molecular polyethylene oxide PEO-S additives into the composition of plaster dry mixes in an optimal amount of 1.5–2% by weight of the dry mixture also yields a rise in the compressive strength of solutions by 16.5–28.5% as compared to compositions in which no such introduction has been performed due to an increase in the water-holding capacity of mortar mixtures from 92.0–92.5 to 97.9–99.87%, respectively.

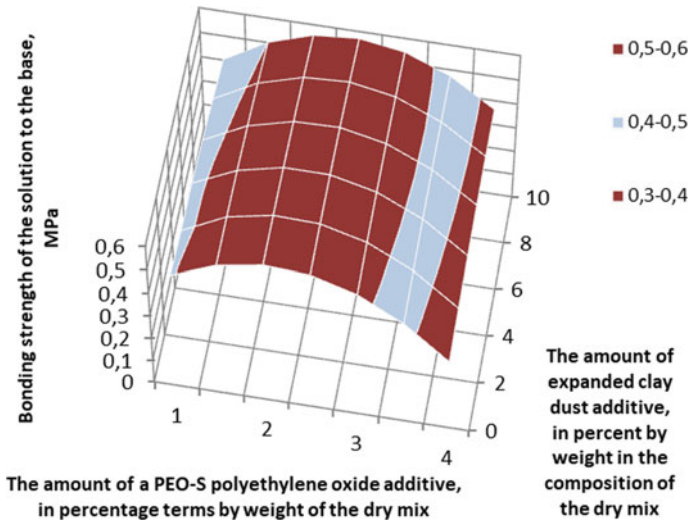


Fig. 2 The effect of a set of modifying additives on the bonding strength to the base of solutions based on plaster dry mixes

The primary influence on the changes in the bonding strength to the base of solutions based on plaster dry mixes comes from by the water-retaining additive PEO-S polyethylene oxide (Fig. 2). When plaster dry mixes are introduced into it in an optimal amount of 1.5–2% by weight of the dry mixture, an increase is observed in the bonding strength of solutions to the base by 2.7–2.9 times as compared to compositions without the introduction of this additive, which is ensured by an increase in the water-holding capacity of mortar mixtures.

The addition of expanded clay dust in optimal amounts up to 4–6% and an expanded clay dust additive in excess of optimal values leads a gradual increase in the water demand of mortar mixtures from 10 to 11–13% and a decrease in the compressive strength of solutions and the bonding strength of solutions to the base.

This shows that maximum compressive strength and bonding strength to the base of solutions based on plaster dry mixes is achieved by having a set of modifying additives introduced into their composition in the following optimal quantities: pozzolan additive expanded clay dust – 4–6% by weight in the dry mixture and a water-retaining additive of high molecular weight polyethylene oxide PEO-S – 1.5–2% of the weight of the dry mix.

The dry plaster mixes that have been developed whose composition is shown in Table 2 comply with the performance standards in terms of basic physical and mechanical properties (Table 3).

The dry plaster mixes that have been developed are commercially viable as their price is 13–23% lower as compared to industrial counterparts thanks to a pozzolan additive used in their composition, expanded clay dust which is the waste of the building materials industry which reduces the consumption of expensive Portland

Table 2 Developed compositions of dry plaster mixes

Components of dry plaster mixes	Unit of measurement	Consumption of components
Portland cement CEM 0 52.5 N	in percent by weight in the composition of a dry mix	20–15
Quartz sand		75
Expanded clay dust (specific surface of 300 m ² /kg)		5–10
PEO-S polyethylene oxide	in percent by weight of the dry mix	1.5–2
Esapon 1214		0.01

Table 3 Indexes of the basic physical and mechanical properties of the developed dry plaster mixes

Property name	Developed dry plaster mixes	Performance standards as per GOST 33,083 (Russian Federation National Standard)
Maximum particle size, mm	2.5	2.5
Average dry density, kg/m ³	1300–1400	more than 1300
Compressive strength class at the age of 28 days/MPa	KP II/2.5–5.0	KP II/2.5–5.0
Water demand, in percent	11	11
Mobility in the depth of immersion of the cone, cm	Pk3 8–12	Pk3 8–12
Water-holding capacity, percent	99.7 – 99.8	at least 95
Bonding strength of the solution to the base, MPa	0.5 – 0.6	at least 0.3
Contact zone frost resistance zone	F50	at least F25
Frost resistance grade, min	F50	at least F25
Capillary water absorption, kg/(m ² ·min ^{0.5})	0.1–0.15	0–0.4
Crack resistance	None	None (sample thickness: 20 mm)
Shrinkage deformations, mm/m	0.32 - 0.35	1.0 max

cement as well as a water-retaining additive of locally produced high-molecular polyethylene oxide PEO-S instead of more expensive imported water-retaining additives.

4 Conclusion

1. The Mathematical Dependences Indicate the Impact of the Set of Modifying Additives in Question - a Ground Pozzolan Additive to a Specific Surface of 300 m²/kg of expanded clay dust and a water-retaining additive of high-molecular polyethylene oxide PEO-S with a molecular weight of 4×10^6 on the compressive strength and bonding strength of solutions based on plaster dry mixes.
2. It has been found that the used set of modifying additives when introduced in optimal quantities, results in a rise in compressive strength and bonding strength to the base of solutions based on plaster dry mixes. The effectiveness of introduction of a ground expanded clay dust additive that shows high pozzolan activity is due to its chemical interaction with portlandite $\text{Ca}(\text{OH})_2$ and other hydration products of Portland cement clinker minerals which yields newly formed phases that are engaged in structure formation and contribute to a rise in the strength of the solution. It has been found that high molecular weight polyethylene oxide PEO-S with a molecular weight of 4×10^6 is an effective water-retaining additive.
3. The obtained dependencies have been used to develop optimal compositions of dry plaster mixes which use a set of modifying additives that comply with performance standards. The developed dry plaster mixes are commercially viable as their price is 13–23% lower as compared to industrial counterparts which reduces the consumption of expensive Portland cement owing to a reduction in the consumption of expensive Portland cement achieved through replacing a portion of it with ground expanded clay dust - industrial waste - and also thanks to the application of a water-retaining additive of locally produced high-molecular polyethylene oxide PEO-S instead of more expensive imported water-retaining additives.

References

1. Stepanov, S., Krasnikova, N., Makarov, D.: Cement stone, modified by galvanic sludge. IOP Conf. Ser. Mater. Sci. Eng. **890**(1), 012086 (2020). <https://doi.org/10.1088/1757-899X/890/1/012086>
2. Mukhametrakhimov, R.K., Galautdinov, A.R., Gilmanshin, I.R.: Modified gypsum-cement-pozzolan composites reinforced with polypropylene fibers. IOP Conf. Ser. Mater. Sci. Eng. **570**(1), 012068 (2019). <https://doi.org/10.1088/1757-899X/570/1/012068>
3. Tokarev, Y., Ginchitsky, E., Sychugov, S., Krutikov, V., Yakovlev, G., Buryanov, A., Senkov, S.: Modification of gypsum binders by using carbon nanotubes and mineral additives. Procedia Eng. **172**, 1161–1168 (2017). <https://doi.org/10.1016/j.proeng.2017.02.135>
4. Galeev, R.R., Nizamov, R.K., Abdрахmanova, L.A.: Filling of epoxy polymers with chemically precipitated chalk from chemical water treatment sludge. Lect. Notes Civil Eng. **147**, 93–97 (2021). https://doi.org/10.1007/978-3-030-68984-1_14
5. Galautdinov, A., Mukhametrakhimov, R., Kupriyanov, V.: Gypsum-fiber radioprotective facing materials. Lect. Notes Civil Eng. **169**, 372–381 (2021). https://doi.org/10.1007/978-3-030-80103-8_40

6. Vdovin, E., Stroganov, V., Kononov, N.: Modification of road soil cement with activated fillers. *Lect. Notes Civil Eng. LNCE* **150**, 335–345 (2021). https://doi.org/10.1007/978-3-030-72404-7_3
7. Mukhametrakhimov, R., Galautdinov, A., Gorbunova, P., Gorbunova, T.: Water-resistant fiber-reinforced gypsum cement-pozzolan composites. In: *E3S Web of Conferences*, vol. 138, p. 01011 (2019). <https://doi.org/10.1051/e3sconf/201913801011>
8. Garg, N., Skibsted, J.: Pozzolan reactivity of a calcined interstratified illite/smectite (70/30) clay. *Cem. Concr. Res.* **79**, 101–111 (2016). <https://doi.org/10.1016/j.cemconres.2015.08.006>
9. Gorin, V.M., Tokareva, S.A., Sukhov, V.Y., Nekhaev, P.F., Avakova, V.D., Romanov, N.I.: Expansion of the field of application of expanded clay gravel. *Constr. Mater.* **11**, 19–21 (2003)
10. Rakhimova, N.R., Rakhimov R.Z.: Influence of calcined clays additions on the composition of reaction products and properties of compositional alkali-activated slag cements with low content of alkali reactant. *News KSUAE* **2**(56), 50–59 (2021). https://doi.org/10.52409/20731523_2021_2_50
11. Taylor-Lange, S.C., Lamon, E.L., Riding, K.A., Juenger, M.C.G.: Calcined kaolinite-bentonite clay blends as supplementary cementitious materials. *Appl. Clay Sci.* **108**, 84–93 (2015). <https://doi.org/10.1016/j.clay.2015.01.025>
12. Khaliullin, M., Gilmanshina, A.: The effect of ground limestone on the properties of composite gypsum binder using thermally activated clay as a pozzolan component. In: *E3S Web of Conferences*, vol. 274, p. 04006 (2021). <https://doi.org/10.1051/e3sconf/202127404006>
13. Korneev, V.I., Zozulya, P.V., Medvedeva, I.N.: *Technology of Dry Building Mixes*, 2nd edn. Lan Publishing House, Saint Petersburg (2018)
14. Demyanova, V.S., Kalashnikov, V.I., Duboshina, N.M.: On the issue of assessing the adhesion strength of building mortars modified with water-soluble polymer additives. *News High. Educ. Inst. Constr.* **1**, 33–35 (2001)
15. Afanasyev, N.M., Tseluiko, M.K.: *Additives in Concrete and Mortars*. Budivelnyk, Kyiv (1989)
16. Potapova, E.N., Manushina, A.S., Zyryanov, S.M., Urbanov, A.V.: Methods for determining pozzolan activity of mineral additives. *Constr. Mater. Equip. Technol. XXI Century* **7–8**(222–223), 29–33 (2017)
17. Hartman, K., Letsky, E., Schaefer, V.: *Experiment Planning in the Study of Technological Processes*. Mir, Moscow (1977)
18. Khaliullin, M., Dimieva, A.: Composite gypsum binder under introducing thermally activated clay as a pozzolan component and adding ground limestone. *IOP Conf. Ser. Mater. Sci. Eng.* **890**(1), 012093 (2020). <https://doi.org/10.1088/1757-899X/890/1/012093>
19. Mukhametrakhimov, R., Galautdinov, A., Lukmanova, L.: Influence of active mineral additives on the basic properties of the gypsum cement-pozzolan binder for the manufacture of building products. In: *MATEC Web of Conferences*, vol. 106, p. 03012 (2017). <https://doi.org/10.1051/matecon/201710603012>
20. Mukhametrakhimov, R., Lukmanova, L.: Features of the hydration process of the modified blended cement for fiber cement panels. In: *MATEC Web of Conferences*, vol. 170, p. 03030 (2018). <https://doi.org/10.1051/matecon/201817003030>

Verification and Validation of Numerical Model of Flow in Supply Opening with Elbow Unit



Juliya Kareeva , Arslan Ziganshin , and Kseniya Narsova

Abstract The existing methods for the calculation of ventilation systems do not take into account all parameters that affect jet performance. Numerical simulation can be used to achieve the most accurate results by eliminating the existing assumptions. The vast variety of turbulence models with different numbers of differential equations leads to a lack of consensus on the model combination that most accurately describes a particular process. It is necessary to confirm their validity when numerically solving specific problems. This study aimed to verify and validate a numerical model for investigating the flow of an air jet from unit containing supply opening and 90-degree sharp elbow located at different distances from opening. It was found that the combination of standard k- ϵ turbulence model and standard near-wall functions showed the best results for both resistance and simulation of jet development.

Keywords Verification · Validation · Computational fluid dynamics · Unit · 90-degree elbow · Supply opening

1 Introduction

A modern ventilation system must provide not only the required indoor climate parameters, but should be energy efficient and cost effective as well. This goal can be achieved if the design process takes into account the characteristic features of the supply jet and other sources of disturbances of indoor air [1, 2] which are not normally considered. It is well known that the duct elbow entails the appearance of vortex zones, resulting in the separation of the jet and the narrowing of the flow. The generated vortices behave as follows: at the inner wall velocity increases and static pressure decreases (confuser effect), and at the outer wall velocity decreases and static pressure increases (diffuser effect) [3]. The velocity epure after the elbow is uneven, but the flow eventually, as it moves away from the elbow, will try to equalize

J. Kareeva (✉) · A. Ziganshin · K. Narsova
Kazan State University of Architecture and Engineering, Kazan, Russia
e-mail: jkareeva2503@gmail.com

[4]. If we consider the situation when the supply opening occurs immediately after the elbow, then, the air suction from the environment will take place [4, 5].

To obtain adequate results of numerical solution it is necessary to choose the most suitable mathematical model (combination of turbulence model and wall functions). The Fluent software includes several turbulence models, each of which has its own varieties, and a number of wall functions.

These models are considered in many works [5–17]. One of the most frequently used turbulence model is the k - ε model combined with the *Standard Wall Function* (SWF) [6]. This turbulence model is used for calculations near walls where vortex zones and jet separation occur. The author compares k - ε SWF, “standard” k - ω and k - ω SST models with the results of physical experiment, and shows that k - ε SWF not only has the least deviations from experimental results, but also is the fastest way of calculation. The “standard” k - ε , k - ε RNG and k - ε *Realizable* turbulence models were compared in [8]. The RNG model is better than the Standard model because it has an additional term in the dissipation equation, which improves the accuracy of the calculations. RNG should not be chosen to solve the problem if the flow velocity is high, as it causes significant errors. The turbulence model k - ε *Realizable* is better to use for circular cross sections, otherwise the results are unsatisfactory [8]. Also, it should be taken into account that the RNG and *Realizable* near-wall functions are very similar at the beginning of the path, but as one moves away from the outlet, the current lines diverge [9]. When comparing k - ε SWF, k - ε N-EWF, k - ω SST with the results of the physical experiment, the scientists concluded that the k - ω SST model gives strong errors at the beginning of the air jet flow; all other values have acceptable errors [10]. Studying local resistance coefficient obtained using various models of turbulence (k - ε SWF, k - ε EWT, RSM SWF, RSM EWT, k - ω) and further comparing the results with values from the handbook by Idelchik [3] and other papers, the authors [10] concluded that RSM SWF and k - ε EWT are the best models, as the values obtained were more close to the experimental. But RSM SWF model has an untypical shape in the vortex zone closure area, so the authors recommend using k - ε EWT model in calculations [11, 12]. For example, the other authors also choose k - ε EWT model for calculations of supply ventilation [13]. In works [14–17], the problem of air distribution in rooms in non-isothermal formulation is considered. Comparison of different models showed that the process is best described by the k - ε RNG model.

Thus, the vast variety of turbulence models with different numbers of differential equations leads to a lack of consensus on the model combination most accurately describing a particular process. So, when solving specific problems, one should verify their validity. Verification and validation are the primary tools for assessing the accuracy, reliability and validity of numerical models, as well as the correctness of their software implementations.

Verification of mathematical model is a confirmation of correctness of mathematical model equations solution. Validation of mathematical model is confirmation of the adequacy of mathematical model to the object being modeled (physical phenomenon or process under study) [18].

This study aims to verify and validate a numerical model for studying the flow of air jet from an air inlet located at different distances from a 90-degree elbow.

To achieve the set aim, the following tasks should be solved:

- to choose an adaptation strategy to obtain adequate results of the numerical study;
- to perform calculations using different combinations of turbulence models and wall functions;
- to compare the obtained results with the known experimental and numerical studies.

2 Methods

2.1 Problem Statement

Considered is the problem of flow of isothermal jet from a supply opening located at different distances from a 90-degree sharp elbow. Gambit program is used to built the geometry of the investigated area (Fig. 1): duct width $b_0 = 0.1$ m, distance from elbow to jet flow section $l = 0.05; 0.1; 0.15; 0.2; 0.25; 0.3; 0.5; 0.6; 0.7; 0.8$ m; computational area width $L = 6$; height $H = 4$ m.

Initial velocity v_0 at boundary AB is uniform and equal to 3 m/s. The problem is solved numerically, using Fluent software package.

The boundary conditions adopted in the problem are the following:

- AB (air supply) - Velocity inlet: velocity is constant and directed along the normal to the boundary: $v_0 = \text{const}; k = 0; \epsilon = 0$;

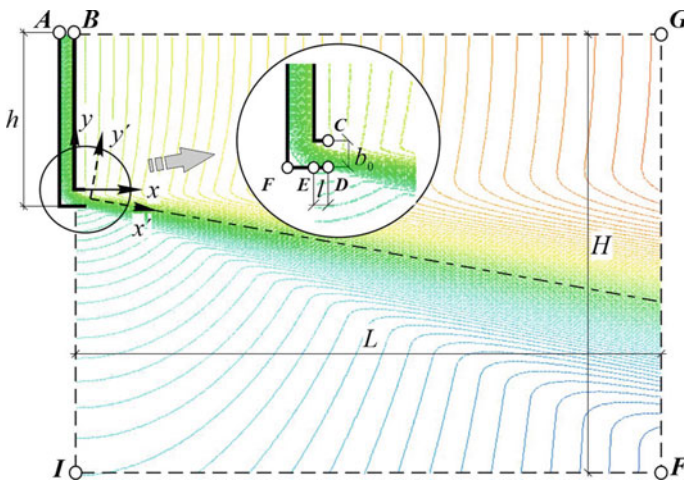


Fig. 1 Geometry and streamlines of the considered problem

- **BG, GK, KI, IE** (free boundary) - Pressure Outlet: overpressure $\Delta P = 0$; velocity is normal to the boundary $v = v_n$, $dk/dn = 0$, $d\varepsilon/dn = 0$;
- **AF, FD, BC** (impermeable walls) Wall: $v = 0$, $dv_n/dn = 0$; (dn is normal to the boundary).

2.2 Verification

To obtain the most adequate results, it is necessary to achieve sufficient resolution of the computational mesh in the process of solution, i.e. to investigate the problem on the mesh dependence. The maximum velocity v_{\max} at the **CD** outlet boundary was taken as a controlled parameter.

At the first stage, mesh refinement was performed on the whole area of the investigated geometry. Further, the area of mesh refinement was reduced. The greatest attention was paid to the mesh refinement in the duct. In this area, key processes occur that most noticeably affect the final result: velocity changes from 0 on the wall to the maximum value in the core of the jet, and vortex zones arise. The adaptation strategy is presented below in Table 1 (Fig. 2).

The results obtained are used to plot the relationship between the controlled parameter (maximum velocity at the outlet v_{\max}) and the refinement of the computational mesh. The degree of refinement is controlled by the dimensionless distance $y+$, the recommended value of which for *SWF* and *NEWF* is not less than 30, and for *EWT* it is about 1 [19].

Table 1 Characteristics of the used mesh

Adapt no.	Adaptation area	Characteristics of the calculation mesh		
		Size of max. cell	Size of min. cell	Number of cells
1	Region (0;0) and (2.7;2)	$2.5 \cdot 10^{-5}$	$2.5 \cdot 10^{-5}$	208,000
2	Region (0;1) and (0.25;2) + Region (0.25;0) and (2.7;1.2)	$2.5 \cdot 10^{-5}$	$6.25 \cdot 10^{-6}$	590,830
3	Region (0;1) and (0.25;2)	$2.5 \cdot 10^{-5}$	$1.5625 \cdot 10^{-6}$	711,370
4	at solid boundaries: 10 cells	$2.5 \cdot 10^{-5}$	$3.90625 \cdot 10^{-7}$	782,968
5	at solid boundaries: 6 cells	$2.5 \cdot 10^{-5}$	$9.765625 \cdot 10^{-8}$	869,215
6	at solid boundaries: 2 cells	$2.5 \cdot 10^{-5}$	$2.441406 \cdot 10^{-8}$	926,806
7	at solid boundaries: 1 cell	$2.5 \cdot 10^{-5}$	$6.103516 \cdot 10^{-9}$	984,412

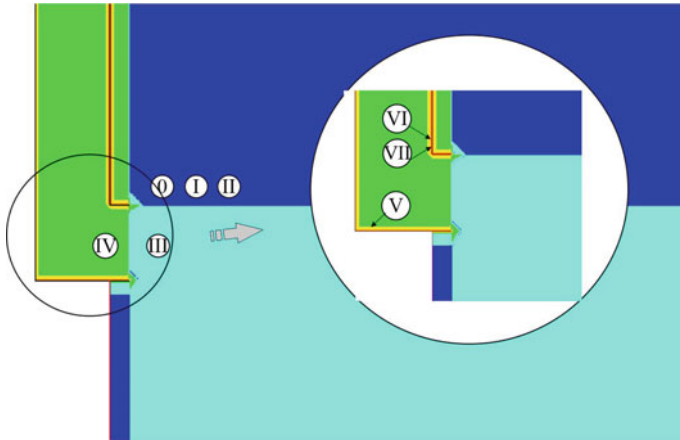


Fig. 2 Mesh adaptation stages

2.3 Validation

To validate the mathematical model, the numerically obtained value of the local density coefficient (LDC) was compared with the known experimental [3] and numerical [12] data at different combinations of turbulence models and near-wall functions. The models most commonly used today in the numerical study of both internal currents in channels and external jet currents have been selected: “standard” $k-\epsilon$ model (*SKE*) combined with standard (*SWF*) and non-equilibrium (*NeWF*) wall functions; extended wall modeling (*EWT*); $k-\epsilon$ “renormalized groups” model (*RNGKE*), “standard” $k-\omega$ (*SKW*), $k-\omega$ SST (*SSTKW*); *RSM* model: *SWF*, *NeWF*, *EWT*.

Figure 3 shows the streamlines and total pressure distribution in a channel for the case with $l = 0.8 \text{ m}$. It should be noted that at the beginning of section (IV) $0 \text{ m} < x < 0.2 \text{ m}$ it seems that the P_{tot} at the start sharply drop and then increases ($0.1 \text{ m} < x < 0.15 \text{ m}$). This is due to the fact that in this area the pressure averaging at the cross sections have been made through the vortex zone. So the values of P_{tot} at this area are not valid, but do not affect at the result. Distribution of P_{tot} is used for LDC determining from the results of numerical solution. In the considered problem, at the initial section (I) of the duct, the pressure change occurs under the influence of boundary conditions. The section (II) presents a nearly constant behavior for the specific pressure drop R , so it occurs due to friction losses only. At the (III) and (IV) sections the changes of R are highly nonlinear, and it is because of flow deformation and a vortex zone here. These losses are so called local pressure losses. And in this case the (V) section shows the similar to section (II) behavior. The friction losses $\Delta P_{fr} = R \cdot l_{(II+III+IV+V)}$. Thus, LDC is determined by the formula:

$$\zeta = \frac{P_1 - P_2 - \Delta P_{fr}}{(\rho v_0^2 / 2)}$$

where P_1 is the pressure at the end of (I) section, $P_2 = 0$ is the pressure at the section far from the outlet.

3 Results and Discussion

In the course of verification process, we plotted the maximum velocities at the outlet found at each stage of mesh refinement and for each of the investigated model combinations (Fig. 4).

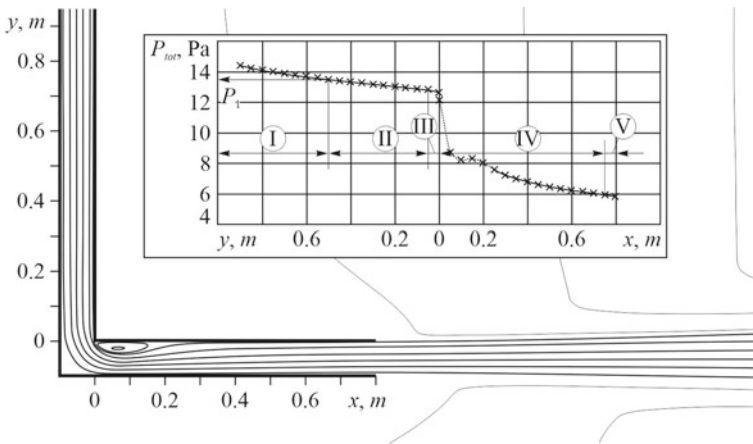


Fig. 3 Streamlines and pressure distribution in a channel for the LDC determination ($l = 0.8\text{ m}$)

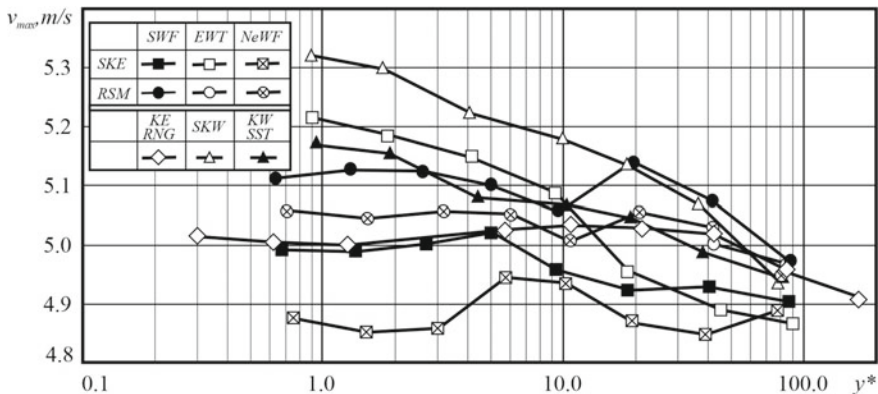


Fig. 4 Maximum velocity at the outlet for different combinations of turbulence models and wall functions

For the combinations *SKE EWT*, *SKW* and *SSTKW* $y + < 1$ at the 6th adaptation, and for the other models another mesh refinement step was performed. When using the *RSM* model in combination with the *EWT* wall function, no jet is formed; the problem diverges. Figure 3 shows that the relatively stable velocity behavior during mesh refinement is observed for the combinations *SKE SWF*, *RNGKE SWF*, and *RSM NeWF*. For these models, the maximum scatter of values at the last mesh adaptations (at $y + < 5$) does not exceed 0.4%. The other models show a scatter from 0.8% to 2%.

To verify the use of models for modeling the jet after leaving the hole, graphs of changes in the dimensionless axial velocity along the length of the jet were plotted (Fig. 5). For this purpose, the maximum velocity v_{max}/v_0 and the coordinate of this maximum were determined for several cross sections. The coordinates were used to determine the distance along the length of the jet axis, represented in the dimensionless form x'/b_0 , and to plot the jet axis (Fig. 6).

The behavior of axial velocity and jet axis does not change qualitatively when using various models. Figure 5 clearly shows that the models can be divided into two groups. $k-\epsilon$ RNG, standard $k-\omega$ and $k-\omega$ SST models are close to each other and differ from the others. In the second group of models, the maximum variation of velocities does not exceed 5%, and it equals 15% when comparing the groups. The jet axis in all cases has a deviation relative to the horizontal surface. The maximum scatter of values at the last point between models standard $k-\epsilon$ EWT and *RSM NeWF* is 18.5%.

Considering the results presented in Figs. 4, 5 and 6, a combination of *SKE SWF* models is taken as the basic calculation one. This model is further used to study the mesh dependence and flow.

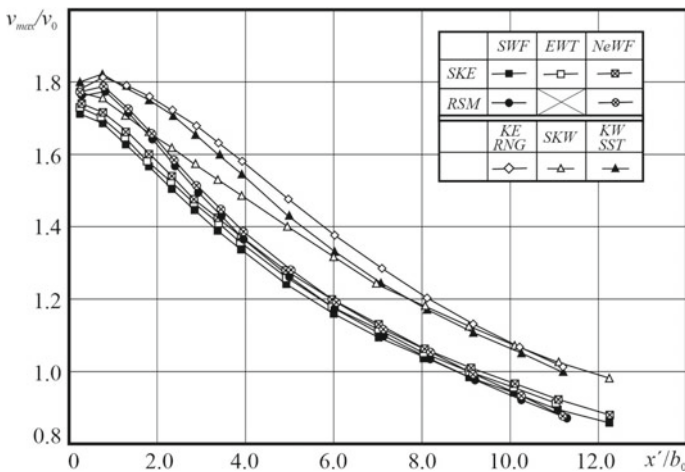


Fig. 5 Change in dimensionless maximum velocity along the length of the jet

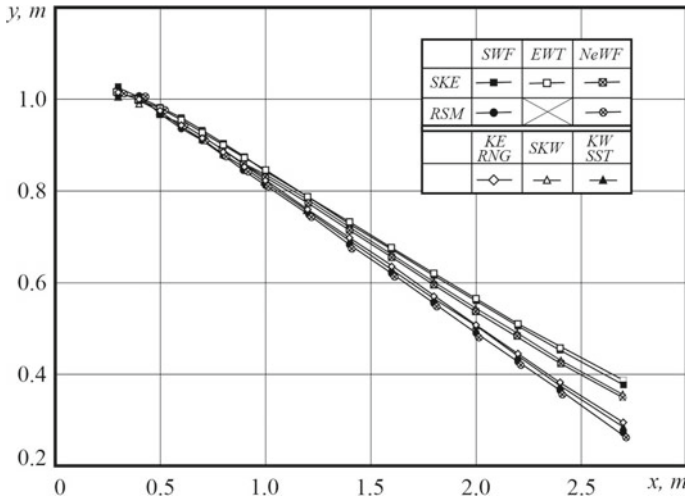


Fig. 6 Jet axis

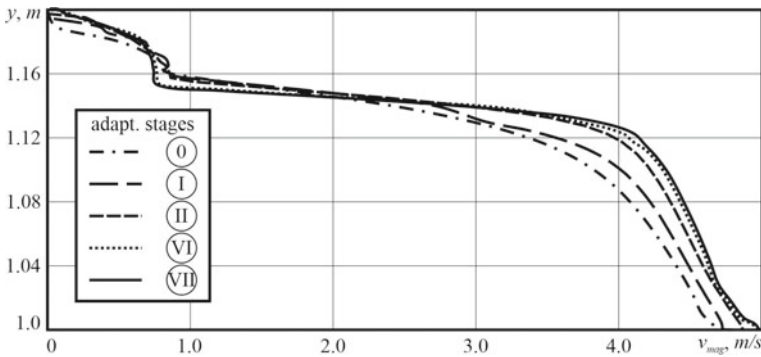
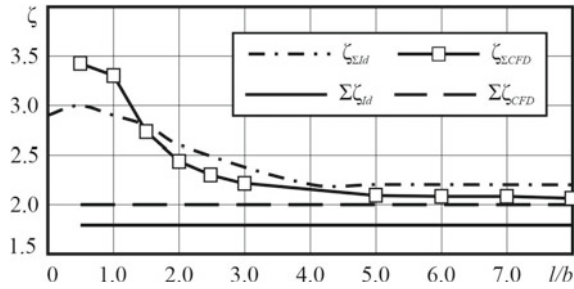


Fig. 7 Velocity magnitude profile at the outlet for the selected turbulence model for various adaptations

Mesh independence study with the profile of magnitude velocity on the outlet (*CD* boundary in Fig. 1) was performed. Figure 7 shows the maximum velocity profiles at the outlet for the *SKE SWF* model for various adaptations. The figure shows that the velocity profile is significantly irregular, which can be explained by the close location of the elbow to the outlet cross section. The flow after a 90° sharp elbow experiences deformation, which leads to distortion of both the velocity profile and deviation of the jet axis from the horizontal. Also, Fig. 7 shows that the velocity magnitude ceases to change, which shows the elimination of the dependence on the used mesh.

Further the combination *SKE SWF* was used to study the relationship between the resistance of a unit containing an elbow and an inlet opening, and the distance

Fig. 8 LDC for the unit “elbow-outlet”



between them for $l/b_0 = 0.5, 1, 1.5, 2, 2.5, 3, 5, 6, 7, 8$. For each problem, a mesh dependence study was carried out, and the LDC value on the most refined mesh and differing from the previous one by no more than 0.4% was taken as the final result. As a result (Fig. 8) the following were plotted: LDC of the unit (with friction deduction) obtained according to results of numerical investigation ($\zeta_{\Sigma CFD}$); LDC of the unit according to experimental data ($\zeta_{\Sigma Id}$ [3]); dependences for the sum of LDC of the elbow and the jet flowing in an unbounded space, which are equal to $\Sigma \zeta_{Id} = 0.79 + 1 = 1.79$ according to experimental data [3] and $\Sigma \zeta_{CFD} = 1.05 + 1 = 2.05$ according to numerical simulation [12].

Figure 8 shows that the developed computer model agrees well both with experimental data (difference is about 15% for $l/b_0 = 0.5$ and not more than 6% for $l/b_0 > 4$), and with numerical studies (difference is about 7%). In addition, it can be concluded that the unit consisting of an elbow and an inlet opening has a much higher resistance than the sum of these two shaped elements separately, in the case when the distance between them is less than $4b$.

4 Conclusion

A detailed validation and verification of the numerical solution of the flow problem in a unit consisting of an elbow and an inlet opening was performed. It was shown that the combination of standard k-ε turbulence model and standard near-wall functions showed the best results both in terms of resistance and modeling of jet development. The study has shown a significant dependence of the resistance of the unit on the distance between its constituent elements. At distances less than $4b$ (which is typical when connecting different supply air diffusers) the resistance of the unit is higher than that of the individual elements. This should be taken into account in aerodynamic calculations of ventilation systems. In the future it is necessary to continue research of distance influence between unit elements on kinematic properties of the jet, and also to expand the investigated constructions, and to consider openings equipped with various types of air diffusers.

References

1. Ignatiev, K.A., Giniyatullin, E.R., Ziganshin, M.G.: Research of the energy efficiency of a combined air and water heating of a public building. *Saf. Reliab. Power Ind.* **14**(2), 124–131 (2021)
2. Ignatyev, K.A., Giniyatullin, E.R., Ziganshin, M.G.: Research of the energy efficiency of a combined air and water heating system in a public building. *Reliabil. Secur. Energy* **14**(2), 124–131 (2021). <https://doi.org/10.24223/1999-5555-2021-14-2-124-131>
3. Idelchik, I.E.: Fluid dynamics of industrial equipment. Hemisphere Pub., 1991. (Translation of *Aerogidrodinamika tekhnologicheskikh apparatov*), p. 351. Mashinostroenie, Moscow (1983)
4. Kareeva, J., Bliznyakova, K., Ashadullina, D., Zakieva, R.: Influence of geometrical parameters of air inlet hole on the kinematic characteristics of jet. *IOP Conf. Ser. Mater. Sci. Eng.* **890**, 012164 (2020). <https://doi.org/10.1088/1757-899X/890/1/012164>
5. Kareeva, J., Zakieva, R.R.: Verification of the numerical model of the process of the jet flow from the inlet hole at an angle. *News KSUAE* **4**(58), 82–89 (2020)
6. Kocharyants, K.V.: Numerical modeling of air distribution by fan overflowing jets. Choice of turbulence model. *Bull. Civil Eng.* **4**(57), 128–133 (2016)
7. Kocharyants, K.V., Denisikhina, D.M.: Impermanence of kinematic coefficient in the flow from modern air diffusers. *Sci. Rev.*, 40–47 (2017)
8. Korkodinov, Y.A.: Review of k- ϵ family of models for modeling turbulence. *Bull. PNRPU Mech. Eng. Mater. Sci.*, 5–16 (2013)
9. Mizher, U.D., Velmisov, P.A. Application of Ansys system for investigation of jet turbulent flows. *Vestnik UIGTU*, 11–14 (2020)
10. Denisikhina, D.M., Ivanova, Yu.V., Mokrov, V.V.: Numerical modeling of outlet of modern air-distributing devices. *Eng. J. Don* **2** (2018)
11. Ziganshin, A., Eremina, S., Safiullina, G., Logachev, K.: Numerical study of the flow in a symmetrical ventilation junction tee with a baffle vane (2021). https://doi.org/10.1007/978-3-030-80103-8_23
12. Ziganshin, A.M., Beljaeva, E.E., Sokolov, V.A.: Pressure losses reduction with profiling of sharp elbow and elbow with dead-end. *News High. Educ. Inst. Constr.* **697**, 108–116 (2017)
13. Posokhin, V.N., Kareeva, Yu.R.: On pressure losses at jet air supply in limited volumes. *News Kazan State Univ. Arch. Eng.* **2**(36), 146–151 (2016)
14. Yusof, S.N.A.A., Sidik, Y., Azwadi, N., Mohamed, C., Japar, S.B., Aziz, W.M.A.: A short review on rans turbulence models. *CFD Lett.* **11**, 83–96 (2020)
15. Dong, X., Zhang, Z., Liu, D., Tian, Z., Chen, G.: Numerical investigation of the effect of meshes and turbulence models on critical heat flux in a vertical pipe. *Front. Energy Res* **6**(58), 1–11 (2018)
16. Huynh, T., Nguyen, Y.Q.: Numerical simulation of a solar chimney for natural ventilation of a building: comparison of different computational domains. *IOP Conf. Ser. Mater. Sci. Eng.* **1109**, 012014 (2021). <https://doi.org/10.1088/1757-899X/1109/1/012014>.
17. Harnane, Y., Bouzid, S., Berkane, S., Brima, A., Kaddour, A.: Simulation of night cooling through natural cross ventilation using ansys (Fluent) (2021). <https://doi.org/10.47238/ijeca.v6i1.146>
18. The Russian State Standard GOST R 57188–2016. Numerical modeling of physical processes. Terms and definitions, p. 12 (2016)
19. <http://www.sharcnet.ca/Software/Fluent12/html/th/node97.htm>. Accessed 03 aPR 2021

Concrete Beams with External Reinforcement of Composite Materials



Gleb Ogurtsov , Gleb Averchenko , Sergey Alekseev ,
Aleksii Ismailov , Anna Zanina , and Irshat Mukharryamov 

Abstract The operation of buildings and structures leads to the appearance of various structural defects. There are constant changes in payload values in the regulatory documents. Schemes of external reinforcement with composite woven material of the superstructure are proposed and considered. The article presents the sequence of mounting a composite material on a reinforced concrete beam. The physical and mechanical properties of a laminate composite material in the field of construction are considered. External reinforcement allows you to increase the bearing capacity of the element in a short time without changing the cross section and material of the element, which requires an increase in mechanical properties. The article presents the results of theoretical studies of mechanical properties. The influence of external reinforcement on the bearing capacity of the beam structure is determined.

Keywords Concrete beams · External reinforcement · Composite materials

1 Introduction

Currently, the state of many buildings and structures requires a comprehensive survey to identify the need for reconstruction and (or) strengthening of the constituent parts and elements. Strengthening the structures of various buildings and constructions using a composite material based on thermosetting plastics [1–3] could become one of the most widespread, technically perfect and cost-effective way in comparison with other methods [4–6]. The need for reinforcement arises both during reconstruction and during operation as a part of emergency repair. Therefore, the need for research on the reinforcement of concrete structures is obvious and not fully disclosed with the known achievements of science and technology. For the purpose of this, the authors

G. Ogurtsov · G. Averchenko · S. Alekseev · A. Ismailov (✉) · A. Zanina · I. Mukharryamov
Peter the Great St. Petersburg Polytechnic University,
Polytechnicheskaya Street, 29, St. Petersburg 195251, Russian Federation
e-mail: ismailov-aleksei@mail.ru

I. Mukharryamov
New Institute, Gouda, The Netherlands

have carried out a number of practical studies on the reinforcement of concrete beams with external reinforcement made of composite materials.

2 Materials and Methods

We used external reinforcement (of a reinforced concrete structure) with composite materials. The installation is fulfilled by gluing prefabricated products made of composite materials (laminates) onto a reinforced concrete structure or layer-by-layer gluing of continuous carbon or glass fiber products (canvases, nets and other woven materials) with thermosetting adhesives, followed by curing and the formation of a single layer or multilayer composite material [7–9]. The main strength and deformation characteristics of composite materials for the design of reinforced concrete structures reinforced externally with composite materials are:

- tensile resistance;
- modulus of elasticity in tension;
- limiting relative deformations;
- the coefficient of transverse deformation [10–12].

For calculations for the first group of limiting states, the following strength and geometric characteristics of materials were taken [13, 14].

For calculating the beam, the following dimensions were taken: $0.3 \times 0.8 \times 6$, (BxHxL). Concrete grades B20 (average strength under uniaxial compression $R_b = 11.7$ MPa), B25 (average strength under uniaxial compression $R_b = 13.1$ MPa), B30 (average strength under uniaxial compression $R_b = 17$ MPa). We use a rod rebar of A-III classes with the design resistance for the limiting states of the first group $R_s = 365$ MPa when calculating 3 rods with a diameter of 10 mm [15, 16]. We apply composite material with critical strength in uniaxial tension $\sigma_r = 1000$ MPa, layer thickness is 8, 10 and 12 mm, and width is 200 mm. Inclined clamps are made from one piece of canvas. First, it is glued to one side of the reinforced beam, its rolling is carried out, after which the actions are repeated with other sides (Fig. 1) [17, 18] (Fig. 2 and Table 2).

Reinforcement scheme A is used when reinforcing the superstructure, in the calculation of which an error was made (or the load requirements changed) and it is required to increase the limiting moment perceived by the section [19, 20]. This method is convenient because the external reinforcement is installed on site and it does not require a change in the superstructure design [21–23].

Reinforcement schemes B and D are used to reinforce the superstructure, the strength of which cannot be ensured with standard reinforcement dimensions. This external reinforcement differs from the previous one with transverse clamps, which are used along an inclined crack that may form during operation. Without transverse clamps, the protective layer of concrete can come off and the outer reinforcement will no longer take the load [24–26].

Fig. 1 Scheme of installing woven materials on beam structures

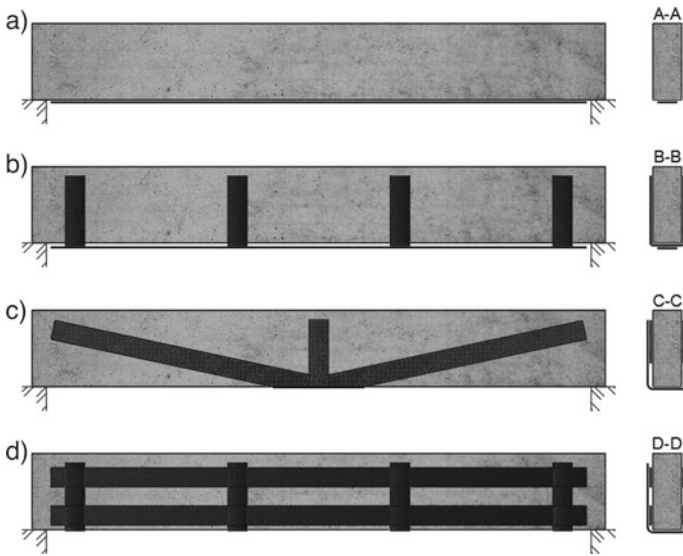
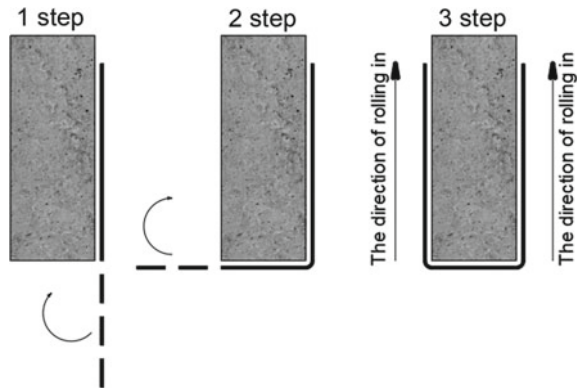


Fig. 2 Accepted schemes of external reinforcement of concrete beams (A, B, C, D)

Reinforcement scheme C is used when an error is made in the calculation of the reinforcement of the superstructure section (or the load requirements have changed) and it is required to ensure the strength along the inclined section [27, 28].

Determining the height of the compressed zone:

$$x = \frac{R_f A_f}{R_b A_b} \tag{1}$$

R_f —tensile strength of external reinforcement.

A_f —external reinforcement area.

Table 1 Strength and deformation characteristics of composite materials

Fiber type	Tensile strength, MPa	Elastic modulus, GPa	Elongation deformation, %	Density, t / m ³
High strength carbon *	4300–4900	230–240	1,9–2,1	1,8
High modulus carbon *	2740–5490	294–329	0,7–1,9	1,78–1,81
High modulus carbon **	2600–4020	540–640	0,4–0,8	1,91–2,12
Aramid ***	3200–3600	124–130	2,4	1,44
Glass	2400–3500	70–85	3,5–4,7	2,6

* On a polyacrylonitrile matrix

** On an epoxy resin matrix.

*** Aramid can have the same strength with a lower modulus of elasticity.

Table 2 The minimum required characteristics of woven materials based on carbon fiber used for external reinforcement according to Table 1 SP 164.1325800.2014 [11]

№ s/p	Indicator name	Unit	Value	Control method
1	Tensile strength	MPa	1000	GOST 25.601
2	Tensile modulus	GPa	55	GOST 25.601
3	Linear thermal expansion coefficient: - longitudinal - transverse	°C ⁻¹	(-1-0) * 10 ⁻⁶ (22-50) * 10 ⁻⁶	GOST 15,173
4	Compressive strength	MPa	650	GOST 25.601
5	Compressive modulus	GPa	65	GOST 25.601

R_b —compressive strength of concrete.

A_b —compressed area of concrete.

Determination of the limiting moment:

$$M_u = R_b \cdot b \cdot x \cdot (h_o - 0,5 \cdot x) + 0,05 \cdot R_f \cdot A_f \text{ for schemes A and B} \quad (2)$$

$$M_u = R_b \cdot b \cdot x \cdot (h_o - 0,5 \cdot x) + 0,9 \cdot R_f \cdot A_f \text{ for schemes C} \quad (3)$$

x —height of the compressed zone of concrete.

The action of shear forces perceived by concrete:

$$Q_b = \frac{1,5 \cdot R_{bt} \cdot b \cdot h_0^2}{c} \quad (4)$$

R_{bt} —tensile strength of concrete.

c —inclined section projection length.

The action of shear forces perceived by external reinforcement:

$$Q_{fw} = 0,95 \frac{A_{fw} \cdot R_{fw} \cdot \sin \alpha \cdot C_{fw}}{S_f} \quad (5)$$

$$C_{fw} = \frac{C(h_{fw} - a)}{h} \quad (6)$$

$$R_{fw} \leq \gamma_{f4} \cdot R_f \quad (7)$$

$$\gamma_{f4} = \frac{k_1 \cdot k_2 \cdot L_f \cdot E_f}{1190 \cdot R_f} \leq 0,75 \quad (8)$$

$$L_f = \frac{23300}{(n \cdot t_f \cdot E_f)^{0,58}} \quad (9)$$

$$k_1 = (0,1 \cdot R_b)^{2/3} \quad (10)$$

$$k_2 = \frac{h_{fw} - L_f}{h_{fw}} \quad (11)$$

h_{fw} —cross clamp sticker height.

A_{fw} —cross-sectional area of the composite material clamp.

R_{fw} —the calculated value of the tensile strength of a composite material when calculating the strength of sections.

γ_{f4} —adhesion safety factor.

L_f —effective anchorage length, mm.

k_1 —coefficient taking into account the strength of concrete.

k_2 —coefficient taking into account the reinforcement scheme (Figs. 3 and 4).

3 Results

The critical (breaking) loads were determined for a beam with external reinforcement using various external reinforcement schemes and various grades of concrete (B20, B25 and B30). Table 3 shows the results of calculations using various sheets for reinforcement. The table shows the results of calculations of the beam superstructure in terms of the bearing capacity for the given strength, deformation and geometric characteristics of the section. The column “Permissible Load” indicates the maximum limit load values without external composite reinforcement [29–33].

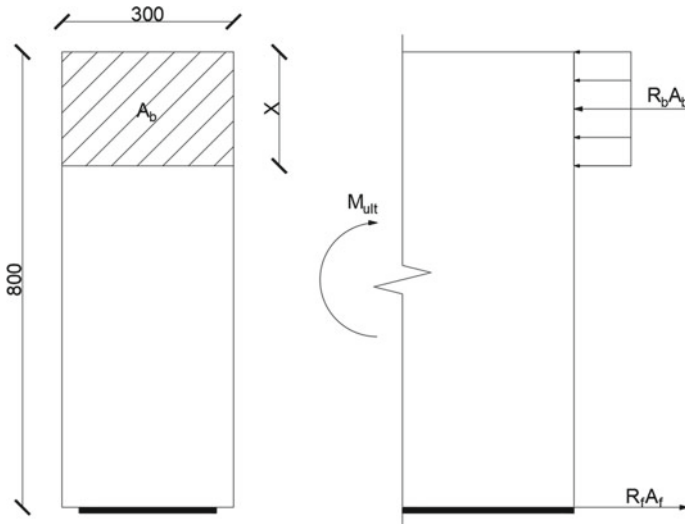


Fig. 3 Design scheme for determining the limiting moment for schemes A and B

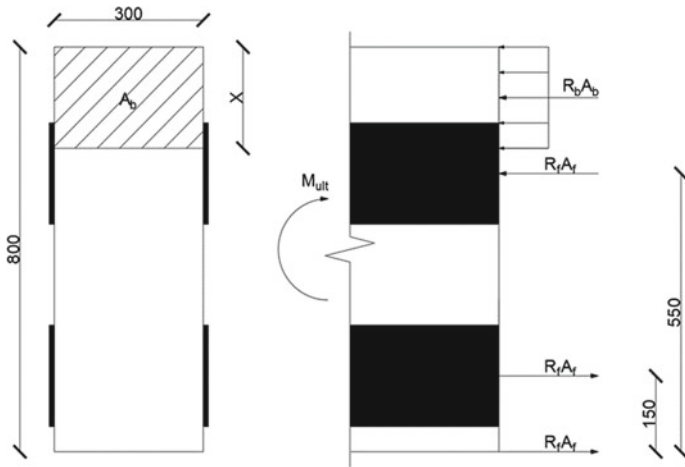


Fig. 4 Design scheme for determining the limiting moment for scheme D

4 Conclusions

According to the data obtained from the calculations, it can be seen that when using external reinforcement made of composite materials, the superstructure can withstand several times more load without changing the composition of concrete, the area of steel reinforcement and geometric characteristics [34].

Table 3 Table of the results obtained

№ s/p	Reinforcement scheme and concrete strength	Permissible load (conditional admissible value or normative), kPa	Ultimate (breaking) load, kPa		
			Canvas Thickness/Width 8 mm/200 mm	Canvas Thickness/Width 10 mm/200 mm	Canvas Thickness/Width 12 mm / 200 mm
Scheme A:					
1	B20	1,404*	2,441	2,725	2,956
2	B25	1,408*	2,721	3,038	3,296
3	B30	1,411*	2,972	3,320	3,602
Scheme B:					
4	B20	1,404*	2,441	2,725	2,956
5	B25	1,408*	2,721	3,038	3,296
6	B30	1,411*	2,972	3,320	3,602
Scheme C:					
7	B20	1,404*	4,656	5,211	5,662
8	B25	1,408*	5,173	5,793	6,298
9	B30	1,411*	5,634	6,314	6,867
Scheme D:					
10	B20	1,404*	4,938	5,423	5,827
11	B25	1,408*	5,485	6,037	6,506
12	B30	1,411*	5,988	6,600	7,123

* - permissible load without external reinforcement.

References

- Pavlenko, A., Mishakova, A., Pertseva, O., Ivanova, V., Olekhovich, Y., Averchenko, G.: Feasibility of using of accelerated test methods for determination of frost-resistance for concrete. In: E3S Web of Conferences (2020). <https://doi.org/10.1051/e3sconf/202015706035>
- Mukharyamov, I., Averchenko, G.: Improvement of analysis and design of road pavements using nepheline sludge. Archit. Eng. (2020). <https://doi.org/10.23968/2500-0055-2020-5-3-63-69>
- McCarthy, C.T., O'Higgins, R.M., Frizzell, R.M.: A cubic spline implementation of non-linear shear behaviour in three-dimensional progressive damage models for composite laminates. Compos. Struct. (2010). <https://doi.org/10.1016/j.compstruct.2009.07.025>
- Jones, R.M., Morgant, H.S.: Analysis of nonlinear stress-strain behavior of fiber-reinforced composite materials. AIAA J. (1977). <https://doi.org/10.2514/3.60835>
- Hassani, F., Shokrieh, M., Lessard, L.: A fully non-linear 3-D constitutive relationship for the stress analysis of a pin-loaded composite laminate. Compos. Sci. Technol. (2002). [https://doi.org/10.1016/S0266-3538\(02\)00003-9](https://doi.org/10.1016/S0266-3538(02)00003-9)
- Van Paepegem, W., De Baere, I., Degrieck, J.: Modelling the nonlinear shear stress-strain response of glass fibre-reinforced composites. Part I: Experimental results. Compos. Sci. Technol. (2006). <https://doi.org/10.1016/j.compscitech.2005.04.014>

7. Dano, M.L., Gendron, G., Picard, A.: Stress and failure analysis of mechanically fastened joints in composite laminates. *Compos. Struct.* (2000).[https://doi.org/10.1016/S0263-8223\(00\)00119-7](https://doi.org/10.1016/S0263-8223(00)00119-7)
8. Bordreuil, C., Hochard, C.: Finite element computation of woven ply laminated composite structures up to rupture. *Appl. Compos. Mater.* (2004).<https://doi.org/10.1023/B:ACMA.0000026474.67067.b6>
9. Ladeveze, P., LeDantec, E.: Damage modelling of the elementary ply for laminated composites. *Compos. Sci. Technol.* (1992).[https://doi.org/10.1016/0266-3538\(92\)90097-M](https://doi.org/10.1016/0266-3538(92)90097-M)
10. Abramovich, H.: Introduction to composite materials. In: *Stability and Vibrations of Thin-Walled Composite Structures* (2017). <https://doi.org/10.1016/B978-0-08-100410-4.00001-6>.
11. Pavan, R.C., Creus, G.J., Maghous, S.: A simplified approach to continuous damage of composite materials and micromechanical analysis. *Compos. Struct.* (2009).<https://doi.org/10.1016/j.compstruct.2009.04.044>
12. Belytschko, T., Black, T.: Elastic crack growth in finite elements with minimal remeshing. *Int. J. Numer. Methods Eng.* (1999).[https://doi.org/10.1002/\(SICI\)1097-0207\(19990620\)45:5<601::AID-NME598>3.0.CO;2-S](https://doi.org/10.1002/(SICI)1097-0207(19990620)45:5<601::AID-NME598>3.0.CO;2-S)
13. Qian, Z., Hu, J.: Fracture properties of epoxy asphalt mixture based on extended finite element method. *J. Cent. South Univ.* (2012). <https://doi.org/10.1007/s11771-012-1412-8>
14. Moës, N., Dolbow, J., Belytschko, T.: A finite element method for crack growth without remeshing. *Int. J. Numer. Methods Eng.* (1999).[https://doi.org/10.1002/\(SICI\)1097-0207\(19990910\)46:1<131::AID-NME726>3.0.CO;2-J](https://doi.org/10.1002/(SICI)1097-0207(19990910)46:1<131::AID-NME726>3.0.CO;2-J)
15. Ismailov A.M.: Optimization-qualimetric model of the process of designing asphalt-concrete mixes of required quality (2019)
16. Menk, A., Bordas, S.P.A.: A robust preconditioning technique for the extended finite element method. *Int. J. Numer. Methods Eng.* (2011).<https://doi.org/10.1002/nme.3032>
17. Asadpoure, A., Mohammadi, S.: Developing new enrichment functions for crack simulation in orthotropic media by the extended finite element method. *Int. J. Numer. Methods Eng.* (2007).<https://doi.org/10.1002/nme.1839>
18. Petit, P.H., Waddoups, M.E.: A method of predicting the nonlinear behavior of laminated composites. *J. Compos. Mater.* (1969).<https://doi.org/10.1177/002199836900300101>
19. Hahn, H.T., Tsai, S.W.: Nonlinear elastic behavior of unidirectional composite laminae. *J. Compos. Mater.* (1973).<https://doi.org/10.1177/002199837300700108>
20. Jones, R.M., Nelson, D.A.R.: A New Material model for the nonlinear biaxial behavior of ATJ-S Graphite*. *J. Compos. Mater.* (1975). <https://doi.org/10.1177/002199837500900102>.
21. Greaves, G.N., Greer, A.L., Lakes, R.S., Rouxel, T.: Poisson's ratio and modern materials (2011).<https://doi.org/10.1038/nmat3134>
22. Sandhu, R.S.: Nonlinear behavior of unidirectional and angle ply laminates *J. Aircr.* (1976).<https://doi.org/10.2514/3.58638>
23. Meng, M., Le, H.R., Rizvi, M.J., Grove, S.M.: 3D FEA modelling of laminated composites in bending and their failure mechanisms. *Compos. Struct.* (2015).<https://doi.org/10.1016/j.compstruct.2014.09.048>
24. Ismailov, A., Bokovaya, N., Averchenko, G.: The impact modifier will Factorit-C on the physico-mechanical properties of asphalt mix. In: Vatin, N., Borodinecs, A., Teltayev, B. (eds.) *Proceedings of EECE 2020. EECE 2020. LNCE*, vol. 150, pp. 525–534. Springer, Cham (2021). https://doi.org/10.1007/978-3-030-72404-7_51
25. Averchenko, G., Kovalev, A., Semyonova, T., Birykov, O., Ermoshin, N.: Definition of movements in arches and the arches massive bridges. In: Vatin, N., Borodinecs, A., Teltayev, B. (eds.) *Proceedings of EECE 2020. EECE 2020. LNCE*, vol. 150, pp. 421–431. Springer, Cham (2021). https://doi.org/10.1007/978-3-030-72404-7_41
26. Anishchenko, D., Novik, A., Boytsov, A., Lazarev, Y., Trubina, D.: Underground streets in residential area: aspects of design on the example of Russia. In: Anatolijs, B., Nikolai, V., Vitalii, S. (eds.) *Proceedings of EECE 2019. EECE 2019. LNCE*, vol. 70, pp. 433–439. Springer, Cham (2020). https://doi.org/10.1007/978-3-030-42351-3_38

27. Vdovin, E., Mavliev, L., Stroganov, V. Interaction of clay soil components with portland cement and complex additive based on octyltriethoxysilane and sodium hydroxide. In: IOP Conference Series: Materials Science and Engineering, vol. 890, no. 1, p. 012031 (2020)
28. Mavliev, L., Vdovin, E.: Structure of road soil cement compositions modified by complex additive based on organosilicon compounds and electrolytes. In: E3S Web of Conferences, vol. 140, p. 02016 (2019)
29. Vdovin, E., Stroganov, V., Kononov, N.: Modification of road soil cement with activated fillers. In: Vatin, N., Borodinecs, A., Teltayev, B. (eds.) Proceedings of EECE 2020. EECE 2020. LNCE, vol. 150, pp. 335–345. Springer, Cham (2021). https://doi.org/10.1007/978-3-030-72404-7_33
30. Vdovin, E.A., Stroganov, V.F.: Optimization of complex frost-resisting additives in line with operational requirements towards freezing temperature in road dressing constructions. In: IOP Conference Series: Materials Science and Engineering, vol. 832, no. 1, p. 012034 (2020)
31. Vdovin, E.A., Stroganov, V.F. Modification of cement-bound mixtures with sodium formate additives for the construction of pavement bases at low air temperatures. IOP Conference Series: Materials Science and Engineering, vol. 786, no. 1, p. 012065 (2020)
32. Drigo, D., Talipova, L.: Modeling the shape of a high-rise building in St. Petersburg to reduce wind flows. In: ISI Science Week. Materials of the All-Russian conference in 3 parts. Civil Engineering Institute of Peter the Great St. Petersburg Polytechnic University. St. Petersburg, pp. 81–83 (2021)
33. Talipova, L., Lyubomirskiy, A., Povarenko, D., Scherbakov, A. Creating public space through urban analysis. In: E3S Web of Conferences. Topical Problems of Green Architecture, Civil and Environmental Engineering, TPACEE 2019, p. 04012 (2020)
34. Rozhina, M., Lyubomirskiy, A., Talipova, L.: Analysis of fire department's location in St. Petersburg. In: E3S Web of Conferences. Topical Problems of Green Architecture, Civil and Environmental Engineering, TPACEE 2019, p. 04013 (2020)

Full-Scale Tests of the Bearing Capacity of a Composite I-Beam with a Solid Web of Pultruded Fiberglass Profiles (PFP)



Marat Salakhutdinov , Daler Aripov , and Arslan Khanekov 

Abstract The article considers the results of full-scale test of a composite I-beam with a solid web of pultruded fiberglass profiles to determine its bearing capacity, deflection, and stress-strain state. A new design solution of a composite I-beam with a solid web of pultruded fiberglass profiles with a 6-m span for floor slabs or covering of buildings and structures has been developed. The significance of a full-scale test lies in determination of the actual operation and the bearing capacity of a composite I-beam of pultruded fiberglass profiles with a three-point bend and the possibility of further implementation of this type of beams in constructions.

Keywords Pultrusion · Fiberglass profile · Bearing capacity · Composite beam · Beam bending

1 Introduction

Currently, the use of pultruded fiberglass products in railway transport, construction, in the petrochemical industry, etc. is relevant [1–6]. The most widespread use of PFP in constructions has been found in pedestrian and road bridges [7, 8], slabbing and covering buildings and structures [9]. The possibility of using PFP in load bearing structures is justified by theoretical studies [10]. Analysis of existing recommendations for the calculation and construction of these profiles shows that one of the problems in the development of fiberglass structures is to ensure the required strength and deformability [11]. At the same time, the strength and deformability of the PFP structure largely depends on the solution of the nodal joints, which are mainly bolted [13].

It is known that truss and frame PFP structures have been designed for more than 30 years [14]. Now, there are no generally accepted standards for the calculation and design of PFP structures at the level of Russian joint ventures or American Codes.

M. Salakhutdinov (✉) · D. Aripov · A. Khanekov
Kazan State University of Architecture and Engineering, Kazan, Russian Federation

D. Aripov
e-mail: architector-1992@mail.ru

Available documents are recommendations of individual industries or standards of various associations [15]. Expanding the scope of application of PFP lattice structures requires the development of methods for calculating and considering the behavior of these materials in various operating conditions [16, 21]. Experimental studies of bolted connections of PFP elements were performed by Mottram and Zheng [17], and Truvey and Cooper [18]. Experimental studies show that the initial stiffness of the nodal joint is determined by the connecting elements. The complete destruction of the connecting elements on the bolts is characterized by a fragile destruction of the material, the shape of which depends on both the strength of each element and the configuration of the connection.

Objective of the study: To determine the bearing capacity of a composite I-beam with a solid web of PFP by full-scale testing.

Tasks:

1. To develop a new design solution for a composite I-beam made of PFP, the belts of which are made of paired corners, the wall is made of sheets of double thickness, installed with an offset in length.
2. To perform full scale three-point bending tests of a composite I-beam with a solid web of PFP.
3. To obtain the deformation dependencies on the load on the composite I-beam with a solid web of PFP.

2 Materials and Methods

The object of a study is a composite I-beam with a solid web of pultruded fiberglass profiles with a 6-m span and a height of 0.5 m. The upper and lower shelves are made of paired pultruded fiberglass corners with a cross-section of 105×13 mm, the web along the entire length of the beam was made of double thickness from pultruded fiberglass sheets with a cross-section of 500×400 mm with a thickness of 10 mm each. The web elements were installed with an offset along the length of the beam to exclude the formation of gaps between the fiberglass sheets. The elements of the shelves and the walls of the beam were interconnected by bolts M16 without controlled tension, installed in increments of 100 mm (Fig. 1).

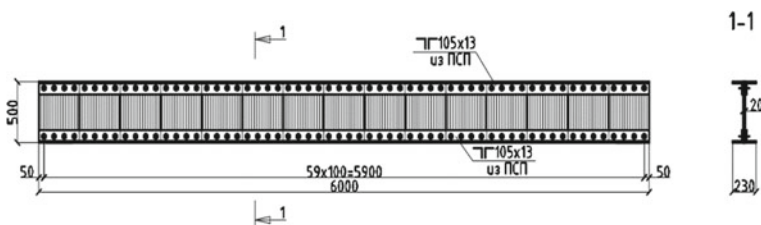


Fig. 1 Design solution of a composite I-beam with a solid web of PFP



Fig. 2 The composite I-beam with a solid web of PFP before full-scale test

Full-scale tests were carried out on the basis of the REC “Strength” of KSUAE. A sample of a composite I-beam with a solid web of PFP for full-scale testing was produced and provided by Tatneft-Presskomposite LLC [19].

For premature destruction of the support zone, support plates were additionally installed along the edges of the beam. As part of the full-scale test, the following sequence of preparation of the beam sample was adopted:

1. Installation of the beam on metal supports made of steel I-beam 20K1. Round pipes with a diameter of 45 mm were used as hinged supports.
2. Installation of a hydraulic universal jack DU20P250 (with a maximum force of 20 tf), equipped with a Ten-zoM70-20.0-S3 power meter with the function of displaying test results on the computer display.
3. Cleaning of PFP element surfaces in places where strain gauges are installed.
4. Installation of strain gages BF120-10AA on the surface of PFP elements (Fig. 2).
5. Installation of metal struts in the middle and at the ends of the beam.

After the described actions, the performance of the measuring system was checked, and the composite I-beam was tested (Fig. 2). Full-scale tests of the beam were carried out on the action of a concentrated short-term load. The loading was produced gradually with the stages of no more than 0,01 of the reference strength load (280 kN). At each stage, the load was held for 10 min. The readings were taken constantly at each loading stage.

The composite I-section beam was tested on a three-point bending. Before loading, the loading devices were aligned with the pre-applied marking drawings on the surface of the beam. Thus, all the resulting stress irregularities in cross-sections were due only to random eccentricities. During the full-scale tests, the beams were fixed at each step of a stepped load application.

- relative deformations in beam elements;
- vertical movements of the beam.

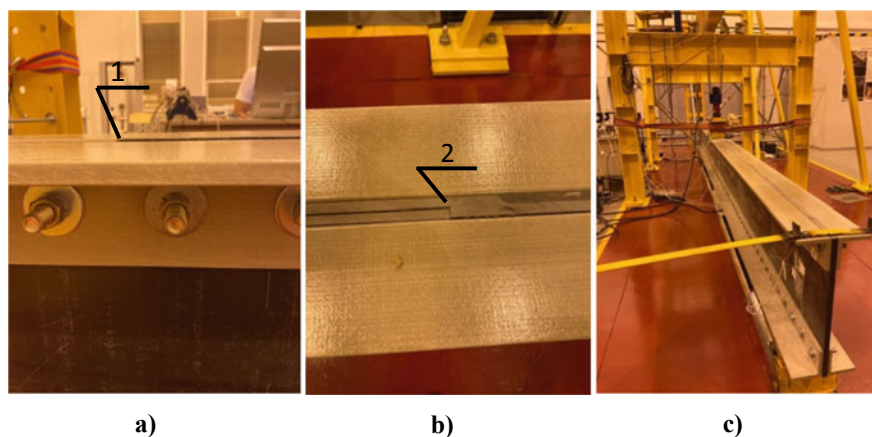


Fig. 3 a, b Displacement of web elements relative to belts (1. Displacement of a sheet gusset, 2. Cut of bolted connection), c The general view of the beam deformation

3 Results

During the full-scale test, the composite I-beam was deformed (Fig. 3).

Based on the results of the full-scale test, the readings of the beam deflections were taken, and dependency graphs were built (Fig. 4). The value of the maximum deflection for the second group of limit states ($f_c = 30$ mm) was achieved at a concentrated short-term load $P_{ult} = 61.3$ kN.

4 Discussion

The results of full-scale tests of a solid-section beam made of PFP for short-term loads are known [10]. This beam with a span of 1.55 m is made with I-beam cross-section with a height and width of shelves of 200 mm, a wall thickness and shelves of 15 mm, respectively.

For the beam under consideration, the theoretical value of the maximum load capacity was $P_{theor} = 114.14$ kN, and the results of full-scale tests showed the maximum short-term load $P_{ult} = 143.14$ kN [20]. Theoretical studies show that solid I-beams can be used only up to spans of not more than 4 m, while the composite I-beams allow to be effectively used at spans of 4 m or more. At the same time, the second limit state (deflection of 30 mm) for the developed composite beam is achieved at a short-term load $P = 61.3$ kN, and the maximum short-term load according to the results of the full-scale test was $P_{max} = 107.91$ kN.

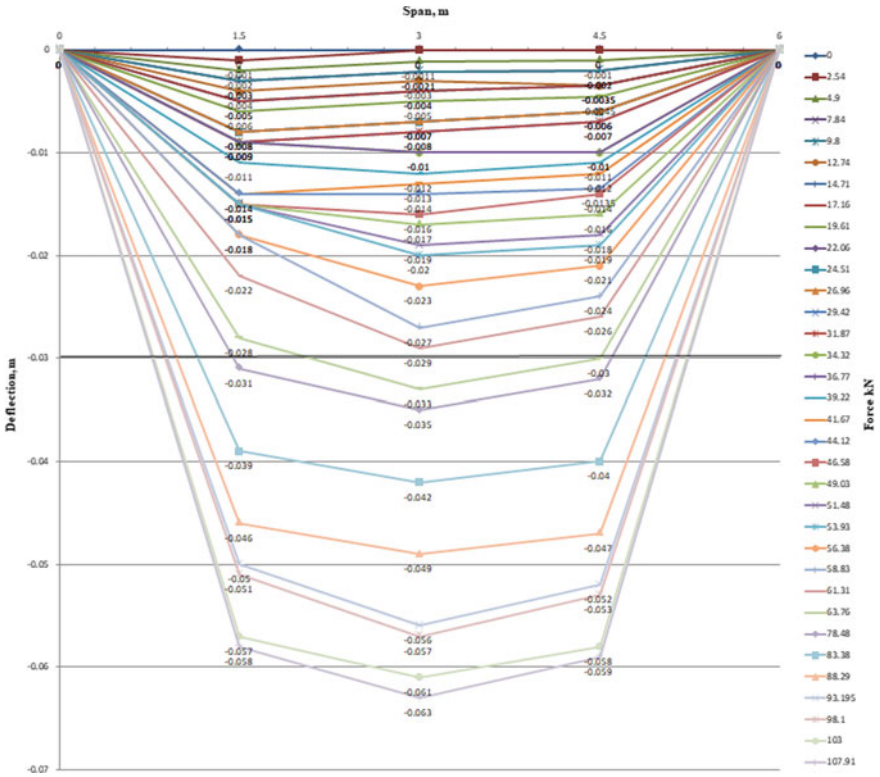


Fig. 4 Graph of the dependence of deflections on the short-term load of a composite I-beam with a solid web of PFP

5 Conclusion

1. We developed new design solution for a composite I-beam made of PFP, the belts of which are made of paired angle bars, and the web is made of double-thickness sheets installed with a displacement along the length.
2. We performed full-scale tests of a composite I-beam with a solid web of PFP for three-point bending.
3. We obtained the values of deformation of a composite I-beam section with a solid web in the form of deflections. It has been established that the bearing capacity of the developed beam according to the first and second group of limit states is ensured. At the same time, the second limit state (deflection of 30 mm) for the developed composite I-beam is achieved at a short-term load $P = 61.3$ kN.

References

1. Kayumov, R., Sulejmanov, A., Strakhov, D.: Model of degradation of composite materials of building structure's load-bearing elements. In: Presented at the (2021). https://doi.org/10.1007/978-3-030-80103-8_26
2. Mirsayapov, I., Nurmukhametov, R., Vasyutkin, E., Burin, D.: FEA analysis of fiberglass piles' bearing capacity at water saturated soft clay. In: Presented at the (2021). https://doi.org/10.1007/978-3-030-72404-7_38
3. Setyanto, D., Antonio, Y.A., Darmawan, M., Ubaidillah, U.: A novel Z profile of pultruded glass-fibre-reinforced polymer beams for purlins. *Sustainability* **14**, 5862 (2022). <https://doi.org/10.3390/su14105862>
4. Vatin, N., Ilizar, M., Nurmukhametov, R.: Composite helical micro pile's bearing capacity. *IOP Conf. Ser. Mater. Sci. Eng.* **890**, 012037 (2020). <https://doi.org/10.1088/1757-899X/890/1/012037>
5. Mukhametrakhimov, R., Aliullova, I.: Construction technology and quality control of expansion joints with rubber compensators. *E3S Web Conf.* **264**, 02066 (2021). <https://doi.org/10.1051/e3sconf/202126402066>
6. Suleimanov, A.M., Tuisina, E.B.: Experimental determination of the significance of the impact of operational factors on the polymer matrix of pultrusion fiberglass profiles. *Vestnik Civ. Eng.* **19**, 98–109 (2022). <https://doi.org/10.23968/1999-5571-2022-19-2-98-109>
7. Sebastian, W.M., Ross, J., Keller, T., Luke, S.: Load response due to local and global indeterminacies of FRP-deck bridges. *Compos. Part B Eng.* **43**(4), 1727–1738 (2012)
8. Adilardi A., Russo, S.: Innovative design approach to a GFRP pedestrian bridge: Structural aspects, engineering optimization and maintenance. *Proc., 15th Int. Conf. on Bridge Maintenance, Safety and Management*. CRC Press/Balkema, Taylor and Francis Group, Leiden, Netherlands, pp. 2455–2459 (2010)
9. Feroldi, F., Russo, S.: Structural behavior of all-FRP beam-column plate-bolted joints. *J. Compos. Constr.* **20**(4), 04016004 (2016). [https://doi.org/10.1061/\(ASCE\)CC.1943-5614.0000667](https://doi.org/10.1061/(ASCE)CC.1943-5614.0000667)
10. Kayumov, R.A., Lukankin, S.A., Paimushin, V.N., Kholmogorov, S.A.: Identification of mechanical properties of fiber-reinforced composites. *Uchenye Zapiski Kazanskogo Universiteta. Seriya Fiziko-Matematicheskie Nauki* **157**(4), 112–132 (2015)
11. Martins, D., Proenca, M., Correira, J.R., Gonilha, J., Arruda, M., Silvestre, N.: Development of a novel beam to column connection system for pultruded GFRP tubular profiles. *Compos. Struct.* **171**, 263–276 (2017). <https://doi.org/10.1016/j.compstruct.2017.03.049>
12. Satasivam, S, Feng, P., Bai, Y., Caprani, C.: Composite actions within steel-FPR composite beam systems with novel blind bolt shear connections. *Eng. Struct.* **138**, 63–73. <https://doi.org/10.1016/j.engstruct.2017.01.068>
13. Kuznetsov, I.L., Fakhrutdinov, A.E., Aripov, D.N. A study of bolted joints pultruded GRP profiles elements: collection of articles of All-Russian scientific and technical conference “Polymer composite materials of new generation. Transfer of innovations from aviation to priority sectors of the Russian economy”/VIAM. Ulyanovsk, pp. 6–15 (2018)
14. Mutsuyoshi, H., Nguyen, H., Zatar, W., Ishihama, T.: Rexural behavior of pultruded hybrid fiber-reinforced polymer I-beam with bonded-and-bolted splice joints. *Transp. Res. Method* **2592**, 45–55 (2016). <https://doi.org/10.3141/2592-06>
15. Aripov, D.N., Kuznetsov, I.L., Salakhutdinov, M.A.: Improvement of node connections on pultrusion fiberglass gusset plates in frame structure. *Bulletin of BSTU named after V.G. Shukhov*, vol. 12, pp. 22–31 (2020). <https://doi.org/10.34031/2071-7318-2020-5-12-22-31>
16. Boscato, G., Russo, S.: Free vibrations of a pultruded GFRP frame with different rotational stiffness of bolted joints. *Mech. Compos. Mater.* **48**(6), 655–668 (2013)
17. Mottram, J.T., Zafari, B.: Pin-bearing strengths for bolted connections in fibre-reinforced polymer structures. *Proc. Inst. Civ. Eng. Struct. Build.* **164**(5), 291–305 (2011). <https://doi.org/10.1680/stbu.2011.164.5.291>

18. Turvey, G.J.: Experimental and analytical investigation of two- and six-plate bonded splice joints on serviceability limit deformations of pultruded GFRP beams. *Compos. Struct.* **111**, 426–435 (2014). <https://doi.org/10.1016/j.compstruct.2013.12.022>
19. Composite materials SMC/BMC. High technology. Good quality. Professional approach. <https://www.tnpc.ru/>. Accessed 10 June 2022
20. Salakhutdinov, M.A., Gimranov, L.R., Kuznetsov, I.L., Fakhrutdinov, A.E., Nurgaleeva, L.M.: PFRP structures under the predominately short term load. *Mag. Civ. Eng.* **96**(4), 3–14 (2020). <https://doi.org/10.18720/MCE.96.1>
21. Kayumov, R.A., Sharafutdinova, A.A.: Ob otsenke dolgovechnosti stroitelnykh konstruksiy iz stekloplastika [About an estimation of operational durability of building designs from fiberglass]. *News KSUAE* **40**(2), 114–123 (2017)

The Possibility of Vibrodynamic Data from Phone Accelerometers for the Rapid Assessment of the Technical Condition of Buildings and Structures Use



Andrey Savinov , Gennadiy Nigmatov , Temir Nigmatov ,
and Rinat Galliulun

Abstract The possibility of diagnosing buildings and structures, from the frequencies of natural oscillations obtained from sensors built into the phone was examined. A special application program to read data from phone sensors was written. Experimental studies on registration of building vibrations using telephone sensors and a software–hardware complex with external accelerometers have been carried out.

Keywords Method of dynamic geophysical testing · Natural frequency of the building · Accelerometer · Rigidity · Wear · Non-destructive testing · Phones

1 Introduction

Google is known to build a worldwide earthquake warning system based on Android software and deploying the first part of the system. It uses the accelerometer in Android phones and will collect data from each phone. After processing the data, the algorithm will detect an earthquake and notify people in the area of possible damage [1–4].

According to Google research, a phone accelerometer’s sensitivity is enough to detect even a weak earthquake. With the help of GPS sensors, the location of the phones is determined, and when reading data from a large number of phones, it allows filtering false data from seismic sensors and determining the real boundaries of the seismic impact, possible accelerations affecting buildings [5–8].

To assess the possibility of using phone accelerometers to determine the vulnerability of buildings, it was necessary to measure building vibrations using a phone. Therefore, a ten-story reinforced concrete frame building was chosen for the experiment. Measurements were taken on the top tenth floor. To assess the quality of the vibration signal from phone accelerometers and the natural vibrations of the building,

A. Savinov (✉) · G. Nigmatov · T. Nigmatov
FGBU NII GO EMERGENCY “FC”, Moscow, Russian Federation
e-mail: savandr198@mail.ru

R. Galliulun
Kazan State University of Architecture and Engineering, Kazan, Russia

a comparison of data from the accelerometer of the phone and two software and hardware systems with accelerometers of the A1638 type from the «Geoacoustics» company and the MA 1E-2 type from the «Elpa» company was made.

To assess the vulnerability of buildings and structures, it is necessary to have the following dynamic parameters:

- natural frequency;
- damping factor.

In addition, acoustic noise carries important information about the state of structures; therefore, with the help of seismic sensors, a building or structure is “listened” for possible cracks, limiting effects of dangerous dynamic loads, and possible deformations in soils. [9–11].

To solve these problems, it is necessary to determine the sensitivity of the accelerometer in the phone and the possibility of their use for the rapid assessment of the technical condition of buildings and structures.

2 Methods

To determine the possibility of using vibrodynamic data from seismic sensors of the phone, the method of dynamic geophysical tests was used to assess the technical condition of the buildings [12–14]. The main feature of the method for diagnosing buildings and structures according to the data of vibrodynamic tests is the integral assessment of their residual life and the category of technical condition [15].

The method of vibrodynamic testing makes it possible to judge the overall rigidity of a structural system based on the measured frequency of natural oscillations of a structural system [16]. For example, the natural frequency of a beam is related to the stiffness, known from structural mechanics by the formula. [17]:

$$F = \frac{\pi^2}{L^2} * \sqrt{\frac{EJ}{m}}, \quad (1)$$

where

- m—linear mass of the beam, kg/m,
- EJ—beam rigidity, N × m²;
- F—natural frequency, Hz;
- L—beam length, m.

By comparing the frequency of natural vibrations of the beam, obtained from the calculation with the design data of the beam, with the frequency of natural vibrations obtained from vibrodynamic tests, it is possible to determine the vulnerability of the beam.

To test the possibility of using a phone accelerometer for vibrodynamic tests and to compare the quality of vibration recording data from a phone, data obtained from highly sensitive piezo ceramic accelerometers of the A1638 type from «Geofon»

and the MA 1E-2 type from «Elpa» were used. The vibration data of the building received from the sensors are converted into vibration frequencies using the Fourier transform. Comparing the normative and experimental data of the building in terms of natural vibration frequencies, we determine its vulnerability or the category of technical condition [16].

The comparison of the sensitivity of three accelerometers was carried out by simultaneous recording of wave impulses during impact on structures. [18]. Impulses were created by striking 25 kg sandbags on load-bearing walls. Three series of experiments were carried out. In the first experiment, the blows were applied in the same room where the sensors were located. In the second experiment, blows were delivered into the next room at a distance of up to 6 m. In the third experiment, the sensors were located at a distance of 20 m from the place where the blows were applied.

The experiment's primary purpose was to evaluate the sensitivity of the phone's accelerometer. [19–21]. As mentioned above, three types of sensors were used for these tests: The accelerometer on the phone, the accelerometer (Fig. 1) manufactured by Geoacoustics, the accelerometer manufactured by Elpa (Fig. 2). The accelerometer made by Geoacoustics is used in most dynamic geophysical complexes used for dynamic testing of buildings. The operating frequencies of the accelerometer type A1638 (made by Geoacoustics) are (0.1–400) Hz. The accelerometer manufactured by Elpa operates at frequencies (0.1–1000) Hz.



Fig. 1 Type A 1638 accelerometer manufactured by «Geoacoustics»



Fig. 2 Sensor manufactured by «Elpa»

3 Results

Based on the results of the experiments, it was found that in the first experiment, all sensors registered the applied pulses (Fig. 3, 5, 6). In the second experiment, all sensors registered the impact of pulses. However, the pulse on the accelerometer on the phone was almost completely hidden by noise. However, in the third experiment, the accelerometer on the phone did not register the impact of impulses (Fig. 4, Table 1).

Experimental data have shown that it is difficult to use the phone's accelerometer to detect weak signals from distant sources. There are two most likely reasons. Firstly, this is a too high noise level in the phone, at which weak vibrations of the structures are not noticeable. Secondly, this is the possibility that the phone has a too low sensitive accelerometer for such measurements.

Fig. 3 Sensor readings from the phone, obtained when exposed to a non-remote source

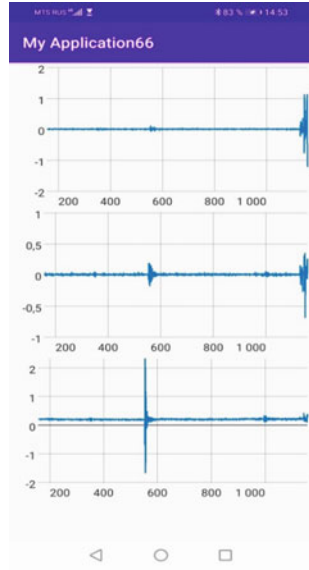
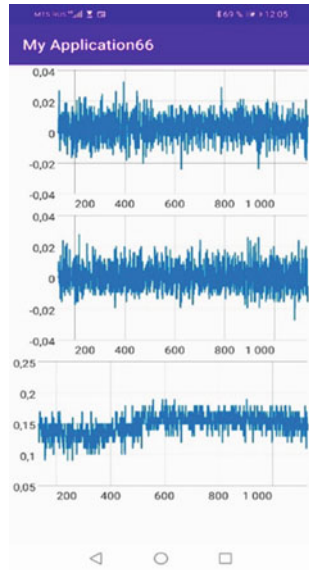


Fig. 4 Sensor readings from the phone, obtained when exposed to a remote source



4 Discussion

The performed experimental studies have shown that phones with built-in accelerometers can detect vibration signals of structural systems.

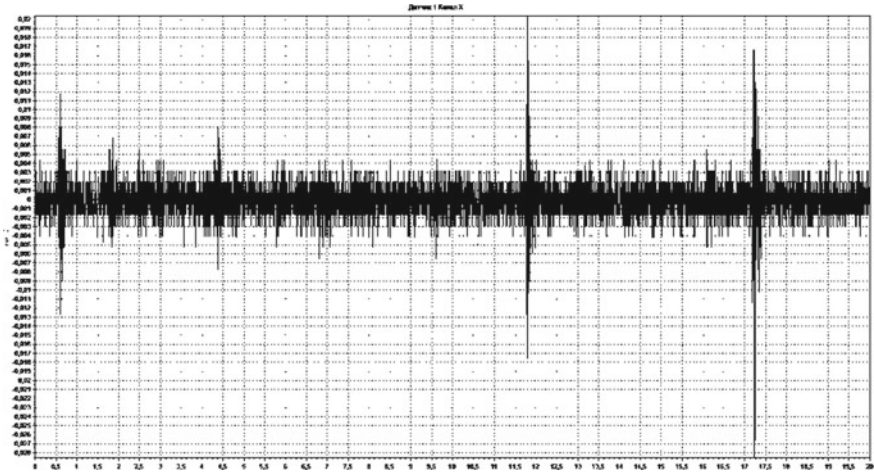


Fig. 5 Readings from a sensor manufactured by «Geoacoustics»

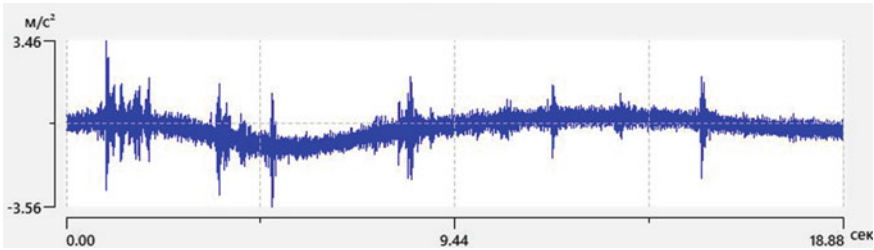


Fig. 6 Readings from a sensor manufactured by «Elpa»

Table 1 The analysis of the capabilities of accelerometers based on tests

Possibility	Sensor A1638 (Geoacoustics)	Sensor«Elpa»	Phone sensor
Get the natural frequency	Available	Available	Available
Get the decrement of natural oscillations	Available	Available	Available
Register a strong external impact (for example, driving piles at a distance of 300 m)	Available	Available	Most impacts are hidden by noise
Register cracks or other damaging effects in the structure	Available	Available	Not available

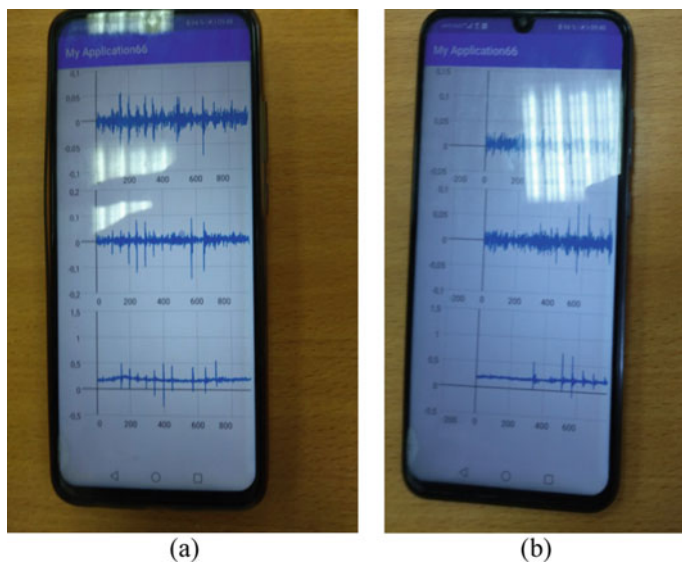


Fig. 7 The fixation of vibrations of the table under impulse action: **a** the phone is connected to the table surface viaplasticine; **b** the phone is on the surface of the table without plasticine

To obtain high-quality vibration signals, it is necessary to apply technical, technological, and software methods to improve the reliability of obtaining proper signals about building vibrations. With the help of technical methods, it is possible to improve signal quality by using more up-to-date phones with sensitive accelerometers or by using external accelerometers connected to the phone.

Using technological methods, it is necessary to correctly select the structure's surface (if the structure is covered with soft material, it is not recommended to place a smartphone on it), where the smartphone should be installed, using plasticine for reliable contact with the surface. Figure 7 shows examples of vibration signals taken with and without plasticine for contact with the surface. It can be seen that in Fig. 7a) the signal quality is better than in Fig. 7b) less background noise. Of course, with the help of software, we can improve the quality of the signal. However, it is essential to follow the technical and technological methods to get a high-quality signal.

5 Conclusion

We can give four main conclusions that by the use of a phone accelerometer sensor it is possible to:

- determine the frequency of natural vibrations of the structure and make a rough assessment of its technical condition;
- determine the damping decrement of oscillations.

It is not possible to:

- assess the impact of external remote sources, even if they have a strong impact, it is not possible with the current level of phone technology;
- detect small cracks (in brickwork, in concrete, etc.), it is not possible with the current level of phone technology.

The accelerometer built-in the phone should not be used to diagnose buildings and structures. To assess the category of the technical condition of buildings using phones, it is proposed to connect an external accelerometer to the phone with the ability to record a signal in a frequency range of at least 0.1–200 Hz.

References

1. Minson, S.E., et al.: Crowdsourced earthquake early warning. *Sci. Adv.* **1**(3) (2015). <https://doi.org/10.1126/sciadv.1500036>, <https://www.science.org/doi/10.1126/sciadv.1500036>
2. Kuyuk, H.S., Susumu, O.: Real-time classification of earthquake using deep learning. *Procedia Comput. Sci.* **140**, 298–305 (2018). <https://doi.org/10.1016/J.PROCS.2018.10.316>
3. McBride, S.K., et al.: Developing post-alert messaging for ShakeAlert, the earthquake early warning system for the West Coast of the United States of America. *Int. J. Disaster Risk Reduction* **50**, 101713 (2020). <https://doi.org/10.1016/J.IJDRR.2020.101713>
4. Sumy, D.F., Jenkins, M.R., McBride, S.K., de Groot, R.-M.: Typology development of earthquake displays in free-choice learning environments, to inform earthquake early warning education in the United States. *Int. J. Disaster Risk Reduction* **102802** (2022). <https://doi.org/10.1016/J.IJDRR.2022.102802>, <https://linkinghub.elsevier.com/retrieve/pii/S2212420922000218>. Date of Application 17 Feb 2022
5. Zhang, H., Wei, X., Ding, Y., Jiang, Z., Ren, J.: A low noise capacitive MEMS accelerometer with anti-spring structure. *Sens. Actuators A Phys.* **296**, 79–86 (2019). <https://doi.org/10.1016/J.SNA.2019.06.051>
6. Bertolini, A., Beverini, N., Cella, G., DeSalvo, R., Fidecaro, F., Francesconi, M., Simonetti, D.: Geometric anti-spring vertical accelerometers for seismic monitoring. *Nucl. Instrum. Methods Phys. Res. Sect. A* **518**(1–2), 233–235 (2004). <https://doi.org/10.1016/J.NIMA.2003.10.069>
7. Kavitha, S., Joseph Daniel, R., Sumangala, K.: Design and analysis of MEMS comb drive capacitive accelerometer for SHM and seismic applications. *Measurement* **93**, 327–339 (2016). <https://doi.org/10.1016/J.MEASUREMENT.2016.07.029>
8. Del Gaudio, V., Zhao, B., Luo, Y., Wang, Y., Wasowski, J.: Seismic response of steep slopes inferred from ambient noise and accelerometer recordings: the case of Dadu River valley, China. *Eng. Geol.* **259**, 105197 (2019). <https://doi.org/10.1016/J.ENGGE.2019.105197>
9. Peng, C., et al.: A new type of tri-axial accelerometers with high dynamic range MEMS for earthquake early warning. *Comput. Geosci.* **100**, 179–187 (2017). <https://doi.org/10.1016/J.CAGEO.2017.01.001>
10. Li, R., Mohammed, Z., Rasras, M., Elfadel, I.A.M., Choi, D.: Design, modelling and characterization of comb drive MEMS gap-changeable differential capacitive accelerometer. *Measurement* **169**, 108377 (2021). <https://doi.org/10.1016/J.MEASUREMENT.2020.108377>
11. Prato, A., Mazzoleni, F., D'Emilia, G., Gaspari, A., Natale, E., Schiavi, A.: Metrological traceability of a digital 3-axis MEMS accelerometers sensor network. *Measurement* **184**, 109925 (2021). <https://doi.org/10.1016/J.MEASUREMENT.2021.109925>
12. Moschas, F., Stiros, S.: Experimental evaluation of the performance of arrays of MEMS accelerometers. *Mech. Syst. Sig. Process.* **116**, 933–942 (2019). <https://doi.org/10.1016/J.YMSSP.2018.07.031>

13. Wang, S., Wei, X., Zhao, Y., Jiang, Z., Shen, Y.: A MEMS resonant accelerometer for low-frequency vibration detection. *Sens. Actuators A Phys.* **283**, 151–158 (2018). <https://doi.org/10.1016/J.SNA.2018.09.055>
14. Preeti, M., Guha, K., Baishnab, K.L., Dusarlapudi, K., Narasimha Raju, K.: Low frequency MEMS accelerometers in health monitoring – A review based on material and design aspects. *Mater. Today Proc.* **18**, 2152–2157 (2019). <https://doi.org/10.1016/J.MATPR.2019.06.658>
15. Nigmatov, G.M., Rybakov, A.V., Savinov, A.M., Nigmatov, T.G.: Modern approaches to assessing the risk of structural collapse. *Civ. Secur. Technol.* **15**(2), 26–29 (2018). <https://doi.org/10.54234/CST.19968493.2018.15.2.56.4.26>, https://elibrary.ru/doi_resolution.asp?doi=10.54234%2FCST.19968493.2018.15.2.56.4.26
16. Savinov, A.M., Nigmatov, G.M., Kovaleva, S.D., Nigmatov, T.G.: Determination of the logarithmic decrement of natural vibrations of buildings and structure determination of the logarithmic decrement of natural vibrations of buildings and structures. *Structural mechanics and analysis of constructions. Struct. Mech. Anal. Constr.* **1**, 62–65 (2021). <https://doi.org/10.37538/0039-2383.2021.1.62.65>, http://stroy-mex.narod.ru/index/2021_1/0-261
17. Methodology for assessing and certifying the engineering safety of buildings and structures. Moscow. Moscow, VNII GOChS (2003)
18. Nigmatov, G., Akatev, V., Savinov, A., Nigmatov, T.: Estimation of seismic resistance of buildings by the dynamic-geophysical method, taking into account the peculiarity of the interaction of the seismic wave with the «soil – construction» system. *Struct. Mech. Anal. Constr.* **1**(276), 24–30 (2018)
19. Nigmatov, G., Savinov, A.: About dynamic-method geophysical evaluation the bearing capacity of structures. *General scientific problems of engineering training of personnel of the Ministry of Emergency Situations of the Russian Federation: Collection*, p. 69 (2018). <https://www.elibrary.ru/item.asp?id=35004570>
20. Ibragimov, R.A., Korolev, E.V., Deberdeev, T.R., Leksin, V.V.: Efficient complex activation of Portland cement through processing it in the vortex layer machine. *Struct. Concr.* **20**(2), 851–859 (2019). <https://doi.org/10.1002/suco.201800008>
21. Stroganov, V., Sagadeev, E., Ibragimov, R., Potapova, L.: Mechanical activation effect on the biostability of modified cement compositions. *Constr. Build. Mater.* **246**, 118506 (2020). <https://doi.org/10.1016/j.conbuildmat.2020.118506>

Experimental and Theoretical Analysis of Crack Resistance and Deformability of Concrete Beams Reinforced with Fiber-Reinforced Polymer Bars



Ishat Mirsayapov, Igor Antakov, and Alexey Antakov

Abstract Along with the known advantages, high tensile strength, low specific density, high fastness to staining and low thermal conductivity, fiber-reinforced polymers (FRP) reinforcement bars have a number of features and disadvantages. One of the main is the relatively low modulus of elasticity compared to steel. As a result, elements with FRP reinforcement have a higher deformability. In this regard, the requirements of the service limit states imposed on structures may become the main obstacle to the use of FRP for reinforcing concrete members. Experimental studies were carried out taking into account and observing the provisions of GOST 8829-2018. Concrete beam specimens were 120×220 mm in cross section and 1810 mm in length, reinforced with two bars in a tension side. The beams were reinforced longitudinally with steel, glass fiber-reinforced polymer (GFRP) and basalt fiber-reinforced polymer (BFRP) bars. The value of the reinforcement ratio varied. Methods for calculating the crack width of guidelines are considered: Russia—Construction rules and regulations 63.13330.2012 and 295.1325800.2017, USA—ACI 440.1R-06. The results of theoretical and experimental studies of the crack resistance of flexural members with FRP reinforcement are obtained. Differences in the considered design methods are revealed. Deviations of theoretical data from experimental data are determined. Inaccurate determination of the cracking moment M_{cr} has a negative impact on the results of calculating the deflection of flexural members with FRP. Features of crack formation in members with FRP reinforcement are recorded, which call into question the possibility of using the design methods by Construction rules and regulations 63.13330.2012 and 295.1325800.2017. Corrected equations for calculating the cracking moment and the crack width are proposed. In the equation for calculating the crack opening width, a coefficient is introduced that takes into account the influence of the diameter of the rods.

Keywords Building · Construction · Non-metallic reinforcement · Fiber-reinforced polymer reinforcement · Concrete structures · Flexural members · Crack width · Concrete beam · Glass fiber-reinforced polymer reinforcement · Basalt fiber-reinforced polymer reinforcement

I. Mirsayapov · I. Antakov (✉) · A. Antakov
Kazan State University of Architecture and Engineering, Kazan 420043, Russia
e-mail: igor788@bk.ru

1 Introduction

Fiber-reinforced polymers (FRP) reinforcement bars have a number of advantages over steel reinforcement: Up to 3,5 times more tensile strength, low specific density, high corrosion resistance, and low thermal conductivity. Moreover, the deformation properties of the FRP bars also differ significantly: Up to 4 times lower modulus of elasticity, the “stress–strain” diagram for short-term loading is almost straight up to the point of failure.

Studies by many scientists have revealed a number of features of the work of flexural concrete members with FRP reinforcement under load:

- first, the external fibers of the reinforcement bars are subjected to tensile, later the internal ones come into operation [1];
- “bending moment—deflection” diagrams for beams under load are characterized mainly by bilinear dependencies with two behavior phases of the flexural members: Without cracks and with cracks [2–8]. At the same time, the deflection values are 3–4 times higher than those of reinforced concrete analogues, and the crack width is correspondingly greater [9–15];
- the compressed region in the normal section significantly, as compared with reinforced concrete members, decreases after the appearance of cracks and then remains almost constant until the failure of the member [16];
- the failure of the normal section is of brittle nature with the implementation of two mode of fracture behavior—from the rupture of tensile reinforcement and from the concrete crushing in the compressed region [3, 4, 6, 10, 11, 15, 17]. Simultaneous failure of concrete and tensile reinforcement is also possible [18]. Due to the low modulus of elasticity of the FRP, when the reinforcement ratio is below a defined level, the failure of the beams from concrete crushing is possible, with loads less than design values [19];
- due to the relatively high susceptibility of FRP reinforcement to creep during sustained load, the deflections of the flexural members increase to 90% of the initial values, depending on the size of load and the type of reinforcement. Moreover, crack formation is possible over time [20]. Depending on the type of FRP, the ultimate strength at sustained load is about 20–65% of the strength at short duration load [21, 22];
- due to the relatively low modulus of elasticity of the FRP, the requirements for deflections and the crack width can be basic when designing FRP—reinforced constructions [10]. It is necessary to improve existing methods for calculating deflections and crack width of flexural members with FRP [6, 15, 23–26]. The most significant variables in the design for serviceability limit states (SLS) are the reinforcement ratio and modulus of elasticity of FRP [6];
- more cracks are formed in beams reinforced with FRP bars than in reinforced concrete analogues [13]. When the reinforcement ratio increases the crack spacing and their width decreases [14, 27];
- in the previous study [28], it was established that the SLS of beams reinforced with FRP bars occur at 26,1–52,9% of the ultimate breaking load, for the reinforced

beams with prestressed FRP bars—at 42,3–70,3% of the ultimate failure load. Using bars of smaller size proves to be more effective.

Thereby, the behavior of flexural members with FRP bars under load is essentially different from that of reinforced concrete constructions, due to physical and mechanical properties of FRP reinforcement.

In 2015, Amendment No. 1 to Construction rules and regulations 63.13330.2012 came into operation, which contains Appendix L with recommendations for the calculation and design of structures with FRP reinforcement. In 2017, Construction rules and regulations 295.1325800.2017 was released which dealt exclusively with the design of structures with FRP reinforcement. In 2019, Construction rules and regulations 63.13330.2018 was put into effect, in which there is no Appendix with recommendations for the design of structures with FRP.

Thus, in the Russian Federation, there were two regulatory guidelines that presented methods for design structures with FRP reinforcement—these are Construction rules and regulations 63.13330.2012 and 295.1325800.2017. A common feature of all considered guidelines and recommendations is that calculation methods are based on existing approaches for steel-reinforced concrete structures. The design methods of Construction rules and regulations 63.13330.2012 and SP 295.1325800.2017 are identical, except for the calculation of the crack width.

In both guidelines, the crack width is determined by Eq. 1.

$$a_{cr,c,i} = \varphi_1 \cdot \varphi_2 \cdot \varphi_3 \cdot \psi_f \cdot \frac{\sigma_f}{E_f} \cdot l_f \quad (1)$$

In contrast to the calculation of steel-reinforced concrete members, the limiting values of the crack width are increased to 0,7 mm—with a short opening of cracks and 0,5 mm—with a long one. The values of the coefficient φ_2 , which takes into account the profile of the longitudinal FRP, have been increased to 0,7 for the reinforcement of a ribbed bar and 1,2 for plain bar. Compressed reinforcement is not taken into account in the calculations.

The basic distance between the cracks l_f is determined differently in the calculation methods. According to p. П.3.4 of Construction rules and regulations 63.13330.2012, calculations for the serviceability limit states are performed according to the method of calculating reinforced concrete members using the characteristics of FRP. That is, l_f is determined by Eq. 2 and is accepted at least $10d_s$ and 10 cm, and no more than $40d_s$ and 40 cm.

$$l_f = 0,5 \frac{A_{bt}}{A_f} d_s \quad (2)$$

In p. 6.2.16 of Construction rules and regulations 295.1325800.2017, l_f is determined by Eq. 3 and is accepted at least $10d_s$ and 10 cm, and not more than $20d_s$ and 20 cm.

$$l_f = 0,25 \frac{A_{bt}}{A_f} d_s \quad (3)$$

In Construction rules and regulations 295.1325800.2017, the calculated value of l_f and the limit value are reduced by 2 times than in 63.13330.2012.

This paper also considered the calculation method for the USA guidelines – ACI 440.1R-06. The crack width is determined by Eq. 4.

$$w = 2 \frac{f_f}{E_f} \beta k_b \sqrt{d_c^2 + \left(\frac{s}{2}\right)^2} \quad (4)$$

in which f_f —reinforcement stress; E_f —reinforcement modulus of elasticity; β —ratio of distance between neutral axis and tension face to distance between neutral axis and centroid of reinforcement; k_b —coefficient that accounts for the degree of bond between FRP bar and surrounding concrete; d_c —thickness of over from tension face to center of closest bar; s —bar spacing.

According to ACI 440.1R-06, depending on the type of fiber, binder and type of surface, the coefficient k_b ranges from 0,6 to 1,72. In the case where the value of k_b is not known from experimental data, it should be taken equal to 1,4. Thus, this coefficient, in contrast to the coefficient φ_2 of the Construction rules and regulations technique 295.1325800.2017 and 63.13330.2012, is not a constant value.

This study was carried out to assess the reliability of the methods for calculating the cracking moments, crack width and deflections presented in Construction rules and regulations technique 63.13330.2012 and 295.1325800.2017, ACI 440.1R-06 and also to develop recommendations for performing calculations for the serviceability limit states.

2 Materials and Methods

In order to obtain experimental data on the behavior of flexible members with FRP reinforcement, experimental studies of beam specimens with glass fiber-reinforced polymer (GFRP) and basalt fiber-reinforced polymer (BFRP) bars.

The experimental specimens were concrete beams with a cross section of 120 × 220 mm and a length of 1810 mm, reinforced with two bars in a tensile region, with a concrete cover of 20 mm. The beams are simply-supported on two sides and loaded with concentrated loads at a distance of L/3 on each side from the supports (Fig. 1), where L is the distance between the supports. Beams specimens were tested under short-term load application. The analysis of the work of beams at the stage of destruction is presented in the previously published article [29]. The results of testing beams under sustained loading are presented in the article [30].

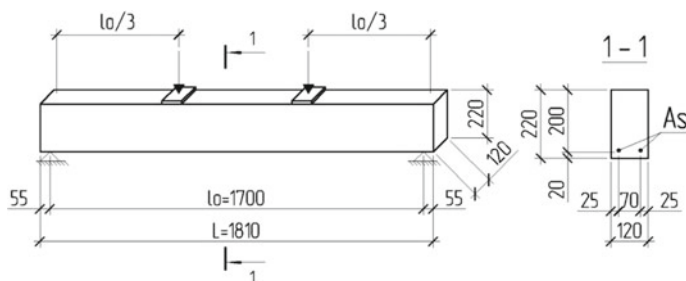


Fig. 1 The scheme of support and loading of the beam specimens

Table 1 Characteristics of the series of beam specimens

Series No.	Strength classes for concrete	Longitudinal reinforcement					
		Number of bar, type, prestressing value	Design diameter, mm	Ratio of reinforcement μ , %	Area of longitudinal reinforcement A_s , mm ²	Modulus of elasticity $E_{s(f)}$, MPa	Ultimate tensile strength $R_{s(f),n}$, MPa
1	C25/30 (B30)	2 Ø12 A400	12	0,942	226	200,000	400
		2 Ø8 A400	8	0,421	101		
		2 Ø6 A400	6	0,238	57		
2	C30/37 (B40)	2 Ø10 GFRP	8,6	0,484	116,12	51,500	1200
		2 Ø8 GFRP	7	0,321	76,93	51,500	1200
		2 Ø6 GFRP	5	0,164	39,25	51,770	1250
3	C30/37 (B35)	2 Ø7 BFRP	7	0,321	76,96	50,730	1100
		2 Ø5 BFRP	5,3	0,184	44,1	52,620	1230
		2 Ø4 BFRP	4	0,105	25,12	53,280	1260

Table 1 presents the characteristics of beam specimens. The study used the following types of reinforcement: series 1—steel bars A400 strength class; series 2—GFRP of a ribbed bars (Fig. 2a), corrugation created by winding basalt fiber; series 3—BFRP bars (Fig. 2b), with a sand-coated surface.

3 Results

3.1 Cracking Moment

Table 2 compares the theoretical and experimental values of the cracking moments. For beams with FRP reinforcement, the deviation of theoretical data according to the Construction rules and regulations 295.1325800.2017 method from the experimental ones is 26,2–59,1%, for the ACI 440.1R-06 method—20,1–57,1%.

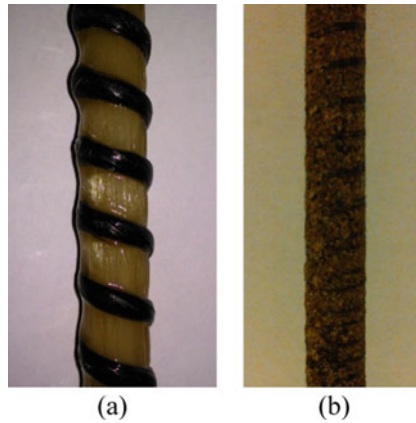


Fig. 2 FRP bars used in the test: **a**—glass fiber-reinforced polymer bar; **b**—basalt fiber-reinforced polymer bar

Table 2 Comparison of the values of experimental and theoretical of cracking moment

Series No.	Number of bar, type	Experimental data		Theoretical data	
		$M^{\text{exp}}_{\text{crc}}$, κN·m	Mean value $M^{\text{exp}}_{\text{crc}}$, κN·m	Construction rules and regulations 63.13330.2012, 295.1325800.2017	ACI 440.1R-06
1	2 Ø12 A400	3,575	3,575	3,995	–
	2 Ø8 A400	3,296–4,18	3,738	3,768	–
	2 Ø6 A400	2,57–3,156	2,863	3,682	–
2	2 Ø10 GFRP	3,24–3,129	3,185	4,317	3,988
	2 Ø8 GFRP	3,016–3,156	3,086	4,295	3,988
	2 Ø6 GFRP	3,296–2,737	3,017	4,274	3,988
3	2 Ø7 BFRP	2,095–2,57	2,333	3,99	3,773
	2 Ø5 BFRP	1,955	1,955	3,973	3,773
	2 Ø4 BFRP	1,201–2,039	1,62	3,962	3,773

The cracking moment of the flexural members without prestressing the reinforcement is proposed to be determined by the method of Construction rules and regulations 295.1325800.2017, taking into account additional components, according to the appropriate equation:

$$M_{cr} = \varphi_f \cdot \gamma_t \cdot R_{bt,ser} \cdot W_{pl} \quad (5)$$

in which φ_f —coefficient taking into account the profile of longitudinal reinforcement: 0,7—for reinforcement of a ribbed bars (with “winding”), 0,5—for reinforcement with a sand-coated surface;

γ_t —coefficient taking into account the duration of the load, taken for a short-term load application equal to 1, for a sustained load—0,9.

The proposed method for calculating M_{cr} gives deviations from the experimental values in the range of 0,8–18,2%, the average deviation is 7,14%.

3.2 Deflections

Figures 3, 4, 5, 6, 7, 8, 9, 10, 11, 12, 13 and 14 show the experimental and theoretical dependences between the values of the bending moment and deflections (M-f) for the test beam specimens of series 2 and 3. For the two considered methods Construction rules and regulations 295.1325800.2017 and ACI 440.1R.-06, four diagrams are defined. In the methods Construction rules and regulations 295.1325800.2017 method, the coefficient ψ_f , which takes into account the uneven distribution of relative deformations of tensile reinforcement between cracks, was assumed to be equal to 1 and $\psi_f = 1 - 0,8 \cdot \frac{M_{cr}}{M}$. ψ_f is allowed to be taken equal to 1 when the condition $f \leq f_{ult}$ is met. According to the ACI method, the data were determined by calculating short-term deflections and taking into account the coefficient $\lambda = 0,6 \times \xi$, where ξ was assumed to be equal to 2 for the sustained load for more than 5 years. The calculations were carried out taking into account the theoretical and experimental values of the cracking moment. In the study [31], ACI and Eurocode calculation methods were considered, where it was noted that the assessment of the cracking moment can have a decisive role in the reliability of the results of deflection calculations.

The behavior of beams with FRP under load is characterized by a predominantly linear M–f dependence after cracking until failure. The calculation diagrams of the considered techniques after the expected crack formation are also straight-line. Diagrams of the Construction rules and regulations 295.1325800.2017 method at the point of crack formation have a horizontal section, which is caused by the transition from calculating the deflections of the member without cracks to calculating them. Evaluating the diagrams of the Construction rules and regulations 295.1325800.2017 method from the start of loading to the failure of beams, it is difficult to choose the most reliable option for calculating deflections. There is no single calculation option that would have the closest results with experimental data for all beams at all stages

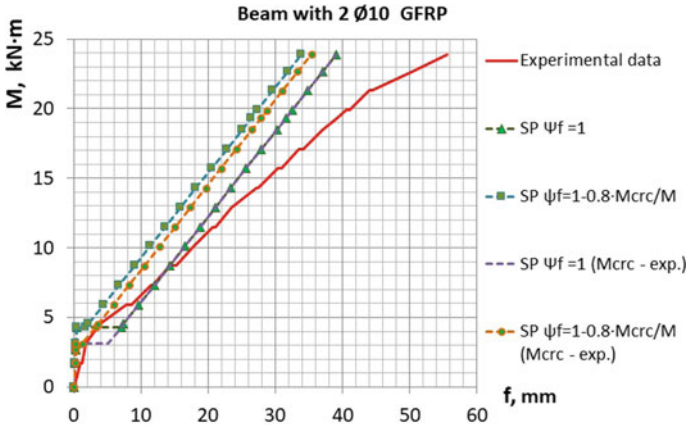


Fig. 3 Comparison of theoretical moment-deflection curves according to the Construction rules and regulations (SP) 295.1325800.2017 method with experimental data for beam reinforced with two bars Ø10 GFRP

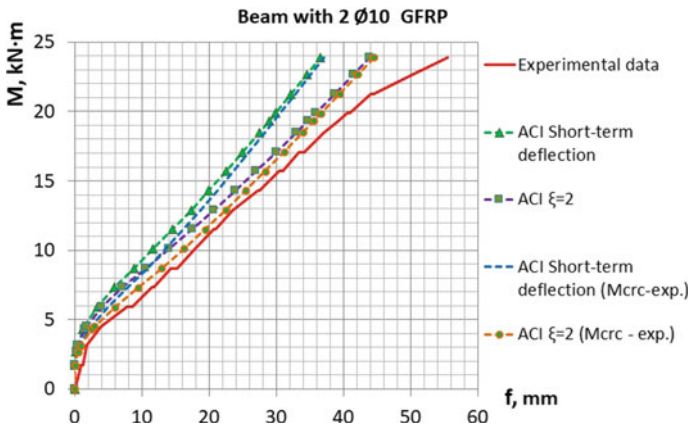


Fig. 4 Comparison of theoretical moment-deflection curves according to the ACI 440.1R-06 method with experimental data for beam reinforced with two bars Ø10 GFRP

of loading. The maximum deviation of the theoretical values of the maximum deflection according to the Construction rules and regulations 295.1325800.2017 method from the experimental data is 53,6%, for the ACI 440.1R-06 method it is 56,1%.

For the ACI 440.1R-06 method, the closest to the experimental data is the calculation with the coefficient $\xi = 2$ and using the experimental values of the cracking moment. In this calculation, the short-term deflection was multiplied by the coefficient $\lambda = 0,6 \cdot \xi = 0,6 \cdot 2 = 1,2$. With this calculation, the maximum deviation of the theoretical values of the maximum deflection from the experimental data is 39,8%. It is worth noting that, unlike the calculated diagrams of the Construction

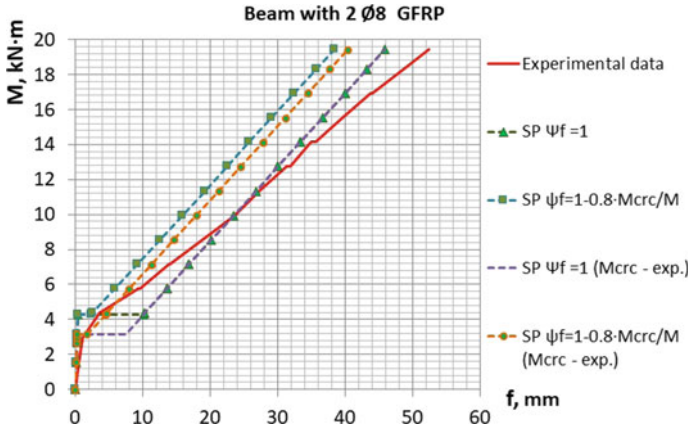


Fig. 5 Comparison of theoretical moment-deflection curves according to the Construction rules and regulations (SP) 295.1325800.2017 method with experimental data for beam reinforced with two bars Ø8 GFRP

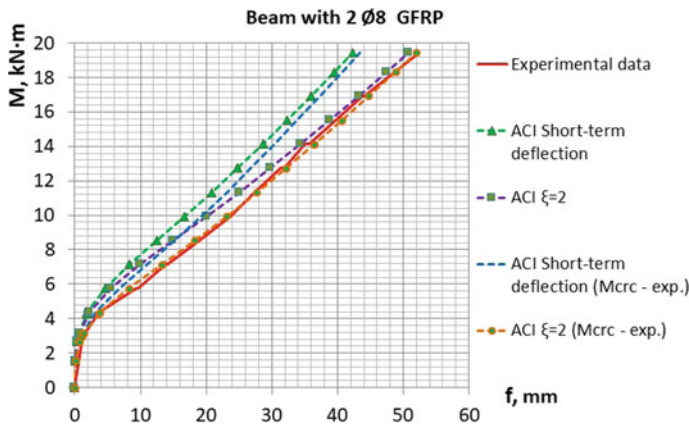


Fig. 6 Comparison of theoretical moment-deflection curves according to the ACI 440.1R-06 method with experimental data for beam reinforced with two bars Ø8 GFRP

rules and regulations 295.1325800.2017 method, the ACI 440.1R-06 diagrams are closest in outline to the experimental ones.

When calculating structures for the serviceability limit states, the requirement $f \leq f_u$ is imposed. That is, the calculated deflection should not exceed the maximum allowable value. The most important section of the diagram for research is the interval $f = (0 \dots f_u)$. Table 3 and Fig. 15 comparison of theoretical and experimental values of deflections of beams corresponding to the maximum allowable value— $f_u = (1/200) l_0 = 8,55$ mm.

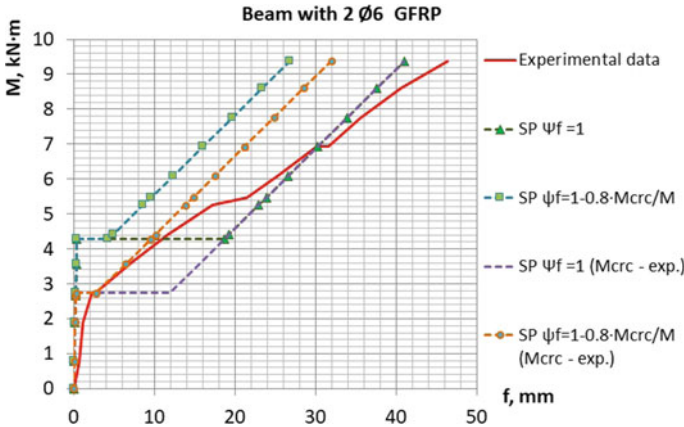


Fig. 7 Comparison of theoretical moment-deflection curves according to the Construction rules and regulations (SP) 295.1325800.2017 method with experimental data for beam reinforced with two bars Ø6 GFRP

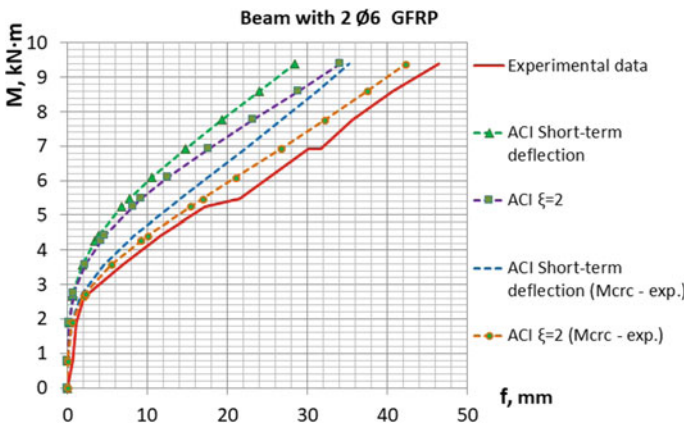


Fig. 8 Comparison of theoretical moment-deflection curves according to the ACI 440.1R-06 method with experimental data for beam reinforced with two bars Ø6 GFRP

Table 4 shows the maximum and average deviations of the theoretical values of deflections, presented in Table 3, from the value $f_u = (1/200)l_0 = 8,55$ mm.

For both calculation methods, the closest results to the experimental data were obtained using the experimental values of the cracking moment. The closest results to the experimental data by the Construction rules and regulations 295.1325800.2017 method were obtained at $\psi_f = 1 - 0,8 \cdot \frac{M_{cr}}{M}$. The maximum deviation from the experimental data is 32,29%. The results closest to the experimental data are obtained by the ACI method at $\xi = 2$. The maximum deviation from the experimental data

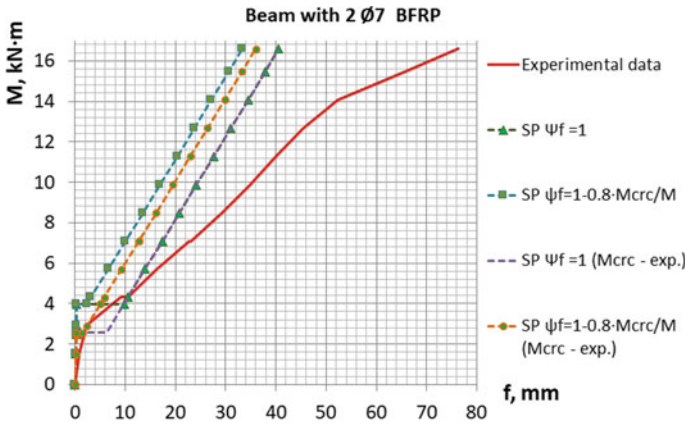


Fig. 9 Comparison of theoretical moment-deflection curves according to the Construction rules and regulations (SP) 295.1325800.2017 method with experimental data for beam reinforced with two bars Ø7 BFRP

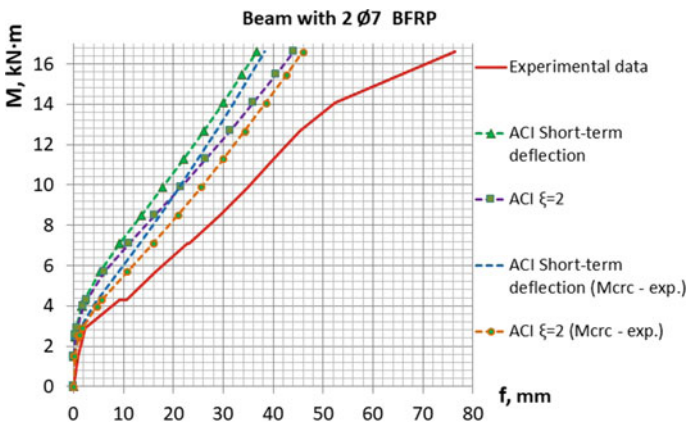


Fig. 10 Comparison of theoretical moment-deflection curves according to the ACI 440.1R-06 method with experimental data for beam reinforced with two bars Ø7 BFRP

is 41,81%. When using the proposed improved M_{crc} values (Eq. 5), the marginal deviation is 29,97%.

3.3 Crack Width

Table 5 shows the experimental values of bending moments with a crack width equal to the maximum allowable value of 0,7 mm, and the corresponding theoretical data on

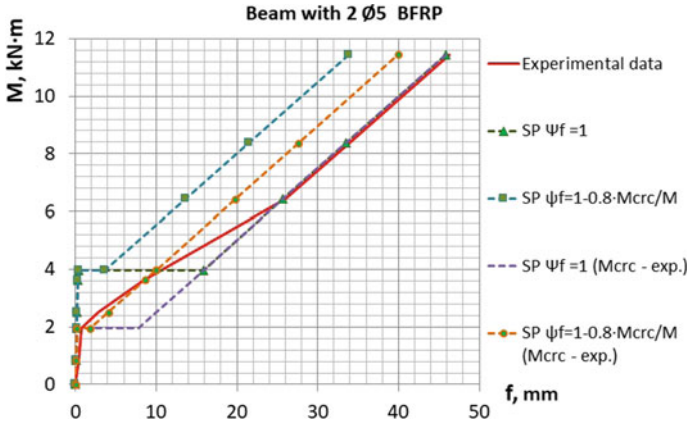


Fig. 11 Comparison of theoretical moment-deflection curves according to the Construction rules and regulations (SP) 295.1325800.2017 method with experimental data for beam reinforced with two bars Ø5 BFRP

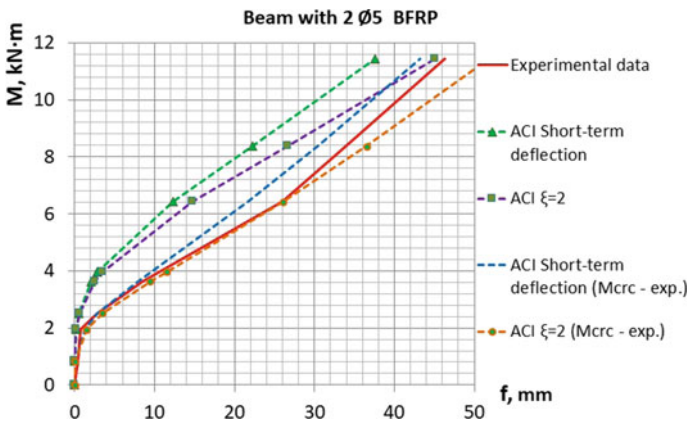


Fig. 12 Comparison of theoretical moment-deflection curves according to the ACI 440.1R-06 method with experimental data for beam reinforced with two bars Ø5 BFRP

the crack width and the distance between the cracks. In calculations according to the Construction rules and regulations 63.13330.2012 and 295.1325800.2017 methods, the coefficient ψ_f was determined by the equation $\psi_f = 1 - 0,8 \cdot \frac{M_{crc}}{M}$. In the l_f values, the first number was used in the calculation of a_{crc} ; in all calculations, it is the limit value of 40ds and 20ds, respectively, of the methods of Construction rules and regulations 63.13330.2012 and 295.1325800.2017. In parentheses, the value determined by Eqs. 2 and 3, in all cases it is greater than the limit value. As might be expected, the value of l_f had a significant effect on the crack width: in the method Construction rules and regulations 295.1325800.2017 it is 2 times less than in 63.13330.2012. As a result, the theoretical data on the crack width for all beams according to the

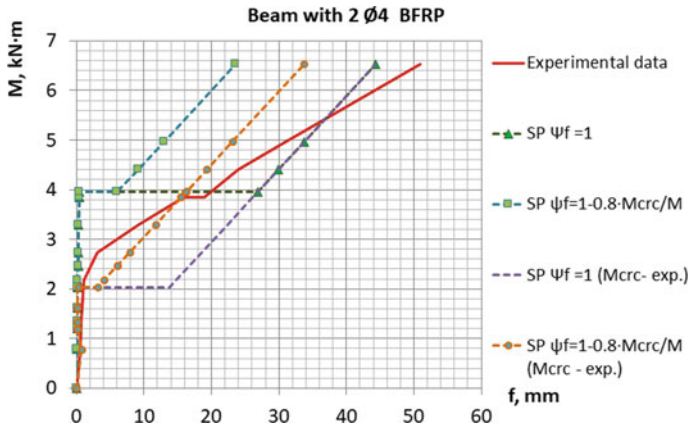


Fig. 13 Comparison of theoretical moment-deflection curves according to the Construction rules and regulations (SP) 295.1325800.2017 method with experimental data for beam reinforced with two bars Ø4 BFRP

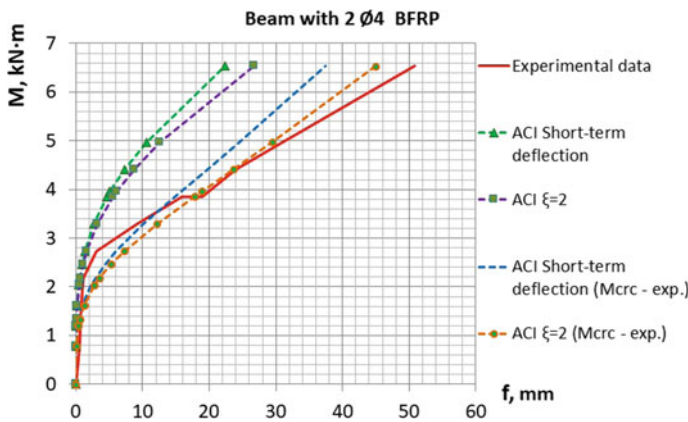


Fig. 14 Comparison of theoretical moment-deflection curves according to the ACI 440.1R-06 method with experimental data for beam reinforced with two bars Ø4 BFRP

Construction rules and regulations 295.1325800.2017 method are underestimated relative to the experimental data. When calculating according to the ACI 440.1R-06 method, the coefficient k_b was taken equal to 1 and 1,4.

The deviation of the theoretical data of the crack opening width according to the Construction rules and regulations 63.13330.2012 method from the value of 0,7 mm reaches 60%, for the 295.1325800.2017 method it is 80%, for the ACI 440.1R-06 method at $k_b = 1$ it is 29,86%, at $k_b = 1,4$ —49,9% (according to theoretical data, beams in which cracks do not form are not taken into account). The study [27] also noted more accurate results of the ACI 440.1R-06 method at $k_b = 1$. However, a number of types of beams have a relatively high spread between experimental data.

Table 3 Findings of the beam studies, including experimental bending moments M at crack deflection $f_u = (1/200)l_0 = 8,55$ mm and corresponding theoretical data on the deflection of beam specimens

Series No.	Reinforcement of beam specimens	Experimental data		Theoretical data – deflection f , mm					
		Bending moment at $f = 8,55$ mm M , kN·m	Crack width a_{cr} , mm	Construction rules and regulations		M_{cr} – theoretical		M_{cr} – experimental	
				ACI 440.1R-06		M_{cr} – theoretical		M_{cr} – experimental	
				$\psi_f = 1$	$\psi_f = 1 - 0,8 \cdot \frac{M_{cr}}{M}$	Short-term	$\xi = 2$	Short-term	$\xi = 2$
1	2 Ø12 A400	11,08	0,15	-	-	-	-	-	-
	2 Ø8 A400	8,1	0,5	-	-	-	-	-	-
	2 Ø6 A400	5,58	0,8	-	-	-	-	-	-
2	2 Ø10 GFRP	5,89	0,5	9,618	4,395	5,789	3,285	4,806	5,768
	2 Ø8 GFRP	5,576	0,8	13,176	5,533	7,718	4,189	6,544	7,853
	2 Ø6 GFRP	3,88	1,1	0,364*	0,364*	6,849	2,477	4,777	5,732
3	2 Ø7 BFRP	4,5	0,5	10,626	3,518	6,519	2,524	5,996	7,196
	2 Ø5 BFRP	3,755	1,1	0,364*	0,364*	8,639	2,386	8,374	10,049
	2 Ø4 BFRP	3,15	1,35	0,305*	0,305*	12,12	2,245	12,243	14,692

Note *— $M < M_{cr}$, means no cracking according to the theoretical data

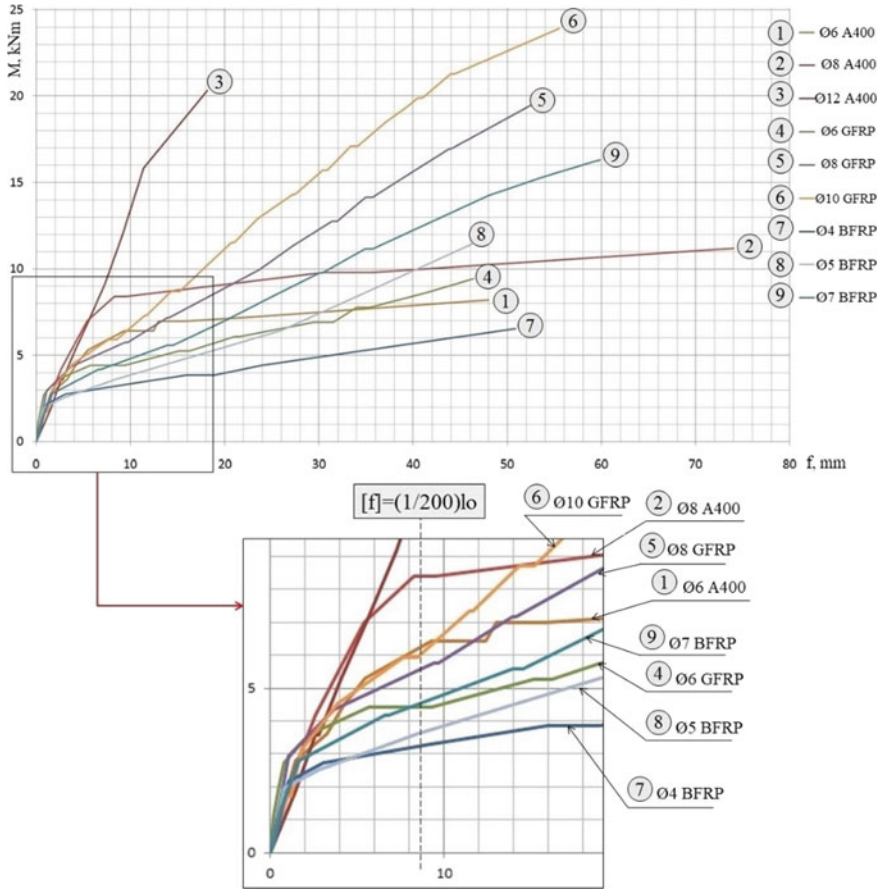


Fig. 15 Moment-deflection curves obtained as a result of testing beam specimens

Table 4 Limit and average deviations of the theoretical values of the deflection (Table 3) from the value $f_u = (1/200) l_0 = 8,55$ mm

Construction rules and regulations 63.13330.2012, 295.1325800.2017		ACI 440.1R-06			
Mcr—theoretical		Mcr—experimental		Mcr—experimental	
$\psi_f = 1$	$\psi_f = 1 - 0,8 \cdot \frac{M_{Mcr}}{M}$	Short-term deflection	$\xi = 2$	Short-term deflection	$\xi = 2$
$\frac{11,1-96,4}{46,4}$	$\frac{25,3-96,4}{59,85}$	$\frac{5,9-32,29}{21,5}$	$\frac{51-73,74}{66,66}$	$\frac{41,2-68,49}{59,99}$	$\frac{2,06-44,1}{28,91}$
					$\frac{8,2-41,81}{24,37}$

Note in the numerator—the minimum and maximum deviations, in the denominator—the average

Table 5 Results of the study of beams—experimental bending moments M at crack width $a_{cr,c} = 0,7$ mm and corresponding theoretical data on crack width and crack spacing

Series No.	Reinforcement of beam specimens	Experimental data		Theoretical data					
		Bending moment at $a_{cr,c} = 0,7$ mm M , kN·m	Mean value M , kN·m	Construction rules and regulations					
				63.13330.2012		295.1325800.2017		ACI 440.1R-06	
				$a_{cr,c}$, mm	l_f , mm	$a_{cr,c}$, mm	l_f , mm	w at $k_b = 1$, mm	w at $k_b = 1,4$, mm
2	2 Ø10 GFRP	5,684–9,412	7,548	0,902	344 (437,7)	0,447	172 (218,8)	0,662	0,926
	2 Ø8 GFRP	7,094–4,968	6,031	0,695	280 (538,7)	0,345	140 (269,3)	0,787	1,1
	2 Ø6 GFRP	3,519–3,423	3,471	–	200 (755,4)	–	100 (377,7)	0,87	1,218
3	2 Ø7 BFRP	7,448–4,128	5,788	0,701	280 (538,6)	0,35	140 (269,3)	0,768	1,074
	2 Ø5 BFRP	3,99	3,99	0,28	212 (712,5)	0,14	106 (356,2)	0,879	1,23
	2 Ø4 BFRP	2,64	2,64	–	160 (944,8)	–	80 (472,39)	0,998	1,397

Note “–” —according to the theoretical data, cracks are not formed



Fig. 16 Typical stages of crack development in beams reinforced with two bars 2 Ø6 A400 and 2 Ø6 GFRP

To assess the reliability of certain distances between cracks l_f , we consider the schemes of crack development for the beams under study. To identify the features of crack formation in members with FRP in Fig. 16, a comparison was made of beams reinforced with 2 Ø6 A400 and 2 Ø6 GFRP. Which have similar results in terms of the failure force and the cracking moment.

Due to the relatively greater deformability, the height of crack development in specimens with FRP is higher than in steel-reinforced concrete beams, and remains practically constant until the failure of the member. Beams with FRP exhibited “branching” of cracks. A similar phenomenon in steel-reinforced concrete beams occurred at the moment when the stresses in the bars reached the yield stress. The supposed reason for the “branching” of cracks is the relatively low modulus of elasticity of the FRP. For steel-reinforced concrete beams, this phenomenon occurs only after reaching the yield stress in the reinforcement.

Figure 17 shows the crack development schemes for beams reinforced with 2 Ø8 GFRP and 2 Ø10 GFRP, Fig. 18—for beams reinforced with 2 Ø7 BFRP, 2 Ø5 BFRP and 2 Ø4 BFRP.

Let’s consider the features of crack development in the studied beams with FRP, when the maximum crack width of 0,7 mm is reached:

1. At this stage, only one crack has formed in the beams reinforced with 2 Ø4 BFRP. These beams have a ratio of reinforcement less than the minimum allowable value.
2. Two cracks formed in the beams reinforced with 2 Ø6 GFRP.
3. Beams reinforced with 2 Ø8 GFRP, 2 Ø10 GFRP, 2 Ø5 BFRP and 2 Ø7 BFRP formed from 5 to 10 cracks, while their “branching” occurred in the tensile region. In beams with 2 Ø8 GFRP and 2 Ø10 GFRP, the “branching” of cracks occurred

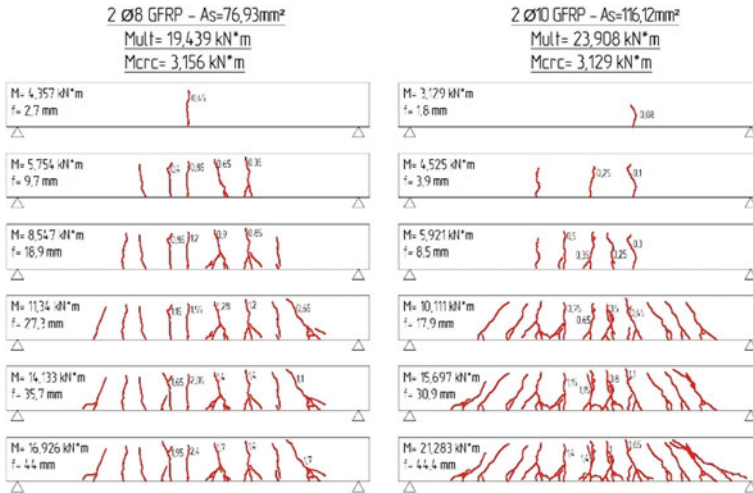


Fig. 17 Typical stages of crack development in beams of series 2, reinforced with two bars 2 Ø8 GFRP and 2 Ø10 GFRP



Fig. 18 Typical stages of crack development in beams of series 3, reinforced with two bars 2 Ø7 BFRP, 2 Ø5 BFRP and 2 Ø4 BFRP

in one of the two beam specimens. The reason for the differences in the cracking of identical beam specimens is not clear. Since the reinforcing bars were used from one coil, the concrete mixture was produced in the factory in one batch for all beams of each series.

At beams with steel reinforcement, when the maximum crack opening width of 0,4 mm was reached, from 5 to 10 cracks formed, no “branching” of cracks occurred.

The approach using the value of the base distance between cracks l_f , presented in Construction rules and regulations 63.13330.2012 and 295.1325800.2017, does not allow for a correct and reliable prediction of the crack width of flexural concrete members with FRP. The approach implemented in the ACI 440.1R-06 method is more reliable, which confirms the smaller (29,86%—at $k_b = 1$) deviation of the theoretical data from the experimental ones.

Based on the performed study, the calculation of the crack width is proposed to be performed according to Eq. (6). The proposed method is based on the approach for determining the crack width of the ACI 440.1R-06 method, with the correction coefficients introduced, taking into account the degree of bond of FRP to concrete and the influence of the diameter of the bars.

$$a_{crc} = \varphi_1 \varphi_2 \varphi_d \frac{\sigma_f}{E_f} \beta \sqrt{a^2 + \left(\frac{s}{2}\right)^2}, \quad (6)$$

in which φ_1 —coefficient taking into account the duration of the load, taken for a short-term load application equal to 1, for a sustained load—1,4;

σ_f —stress in FRP reinforcement in tension;

E_f —elastic modulus for FRP;

β —ratio of distance between neutral axis and tension face to distance between neutral axis and centroid of reinforcement;

a —thickness of over from tension face to center of closest bar;

s —bar spacing;

φ_2 —coefficient that accounts for the degree of bond between FRP bar and surrounding concrete (for the studied beams is equal to 2);

φ_d —coefficient taking into account the influence of the FRP diameter.

$$\varphi_d = \sqrt[3]{d_f} - 1.$$

Coefficient φ_2 is determined by the equation

$$\varphi_2 = \frac{\tau_s}{\tau_f},$$

in which τ_s —bond strength of steel reinforcement A400 with concrete; τ_f —bond strength of FRP reinforcement with concrete.

The value of the coefficient φ_2 is determined based on the results of the study [32] in which the values of bond of various types of FRP and steel reinforcement of A400 with concrete were determined. The bond values were considered when the rod slipped by 0,1 mm. The bond of FRP reinforcement to concrete can be very different from the bond of steel reinforcement, it depends on the type of fiber, profile, and concrete strength [32, 33]. The bond value is also affected by high temperatures, aggressive media, and operating conditions [32].

Table 6 Results of the study of beams—experimental bending moments M at crack width $a_{cre} = 0,7$ mm and corresponding theoretical data on crack width, determined by the proposed Eq. 6

Series No.	Reinforcement of beam specimens	Experimental data		Theoretical data for Eq. (6)	Deviation of theoretical data from experimental data, %
		Mean value M , $\kappa\text{N}\cdot\text{m}$	Crack width a_{cre} , mm	Crack width a_{cre} , mm	
2	2 Ø10 ACK	7,548	0,7	0,707	0,99
	2 Ø8 ACK	6,031		0,732	4,372
	2 Ø6 ACK	3,471		0,64	8,571
3	2 Ø7 ABK	5,788	0,7	0,711	5,788
	2 Ø5 ABK	3,99		0,663	3,99
	2 Ø4 ABK	2,64		0,598*	14,571

Note *—ratio of reinforcement less than the minimum allowable value, in accordance with p. 8.2.5 of Construction rules and regulations 295.1325800.2017

The value of the coefficient $\varphi_1 = 1,4$, with sustained load, was adopted in accordance Construction rules and regulations 295.1325800.2017. Clarification of the value of this coefficient under sustained load requires additional research.

The introduction of the coefficient φ_d is due to the revealed influence of the diameter of the FRP on the parameters of serviceability limit states of the beams under study. As a result of experimental studies, it was found that with a decrease in the diameter of the FRP, the proportion of bending moments corresponding to the limit states for serviceability from failure moments increases. More effective is the use of reinforcement of smaller diameter [28]. This was also noted in studies [32].

Table 6 presents the experimental values of the bending moments with a crack width equal to the maximum allowable value of 0,7 mm, and the corresponding theoretical data on the crack width, determined by the proposed Eq. 6. The cracking moment is determined by Eq. 5.

The proposed method of calculating a_{cre} gives deviations from experimental values in the range of 0,99–8,57%, the average deviation is 3,31% (beams with reinforcement 2 Ø4 BFRP are not taken into account, in which the ratio of reinforcement $\mu = 0,105\%$ is less than the minimum allowable value $\mu_{min} = 0,13\%$) (Fig. 19).

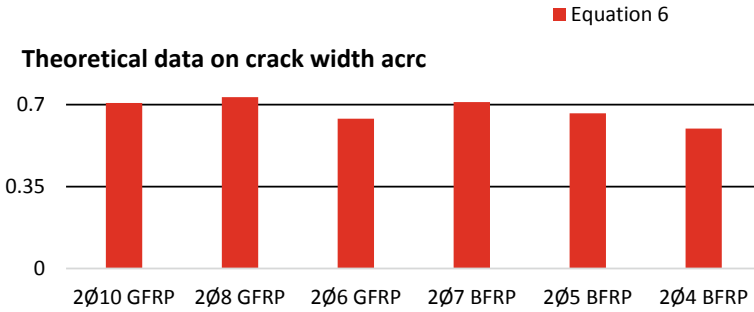


Fig. 19 Comparison of theoretical and experimental data on the crack width of Table 6

4 Conclusions

The results of the study showed that inaccurate determination of the cracking moment has a negative impact on the results of deflection calculation. Calculation of deflections according to the methods of Construction rules and regulations 295.1325800.2017 and ACI 440.1R-06 is more accurate when using experimental values of the cracking moment M_{cr} than with theoretical ones. For beams with FRP reinforcement, the deviation of theoretical data according to the Construction rules and regulations 295.1325800.2017 method from the experimental ones is 26,2–59,1%, for the ACI 440.1R-06 method—20,1–57,1%.

Evaluating the theoretical dependences between the values of the bending moment and deflections from the start of loading to the destruction of the beams, it can be concluded that the closest to experimental data on the values of deflection and the shape of diagrams is the ACI 440.1R-06 method. More accurate is the algorithm in which the deflection is calculated taking into account the coefficient $\lambda = 0,6 \cdot \xi = 0,6 \cdot 2 = 1,2$ and the experimental values of the cracking moment are used. With this calculation, the maximum deviation of the theoretical values of the maximum deflection from the experimental data is 39,8%.

The closest results to the experimental data with the deflection $f_u = (1/200)l_0 = 8,55$ mm are obtained by the method Construction rules and regulations 295.1325800.2017 with $\psi_f = 1 - 0,8 \cdot \frac{M_{cr}}{M}$ and using the experimental values of M_{cr} . The maximum deviation from the experimental data is 32,29%.

The results obtained showed the need to improve the method of Construction rules and regulations 295.1325800.2017 in terms of calculating the deflections of flexural members with FRP. At the first stage, it is possible to approximate the theoretical values of the cracking moment to the experimental data by introducing correction coefficients into the expression according to the definition of M_{cr} : For beams with an FRP of a ribbed bars—0,7, for FRP bars with a sand-coated surface—0,5. With adjusted M_{cr} values, the maximum deviation of the theoretical data with a deflection $f_u = (1/200)l_0 = 8,55$ mm from the experimental ones is 30%.

Features of crack formation in members with FRP reinforcement are recorded, which call into question the possibility of using the design methods by Construction rules and regulations 63.13330.2012 and 295.1325800.2017. The approach using the value of the base distance between cracks l_f does not allow for a correct and reliable prediction of the crack width of flexural concrete members with FRP. Based on the conducted study, an equation for determining the crack width a_{cr} was developed, based on the approach for determining the crack width of the ACI 440.1R-06 method, with the correction coefficients introduced, taking into account the degree of bond of FRP to concrete and the influence of the diameter of the bars. Deviations of theoretical data from experimental data range from 8,57%.

References

1. Rimshin, V.I., Merkulov, S.I.: About normalization of characteristics of rod non-metallic composite reinforcement. *Promyshlennoe i grazhdanskoe stroitel'stvo [Ind. Civ. Eng.]* **5**, 22–26 (2015). (in Russian)
2. Attia, K., El Refai, A., Alnahhal, W.: Flexural behavior of basalt fiber-reinforced concrete slab strips with BFRP bars: experimental testing and numerical simulation. *J. Compos. Constr.* **24**(2), 04020007 (2020). [https://doi.org/10.1061/\(ASCE\)CC.1943-5614.0001002](https://doi.org/10.1061/(ASCE)CC.1943-5614.0001002)
3. Salih, R., Zhou, F.: Numerical investigation of the behavior of reinforced concrete beam reinforced with FRP bars. *Civ. Eng. J.* **5**(11), 2296–2308 (2019). <https://doi.org/10.28991/cej-2019-03091412>
4. Pawłowska, D., Szumigala, M.: Flexural behaviour of full-scale basalt FRP RC beams – experimental and numerical studies. In: 7th Scientific-Technical Conference Material Problems in Civil Engineering (MATBUD'2015). *Procedia Engineering*, vol. 108, pp. 518–525 (2015). <https://doi.org/10.1016/j.proeng.2015.06.114>
5. Acciai, A., D'Ambrisi, A., De Stefano, M., Feo, L., Focacci, F., Nudo, R.: Experimental response of FRP reinforced members without transverse reinforcement: failure modes and design issues. *Compos. Part B Eng.* **89**, 397–407 (2016). <https://doi.org/10.1016/j.compositesb.2016.01.002>
6. Adam, M.A., Said, M., Mahmoud, A.A., Shanour, A.S.: Analytical and experimental flexural behavior of concrete beams reinforced with glass fiber reinforced polymers bars. *Constr. Build. Mater.* **84**, 354–366 (2015). <https://doi.org/10.1016/j.conbuildmat.2015.03.057>
7. El-Nemr, A., Ahmed, E.A., El-Safty, A., Benmokrane, B.: Evaluation of the flexural strength and serviceability of concrete beams reinforced with different types of GFRP bars. *Eng. Struct.* **173**, 606–619 (2018). <https://doi.org/10.1016/j.engstruct.2018.06.089>
8. Ju, M., Park, Y., Park, C.: Cracking control comparison in the specifications of serviceability in cracking for FRP reinforced concrete beams. *Compos. Struct.* **182**, 674–685 (2017). <https://doi.org/10.1016/j.compstruct.2017.09.016>
9. Al-Sunna, R., Pilakoutas, K., Hajirasouliha, I., Guadagnini, M.: Deflection behavior of FRP reinforced concrete beams and slabs: An experimental investigation. *Compos. B Eng.* **43**(5), 2125–2134 (2012). <https://doi.org/10.1016/j.compositesb.2012.03.007>
10. Urbanski, M., Garbacz, A., Lapko, A.: Investigation on concrete beams reinforced with basalt rebars as an effective alternative of conventional R/C structures. In: *Proceedings of the 11th International Conference on Modern Building Materials, Structures and Techniques. Procedia Engineering*, vol. 57, pp. 1183–1191 (2013). <https://doi.org/10.1016/j.proeng.2013.04.149>
11. Ruan, X.J., Lu, C.H., Xu, K., Xuan, G.Y., Ni, M.Z.: Flexural behavior and serviceability of concrete beams hybrid-reinforced with GFRP bars and steel bars. *Compos. Struct.* **235**, 111772 (2020). <https://doi.org/10.1016/j.compstruct.2019.111772>

12. Barris, C., Torres, L., Vilanova, I., Miàs, C., Llorens, M.: Experimental study on crack width and crack spacing for Glass-FRP reinforced concrete beams. *Eng. Struct.* **131**, 231–242 (2017). <https://doi.org/10.1016/j.engstruct.2016.11.007>
13. Kim, S., Kim, S.: Flexural behavior of concrete beams with steel bar and FRP reinforcement. *J. Asian Archit. Build. Eng.* **18**(2), 94–100 (2019). <https://doi.org/10.1080/13467581.2019.1596814>
14. Pan, M.X., Xu, X.S.: Study on crack development of concrete beams in bending reinforced with FRP bars. In: 3rd International Conference on Energy Materials and Environment Engineering (ICEMEE). Bangkok, Thailand (2017). <https://doi.org/10.1088/1755-1315/61/1/01203>
15. Lapko, A., Urbański, M.: Experimental and theoretical analysis of deflections of concrete beams reinforced with basalt rebar. *Arch. Civ. Mech. Eng.* **15**(1), 223–230 (2015). <https://doi.org/10.1016/j.acme.2014.03.008>
16. Barris, C., Torres, L., Turon, A., Baena, M., Mias, C.: Experimental study of flexural behaviour of GFRP reinforced. In: Fourth International Conference on FRP Composites in Civil Engineering (CICE2008). Zurich, Switzerland (2008)
17. Peng, F., Xue, W.: Design approach for flexural capacity of concrete T-beams with bonded prestressed and nonprestressed FRP reinforcements. *Compos. Struct.* **204**, 333–341 (2018). <https://doi.org/10.1016/j.compstruct.2018.07.091>
18. Sun, Y., Liu, Y., Wu, T., Liu, X., Lu, H.: Numerical analysis on flexural behavior of steel fiber-reinforced LWAC beams reinforced with GFRP bars. *Appl. Sci. Basel* **23**(9), 5128 (2019). <https://doi.org/10.3390/app9235128>
19. Imomnazarov, T.S., Al-Sabri, S.A.M., Dirie, M.H.: The use of composite reinforcement. *Sistemnye tekhnologii* [Syst. Technol.] **2**(27), 24–29 (2018). (in Russian)
20. Gross, S., Yost, J., Kevgas, G.: Time-dependent behavior of normal and high strength concrete beams reinforced with GFRP bars under sustained loads. In: International Conference on High Performance Materials in Bridges, American Society of Civil Engineers, pp. 451–462 (2003). [https://doi.org/10.1061/40691\(2003\)40](https://doi.org/10.1061/40691(2003)40)
21. Benmokrane, B., Brown, V.L., Mohamed, K., Nanni, A., Rossini, M., Shield, C.: Creep-rupture limit for GFRP bars subjected to sustained loads. *J. Compos. Constr.* **23**(6), 06019001 (2019). [https://doi.org/10.1061/\(ASCE\)CC.1943-5614.0000971](https://doi.org/10.1061/(ASCE)CC.1943-5614.0000971)
22. D'Antino, T., Pisani, M.A.: Long-term behavior of GFRP reinforcing bars. *Compos. Struct.* **227**, 111283 (2019). <https://doi.org/10.1016/j.compstruct.2019.111283>
23. Barris, C., Torres, L., Comas, J., Mias, C.: Cracking and deflections in GFRP RC beams: an experimental study. *Compos. Part B* **55**, 580–590 (2013). <https://doi.org/10.1016/j.compositesb.2013.07.019>
24. Feizbahr, M., Jayaprakash, J., Jamshidi, M., Keong, C.K.: Review on various types and failures of fibre reinforcement polymer. *Middle East J. Sci. Res.* **13**(10), 1312–1318 (2013). <https://doi.org/10.5829/idosi.mejsr.2013.13.10.1180>
25. Begunova, N.V., Grahov, V.P., Vozmishchev, V.N., Kislyakova, I.G.: Comparative evaluation of results on test of concrete beams with fiberglass rebar and calculated data. *Nauka i tekhnika* [Sci. Tech.] **18**(2), 155–163 (2019). (in Russian)
26. Ng, P.L., Barros, J.A.O., Kaklauskas, G., Lam, J.Y.K.: Deformation analysis of fibre-reinforced polymer reinforced concrete beams by tension-stiffening approach. *Compos. Struct.* **234**, 111664 (2020). <https://doi.org/10.1016/j.compstruct.2019.111664>
27. Miàs, C., Torres, L., Guadagnini, M., Turon, A.: Short and long-term cracking behaviour of GFRP reinforced concrete beams. *Compos. B Eng.* **77**, 223–231 (2015). <https://doi.org/10.1016/j.compositesb.2015.03.024>
28. Antakov, I.A.: Features of behavior of flexural members with composite polymeric reinforcement under load. *Zhilishchnoe Stroitel'stvo* [Housing Constr.] **5**, 15–18 (2018). (in Russian)
29. Mirsayapov, Il., Antakov, I., Antakov, A.: Improving methods of strength design of normal sections of flexural concrete members reinforced with fiber-reinforced polymer bars. In: Socio-Technical Construction and Civil Engineering (STCCE-2020). IOP Conference Series: Materials Science and Engineering, vol. 890, p. 012057 (2020). <https://doi.org/10.1088/1757-899X/890/1/012057>

30. Antakov, A.B., Antakov, I.A.: Experimental studies of flexural members with fiber-reinforced polymer reinforcement under sustained load application. In: *New in Architecture, Design Construction and Renovation: Proceedings of the III International (IX All-Russia) Conference (NADCR – 2016)*. The Chuvash State University, Cheboksary, pp. 67–72 (2016). (in Russian)
31. Pecce, M., Manfredi, G., Cosenza, E.: A probabilistic assessment of deflections in FRP RC beams. In: *Proceedings of 5th International Conference on Non-metallic Reinforcement for Concrete Structures - FRPRCS-5*, Cambridge, Thomas Telford Publishing, vol. 2, pp. 887–896, 16–18 July 2001
32. Gizdatullin, A.R.: Collaboration of FRP reinforcement and cement concrete in structures. Candidate's thesis. Kazan, p. 190 (2018). (in Russian)
33. Zinnurov, T.A., Majstrenko, I.Yu., Erokhin, D.I., Zamilova, A.Kh., Umarov, B.Sh.: Investigation of the effect of thickenings in fiberglass reinforcement (FRP) on adhesion to concrete. *Izvestija KGASU [News KSUAE]* **2**(56), 84–93 (2021). https://doi.org/10.52409/20731523_2021_2_84. (in Russian)

Complex Modification of Bituminous Binders by Linear Styrene-Butadiene-Styrene Copolymer and Sulfur



Pavel Bulanov , Evgenii Vdovin , Victor Stroganov , Lenar Mavliev ,
and Igor Juravlev 

Abstract It is known that the load on roads is constantly increasing due to a sharp increase in the number of heavy trucks and formation of so-called “traffic jams”. Therefore, it became necessary to improve the quality of bituminous binders. The use of modified bitumen with polymers in asphalt concrete pavements makes it possible to increase the resistance to plastic rutting, fatigue and low-temperature cracks, wear resistance, and aging. Styrene-butadiene-styrene rubbers belonging to the elastomers group are among the most effective polymers in the world for polymer-bitumen binder production. Studies have been carried out on bitumen modification by linear styrene-butadiene-styrene copolymer and sulfur for the following physical and technical properties: Softening point, dynamic viscosity at 105, 135 and 165 °C, penetration at 25 °C, extensibility at 0 °C, Fraas brittleness temperature, as well as the difference in softening temperature after aging in the RTFOT oven. The optimal dosages of sulfur and linear styrene-butadiene-styrene copolymer in the polymer-bitumen binder production were determined, the modification of which makes it possible to significantly improve the properties of bituminous binders and asphalt concretes based on them.

Keywords Polymer-modified bitumen · Modification · Styrene-butadiene-styrene copolymer · Sulfur · Aging

1 Introduction

While making the asphalt concrete pavements, special attention was paid to the bituminous binder choice. It is the binder that primarily determines the coating strength and its resistance to the formation of various kinds of defects: Ductility ruts, fatigue and low-temperature cracking. However, the roads load has grown significantly due to a sharp increase in the number of heavy trucks and the formation of so-called

P. Bulanov · E. Vdovin (✉) · V. Stroganov · L. Mavliev · I. Juravlev
Kazan State University of Architecture and Engineering, Kazan, Russia
e-mail: vdovin007@mail.ru

“traffic jams”. Therefore, it became necessary to improve the bituminous binders quality [1, 2].

The improvement of the quality of bituminous binders means their modification [3, 4]. According to [5, 6], there are 2 ways to modify bituminous binders: Technological and prescription.

Technological ones are divided into: Preparation conditions (pressure, temperature, foaming, compounding, etc.) and physical effects (ultrasonic treatment, electromagnetic radiation, IR exposure, microwave activation, mechanical activation, X-ray irradiation, cavitation treatment, etc.) [6–9].

The technological methods application requires complex hardware, high labor intensity, energy costs and large investments. In this connection, a more accessible, effective and simple way of bitumen modification is prescription, which was based on the introduction of additional bituminous binders into the composition that change the original structure and properties at various stages of their production and processing [10].

The research aimed at improving the bitumen properties (resistance to aging and increase in operating temperature) through the modifiers usage began in 1843 [11, 12]. In recent years, polymeric materials often have been used as bitumen modifiers [13, 14]. The use of synthetic polymers to improve bitumen characteristics began in the 1970s [15]. Around the world, among the additives used, approximately 75% are elastomers, 15% are thermoplastics [17].

The use of polymer-modified bitumen in asphalt concrete pavements makes it possible to increase the resistance to plastic rutting, fatigue and low-temperature cracks, wear resistance, and aging [18–20]. However, polymer-modified bitumen (PMB) strongly depends on both the type of polymer added and its percentage [21, 22].

Among the polymers used in a number of countries for the PMBs production, the preference is given to styrene-butadiene-styrene rubbers (SBS), which belong to the group of elastomers [23]. The main advantage of PMB based on elastomers in comparison with traditional road bitumen is the creation of a uniform elastic polymer network in a bituminous binder, capable of reversible plasticization with temperature changes [24].

To improve the high-temperature properties of bitumen and PMB based on SBS, the introduction of sulfur is recommended [25]. When sulfur is added to SBS-based PMB, as a result of dynamic vulcanization, a chemically crosslinkable polymer network is formed in the bitumen matrix. However, low-temperature properties continuously decrease with a further increase of the sulfur amount in PMB due to an increased polysulfide bonds number, which leads to restriction of polymer molecules movement [26].

In this regard, **the aim** of this work is to study the physical and technical properties of polymer-bitumen binders modified by sulfur.

To achieve this goal, the following **tasks** were solved:

- the study of the physical and technical characteristics of bitumen modified by SBS;

- the determination of the sulfur effect on the physical and technical properties of the polymer-bitumen binder.
- the study of short-term aging of polymer-bitumen binders modified by sulfur.

2 Materials and Methods

To conduct research, bitumen was used as a binder, corresponding to the BND 70/100 brand according to GOST 33,133-2014 produced by JSC TAIF-NK.

The test results of bitumen in accordance with GOST 33,133-2014 are presented in Table 1.

To obtain PMB, SBS polymer (Kraton D-1101 A) was used. The manufacturer is Kraton Polymers, Korea. This polymer has the following characteristics: Styrene content—31%, molecular structure—linear, viscosity (on a Brookfield viscometer) in a toluene solution (25%, 25° C)—4 Pa*s, specific density—0.94 t/m³, indicator melt flow rate 200 °C/5 kg—<1 g/10 min, bulk density—0.4 t/m³, Shore A hardness, 30 s—72, tensile strength—33 MPa, modulus of elasticity 300%—2.9 MPa, elongation at break—880%.

Table 1 Physical and technical properties of bitumen grade BND 70/100

№	Name of indicator	Unit of measurement	Actual values	Requirements GOST 33,133-2014	GOST test methods
1	2	3	4	5	6
1	Needle penetration depth, at 25 °C, 0,1 mm	mm	74	71–100	GOST 33,136
2	Softening point	°C	48	not lower than 47	GOST 33,142
3	Extensibility, at 0 °C	cm	3.8	not less than 3.7	GOST 33,138
4	Softening temperature change after warming up	°C	6.2	No more than 7.0	GOST 33,140 GOST 33,142
5	Brittleness temperature	°C	–19	Not higher than -18	GOST 33,143
6	Flash temperature °C, not lower	°C	230	230	GOST 33,141
7	Sample mass change after aging, %, no more	%	0.07	0.6	GOST 33,140

Table 2 Physical and technical properties of sulfur

Nº	Name of indicator	Actual	Requirements TU 38.1011217-89
1	Appearance	98.8	92
2	Mass fraction of granules with a diameter of 2,0–5,0 mm, %, not less than	Yellow granules	Yellow granules
3	Bulk density, g/cm ³	99.99	99.98
4	Mass fraction of sulfur, %, not less than	1.3	1.1–1.3
5	Mass fraction of ash, %, no more	0.007	0.02
6	Mass fraction of organic substances, %, no more	0.01	Not higher than 36
7	Mass fraction of acids in terms of sulfuric acid, %, no more	Absence	Absence
8	Mass fraction of water, %, no more	Traces	Traces
9	Mechanical pollution (paper, wood, sand, etc.)	0.01	Not more than 0.01

Modification of bitumen and PBB was carried out by sulfur produced by JSC TAIF-NK, the main properties are presented in Table 2.

The polymer-bitumen binders preparation was carried out on a SILVERSON L5M laboratory mixer (Great Britain). For dissolution of SBS in PBB, a double mixing nozzle DUPLEX (Great Britain) was used. PMB mixing was carried out in tin cans with a volume of 1 L. An oil bath Memmert ONE 22 (Germany) was used to heat and maintain the required operating temperature during the preparation and ripening process. Silicone oil PMS-100 (LLC Penta Junior) was used as a heat carrier. A tin can with a pre-weighed bitumen amount was immersed in oil bath, while the liquid did not reach the top of the tin by 2–3 cm.

The following method was used to prepare PMB from SBS. A pre-weighed bitumen amount and plasticizer (if necessary) in a can was immersed in oil bath. The bitumen was heated up to the working temperature of PMB preparation—180 °C. The mixer nozzle was immersed in bitumen and a mixing speed of 4500 rpm was created. The necessary additives were introduced at a rate of 5 g/min. After the completion of the additives introduction, mixing was carried out for 0.5 h at a temperature of 180 °C and a rotation speed of 4500 rpm. Further, for the next 2 h, the process of PMB ripening was carried out at a rotation speed of 1500 rpm and uniform cooling from 180 to 160 °C.

Bitumen and polymer-bitumen binders were tested in accordance with GOST 33,133-2014. The tests were carried out according to the following indicators.

The depth of needle penetration at 25 °C according to GOST 33,136-2014 was determined. As a device, a Lintel PN-20 penetrometer, produced by JSC Bashkir Special Design Bureau Neftekhimavtomatika, was used.

The softening point on ring and ball was determined according to GOST 33,142-2014. As a device, an automatic apparatus for softening temperature determining of petroleum bitumen Lintel KISH-20, manufactured by JSC Bashkir Special Design Bureau Neftekhimavtomatika, was used.

The extensibility (ductility) at 0 °C was determined according to GOST 33,138-2014. As a device, an automatic apparatus for determining the extensibility of oil bitumen LinteL DB-20–100, manufactured by JSC Bashkir Special Design Bureau Neftekhimavtomatika, was used.

The brittleness temperature according to Fraas was determined in accordance with GOST 33,143-2014. As a device, an automatic apparatus for determining the temperature of oil bitumen LinteL ATX-20, manufactured by JSC Bashkir Special Design Bureau Neftekhimavtomatika, was used.

The sample mass change and softening temperature change after aging in the RTFOT furnace was determined according to GOST 33,140-2014. Rolling thin-film B066N1 equipment (Matest, Italy) was used as a device for bitumen and PMB aging.

The dynamic viscosity at 105, 135 and 165 °C was determined according to GOST 33,137-2014. The test method is to measure the relative resistance to flow caused by shearing bitumen by rotating configuration elements. Dynamic viscosity is calculated as the ratio between applied shear stress and shear rate. A Brookfield DV2T viscometer (Brookfield, USA) was used.

3 Results and Discussion

It was found that when bitumen has been modified by sulfur containing 0.05–0.15%: Softening point and dynamic viscosity at 105 °C, 135 °C and 165 °C increased by 4.1–8.9%, 9.6–30.9%, 13.5–37.8%, 54.5–172.7%, respectively; penetration at 25 °C decreased by 1.4–2.7%; extensibility at 0 °C decreased by 13.2–42.1%; brittleness temperature according to Fraas increased by 10.5–36.8%.

According to the results, it can be seen that when bitumen is modified by sulfur, high-temperature properties improve, while low-temperature characteristics deteriorate, which is consistent with the following studies [27].

When PMB based on SBS (in the amount of 2–6%) is modified by sulfur (in the amount of 0.05–0.15%), it was found that the softening point and dynamic viscosity at 105 °C, 135 °C and 165 °C increased by 2.4–8.9%, 18.8–86.5%, 8.5–49.5%, 21.5–135.9%, respectively. Penetration at 25 °C decreased by 1.4–8.6%; extensibility at 0 °C increased by 4.2–31.3%; brittleness temperature according to Fraas decreased by 4.3–12.0%.

Based on the low-temperature properties (extensibility at 0 °C, brittleness temperature according to Fraas) of PMB modified by sulfur, the optimal sulfur content was determined: At 4% SBS in PMB—0.1% sulfur; at 6% SBS—0.05–0.10% sulfur.

As the sulfur content in bitumen increases, the softening temperature difference after aging in the RTFOT furnace increases too. However, the PMB modification by sulfur causes the opposite effect (change in softening temperature after aging in the

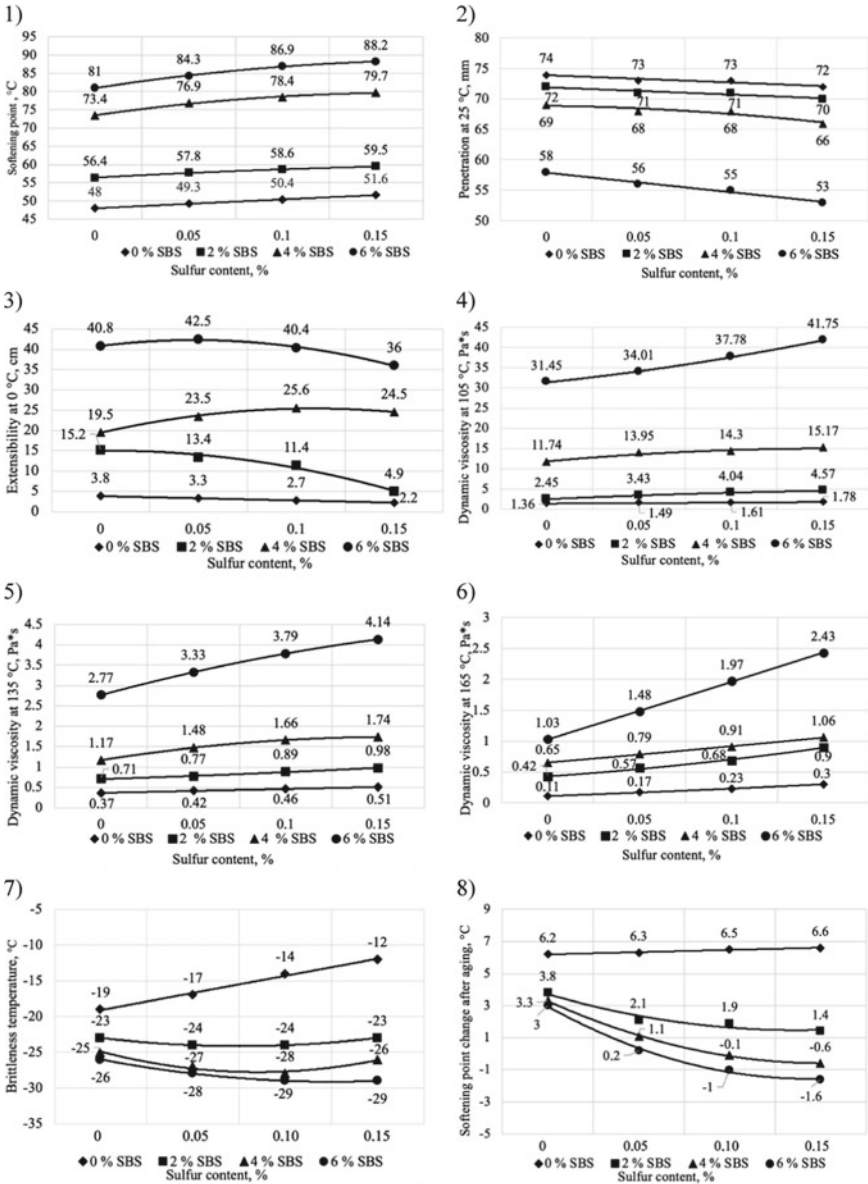


Fig. 1 Influence of sulfur and SBS on the physical and technical characteristics of modified bitumen: 1—softening point; 2—needle penetration depth at 25 °C; 3—extensibility (ductility) at 0 °C; 4—dynamic viscosity at 105 °C; 5 – dynamic viscosity at 135 °C; 6—dynamic viscosity at 165 °C; 7—brittleness temperature according to Fraas; 8—softening point change after aging in the RTFOT oven

RTFOT furnace of bitumen modified by SBS in an amount of 6% and sulfur in an amount of 0.15% – -1.6 °C).

The oxidative aging effect on the PMB high-temperature properties is divided into two main mechanisms. First, the increase amount of solid components of bitumen, such as asphaltenes and resins, as a result of aging, increases the high temperature properties of the binders and reduces the low temperature characteristics. Second, the polymer network destruction dispersed in bitumen after aging can lead to the opposite effect [24].

The formed polysulfide bonds $-(S)_x-$ ($x = 4-6$) between SBS molecules in PMB modified by sulfur are relatively weak. In $C = C$ carbon-carbon double bonds, the butadiene structure has a reactive n-bond. During SBS dynamic vulcanization, the reactive n-bond breaks and turns into a carbon-sulfur C-S bond, therefore, a cross-linked polymer network is formed in the bitumen matrix, which leads to an increase in high-temperature properties [28, 29].

However, the length of the polysulfide bond is longer and its binding energy is lower. Under the influence of thermal and dynamic shear, these weak polysulfide bonds are broken and the cross-linked polymer network is destroyed, which probably leads to a decrease in high-temperature properties after aging of PMB based on SBS modified by sulfur [29, 30] (Fig. 1).

4 Conclusions

- 1) It was found that when bitumen is modified by sulfur containing 0.05–0.15%: The softening point and dynamic viscosity at 105 °C, 135 °C and 165 °C increases by 4.1–8.9%, 9.6–30.9%, 13.5–37.8%, 54.5–172.7%, respectively; penetration at 25 °C decreases by 1.4–2.7%; extensibility at 0 °C decreases by 13.2–42.1%; brittleness temperature according to Fraas increases by 10.5–36.8%.
- 2) When polymer-bitumen binder based on SBS (in the amount of 2–6%) is modified by sulfur (in the amount of 0.05–0.15%), the softening point and dynamic viscosity at 105 °C, 135 °C and 165 °C increases by 2.4–8.9%, 18.8–86.5%, 8.5–49.5%, 21.5–135.9%, respectively. Penetration at 25 °C decreases by 1.4–8.6%; extensibility at 0 °C increases by 4.2–31.3%; brittleness temperature according to Fraas decreases by 4.3–12.0%.
- 3) Based on the low-temperature properties (extensibility at 0 °C and brittleness temperature according to Fraas) of the polymer-bitumen binder modified by sulfur, the optimal modifier content was determined. If the polymer-bitumen binder SBS content is 4%, optimal sulfur content is 0.1%. If SBS content is 6%, optimal sulfur content is 0.05–0.10%.
- 4) It is found that with sulfur content increasing in bitumen, the softening temperature difference after aging in the RTFOT furnace increases too. However, the polymer-bitumen binder modification by sulfur gives the opposite effect, up to negative values due to the destruction of polysulfide bonds as a result of thermal exposure and dynamic shear.

References

1. Celauro, C., Teresi, R., Dintcheva, N.: Effect of short-term and UV irradiation aging on the behaviour of SBS-modified bitumen. *Sustainability* **14**(11), 6915 (2022)
2. Wei, H., et al.: Aging mechanism and properties of SBS modified bitumen under complex environmental conditions. *Materials* **12**(7), 1189 (2019)
3. Rasool, R.T., Hongru, Y., Hassan, A.A., Wang, S., Zhang, H.: In-field aging process of high content SBS modified asphalt in porous pavement. *Polym. Degrad. Stab.* **155**, 230–237 (2018)
4. Ayupov, D.A., Potapova, L.I., Kazakulov, R.I., Khakimullin, Y.N.: Road surfactants composition investigation. *News KSUAE* **3**(45), 178–188 (2018)
5. Diab, A., Pais, J., Chen, S., Gupta, A., Li, X., You, L., Hasan, M.: High, intermediate and low temperature performance appraisal of elastomeric and plastomeric asphalt binders and mixes. *J. Elastomers Plast.* **54**(2), 225–246 (2022)
6. Volkova, G., Morozova, A.: Structural transformations of bitumen asphaltenes after ultrasonic treatment. *Solid Fuel Chem.* **56**(2), 133–137 (2022)
7. Ben, Zh., Chen, H., Zhang, H., Kuang, D., Wu, J., Zhang, X.: A study on physical and rheological properties of rubberized bitumen modified by different methods. *Materials* **12**(21), 3538 (2019)
8. Fathy, E.S., El-Nemr, K.F., Youssef, H.A., El-Shafie, M.: Effect of gamma irradiation and oxidized bitumen on the performance of the modified crumb rubber for various applications. *Radiochimica Acta* **109**(1), 47–54 (2021)
9. Mohapatra, D., Kirpalani, D.: Bitumen heavy oil upgrading by cavitation processing: effect on asphaltene separation, rheology, and metal content. *Appl. Petrochem. Res.* **6**(2), 107–115 (2016)
10. Ratajczak, M., Babiak, M., Bilski, M., Zieliński, K., Kosno, J.: Innovative methods of bitumen modification used in waterproofing. *Int. J. Eng. Technol.* **10**(4), 308–314 (2018)
11. Yalçın, E., et al.: Effect of gilsonite use on storage stability of styrene-butadiene-styrene modified bitumen. *Periodica Polytechnica Civ. Eng.* **63**(3), 833–844 (2019)
12. Xiong, J.P., Xuan, W., Feng, M., Ma, F.: The Performance of SBS modified asphalt binder base on the MSCR test. *IOP Conf. Ser. Mater. Sci. Eng.* **631**, 022018 (2019)
13. Hu, M., et al.: Quantifying weathering-aging test parameters of high viscosity-modified asphalt by establishing a conversion relationship with standard PAV aging. *J. Mater. Civ. Eng.* **34**(6), 04022089 (2022)
14. Derya, K., Topal, A., McNally, T.: Correlation of processing parameters and ageing with the phase morphology of styrene-butadiene-styrene block co-polymer modified bitumen. *Mater. Res. Express* **6**(10), 105309 (2019)
15. Nivitha, M.R., Devika, R., Murali, K.J., Roy, N.: Influence of bitumen type and polymer dosage on the relaxation spectrum of styrene-butadiene-styrene (SBS)/styrene-butadiene (SB) modified bitumen. *Mech. Time Dependent Mater.* **1**(20), 143 (2022)
16. Keyf, S.: The modification of bitumen with styrene-butadiene-styrene, ethylene vinyl acetate and varying the amount of reactive ethylene terpolymer. *J. Elastomers Plast.* **50**(3), 241–255 (2018)
17. Jianhui, X., Tian, X., Li, Zh., Bo, Y., Mingbo, Y.: Correlation between phase separation and rheological behavior in bitumen/SBS/PE blends. *RSC Adv.* **8**(73), 41713–41721 (2018)
18. Mandrawalia, A.K., Gaur, A., Mittal, A.: Investigation of rheological and performance characteristics of oxidized polyethylene polymer blended with SBS modified bitumen. *IOP Conf. Ser. Mater. Sci. Eng.* **1017**(1), 012030 (2021)
19. Kók, B.V., Erkuş, Y., Yılmaz, M.: Evaluation of the cohesive properties of SBS-modified binders at low temperatures. *Slovak J. Civ. Eng.* **29**(1), 21–27 (2021)
20. Zheng, C., Li, G., Xu, Y., Wang, D., Lv, D.: Analysis of the effects of ageing on the cohesive strength of polymer-modified bitumen at low temperatures. *Baltic J. Road Bridge Eng.* **13**(2), 156–164 (2018)
21. Ratajczak, M., Wilmański, A.: Evaluation of laboratory methods of determination of SBS content in polymer-modified bitumens. *Materials* **13**(22), 5237 (2020)

22. Joohari, I.B., Maniam, S., Giustozzi, F.: Enhancing the storage stability of SBS-plastic waste modified bitumen using reactive elastomeric terpolymer. *Int. J. Pavement Res. Technol.* 1–15 (2022)
23. Jiang, Zh., Hu, Ch., Easa, S.M., Zheng, X., Zhang, Y.: Evaluation of physical, rheological, and structural properties of vulcanized EVA/SBS modified bitumen. *J. Appl. Polym. Sci.* **134**(21), 44850 (2017)
24. Singh, S.K., Kumar, Y., Ravindranath, S.S.: Thermal degradation of SBS in bitumen during storage: influence of temperature, SBS concentration, polymer type and base bitumen. *Polym. Degrad. Stab.* **147**, 64–75 (2018)
25. Pang, J., Du, S., Chang, R., Cui, D.: Rheological properties of SBS-modified asphalt in the presence of dithiodimorpholine and tetraethyl thiuram disulfide. *Polym. Compos.* **37**(3), 943–948 (2016)
26. Le, H.T., Korolev, E.V., Grishina, A.N., Gladkikh, V.A.: Reasons for reduced moisture resistance of sulfur-extended asphalt concrete. *Materials* **14**, 7218 (2021)
27. Zhang, F., Hu, C.: Physical and rheological properties of crumb rubber/styrene–butadiene–styrene compound modified asphalts. *Polym. Compos.* **38**(9), 1918–1927 (2017)
28. Zhang, F., Yu, J., Wu, Sh.: Influence of ageing on rheology of SBR/sulfur-modified asphalts. *Polym. Eng. Sci.* **52**, 71–79 (2012)
29. Yang, L., Liu, K., Du, A.: The effect of network structure on compressive fatigue behavior of unfilled styrene-butadiene rubber. *Adv. Mater. Sci. Eng.* **20**, 6729754 (2020)
30. Entezam, M., Zarei, I., Khonakdar, H.A.: Effect of accelerator solubility on the curing characteristics and physico-mechanical properties of SBR/NBR blends: correlation with feeding sequence and blend composition. *Polym. Bull.* **79**(3), 1501–1519 (2022)

Fiber-Reinforced Building Composites Based on Mineral Binders



Albert Galautdinov  and Rustem Mukhametrakhimov 

Abstract Currently, the volume of production of modified fiber composites based on mineral binders tends to decrease, due to a drop in demand for them as the alternative materials, including foreign ones, have entered the market. Traditionally obtained fibrous composite materials and products have a number of disadvantages, which significantly limits the range and scope of their application. Due to that fact, the significant interest is in the development of modified fibrous composite materials based on mineral binders, the study of the processes of their structure formation, properties and improvement of production technology. The paper studies the role of the type of reinforcing fibers in the formation of the structure and properties of composites based on cement and gypsum binders. It is shown that the maximum strength of fiber-cement composites is provided at a degree of fineness of cellulose fibers of 30–40°ShR with their content in the matrix in amount of 5–6% by the mass of solid components, the best records are achieved with a specific surface of silica sand of 310 m²/kg. It was revealed that the optimal coefficient of fiber reinforcement of a gypsum-cement-puzzolanic matrix with cellulose fibers is 0.5–1% by the binder mass at a degree of fineness of cellulose fibers of 30°ShR. The significance of the results for the construction industry lies in the possibility of obtaining fiber composites based on mineral binders with improved performance characteristics and durability, which will expand the scope of their application and increase their competitiveness in comparison with analogues.

Keywords Building materials · Composite materials · Dispersed reinforcement · Mineral binders · Cement · Gypsum · Structure

1 Introduction

At this time production of modified fiber composites based on mineral binders is among upcoming trends of manufacturing of high grade and environmentally clean

A. Galautdinov · R. Mukhametrakhimov (✉)
Kazan State University of Architecture and Engineering, 420043 Kazan, Russia
e-mail: muhametrakhimov@mail.ru

materials and products. The volume of their home production tends downward, which is connected with reduction of demand due to alternative materials appearance on the market. At the present time the part of them is imported from foreign countries and is used as surfacing material during hinged ventilated facade installation, for interior and exterior walls facing, for window sills, floating ceiling, partitions preparation. Moreover, traditionally produced fiber composite materials and products have number of shortcomings: significant specific weight, which confines the scope of their use; low physical and mechanical characteristics and durability.

There are the following directions of correction of these shortcomings: matrix composition modification by mineral [1–3], chemical and complex additives [4–8], nanomodifiers [9, 10], fiber reinforcement of composites based on mineral binders [11–20], optimization of processing methods of production that will fit the requirements of energy-output ratio reduction [21–23], materials consumption and manufacturing cost, their increasing scope, materials recycling [24], environmental improvement and environment preservation, and also imports phase-out. The competitive advantages of modified fiber composite materials based on mineral binders are their small weight, increase of physical and mechanical performance, durability and environmental friendliness during conjoined cost reduction of products and increase of competitive ability in comparison with foreign analogues.

The application problem of basic low-graded construction raw material, gypsum binder, the volume of explored stocks of which makes up about the half of world reserves, is limited by its low water resistance. Weak points of fiber cement products are relatively low performance of their resistance in relation to environmental effect, which is expressed in high deformations of shrinkage/swelling, water absorption, low frost proof et al.

Therefore, the question of present interest is the development of modified fiber composite materials and products based on it, the research of processes of their structure formation and technological improvements of their production, which helps to increase their working properties and durability, expand areas of use, save benefits and make good existing shortcomings.

The performance characteristics of fiber composites based on mineral binders are conditional upon their density, adhesional strength of mineral matrix with fiber, fiber content and degree of their opening. It is necessary to regulate all of these factors in production processes of products. Two reasons of fiber composites damage are possible (Fig. 1):

- fiber breaking when there is exceed of its tension resistance equal to: $\frac{\pi * d^2}{4} * R_{a.p.}$;
- fiber pulling from matrix when there is exceed of shearing resistance equal to: $\frac{\pi * d * l * \tau}{2}$.

Condition of identical fiber resistance to tension and shear, according to theoretical strength research by P.N. Sokolov, leads to formation of mathematical relation between fiber length and diameter of the following type:

$\frac{l}{d_{crit}} = \frac{R_{a.p.}}{2 * \tau}$, where $R_{a.p.}$ —ultimate tensile strength; τ – ultimate strength of experimental fiber type under shear loading.

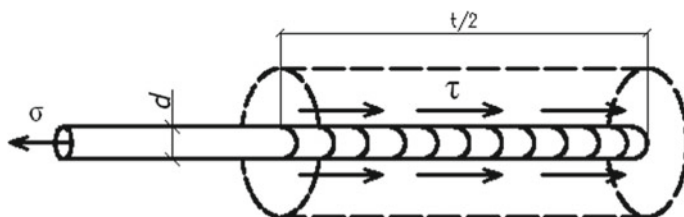


Fig. 1 Diagram of mechanical cooperation of fiber and matrix

The analysis of above-mentioned relation allows deducing that the increase of potential of short fibers use, length-to-diameter ratio of which is not too large, is possible at accretion of adhesive strength of fibers with matrix. At high degree of fiber opening: $\frac{l}{d} > (\frac{l}{d})_{crit}$, deformations and damages of composite fiber material will be conditioned by fiber breaking. At low degree of fiber opening strength parameters of fibers will be not fully used. Overall, the research of influence of cellulosic fiber opening degree on structure and physical and mechanical performance of fiber composites (especially ultimate strength performance) is the question of present interest.

The purpose of the present study is the development of effective modified fiber composites based on mineral binders (portland cement and gypsum), research of processes of their structure formation and properties for creation of thin-wall facing products with increased performance characteristics.

According to the purpose in view on the first phase of experimental research the influence of type and content of reinforcement fiber in composite composition based on mineral binders on their physical and mechanical performance was observed, optimal degrees of fiber opening and coefficients of fiber reinforcement were determined. On the second phase special aspects of microstructure formation of modified fiber composites based on mineral binders were observed.

2 Materials and Methods

During experimental investigations the following materials were used:

- portland cement CEM I 42.5 H produced by Belgorodskij and Volskij cement plants, CEM II/A-K (III-II) 32.5H produced by Ulyanovskij cement plant;
- gypsum cement graded G6BII produced by LLC “Arakchinskij gips”;
- active mineral additive—metakaolin with hydraulic activity not less 1200 mg/g selected from a wide range of natural and technogeneous AMA based on earlier investigations [25–27] and analysis of literature sources [28–30];
- fine aggregate—sand from Kama mineral assets with specific surface 410, 310, 210, 192 m²/kg;
- water that meets the requirements of GOST 23,732.

The ratio of components in composition of raw mixes is accepted according to [31, 32]. The modification of composites was made by chemical admixtures developed earlier, including plastifying [32], waterproofing [33], flocculating [34] ones.

In the capacity of fiber material, we used coniferous sulfate unbleached cellulose with grade NSK-0 opened before until 20, 30, 50° ShR. Cellulose opening was made in disintegrating mill permitting separate it on individual fibers without morphological structure damage according to GOST 14,363.4–89. Cellulosic fibers appertain to high-modulus organic ones, tensile strain at break of which is up to 0.5–4%, tensile strength is 300–500 MPa, average diameter of fibers is 10–35 μm, length is 200–1000 μm and more.

Easy opening, relatively high mechanical strength and flexibility, resistance to aggressive environments, biopositivity, and also ability to soot and hold tightly of particles of cement and gypsum binders on the surface, which is conditioned by high adsorptive capacity of fibers, can be considered as the benefits of cellulose fibers. Reinforcing properties of investigated type of fibers determine high properties of ultimate strength of bend and tension, impact ductility of consolidated composite. Coefficient of fiber reinforcement of the composites were estimated by ratio of fiber material mass to gypsum-cement-puzzolan or cement binder mass.

The test of samples was made according to GOST 8747–88, GOST R 51,829–2001. The investigations of microstructure of modified fiber composites based on mineral binders were undertaken by means of raster scanning election microscope “Philips XL-30”.

3 Results and Discussion

“Degree of fiber fineness—time” relations are shown in Fig. 2.

It is found out that the significant impact on structure formation and properties of fiber composites based on cement binder has the degree of fineness of cellulosic fibers. The dependence of bend strength of cement-fiber composite on degree of fiber fineness is represented by the quadratic of the following form:

$R_{bend} = 0,0125x^2 + 0,885x - 0,8491$, according to which the maximum parameters are achieved at degree of cellulose fineness equal to 30–40 °ShR. Optimal coefficient of fiber reinforcement of cement matrix amounts to 5–6% by mass of binder. At fiber reinforcement content less than 5% and more than 6% the decrease of ultimate strength of cement-fiber composites can be observed. It should be noted that the best performance of bend strength is found in cement-fiber composites based on silica sand with specific surface equal to 310 m²/kg. The further increase of specific surface of silica sand significantly drives up energy costs in the process of manufacturing that are conditioned by time of fineness at slight increase of strength properties of end products.

We used existing complex chemical additive including plastifying and hydrophobic components for modifying the cellulose fiber-reinforced composites

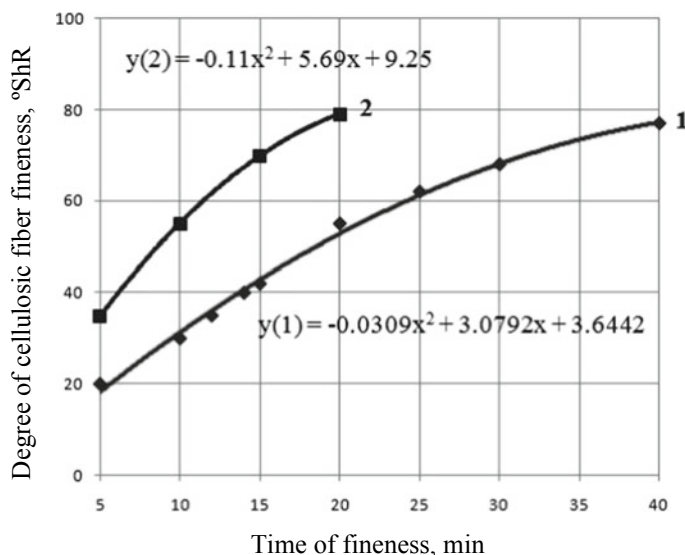


Fig. 2 “Degree of cellulosic fiber fineness—time of fineness” relations: 1—without SAA, 2—with SAA (1% SP “Odolit-K”) (authors’ illustrations)

based on gypsum-cement-puzzolan binder. Physicotechnical fiber characteristics and properties of fiber composites based on it largely depend on opening degree.

The analysis of the findings has allowed establishing significant influence of cellulosic fibers on strength performance of investigated gypsum-cement-puzzolan composites. For example, the best performance is achieved at cellulosic fibers content in composite composition in the quantity of 0.5–1% by mass of binder. Strength performance reduce at increase of cellulosic fibers content in the mix is connected with their lump formation that provides unequal distribution in material volume and with increase of required quantity of gauged water.

The best performance of ultimate bending and compressive strength is achieved at fineness of cellulosic fibers up to 30°ShR. The decrease of strength performance of end products at the increase of degree of cellulosic fibers fineness, in our opinion, is conditioned by significant growth of their damage by opening.

The performed microstructure analysis of the composites by the method of raster scanning electron microscopy gave the opportunity to make electron micrographs at various extents of increase, where we can observe the special aspects of structure formation of the matrixes fiber-reinforced by cellulosic fibers (Figs. 3, 4 and 5).

The analysis of pattern of distribution of fiber material in the volume of matrix according to the study of microstructure at a sections of damage and electron micrographs shows their relatively homogeneous and random distribution.

Fiber reinforcement by the investigated fibers results in high strength performance of modified composites. Besides, hydrated newgrowths received during modifying of mineral binders by complex chemical additives, promotes the conditions for fibers

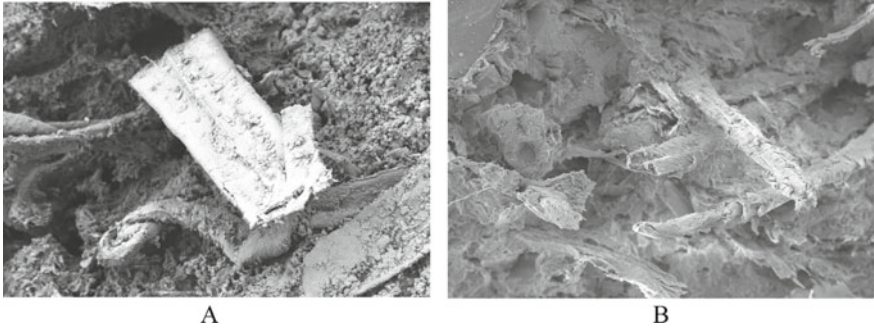


Fig. 3 Electron micrographs of fiber composites at increase $\times 500$: A—based on gypsum binder; B—based on cement binder (authors' illustrations)

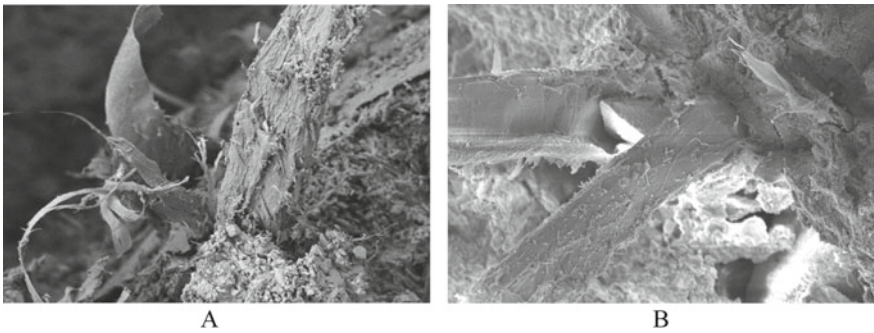


Fig. 4 Electron micrographs of fiber composites at increase $\times 1000$: A—based on gypsum binder; B—based on cement binder (authors' illustrations)

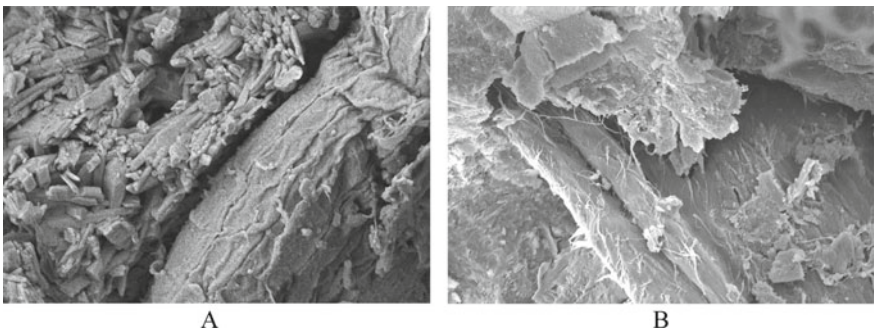


Fig. 5 Electron micrographs of fiber composites at increase $\times 5000$: A—based on gypsum binder; B—based on cement binder (authors' illustrations)

protection from aggressive actions of environment and the best interaction between fibers under mechanical effects.

The analysis of Fig. 4 at increase $\times 1000$ shows connected fibers formation in matrix of the composites in the absence of mesh reinforcement with linear and planar fiber orientation, which is due to existence of contact zones between individual fibers at their configuration and orientation in different planes. Having regard to the above, it can be concluded that the increase of strength performance of end products depends on the fiber equal distribution in the volume of material with predominantly directionally-framed reinforcement with linear fiber orientation in composite's plane.

The elemental analysis of electron micrographs at increase $\times 5000$ (Fig. 5) highlighted low-basic hydrated calcium sulfoaluminates with high degree of amorphism in the form of shapeless submicrocrystalline structures.

4 Conclusions

1. It is shown that in spite of variety of national and foreign scientists' investigations oriented to the increase of quality and effectiveness of composite materials based on mineral binders, research of new ways of improvement of their effectiveness is highly relevant; one of these ways is scientifically grounded technological concept of fiber composites development that consists in cellulosic fibers introduction into modified mineral matrix, which allows to make composite structure stronger, to increase the physicochemical product performance and to simplify the technology of their production.
2. The obtained dependences of strength performance on degree of fineness of the fibers type allowed determining its optimal interval equal to 30–40 °ShR for cement matrix and 30°ShR gypsum matrix that provides the highest increase of ultimate bend strength of modified fiber composites based on them.
3. The optimal coefficient of fiber reinforcement by cellulosic fibers of cement matrix is equal to 5–6%, gypsum-cement-puzzolan matrix—0.5–1%.
4. The analysis of microstructure of modified fiber composites based on mineral binders allowed to detect the positive influence of cellulosic fibers on the structure and the properties of end products, which is conditioned by their optimal degree of opening, relatively homogeneous and random distribution in the volume of modified matrixes based on mineral binders with predominantly directionally-framed reinforcement with linear fiber orientation in composite's plane.

Summing up, the effective modified fiber composites based on cement and gypsum binders with high performance that helps to expand the scope of their application and increase their competitive ability in comparison with foreign analogues have been obtained.

References

1. Rakhimova, N., Rakhimov, R.: Advances in development of calcined clays as supplementary cementitious materials. IOP Conf. Ser. Mater. Sci. Eng. (2020). <https://doi.org/10.1088/1757-899X/890/1/012085>
2. Khaliullin, M., Dimieva, A.: Composite gypsum binder under introducing thermally activated clay as a pozzolanic component and adding ground limestone. IOP Conf. Ser. Mater. Sci. Eng. (2020). <https://doi.org/10.1088/1757-899X/890/1/012093>
3. Rakhimova, N.R., Rakhimov, R.Z.: Influence of calcined clays additions on the composition of reaction products and properties of compositional alkali-activated slag cements with low content of alkali reactant. IZV KGASU **2**, 50–59 (2021). https://doi.org/10.52409/20731523_2021_2_50
4. Khozin, V., Khokhryakov, O., N, R.: A «carbon footprint» of low water demand cements and cement-based concrete. IOP Conf. Ser. Mater. Sci. Eng. **890**, 012105 (2020). <https://doi.org/10.1088/1757-899X/890/1/012105>
5. Mukhametrakhimov, R.K., Izotov, V.S.: Improving the physical and mechanical properties and durability of fiber cement boards based on cellulose fibers. Izv. Vyss. uchebnyh Zaved. Stroit. **9**, 101–107 (2012)
6. Vdovin, E., Mavliev, L., Stroganov, V.: Interaction of clay soil components with portland cement and complex additive based on octyltriethoxysilane and sodium hydroxide. IOP Conf. Ser. Mater. Sci. Eng. (2020). <https://doi.org/10.1088/1757-899X/890/1/012031>
7. Organomineral modifier for fiber cement compositions: pat. 2500633 Russian Federation. № 2012118735/03 ; declared 04.05.12 ; published 10.12.13. bulletin № 34. 5c
8. Kalabina, D.A., Yakovlev, G.I., Kuzmina, N.V.: Non-shrinking fluoroanhydrite compositions for flooring. Izv KGASU **1**, 24–38 (2021). https://doi.org/10.52409/20731523_2021_1_24
9. Galeev, R., Abdrakhmanova, L.A., Nizamov, R.: Nanomodified organic-inorganic polymeric binders for polymer building materials. Solid State Phenom. **276**, 223–228 (2018). <https://doi.org/10.4028/www.scientific.net/SSP.276.223>
10. Galeev, R.R., Nizamov, R.K., Abdrakhmanova, L.A.: Filling of epoxy polymers with chemically precipitated chalk from chemical water treatment sludge (2021). https://doi.org/10.1007/978-3-030-68984-1_14
11. Vdovin, E., Stroganov, V., Amel'chenko, M., Kraus, E., Fazleev, I.: Biostability of road cement-mineral materials reinforced with dispersed fibre. In: Presented at the (2021). https://doi.org/10.1007/978-3-030-80103-8_31
12. Potapova, E., Dmitrieva, E., Nian, A.K., Tsvetkova, E.: Gypsum composite reinforced with polymer fibers. Key Eng. Mater. **910**, 880–886 (2022). <https://doi.org/10.4028/p-dgyem5>
13. Potapova, E., Krivoborodov, Y., Sivkov, S., Sycheva, L., Burlov, I.: Properties of cements with carbon nanofibers grown on kaolin clay. In: Presented at the September, vol. 20 (2020). <https://doi.org/10.5593/sgem2020/6.1/s24.016>
14. Klyuev, S.V., Klyuev, A.V., Vatin, N.I., Shorstova, E.S.: Technology of 3-D printing of fiber reinforced mixtures. In: Presented at the (2021). https://doi.org/10.1007/978-3-030-67654-4_25
15. Klyuev, S.V., Khezhev, T.A., Pukharenko, Y.V., Klyuev, A.V.: To the question of fiber reinforcement of concrete. Mater. Sci. Forum. **945**, 25–29 (2019). <https://doi.org/10.4028/www.scientific.net/MSF.945.25>
16. Klyuev, S.V., Khezhev, T.A., Pukharenko, Y.V., Klyuev, A.V.: Fibers and their properties for concrete reinforcement. Mater. Sci. Forum. **945**, 125–130 (2019). <https://doi.org/10.4028/www.scientific.net/MSF.945.125>
17. Klyuev, S.V., Bratanovskiy, S.N., Trukhanov, S.V., Manukyan, H.A.: Strengthening of concrete structures with composite based on carbon fiber. J. Comput. Theor. Nanosci. **16**, 2810–2814 (2019). <https://doi.org/10.1166/jctn.2019.8132>
18. Klyuev, S.V., Khezhev, T.A., Pukharenko, Y.V., Klyuev, A.V.: Experimental study of fiber-reinforced concrete structures. Mater. Sci. Forum. **945**, 115–119 (2019). <https://doi.org/10.4028/www.scientific.net/MSF.945.115>

19. Klyuev, S.V., Khezhev, T.A., Pukhareno, Y.V., Klyuev, A.V.: Fiber concrete for industrial and civil construction. *Mater. Sci. Forum.* **945**, 120–124 (2019). <https://doi.org/10.4028/www.scientific.net/MSF.945.120>
20. Stepanov, S., Krasinikova, N., Makarov, D.: Cement stone, modified by galvanic sludge. *IOP Conf. Ser. Mater. Sci. Eng.* (2020). <https://doi.org/10.1088/1757-899X/890/1/012086>.
21. Mukhametrakhimov, R.K., Lukmanova, L.V.: Decreasing of energy expenditures connected with production of fiber cement panels for building finish. *IOP Conf. Ser. Earth Environ. Sci.* (2017). <https://doi.org/10.1088/1755-1315/90/1/012112>
22. Pimenov, S.I.: Features of the structure formation of a cement stone after hydro-mechanochemical activation of cement. *Russ. J. Build. Constr. Archit.* **49**, 46–58 (2019)
23. Izotov, V.S., Mukhametrakhimov, R.K., Galautdinov, A.R.: Method for preparing gypsum-cement-pozzolanic composition: pat. RU 2552274 C1. RU (2015)
24. Morozov, N.M., Stepanov, S.V., Galeev, A.F.: The use of industrial waste in cement compositions. In: *Integraciya nauki, obshchestva, proizvodstva i promyshlennosti*. pp. 36–39 (2016)
25. Mukhametrakhimov, R., Galautdinov, A., Lukmanova, L.: Influence of active mineral additives on the basic properties of the gypsum cementpozzolan binder for the manufacture of building products. In: *MATEC Web of Conferences* (2017). <https://doi.org/10.1051/mateconf/201710603012>
26. Mukhametrakhimov, R., Galautdinov, A., Garafiev, A.: The concrete modified by conductive mineral for electrode heating. *IOP Conf. Ser. Mater. Sci. Eng.* (2020). <https://doi.org/10.1088/1757-899X/890/1/012124>
27. Mukhametrakhimov, R.K., Galautdinov, A.R., Garafiev, A.M.: Structure and properties of fiber composites based on modified mineral binders. *News KSUAE.* **4**, 62–71 (2020)
28. Khaliullin, M., Gilmanshina, A.: The effect of additives of mechanically activated mineral fillers on the properties of composite gypsum binders. In: Presented at the (2021). https://doi.org/10.1007/978-3-030-80103-8_36
29. Khaliullin, M., Gilmanshina, A.: The effect of ground limestone on the properties of composite gypsum binder using thermally activated clay as a pozzolanic component. In: *E3S Web of Conference*, vol. 274, p. 04006 (2021). <https://doi.org/10.1051/e3sconf/202127404006>
30. Tironi, A., Tressa, M., Sian, A., Irassar, E.F.: Thermal activation of kaolinite clays. *Cem. i ego Primen.* **6**, 145–148 (2012)
31. Fiber cement mixture: pat. 2486150. Russian Federation. № 2012101728/03; de-clared 18.01.12; published 27.06.13. bulletin № 18.6c
32. Complex additive: pat. 2519313. Russian Federation. № 2013103948/03; declared 29.01.13; published 10.06.14. bulletin № 16. 5c
33. Mukhametrakhimov, R., Galautdinov, A., Gorbunova, P., Gorbunova, T.: Water-resistant fiber-reinforced gypsum cement-pozzolanic composites. In: *E3S Web of Conferences* (2019). <https://doi.org/10.1051/e3sconf/201913801011>
34. Mukhametrakhimov, R.: Fiber-cement compositions modified by flocculating additives. *Constr. Unique Build. Struct.* **10**, 28–37 (2018). <https://doi.org/10.18720/CUBS.73.3>

Structure of 3D-Printed Concrete by X-ray Computed Tomography



Rustem Mukhametrakhimov , Liliya Ziganshina , Rail Kadyrov ,
and Evgeny Statsenko 

Abstract The problem of increased porosity and heterogeneity is typical for concrete products obtained by layered extrusion (3D-printing). It can be partially solved by using organomineral additives, and the optimal ratio of mixture components (binder, fine aggregate, mineral and chemical additives, water), as well as by optimizing technological parameters of the printing process. This work aims to study the peculiarities of formation of micro- and macrostructure of basic and modified composition of concrete formed by layered extrusion (3D-printing). The object of the study is the basic and modified fine-grained cement concrete. The subject of the study is the structure and properties of a single layer of concrete, printed on a 3D-printer by layered extrusion. The control (basic) composition of PC CEM I 42,5H + fine aggregate + water and the modified composition of PC CEM I 42,5H + organomineral additive (metakaolin 10% + complex additive “Relamix PC” 1%) + fine aggregate + water were investigated. The investigated compositions had cement to sand ratio of 1/3, and the Pk-3 mobility of concrete mixes. The X-ray computed tomography using General Electric Vtome|X S 240 (Germany) was used to study the structure of fine-grained 3D- printed concretes. The examined samples were selected from identical places within the thickness of one printed layer (not along the border of layers). The results obtained proved the efficiency of modification of fine-grained concrete mixtures of Pk 3 mobility by a complex additive containing metakaolin and copolymer based on polyoxyethylene derivatives of unsaturated carboxylic acids. The increased density and strength of 3D-printed concrete were registered. X-ray computed tomography showed that the developed compositions of the modified fine-grained concrete formed by the layered extrusion are characterized by less porous and more homogeneous structure with prevalence of an equivalent pore diameter of a smaller size (0.1–0.8 mm) in comparison with the basic composition (0.9–1.4, 1.6 mm) Concrete modified with organomineral additive has a 10.3% lower total pore volume, a 23.9% lower volume of open capillary pores, a 77% lower volume

R. Mukhametrakhimov (✉) · L. Ziganshina · E. Statsenko
Kazan State University of Architecture and Engineering, Kazan 420043, Russia
e-mail: muhametrahimov@mail.ru

R. Kadyrov · E. Statsenko
Institute of Geology and Petroleum Technologies of Kazan Federal University, Kazan, Russia

of open non-capillary pores, a 57% higher volume of conditionally closed pores, an 0.31–0.84 increase in microporosity as compared with the basic composition.

Keywords Concrete · Cement · Mortars · 3D concrete printing · 3DCP · Additive manufacturing · X-ray computed tomography

1 Introduction

The development and introduction of automation and robotics techniques in manufacturing contributes to the improved efficiency of various industries, including construction [1–5].

Additive technologies are used to produce parts, products, small architectural forms, structures, building frameworks [6–8], bridge structures [9, 10] based on creating a physical object using an electronic geometric model by adding material, usually layer by layer, unlike subtractive production (mechanical treatment) and traditional shaping production (casting, stamping) [8].

The prospects of additive technologies in construction are discussed by many authors [9–13]. These technologies are cost-effective and make it possible to significantly reduce the construction time and labor costs, and to make products of different configurations in the absence of significant waste during production.

3DCP technologies are studied at various Universities, for example, Eindhoven University of Technology [11–13], Swinburne University of Technology [14–16], Singapore Centre for 3D Printing [17–19] Moscow State University of Civil Engineering [20–22], Belgorod State Technological University named after V. G. Shukhov [23–31], Voronezh State Technical University [32–34], Kazan State University of Architecture and Engineering [35–43] and others.

The most important physical and mechanical properties and durability of fine-grained concretes formed by layered extrusion depend on the composition of raw mixes, their rheological properties, the nature of interaction of particles of initial components and new formations, pore structure of the hardened composite, curing conditions. The combination of these factors makes the basis for the optimal mechanisms of hydration and structure formation processes.

The problem of increased porosity and heterogeneity, which is typical for concrete products obtained by layered extrusion (3D-printing) [44] is partially solved by using active mineral additives, and the optimal ratio of mixture components [36, 45] (binder, fine aggregate, mineral and chemical additives, water) [39], and by optimizing the technological parameters of the printing process [40].

The need for the use of active mineral and chemical additives in 3DCP technology is also explained by the need to obtain raw mixes with the required rheological properties, increased physical and mechanical characteristics and durability, which is the most affordable and simple way to optimize the specified properties.

The method of X-ray computed tomography (XRCT) is very effective for studying the structure of building materials [46, 47]. The authors [48] used SEM and X-ray

computed tomography to investigate the structural features of fine-grained PC CEM I 52,5B concrete, modified with limestone powder, calcined clay, plasticizing additive based on polycarboxylate esters and a viscosity modifier created by 3D-printing. It was found that a significant volume of pores with the 10–1000 μm diameters are evenly distributed in the layer area of the printed samples, large pores (1000–6000 μm) are concentrated mainly on the border of the printed layers. In addition, most of the pores have an irregular and elongated shape, which, according to [48], can be explained by the extrusion processes in 3D-printing technology.

In the previous studies we have developed compositions of fine-grained concrete modified by active mineral additive and hyperplasticizer, which made it possible to increase the form stability of the printed mixture, density and strength of the hardened composite.

This work aims to study the peculiarities of formation of micro- and macrostructure of basic and modified concrete composition molded by layered extrusion (3D-printing).

The object of the research is the basic and modified fine-grained cement concrete.

The subject of the research is the structure of a single layer of concrete printed on a 3D printer by layered extrusion.

2 Materials and Methods

The research was carried out in the laboratory of additive manufacturing in construction (Kazan State University of Architecture and Engineering, Russia).

The following materials were used:

- Portland cement CEM I 42,5 N (manufacturer “Sukholozhskcement”) complying with GOST 31,108-2016 (Russian standard);
- fine aggregate: quartz sand with a fineness module $M_k = 2.3$ complying with GOST 8736-2014 (Russian standard);
- active mineral admixture metakaolin from the “Crane’s Elbow” deposit. Specific surface area is 2068 m^2/kg ;
- polyfunctional chemical additive “Relamix PK”, including copolymer based on polyoxyethylene derivatives of unsaturated carboxylic acids produced by LLC “Polyplast Kazan”.
- tap drinking water complying with GOST 23,732-2011 (Russian standard).
- Mixing of raw materials was carried out in a forced action concrete mixer for 10 min until homogeneous mass was obtained.

The mobility of the mortar and concrete mixes was determined according to GOST 5802-86 (Russian standard) by the depth of the reference cone immersion in it.

The sample was formed from a sand-cement mix by extrusion in workshop 3D printer “AMT S-6044” from SPETSAVIA LLC (Yaroslavl, Russia), organized by a portal system, in accordance with a specified digital three-dimensional model (G-code).

The printed samples hardened for 28 days under natural conditions: temperature of 20 ± 2 °C, relative humidity of $50 \pm 20\%$.

3DCP-samples for testing were prepared by cutting them into prisms with dimensions of $40 \times 40 \times 160$ mm.

The average density of hardened cement-sand mortars was determined according to GOST 5802-86, the average density of concretes was determined according to GOST 12,730.1-78 (Russian standard).

Water absorption of mortars was determined according to GOST 5802-86, water absorption of concretes was determined according to GOST 12,730.3-78 (Russian standard).

The flexural and compression strength of the hardened mortars and concretes was determined on samples-beams with dimensions of $40 \times 40 \times 160$ mm and halves of prism samples obtained after flexural tests, according to GOST 5802-86 using testing machines IP-1000-0, MII-100. This method was chosen to investigate fine-grained concretes because of the absence of coarse aggregate (more than 5 mm) in them, which makes it possible to produce samples of smaller sizes, regulated by GOST 10,180-2012 (Russian standard) for concretes, the complexity of forming samples on a 3D printer with the dimensions specified in GOST 10,180-2012.

To study physical and mechanical properties and microstructure of fine-grained 3D-printed concrete (distribution of pores by volume and diameter), X-ray computed tomography was performed for the following compositions:

- 1) Control (basic) composition: PC CEM I 42,5H + fine aggregate + water;
- 2) Modified composition: PC CEM I 42,5H + KD1 (metakaolin 10% + factory complex additive "Relamix PK" 1%) + fine aggregate + water.

The studied compositions had cement to sand ratio of 1/3, and the Pk-3 mobility of concrete mixes.

Samples studied by XRCT were taken from identical places - within the thickness of one printed layer (not on the border of the layers).

The structure of fine-grained concretes printed on a 3D printer was investigated by X-ray computed tomography using the General Electric VtomeIX S 240 (Germany).

Imaging of the samples was performed using a microfocus tube at 130 kV, 130 mA. Imaging conditions for each sample were adjusted separately depending on the density characteristics of the minerals composing the sample.

3 Results and Discussions

At the first stage of the study, the influence of the developed organomineral additive on the physical and mechanical characteristics of 3D-printed concrete was studied (Table 1).

Table 1 shows that the modification of concrete with organomineral additive makes it possible to increase by 224% the ultimate compressive strength, by 208% the ultimate bending strength, and to reduce water absorption by 44.5%.

Table 1 The influence of the organomineral additive on the physical and mechanical characteristics of fine-grained 3D-printed concrete

No. of additive	Components of organomineral additive	Content, % of PC weight	Average density, kg/m ³	FS, MPa	CS, MPa	W, %
1	2	3	4	5	6	7
–	–	–	2090	4.6	20.4	10.7
KD 1	Metakaolin Relamix PK	10 1.0	2150	9.6	45.8	7.4

At the second stage, obtained were XRCT images of the examined samples of fine-grained concrete, molded by layered extrusion (3D-printing), which are shown in Figs. 1, 2, 3, 4 and 5. The distribution of pores in concrete samples (control and modified) by the equivalent pore diameter is shown in Table 2.

Figures 1, 2, 3, 4 and 5 show that the samples molded by layered extrusion (3D-printing) have not only isotropic pores, but also anisometric and slotted pores, which are most typical for the technology of construction 3D-printing in contrast to the traditional injection molding method. The orientation of the anisometric and slotted pores in the concrete corresponds to the extrusion direction of the mixture. The data obtained are consistent with the results of [49, 50]. In addition, concrete samples from the modified composition have a denser and more homogeneous structure compared to the concrete samples from the control composition, which results in the improved physical and mechanical characteristics (see Table 1).

The analysis of Table 2 shows that concrete samples from the control and modified compositions, molded by layered extrusion (3D-printing) have different distributions of pores by equivalent diameter. The samples from the modified composition predominantly have 0.1–0.8 mm pores, pores with sizes 0.9–1.4, 1.6 mm prevail in a concrete sample from a control (unmodified composition). So, the share of rather large pores

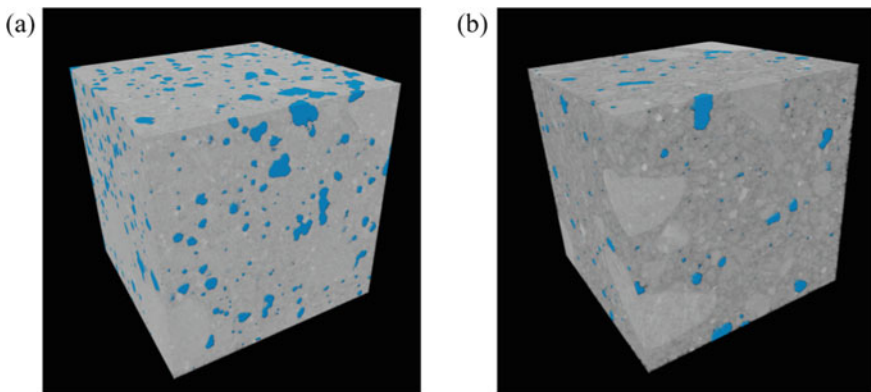


Fig. 1 XRCT image of 3D visualization of concrete samples: **a** control; **b** modified

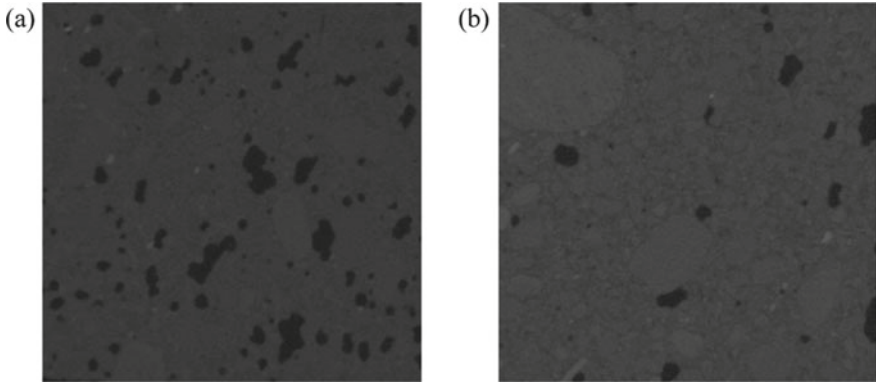


Fig. 2 XRCT image of a 8.3 × 8.3 mm cut along the XY axis of concrete samples: **a** control; **b** modified

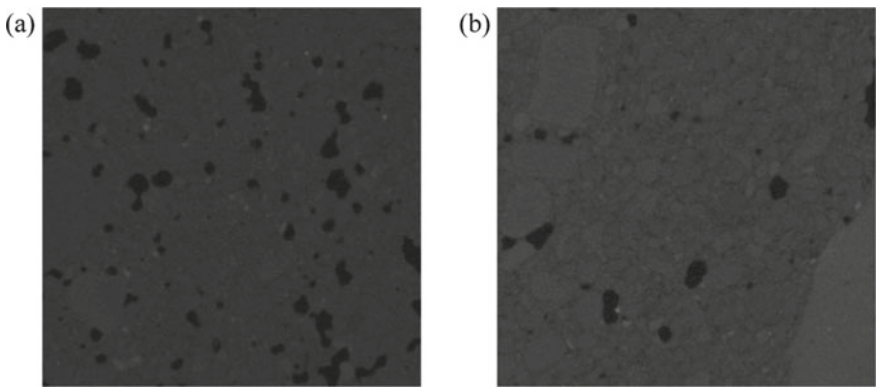


Fig. 3 XRCT image of a 8.3 × 8.3 mm cut along the XZ axis of concrete samples: **a** control; **b** modified

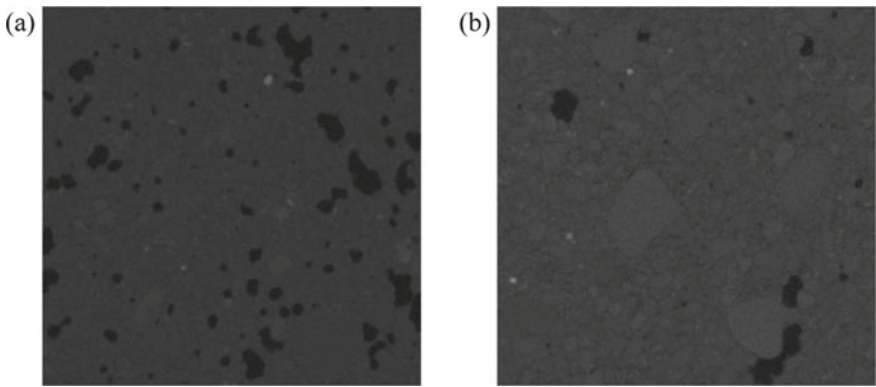


Fig. 4 XRCT image of a 8.3 × 8.3 mm cut along the YZ axis of concrete samples: **a** control; **b** modified

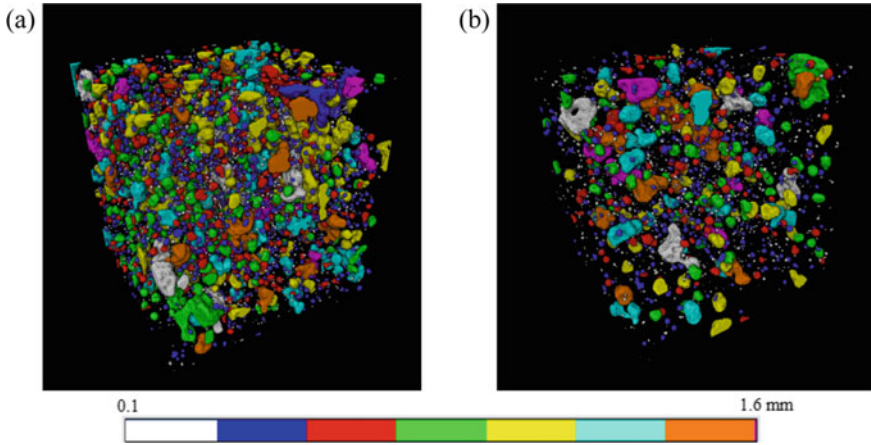


Fig. 5 XRCT image of 3D visualization of pores of various diameters: **a** control; **b** modified

Table 2 Pore distribution in concrete samples (control and modified) by equivalent pore diameter

Equivalent pore diameter, mm	Proportion of total pore volume, %	
	Control	Modified
1	2	3
0.1	1.15	6.36
0.2	4.58	5.13
0.3	7.61	8.25
0.4	9.70	10.75
0.5	12.35	12.92
0.6	12.98	14.50
0.7	10.10	12.44
0.8	6.45	10.19
0.9	11.84	7.85
1.0	4.10	3.70
1.1	4.27	1.89
1.2	5.07	4.78
1.3	4.50	0
1.4	1.92	0
1.5	0	1.22
1.6	3.37	0

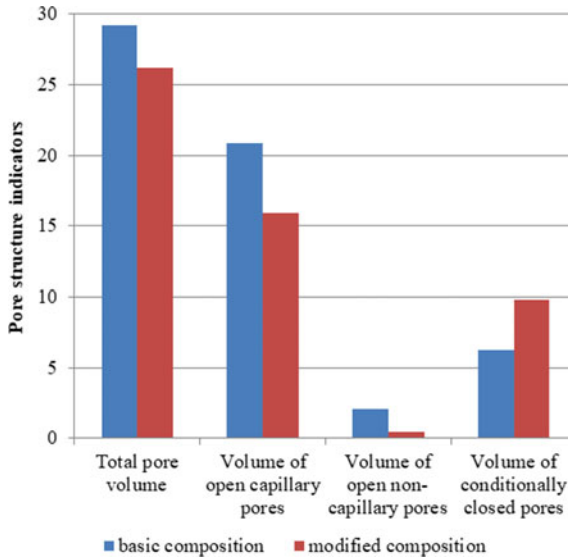


Fig. 6 Indicators of the pore structure of 3D-printed concretes

(with diameter more than 0.9 mm) decreases in modified samples and the share of small pores (less than 0.9 mm) increases.

Thus, the XRCT method was used to determine that the developed compositions of the modified fine-grained concrete made by layered extrusion (3D-printing) are characterized by a less porous structure with the prevalence of an equivalent pore diameter of a smaller size (0.1–0.8 mm) as compared with the basic composition (0.9–1.4, 1.6 mm).

At the third stage, the indicators of pore structure of concretes were studied. The results obtained are shown in Figs. 6 and 7.

Figures 6 and 7 show that the introduction of organomineral additive into the composition of fine-grained concrete mixtures results in redistribution of indicators of pore structure of 3D-printed concrete. Concrete modified with organomineral additive has a 10.3% lower total pore volume, a 23.9% lower volume of open capillary pores, a 77% lower volume of open non-capillary pores, a 57% higher volume of conditionally closed pores, an 0.31–0.84 increase in microporosity as compared with the basic composition. The obtained data are consistent with the determined physical and mechanical characteristics (see Table 1), indicating the effectiveness of the application of organomineral additive to modify the structure of fine-grained concrete in the technology of additive production.

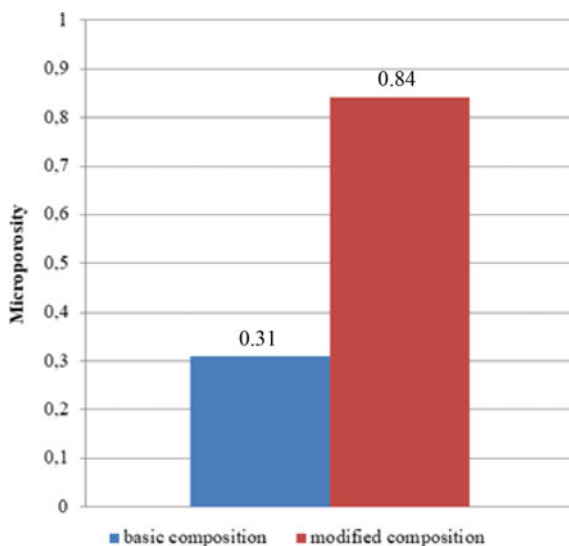


Fig. 7 Miscoporosity of 3D-printed concretes

4 Conclusions

1. The paper proved the efficiency of modification of fine-grained concrete mixtures of Pk-3 mobility by a complex additive containing metakaolin and copolymer based on polyoxyethylene derivatives of unsaturated carboxylic acids, which provides an increased density and strength of concrete in 3D-printing technology.
2. X-ray computed tomography showed that the developed compositions of the modified fine-grained concrete formed by 3D-printing are characterized by less porous and more homogeneous structure with prevalence of an equivalent pore diameter of a smaller size (0.1–0.8 mm) in comparison with the basic composition (0.9–1.4, 1.6 mm).
3. It was established that the structure of the developed fine-grained concrete modified with KD1 has a 10.3% lower total pore volume, a 23.9% lower volume of open capillary pores, a 77% lower volume of open non-capillary pores, a 57% higher volume of conditionally closed pores, an increase in microporosity from 0.31 to 0.84 compared to the base composition, which causes their compaction and hardening.

Acknowledgements This research was funded by President of Russia Scholarship for young scientists and graduate students (SP-1051.2021.1). This paper has been supported by the Kazan Federal University Strategic Academic Leadership Program.

References

1. Vatin, N., et al.: 3D printing in construction. *Constr. Unique Build. Struct.* **52**, 27–46 (2017). <https://doi.org/10.18720/CUBS.52.3>
2. Klyuev, S.V., Klyuev, A.V., Vatin, N.I., Shorstova, E.S.: Technology of 3-D Printing of Fiber Reinforced Mixtures. Presented at the (2021)
3. Khozin, V., Khokhryakov, O., Nizamov, R.: A «carbon footprint» of low water demand cements and cement-based concrete. In: *IOP Conference Series: Materials Science and Engineering* (2020)
4. Stroganov, V.F., Amel'chenko, M.O., Mukhametrakhimov, R.K., Vdovin, E.A., Tabaeva, R.K.: Increasing the adhesion of styrene–acrylic coatings modified by schungite filler in protection of building materials. *Polym. Sci. Ser. D* **15**, 162–165 (2022). <https://doi.org/10.1134/S1995421222020277>
5. Mukhametrakhimov, R.K., Galautdinov, A.R., Potapova, L.I., Garafiev, A.M.: The study of structure formation of modified cement stone containing shungite by infrared spectroscopy. *News KSUAE* **4**, 70–81 (2021). <https://doi.org/10.52409/20731523>
6. Anton, A., Reiter, L., Wangler, T., Frangez, V., Flatt, R.J., Dillenburger, B.: A 3D concrete printing prefabrication platform for bespoke columns. *Autom. Constr.* **122**, 103467 (2021). <https://doi.org/10.1016/j.autcon.2020.103467>
7. He, Y., Zhang, Y., Zhang, C., Zhou, H.: Energy-saving potential of 3D printed concrete building with integrated living wall. *Energy Build.* **222**, 110110 (2020). <https://doi.org/10.1016/j.enbuid.2020.110110>
8. Hager, I., Golonka, A., Putanowicz, R.: 3D printing of buildings and building components as the future of sustainable construction? *Procedia Eng.* **151**, 292–299 (2016). <https://doi.org/10.1016/j.proeng.2016.07.357>
9. Salet, T.A.M., Ahmed, Z.Y., Bos, F.P., Laagland, H.L.M.: 3D printed concrete bridge. In: *Proceedings of the International Conference on Progress in Additive Manufacturing*, pp. 2–9. Pro-AM (2018)
10. Salet, T.A.M., Ahmed, Z.Y., Bos, F.P., Laagland, H.L.M.: Design of a 3D printed concrete bridge by testing. *Virtual Phys. Prototyp.* **13**, 222–236 (2018). <https://doi.org/10.1080/17452759.2018.1476064>
11. Bos, F.P., et al.: The realities of additively manufactured concrete structures in practice. *Cem. Concr. Res.* **156**, 106746 (2022). <https://doi.org/10.1016/j.cemconres.2022.106746>
12. van Overmeir, A.L., Figueiredo, S.C., Šavija, B., Bos, F.P., Schlangen, E.: Design and analyses of printable strain hardening cementitious composites with optimized particle size distribution. *Constr. Build. Mater.* **324**, 126411 (2022). <https://doi.org/10.1016/j.conbuildmat.2022.126411>
13. Mechtcherine, V., et al.: Extrusion-based additive manufacturing with cement-based materials—production steps, processes, and their underlying physics: a review. *Cem. Concr. Res.* **132** (2020). <https://doi.org/10.1016/j.cemconres.2020.106037>
14. Marchment, T., Sanjayan, J.: Lap joint reinforcement for 3D concrete printing. *J. Struct. Eng.* **148** (2022). [https://doi.org/10.1061/\(ASCE\)ST.1943-541X.0003361](https://doi.org/10.1061/(ASCE)ST.1943-541X.0003361)
15. Jayathilakage, R., Sanjayan, J., Rajeev, P.: Comparison of rheology measurement techniques used in 3D concrete printing applications (2021)
16. Muthukrishnan, S., Ramakrishnan, S., Sanjayan, J.: Effect of microwave heating on interlayer bonding and buildability of geopolymer 3D concrete printing. *Constr. Build. Mater.* **265** (2020). <https://doi.org/10.1016/j.conbuildmat.2020.120786>
17. Geng, Z., Pan, H., Zuo, W., She, W.: Functionally graded lightweight cement-based composites with outstanding mechanical performances via additive manufacturing. *Addit. Manuf.* **56**, 102911 (2022). <https://doi.org/10.1016/j.addma.2022.102911>
18. Andrew Ting, G.H., Noel Quah, T.K., Lim, J.H., Daniel Tay, Y.W., Tan, M.J.: Extrudable region parametrical study of 3D printable concrete using recycled glass concrete. *J. Build. Eng.* **50**, 104091 (2022). <https://doi.org/10.1016/j.job.2022.104091>

19. Weng, Y., Li, M., Zhang, D., Tan, M.J., Qian, S.: Investigation of interlayer adhesion of 3D printable cementitious material from the aspect of printing process. *Cem. Concr. Res.* **143** (2021). <https://doi.org/10.1016/j.cemconres.2021.106386>
20. Korolev, E. V., Zuong, T.K., Inozemtsev, A.S.: A method for providing internal care for cement hydration in 3D printing formulations. *Vestn. MGSU* **6**, 834–846 (2020). <https://doi.org/10.22227/1997-0935.2020.6.834-846>
21. Inozemtsev, A.S., Korolev, E.V., Zuong, T.K.: Analysis of existing technological solutions for 3D printing in construction. *Vestn. MGSU* **7**, 863–876 (2018). <https://doi.org/10.22227/1997-0935.2018.7>
22. Zuong, T.: High-strength lightweight fiber-reinforced concrete for structural purposes: Thesis, Moscow (2020)
23. Poluektova, V.A.: Patterns of surface phenomena and modification of polymer-mineral dispersions for additive technologies: Thesis (2022)
24. Novosadov, N.I., Poluektova, V.A.: Strength characteristics of a polymer-cement composite for additive technologies. In: III International Scientific and Practical Conference, pp. 133–137 (2017)
25. Chernysheva, N.V., Lesovik, V.S., Volodchenko, A.A., Glagolev, E.S., Drebezgova, M.Y.: Composite materials using energy-saving technogenic raw materials for 3D additive technologies. In: Science-Intensive Technologies and Innovations Collection of Reports of the International Scientific-Practical Conference, pp. 452–456 (2016)
26. Lesovik, V.S., et al.: Modern three-dimensional technologies and factors restraining them. *Bull. BSTU* **1**, 22–30 (2016). <https://doi.org/10.12737/23011>
27. Klyuev, S.V., Khezhev, T.A., Pukharenko, Y.V., Klyuev, A.V.: Experimental study of fiber-reinforced concrete structures. *Mater. Sci. Forum.* **945**, 115–119 (2019). <https://doi.org/10.4028/www.scientific.net/MSF.945.115>
28. Klyuev, S.V., Khezhev, T.A., Pukharenko, Y.V., Klyuev, A.V.: Fibers and their properties for concrete reinforcement. *Mater. Sci. Forum.* **945**, 125–130 (2019). <https://doi.org/10.4028/www.scientific.net/MSF.945.125>
29. Klyuev, S.V., Bratanovskiy, S.N., Trukhanov, S.V., Manukyan, H.A.: Strengthening of concrete structures with composite based on carbon fiber. *J. Comput. Theor. Nanosci.* **16**, 2810–2814 (2019). <https://doi.org/10.1166/jctn.2019.8132>
30. Klyuev, S.V., Khezhev, T.A., Pukharenko, Y.V., Klyuev, A.V.: Fiber concrete for industrial and civil construction. *Mater. Sci. Forum.* **945**, 120–124 (2019). <https://doi.org/10.4028/www.scientific.net/MSF.945.120>
31. Klyuev, S.V., Khezhev, T.A., Pukharenko, Y.V., Klyuev, A.V.: To the question of fiber reinforcement of concrete. *Mater. Sci. Forum.* **945**, 25–29 (2019). <https://doi.org/10.4028/www.scientific.net/MSF.945.25>
32. Slavcheva, G.S., Artamonova, O.V.: Rheological behavior of 3D printable cement paste : critical evaluation. *Инженерно-строительный журнал.* **8**, 97–108 (2018). <https://doi.org/10.18720/MCE.84.10>
33. Slavcheva, G.S., Britvina, E.A., Ibrayeva, A.I.: 3D construction printing: an operational method for controlling the rheological characteristics of mixtures. *Bull. Eng. Sch. Far East. Fed. Univ.* **41**, 134–143 (2019)
34. Slavcheva, G.S., Artamonova, O.V.: Rheological behavior of dispersed systems for building 3D printing: a control problem based on the capabilities of the Nano arsenal. *Nanotechnol. Constr. Sci. Internet J.* **3**, 107–122 (2018). <https://doi.org/10.15828/2075-8545-2018-10-3-107-122>
35. Mukhametrahimov, R.K., Gorbunova, P.S.: The role of dispersed reinforcement in the formation of technological properties and rheological properties of concrete mixtures for building 3D printing. In: Actual Problems and Prospects for the Development of the Construction Complex, pp. 270–274 (2019)
36. Mukhametrakhimov, R., Lukmanova, L.: Influence of cement-sand mortar mobility on the quality of 3D printed hardened composite. *Constr. Unique Build. Struct.* **94**, 9404 (2021). <https://doi.org/10.4123/CUBS.94.4>

37. Mukhametrakhimov, R., Lukmanova, L.: Structure and properties of mortar printed on a 3D printer. *Mag. Civ. Eng.* **102** (2021). <https://doi.org/10.34910/MCE.102.6>
38. Mukhametrakhimov, R., Lukmanova, L.: Influence of the technological properties of cement-sand mortar on the quality of 3D printed products. In: *IOP Conference Series: Materials Science and Engineering* (2020)
39. Mukhametrakhimov, R., Lukmanova, L.: Investigation of Portland cement in 3D concrete printing. In: Vatin, N. (eds.) *Proceedings of STCCE 2021*. STCCE 2021. LNCE, vol. 169, pp. 1–13. Springer, Cham (2021). https://doi.org/10.1007/978-3-030-80103-8_1
40. Mukhametrakhimov, R.K., Ziganshina, L.V.: Technology and quality control of 3DCP. *News KSUAE* **59**, 64–79 (2022). https://doi.org/10.52409/20731523_2022_1_64
41. Khaliullin, M., Dimieva, A.: Composite gypsum binder under introducing thermally activated clay as a pozzolanic component and adding ground limestone. In: *IOP Conference Series: Materials Science and Engineering* (2020)
42. Khaliullin, M., Gilmanshina, A.: The Effect of Additives of Mechanically Activated Mineral Fillers on the Properties of Composite Gypsum Binders. Presented at the (2021)
43. Khaliullin, M., Gilmanshina, A.: The effect of ground limestone on the properties of composite gypsum binder using thermally activated clay as a pozzolanic component. *E3S Web Conf.* **274**, 04006 (2021). <https://doi.org/10.1051/e3sconf/202127404006>
44. Mukhametrakhimov, R.K., Lukmanova, L.V.: Structure and properties of mortar printed on a 3D printer. *Mag. Civ. Eng.* **102**, 10206 (2021). <https://doi.org/10.34910/MCE.102.6>
45. Mukhametrakhimov, R., Lukmanova, L.: Influence of the technological properties of cement-sand mortar on the quality of 3D printed products. In: *IOP Conference Series: Materials Science and Engineering*. Institute of Physics Publishing (2020)
46. Garboczi, E.J.: Three-dimensional mathematical analysis of particle shape using X-ray tomography and spherical harmonics: application to aggregates used in concrete. *Cem. Concr. Res.* **32**, 1621–1638 (2002). [https://doi.org/10.1016/S0008-8846\(02\)00836-0](https://doi.org/10.1016/S0008-8846(02)00836-0)
47. Xue, G., Fu, Q., Xu, S., Li, J.: Macroscopic mechanical properties and microstructure characteristics of steel slag fine aggregate concrete. *J. Build. Eng.* **56**, 104742 (2022). <https://doi.org/10.1016/j.job.2022.104742>
48. Chen, Y., Çopuroğlu, O., Romero Rodriguez, C., Mendonca Filho, F.F.D., Schlangen, E.: Characterization of air-void systems in 3D printed cementitious materials using optical image scanning and X-ray computed tomography. *Mater. Charact.* **173**, (2021). <https://doi.org/10.1016/j.matchar.2021.110948>
49. Liu, J., Li, S., Gunasekara, C., Fox, K., Tran, P.: 3D-printed concrete with recycled glass: effect of glass gradation on flexural strength and microstructure. *Constr. Build. Mater.* **314**, 125561 (2022). <https://doi.org/10.1016/j.conbuildmat.2021.125561>
50. Kruger, J., du Plessis, A., van Zijl, G.: An investigation into the porosity of extrusion-based 3D printed concrete. *Addit. Manuf.* **37**, 101740 (2021). <https://doi.org/10.1016/j.addma.2020.101740>

Economic Feasibility of Manufacturing of Multi-hollow Floor Slabs from High-Strength Sand Concrete



Nikolai Palagin  and Marat Akhmetov

Abstract The authors carried out studies to identify the economic feasibility of manufacturing multi-hollow floor slabs of 220 mm height with round hollow cores of 159 mm in diameter, reinforced with non-stressed reinforcement of class A500C (series 1.141-1, issue 60) and prestressed reinforcement of class A800 (series 1.141-1, issue 63), made from high-strength sand concrete of classes HSSC60 and HSSC80 in comparison with slabs of heavy concrete of classes B15 ... B80 for Kazan (Russia, Tatarstan). The research was carried out due to the absence of large aggregate deposits in a large part of the European territory of the Russian Federation and the presence of deposits of sedimentary rocks that are limitedly suitable for use in reinforced concrete, with the widespread presence of sand, as well as the well-known economic efficiency of using high-strength concrete when manufacturing a load-bearing structures. The objectives of the research were to compare the technical and economic indicators of slabs of high-strength sand concrete of HSSC60 and HSSC80 classes with those of slabs of heavy concrete of classes B15...B80. Authors carried out the studies by the engineering method of calculation according to the current standards using the PC MS Excel. The strength and deformation characteristics of high-strength sand concrete were based on the results of the experiments of the department “Technology of building materials, products and structures” of the Kazan State University of Architecture and Engineering, obtained for concretes on the sands of local deposits. Studies have shown that increasing the class of heavy and high-strength sand concrete does not affect the overall consumption of steel. In terms of the cost of materials, in all cases the most economical is the use of heavy concrete of the minimum class (B15 in slabs with non-stressed reinforcement and B20 in slabs with pre-stressed reinforcement). The significance of the obtained results lies in the identification of economical solutions for the consumption of materials depending on the class of heavy and high-strength sand concrete for multi-hollow floor slabs up to 6.3 m

N. Palagin (✉)

Kazan State University of Architecture and Engineering, Kazan, Russia

e-mail: pal_nik11@mail.ru

M. Akhmetov

LLC Artemida», Izhevsk, Russia

long with A500C class non-stressed reinforcement and pre-stressed reinforcement of A800 class.

Keywords High-strength sand concrete · Heavy concrete · Multi-hollow floor slabs with non-stressed and pre-stressed reinforcement · Design load · Standard size · Economic efficiency

1 Introduction

In foreign construction, high-strength heavy concretes are increasingly used. It makes it possible to reduce the size of the sections of elements and save concrete and reinforcement [1]. In the Russian Federation, we began to use such concretes much later than abroad. The most famous buildings in our country made from heavy concrete of B80 ... B90 classes are the «Federation» complexes of the MIBC «Moscow City» in Moscow [2] and the «Lakhta Center» in St. Petersburg [3].

An alternative solution is the use of high-strength sand concrete (HSSC) [4]. Its composition includes quartz sand, divided into fractions, highly active binder, mineral and chemical additives, and organic-mineral modifiers. As a rule, plasticizers are used as chemical additives, which make it possible to significantly reduce the consumption of cement and the water-cement ratio of the concrete mixture: Sika VC5-800, Melflux 2651, C-3 [7] and others (SP-1, Sika 5NEW, Reotech DR8500, Melflux 2641).

The use of sand concrete has the following important advantages compared to heavy concrete: A homogeneous high quality structure and increased manufacturability, no need for storage and sorting facilities for the acceptance, processing and storage of large aggregates, lower energy consumption and less labor intensity, the possibility of building thin-walled structures and production of decorative concrete [5, 6].

In addition high-strength sand concrete, in comparison with equal-strength heavy concrete, has increased compressive and tensile strength, water and gas impermeability, wear and frost resistance, and higher corrosion resistance. This is due to an increase in the number of contacts of cement stone with fine aggregates, and also, due to the use of superplasticizers and mineral additives, a decrease in porosity in the zone of their contact.

It should be noted that, due to the large surface of the aggregates, sandy concretes, in comparison with heavy concretes of the same class, have increased cement consumption by 15–20%. For this reason, mineral additives are also introduced into their composition together with plasticizers, or cements of low water demand; or composite cements are used in their production. Also, sandy concretes have increased air entrainment. Highly effective thinners (for example, ground quartz sand, MK-85 microsilica, Melflux 2651 F superplasticizer) or foam carriers are used to reduce it [7].

The use of sand concrete in the construction industry of our country is due to the widespread presence of sand deposits. For example, in the Republic of Tatarstan there are more than 50 sand deposits. At the same time, the reserves of building sands are almost 1 billion m^3 , available for use—almost 300 million m^3 . In accordance with the concept of the ecological safety of the republic and the development of its natural resource complex in the period up to 2030, the building materials industry has set the goal to increase the composition of products based on local natural resources.

Due to the fact that the European part of the Russian Federation mainly has deposits of sedimentary carbonate rocks that are not very suitable for use in reinforced concrete structures, and the reserves of igneous rocks of coarse aggregate are limited, the use of sand concrete in their manufacture is relevant. In addition, a significant amount of energy and labor resources must be spent on the extraction of stone and its further processing into crushed stone. A concomitant result in obtaining crushed stone of a fraction of more than 5 mm is the formation of a significant amount (up to 20–30%) of screenings of a fraction, which occupy large areas and thereby violate the ecological balance of nature. Only a small amount of this waste is used in the production of limestone flour and mineral powder in the production of asphalt concrete. The mountains destruction during the extraction of crushed stone caused irreversible climatic consequences in Karelia, the Volga region and the North Caucasus. The use of sand instead of crushed stone as a filler for concrete is more environmentally friendly.

The use of high-strength sand concretes based on fractionated river sands of the Republic of Tatarstan with the use of chemical and mineral additives is an alternative solution compared to traditional heavy concretes, which include high-strength crushed stone from the Urals.

In KSUAE at the department of TBMPS the scientists obtained compositions of high-strength sandy concretes of classes HSSC60 ... HSSC80 based on sands from local deposits of the Volga and Kama rivers, the strength characteristics of which (R_b , R_{bt} , $R_{b,ser}$, $R_{bt,ser}$) are greater than the values for heavy concrete of the same classes by 1.05...2.05 times, and the elastic modulus E_b is 1.02...1.04 times less [8].

The review showed that in foreign and Russian sources there are practically no results of studies on the use of sand concrete in load-bearing structures. As a rule, authors studied questions of selection of their composition [9–13] and durability [14, 15]. They carried out studies to determine their various mechanical characteristics [16–19].

The papers [20] and [21] provide information about the great potential of using sand concrete in the construction of buildings and structures using 3D printing. A significant number of studies confirm the effectiveness of their use, due to the absence of large aggregates in the composition, the presence of which leads to defects in the concrete structure and large deformations of freshly printed layers.

Authors studied the issue of the cost-effectiveness of using high-strength sand concrete in load-bearing structures in [22–24].

The results of studies to identify the economic feasibility of manufacturing long cylindrical shells from prefabricated and monolithic high-strength sandy concrete of HSSC60 and HSSC80 classes compared from heavy concrete of classes B20...B80

are given in [22]. It has been established that, concerning Kazan, the use of HSSC compared to heavy one makes it possible to reduce significantly the consumption of materials (steel—up to 30.6%, concrete—up to 15.9%) and their total cost (up to 20.3%). It was found in [23] that the use of shallow shells of positive Gaussian curvature from prefabricated and monolithic high-strength sandy concrete of the HSSC60 and HSSC80 classes, compared with their use from the heavy B25...B80 classes concerning Kazan, also significantly reduces the consumption of materials (steel—up to 43.0%, concrete—up to 12.9%) and the total cost of materials—up to 29.4%. In [24], it was established that, concerning Kazan, the production of rectangular columns of one-story industrial buildings with bridge cranes (series 1.424.1–5) from high-strength sand concrete of the HSSC60 and HSSC80 classes is, as a rule, more economical than from heavy concrete of traditional classes B20...B40. Savings range from 24.8 to 109.5%, on the total consumption of materials, and 53.8...71.5% on the total consumption of steel.

Despite the advantages above, at the moment in Russia and the Republic of Tatarstan, the use of sand concrete is mainly limited to floor coverings for industrial buildings and the manufacture of small-piece and decorative finishing products.

According to the above, we should continue to work on the use of HSSC in the manufacture of various building structures, including bearing ones. Economic efficiency is one of the main criteria for the expediency of its use. In accordance with this, the authors considered the topic in the article is relevant for the development of the construction industry of both the Republic of Tatarstan and Russia as a whole.

The purpose of the research was to identify the economic feasibility of manufacturing multi-hollow floor slabs with 220 mm height with round hollow cores of 159 mm diameter, reinforced with A500C class non-stressed reinforcement (series 1.141-1, issue 60) and pre-stressed reinforcement of class A800 (series 1.141-1, issue 63) made from high-strength sand concrete of classes HSSC60 and HSSC80 in comparison with slabs of heavy concrete of classes B15...B80 concerning to Kazan.

The tasks of the research were the following:

1. To identify the effect of increasing the class of heavy and high-strength sand concrete of multi-hollow floor slabs with non-stressed and pre-stressed reinforcement on the required and accepted steel consumption, as well as on the total cost of materials;
2. To compare the technical and economic indicators of slabs made from high-strength sand concrete of HSSC60 and HSSC80 classes with the indicators of slabs with non-stressed reinforcement made from heavy concrete of B15 class and pre-stressed slabs with pre-stressed reinforcement of A800 class made from heavy concrete of B20 class.

2 Materials and Methods

The authors studied reinforced concrete multi-hollow slabs made from heavy concrete of medium strength of B15, B25, B40 classes and heavy high-strength

concrete of B60, B80 classes (with non-stressed reinforcement), slabs made from heavy concrete of medium strength of B20, B30, B40 and heavy high-strength concrete of B60, B80 classes (with pre-stressed reinforcement), slabs made from high-strength sand concrete of HSSC60 and HSSC80 classes (with non-stressed and pre-stressed reinforcement). Dimensions of slabs in plan with non-stressed reinforcement are 2380×990 , 2380×1490 , 4180×990 , 4180×1490 mm, with pre-stressed reinforcement are 4780×990 , 4780×1490 , 6280×990 , 6280×1490 mm.

The calculated load without slab's own weight was 3 and 8 kN/m². The authors took the length of the slabs and loads as the minimum and maximum used in the standard series. The class of longitudinal working reinforcement is A500C (in slabs with non-stressed reinforcement), A800 (in slabs with pre-stressed reinforcement), transverse and structural reinforcement—B500C, mounting loops—A240C. The authors used electro-thermal method on the mold stops as the tension method. We considered 16 variants of slabs different in standard sizes and (or) load. The whole amount of considered results was 112.

The authors performed the calculations of slabs for I and II groups of limit states in the operation stage. The following regulatory documents were used: The Set of Rules SP 63.13330.2018 «SNiP 52-01-2003 Concrete and reinforced concrete structures. Basic provisions» (amended No. 1, No. 2), SP 311.1325800.2018 «Concrete and reinforced concrete structures made from high-strength concrete. Design Rules», methodological guide «Calculation of reinforced concrete structures without pre-stressed reinforcement (to SP 63.13330.2012)»—M., 2015, «Methodological guide for the calculation of pre-stressed reinforced concrete structures (to SP 63.13330.2012)»—M., 2015.

The authors took the strength and deformation characteristics of heavy concrete and reinforcement in accordance with the above standards, and high-strength sand concrete of HSSC60 and HSSC80 classes—according to the results of research by the Department of TBMPs KSUAE obtained for concrete on the sands of local deposits. For heavy concrete of B80 class and high-strength sand concrete of HSSC80 class, the values of the design resistance of concrete to axial compression (R_b) and tension (R_{bt}) are taken considering a reduction factor that takes into account the increase in the fragility of high-strength concrete due to a decrease in creep deformations ($\gamma_{b,br}$), equal to

$$\gamma_{b,br} = (360 - B)/300, \quad (1)$$

where B is the class of concrete.

Partial safety for intended purpose reliability (γ_n) was assumed to be 1.0.

To automate the calculations, 8 flowcharts and the corresponding unified calculation program in MS Excel were compiled. Testing of the program showed complete convergence with the results of manual counting. According to this program calculations were performed for all the above 112 cases of various variants of slabs, types and classes of concrete.

The design of the slabs was carried out in compliance with the following design requirements. Longitudinal working reinforcement was installed through two

hollow-cores. If there was no need for calculation transverse reinforcement was not installed. The minimum diameter of the reinforcement class A500C is 6 mm, A800 is 10 mm, B500C is 3 mm. Grids and frames were made with the fulfillment of the weldability condition. The design of the mounting loops was taken according to the standard series.

For all the cases considered, using the program compiled in MS Excel, the consumption of materials (concrete and reinforcement), as well as their total cost, was determined. The cost of both types of concrete and reinforcement was taken at prices relevant for Kazan for the II quarter of 2022.

3 Results

Some calculation results are shown in Figs. 1, 2, 3 and 4, on which the following marking of slabs is adopted: «PK»—a round-hollow slab, the first digit is the length of the slab in dm., the second is the width in dm., the third is the design load without taking into account the own weight of the slab, kN/m².

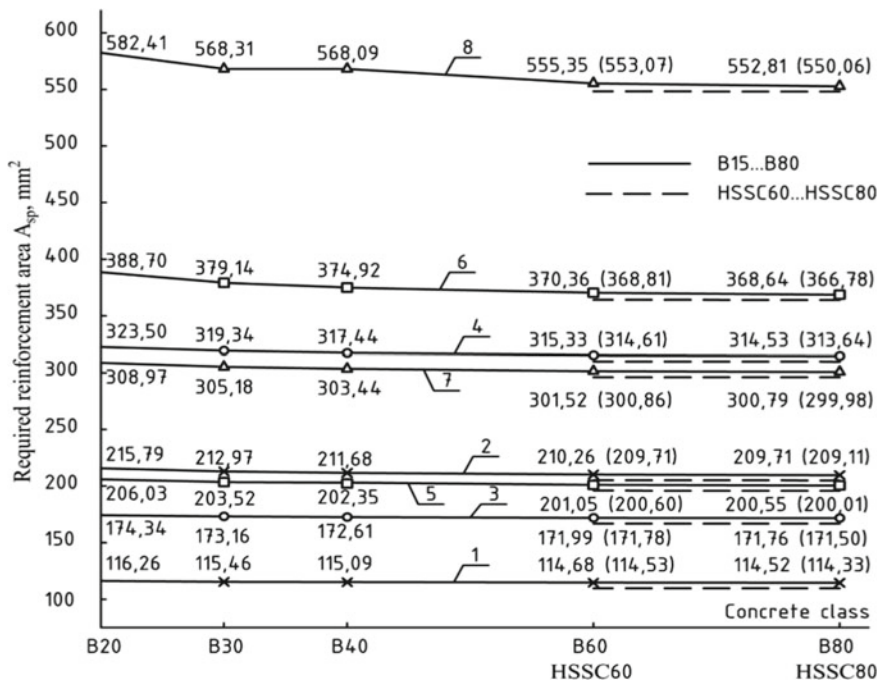


Fig. 1 Graphs of the required area of pre-stressed reinforcement on the type and class of concrete. 1—PK48.10.3; 2—PK48.10.8; 3—PK48.15.3; 4—PK48.15.8; 5—PK63.10.3; 6—PK63.10.8; 7—PK63.15.3; 8—PK63.15.8. The values in brackets are for the HSSC60 and HSSC80 classes

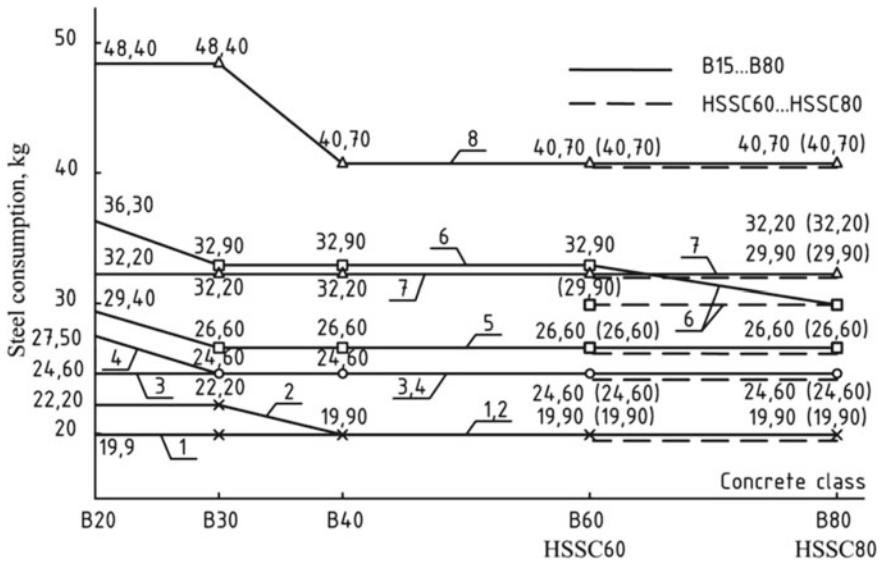


Fig. 2 Graphs of the accepted total consumption of steel in pre-stressed slabs on the type and class of concrete. 1—PK48.10.3; 2—PK48.10.8; 3—PK48.15.3; 4—PK48.15.8; 5—PK63.10.3; 6—PK63.10.8; 7—PK63.15.3; 8—PK63.15.8. The values in brackets are for the HSSC60 and HSSC80 classes

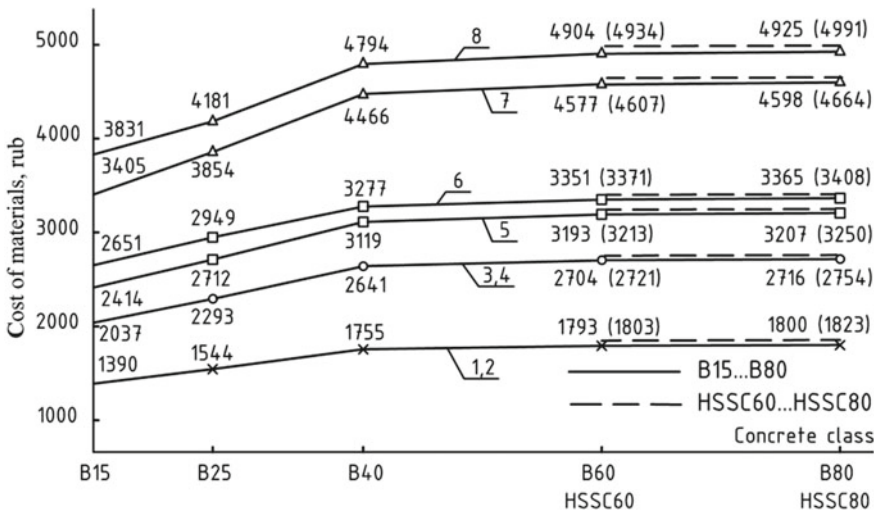


Fig. 3 Graphs of the total cost of materials for slabs with non-tensioned reinforcement on the type and class of concrete. 1—PK24.10.3; 2—PK24.10.8; 3—PK24.15.3; 4—PK24.15.8; 5—PK42.10.3; 6—PK42.10.8; 7—PK42.15.3; 8—PK42.15.8. The values in brackets are for the HSSC60 and HSSC80 classes

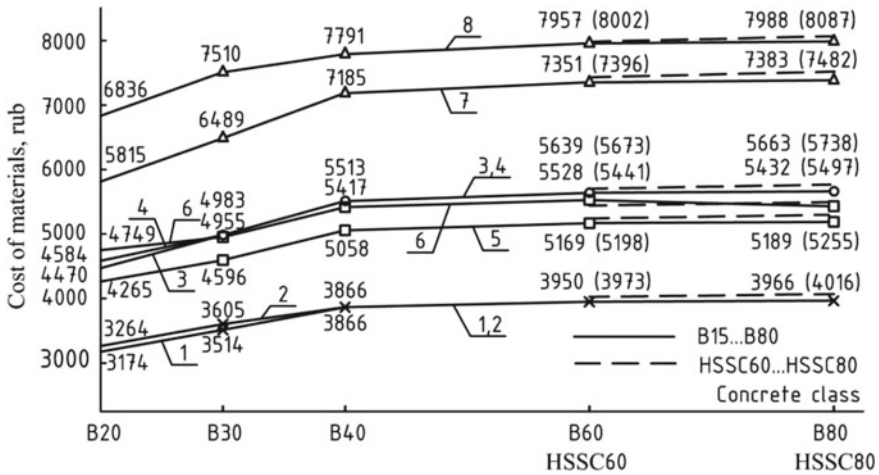


Fig. 4 Graphs of the total cost of materials for slabs of pre-stressed reinforcement on the type and class of concrete. 1—PK48.10.3; 2—PK48.10.8; 3—PK48.15.3; 4—PK48.15.8; 5—PK63.10.3; 6—PK63.10.8; 7—PK63.15.3; 8—PK63.15.8. The values in brackets are for the HSSC60 and HSSC80 classes

Comparison of the technical and economic indicators of heavy concrete slabs of B15 ... B80 classes, HSSC60 and HSSC80 with non-stressed and pre-stressed reinforcement for all considered cases showed the following:

- with an increase in the class of heavy and high-strength sand concrete, the required cross-sectional area of non-stressed (A_s) and pre-stressed reinforcement (A_{sp}) decreases. Thus, in slabs with non-stressed reinforcement, with an increase in the class of heavy concrete from B15 to B80, the decrease in the required A_s was from 0.51 to 3.18%, depending on the size of the slab and the load, and from HSSC60 to HSSC80—from 0.04 up to 0.23%. In pre-stressed slabs, with an increase in the class of heavy concrete from B20 to B80, the decrease in the required A_{sp} was from 1.48 to 5.16%, and from HSSC60 to HSSC80—from 0.16 to 0.55% (Fig. 1);
- the use of high-strength sand concrete of HSSC60 and HSSC80 classes compared with heavy concrete of classes B15 and B20 reduces the required cross-sectional area of reinforcement A_s by 0.56 ... 3.39%, reinforcement A_{sp} —by 1.63 ... 5.64% (Fig. 1);
- the manufacture of slabs from high-strength sand concrete of HSSC60 and HSSC80 classes, in comparison with their manufacture from high-strength heavy concrete of B60 and B80 classes, leads to a decrease in the required cross-sectional area of reinforcement A_s by 0.06 ... 0.41%, reinforcement A_{sp} by 0.28 ... 0.097% (Fig. 1);
- increasing the class of heavy and high-strength sand concrete has practically no effect on the accepted total steel consumption, which, as a rule, remains constant for a specific slab size for one load. It decreased in slabs with non-tensioned reinforcement only in 2 cases out of 56 (i.e., in 3.5% of cases)—by 9.8 and

- 10.4%—and in pre-stressed slabs in 7 cases out of 56 (12.5%)—by 9.1...15.9% (Fig. 2);
- the use of high-strength sand concrete of HSSC60 and HSSC80 classes in comparison with high-strength heavy concrete of B60 and B80 classes in 31 cases out of 32 gives the same accepted total consumption of steel. Only in 1 case (3.1%)—in the slab PK63.10.8 with concrete HSSC60 class—there was a decrease by 3.0 kg (9.1%) compared with the use of B60 class concrete (Fig. 2);
 - in terms of the total cost of materials (rebar and concrete), in all cases, the most economical was the use of heavy concrete of the minimum class (B15 in slabs with non-stressed reinforcement and B20 in pre-stressed ones) (Figs. 3 and 4). Savings in comparison with the use of heavy concrete of B80 class amounted to 26.9 to 35.0% in slabs with non-stressed reinforcement, from 14.4 to 27.0% in pre-stressed ones. Compared with the use of high-strength sand concrete of the HSSC80 class—from 28.6 to 37.0% in slabs with non-stressed reinforcement and from 15.8 to 28.7% in pre-stressed ones;
 - the total cost of materials in the manufacture of both slabs with non-stressed reinforcement and pre-stressed slabs from high-strength heavy concrete of B60 and B80 classes is almost always lower than when they are made from high-strength sand concrete HSSC60 and HSSC80, respectively (by 0.6 ... 0.7% when comparing B60 and HSSC60 and by 1.2...1.4% when comparing B80 and HSSC80). Only in 1 case out of 16 (6.3%)—for the slab PK63.10.8 when using heavy concrete of B60 class—it turned out to be higher by 1.6% compared to the use of high-strength sandy concrete of class HSSC60, which is associated with a higher by 3.0 kg (9.1%) with the total consumption of steel (Fig. 2).

In addition as a result of the calculations, it was revealed that:

- in 98 cases out of 112 (87.5%), transverse reinforcement was not required by calculation and therefore was not installed;
- in 98 cases out of 112 (87.5%) normal cracks were not formed;
- in all cases the longitudinal working reinforcement, taken from the calculation for the I group of limit states, turned out to be sufficient to meet the requirements of the II group.

4 Discussion

The analysis of the obtained results shows that an increase in the class of heavy and high-strength sand concrete leads to a decrease in the required amount of longitudinal tensile non-stressed reinforcement A_s and pre-stressed reinforcement A_{sp} , and also, in most cases, to the rejection of the installation of transverse reinforcement.

At the same time, this has practically no effect on the accepted total steel consumption, which, as a rule, remains constant for a specific slab size for one load.

In all cases, the most economical in terms of the total cost of materials was the use of heavy concrete of the minimum class (B15 in slabs with non-stressed reinforcement and B20 in slabs with pre-stressed reinforcement). The production of slabs from high-strength sand concrete of the HSSC60 and HSSC80 classes turned out to be the most expensive in terms of the cost of materials. Compared to B15 class heavy concrete slabs with non-stressed reinforcement, they turned out to be 28.6...37.0% more expensive, compared to B20 class heavy concrete slabs with pre-stressed reinforcement—by 15.8... 28.7%.

The results obtained were the result of: 1. the impossibility of increasing or decreasing the height of the section of the slabs, which significantly limited the increase in the shoulder of the internal pair of forces with an increase in the strength of concrete in the compressed zone, and also did not lead to a decrease in concrete consumption; 2. the need to fulfill structural requirements when reinforcing with tensile longitudinal and transverse reinforcement; 3. obtaining in all cases the value of the relative height of the compressed zone, not exceeding its boundary value $\xi \leq \xi_R$, as a result of which the compressed reinforcement was installed according to design requirements.

In all previous similar studies [22–24] indicated in the Introduction section, the use of high-strength sand concrete of the HSSC60 and HSSC80 classes led to a decrease in the total consumption of steel and the total cost of materials. This was a consequence of: 1. the possibility of reducing the cross section of elements ([22, 23]); 2. by exceeding the design values obtained by calculation of the area of the working reinforcement; 3. different ratio of the cost of reinforcement and concrete at the time of the study.

The results obtained in these studies are significant, because they made it possible to identify cost-effective solutions for the consumption of materials, depending on the type and class of heavy and high-strength sand concrete used for multi-hollow floor slabs up to 6.3 m long with non-stressed reinforcement (with reinforcement A500C class) and with pre-stressed reinforcement (with reinforcement A800 class).

5 Conclusion

Based on the results of the studies performed, the authors made the following conclusions:

1. An increase in the class of heavy and high-strength sand concrete leads to a decrease in the required amount of longitudinal tensioned non-stressed and pre-stressed reinforcement, and also, in most cases, to the abandonment of the installation of transverse reinforcement. At the same time, this has practically no effect on the accepted total steel consumption, which, as a rule, remains constant for a specific slab size for one load;
2. In all cases, the most economical in terms of the total cost of materials was the use of heavy concrete of the minimum class (B15 in slabs with non-tensioned

- reinforcement and B20 in slabs with pre-stressed reinforcement). The production of slabs from high-strength sand concrete of the HSSC60 and HSSC80 classes turned out to be uneconomical;
3. The main results obtained are explained by the following: 1) the impossibility of increasing or decreasing the height of the section of the slabs, which significantly limited the increase in the shoulder of the internal pair of forces with an increase in the strength of concrete in the compressed zone, and also did not lead to a decrease in concrete consumption; 2) the need to fulfill structural requirements when reinforcing with tensile longitudinal and transverse reinforcement; 3) obtaining in all cases the value of the relative height of the compressed zone, not exceeding its boundary value, as a result of which the compressed reinforcement was installed according to design requirements;
 4. The studies carried out made it possible to identify economical solutions for hollow-core floor slabs up to 6.3 m long with A500C class non-stressed reinforcement and A800 class pre-stressed reinforcement, taking into account the type and class of concrete used.

References

1. Mindess, S.: Developments in the formulation and reinforcement of concrete, p. 423 (2019). <https://doi.org/10.1016/C2017-0-03347-5>
2. Kaprielov, S.S., Travush, V.I., Karpenko, N.I.: Modified high-strength concretes of classes B80 and B90 in monolithic structures. *Build. Mater.* **3**, 9–13 (2008)
3. Ilyukhina, E.A., Lakhman, S.I., Miller, A.B., Travush, V.I.: Constructive solutions for the high-rise building “Lakhta center” in St Petersburg. *Stroitelnye nauki* **3**, 110–121 (2019)
4. Karpenko, N.I., Kaprielov, S.S., Bezgodov, I.M., Moiseenko, G.A., Stepanov, M.V.: Study of shrinkage deformations of fine-grained high-strength concrete and steel-fiber-reinforced concrete with a rational fiber content. *Izvestia of Higher Educational Institutions. Series “Technology of the Textile Industry”*, vol. 3, pp. 227–230 (2018)
5. Vdovin, E., Mavliev, L., Konovalov, N.: Modification by zeolite-containing additive the road-building materials based on carbonate crushed stone-sand mixtures and cements. In: Vatin, N. (ed.) *Proceedings of STCCE 2021*. STCCE 2021. LNCE, vol. 169, pp. 308–317. Springer, Cham (2021). https://doi.org/10.1007/978-3-030-80103-8_33
6. Mavliev, L., Vdovin, E., Stroganov, V., Konovalov, N.: Road cement-mineral materials with granulometric and hydrophobic additives. In: Sinitsyn, A. (ed.) *Sustainable Energy Systems: Innovative Perspectives*. SES 2020. LNCE, vol. 141, pp. 20–28. Springer, Cham (2021). https://doi.org/10.1007/978-3-030-67654-4_3
7. Morozov, N.M., Khozin, V.G., Muginov, Kh.G.: Features of the formation of the structure of modified sandy concrete. *Stroitelnye Materialy* **9**, 72–73 (2010)
8. Morozov, N.M., Khozin, V.G.: Sandy concrete of high strength. *Build. Mater.* **11**, 25–26 (2005)
9. Khozin, V.G., Khokhryakov, O.V., Nizamov, R.K.: Carbonate cements of low water demand - promising binders for concrete. *Concr. Reinforced Concr.* **601**(1), 15–28 (2020)
10. Khozin, V.G., Khokhryakov, O.V., Nizamov, R.K., Kashapov, R.R., Baishev, D.I.: Experience of nanomodification of cements of low water demand. *Ind. Civ. Constr.* **1**, 53–57 (2018)
11. Vdovin, E.A., Khozin, V.G., Ilyina, O.N., Kuklin, A.N., Gizdatullin, A.R., Sharafutdinov, B.D.: Experience in the use of polymer composite reinforcement in the construction of concrete airfield pavements in the airport complex in Kazan. *Sat. scientific papers: innovative materials*,

- technologies and equipment for the construction of modern transport facilities. Belgorod State Technological University. V.G. Shukhov, pp. 86–90 (2013)
12. Boucedra, A., Bederina, M., Ghernouti, Y.: Study of the acoustical and thermo-mechanical properties of dune and river sand concretes containing recycled plastic aggregates. *Constr. Build. Mater.* **256** (2020). <https://doi.org/10.1016/j.conbuildmat.2020.119447>
 13. Ouassila, B., Houria, H., Leila, K., Mouloud, B., Assia, A., Chaher, R.: Valorization of marble's waste as a substitute in sand concrete. *Adv. Concr. Constr.* **2**(9), 217–225 (2020). <https://doi.org/10.12989/acc.2020.9.2.217>
 14. Thangapandi, K., et al.: Durability phenomenon in manufactured sand concrete: Effects of zinc oxide and alcofine on behavior. *Silicon* **13**(4), 1079–1085 (2021). <https://doi.org/10.1007/s12633-020-00494-2>
 15. Tolstoy, A.D., Fomina, E.V., Milkina, A.S.: Durability of fine-grained high-strength concrete in corrosive environment. In: Paper Presented at the IOP Conference Series: Materials Science and Engineering, vol. 753, no. 3 (2020). <https://doi.org/10.1088/1757-899X/753/3/032036>
 16. Peng, Z., Li, D., Zhou, Y., Ren, S.: Failure criterion in stress space for coral reef sand concrete under biaxial compression. *Wuhan Ligong Daxue Xuebao/J. Wuhan Univ. Technol.* **40**(5), 66–70 (2018). <https://doi.org/10.3963/j.issn.1671-4431.2018.05.011>
 17. Li, Z., Wang, G., Yang, S., Ju, G.: Experimental study on mechanical properties and stress-strain constitutive relations of desert sand concrete. *Yingyong Lixue Xuebao. Chin. J. Appl. Mech.* **36**(5), 1131–1137 (2019). <https://doi.org/10.11776/cjam.36.05.B063>
 18. Li, B., Yin, L., Fan, L.: Analysis on flexural fatigue performance of manufactured sand concrete. *Jianzhu Cailiao Xuebao. J. Build. Mater.* **20**(5), 801–807 (2017). <https://doi.org/10.3969/j.issn.1007-9629.2017.05.024>
 19. Dong, Z., Wu, G., Xu, Y.: Bond and flexural behavior of sea sand concrete members reinforced with hybrid steel-composite bars presubjected to wet-dry cycles. *J. Compos. Constr.* **21**(2) (2017). [https://doi.org/10.1061/\(ASCE\)CC.1943-5614.0000749](https://doi.org/10.1061/(ASCE)CC.1943-5614.0000749)
 20. Mukhametrakhimov, R., Lukmanova, L.: Influence of the technological properties of cement-sand mortar on the quality of 3D printed products. *IOP Conf. Ser. Mater. Sci. Eng.* **890**, 012082 (2020). <https://doi.org/10.1088/1757-899X/890/1/012082>
 21. Mukhametrakhimov, R.K., Lukmanova, L.V.: Structure and properties of mortar printed on a 3D printer. *Mag. Civ. Eng.* **102**(2), Article number 10206 (2021). <https://doi.org/10.18720/MCE.10206>
 22. Palagin, N., Dul'miyeva, A.: Cost-effective design of long cylindrical shells of high-strength sand concrete. *IOP Conf. Ser. Mater. Sci. Eng.* **890**, 012078 (2020). <https://doi.org/10.1088/1757-899X/890/1/012078>
 23. Palagin, N., Nikitin, G., Sadrutdinova, A.: Erection of flat shells of positive Gaussian curvature made from high-strength sand concrete and its economic efficiency. In: Vatin, N.I., Tamrazyan, A.G., Plotnikov, A.N., Leonovich, S.N., Pakrastins, L., Rakhmonzoda, A. (eds.) *Advances in Construction and Development*. CDLC 2020. LNCE, vol 197. Springer, Singapore (2022). https://doi.org/10.1007/978-981-16-6593-6_11
 24. Palagin, N.G., Nikitin, G.P., Trunov, A.N.: Economic efficiency of manufacturing rectangular columns of one-story industrial buildings with overhead cranes from high-strength sand concrete abstract. *News KSUAE 2022* **59**(1), 41–53 (2022). https://doi.org/10.52409/20731523_2022_1_41

Perspectives of Interactions CAD and GIS Systems



Liliia Talipova , Egor Grebenyuk , Gleb Ogurtsov , Aleksei Ismailov , and Yuriy Lazarev 

Abstract Methods of data transformations from CAD-environmental to GIS and back were studied in the article. Geographical auxiliary info was added by height, rotation angle and dependencies by other elements. Visual displaying elements in GIS-environmental, rendering in 3d, logic of keeping source information models, requirements for geometry representation and features for working with unique objects were considered.

Keywords GIS · CAD · Interactions GIS CAD · Open street map · Coordinate systems transformation · Keeping information models · Description of geography position

1 Introduction

Evolution of program software and government policy in area of digitalization of industry, building and objects exploitation leads to necessity to working with big data frames, with extended information about physical material properties or cost estimation of its repairing.

The aggregator of information in this case is a territorial or federal executive authority that establishes a set of requirements for the objects of information models or documentation that is submitted within the framework of the project. In other cases, the information storage scheme may imply links to other databases of other departments.

In general, geoinformation systems (hereinafter, GIS) are characterized by working with a large set of objects and sets of attributes (properties) of a limited type of storage (geometric representation). A great difficulty in this case is the process of data exchange between GIS and computer-aided design systems (hereinafter, CAD) both in one direction and in the other. A two-way exchange is needed because work on attributing elements and uploading them to geoinformation systems is carried out

L. Talipova (✉) · E. Grebenyuk · G. Ogurtsov · A. Ismailov · Y. Lazarev
Peter the Great St. Petersburg Polytechnic University, 29 Politechnicheskaya Street, St.
Petersburg 195251, Russia
e-mail: talipova_lv@spbstu.ru

in parallel with the preparation of working/project documentation, where basic information is stored initially in the information model of the object. The reverse side of data transmission is more typical for the case of providing information to individual design organizations as initial data on design objects, as well as for internal use and revision by employees of a state authority.

Building information modeling performed using CAD and GIS provides an architectural representation of objects. CAD focuses on the micro-level representation of the buildings themselves or individual structures, and GIS provides a macro-level representation of the external environment. Thus, CAD systems have advantages in terms of extended geometric and semantic information throughout the life cycle of an object, but they do not contain and do not allow to manage geographical information, while the GIS system is a wide area covering decision-making based on geovisualizations and geospatial modeling, but they do not store the information required building codes [1]. Thus, for many years, the purpose of spatial databases created using GIS was to provide information about large spaces and areas outside buildings, and CAD technologies were focused mainly on small rooms, internal and external objects. The significant development of GIS technologies and new tools for rapid data collection (for example, laser scanning) and the growing needs of users led to geoinformation modeling of the space inside buildings, and CAD technologies, in turn, began to be used for increasingly large spaces outside buildings. The combination of technologies allows you to create a comprehensive view of the environment based on integrated data. The use of integrations in the industry requires systematic theories. Integration hypotheses make it possible to create more complex applications throughout the entire project lifecycle [2].

As a result of the research, three typical modes of CAD-GIS integration are distinguished, namely: “CAD sources and loading to GIS”, “GIS sources and CAD import” and “CAD and GIS are equally involved”, which are classified based on the different dominant positions of the two technologies [3]. Developers, users and scientists note that some CAD and GIS work is repetitive, which confirms the need to combine technologies. Their proposed integrated CAD/GIS spatial database environment allows storing GIS and CAD data and using the same data by both types of systems simultaneously and in a consistent manner. This allows CAD systems to get simultaneous access to CAD and GIS data, which may be required, for example, in the process of analyzing a building and its immediate use of the environment. At the same time, GIS can obtain up-to-date building data needed for spatial analysis, building management, or route mapping in navigation applications. The concept assumes a pragmatic approach based on the joint use of Industry Foundation Classes (IFC) and CityGML schemas from a single database for CAD and GIS applications in their original forms of practical applications using an additional integrated CAD-GIS scheme [4–10].

There are also studies describing the disadvantages of this approach in terms of using a bundle to create visualizations and analysis, suggesting the use of a shapefile. The results of this study show that converting IFC to a shapefile is easier and more flexible to implement than converting IFC to CityGML, as well as the computer graphics method can increase the efficiency and reliability of converting CAD to GIS [11–15]. Shapefiles do not support a three-dimensional description of objects,

unlike more modern IFC or CityGML specifications, in addition, the format has limitations in terms of field sizes, weights, and in general is much less flexible than the designated modern formats.

Public media resources (by web-cameras or Google-panoramas) have become an important source for collecting geospatial data and urban analytics, obtaining information and supporting informed decisions. This was caused by the proliferation of large-scale image processing platforms, advances in computer vision and machine learning, as well as the availability of computing resources. Most of the research on this topic is based on data from Google Street View, as a result of which it was concluded that street images have now become an integral component of urban analytics and GIS science, which is used in many areas with numerous applications—from vegetation and transport analysis to medical and socio-economic research. Researchers also highlight the trend of using crowdsourcing images for street viewing, which is facilitated by services such as Mapillary, Google Street View and KartaView [17]. The use of Google Street View is also used to obtain data on the Sky Survey Coefficient (SVF)—an indicator of urban geometry, which at street level was quite limited due to the high cost of field research. However, the automatic extraction of SVF from Google Street View panoramas involves a lot of computational processes. Based on this, a tool integrated with GIS (GSV2SVF) was developed to simplify the workflow of extracting SVF data from GSV images. As by-products, in addition to SVF, the results of each panorama are accompanied by a tree viewing coefficient (TVF) and a building viewing coefficient (BVF), which together can provide a more holistic characterization of the external built environment [18]. The use of by-products of such services allows for further research to assess the sustainability of urban development and change the compactness of the urban form. The research is aimed at comparing the level of compactness of quarters in the GIS environment by six broad indicators, for the evaluation of which a composite compactness index (CCI) based on a multi-criteria approach to decision-making (MCDM) was developed. The research results can serve as a preliminary guide for planners, policy makers and development agencies when designing a more sustainable and efficient urban form due to compact urban development on the scale of a microdistrict [19–24].

Technologies using satellite images, GIS and landscape indicators are also used to assess and monitor the use of urban land. Research in this area is based on a two-component method: Land classification based on remote sensing and analysis of land changes based on GIS. In particular, a stratified image classification strategy was adopted in combination with a GIS-based spatial reclassification procedure to display land classes from Landsat Thematic Mapper (TM) scenes. The research results indicate the usefulness of integrating remote sensing with GIS and landscape metrics in the analysis of land changes [25, 26].

The CAD-GIS bundle allows assessing the vulnerability of interdependent infrastructures. So, based on the interaction of technologies, studies were conducted on the relationship of storm sewers, construction and road transport during flooding in cities. The study examines the synchronization of available tools, such as building information modeling (CAD systems), GIS and specialized computing mechanisms

(DCE) to perform interdisciplinary tasks. The proposed approach consists of the following key components: Collection of building information from a BIM model, physical modeling of infrastructure performance before and after hazards using DCE, and data integration and geospatial analysis for decision-making on a GIS platform. The integration under consideration is a new modeling paradigm that will provide an effective opportunity to formalize joint efforts between various infrastructure stakeholders and intelligently generate reliable high-resolution vulnerability assessment results [27–29].

Using CAD and GIS integration it is also possible to create an infrastructure information platform—a shared data environment used to help manage a city using geographical information and data about buildings and objects. At the same time, it is important to integrate technologies into the management of underground utilities during excavation. The problem with the traditional system is the use of two-dimensional drawings and the storage of unreliable information in the absence of updates, which makes the system as a whole inefficient. The research suggests the introduction of a new integrated structure for management systems based on the comparison of IFC and CityGML, which provides an effective management system and facilitates the optimization of the project by providing three-dimensional spatial information in real time during the construction process and acts as an integrated information database [30–37].

In emergency response and pedestrian route planning, indoor and outdoor geospatial data with a network data model is largely used, however, indoor geospatial data collection requires a large amount of time. Several studies have used the Architecture, Design and Construction (AEC) model to create models of internal networks. These models are subject to input data types, and attributes of internal construction objects are usually incomplete; Consequently, the integration of building information modeling (BIM) and Geographic Information Systems (GIS) can benefit integrated indoor and outdoor applications. To enable data interaction with buildingSMART, an open BIM standard called Industry Foundation Classes (IFC) is supported. The study suggests the use of a multi-purpose geometric network model (MGNM) based on CAD. To ensure interaction, the transformation of IFC to MGNM includes the following steps: Extracting building information from IFC, isolating MGNM information from building information, and constructing topological information of MGNM communication with a GIS geodata. Studies have shown that MGNM can be automatically generated from CAD and applied to connect internal and external functions in a multi-purpose application [38].

The research also touches upon the possibility of creating a multi-scale historical bundle of technologies with digital recording tools with geospatial information. The creation of an integrated historical CAD-GIS bundle for a complex of monuments included in the UNESCO list is being discussed. The work is aimed at studying the pros and cons of a new parametric 3D environment capable of integrating data, methods and tools for processing both BIM and GIS in the case of historical buildings and sites [39].

Integration of CAD and GIS is also possible using LiDAR technologies. Parameterization of roads, in this case, performed for the purpose of traffic monitoring,

autonomous vehicle navigation, condition assessment and delivery of data in real time to drivers is possible using a point cloud, which is collected using LiDAR and is a solution for fixing in real conditions. The proposed system makes the creation of a CAD-GIS bundle more flexible and is not limited to the use of certain algorithms for processing point clouds [40–42].

As a perspective of working with CAD-GIS integration, research has proposed a solution to one of the existing GIS problems. According to the research data, it is proposed to use public relations in order to supplement and clarify the existing information necessary for making spatial decisions. Accordingly, these studies used GIS as a result of public participation or information generated by citizens as reference data to verify the results of processes [43–45].

Also, with the increase in the number of intelligent devices, spatial data has grown exponentially, which has led to the problem of storing volumes of data, which requires a scalable and efficient system capable of storing, querying, analyzing and visualizing large spatiotemporal data. The research suggests building an integrated GIS platform of a cloud terminal designed to meet a large volume of spatiotemporal data. As a result of the conducted studies deployed on an internal organizational cluster using real-time datasets, it was proved that the SuperMap GIS data engine provides the necessary performance [46–49].

Other studies solve the problem of simplifying the GIS model by developing a framework for creating simplified solid-state models of buildings. In the proposed structure, a set of levels of detail was defined to correspond to solid-state models of buildings and three unique implementation problems were identified that can be solved using a semantic approach, including the identification of external objects, the definition of overlap differences and the creation of actual external walls. The results of the study show that the use of semantics from CAD makes it possible to simplify the transformation and simplification of building models, which makes information from CAD the most practical for use in GIS [50–53].

Despite the number of studies conducted, the question of the compatibility of CAD and GIS technologies remains open, and the existing numerous implementation methods are contradictory and cover only high-level and semantic aspects.

According to the researchers' experimental results, three main integration problems are identified: Automated processing of complex IFC architectural models, integration of existing GIS data on subsurface resources into CAD and geographical linking of CAD models for their use in GIS software [54, 55].

Based on the analysis, it was revealed that this problem has not received due attention in the works of compatriots and most of the scientific works are not relevant at the moment.

The development of the Internet and the principles of open source against the background of expensive commercial access to resources has led to the emergence and development of a community of users from all over the world who are engaged in daily updating of available information on buildings and infrastructure within the framework of the Open Street Maps project (hereinafter, OSM). Many companies

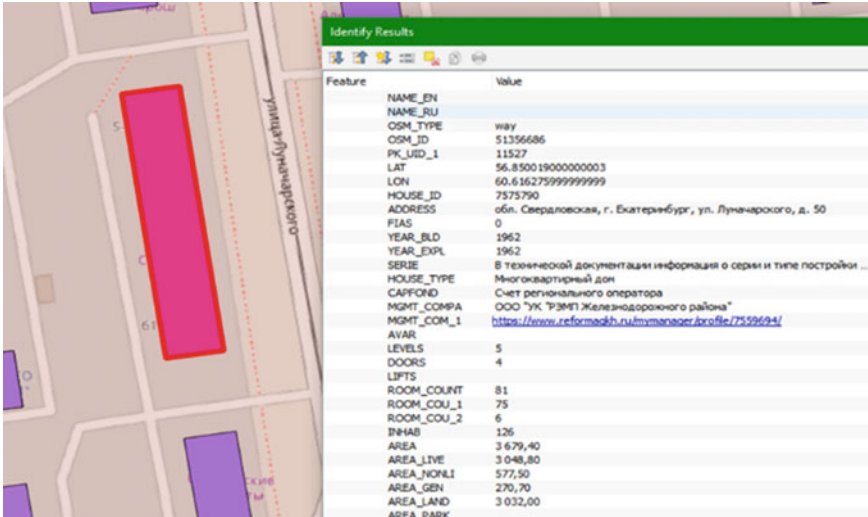


Fig. 1 Data for residential house with extended-info in QGIS environmental

around the world are also improving this database with the help of hired employees—and in some places OSM data is superior in quality to data acquired commercially (with the exception of materials from real research and design projects).

OSM data is present in the form of vector data (objects peculiar to all GIS—points, lines, polygons and groups) with attributes of a fixed type (Fig. 1). Individual executive authorities provide commercial access to extended data on the geometric content of OSM. For example, the Russian Ministry of Housing and Communal Services within the framework of the program “Housing and Communal Services Reform” allows you to download the above-mentioned expanded information on some buildings as part of commercial access. The file raster version of OSM is also used—which is used as a base map-substrate in many services.

This article will be devoted to the consistent coverage of individual moments of the transfer of information models from the design environment to the GIS environment and back:

- real coordinates and the combination of the used coordinate system with the world geographical;
- addition of the description of the geospatial position by height, angle of rotation, dependence on other elements;
- visual display of elements in GIS, as in a real model; visualization in 3d;
- logic of tabular data storage;
- storage of initial information models, requirements for geometric representation and features of working with unique non-typical objects.

2 Methods

The coverage of all the issues raised was based on the practical experience of the authors in solving the tasks set within the framework of the state tender for updating the technical means of traffic management in St. Petersburg, as well as the early research of the authors when borrowing individual practices from the experience of domestic and foreign colleagues, whose materials were partially presented in the review of literary sources.

The use of common coordinates (in a specific system) in the project is regulated by the terms of reference and, as a rule, there is a key for translating data into the world geographical coordinate system WGS-84. Of interest are cases when modeling is not conducted in general coordinates, or there is a need to linearly transform the representation of the model for unloading into the used coordinate system in the form of a common solid model, or in the form of separate geometric entities with a set of attributes. If the functionality of the software used is available, the first case is possible when using the description of the current coordinate system (or numerical parameters of the transition to it) in the header information of 3d data representation files—for example, the IFC specification, the `IfcCoordinateReferenceSystem` class or CityGML format. In the absence of any other possibility, or the unavailability of the mentioned options in data formats, there is an option for direct transformation of the coordinates of the object or the site on which it is located in the private formulation of the problem 7-parametric Helmert transformation.

An alternative option for reprojecting may be the case of exporting descriptions of all elements to a set of attributes with replacing the geometric position of the object with a point/line and re-inserting elements into the primary modeling environment already in common coordinates. But as a rule, this is used only at the initial stage of the project for geometric and textual primitives, or for more complex objects, but with the condition that they can be specified in their original form (with a set of properties) in the software data format, which is not feasible due to the proprietary format of almost all popular CAD systems on the market, whereas general specifications of the type IFC returns only non-editable geometry when opened.

An important place of data transmission is the possibility of their subsequent “reproduction” in another environment in the same form, or in a form reflecting their properties and position, as in the original CAD. In this question, we can conditionally divide the elements into typical and unique, if we talk about the set of information that needs to be transferred to the knowledge base and how to replace it, so as not to store the element as an integral information model.

For example, when transferring an information model of a building to GIS for operation, then no tables will be enough to completely replace the model with data—you will have to store a geometric representation in the form of a 3D model in the form of a file path in the attributes of the object in addition to the uploaded general metrics of the object in the form of a set of attributes; on the other hand, the same models of public transport stops represent they are typical models whose characteristics do not change, which allows you to replace a stop point in GIS with a polygon/point

with the attribute of the series of this object. As for the reverse import of objects from GIS to CAD, the situation is a little more complicated here. If we talk about standard objects, they can be created from the database of families of this software with parameters from the attributes of an object from GIS, whereas integral models of buildings are in the form of open/closed specifications of the IFC type, CityGML in general are not transmitted as editable entities, and in this case it is necessary in addition to presenting the information model in one from open formats, store the representation of the model in the original design format, which loses the advantage of GIS as an aggregator system of various topology data and free exchange of them between CAD systems.

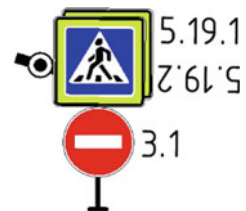
Let's focus more specifically on the possibility of representing an array of objects (a complex object) by a group of simple/one simple. For example, a group of road signs of various types on one rack.

In this article it was mentioned that in GIS objects exist in the form of simple geometric shapes (points, lines, polygons and their groups)—this concerns elements whose geospatial position is important for displaying and using the object/its properties. Separately, in the form of tables or classifier tables, groups of parameters describing the properties of a given object or individual objects related to the data geometrically can be stored so that their position on this can be easily reproduced—this allows you not to store the position of all the components of a complex object, but to fix only the supporting parts. Another example is that a multi-layered wall of a building can be represented as a flat line with the attribute of the thickness of the structural layers, the marks of the bottom and top of the wall, also with the properties of the useful area of voids/materials—adjusted for holes and structural nodes that are not transmitted by individual elements (or that are not needed for the model as a whole within this GIS).

With regard to the earlier mentioned example of a rack with road signs, in addition to the location of the rack, the following parameters are introduced that make it possible to link individual elements to this: The serial number of the sign relative to the bottom/side of the support, the angle of rotation of the sign relative to the direction of movement of the road, the type of support (single rack—then the signs will be placed vertically; U-shaped support—then horizontally, and the support itself will be set by two or more coordinates—at the location of the supports) (Fig. 2).

The need for repeated modeling in CAD of a group of elements from GIS leads to the need to use a hierarchy of elements, which was not initially implemented directly in the GIS data tables—that is, assigning each element within a group of elements

Fig. 2 The example of representation the road sign in environmental of IndoorTrafficPlan



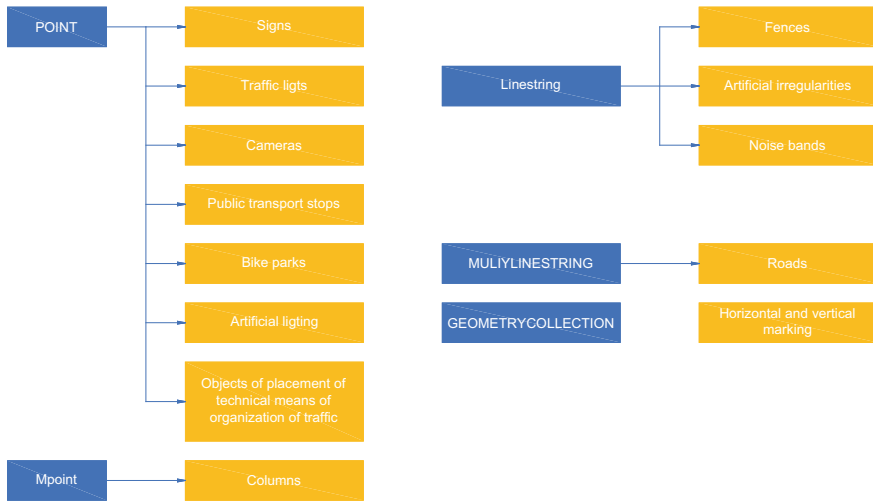


Fig. 3 Dataview of IndorTrafficPlan’s objects to standard GIS objects

(signs, posts, fences—if we talk about roadside arrangement) a link to the parent element. For individual signs, this is the place of attachment, for fencing—the edge of the lane, for racks—the axes of roads and the side of traffic, etc. The best way to represent an identifier is a unique value of a parameter that exists in the singular in this database table. Almost everywhere, the so-called GUID—128-digit character sets with a probability of meeting the same one equal to $1/2^{128}$ are taken as such a parameter. Then the visible method of loading data from GIS to CAD may look like loading an array of data within the desired polygon, modeling a geometric representation in the form of axes in a hierarchy from bottom to top, applying additional geometric transformation operations to accurately position objects on the ground, replacing simple display forms with typical objects/blocks/families using object parameters. The reverse method of loading modified/new data will be based on the principle of matching element identifiers and updating existing/forming new ones (Fig. 3).

In recent years, there has been a tendency for CAD to switch to a database structure, that is, the model project is essentially a set of metadata and properties (in tabular form), where geometry objects are stored in the database of standard program families and in the model description file are present only in the form of records, and not a whole representation, copied from the model. A striking representative of the current logic (storing each new instance of an element in the model file) is the structure of the model in IFC, the size of which is inflated to huge values when using a large number of identical objects located in different places of the model.

In the case of the transition of the storage logic to the database form, it will become much easier to transfer information to GIS—it will already be stored in tabular form, and have a related structure with other elements through, again, unique identifiers.

3 Results and Discussion

As in our own and in the works of other authors, the logic of reducing the representation of the information model to databases, a smooth transition from a set of geometry to a hierarchical structure of the model, or rather its elements among themselves, is traced.

It is worth noting that software vendors are in no hurry in the long term to provide full access to read their proprietary formats for models. This actually leads to the loss of the market by them and the very need to constantly buy both software ownership licenses and additional support packages and modules for this. Individual developers and companies, being members of the so-called Open Design Alliance, can access these proprietary formats, but this is not a universal solution to the problem.

Table 1 shows the general order of data presentation.

Table 1 Logic of working for data transferring

Source environmental	Target environmental	Method of the data transferring	Description of method
IndorTrafficPlan	QGIS	Reading XML-file with program code (C#)	All model elements are replaced to planar GIS-objects (points, lines, polygons) that were generated programmatically from XMK project's file
QGIS	IndorTrafficPlan	Saving scene to raster	Current scene with objects and their styles in QGIS is saving as georeferencing raster image; in environmental target again creating objects by it Note: Variant with generation of XML scheme of project is difficult because the tools of development from vendor are missing
(AutoCAD) Civil3D	QGIS	By embedded export in vector data formats	The CAD primitives (points, lines, polygons) are converted automatically; more compound elements (alignments, surfaces and etc.) are simplified to simple objects The transferring is possible only for old-data formats. In general, for necessary scenarios, we need to use programmatically export with API

(continued)

Table 1 (continued)

Source environmental	Target environmental	Method of the data transferring	Description of method
QGIS	Civil3D (AutoCAD)	By embedded import from vector formats	Inserted GIS data as CAD's drawing primitives need to be changed programmatically. Embedded CAD's functional lets only change visual style of objects and manage their layer's relationships. Only old GIS data formats are supported

The visible way to apply a unified strategy for working with data in a particular model development environment (CAD), while maintaining the ability to export data without restrictions to external GIS databases and vice versa, is to use standard forms of exporting geometric and attribute representation of the model to open specifications like IFC, and in some cases also use additional features of the software interface uploading information (its API). The popularity of the IFC format and its support by almost all CAD systems allows at least in one direction—data transfer from CAD to GIS to adhere to one approach of data flow migration, while in the opposite direction—if necessary, to upload a data package from GIS back to CAD, you have to use exclusively the capabilities of the software interface in the absence of other specifications supported by the data Software for importing objects in editing mode.

The disadvantage of the IFC format for GIS is obvious—the specification implies storing all elements of the model as a text file, all occurrences of a particular family are duplicated many times, the size of the model and the presence of complex curved surfaces in it is directly proportional to the weight of the file and the convenience of working with it. Popular movements in the world in support of Open Source are trying to link IFC as a de facto standard for data information models from CAD with the standard for presenting information models in the context of a geoinformation model—CityGML, but all this is a rather lengthy process due to the disinterest in the development of such a scheme by large monopolists in the GIS market—Esri, which promotes its own GeobIM ecosystem, closely integrated with the global CAD market leader Autodesk through its cloud model repositories. As a planning scenario for future work, we consider the next scheme (Fig. 4).

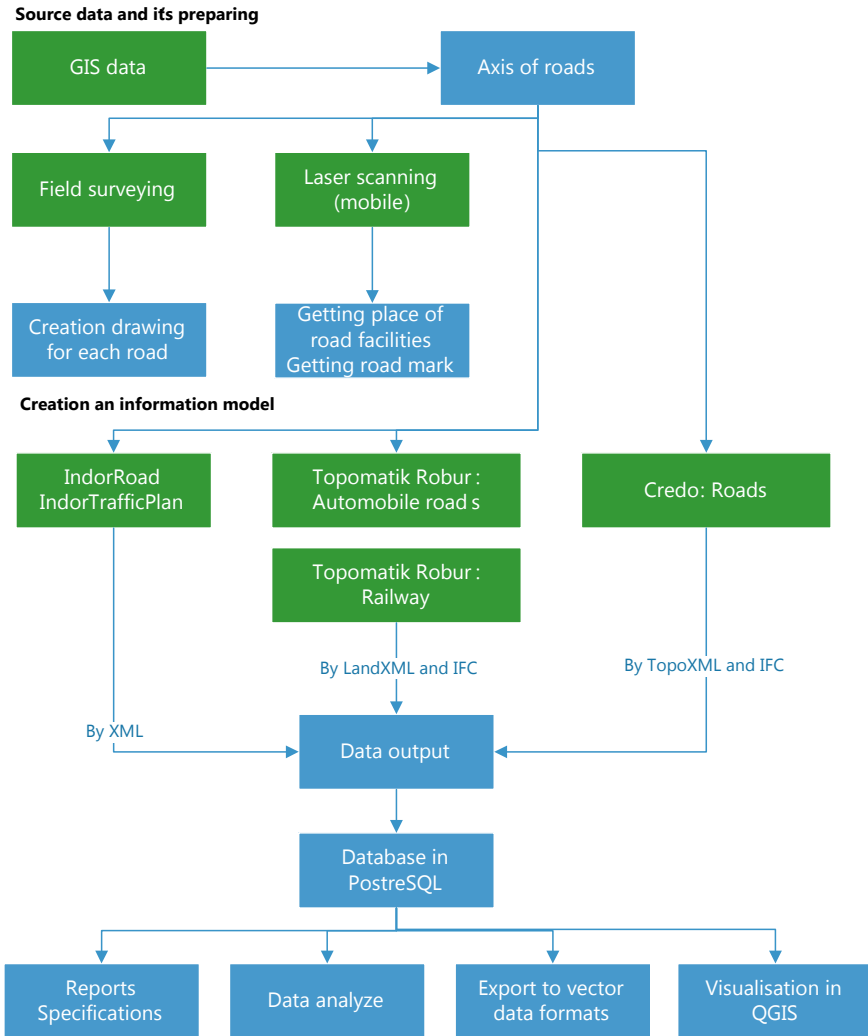


Fig. 4 A planning scenario for work

4 Conclusions

It is worth noting the growing interest in the issues of data exchange between CAD and GIS both on the part of users and on the part of public authorities interested in a unified approach to the organization of data storage and transmission between individual executive bodies and directly for the project organizations themselves. The increasing functionality of geoinformation systems and the openness of the source

code of the modules make it possible to expand the use of individual data analytics algorithms indefinitely to the sides.

References

1. Demir Altıntaş, Y., Ilal, M.E.: Loose coupling of GIS and BIM data models for automated compliance checking against zoning codes. *Autom. Constr.* **128**(January) (2021). <https://doi.org/10.1016/j.autcon.2021.103743>
2. Song, Y., et al.: Trends and opportunities of BIM-GIS integration in the architecture, engineering and construction industry: a review from a spatio-temporal statistical perspective **6**(12) (2017)
3. Wang, H., Pan, Y., Luo, X.: Integration of BIM and GIS in sustainable built environment: a review and bibliometric analysis. *Autom Constr* **103**, 41–52 (2019). <https://doi.org/10.1016/j.autcon.2019.03.005>
4. Wyszomirski, M., Gotlib, D.: A unified database solution to process BIM and GIS data. *Appl. Sci.* **10**(23), 1–19 (2020). <https://doi.org/10.3390/app10238518>
5. Tobiáš, P.: An investigation into the possibilities of BIM and GIS cooperation and utilization of GIS in the BIM process. *Geoinform. FCE CTU* **14**(1), 65–78 (2015). <https://doi.org/10.14311/gi.14.1.5>
6. Khan, M.S., Park, J., Seo, J.: Geotechnical property modeling and construction safety zoning based on GIS and BIM integration. *Appl. Sci. (Switzerland)* **11**(9) (2021). <https://doi.org/10.3390/app11094004>
7. Wilhelm, L., Donaubaauer, A., Kolbe, T.H.: Integration of BIM and environmental planning: the CityGML EnvPlan ADE. *J. Digit. Landscape Archit.* **6**, 332–343 (2021). <https://doi.org/10.14627/537705030>
8. Deng, Y., Cheng, J.C.P., Anumba, C.: Mapping between BIM and 3D GIS in different levels of detail using schema mediation and instance comparison. *Autom. Constr.* **67**, 1–21 (2016). <https://doi.org/10.1016/j.autcon.2016.03.006>
9. Jusuf, S., Mousseau, B., Godfroid, G., Soh, J.: Path to an integrated modelling between IFC and CityGML for neighborhood scale modelling. *Urban Sci.* **1**(4), 25 (2017). <https://doi.org/10.3390/urbansci1030025>
10. Gilbert, T., Barr, S., James, P., Morley, J., Ji, Q.: Software systems approach to multi-scale GIS-BIM utility infrastructure network integration and resource flow simulation. *ISPRS Int. J. Geo Inf.* **7**(8), 310 (2018). <https://doi.org/10.3390/ijgi7080310>
11. Zhu, J., Wu, P., Chen, M., Kim, M.J., Wang, X., Fang, T.: Automatically processing IFC clipping representation for BIM and GIS integration at the process level *Appl. Sci. (Switzerland)* **10**(6) (2020). <https://doi.org/10.3390/app10062009>
12. Gabriele, M., Previtali, M., Information, G.: HBIM-GIS integration with an IFC-to-shapefile approach : THE2021 **8**(October), 11–14 (2020)
13. Zhu, J., Wu, P.: Towards effective BIM/GIS data integration for smart city by integrating computer graphics technique. *Remote Sens.* **13**(10) (2021). <https://doi.org/10.3390/rs13101889>
14. Chen, Q., Chen, J., Huang, W.: Visualizing large-scale building information modeling models within indoor and outdoor environments using a semantics-based method. *ISPRS Int. J. Geo Inf.* **10**(11) (2021). <https://doi.org/10.3390/ijgi10110756>
15. Özsoy Özbay, A.E., Sanrı, K.I., Ünün, H.C.: Visualization of seismic vulnerability of buildings with the use of a mobile data transmission and an automated GIS-based tool. *Structures* **24**, 50–58 (2020). <https://doi.org/10.1016/j.istruc.2020.01.004>
16. Hijazi, I., Donaubaauer, A., Kolbe, T.H.: BIM-GIS integration as dedicated and independent course for geoinformatics students: merits, challenges, and ways forward. *ISPRS Int. J. Geo Inf.* **7**(8), 1–12 (2018). <https://doi.org/10.3390/ijgi7080319>

17. Biljecki, F., Ito, K.: Street view imagery in urban analytics and GIS: a review. *Landscape Urban Plan.* **215**, 104217 (2021). <https://doi.org/10.1016/j.landurbplan.2021.104217>
18. Liang, J., Gong, J., Zhang, J., Li, Y., Wu, D., Zhang, G.: GSV2SVF—an interactive GIS tool for sky, tree and building view factor estimation from street view photographs. *Build. Environ.* **168** (2020). <https://doi.org/10.1016/j.buildenv.2019.106475>
19. Rahman, M.H., Islam, M.H., Neema, M.N.: GIS-based compactness measurement of urban form at neighborhood scale: the case of Dhaka, Bangladesh. *J. Urban Manage.* (2021). <https://doi.org/10.1016/j.jum.2021.08.005>.
20. Ritcher, C.: From base map to inductive mapping—three cases of GIS implementation in cities of Karnataka, India. *Compr. Geogr. Inf. Syst.* **3**, 411–421 (2018). <https://doi.org/10.1016/B978-0-12-409548-9.09688-3>
21. Pedro, J., Silva, C., Pinheiro, M.D.: Integrating GIS spatial dimension into BREEAM communities sustainability assessment to support urban planning policies, Lisbon case study. *Land Use Policy* **83**, 424–434 (2019). <https://doi.org/10.1016/j.landusepol.2019.02.003>
22. Koopmans, S., Heusinkveld, B.G., Steeneveld, G.J.: A standardized physical equivalent temperature urban heat map at 1-m spatial resolution to facilitate climate stress tests in the Netherlands. *Build. Environ.* **181**, 106984 (2020). <https://doi.org/10.1016/j.buildenv.2020.106984>
23. Moretti, N., Ellul, C., Re, C.F., Papapetros, N., Dejaco, M.C.: GeoBIM for built environment condition assessment supporting asset management decision making. *Autom. Constr.* **130**, 103859 (2021). <https://doi.org/10.1016/j.autcon.2021.103859>
24. Ferla, G., Caputo, P., Colaninno, N., Morello, E.: Urban greenery management and energy planning: a GIS-based potential evaluation of pruning by-products for energy application for the city of Milan. *Renew. Energy* **160**, 185–195 (2020). <https://doi.org/10.1016/j.renene.2020.06.105>
25. Liu, T., Yang, X.: Monitoring land changes in an urban area using satellite imagery, GIS and landscape metrics. *Appl. Geogr.* **56**, 42–54 (2015). <https://doi.org/10.1016/j.apgeog.2014.10.002>
26. Vdovin, E., Mavliev, L., Stroganov, V.: Interaction of clay soil components with Portland cement and complex additive based on octyltriethoxysilane and sodium hydroxide. *IOP Conf. Ser. Mater. Sci. Eng.* **890**(1), 012031 (2020)
27. Yang, Y., et al.: GIS-DCEs enabled vulnerability assessment of interdependent infrastructures – A case of stormwater drainage-building-road transport Nexus in urban flooding. *Autom. Constr.* **125**, 103626 (2021). <https://doi.org/10.1016/j.autcon.2021.103626>
28. Nefros, K.C., Kitsara, G.S., Photis, Y.N.: Using geographic information systems (GIS) to develop prioritization maps in urban search and rescue operations, after a natural disaster. Case study: the municipality of Agia Paraskevi, Athens, Greece. *IFAC PapersOnLine* **30**(51), 360–395 (2018). <https://doi.org/10.1016/j.ifacol.2018.11.332>
29. Abbas, A., et al.: Modelling data of an urban drainage design using a geographic information system (GIS) database. *J. Hydrol.* **574**, 450–466 (2019). <https://doi.org/10.1016/j.jhydrol.2019.04.009>
30. Mavliev, L., Vdovin, E.: Structure of road soil cement compositions modified by complex additive based on organosilicon compounds and electrolytes In: *E3S Web of Conferences*, vol. 140, p. 02016 (2019)
31. Huang, Y.S., Shih, S.G., Yen, K.H.: An integrated GIS, BIM and facilities infrastructure information platform designed for city management. *J. Chinese Inst. Eng. Trans. Chinese Inst. Eng. Ser. A* **4**(44), 293–304 (2021). <https://doi.org/10.1080/02533839.2021.1897481>
32. Vdovin, E., Stroganov, V., Kononov, N.: Modification of road soil cement with activated fillers. In: Vatin, N., Borodinecs, A., Teltayev, B. (eds.) *Proceedings of EECCE 2020. EECCE 2020. LNCE*, vol 150, pp. 335–345. Springer, Cham. https://doi.org/10.1007/978-3-030-72404-7_33
33. Zadeh, P.A., Wei, L., Dee, A., Pottinger, R., Staub-French, S.: BIM-CityGML data integration for modern urban challenges. *J. Inf. Technol. Constr.* **24**, 318–340 (2019). <https://doi.org/10.36680/j.itcon.2019.017>
34. Gröger, G., Plümer, L.: Interoperable semantic 3D city models. *ISPRS J. Photogrammetry Remote Sens.* **71**, 12–33 (2012). <https://doi.org/10.1016/j.isprsjprs.2012.04.004>

35. Hajji, R., Yaagoubi, R., Meliana, I., Laafou, I., Gholabzouri, A.El.: Development of an integrated BIM-3D GIS approach for 3D Cadastre in Morocco. *ISPRS Int. J. Geo Inf.* **10**(5) (2021). <https://doi.org/10.3390/ijgi10050351>
36. Han, Z.H., Wang, Z.K., Gao, C., Wang, M.X., Li, S.T.: Application of GIS and BIM integration technology in construction management. *IOP Conf. Ser. Earth Environ. Sci.* **526**(1) (2020). <https://doi.org/10.1088/1755-1315/526/1/012161>.
37. Sani, M.J., Rahman, A.A.: GIS and BIM integration at data level: a review. In: *International Archives of the Photogrammetry, Remote Sensing and Spatial Information Sciences - ISPRS Archives*, vol. 42, no. 4/W9, pp. 299–306. <https://doi.org/10.5194/isprs-archives-XLII-4-W9-299-2018>
38. Teo, T.A., Cho, K.H.: BIM-oriented indoor network model for indoor and outdoor combined route planning. *Adv. Eng. Inform.* **30**(3), 268–282 (2016). <https://doi.org/10.1016/j.aei.2016.04.007>
39. Barazzetti, L., Roncoroni, F.: Generation of a multi-scale historic BIM-GIS with digital recording tools and geospatial information. *Heritage* **4**(4), 3331–3348 (2021). <https://doi.org/10.3390/heritage4040185>
40. Barazzetti, L., Previtali, M., Scaioni, M.: Roads detection and parametrization in integrated BIM-GIS using LiDAR. *Infrastructures* **5**(7) (2020). <https://doi.org/10.3390/infrastructures5070055>
41. Zubaer, K.H., Alam, Q.M., Toha, T.R., Salim, S.I., Islam, A.B.M.A..Al.: Towards simulating non-lane based heterogeneous road traffic of less developed countries using authoritative polygonal GIS map. *Simul. Model. Pract. Theory* **105**, 102516 (2020). <https://doi.org/10.1016/j.simpat.2020.102156>
42. Salim, M., Jassal, K.: Feasibility study of a peripheral ring road around Chandigarh city using GIS. *Mater. Today Proc.* (2021). <https://doi.org/10.1016/j.matpr.2021.03.323>
43. Depietri, Y., Ghermandi, A., Campisi-Pinto, S., Orenstein, D.E.: Public participation GIS versus geolocated social media data to assess urban cultural ecosystem services: instances of complementarity. *Ecosyst. Serv.* **50**, 101277. <https://doi.org/10.1016/j.ecoser.2021.101277>
44. Vdovin, E.A., Stroganov, V.F.: Optimization of complex frost-resisting additives in line with operational requirements towards freezing temperature in road dressing constructions. *IOP Conf. Ser. Mater. Sci. Eng.* **832**(1), 012034 (2020)
45. Hasanzadeh, K., Kajosaari, A., Häggman, D., Kyttä, M.: A context sensitive approach to anonymizing public participation GIS data: from development to the assessment of anonymization effects on data quality. *Comput. Environ. Urban Syst.* **83**, 101513 (2020). <https://doi.org/10.1016/j.compenvurbsys.2020.101513>
46. Li, W., Winter, P.L., Milburn, L.A., Padgett, P.E.: A dual-method approach toward measuring the built environment - sampling optimization, validity, and efficiency of using GIS and virtual auditing. *Health Place* **67**, 102482 (2021). <https://doi.org/10.1016/j.healthplace.2020.102482>
47. Vdovin, E.A., Stroganov, V.F.: Modification of cement-bound mixtures with sodium formate additives for the construction of pavement bases at low air temperatures. *IOP Conf. Ser. Mater. Sci. Eng.* **786**(1), 012065 (2020)
48. Sharma, M., Bunde, M.: Analysis of NoSQL schema design approaches using HBase for GIS data. *Procedia Comput. Sci.* **152**, 59–65 (2019). <https://doi.org/10.1016/j.procs.2019.05.027>
49. Ashkezari, A.D., Hosseinzadeh, N., Chebli, A., Albadi, M.: Development of an enterprise geographic information system (GIS) integrated with smart grid. *Sustain. Energy Grids Networks* **14**, 25–34 (2018). <https://doi.org/10.1016/j.segan.2018.02.001>
50. Cooper, C.H.V., Chiaradia, A.J.F.: 3-D spatial network analysis for GIS, CAD, Command Line and Python. *SoftwareX* **12**, 100525 (2020). <https://doi.org/10.1016/j.softx.2020.100525>
51. Zhu, J., Wu, P., Anumba, C.: A semantics-based approach for simplifying IFC building models to facilitate the use of BIM models in GIS. *Remote Sens.* **13**(22) (2021). <https://doi.org/10.3390/rs13224727>
52. Kang, T.W., Hong, C.H.: A study on software architecture for effective BIM/GIS-based facility management data integration. *Autom. Constr.* **54**, 25–38 (2015). <https://doi.org/10.1016/j.autcon.2015.03.019>

53. Beck, S.F., Abualdenien, J., Hijazi, I.H., Borrmann, A., Kolbe, T.H.: Analyzing contextual linking of heterogeneous information models from the domains BIM and UIM. *ISPRS Int. J. Geo Inf.* **10**(12), 807 (2021). <https://doi.org/10.3390/ijgi10120807>
54. Zhu, A.X., Zhao, F.H., Liang, P., Qin, C.Z.: Next generation of GIS: must be easy. *Ann. GIS* **1**(27), 71–86 (2021). <https://doi.org/10.1080/19475683.2020.1766563>
55. Ohori, K.A., Diakit , A., Krijnen, T., Ledoux, H., Stoter, J.: Processing BIM and GIS models in practice: experiences and recommendations from a GeoBIM project in The Netherlands. *ISPRS Int. J. Geo Inf.* **7**(8) (2018). <https://doi.org/10.3390/ijgi7080311>

Corrosion Processes in Building Materials, Products and Structures



Vladimir Berdnikov, Victor Stroganov , Evgenii Vdovin , Ilya Stroganov, and Viktor Gasilov

Abstract The object of the study is the oxidation–reduction reactions of nitrogen and the known values of standard electrode potentials of the corrosion processes in building materials, products, and structures. The importance of searching for consistent (consistent with the known) values, determination of missing and correction of available reference data is relevant and in demand both for specialists who study electrochemical and corrosion processes and engineers who calculate durability of buildings and structures. The available reference data on oxidation–reduction half-reactions and the known values of standard electrode potential was analyzed. The peculiarities of nitrogen half-reaction behavior in acid and alkaline media were established. As a result, three groups of components in the media were identified. The first group of components is stable in acid and alkaline media, the second group is stable in acid and the third group is stable in an alkaline medium. The components of the second and third groups can pairwise change each other under the change of the medium pH. The peculiarities of the components behavior in media have necessitated the search for the consistent values of standard electrode potential for the acid and alkaline media. The relationship between these values for $\text{pH} = 0$ and $\text{pH} = 14$ was established. The reference array was supplemented with eight oxidation–reduction half-reactions with the known values of standard electrode potential. A full search of the consistent values of standard electrode potential for acid and alkaline media was carried out and structuring with the use of potential schemes was performed. The information array of standard electrode potentials and oxidation–reduction half-reactions is not fully described in the reference literature, which complicates and hinders both the calculations and practical application of corrosion processes, and restrains the development of promising directions in various branches of chemistry and construction materials science. The developed technique

V. Berdnikov

Moscow Automobile and Road Construction State Technical University, Cheboksary, Russia

V. Stroganov · E. Vdovin (✉)

Kazan State University of Architecture and Engineering, Kazan, Russia

e-mail: vdovin007@mail.ru

I. Stroganov · V. Gasilov

Kazan National Research Technological University, Kazan, Russia

of searching for consistent values was used to supplement the existing information array of standard electrode potentials and oxidation–reduction half-reactions.

Keywords Corrosion processes in construction • Consistent values of standard electrode potentials

1 Introduction

The importance and significance of the use of reference quantitative characteristics of substances and chemical reactions (standard electrode potentials (SEP), Gibbs energy) [1–4] in various physical and chemical calculations are commonly accepted. The absence of certain data and characteristics in the reference literature makes it difficult and hinders not only the calculations and practical application of corrosion processes [5–7], durability of buildings and structures [5], but also the development of promising areas of chemistry, electrochemistry, and construction materials science [6].

The electrode reactions in aqueous solutions and SEP values are widely enough discussed in scientific, technical, and educational literature on electrochemistry [1, 2, 8–10]. It is known that electrode reactions are oxidation–reduction (redox) half-reactions occurring in the presence of electrodes [11–13]. Each oxidation–reduction half-reaction includes an oxidizer and a reducer (hereafter referred to as components), electrons, and it can also include water and its ions [14–16]. In redox half-reactions, the material and charge balances are observed. The nitrogen oxidation–reduction half-reactions were chosen due to several reasons. First, the array of these data is rather extensive; secondly, the oxidation–reduction half-reactions of the array are the basis for gas and redox electrodes [1, 13]. It should be noted that it is possible to calculate the standard electrode potentials of this array with a sufficiently high accuracy, up to the third decimal place [9, 10]. These circumstances indicate that the reference material on oxidation–reduction half-reactions of nitrogen is a necessary and sufficiently acceptable object for the application of a multistage technique of searching for consistent values that are verifiably consistent with each other. This is the aim of the study.

To achieve the set aim, the following tasks were solved:

- Analysis of the available reference data on oxidation–reduction half-reaction (ORHR) and SEP;
- Determination of the peculiarities of the ORHR components' behavior in an aqueous medium;
- Structuring of ORHR by selected components (oxidizer and reducer) by means of potential schemes (PD);
- Performing correlation of complete sets of three-member electrochemical cycles (ECC) for each PD.

2 Materials and Methods

The objects of the study are published reference data on nitrogen oxidation–reduction half-reaction and standard electrode potentials in corrosion processes of building materials, products and structures.

The methods of the study are analysis and comparison, correlation of SEP values, their structuring according to schemes for aqueous media ($\text{pH} = 0$) and ($\text{pH} = 14$); choice of paths and reference points.

3 Results and Discussion

Traditionally, electrode reactions are listed in order of increasing standard electrode potentials. It should be noted that the notations do not include the ORHR sequential number, do not specify the reaction medium, for example SEP $E^0(\text{pH} = 0)$ for the acid medium or SEP $E^0(\text{pH} = 14)$ for the alkaline medium [14]. This was taken into account during the compilation of the tables. The tables consist of three parts. The first part (Reference ORHR array) contains the data (Table 1) given in the reference literature (numbers from 1 to 58). The second part (Supplementation of ORHR array) contains the calculated data (Table 2) obtained from the reference data (8 names denoted by 32.1, 36.1 ... 49.1) and the third part (Addition of ORHR array) contains data (Table 3) obtained by completing the search.

The first 58 reference ORHRs (Table 1) with known SEP values contain 27 components. To ensure the reliability and accuracy of the results during the search for consistent SEP values, 12 components are excluded: $\text{HN}_3(r)$, HN_3aq , CNO^- , CN^- , N_3^- , HCNO , $\text{C}_2\text{N}_2(r)$, NOH , HCNaq , $(\text{SCN})_2$, SCN^- , $\text{NO}_2(r)$, which are part of the excluded ORHRs with sequential numbers 1, 2, 7, 9, 10, 11, 21, 26, 30, 31. Also excluded are complex ORHRs with sequential numbers 9 and 50, which include three components. The remaining 15 components are included in three or more ORHRs. It should be noted that these components behave preferentially with respect to the medium pH.

The first group of components (gases N_2O_4 , NO , N_2O , N_2) does not change composition when the solution pH changes. The second group of components (HNO_2aq , $\text{H}_2\text{N}_2\text{O}_2$, NH_3OH^+ , N_2H_5^+ , NH_4^+) is stable in the acid medium, but when alkalized, it changes, respectively, to NO_2^- , $\text{N}_2\text{O}_2^{2-}$, NH_2OH , N_2H_4 , NH_4OH . The third group of components (NO_2^- , $\text{N}_2\text{O}_2^{2-}$, NH_2OH , N_2H_4 , NH_4OH) is stable in the alkaline medium, and upon acidification these components change to HNO_2aq , $\text{H}_2\text{N}_2\text{O}_2$, NH_3OH^+ , N_2H_5^+ , NH_4^+ . The nature of the medium, in which the ORHR takes place, is determined by its composition. For example, if the ORHR has both components from the first group, the acid medium is characterized by the presence of H^+ (H_3O^+) ions on the left side of the ORHR, and the alkaline medium is characterized by the presence of OH^- ions on the right side of the ORHR. For other components of the third group, the nature of the medium is established by the

Table 1 ORHR reference data array

No.	ORHR	SEP, V			
		[3]	[2]	[4]	Consistent values
1	2	3	4	5	6
1	$3\text{N}_2(\text{r}) + 2\text{H}^+ + 2\text{e} = 2\text{HN}_3(\text{r})$	-3.40			
2	$3\text{N}_2(\text{r}) + 2\text{H}^+ + 2\text{e} = 2\text{HN}_3(\text{ng})$	-3.09	-3.09		
3	$\text{N}_2(\text{r}) + 4\text{H}_2\text{O} + 2\text{e} = 2\text{NH}_2\text{OH} + 2\text{OH}^-$	-3.04		-3.044	-3.044
4	$\text{N}_2(\text{r}) + 2\text{H}_2\text{O} + 4\text{H}^+ + 2\text{e} = 2\text{NH}_3\text{OH}^+$	-1.87		-1.87	-1.87
5	$\text{N}_2(\text{r}) + 4\text{H}_2\text{O} + 4\text{e} = \text{N}_2\text{H}_4 + 4\text{OH}^-$	-1.15		-1.157	-1.157
6	$\text{N}_2\text{O}(\text{r}) + 5\text{H}_2\text{O} + 4\text{e} = 2\text{NH}_2\text{OH} + 4\text{OH}^-$	-1.05		-1.05	-1.053
7	$\text{CNO}^- + \text{H}_2\text{O} + 2\text{e} = \text{CN}^- + 2\text{OH}^-$	-0.970			
8	$\text{N}_2 \text{O}_2^{2-} + 6\text{H}_2\text{O} + 4\text{e} = 2\text{NH}_2\text{OH} + 6\text{OH}^-$	-0.73		-0.73	-0.719
9	$\text{N}_3^- + 7\text{H}_2\text{O} + 6\text{e} = \text{N}_2\text{H}_4 + \text{NH}_3(\text{ng}) + 7\text{OH}^-$	-0.62			
10	$\text{HCNO} + \text{H}^+ + \text{e} = \text{C}_2\text{N}_2(\text{r}) + \text{H}_2\text{O}$	-0.330			
11	$\text{NO}(\text{r}) + \text{H}^+ + \text{e} = \text{NOH}$	-0.3			
12	$\text{NO}_3^- + 5\text{H}_2\text{O} + 6\text{e} = \text{NH}_2\text{OH} + 7\text{OH}^-$	-0.30		-0.30	-0.297
13	$\text{N}_2(\text{r}) + 5\text{H}^+ + 4\text{e} = \text{N}_2$	-0.23		-0.225	-0.225
14	$2\text{NO}_2^- + 2\text{H}_2\text{O} + 4\text{e} = \text{N}_2 \text{O}_2^{2-} + 4\text{OH}^-$	-0.180	-0.18	-0.180	-0.180
15	$\text{NO}_2^- + 6\text{H}_2\text{O} + 6\text{e} = \text{NH}_4\text{OH} + 7\text{OH}^-$	-0.15		-0.16 (3)	0.59 (6)
16	$\text{N}_2\text{O}(\text{r}) + \text{H}_2\text{O} + 6\text{H}^+ + 4\text{e} = 2 \text{NH}_3\text{O H}^+$	0.05		-0.05	-0.052
17	$\text{NO}_3^- + \text{H}_2\text{O} + 2\text{e} = \text{NO}_2^- + 2\text{OH}^-$	0.01	0.01	0.01	0.007
18	$2\text{NO}(\text{r}) + 2\text{e} = \text{N}_2 \text{O}_2^{2-}$	0.1		0.124	0.095
19	$\text{N}_2\text{H}_4 + 4\text{H}_2\text{O} + 2\text{e} = 2\text{NH}_4\text{OH} + 2\text{OH}^-$	0.11		0.11	0.11
20	$\text{N}_2(\text{r}) + 8\text{H}^+ + 6\text{e} = 2 \text{N}$	0.26		0.275	0.275
21	$\text{C}_2\text{N}_2 + 2\text{H}^+ + 2\text{e} = 2\text{HCN}(\text{ng})$	0.373			

(continued)

Table 1 (continued)

No.	ORHR	SEP, V			
		[3]	[2]	[4]	Consistent values
1	2	3	4	5	6
22	$\text{H}_2\text{N}_2\text{O}_2 + 6\text{H}^+ + 4\text{e} = 2\text{NH}_3\text{OH}^+$	0.387		0.387	0.387
23	$2\text{NO}_2^- + 4\text{H}_2\text{O} + 6\text{e} = \text{N}_2(\text{r}) + 8\text{OH}^-$	0.41		0.408	0.415(3)
24	$\text{NH}_2\text{OH} + 2\text{H}_2\text{O} + 2\text{e} = \text{NH}_4\text{OH} + 2\text{OH}^-$	0.42		0.42	0.42
25	$\text{HNO}_2\text{aq} + 5\text{H}^+ + 4\text{e} = \text{NH}_3\text{OH}^+ + \text{H}_2\text{O}$	0.62		0.62	0.6225
26	$\text{HN}_3\text{aq} + 11\text{H}^+ + 8\text{e} = 3\text{N}$	0.695			
27	$2\text{NO}(\text{r}) + 2\text{H}^+ + 2\text{e} = \text{H}_2\text{N}_2\text{O}_2$	0.712			0.713
28	$2\text{NH}_2\text{OH} + 2\text{e} = \text{N}_2\text{H}_4 + 2\text{OH}^-$	0.73			0.73
29	$\text{NO}_3^- + 8\text{H}^+ + 6\text{e} = \text{NH}_3\text{OH}^+ + 2\text{H}_2\text{O}$	0.73		0.721(6)	0.726(3)
30	$(\text{SCN})_2 + 2\text{e} = 2\text{SCN}^-$	0.77			
31	$\text{NO}_3^- + 2\text{H}^+ + \text{e} = \text{NO}_2(\text{r}) + \text{H}_2\text{O}$	0.80			
32	$2\text{NO}_3^- + 4\text{H}^+ + 2\text{e} = \text{N}_2\text{O}_4(\text{r}) + 2\text{H}_2\text{O}$	0.803	0.803	0.803	0.803
33	$2\text{NO}_3^- + 17\text{H}^+ + 14\text{e} = \text{N}_3 + 6\text{H}_2\text{O}$	0.84		0.821	0.826
34	$2\text{HNO}_2\text{aq} + 4\text{H}^+ + 4\text{e} = \text{H}_2\text{N}_2\text{O}_2 + 2\text{H}_2\text{O}$	0.86	0.86	0.853	0.858
35	$\text{NO}_3^- + 10\text{H}^+ + 8\text{e} = \text{N} + 3\text{H}_2\text{O}$	0.87		0.878	0.882
36	$\text{NO}_3^- + 4\text{H}^+ + 3\text{e} = \text{NO}(\text{r}) + 2\text{H}_2\text{O}$	0.96	0.957	0.94(6)	0.957
37	$\text{HNO}_2\text{aq} + \text{H}^+ + \text{e} = \text{NO}(\text{r}) + \text{H}_2\text{O}$	1.00	0.983	1.013	1.003
38	$\text{N}_2\text{O}_4(\text{r}) + 4\text{H}^+ + 4\text{e} = 2\text{NO}(\text{r}) + 2\text{H}_2\text{O}$	1.03	1.035	1.03	1.034
39	$\text{N}_2\text{O}_4(\text{r}) + 2\text{H}^+ + 2\text{e} = 2\text{HNO}_2\text{aq}$	1.07	1.065	1.047	1.065
40	$2\text{NO}_3^- + 12\text{H}^+ + 10\text{e} = \text{N}_2(\text{r}) + 6\text{H}_2\text{O}$	1.24		1.24	1.2456

(continued)

Table 1 (continued)

No.	ORHR	SEP, V			
		[3]	[2]	[4]	Consistent values
1	2	3	4	5	6
41	$N_2 + 3H^+ + 2e = 2 N$	1.275	1.275	1.275	1.275
42	$2HNO_2aq + 4H^+ + 4e = N_2O(r) + 3H_2O$	1.29	1.297	1.29	1.297
43	$NH_3OH^+ + 2H^+ + 2e = N + H_2O$	1.35		1.3475	1.3475
44	$N_2O_4(r) + 8H^+ + 8e = N_2(r) + 4H_2O$	1.35		1.349	1.356
45	$2NH_3OH^+ + H^+ + 2e = N_2 + 2H_2O$	1.42	1.42	1.42	1.42
46	$2HNO_2aq + 6H^+ + 6e = N_2(r) + 4H_2O$	1.44		1.45	1.45(3)
47	$2NO(r) + 2H^+ + 2e = N_2O(r) + H_2O$	1.59	1.591	1.59	1.591
48	$2NO(r) + 4H^+ + 4e = N_2(r) + 2H_2O$	1.68		1.68	1.6785
49	$N_2O(r) + 2H^+ + 2e = N_2(r) + H_2O$	1.77	1.766	1.77	1.766
50	$HN_3aq + 3H^+ + 2e = N + N_2(r)$	1.96			
51	$H_2N_2O_2 + 2H^+ + 2e = N_2(r) + 2H_2O$	2.65	2.65	2.644	2.644
52	$N_2(r) + 2H_2O + 6H^+ + 6e = 2NH_4OH$		0.092		
53	$N_2O_4(r) + 2e = 2 NO_2^-$		0.867		0.867
54	$2NO(r) + H_2O + 2e = N_2O(r) + 2OH^-$		0.76		0.763
56	$NO_2^- + N_2O + e = NO(r) + 2OH^-$		-0.46		- 0.455
57	$2NO_2^- + 3H_2O + 4e = N_2O(r) + 6OH^-$		0.15		0.154
58	$NO_3^- + 3H^+ + 2e = HNO_2aq + H_2O$		0.934		0.934
59	$N_2O(r) + H_2O + 2e = N_2(r) + 2OH^-$	0.942	0.938	0.942	0.938

Table 2 Supplementation of the reference array of nitrogen ORHR

No.	ORHR	SEP, V			
		[3]	[2]	[4]	Consistent values
1	2	3	4	5	6
32.1	$2\text{NO}_3^- + 2\text{H}_2\text{O} + 2\text{e} = \text{N}_2\text{O}_4(\text{r}) + 4\text{OH}^-$			-0.853	
36.1	$\text{NO}_3^- + 2\text{H}_2\text{O} + 3\text{e} = \text{NO}(\text{r}) + 4\text{OH}^-$			-0.147	
38.1	$\text{N}_2\text{O}_4(\text{r}) + 2\text{H}_2\text{O} + 4\text{e} = 2\text{NO}(\text{r}) + 4\text{OH}^-$			0.206	
40.1	$2\text{NO}_3^- + 6\text{H}_2\text{O} + 10\text{e} = \text{N}_2(\text{r}) + 12\text{OH}^-$			0.252	
44.1	$\text{N}_2\text{O}_4(\text{r}) + 4\text{H}_2\text{O} + 8\text{e} = \text{N}_2(\text{r}) + 8\text{OH}^-$			0.528	
47.1	$2\text{NO}(\text{r}) + \text{H}_2\text{O} + 2\text{e} = \text{N}_2\text{O}(\text{r}) + 2\text{OH}^-$			0.763	
48.1	$2\text{NO}(\text{r}) + 2\text{H}_2\text{O} + 4\text{e} = \text{N}_2(\text{r}) + 4\text{OH}^-$			0.8505	
49.1	$\text{N}_2\text{O}(\text{r}) + \text{H}_2\text{O} + 2\text{e} = \text{N}_2(\text{r}) + 2\text{OH}^-$			0.938	0.938

character of the stability of the component in the right part of the ORHR. When components are stable in the acid medium, their transformation occurs in the acid medium with a SEP value equal to $E^0(\text{pH} = 0)$, and in the alkaline medium with $\text{SEP} = E^0(\text{pH} = 14)$. For example, ORHR (18) occurs in the alkaline medium, and ORHR (4) in the acid medium.

It is known that the theoretical state of the gas hydrogen electrode in acid and alkaline aqueous solution can be described by the equation [13]:

$$E^0(\text{pH} = 0) = E^0(\text{pH} = 14) - \frac{RT}{F} \ln K \quad (1)$$

where: K is the electrolytic dissociation constant of water, acidity constant of water. As it is known [3], $E^0(\text{pH} = 0) = 0.000 \text{ V}$, $E^0(\text{pH} = 14) = -0.828 \text{ V}$, which is confirmed by calculations for standard conditions. Using theoretical calculations involved in the derivation of Eq. (1) for the hydrogen gas electrode in aqueous solutions, a generalized Eq. (1) was obtained in the form:

$$E^0(\text{pH} = 0) = E^0(\text{pH} = 14)0.828 \quad (2)$$

where n_1 and n_2 is the number of moles of $\text{H}^+(\text{H}_3\text{O}^+)$ ions and electrons in ORHR for the acid medium.

It should be noted that Eq. (2) satisfies two ORHRs of a chemical element: one with $\text{SEP} = E^0(\text{pH} = 0)$ for the acid medium, the other with $\text{SEP} = E^0(\text{pH} = 14)$ for the alkaline medium. The left side of the first ORHR should have $\text{H}^+(\text{H}_3\text{O}^+)$ components and electrons, the right side of the ORHR should have H_2O components. The left side of the other ORHR has H_2O and electrons, the right side has OH^- components.

Table 3 Addition of the reference array of nitrogen ORHR

No.	ORHR	SEP, V			
		[3]	[2]	[4]	Consistent values
1	2	3	4	5	6
59	$2 \text{ N } O_3^- + 4\text{H}_2\text{O} + 8\text{e} = \text{N}_2 O_2 + 8\text{OH}^-$				-0.0865
60	$\text{N}_2\text{O}(\text{r}) + 7\text{H}^+ + 6\text{e} = \text{N}_2 + \text{H}_2\text{O}$				0.438(6)
61	$\text{N}_2\text{O}(\text{r}) + 10\text{H}^+ + 8\text{e} = 2 \text{ N} + \text{H}_2\text{O}$				0.648
62	$\text{NO}(\text{r}) + 4\text{H}^+ + 3\text{e} = \text{NH}_3\text{OH}^+$				0.496
63	$2\text{NO}(\text{r}) + 9\text{H}^+ + 8\text{e} = \text{N}_2 + 2\text{H}_2\text{O}$				0.727
64	$\text{NO} + 6\text{H}^+ + 5\text{e} = \text{NH}_4^+ + \text{H}_2\text{O}$				0.8364
65	$2\text{HNO}_2\text{aq} + 11\text{H}^+ + 10\text{e} = \text{N}_2\text{H}_5^+ + 4\text{H}_2\text{O}$				0.782
66	$\text{HNO}_2\text{aq} + 7\text{H}^+ + 6\text{e} = \text{N} + 2\text{H}_2\text{O}$				0.864
67	$\text{N}_2\text{O}_4(\text{r}) + 6\text{H}^+ + 6\text{e} = \text{N}_2\text{O}(\text{r}) + 3\text{H}_2\text{O}$				1.219(6)
68	$\text{N}_2\text{O}_4(\text{r}) + 12\text{H}^+ + 10\text{e} = 2\text{NH}_3\text{OH}^+ + 2\text{H}_2\text{O}$				0.711
69	$\text{N}_2\text{O}_4(\text{r}) + 13\text{H}^+ + 12\text{e} = \text{N}_2 + 4\text{H}_2\text{O}$				0.829
70	$\text{N}_2\text{O}_4(\text{r}) + 16\text{H}^+ + 14\text{e} = 2 \text{ N} + 4\text{H}_2\text{O}$				0.893
71	$2\text{NO}_3^- + 10\text{H}^+ + 8\text{e} = \text{N}_2\text{O}(\text{r}) + 5\text{H}_2\text{O}$				1.1155
72	$\text{H}_2\text{N}_2\text{O}_2 + 7\text{H}^+ + 6\text{e} = \text{N}_2 + 2\text{H}_2\text{O}$				0.734(3)
73	$\text{H}_2\text{N}_2\text{O}_2 + 10\text{H}^+ + 8\text{e} = 2 \text{ N} + 2\text{H}_2\text{O}$				0.867
74	$\text{N}_2\text{O}_4(\text{r}) + 6\text{H}^+ + 6\text{e} = \text{H}_2\text{N}_2\text{O}_2 + 2\text{H}_2\text{O}$				0.927
75	$2\text{NO}_3^- + 10\text{H}^+ + 8\text{e} = \text{H}_2\text{N}_2\text{O}_2 + 4\text{H}_2\text{O}$				0.896
52	$\text{N}_2(\text{r}) + 8\text{H}_2\text{O} + 6\text{e} = 2\text{NH}_4\text{OH} + 6\text{OH}^-$				-0.734(6)
76	$\text{N}_2(\text{r}) + 4\text{H}_2\text{O} + 4\text{e} = \text{N}_2\text{H}_4 + 4\text{OH}^-$				-1.0573
77	$\text{N}_2(\text{r}) + 8\text{H}_2\text{O} + 6\text{e} = 2\text{NH}_4\text{OH} + 6\text{OH}^-$				-0.3165
78	$\text{NO}(\text{r}) + 3\text{H}_2\text{O} + 3\text{e} = \text{NH}_2\text{OH} + 3\text{OH}^-$				-0.447(6)
79	$2\text{NO}(\text{r}) + 6\text{H}_2\text{O} + 8\text{e} = \text{N}_2\text{H}_4 + 8\text{OH}^-$				-0.153
80	$\text{NO}(\text{r}) + 5\text{H}_2\text{O} + 5\text{e} = \text{NH}_4\text{OH} + 5\text{OH}^-$				-1.006
81	$\text{N } O_2^- + 4\text{H}_2\text{O} + 4\text{e} = \text{NH}_2\text{OH} + 5\text{OH}^-$				-0.4495
82	$2 \text{ N } O_2^- + 8\text{H}_2\text{O} + 10\text{e} = \text{N}_2\text{H}_3 + 12\text{OH}^-$				-0.2136
83	$\text{N}_2\text{O}_4(\text{r}) + 3\text{H}_2\text{O} + 6\text{e} = \text{N}_2\text{O}(\text{r}) + 6\text{OH}^-$				0.391(6)
84	$\text{N}_2\text{O}_4(\text{r}) + 8\text{H}_2\text{O} + 10\text{e} = 2\text{NH}_2\text{OH} + 10\text{OH}^-$				0.1863
85	$\text{N}_2\text{O}_4(\text{r}) + 8\text{H}_2\text{O} + 10\text{e} = \text{N}_2\text{H}_4 + 12\text{OH}^-$				-0.0335
86	$\text{N}_2\text{O}_4(\text{r}) + 12\text{H}_2\text{O} + 14\text{e} = 2\text{NH}_4\text{OH} + 14\text{OH}^-$				-0.013
87	$2 \text{ N } O_3^- + 5\text{H}_2\text{O} + 8\text{e} = \text{N}_2\text{O}(\text{r}) + 10\text{OH}^-$				0.0805

(continued)

The sequential numbers of the ORHRs are written under the line, and their SEP values are written above the line. Note that N_2O_4 , NO , N_2O , N_2 are gases. In the PDL pair for the acid medium component, N_2O is replaced by $H_2N_2O_2$; for the alkaline medium, N_2O is replaced by $N_2O_2^{2-}$.

At the second stage of the searching technique, each PDL was correlated with six schemes of three-member electrochemical cycles. Each three-member cycle was composed of two initial ORHRs (1) and an ORHR (2) having a common component resulting in an ORHR (3) lacking a common component. For example, in ORHR (1) the common component is a reducer, in ORHR (2) it is an oxidizer. In ECC, the material balance and charge balance are observed, and the condition is fulfilled which is written in the form of the equation [2]:

$$n_1 E^0(1) + n_2 \cdot E^0(2) = (n_1 + n_2) E^0(3) \quad (3)$$

where n_1 and n_2 are the number of moles of electrons at the charge balance at ORHR (1) and ORHR (2); $E^0(1)$, $E^0(2)$, $E^0(3)$ are SEP values.

The ECC notation is presented as one line: ECC sequential numbers; ORHR (3); ORHR (1); ORHR (2); and condition (3).

Since the structure of all PDLs is the same for the selected set of components, one of them (PDL1) was used to demonstrate the way of making schemes.

Assign sequential numbers 1,2...9 from right to left to the components of the PDL1 chain. These numbers were not shown in Figs. 1 and 2 to not overload the figure. They are needed to describe the algorithm for making the scheme. It is clear that the NO_3^- components in all PDLs have a sequential number 9. The N component for the acid medium and the NH_4OH component for the alkaline medium have sequential number 1. Equations (2) are written for two ORHRs of the chemical element, one with $SEP = E^0$ ($pH = 0$) for the acid medium and the other with $SEP = E^0$ ($pH = 14$) for the alkaline medium (as noted above).

Further the chain of four right components is connected with the third component to the first component at the top of the chain with a line, and the fourth component to the second and first components at the bottom of the chain. As a result, the calculation scheme is obtained (Fig. 3).

Scheme 1

This calculation scheme shows six ORHRs with sequential numbers (43, 4, 45, 41, 13, and 20) indicated below the lines, four ECCs. The sequential numbers **1,2,3** of the ECC cycles are indicated in the scheme, and the sequential number 4 of the cycle is not shown in the scheme.

ECC (1) contains three components NH_3OH^{+1} , N_2 , N. In it, ORHR (45) and ORHR (41), which have a common component N_2 (reducer in ORHR (45) and oxidizer in ORHR (41)) are used to form ORHR (43), which contains NH_3OH^{+1} (oxidizer) and N (reducer), and N_2 is missing.

Write these ECC(1-4):

$$1 - 43 \ 45 \ 41 \ 4 \ E^0(43) = 2E^0(45) + 2E^0(41)$$

$$2 - 13 \ 4 \ 45 \ 4 \ E^0(13) = 2E^0(4) + 2E^0(45)$$

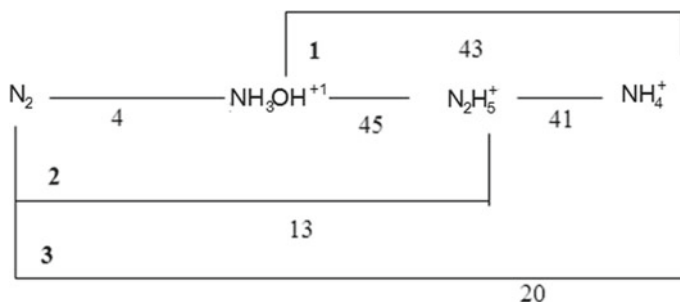


Fig. 3 The calculation scheme for the correlation of ORHR values: 1 (43, 45, 41); 2 (13,4, 45); 3 (20, 13, 41); 4 (20, 4, 43)

$$3 - 20 \ 13 \ 416 \ E^0(20) = 4E^0(13) + 2E^0(41)$$

$$4 - 20 \ 4 \ 436 \ E^0(20) = 2E^0(4) + 4E^0(43)$$

This notation of ECC (1–4) is a truncated form of scheme notation. Both scheme notations are equivalent, because the four columns of the truncated notation can be easily used to reconstruct the last column of the short entry.

The first column contains the sequential numbers of ECCs. The next three columns show the composition of the ECC. The third and fourth columns show the sequential numbers of the pairs of original ORHRs that have common components. Each pair forms an ORR the sequential number of which is given in the second column and which does not contain a common component.

Let us denote ECC (1) by ECC of upper tier, since besides chain lines it has a line above the chain. Let us denote ECC (2) and ECC (3) by ECC of lower tier, since besides chain lines they have lines below the chain. The common requirement is that all schemes must not have line crossings.

Similarly, the second calculation scheme is obtained (Scheme 2). The fifth component is added to the four connected components (Scheme 1) on the left side and then the ECC of the bottom tier of Scheme 1 is transferred without changes to the top tier of scheme 2 (Fig. 3) and the fifth component is connected with the third, second, and first components below the chain. So, nine lines are in the second scheme, with two lines being additional ORHRs with unknown SEP values. In addition, there are seven ECCs, five of which are new, numbered 5 to 9.

Scheme 2

The SEP calculation scheme (Fig. 4) also contains data on the ORHRs of the lower, upper, and adjacent tiers. The upper tier ORHRs (20,13,49,4,45,41,16) are ORHRs from the reference ORHR array (Table 2), and ORHRs (60,61) are from the supplemental reference nitrogen ORHR array (Table 3).

$$2. \ 13 \ 4 \ 45 \quad 7. \ 61 \ 60 \ 41$$

$$3. \ 20 \ 13 \ 41 \quad 8. \ 61 \ 13 \ 20$$

5. 1649 4 9. 60 49 13

6. 601645

It would have been sufficient to use the truncated form of the notation and to exclude condition (3), the last column. Conditions (3) for ECC [2] are omitted, i.e. a truncated form of the notation (without the last column) is given.

Similarly, supplementing and lengthening the chain with components up to the ninth, were obtained six schemes containing forty-nine different ECCs. It was found that each ORHR in the chain is included in seven ECCs and that each ECC contains one or two ORHRs from the chain.

Thus, as a result of the search for each of the media considered, the two PDLs were obtained, differing in one component, twelve schemes which contain 62 different ECC cycles.

At the third stage of the search for consistent values according to the tested method [4], analyzed were sixty-two ECCs for each medium, and also considered were ECCs in which ORHRs with known SEP values were collected. In cases when condition (3) [1] was fulfilled for some of them, ORHRs of such ECCs were designated as references, and their SEP values were considered as consistent and were transferred to other ECCs. In cases where this option of searching a reference point was depleted, then ORHRs from the chain, in which the SEP value was known up to the third decimal place, were assigned as reference points. If condition (3) was not satisfied in the ECC with three known SEP values, then, fixing two values, we found all triples of SEP values in which this condition was satisfied. The triples of SEP values found were compared with similar triples of other ECCs, and repetitive values were identified, thus determining the reference point, and so on. The results of the search for reliable values are presented in Table 3.

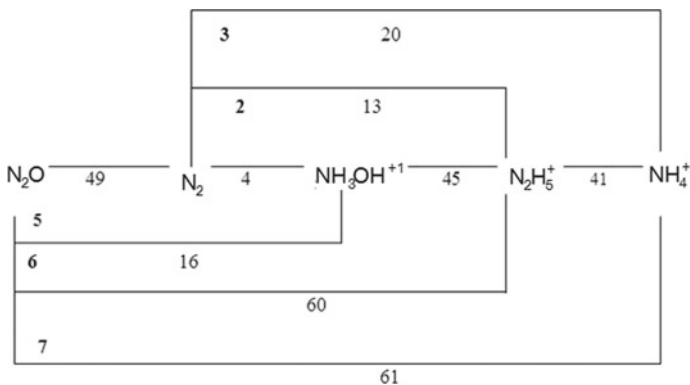


Fig. 4 The calculation scheme for the correlation of SEP values: 3 (20,13,41); 2 (13,4,45); 5 (16,49,4); 6 (16,60,45); 7 (61,60,41); 8 and 9 ECC are not denoted

It should be noted that if the ORHRs in the component chain have SEP consistent values, then the proposed method of scheme-making provides obtaining consistent SEP values for the full set of ORHRs on the selected set of components in the chain.

In addition, the available reference arrays of some chemical elements, particularly nitrogen, make it possible to supplement the basic (main) scheme proposed above to find consistent SEP values, for example, by using a joint analysis of fragments of different schemes. The fragments are part of linked ECC schemes. Forty-nine ECCs are consistent to each PDL as part of six schemes. The search for consistent SEP values is demonstrated on the example of PDL 1 (the acid medium; $N_2O_{(f)}$). It has the greatest number of ORHR reference data (Table 1), all SEP values are known up to the third decimal place. The forty-nine ECCs contain both reference ORHRs with known SEP values, ORHRs from the supplement (Table 2) with our calculated SEP values (for the alkaline medium; for PDL 3 and PDL 4), and additional ORHRs with unknown SEP values (Table 3).

For example, for PDL 1, only three reference ORHRs with known SEP values of the seventeen ECCs were found, two were found in the nineteen ECCs, and one was found in the thirteen ECCs. Taking these initial data into account, the search was started with the first seventeen ECCs, in which we checked that condition (3) is satisfied. It was found that it is directly fulfilled in ECCs with sequential numbers 2, 3 (Scheme 1 and 2) and 37 (Scheme 6).

2	13	4	45	$4E^0(13) = 2E^0(4)2E^0(45)$
3	20	13	41	$6E^0(20) = 4E^0(13) + 2E^0(41)$
37	57	32	39	$4E^0(57) = 2E^0(32) + 2E^0(39)$

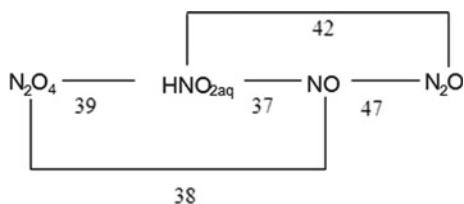
$E^0(13) = -0.225$	$E^0(4) = -1.87$	$E^0(45) = 1.42$
$E^0(20) = 0.275$	$E^0(41) = 1.275$	
$E^0(57) = 0.934$	$E^0(32) = 0.803$	$E^0(39) = 1.065$

Let us denote ORHRs with the sequential numbers listed above as the reference ones. Let us consider SEP values as consistent and transferable to other ECCs. SEP (32) is fixed in ECC with numbers 37, 44, 45, 46, 47, 48, 49; SEP (39) is fixed in ECC with numbers 37, 26, 32, 33, 34, 35, 36; SEP (57) is fixed in ECC with numbers 37 and 38. Assign ORHR (36) with $E^0(36) = 0.9577$ as a reference point. ORHR (37) with the value of $E^0(37)$ is determined in ECC (38) and ORHR (38) with the value of SEP (38) is determined in ECC (26). SEP (37) is fixed in seven ECCs. The next one in the chain of components ORHR (47) with $E^0(47) = 1.591$ is chosen as the reference point and the search is continued for consistent SEP values.

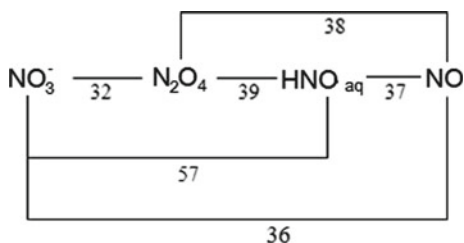
Let us recall that the SEP values of the reference points must be known to the third decimal place. Note that besides the basic (main) paths for the choice of references from the chain of components, other paths can also be quite effective. For example, when searching for $E^0(38)$ and $E^0(37)$ values, the joint consideration of fragments

of two schemes (schemes 5 and 6) proved to be effective, with ORHR (39), ORHR (42) and ORHR (47) and the values $E^0(39) = 1.065$; $E^0(42) = 1.297$; $E^0(47) = 1.591$; and with reference points ORHR (32), ORHR (39), ORHR (37), ORHR (36) and $E^0(32) = 0.803$; $E^0(39) = 1.065$; $E^0(57) = 0.934$; $E^0(37) = 0.957$.

A fragment of scheme 5 is shown below.



A fragment of scheme 6 is shown below.



It is necessary to pay attention to the fact that in the considered fragments ORHR the values of SEP set to the third sign after the decimal place are consistent, and ORHR (39) and ORHR (37) are included in both fragments.

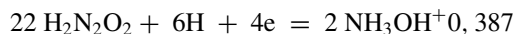
$$\text{Determine: } E^0(38) = 1.034 \neq 1.035$$

$$E^0(37) = 1.003 \neq 0.983.$$

Note that the correctness of the methodology is indirectly confirmed by the fact that three SEP reference values are agreed (as a rule) in ECC, each of which is known to the third decimal place.

It is reasonable to keep the ordinal ECC numbers when switching from the schemes for PDL 1 to the schemes for PDL 2, PDL 3, and PDL 4. The pair PDL 1 and PDL 2 for the acid medium and the pair PDL 3 and PDL 4 for the alkaline medium differ in one component, so 36 ECCs are repeated in the schemes for each medium. So there will be 62 different ECCs for each medium.

Turning from the schemes for PDL 1 to the schemes for PDL 2, the set of reference points for PDL 1 is added by the reference point



Reference ORHRs and additional ORHRs were involved when considering Supplements to the acid medium. For the alkaline medium, the role of the ORHR of supplements is great.

Out of 49 ECCs consistent with PDL 3, condition (3) is fulfilled in three ECCs.

1	24	28	13	$4E^0(24) = 2E^0(28) + 2E^0(13)$
10	48.1	47.1	49.1	$4E^0(48.1) = 2E^0(47.1) + 2E^0(49.1)$
49	36.1	32.1	38.1	$6E^0(36.1) = 2E^0(32.1) + 4E^0(38.1)$

$E^0(24) = 0.42$	$E^0(28) = 0.78$	$E^0(19) = 0.11$
$E^0(48.1) = 0.8505$	$E^0(47.1) = 0.763$	$E^0(49.1) = 0.938$
$E^0(36.1) = -0.147$	$E^0(32.1) = -0.853$	$E^0(38.1) = 0.206$

Reference ORHRs with sequential numbers 24, 28, 19, 48.1, 47.1, 49.1, 36.1, 32.1, 38.1 are presented above. The search for consistent SEPs for the alkaline medium is performed by the same paths as for the acid medium.

4 Conclusions

1. The reliability and efficiency of the developed algorithm for searching consistent SEP values for an extended array of reference data on nitrogen reactions has been confirmed. It is highly relevant both for scientific research in electrochemistry, physical chemistry, and in practical activities related to corrosion processes of materials and structures.
2. It is shown that application of the derived generalized Eq. (2) makes it possible not only to supplement the array of reference data but also to search for SEP values equally for both alkaline and acid media.
3. It is established that the correct selection of reference points is important in the process of search of values, as they are used for checking the correctness of the chosen path.

References

1. Zoski, S. (ed.) Handbook of Electrochemistry, p. 937. Elsevier (2006)
2. Younis, A., Chu, D., Li, S.: Handbook of manufacturing engineering and technology. In: Electrochemical Processes in Manufacturing, pp 2851–2889 (2014)
3. Ravdel, A., Ponamareva, A. (eds.): Handbook of Physico-Chemical Quantities, p. 232. St. Petersburg (1999)
4. V.N. Kazin, E.M. Pliss, A.I. Rusakov. Physical chemistry. Publishing house “Yurait”. Moscow, 2020, 182 p.
5. Al-Sherrawi, M.H., Lyashenko, V., Edaan, E.M., Sotnik, S.: Corrosion as a source of destruction in construction. *Int. J. Civil Eng. Technol.* **9**(5), 308–314 (2018)
6. Ueli, M.: Angst challenges and opportunities in corropsion of steel in concrete. *Mater. Struct.* **51**, 4 (2018)
7. Glass, G.K., Roberts, A.C., Davidson, N.: Hybrid corrosion protection of chloride-contaminated concrete. *Constr. Mater.* **161**, 163–172 (2008)
8. Berdnikov, V.I., Zhitar, S.V.: Testing of standard electrode potentials for aqueous solutions: methodology and testing results. The monograph. Cheboksary, p. 179. Volga Branch of MADI (2012)
9. Berdnikov, V.I., Stroganov, V.F., Stroganov, I.V., Soldatova, V.A.: *Bull. Technol. Univ.* **19**(22), 22–25 (2014)
10. Berdnikov, V.I., Stroganov, V.F., Soldatova, V.A., Stroganov, I.V.: *Bull. Technol. Univ.* **21**(248), 5–10 (2018)
11. Morozov, I.V., Boltalin, A.I., Karpova, E.V.: Oxidizing-reduction processes. Textbook. Publishing house of the Moscow University, p. 79 (2003)
12. Beiser, M., Lund, H. (eds.): Organic Electrochemistry, p. 469. Khimiya, Moscow (1988)
13. Rotinyan, A.L., Tikhonov, K.N., Shoshina, I.A.: Theoretical Electrochemistry, p 424. Khimiya, Leningrad (1981)
14. Sorokina, O.V., Zykova, E.S.: Modern forms of presentation oxidation-reducion processes by diagrms of Latimer, Frost, Purbe. *Fine Chem. Technol.* **1**(3), 50–55 (2006)
15. Dutton, K.G., Lipke, M.C.: Correcting frost scheme misconceptions using interactive frost schemes. *J. Chem. Educ.* **98**(8), 2578–2583 (2021)
16. Koleva, D.A., Hu, J., Fraaij, A.L.A.: Durable building technology benefiting electrochemical methods as a preventive. *Trans. Eng. Sci.* **48**, 87–98 (2005)

Author Index

A

Abdrakhmanova, Lyaylya, [191](#), [201](#)
Akhmetov, Marat, [437](#)
Alekseev, Sergey, [353](#)
Amel'chenko, Maxim, [155](#)
Antakov, Alexey, [381](#)
Antakov, Igor, [381](#)
Aripov, Daler, [363](#)
Averchenko, Gleb, [353](#)
Aysin, Niyaz, [99](#)

B

Barysheva, Alina, [227](#)
Barysheva, Olga, [227](#)
Belayeva, Kamilya, [321](#)
Berdnikov, Vladimir, [465](#)
Bezmenov, Vladimir, [149](#)
Biktemirova, Ella, [263](#)
Bogdanov, Andrey, [285](#)
Bulanov, Pavel, [125](#), [405](#)

E

Erohin, Dmitriy, [245](#)

F

Fattakhov, Irik, [209](#), [311](#)

G

Galautdinov, Albert, [415](#)
Galiev, Ilyas, [219](#)
Galliulun, Rinat, [371](#)
Galyamichev, Alexander, [43](#)

Garipov, Aidar, [273](#)
Gasilov, Viktor, [465](#)
Gilmanshina, Alsu, [333](#)
Giniyatova, Kamilya, [255](#)
Grebenyuk, Egor, [449](#)
Grishin, Iliya, [245](#)
Grishin, Ilya, [321](#)

I

Iangirov, Farit, [311](#)
Ibragimov, Ruslan, [219](#)
Ibragimova, Aigul, [299](#)
Ilgamovich, Garaev Almaz, [109](#)
Islamov, Anvar, [191](#)
Ismailov, Aleksei, [15](#), [353](#), [449](#)

J

Juravlev, Igor, [405](#)

K

Kadyrov, Rail, [425](#)
Kareeva, Julia, [209](#)
Kareeva, Juliya, [311](#), [343](#)
Karimullin, Timur, [65](#)
Kayumov, Rashit, [321](#)
Khaliullin, Marat, [333](#)
Khanekov, Arslan, [363](#)
Khantimirov, Ayaz, [201](#)
Khozin, Vadim, [201](#), [273](#)
Khuziakhmetova, Karina, [191](#)
Kochetkov, Alexander, [209](#)
Konovalov, Nikita, [169](#)
Kraynov, Dmitriy, [299](#)

L

Lazarev, Yuriy, [449](#)
Logachev, Konstantin, [65](#)

M

Makarov, Dmitry, [273](#)
Martynov, Pavel, [263](#)
Mavliev, Lenar, [125](#), [405](#)
Medvedeva, Galina, [255](#), [299](#)
Minikaeva, Kamilla, [255](#)
Mirsayapov, Ilizar, [1](#), [31](#), [73](#), [99](#), [135](#)
Mirsayapov, Ilshat, [381](#)
Mukhametrakhimov, Rustem, [83](#), [415](#), [425](#)
Mukharryamov, Irshat, [353](#)

N

Narsova, Kseniya, [343](#)
Nigmatov, Gennadiy, [371](#)
Nigmatov, Temir, [371](#)
Nizamov, Rashit, [191](#), [201](#)
Novik, Anatoly, [15](#)

O

Ogurtsov, Gleb, [353](#), [449](#)

P

Palagin, Nikolai, [437](#)

R

Romanova, Anna, [263](#)

S

Sadykov, Renat, [299](#)
Safin, Kamil, [149](#)

Safullin, Rinat, [181](#)
Salakhutdinov, Marat, [363](#)
Savinov, Andrey, [371](#)
Semanov, Alexander, [311](#)
Semanova, Aigul, [311](#)
Sentsov, Igor, [15](#)
Shagiakhmetova, Elvira, [263](#)
Sibgatullin, Nazir, [181](#)
Smirnov, Denis, [321](#)
Statsenko, Evgeny, [425](#)
Stepanov, Sergey, [149](#), [273](#), [285](#)
Stroganov, Ilya, [465](#)
Stroganov, Victor, [125](#), [155](#), [169](#), [405](#), [465](#)
Suleymanov, Alfred, [321](#)

T

Tabaeva, Radmilla, [155](#)
Talgatovich, Mirsayapov Ilizar, [109](#)
Talipova, Liliia, [449](#)

V

Vdovin, Evgenii, [125](#), [155](#), [169](#), [405](#), [465](#)

Y

Yagfarov, Emil, [65](#)
Yusupova, Alsu, [255](#)

Z

Zanina, Anna, [353](#)
Zigangirova, Leysan, [219](#)
Ziganshin, Arslan, [65](#), [343](#)
Ziganshina, Liliya, [83](#), [425](#)
Zinnurov, Tagir, [245](#)
Zolotonosov, Yakov, [263](#)